THE FRACTURE TOUGHNESS OF LOW CARBON STEELS;

THE EFFECTS OF GRAIN SIZE AND TEMPERATURE

A thesis
submitted in fulfilment
of the requirements for the Degree
of
Doctor of Philosophy
in
Mechanical Engineering
in the
University of Canterbury

by

M.C. Tunnicliffe

University of Canterbury,
Christchurch, New Zealand.

1991

To my parents,
for the faith they have in their children
and the love they show them.

ABSTRACT

For materials that exhibit a fracture mode transition as temperature is lowered one of the important criteria for material performance is the material's fracture mode transition temperature and not necessarily the specific fracture toughness at any temperature. Therefore, it is important to establish whether operating conditions place a structure below the selected material's transition temperature or that a material is selected with a transition below that of the structure's operating conditions.

Quantitative design processes, based on linear elastic (K_{IC}) and elastic-plastic (CTOD) fracture mechanics using experimental fracture toughness data, allow the design of safer structures. In recent years standard procedures have been adopted for K_{IC} and CTOD testing. Using the traditional Charpy V-notch impact test, detailed information on the effects of composition and grain size on the fracture mode transition temperature are known. The fracture mode transition temperature is not as equally well understood in CTOD or K_{IC} testing, especially for low carbon steels.

The CTOD and Charpy impact tests have been used to determine the grain size dependence of the fracture mode transition temperature for two low carbon (structural) steels, one of low active nitrogen content and one of high active nitrogen content. Both the CTOD and Charpy tests show a fracture mode transition over a narrow temperature range. It was established from theoretical derivation and experimental observation that there is a linear dependence of the transition temperature T_c on the reciprocal square root of grain size ($d^{-1/2}$) for both the CTOD and Charpy tests i.e. $T_c = B_0 + B_1 d^{-1/2}$ where B_0 and B_1 are constants. When the results of the CTOD and Charpy tests are compared the magnitude of B_1 is significantly different for each test. It was concluded that the difference in B_1 between the two tests is due to the different strain rates of the tests and that the strain rate significantly affects the local yield stress around the crack tip or notch.

Micromechanical modelling of fracture toughness predicted a variation in transition temperature with variation of grain size but this did not show a linear dependence on $d^{-1/2}$. The predicted

transition temperature was a lower bound of the range in transition temperature.

The observed decrease in transition temperature with grain refinement when using the CTOD test is explained by the increase in crack initiation and crack propagation energy necessary to overcome grain boundary resistance to fracture. For example, at the fracture mode transition temperature for the low nitrogen steel, the proportion of energy required to overcome grain boundary resistance to fracture increased from 39% at $d^{-1/2}$ = 4.218 $mm^{-1/2}$ to 55% at $d^{-1/2}$ = 9.939 $mm^{-1/2}$ of the total critical energy released. Also, it is thought that grain refinement means a lower critical crack-tip strain is needed for transition.

Correlations between Charpy Impact Energy (C_v) and CTOD (δ_c) or K_{IC} suggested a suitable relationship was δ_c (or K_{IC}) = $D(C_v)^n$. The constants D and n were independent of grain size but were composition dependent. The temperature shift showed a grain size dependence, given as $\Delta T = \Delta B_0 + \Delta B_1 d^{-1/2}$ for the data available.

The CTOD measured from Clip Gauge Displacement was determined to be grain size and composition dependent. From a technique using silicone-rubber replicas of the crack tip the CTOD was found to be a function clip gauge displacement (V_g) and grain size (d), namely, $\delta_t = 0.121113\ V_g + 0.034222\ V_g^2 d^{1/2}$, for the compact tension specimens tested.

For toughness calculations and determining the fracture mode transition the temperature and grain size dependence of the steels' yield stress (at constant strain rate) was determined. Using the Hall-Petch equation ($\sigma_{ys} = \sigma_i + k_y d^{-1/2}$), a suitable model was found to be $\sigma_{ys} = A_1 + A_2T + A_3T^2 + A_4T^3 + k_y d^{-1/2}$ where the constants A_1, A_2, A_3, A_4 and k_y were determined by multiple-linear regression analysis from experimental data over the temperature range -196 to +65°C.

ACKNOWLEDGEMENTS

To complete a project, such as the one presented in this thesis, requires the help and support of many people. The support, advice and encouragement received by me during the course of this project has been wonderful. I would like to thank:

Professor L.A. Erasmus for his supervision and knowledge. Words, alone, cannot express the deep gratitude felt for his advice, encouragement and humour brought to this project.

Dr. J.S. Smaill, my co-supervisor, for his invaluable advice and time, and for helping me see the answers.

My family, whose continued interest, support and encouragement throughout my education have kept me going.

Also, I would like to thank:

Professor H. McCallion, Head of the Mechanical Engineering Department, for the use of the facilities for this project.

The technical staff of the Department of Mechanical Engineering who have provided assistance and support during the course of this project; particularly, the late **Mr. P. O'Hagan** but also **Messrs. H.A. Mobbs**, **D.K. Healy** and **M.J. Flaws** of the Materials Laboratory, **Messrs. O. Bolt** and **K. Brown** of the workshop for specimen preparation, and **Mr. H.J. Anink** for keeping machines running.

To **Diane Sanders** of the Chemistry Department, many thanks for her patient and meticulous typing of this long thesis. It has been very much appreciated.

This project was assisted by financial grants provided in the form of the **New Zealand Steel Research Scholarship**, the **Todd Motors Research Scholarship**. Also, the **Kippenberger Memorial Fellowship** was provided by the **New Zealand Returned Services' Association**. These are gratefully acknowledged.

Finally, to **my friends and fellow postgraduates,** many thanks for making a Ph.D. not so lonely.

CONTENTS

LIST OF FIGURES

LIST OF TABLES

NOMENCLATURE

Symbol	Description
a	Flaw size (Crack length)
a_0	Length of crack to tip of fatigue crack
a_p	Physical crack length
B	Thickness of fracture toughness specimen
b	Burger's vector
b_0	(i) Equilibrium atomic spacing (ii) Length of uncracked ligament of toughness specimen (= W - a_0)
C_o	Carbide Thickness
COD	Crack Opening Displacement
CTOD	Crack-Tip Opening Displacement
CTODi	CTOD at initiation of stable crack extension
D	Solute diffusion coefficient
d	Grain size
d_g	Grain diameter
D_{pin}	Load-Pin displacement
E	Young's modulus of elasticity
E_K	Energy of a single kink.

F	External work performed on cracked plate
f(a/W), $f(a_o/W)$	Compliance function
FMTT	Fracture Mode Transition Temperature
G	(i) Energy release rate (ii) Shear Modulus of Elasticity
G_c	Critical energy release rate
G_{IC}	Plane strain critical energy release rate
H	Activation energy
H_K	Activation energy of a single kink
H_o	Activation energy at ambient temperature
J	J-integral
J_c	Critical J-integral
J_{IC}	Plane strain J-integral
K	Stress Intensity Factor
K_c	(i) Plane Stress critical stress intensity factor (ii) Experimental fracture toughness
K_f	Fatigue Stress Intensity Factor
K_I	Mode I opening stress intensity.
K_{IC}	Plane strain critical stress intensity factor
K_i	Stress intensity factor at initiation of stable crack extension

K_o	Stress intensity factor at point of critical crack extension
K_{plat}	Plateau level of K_R curve
K_Q	Apparent fracture toughness
k_F	Slope of "fracture stress - $d^{-1/2}$" relationship
k_F'	Slope of "fracture stress - $d^{-1/4}$" relationship
k_y	Slope of the Hall-Petch relationship
k_y^s	Slope of the shear Hall-Petch relationship
k_ε	Slope of the "flow stress - $d^{-1/2}$" relationship
L	Length of slip band
L_f	Length of ferrite fraction for linear intercept method
L_p	Length of pearlite fraction for linear intercept method
L_i	Total length of linear intercept lines
m, M	Plastic stress intensification factor.
M	Net elastic response of the test specimen, grips and test machine
m^*	Temperature dependent material characteristic
N	Ramberg-Osgood strain-hardening index
n	(i) Holloman strain-hardening index (ii) Number of dislocations

$N.a$	Maximum displacement of crack faces
N_f	Number of intercepts for linear intercept method
n_s	Number of sites for loop formation
$\dot{n}$	Rate of loop formation
P	Applied load
P_c	Critical load
P_f	Fatigue load
P_{max}	Maximum applied load
P_Q	Load at instability
$P_{0.5}$	Load found from 5% secant line
q	Macroscopic work-hardening coefficient
R	Fracture toughness
r	(i) Distance from crack tip (ii) Distance between blocked slip-line and locked dislocation sources
r_{CH}	Plastic rotation factor for crosshead displacement measurement of CTOD
r_p	Plastic rotation factor
r_y	Radius of plane stress plastic zone
s	Slot width
s_c	Critical slot width

SZW	Stretch zone width
$\dot{s}$	Average velocity of dislocations
T	(i) Temperature (ii) Ageing Temperature
t	(i) time (ii) Ageing time at temperature T
T_A, T_r	Ambient temperature
T_c	Transition temperature
$T(K_i)$	Transition temperature for K_i criterion
t_r	Ageing time at ambient temperature T_r
T_{mat}	Material tearing modulus
T_{app}	Applied tearing modulus
T	Traction vector
T_{27}	27 Joule Charpy transition temperature
$T(\delta_{0.10})$	0.10 mm CTOD transition temperature
$T(\delta_{0.15})$	0.15 mm CTOD transition temperature
u	Displacement vector
u	Displacement in the x direction
U	(i) Activation Energy (ii) Total energy of a plate
U_a	Change in elastic energy caused by introducing crack into a body

U_c	Energy of a cracked specimen
U_e	Elastic energy of a specimen
U_{nc}	Energy of an uncracked specimen
U_o	Energy of a loaded, uncracked plate
U_p	(i) Plastic energy of specimen (ii) Potential energy
U_t	Total energy of specimen
U_γ	Change in elastic surface energy caused by the formation of two new crack surfaces
v	(i) Displacement in y direction (ii) Dislocation velocity
v^*	Activation volume
V_{CH}	Crosshead Displacement
V_e	Elastic component of clip gauge displacement
V_g, V_t	Total clip gauge displacement
V_p	Plastic component of clip gauge displacement
W	(i) Width of fracture toughness specimen (ii) Total strain energy density
W_o	Athermal component of W_p
W_p	Plastic work for crack propagation
X_o	Characteristic distance of cleavage fracture
Y	Compliance function

z	Height of knife edges above surface of SENB specimen or from load-line of CT specimen
β	(i) Stress state (ii) Amplitude of stress singularity at crack tip
Γ	Contour anti-clockwise from lower to the upper crack face
γ	Effective surface energy of matrix
γ_e	Elastic surface energy
γ_p	(i) Plastic strain work (ii) Effective surface energy of ferrite matrix
$\dot{\gamma}$	Shear strain rate
Δ	Load-point displacement
δ, δ_t	Crack-Tip Opening Displacement
δ_c	Critical CTOD
δ_e	Elastic component of CTOD
δ_i	CTOD at initiation of stable crack extension
δ_m	CTOD at maximum load
δ_p	Plastic component of CTOD
δ_u	CTOD at "pop-in"
ε	(i) Critical break-away strain (ii) True strain
ε_f	Uniaxial tensile fracture strain

ε_{fi}	Critical crack-tip strain (Notched ductility)
ε_n	Critical macroscopic strain
$\bar{\varepsilon}_p$	Plastic strain at crack tip
ε_x	Strain in x direction
$\dot{\varepsilon}$	Strain rate
$\dot{\varepsilon}_e$	Elastic strain rate
$\dot{\varepsilon}_p$	Plastic strain rate
θ	Angle of element from crack tip
λ	(i) Wavelength (ii) Width of plastic zone at crack tip
μ	Shear modulus of elasticity
ν	(i) Poisson's ratio (ii) Frequency factor
ρ	Dislocation density
ρ_o	Average density of unlocked dislocations
σ, σ_{app}	Applied stress
σ_A	Yield stress at ambient temperature
$\bar{\sigma}$	Equivalent stress
σ_c	(i) Critical applied stress (ii) Creation stress for creation of mobile dislocations
σ_f, σ_o	Flow Stress

σ_F	Cleavage fracture stress
σ_i	Friction stress
σ_i^*	Thermal component of friction stress
$\sigma_i(st)$	Athermal component of friction stress
σ_{iF}	Friction stress at fracture
$\sigma_L(a/W)$	Plastic collapse stress
σ_m	Mean stress
σ_{max}	Maximum stress
σ_p^*	Peierls-Nabarro stress
σ_u, σ_{uts}	Ultimate tensile stress
σ_{uy}	Upper yield stress
σ_{ys}, σ_{ly}	Lower yield stress
σ_x	Stress in x direction
σ_y	Stress in y direction
σ_{yy}	Local tensile stress
σ_{0K}	Yield stress at 0 K.
τ_{app}	Applied shear stress
τ_{eff}	Effective shear stress
τ_i	Shear friction stress
τ_p	Shear Peierl's stress

τ_{ys}	Shear yield stress
τ_{xy}	Shear stress in the XY plane
Φ	Dimensionless CTOD
ϕ	Diameter

CHAPTER 1

Introduction

"The fault that leaves six thousand ton a log upon the sea"
- Rudyard Kipling, "McAndrew's Hymn" (1893)

1.1 Scope of the Thesis

Developments in the understanding of fracture fundamentals and of materials testing procedures in the past forty years have considerably reduced the risk of catastrophic fracture in steel structures and pressure vessels. A number of factors have influenced the development of fracture mechanics. The advent of the "all-welded" Liberty ships and T-2 tankers of World War II led to a new era of accidents. Of 4694 Liberty ships constructed in the U.S.A. 1289 structural failures were reported, 233 being catastrophic and the vessels were either lost or considered unsafe [1]. These predominantly brittle failures led to a concentrated research effort on the problem of brittle fracture in low carbon steel plate [2]. The solution was to select steels of a low fracture mode transition temperature, eliminate stress concentrations in the design and to use improved welding procedures.

The increased use of high strength materials for structural applications requires a more sophisticated design approach since although the high strength materials are not intrinsically brittle the energy for fracture is low (shown schematically in Figure 1.1). This is particularly important in the aerospace industry where the minimum weight-strength ratio is used. One of the first applications of fracture mechanics was the introduction of stringent criteria for damage tolerance by the United States' Air Force after failure of a F-111A military aircraft in 1969 [3].

There are three main factors which will contribute to the change from ductile to brittle fracture in any one steel; a triaxial state of stress, low temperatures and a high strain rate. Low and medium carbon steels (typically structural and pressure vessel steels) show a fracture mode transition as the test temperature is lowered (shown schematically in Figure 1.1). This occurs over a narrow temperature

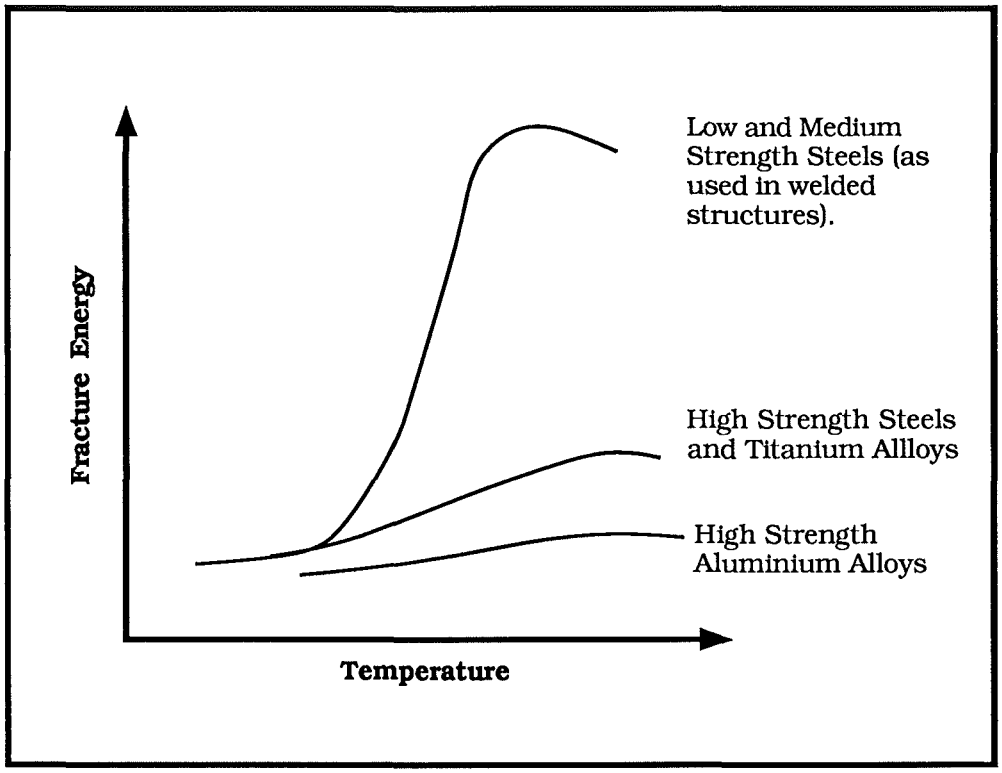

Figure 1.1 : Schematic of the general effect of temperature on the fracture resistance of structural steels.

range. At temperatures above the fracture mode transition temperature (FMTT) failure is ductile by microvoid coalescence and below the FMTT fracture is predominantly brittle by cleavage. Since fracture toughness above the transition temperature is an order of magnitude greater than it is below the transition temperature it is only economically viable to design for fracture toughness values obtained above the transition temperature [4].

It would appear that one of the most important performance criteria for fracture resistance in structural and pressure vessel grade steels is the fracture mode transition temperature. The transition temperature is a function of grain size, the composition of the material (which affects the Peierls-Nabarro stress and the strength of dislocation locking), stress state and strain rate. Detailed information on the variation of the Charpy V-notch Impact test transition temperature resulting from changes in chemical composition and grain size is available [5-15]. The transition temperature found by plane-strain fracture toughness testing or the crack-tip opening displacement (CTOD) test is not as equally well understood.

For selected structural grade steels it is the purpose of this thesis to:

(i) investigate the variation in fracture mode transition temperature due to variation of grain size when using the CTOD test applied to structural grade steels.

(ii) compare the grain size dependence of the FMTT between the CTOD test and the Charpy V-notch impact test. Previous investigation of the FMTT using the CTOD test has shown that strain-age embrittlement of the plastic zone ahead of the fatigue crack used in specimens for CTOD testing causes an increase in the FMTT of about 10°C [16]. However the FMTT found by the CTOD test was between 33 and 56°C lower than the 27 Joule transition temperature given by the Charpy V-notch impact test. This was despite an approximate 30°C increase in transition temperature that would be expected by using a fatigue crack instead of the standard notch in the Charpy test [17]. Strain rate, therefore, has a large effect on the fracture mode transition temperature.

(iii) attempt some correlation between the CTOD test and Charpy V-notch impact test when some variation in grain size is included.

(iv) investigate the temperature and grain size dependence of the lower yield stress since the lower yield stress is used in toughness calculations.

(v) establish the region of overlap at low temperatures between toughness results given by linear elastic fracture mechanics (plane-strain fracture toughness testing) and elastic-plastic fracture mechanics (CTOD testing).

(vi) to distinguish whether there is any influence on the energy required for crack initiation and crack propagation due to the variation in grain size. It has been suggested that CTOD or plane-strain fracture toughness tests measure only the energy required for crack propagation because these tests use a sharp fatigue crack whereas the Charpy V-notch impact test measures the energy required to initiate and propagate a crack from a blunt notch [17]. Therefore, by varying the size of the plastic zone ahead of the crack tip in the CTOD test and varying the degree of ageing in the plastic zone (by varying nitrogen content) progress could be made towards differentiating between the energy required for crack initiation and crack propagation [4].

The selected method of fracture toughness testing should be able to focus on the problem area, namely the crack tip, using economic and realistic specimens. For this purpose the CTOD test is the most attractive and because the testing methods for critical CTOD and plane-strain fracture toughness K_{IC} are similar then at low temperatures valid K_{IC} values may be found.

1.2 The Development of Fracture Mechanics

The concept of flaw tolerance was predicted by Griffith in 1920 on experiments with glass and glass fibres [18]. From analysis of a plate with an introduced elliptical crack in it Griffith showed that crack propagation would occur if an overall reduction in energy occurred. The critical stress σ_c for instability was given by

$$\pi\sigma_c^2 a/E' = 2\gamma_e \qquad (1.1)$$

where γ_e is the elastic surface energy, $E' = E$ for plane stress and $E' = E/(1-\nu^2)$ for plane strain, and where ν is Poisson's ratio and $2a$ is the flaw size. This was experimentally verified by Griffith in his work with glass fibres. From the time this analysis was published until the late nineteen-forties the concept of flaw tolerance was largely ignored since the materials in use were either:

(i) mild steels which were ductile and could tolerate large defects before failure or,

(ii) cast irons which were used for applications where little tension was expected.

The analysis of Griffith is only suitable for completely brittle materials. In a ductile material energy absorption occurs due to blunting of the crack tip by plastic deformation. Orowan and Irwin independently suggested a term to account for the work of plastic deformation at the crack tip [19,20]. The Griffith criterion is then

$$G_c = \pi\sigma_c^2 a/E' = 2(\gamma_e + \gamma_p) = R \qquad (1.2)$$

where γ_p is the plastic strain work accompanying crack extension, G_c is the critical strain energy release rate at instability of the crack and R is the fracture toughness of the material. Usually R is mainly plastic energy and the surface energy (γ_e) can be neglected. The

usefulness of this expression is limited since it is difficult to test for these energy terms.

Irwin developed the stress intensity approach using linear elastic theory in the nineteen-fifties [21]. Linear elastic fracture mechanics determines the magnitude of the elastic stress field (the stress intensity factor) at the crack tip as the product of the remote stress and the square root of the crack length. Under plane-strain conditions the elastic stress intensity factor is a constant designated the plane-strain critical stress intensity factor K_{IC} where

$$K_{IC} = \sigma_c(\pi a)^{1/2} \tag{1.3}$$

and K_{IC} is a material property. Equation (1.3) represents the result of the analysis for an infinite plate with a crack introduced into it.

Brown and Srawley concentrated on the design of testing methods for plane-strain fracture toughness and showed the importance of thickness of the specimen [22]. For different loading applications the fracture toughness is given by

$$K_{IC} = Y\sigma_c a^{1/2} \tag{1.4}$$

where Y is a dimensionless parameter to account for applied loading, crack configuration and specimen geometry; it is given as a function of the crack length to specimen width ratio. The methods of and specimens for testing for plane-strain fracture toughness have been standardised, based on compliance measurements of the specimen [23,24].

Since plane-strain fracture toughness testing is based on linear elastic fracture mechanics (LEFM) only a small degree of plastic yielding around the crack tip can be tolerated. This means that testing is limited to quasi-brittle conditions. This confines testing at ambient temperature to materials with a yield stress greater than 800 MNm^{-2} and for lower strength materials quasi-brittle conditions are imposed by lowering the test temperature or by using unrealistically large test specimens.

The development of elastic-plastic fracture mechanics (EPFM) has provided alternative parameters which allow the measurement of a material's toughness after yielding around the crack tip. The two most common methods used are the crack-tip

opening displacement (CTOD) test and the J-integral test. Both Wells and Cottrell considered the amount of crack opening prior to crack extension as a parameter to characterise the crack-tip region's strain field for a given set of conditions [25,26]. The fracture criterion is a critical value of CTOD where the crack reaches a point of instability. The usual derivation of crack opening displacement is that of Burdekin and Stone given as

$$\delta_t = \frac{8\sigma_{ys}a}{\pi E} \ln \sec\left(\frac{\pi\sigma}{2\sigma_{ys}}\right) \qquad (1.5)$$

where δ_t is the CTOD, σ_{ys} the material's yield stress, a is the crack length and σ is the applied stress [27]. Under LEFM conditions the critical strain energy release rate (G_{IC}) is

$$G_{IC} = M\sigma_{ys}\delta_c \qquad (1.6)$$

where M is a plastic stress intensification factor to account for different stress states, specimen geometries and work-hardening. The value of M varies from 1 for plane stress and non-work hardening materials to 2 for a highly constrained crack tip [28-32]. The CTOD concept provides an alternative to the K_{IC} test when the applied stress is much less than the yield stress.

The J-integral is an energy balance approach and is not focused on the crack tip. It is defined as the path independent integral taken around the crack tip. It is interpreted as the potential energy difference between two identically loaded bodies having slightly different crack lengths so that for unit thickness

$$J = -dU_p/da \qquad (1.7)$$

where U_p is the potential energy of all energy terms contributing to non-linear elastic behaviour and a is the crack length [33]. Under plane strain conditions the critical fracture criterion is

$$J_{IC} = G_{IC} = K_{IC}^2(1-\nu^2)/E. \qquad (1.8)$$

The relationship between CTOD and the J-integral is well established and is written

$$J = m\sigma_{ys}\delta_t \qquad (1.9)$$

where m varies between 1.15 and 2.95 depending on specimen geometry, constraint and other factors [30,31,33-38]. The relationships between G_{IC} and J_{IC}, G_{IC} and δ_c and J_{IC} and δ_c mean that the plane strain fracture toughness K_{IC} may be described in terms of CTOD under small-scale yielding conditions as

$$K_{IC} = [EM\sigma_{ys}\delta_c/(1-\nu^2)]^{1/2} \qquad (1.10)$$

which demonstrates the overlap between linear-elastic and elastic-plastic fracture mechanics [16]. The criterion for overlap has not been established.

Although there are areas of conflict about the critical fracture event and the size independence of the results when using these tests, both the CTOD test method and the J-integral test method have been standardised [39-44]. Other methods of analysis have been successful in analysing fracture toughness data and there is a standard for the equivalent energy method [45-50].

1.3 Fracture Toughness Testing

The usual method of assessing fracture toughness is the Charpy V-notched bar impact test. This test measures the energy absorbed by the specimen during impact of a swinging pendulum. For materials exhibiting a fracture mode transition (e.g. structural steels) it is usually carried out with a number of specimens to determine the fracture mode transition temperature (FMTT) or the fracture appearance transition temperature (FATT). Below the FMTT the fracture is 100% cleavage while above the FMTT there is an increasing amount of ductile fracture present.

The disadvantages of the Charpy test have been given as:

(i) It gives energy as a test result which is of little use to the design engineer. By comparison LEFM and EPFM provide quantitative data which characterise the material's resistance to fracture for design analysis.

(ii) Fracture toughness tests measure the energy required for instability of the material at a stationary sharp crack whereas the Charpy test measures the energy required to initiate a sharp crack

from a blunt notch and propagate it through the specimen at high velocity. It has been suggested that energy is only needed for crack propagation in CTOD and K_{IC} tests [17].

(iii) The measurement of fracture toughness from specimens using a fatigue crack is more realistic of practical situations than the impact loading, blunt notch and smaller specimens of the Charpy test [4].

Testing for plane-strain fracture toughness K_{IC} is governed by standards using a fatigue cracked specimen [23,24]. Testing is conducted to find the load at instability of the specimen to give an apparent fracture toughness value K_Q. If certain conditions are met then the apparent toughness value is called the plane-strain fracture toughness K_{IC}.

The same specimens used to find K_{IC} can be used for J-integral or CTOD testing. The initial procedure to find J_{IC} was a graphical method from load-load-point displacement diagrams which was slow [34]. Use of the geometrical relationship between J and the load point displacement has made testing much simpler [35]. This has led to the adoption of testing standard for J_{IC} [39,40].

Testing for and calculating the CTOD are relatively simple. The CTOD is calculated from a geometric relationship using a rigid specimen rotating about a neutral axis. The formula proposed by Dawes is commonly used to calculate the CTOD where

$$\delta_c = \frac{K_I^2(1-\nu^2)}{2\sigma_{ys}E} + \frac{V_p r_p b_0}{r_p b_0 + a_0 + z} \qquad (1.11)$$

and V_p is the plastic component of clip gauge displacement, a_0 is the original crack length, b_0 is $(W - a_0)$ and is the original uncracked ligament length, W is the specimen width, z is the height of the gauge's knife edges above the specimen surface, K_I is the elastic stress intensity at the critical load and r_p is the rotation factor [37]. The rotation factor r_p depends on specimen geometry and the crack length to specimen width ratio [41,44]. To use the results of J_c or δ_c to calculate a critical crack length in a structure or a safe working stress then the COD or J-design curve is used [51,52]. Other methods exist for determining fracture toughness values the most promising being the tearing modulus concept based on J-R diagrams [53]. Standard methods for finding the critical CTOD of a material

have been formed and guidance on how to interpret results is available [41-44,54].

Reliable correlations between Charpy V-notch impact energy and CTOD or K_{IC} are attractive since fracture toughness testing would cost less and be simplified. The two tests differ in the manner of execution and in the properties they measure. The differences include strain rate, stress state and notch size. It means that any correlation between CTOD or K_{IC} test results and Charpy V-notch test results will be empirical. There have been a number of successful correlations published although most of these correlations are for specific materials, which limit their use [16,55-60]. However, if a dependence of the fracture mode transition temperature on grain size is found using LEFM or EPFM techniques then this dependence may be included in the correlation.

1.4 Mechanisms of Fracture

Fracture in steels is broadly classified into ductile and brittle fracture. A characteristic of ductile fracture is that appreciable amounts of plastic deformation occur both prior to and during the fracture process, whereas brittle fractures show none of this gross deformation.

A further sub-classification is necessary to adequately describe all fractures. Fatigue fracture produced by alternating stress conditions appears to be brittle macroscopically since the fractures show no noticeable plastic deformation. However most fatigue fractures occur by one or other of a series of plastic blunting processes where deformation is localised at the tip of the advancing fatigue crack, as may be seen on a microscopic scale [61,62].

Brittle fracture can also be classified as transgranular (cleavage) and intergranular (stress corrosion etc.) fracture. The most common form of ductile fracture in polycrystalline materials is microvoid coalescence [63]. A comprehensive discussion of these types of fracture is given elsewhere [62,63].

1.4.1 CLEAVAGE FRACTURE

The fracture toughness of a material is influenced by the microstructure, grain size and yield strength of the material, the test temperature, strain rate and stress state (specimen geometry and thickness) among other things.

Cleavage fracture can be described as the transgranular splitting of a metal along certain low index crystallographic planes called cleavage planes. The {100} planes have been shown to be common cleavage planes in the BCC metals e.g.V, Cr, Mo, W, Fe and most steels, and the {0001} planes in the CPH metals, e.g. Mg, Zn, Sn. FCC metals do not normally exhibit cleavage fracture. The bright granular appearance of cleavage fracture in low carbon steels occurs due to light being reflected from the flat "cleaved" surface of each grain.

Cleavage fracture is controlled by the tensile stress normal to the fracture plane since cleavage is the result of pulling atom planes apart as opposed to shearing [64]. Cleavage fracture is more likely to occur when the ratio of tensile stress (σ) to shear stress (τ) is high i.e. triaxially stressed structures are more likely to fail by cleavage than uniaxially stressed structures.

Various micromechanisms for the initiation and propagation of cleavage fracture have been proposed [65-72]. For low carbon steels the mechanisms, considered in order of increasing test temperatures, are:

(i) The intersection of a deformation twin with a grain boundary, a hard second phase particle or a second twin can form a cleavage crack [73]. This will occur at low temperatures or high strain rates. The deformation twins spread more rapidly than slip bands and since little relaxation of stress is able to occur when the twin is blocked by an obstacle sufficient energy is available for cleavage fracture.

(ii) Dislocations pile up against an obstacle such as a grain boundary and coalesce to form a wedge-shaped crack [65,66]. Fracture is then nucleation controlled as is observed at low temperatures.

(iii) Dislocations on intersecting slip planes may glide together to coalesce along the line of intersection to form a sessile dislocation and its Burgers vector is normal to the cleavage plane [67,68]. After the crack attains a critical size it propagates as a Griffith crack under the influence of the normal stress (σ). Cleavage fracture is then propagation controlled.

(iv) The cracking of carbides under impinging dislocation pile-ups. These microcracks propagate as Griffith defects under the combined action of the pile-ups and the applied stress into the surrounding ferrite matrix [69,70]. Again cleavage fracture is

propagation controlled. At higher temperatures, in the transition region, cracks may be non-propagating so that stable grain-sized cracks may exist. In these cases the critical event becomes crack propagation across the first ferrite/ferrite boundary.

For cleavage fracture to occur small scale plastic deformation must occur at the crack tip [74,75]. It is accepted that cleavage crack propagation occurs when a critical stress is achieved over a minimum microstructural scale [72]. This characteristic distance was thought to be of the order of 1 or 2 grains in size but it should be viewed as representing the probability of finding a sufficiently large microcrack nucleus in a highly stressed region to cause cleavage fracture [16,76,77]. The model predicts fracture toughness as

$$K_{IC} \leq \sigma_F(2\pi X_0)^{1/2} \qquad (1.12)$$

where σ_F is the fracture stress and X_0 is the characteristic distance. If X_0 is temperature independent then the predicted temperature dependence of fracture toughness arises solely from the temperature dependence of yield stress.

1.4.2 DUCTILE FRACTURE

Ductile fracture is usually considered to be by transgranular microvoid coalescence. Fracture occurs by nucleation of voids at second phase particles (either by cracking or decohesion) or at inclusions (by decohesion) and growth of individual voids until the voids coalesce and join up with the crack tip. Ductile fracture is stress and strain controlled; one model describes the nucleation condition in terms of a critical macroscopic strain (ε_n) since the matrix has to locally work-harden to reach the criterion for voiding to occur [78]. Once initiated voids grow under the influence of an applied tensile stress, as described by several models [79-81].

The crack-tip ductility in fibrous fracture is affected by the inclusion content of the steel and its work-hardening capacity. At high strains the steel may lose its capacity for work-hardening and shear fracture may occur along localised shear bands instead of void growth [82]. In toughness testing the maximum value of CTOD is limited by the amount of strain the material can sustain at the crack tip and therefore by the initial radius of the notch ρ. At the critical

notch radius below which the CTOD for the initiation of ductile crack extension (δ_i) is constant, a critical crack-tip strain known as the notched ductility (ε_{fi}) is defined [83]. When ductile fracture is initiated ahead of a fatigue crack similar values of ε_{fi} will be attained over a critical length parameter (l_f) of the material so that

$$\delta_i = l_f \varepsilon_{fi} \qquad (1.13)$$

where l_f has been found to be in good agreement with the initial MnS inclusion spacing [84]. The critical length parameter has also been shown to depend on the grain size for ferritic steels where

$$\ln(\delta_i/l_f) = \bar{\varepsilon}_p \qquad (1.14)$$

where $\bar{\varepsilon}_p$ is the plastic strain at the crack tip and l_f is twice the grain size [85]. It has also been found that the notched ductility did not change after strain-ageing of the plastic zone around the crack tip [16].

In the transition region it has been observed that the appearance of ductile shear between the blunted crack-tip and cleavage microcracks or ductile microcracks ahead of the crack tip completes the instability necessary for final fracture of the material [86].

1.4.3 THE FRACTURE MODE TRANSITION TEMPERATURE

Previous studies using the Charpy test have shown that the fracture mode transition temperature can vary by as much as 100°C within one grade of steel assuming extremes for composition and grain size [10]. It was also reported that a survey of NZ3402 Grade 275 reinforcing bar showed that the 27 Joule Charpy transition temperature varied between -42 and 20°C for the 60 heats examined [4]. Therefore, it becomes important to establish whether operating conditions place the structure above or below the transition temperature for the proposed steel or, alternatively, that the steel may be selected for the structure with a transition temperature below the appropriate operating temperature.

The fracture mode transition temperature (T_c) has been described as

$$DT_c = \sigma_i(st) + C - \left(\frac{\beta\mu\gamma}{k_y} - k_y\right)d^{-1/2} \qquad (1.15)$$

where D and C are constants, $\sigma_i(st)$ is the athermal structural component of yield stress, β is a constant to account for stress state, μ is the shear modulus, γ is the effective surface energy of the matrix, k_y accounts for the strength of dislocation locking and $d^{-1/2}$ is the reciprocal square root of grain size [8,87]. This makes the transition temperature a function of grain size, composition (through the Peierls-Nabarro stress and the strength of dislocation locking), stress state and strain rate. It predicts a linear dependence of the transition temperature on $d^{-1/2}$ which has been shown by various workers for the Charpy V-notch impact test [6,7,10].

Previous investigation of the fracture mode transition temperature of three structural grade steels had found that the Charpy test gave a range of 19°C for the 27 Joule transition temperature [16]. The CTOD test showed no discernible variation in the FMTT of the three steels. This difference might be a result of the crack initiation energy being greater in the Charpy test. It has also been suggested that energy is not needed for crack initiation in toughness testing since a sharp fatigue crack is used [17].

The transition temperature given by the CTOD test was also between 31 and 66°C less than the results of the Charpy test when a 30°C increase was expected by use of the fatigue crack. These results indicate that strain rate is significant in determining the transition temperature and that the "static" CTOD test may not be able to detect differences in material properties due to strain rate sensitivity.

By finding the temperature and grain size dependence of fracture toughness using the Charpy Impact and CTOD tests it may be established whether there is a linear dependence of fracture mode transition temperature on grain size for the CTOD test and whether this differs from the dependence of FMTT on grain size for the Charpy test. The reasons for any difference can be investigated, and the sensitivity of the CTOD test or lack of it will be highlighted.

Concern has also been raised about the effect of the plastically damaged zone ahead of the fatigue crack used in CTOD testing on the transition temperature [4]. Studies on the strain-age embrittlement of structural steel showed that significant changes in the FMTT given

by the Charpy test result from plastic deformation in the absence of ageing [13]. A significant increase in transition temperature due to strain-age embrittlement has been found after significant plastic deformation at the root of the notch in CTOD tests [88]. Also, an increase in FMTT of about 10°C has been shown to occur after strain-ageing of the plastic zone surrounding the fatigue crack in the CTOD test [16]. It is possible that by increasing the fatigue amplitude during fatigue cracking that the larger resulting plastic zone could significantly increase the FMTT in the absence of ageing.

The size of the plastic zone ahead of the crack may be increased by an increase in the grain size (due to the decrease in lower yield stress). Hence the effect of the plastic zone size on the FMTT may be studied by variation of the grain size. This means that the energy required to overcome grain boundary resistance may be distinguished and progress made towards differentiating between the energy required for crack initiation and crack propagation. It would be expected that if the CTOD test measures only the energy for crack propagation then little or no difference in FMTT would result for the variation in grain size.

It has been suggested that

$$K_{IC} \leq \sigma_F(2\pi X_0)^{1/2} \qquad (1.12)$$

may be used to predict a lower bound to the transition temperature [72]. If the temperature, grain size and strain rate dependence of K_{IC} is known then this prediction is possible. This has been given as

$$K_{IC} = \left(\frac{X_0\sigma_F^{(N+1)}}{\beta^{(N+1)}\sigma_{ys}^{(N-1)}}\right)^{1/2} \qquad (1.16)$$

where β is the amplitude of the stress singularity at the crack tip, N is the Ramberg-Osgood strain hardening index, σ_F is the fracture stress, X_0 is the characteristic distance and σ_{ys} is the yield stress [89-91]. From knowledge of the grain size dependence of the fracture stress and the grain size, temperature and strain rate dependence of yield stress the transition temperature may be found.

1.5 The Lower Yield Stress

To find the fracture toughness of the material using the CTOD test the 0.2% proof or lower yield stress of the material at the test temperature of interest should be known. Therefore testing is performed to find the yield stress (throughout the thesis yield stress refers to the lower yield stress) over the same temperature range as fracture toughness testing. The temperature dependence of fracture toughness arises almost solely from the temperature dependence of the yield stress [72]. The size of the plastic zone ahead of the crack tip also depends on the yield stress, the lower the yield stress the larger the size of the plastic zone that develops. Since plastic damage at the crack tip is expected to influence the FMTT and since fracture toughness is dependent on the temperature dependence of yield stress it is important to establish the temperature and grain size dependence of the yield stress of the material tested.

The Hall-Petch equation is often used to present the grain size dependence of yield stress, written as

$$\sigma_{ys} = \sigma_i^* + \sigma_i(st) + k_y d^{-1/2} \qquad (1.17)$$

where σ_i^* is the thermal component of yield stress dependent on temperature and strain rate, $\sigma_i(st)$ is an athermal component dependent on composition of the material, k_y is a constant dependent on the strength of dislocation locking and $d^{-1/2}$ is the reciprocal square root of mean grain diameter. If equation (1.17) is used to describe the temperature and grain size dependence of yield stress then σ_i^* must be determined. The temperature dependence of yield stress is commonly given as

$$\sigma_i^* = A\exp[-(\beta_0 + \beta_1 \log\dot{\varepsilon})T] \qquad (1.18)$$

where A is the Peierls-Nabarro stress, β_0 and β_1 are constants, $\dot{\varepsilon}$ is the strain rate and T is the absolute temperature in Kelvin [87]. Alternatively the break-away theory of yield predicts that σ_i^* is proportional to 1/T[92-94]. This theory depended upon the unlocking of dislocations at yield but subsequent work showed that yield was the result of the generation and rapid multiplication of new dislocations [95]. Also k_y, the strength of dislocation locking, should vary with temperature if the break-away theory applies but

experimental evidence showed that it was constant with temperature except in lightly pinned steels (e.g. quenched steels) [96].

The temperature dependence of yield stress based on multiplication theory is explained using thermal activation parameters [97,98]. The constants used in equation (1.18) have been shown to be based on the thermal activation parameters [99]. Combining equations (1.17) and (1.18) makes the subsequent model of yield stress a function of the Peierls-Nabarro stress, the interstitial content, the strength of dislocation locking and grain size. Whether this combined model provides an adequate description of experimental yield stress results has not been shown; it may be that σ_i^* needs to be changed. It is also important that the model developed may be applied to practical engineering situations and therefore the derived temperature dependence of yield need not explicitly show the controlling mechanism of temperature dependence.

It may then be possible to describe the fracture mode transition temperature according to the conditions that any description includes [100]:

(i) A mechanical equation of state including work-hardening;

(ii) Dislocation dynamics or strain-rate sensitivity parameters which account for solid-solution hardening;

(iii) A cleavage criterion for simple stress states which includes the above as well as grain size effects and

(iv) A cleavage criterion for cracks or notches incorporating all of the above.

It is, therefore, necessary to review linear elastic and elastic-plastic fracture mechanics, mechanisms of fracture including a description of the fracture mode transition temperature and the theories of yield.

CHAPTER 2

Fracture Mechanics Review

2.1 Linear Elastic Fracture Mechanics (LEFM)

In this chapter a review of linear elastic and elastic-plastic fracture mechanics and the testing procedure using them is presented.

2.1.1 IDEAL FRACTURE

The ideal fracture strength of a material would be the stress needed to break atomic bonds. Figure 2.1 shows the energy-displacement and force-displacement relationships for a pair of isolated atoms. The atomic stress-strain relationship (from the force-displacement curve) is approximately given by a half sine wave (shown in Figure 2.2), so that

$$\sigma = \sigma_{max}\sin(2\pi\, x/\lambda) \qquad [19,\ 101]. \qquad (2.1)$$

The energy (U_o) required to separate the two atoms to infinity is equal to the total area under the stress-strain curve. This energy in a crystalline solid is equal to twice the surface tension (γ) of a unit area of a free surface of the appropriate plane of the solid, such that

$$U_o = 2\gamma. \qquad (2.2)$$

Therefore by integration of equation (2.1) between 0 and $\lambda/2$ the area under the atomic stress-strain curve can be equated to 2γ,

$$\frac{\lambda}{2\pi}\sigma_{max}\left[-\cos\left(\frac{2\pi x}{\lambda}\right)\right]_o^{\lambda/2} = 2\gamma, \qquad (2.3)$$

which reduces to

$$(\lambda/\pi)\sigma_{max} = 2\gamma. \qquad (2.4)$$

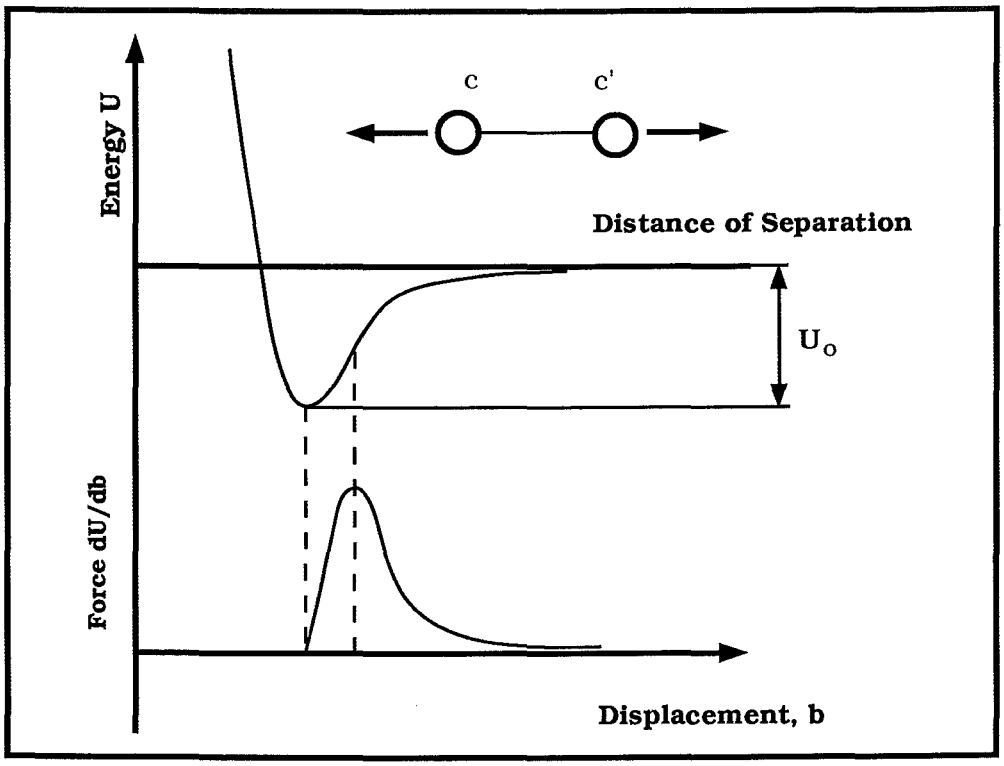

Figure 2.1 : Bonding energy as a function of the distance of separation and the force-displacement curve.

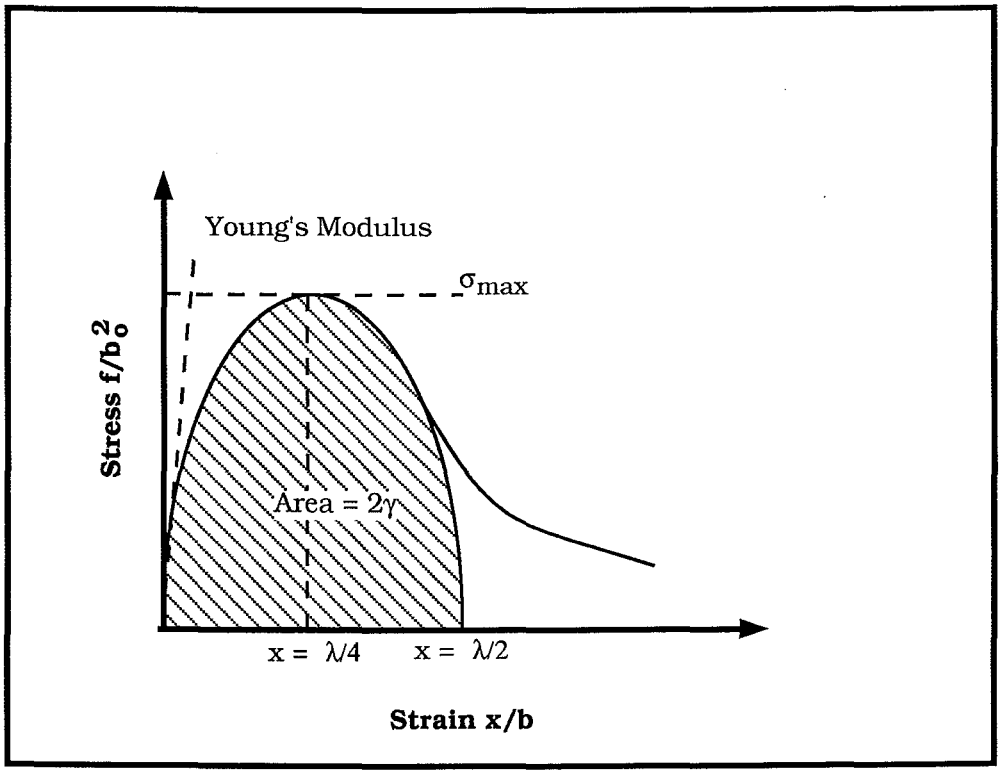

Figure 2.2 : The atomic stress-strain curve

If the displacement is very small then sin x ≈ x and equation (2.1) becomes,

$$\sigma = \sigma_{max} 2\pi x/\lambda = Ex/b_0 \qquad (2.5)$$

which gives λ as

$$\lambda = \sigma_{max} 2\pi b_0/E \qquad (2.6)$$

where b_0 is the distance between the atom planes and E is Young's modulus. Substitute for λ in equation (2.4) and rearrange equation (2.4) to give the ideal fracture strength as,

$$\sigma_{max} = (E\gamma/b_0)^{1/2}. \qquad (2.7)$$

This derivation considers the energy of interaction of a pair of atoms across the fracture plane. A more accurate method is to use interaction energies expressed as Morse potentials [102]. The expression for fracture stress is derived by considering the interaction energies between an atom and all its neighbours and differentiating the energy equation to give atomic force-displacement curves,

$$U(b-b_0) = U\{\exp[-2s(b-b_0)] - 2\exp[-s(b-b_0)]\} \qquad (2.8)$$

where s is the reciprocal of the "range" of the inter-atomic forces.

In other cases the interatomic forces have been given as [103],

$$F = \text{Constant}\left[\left(\frac{b_0}{b}\right)^m - \left(\frac{b_0}{b}\right)^n\right] \qquad (2.9)$$

where m is representative of the repulsive forces and n is dependent on attractive forces. As interatomic potentials are often not well defined pseudo-potential functions like equation (2.8) are accepted to evaluate the various constants. The atomic stress-strain curve may then be calculated, with the result that the fracture stress of a crystalline solid is about 0.1 E [104].

2.1.2 THE GRIFFITH ENERGY CRITERION

An apparently homogeneous material contains pre-existing flaws such as microscopic cracks, atomic deformations which could nucleate cracks, or local inhomogeneity of composition. Therefore the theoretical strength of a crystalline solid is never reached and the observed strength is about two orders of magnitude lower than 0.1 E. The concept of flaw tolerance was predicted by Griffith in 1920 on experiments with glass and glass fibres [18]. Using the stress concentration developed by Inglis for a macroscopic elliptical hole Griffith used it for an elliptical crack introduced into an infinite plate strained between fixed grips [18,105]. Consider Figure 2.3a which shows an infinite plate of unit thickness with a remote stress σ applied. If an elliptical crack of length 2a is introduced into the body then the energy balance of the plate is

$$U = U_o + U_a + U_\gamma - F \qquad (2.10)$$

where (i) U is the total energy of the plate,

(ii) U_o is the elastic energy of the loaded uncracked plate and is constant,

(iii) U_a is the change in elastic energy caused by introducing the crack into the plate, due to stress free areas about and below the crack and

$$U_a = \frac{-\pi\sigma^2 a^2}{E'} \qquad (2.11)$$

where $E' = E$ (in plane stress) (2.12a)

and $E' = E/(1-\nu^2)$ (in plane strain) (2.12b)

and ν is Poisson's ratio.

(iv) U_γ is the change in the elastic surface energy caused by formation of two new crack surfaces. If γ_e is the elastic surface energy then

$$U_\gamma = 2(2a\gamma_e). \qquad (2.13)$$

(v) F is the work performed by external forces and for the fixed grip condition is equal to zero; that is no external work is performed. Therefore, in plane stress, the total energy of the plate is,

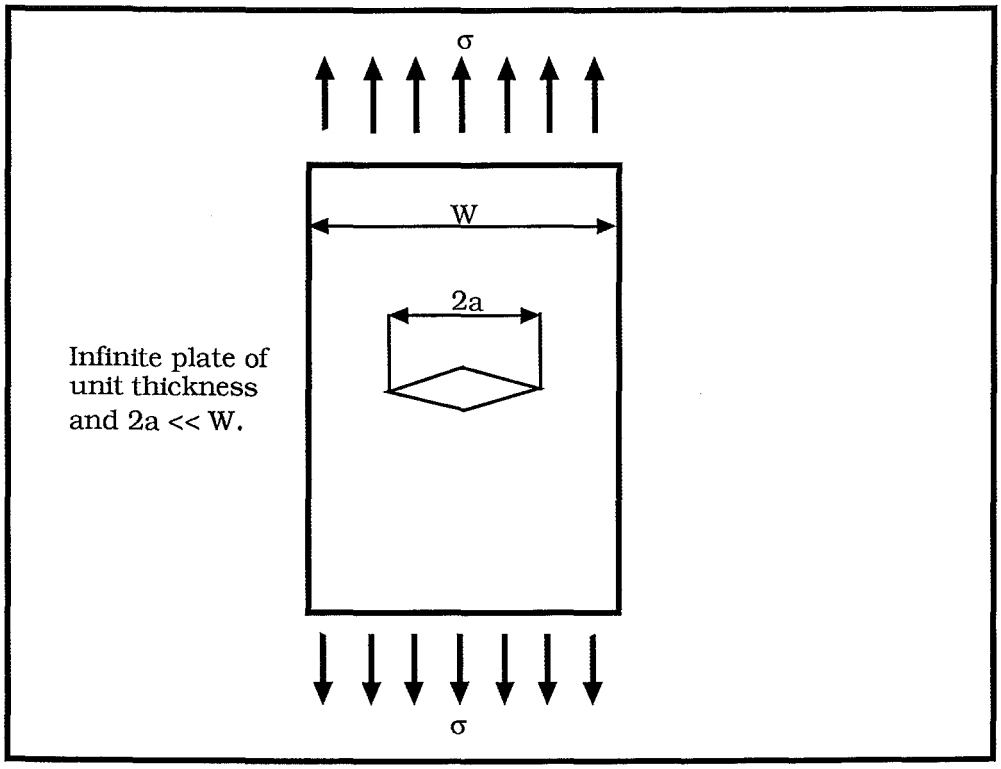

Figure 2.3a : A through-cracked plate of unit thickness with a remote stress applied.

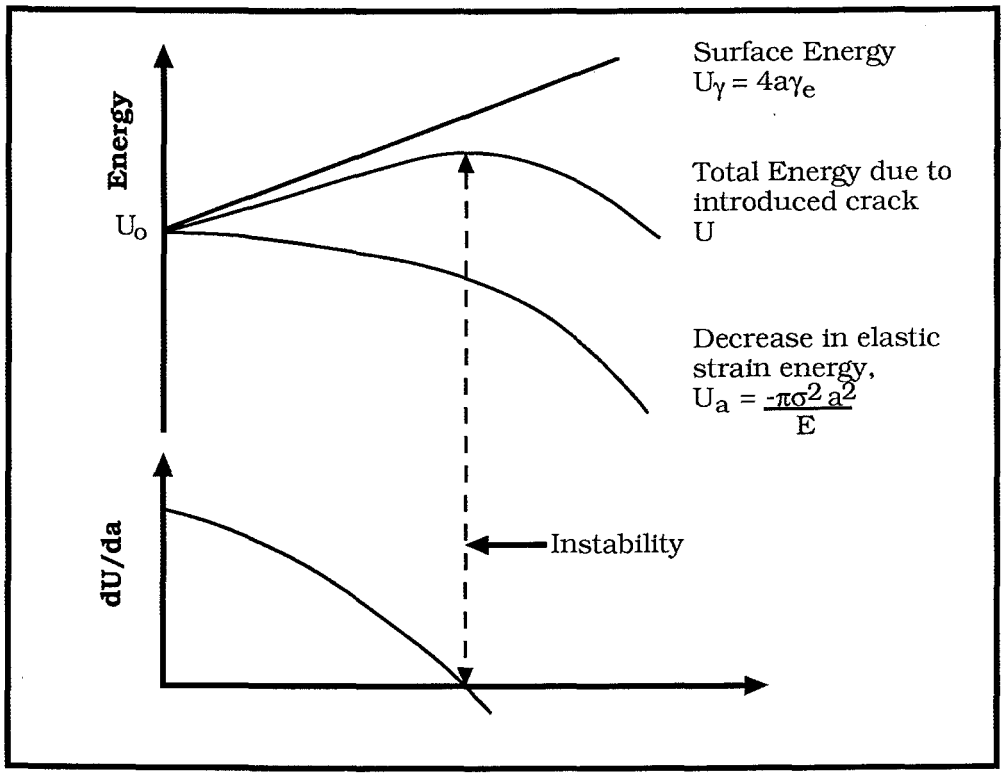

Figure 2.3b : Schematic of the energy balance of an infinite plate with an introduced crack, length 2a, and no work is done by external forces.

$$U = U_o - \frac{\pi\sigma^2 a^2}{E} + 2(2a\gamma_e). \qquad (2.14)$$

Figure 2.3b shows the energy balance of the plate schematically. This shows that with an increase in crack length the energy passes through a maximum and then decreases. If the change in energy of the plate is considered when the crack of length 2a extends by a small amount δa then an energy criterion below which no crack extension occurs is established. By differentiating equation (2.14) with respect to a then an instability occurs when the rate of change of energy with respect to a is less than or equal to zero and

$$\frac{\partial U}{\partial a} = 4\gamma_a - \frac{2\pi\sigma^2 a}{E} \leq 0. \qquad (2.15)$$

By rearranging equation (2.15) the critical stress at instability ($\partial U/\partial a = 0$) is,

$$\sigma_c a^{1/2} = \left(\frac{2E'\gamma_e}{\pi}\right)^{1/2} \qquad (2.16)$$

where $E' = E$ for plane stress and $E' = E/(1-\nu^2)$ for plane strain. The expression developed here is suitable only for a completely brittle material. For example, in a ductile material energy absorption occurs due to blunting of the crack tip during plastic deformation which the Griffith criterion does not take account of.

2.1.3 THE CRITICAL ENERGY RELEASE RATE

The parameter controlling fracture is designated G, the critical energy release rate per unit thickness, and

$$G = \frac{\partial}{\partial a}(F - U_a) \qquad (2.17)$$

which is the amount of energy available for crack extension. Then the crack resistance per unit thickness R, which is the energy needed for crack extension is

$$R = \frac{\partial U_\gamma}{\partial a} = \frac{\partial}{\partial a} 2(2a\gamma_e). \qquad (2.18)$$

For unstable crack propagation

$$\frac{\partial}{\partial a}(F-U_a) \geq \frac{\partial U_\gamma}{\partial a} \tag{2.19}$$

or $$G \geq R \tag{2.20}$$

It follows that R is an intrinsic material property called the fracture toughness of the material.

2.1.4 STRESS INTENSITY

The fracture criteria may be found by considering only the stresses around the crack tip and not those acting over the entire body. Consider Figure 2.4a which shows the stresses on a element ahead of a crack tip. Westergaard provided a semi-inverse method for solving a certain class of plane-strain or plane-stress problems [106]. Irwin used these methods to calculate the "crack-tip stress distribution" using linear elastic theory [21]. The analysis proceeds using the Airy Stress function but the final solution is more usually presented in terms of polar co-ordinates at the crack tip as shown in Figure 2.4a. The solutions are

$$\sigma_x = \frac{\sigma(\pi a)^{1/2}}{(2\pi r)^{1/2}} \cos \theta/2 \, (1 - \sin \theta/2 \sin 3\theta/2) \tag{2.21a}$$

$$\sigma_y = \frac{\sigma(\pi a)^{1/2}}{(2\pi r)^{1/2}} \cos \theta/2 \, (1 + \sin \theta/2 \sin 3\theta/2) \tag{2.21b}$$

$$\tau_{xy} = \frac{\sigma(\pi a)^{1/2}}{(2\pi r)^{1/2}} \sin \theta/2 \cos \theta/2 \cos 3\theta/2. \tag{2.21c}$$

As r approaches zero the stresses tend to infinity so there is a singularity at the crack tip. The stresses are a product of $f(\theta)/(2\pi r)^{1/2}$ and $\sigma(\pi a)^{1/2}$. The product of the remote stress and the root of crack length, $\sigma(\pi a)^{1/2}$, determines the magnitude of the elastic stress field and is called the mode I stress intensity factor,

$$K_I = \sigma(\pi a)^{1/2}. \tag{2.22}$$

For plane strain conditions

$$\sigma_z = \nu(\sigma_x + \sigma_y) \tag{2.23}$$

These results are valid for a crack with zero radius at the crack tip. The solution for a crack with finite tip radius was provided by Creager and Paris, who shifted the origin by the crack-tip radius ρ [107].

The elastic displacements associated with the stresses may be found using Hooke's Law. In plane strain

$$E\varepsilon_x = \sigma_x - \nu(\sigma_y + \sigma_z). \tag{2.24}$$

The strain is $\varepsilon_x = \partial u/\partial x$ so therefore u, the elastic displacement in the x direction, is

$$u = \frac{1}{E}\int((1-\nu^2)\sigma_x - \nu(1+\nu)\sigma_y)dx \tag{2.25}$$

substituting for σ_z using equation (2.23). Upon integrating and substituting for Re$\bar{\phi}$(z) and Imϕ(z)

$$u = 2(1+\nu)\frac{K_I}{E}\left(\frac{r}{2\pi}\right)^{1/2}\cos\theta/2(2-2\nu-\cos^2\theta/2). \tag{2.26}$$

Using similar arguments for v, the displacement in the y direction,

$$v = 2(1+\nu)\frac{K_I}{E}\left(\frac{r}{2\pi}\right)^{1/2}\sin\theta/2(2-2\nu-\cos^2\theta/2). \tag{2.27}$$

The results for plane stress displacement are more complicated since the integration constant is not zero.

The elastic strain energy release rate (G) may also be found by considering a crack closing from (a + δa) to a, as in Figure 2.4b. The total strain energy absorbed is equal to the input energy rate δU_a, which is equal to the strain energy release rate for crack extension δa. In this case the stress and displacement ahead of the crack tip are,

$$\sigma_y = \frac{\sigma x}{(x^2 - a^2)^{1/2}} \tag{2.28}$$

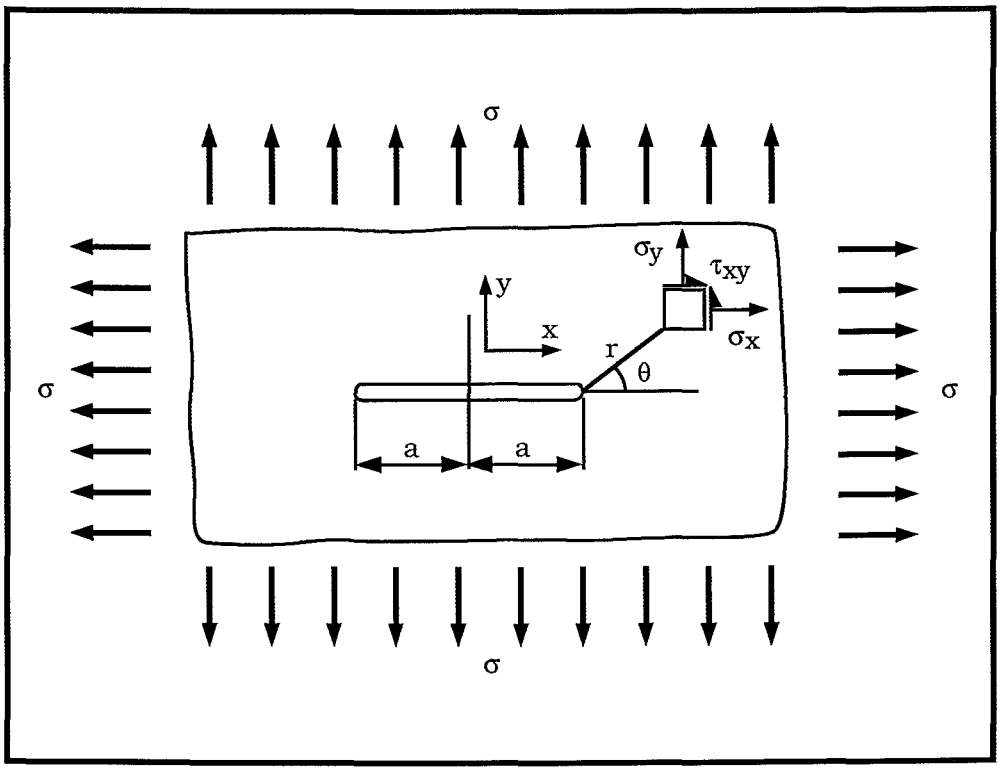

Figure 2.4a : Stresses on an element a distance r, angle θ , ahead of a crack in an infinite plate.

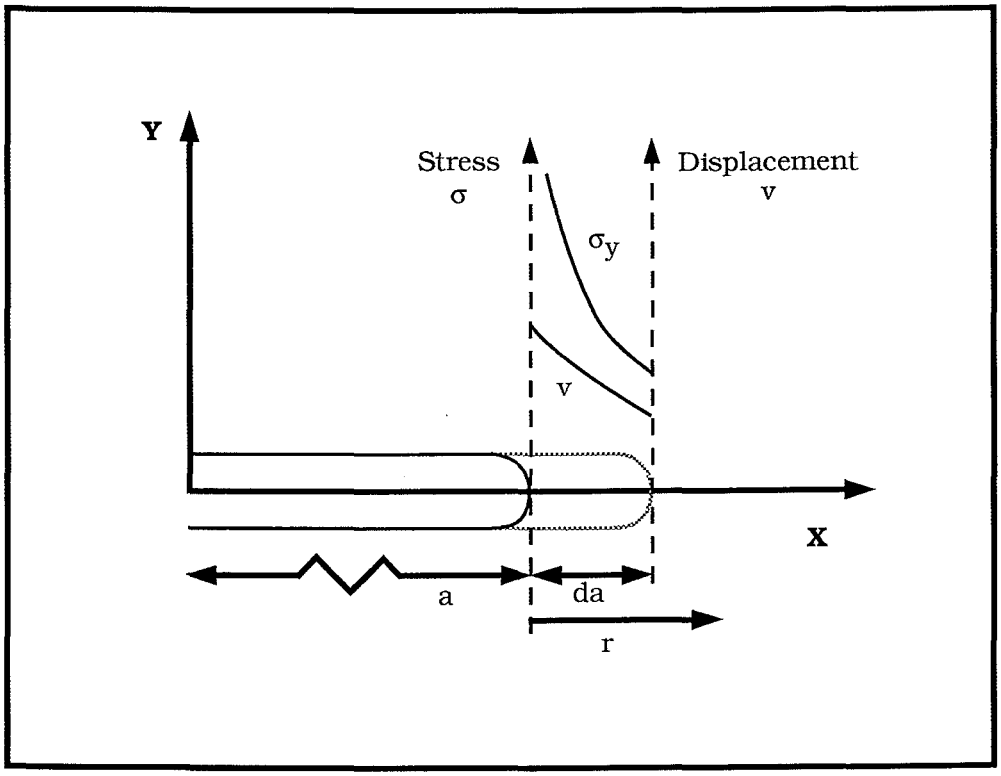

Figure 2.4b : Calculation of G by considering a crack closing from (a+δa) to a.

and $$v = 2(1-\nu^2)(\sigma/E)(a^2-x^2)^{1/2}. \tag{2.29}$$

By letting x = r+a and assuming δa, r<< a then σ_y and v may be written,

$$\sigma_y = \frac{\sigma(\pi a)^{1/2}}{(2\pi r)^{1/2}} \tag{2.30}$$

$$v = 2(1-\nu^2)(\sigma/E)(2a)^{1/2}(\delta a-r)^{1/2}. \tag{2.31}$$

The strain energy release rate per unit thickness is then

$$G\delta a = \int_0^{\delta a} \sigma_y \, v \, dr \tag{2.32a}$$

which upon substituting for σ_y and v becomes

$$G\delta a = 2(1-\nu^2)\,\frac{\sigma^2 a}{E}\int_0^{\delta a}\left(\frac{\delta a-r}{r}\right)^{1/2} dr. \tag{2.32b}$$

Since the crack is elliptical then $r = \delta a \sin^2\omega$ and the integral when evaluated becomes

$$G\delta a = \frac{\sigma\pi^2 a}{E}(1-\nu^2)\delta a \tag{2.33}$$

from which

$$G_I = K_I^2/E' \tag{2.34}$$

where again E' = E in plane stress and $E' = E/(1-\nu^2)$ in plane strain.

These conditions have been found for Mode I tensile opening. Similar expressions may be found for Mode II sliding opening and Mode III tearing opening. When a crack experiences a combination of Modes I, II and III opening then the work involved in opening the crack may be found by superposition of the respective mode strain energy release rates. Hence, the resultant strain energy is

$$G = G_I + G_{II} + G_{III} \tag{2.35}$$

$$= \frac{1}{E'}[K_I^2 + K_{II}^2 + \frac{K_{III}^2}{(1-\nu)}] \tag{2.36}$$

where E' is as for previous equations.

Equations (2.34) and (2.35) have an important role in fracture mechanics and can reduce a complicated situation to a relatively simple mathematical one. Mathematically the stress intensity for different loading applications is given by

$$K = Y\sigma a^{1/2} \tag{2.37}$$

where $$Y = f(a/W). \tag{2.38}$$

Y is a dimensionless parameter to account for applied loading, crack configuration and specimen geometry and it is given as a function of the crack length to specimen width ratio. This is often a numerical approximation in the form of a truncated power series, with a maximum error of about 5%. Y has been found for many situations and compendiums of the value of Y are available, for example, the compendium of stress intensity values written by Rooke and Cartwright [108].

2.1.5 CRACK-TIP PLASTICITY

When linear elastic theory is used to analyse stresses around the crack tip there is a singularity at the crack tip where the stress rises to infinity. In reality structural materials will deform plastically above their yield stress and a plastically deformed zone will form around the crack tip.

Irwin *et al.* found that the critical stress for fracture in large, thin sheets of aluminium containing central cracks was

$$\sigma_c = \left(\frac{E.\text{constant}}{\pi a}\right)^{1/2} \tag{2.39}$$

but the constant was greater than that expected if it was a result only of elastic surface energy of the crack [109].

Orowan and Irwin both suggested independently that energy released in these specimens was due to plastic flow around the

crack. The amount of plastic flow at instability was found to be much smaller compared to the crack length or the width of the specimen. Therefore, linear elastic theory could still be used to relate crack-tip events to the applied stress. Irwin and Orowan re-wrote the Griffith criterion as

$$G_c = \frac{\pi\sigma_c^2 a}{E} = 2(\gamma_e + \gamma_p) = R \qquad (2.40)$$

where γ_p is the plastic strain work accompanying crack extension [10,110]. For relatively ductile materials R is mainly plastic energy and the surface energy can be neglected i.e. $\gamma_p >> \gamma_e$. The amount of plastic work in the crack-tip region which preceded unstable crack propagation was found to be independent of the initial crack length [109]. Therefore the plastic work was a measure of the material's resistance to fracture. The critical strain energy release rate (G_c) provided a convenient parameter to include all energy terms, and it could be used to characterise the material's resistance to fracture. However fracture need not occur at a constant value of G_c since R need not be constant; it is dependent on the experimental testing conditions. It has been determined that R and hence G_c are constant only for plane strain conditions. Therefore Irwin wrote the fracture criteria as [111]

$$G_{IC} = (1-\nu^2)\pi\sigma^2 a/E \qquad (2.41)$$

and

$$K_{IC} = [EG_{IC}/(1-\nu^2)]^{1/2}. \qquad (2.42)$$

The formation of a plastic zone will alter the stress distribution ahead of the crack tip. The actual shape of the plastic zone is difficult to find but a first approximation of the plastic zone assumes that small scale yielding produces a notional crack of length $(a + r_y)$ in plane stress where r_y is the radius of the crack-tip plastic zone [112,113]. Irwin assumed the material to behave elastic-perfectly-plastically so that no strain-hardening occurs in the plastic zone, which gives a stress distribution ahead of the crack tip as shown schematically in Figure 2.5 [112,113]. In this simple approximation the plastic zone is considered to be circular where

$$r_y = \frac{1}{2\pi}\left(\frac{K_I}{\sigma_{ys}}\right)^2 \qquad (2.43)$$

with σ_{ys} being the yield stress of the material. Unstable fracture will occur in the presence of a plastic zone when

$$G_c = \frac{\pi\sigma_F{}^2 a}{E}\,[1 + {}^1/_2(\sigma/\sigma_{ys})^2] \qquad (2.44)$$

where σ_F is the fracture stress, σ is the applied stress and σ_{ys} is the yield stress. The tip of the extended crack is at the centre of the plastic zone. The stress intensity is then

$$K_c = \sigma_F[\pi a\,(1 + \sigma_F{}^2/2\sigma_{ys}{}^2)]^{1/2} \qquad (2.45)$$

where K_c is the critical stress intensity factor.

A plastic zone size correction can also be found using Dugdale's model, which considers that all plastic deformation concentrates in a plastic strip in front of the crack, the strip yield model [114]. The effective crack length is assumed to carry the yield stress as shown in Figure 2.6 and, again, the assumption of elastic-perfectly plastic behaviour is made. The effective crack length is then,

$$\Delta a_n \approx \frac{\pi}{8}\left(\frac{K_I}{\sigma_{ys}}\right)^2 \qquad (2.46)$$

and the critical stress intensity is then

$$K_c = \sigma_F[\pi a\,(1 + \pi^2\sigma_F{}^2/8\sigma_{ys}{}^2)]^{1/2}. \qquad (2.47)$$

It should be noted that these derivations result from conditions of plane stress in an infinite plate. Different expressions result for predominantly plane-strain conditions, the effective crack length is generally smaller except at the plate surface where plane stress conditions will prevail.

Equations (2.45) and (2.47) can be used when $\sigma_F/\sigma_{ys} > 0.4$ but at high values of σ_F/σ_{ys} the elastic equivalent concept becomes doubtful.

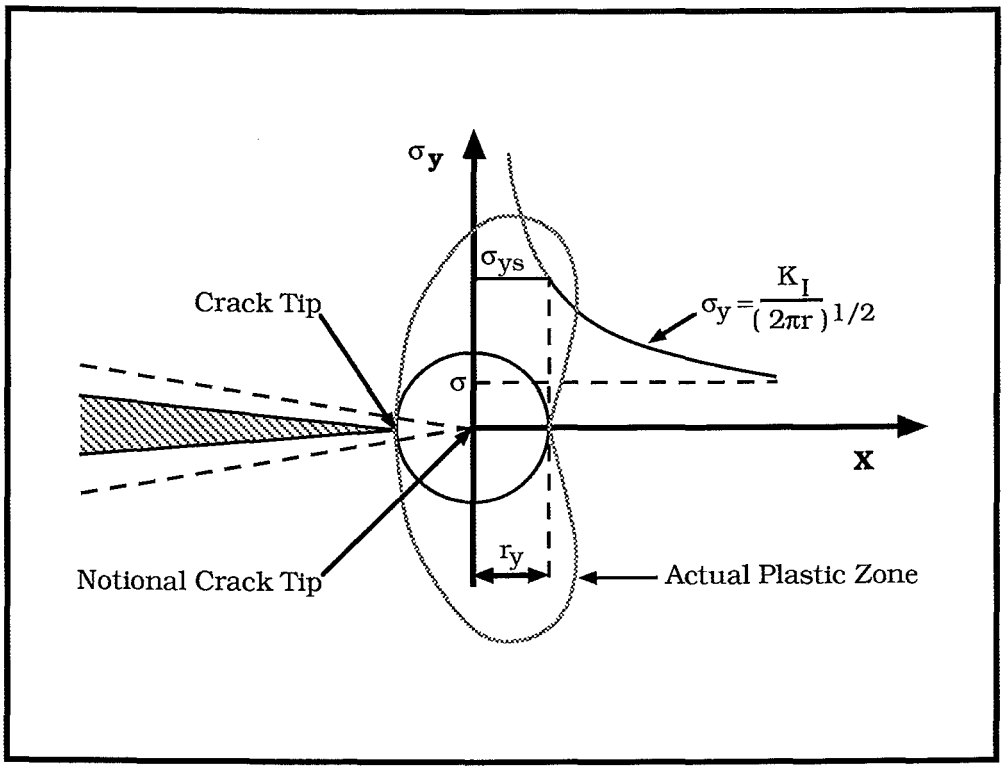

Figure 2.5 : Irwin's approximation of the crack-tip plastic zone after yielding.

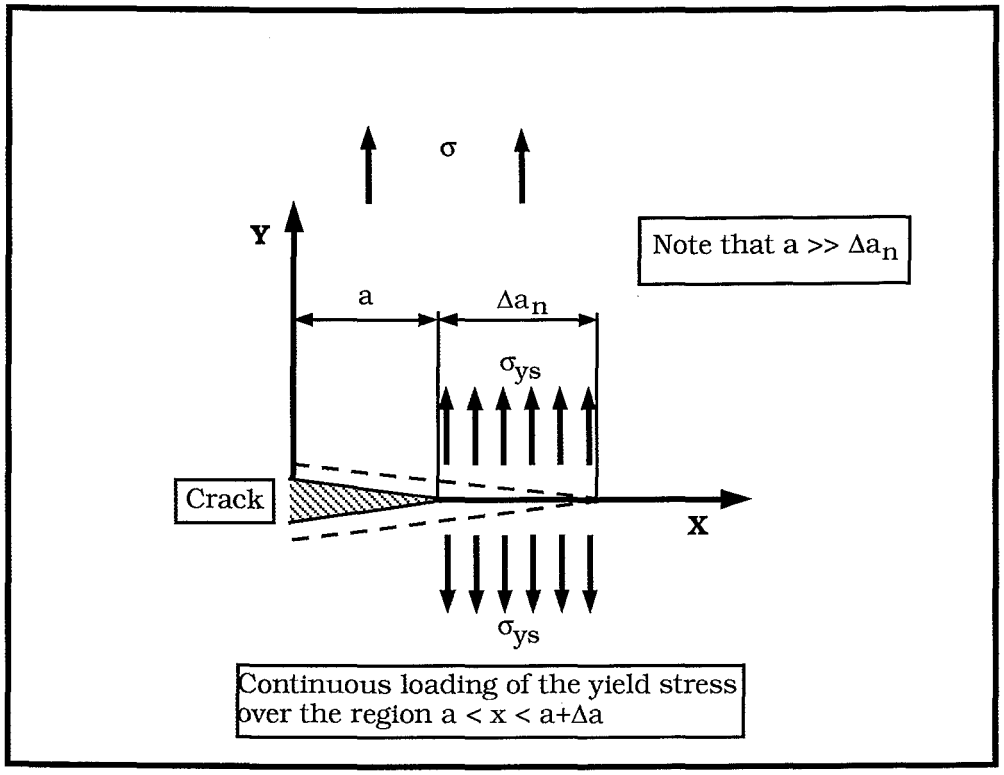

Figure 2.6 : Schematic of the strip-yield model of the plastic zone from Dugdale's analysis[114].

2.1.6 *QUASI-BRITTLE FRACTURE*

The development of linear elastic theory of fracture has led to development of experimental methods to determine the fracture properties of materials. In 1952 Irwin and Kies described a method for engineers to determine the safety of a structure [115]. Brown and Srawley concentrated on the design of testing methods for plane strain fracture toughness and found thickness effects to be very important [22]. Srawley and Brown showed a large variation in toughness using the results of Krafft *et al.*, who had investigated the effects of specimen thickness upon fracture toughness using an age-hardened 7075-T6 aluminium alloy, as shown in Figure 2.7 [116,125]. Figure 2.7 shows the toughness curve can be divided into 3 regions.

(a) Region A: When the specimen is very thin fracture toughness tends to increase with increasing thickness. The fracture is slant (45° mode) and the load-displacement curve is linear. Knott explained this in terms of a K_{III} (antiplane strain) mode of separation at the crack tip as fracture occurs by sliding off on a through-thickness plane inclined at 45° to the tensile axis, the process being completely ductile [117]. However the total fracture would be regarded as brittle. The criterion for first crack extension is

$$\tau_{app} = [\frac{2^{3/2}\mu\tau_{ys}B}{\pi a}]^{1/2} \qquad (2.48)$$

where τ_{app} is the applied shear stress, τ_{ys} is the shear yield stress, μ is the shear modulus, B is specimen thickness and provided that the extent of screw dislocation pile-up is small compared to the width of the sheet. Rewriting equation (2.48) in terms of tensile stresses gives [117]

$$\sigma_{app} = [\frac{2^{3/2}E\sigma_{ys}B}{\pi a(1+\nu)}]^{1/2}. \qquad (2.49)$$

This gives the condition for instability since B remains constant as a increases. A maximum in applied load is obtained and the critical energy release rate is

$$G_c = 2^{3/2}\sigma_{ys}B/(1+\nu) \approx 2\sigma_{ys}B. \qquad (2.50)$$

Therefore the toughness of the sheet increases very rapidly with increase in thickness.

(b) Region B: In this region fracture is mixed as shown in Figure 2.8. The fracture profile is a mixture of slant and square fracture, the amount of square fracture increasing as specimen thickness increases. A maximum in toughness occurs when a small amount of square fracture occurs. The square fracture may produce a step in the load-displacement curve if it occurs quickly (a "pop-in") or the slope may simply decrease if it occurs more gradually. This initial square fracture does not have to produce instability in the specimen as a whole because the shear lips formed require increased load and strain before they separate.

In this region the Irwin fracture criterion breaks down since it was postulated that the amount of crack growth to the point of instability was independent of initial crack length, therefore the scaling with $a^{1/2}$ does not follow [117]. For these situations a curve must be obtained of resistance to crack growth (a R-curve) versus crack length before critical values of G or K relevant to specific service applications may be determined. The R-curve analysis is described in Section 2.1.8.

When the service application uses thin sheets, such as the aircraft industry, then testing is usually carried out using specimens of the same dimensions of the sheets used in service.

(c) Region C: If the fracture is predominantly a square fracture then G_c is independent of crack length; instability is coincident with "pop-in". Plane-strain conditions are assumed to exist at the centre of the specimen and a triaxial stress state is developed. In mild steel Knott has shown that the onset of low strain cleavage cracking is enhanced by a triaxial stress state because the maximum value of σ_{yy} is raised by plastic constraint and is more able to propagate crack nuclei [64]. The constant value of G_c attained is designated G_{IC}, the plane-strain fracture toughness, and it is the subject of the majority of fracture toughness testing. In this region linear elastic theory may be successfully applied to fracture.

Although the general trend is for decreasing toughness with increasing thickness of specimens Gurumoorthy *et al.* in 1988 showed that for alumina specimens toughness, using standard techniques, increased from about 0.5 to 2.25 $MPam^{1/2}$ with thickness increasing from 1.27 to 19.81 mm [118]. Their

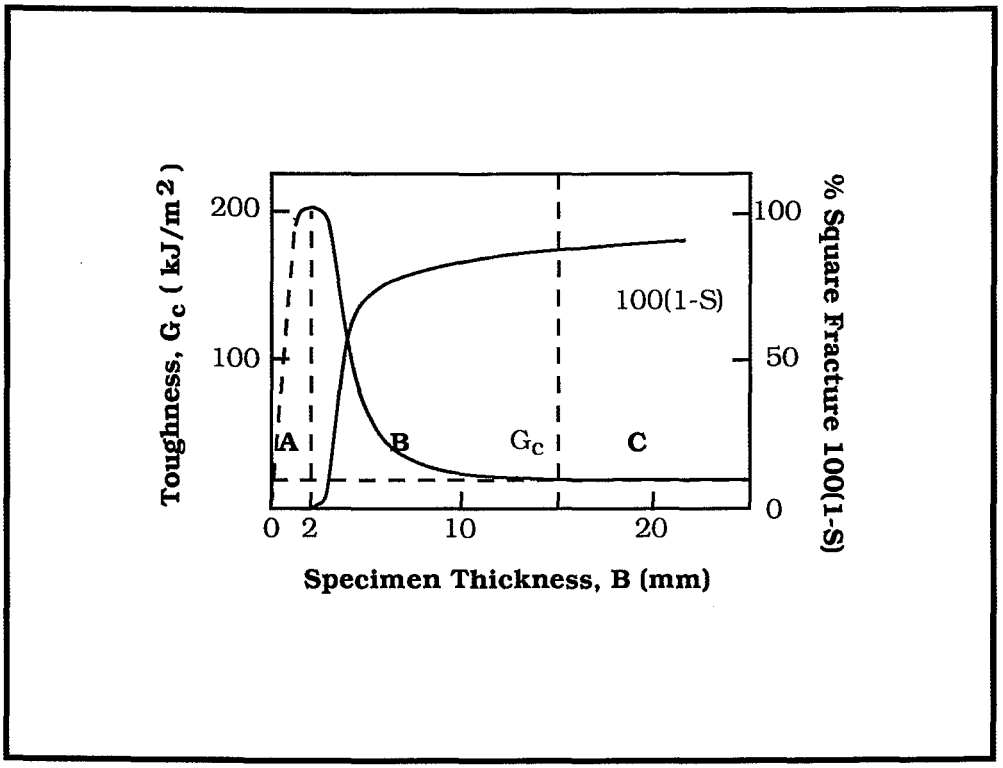

Figure 2.7 : The variation of toughness with thickness of 7075 alloy(Al-Zn-Mg)- T6 [116].

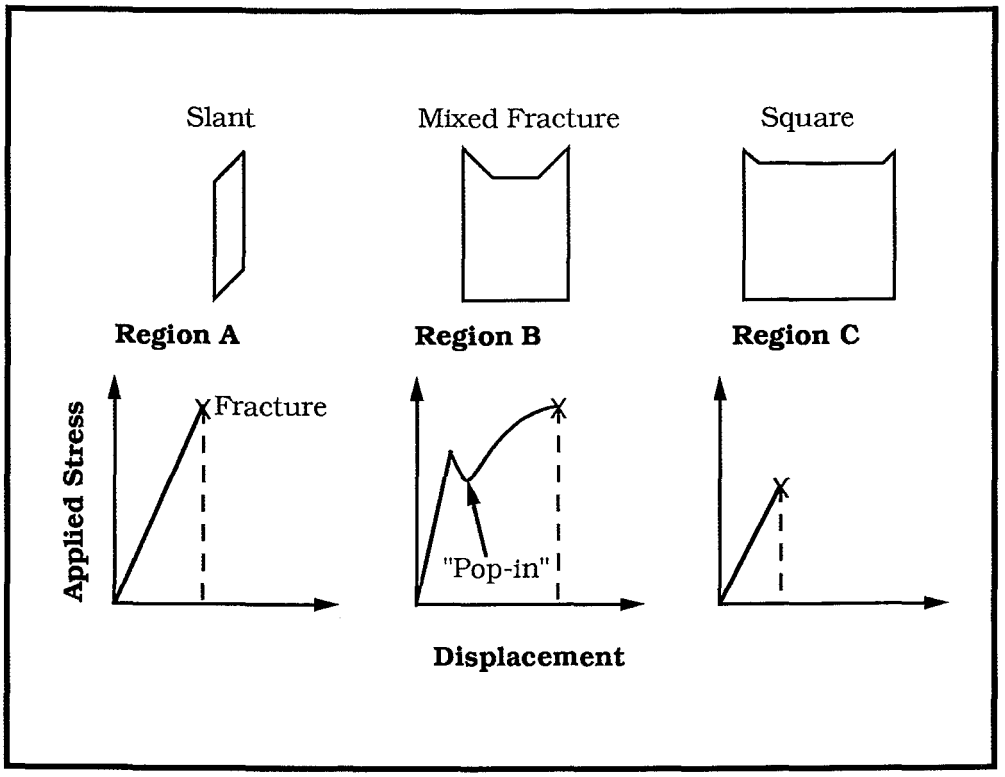

Figure 2.8 : The variation of fracture profile with increasing thickness and typical stress-displacement curves from regions A, B and C.

explanation attributed the increase in toughness due to the crack propagating by first running across the crack front, then becoming unstable and running through the ligament in front of the crack. This result would mean toughness would increase as the square root of thickness. It demonstrates the incomplete understanding of thickness effects on the toughness of the material.

Fracture toughness results for an A533B-1 steel were given as a function of thickness and temperature [119]. This investigation showed small specimens could be used to predict the toughness of larger specimens. It was found that the size effect could be quantified in terms of a shift in temperature for a given toughness level implying FMTT increases with increasing thickness.

2.1.7 PLANE-STRAIN FRACTURE TOUGHNESS TESTING

The emphasis in toughness testing has been the determination of the plane-strain fracture toughness (K_{IC}) in specimens sufficiently thick to ensure that instability occurs as soon as the first plane-strain crack extension begins.

Early research, such as that of Srawley and Brown and Srawley *et al.*, used LEFM theory to develop suitable loading systems, specimen geometries and analysis of data [22,116,120]. After considerable study and experimental verification the American Society for Testing and Materials (ASTM) published a standard method for K_{IC} testing (a later revision is referenced) [23]. The British Standards Institution published a draft for development in 1971 on plane-strain fracture toughness testing which was followed by a standard in 1977 [24,121]. The specimens used have to meet the following requirements:

(i) For LEFM to apply the size of the plastic zone at fracture must be small compared to the uncracked ligament of the specimen at fracture.

(ii) The plastic zone must also be small compared to the initial crack length if the crack-tip stress field is to be characterised by a single value of stress intensity.

(iii) The thickness of the specimen must be sufficient to give plane-strain fracture toughness.

Commonly two specimen geometries are used, the 3-point single-edge-notched bend specimen (SENB) and the compact tension specimen (CT). Testing of both involves loading of the

specimen to open a pre-existing crack (usually a fatigue crack) and recording the applied load against the displacement at the mouth of the crack. The critical load P_Q at instability is determined from the load-displacement curve and the apparent fracture toughness K_Q is calculated, which is

$$K_Q = \frac{P_Q}{BW^{1/2}} \cdot f(a_0/W) \tag{2.51}$$

where B is the specimen thickness and W is the specimen width for the CT specimen. The function $f(a_0/W)$ accounts for different specimen geometries and is based on the crack length to width of the specimen ratio. Values of $f(a_0/W)$ are normally tabulated over the accepted testing range of a/W [23,24].

There are criteria to be met when fatigue pre-cracking and bend or tension testing for K_Q to be accepted as a valid test result. Brown and Srawley found that if K_Q meets the criteria,

$$B,\ W-a_0,\ a_0 \geq 2.5(K_Q/\sigma_{ys})^2 \tag{2.52}$$

where a_0 is the initial crack length and σ_{ys} is the yield stress at the test temperature then K_Q can be accepted as K_{IC} the plane-strain fracture toughness [22]. Therefore

$$B,\ W-a_0,\ a_0 \geq 2.5(K_{IC}/\sigma_{ys})^2 \tag{2.53}$$

which implies that the maximum size of the plastic zone possible from Irwin's analysis (equation (2.43)) is

$$r_{Iy} \approx \frac{1}{3} r_y \approx \frac{1}{6\pi}(K_{IC}/\sigma_{ys})^2. \tag{2.54}$$

So the error in using a single value of K to characterise the crack-tip stresses could be as much as 8% (at $r_{Iy}/a \approx 0.02$) [117].

Two of the major effects on plane-strain fracture toughness testing are test temperature and test strain rate. For low to medium strength steels results for K_{IC} show a large increase in K_{IC} over a small temperature range similar to the notched-bar impact test; that is the results show a fracture mode transition temperature (FMTT).

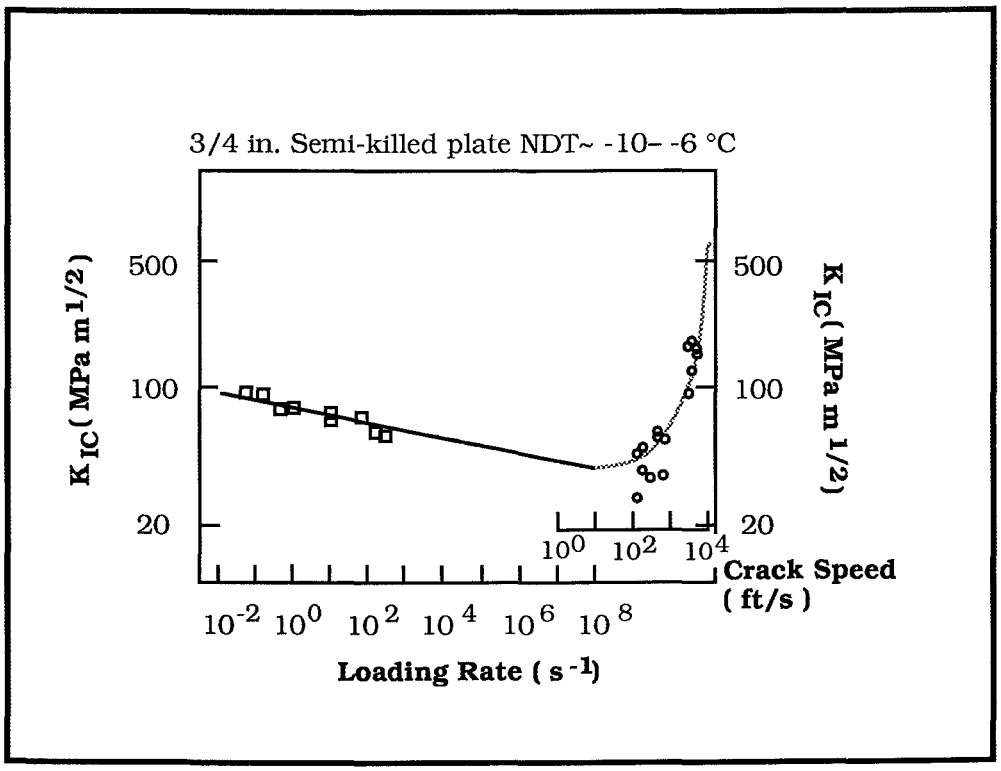

Figure 2.9a : Fracture toughness versus Loading Rate and Crack Speed for a Semi-killed Steel[122].

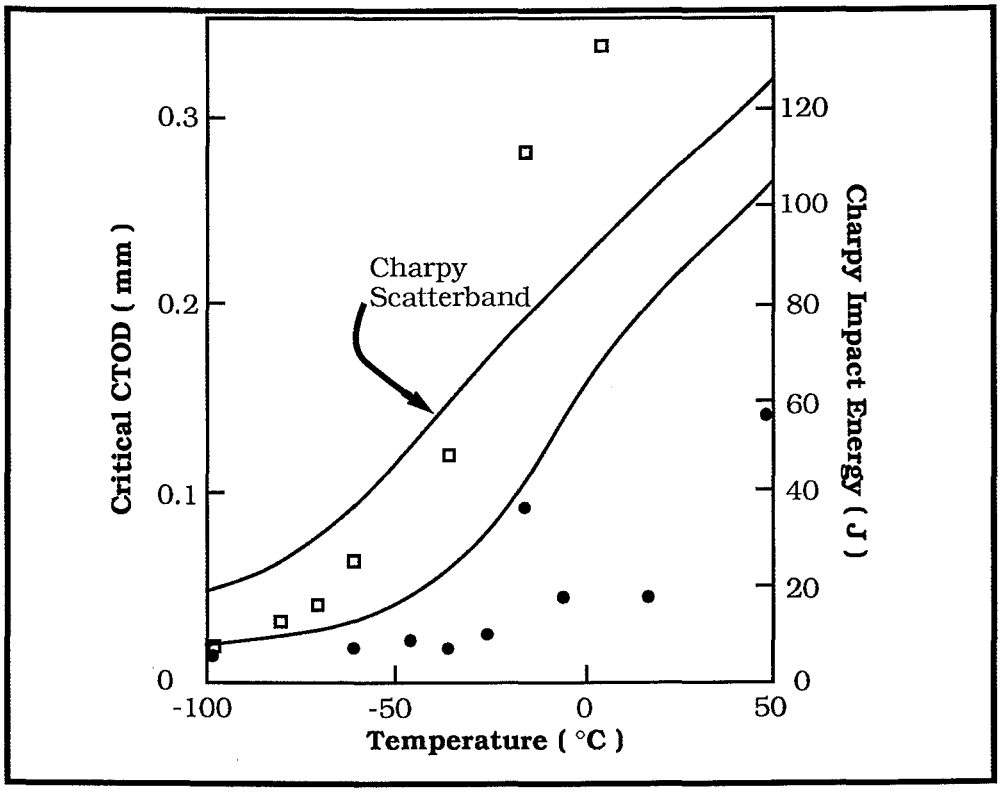

Figure 2.9b : Static and Dynamic Fracture Toughness of Weld Metal; □-Static CTOD, ●- Dynamic CTOD[123].

Results of the change in fracture toughness as a function of change in strain rate are shown in Figure 2.9a and results of the change in fracture toughness as a function of temperature in Figure 2.9b [122,123]. From Figure 2.9a an order of magnitude increase in loading rate results in a 10% decrease in K_{IC}. At very high crack speeds an adiabatic condition may exist ahead of the crack tip and heat generated by plastic flow cannot be dissipated quickly enough into the bulk of the specimen and the apparent fracture toughness may rise. The results of Sumpter and Caudrey in Figure 2.9b show that dynamic loading substantially increases the fracture mode transition temperature, so that the significant effect is not the increase in apparent fracture toughness but the increase in transition temperature.

There isn't a standard method for plane-stress fracture toughness (K_c) testing. However the engineering approach of Feddersen is suited to practical use. It considers the residual strength diagram for a thin plate under plane stress with a central crack $2a_0$ loaded in tension. The plane stress fracture toughness test is detailed elsewhere [63,124].Experimental tests for K_c are conducted with material thicknesses the same as to be used in service and are conducted with centre-cracked panels where stress intensity factors are well defined.

2.1.8 R-CURVE DETERMINATION

A significant limitation on K_c and K_{IC} testing is that the effect of slow stable crack growth is not properly characterised. For plane stress and intermediate plane stress-plane strain conditions the crack resistance R of the material is no longer constant. Instability is preceded by a certain amount of slow stable crack growth and the energy balance approach to this is illustrated in Figure 2.10a. This shows that for instability to occur it is necessary that $G = R$ and $\partial G/\partial a = \partial R/\partial a$, the second condition being a result of assuming a rising R-curve. It is found that an invariant R-curve has the following results:

(i) Initiation of crack growth is independent of initial crack length (a_0),

(ii) Instability depends on a_0 and hence on the total crack length (a) since an increase in a_0 results in more stable crack growth and a higher value of G at instability.

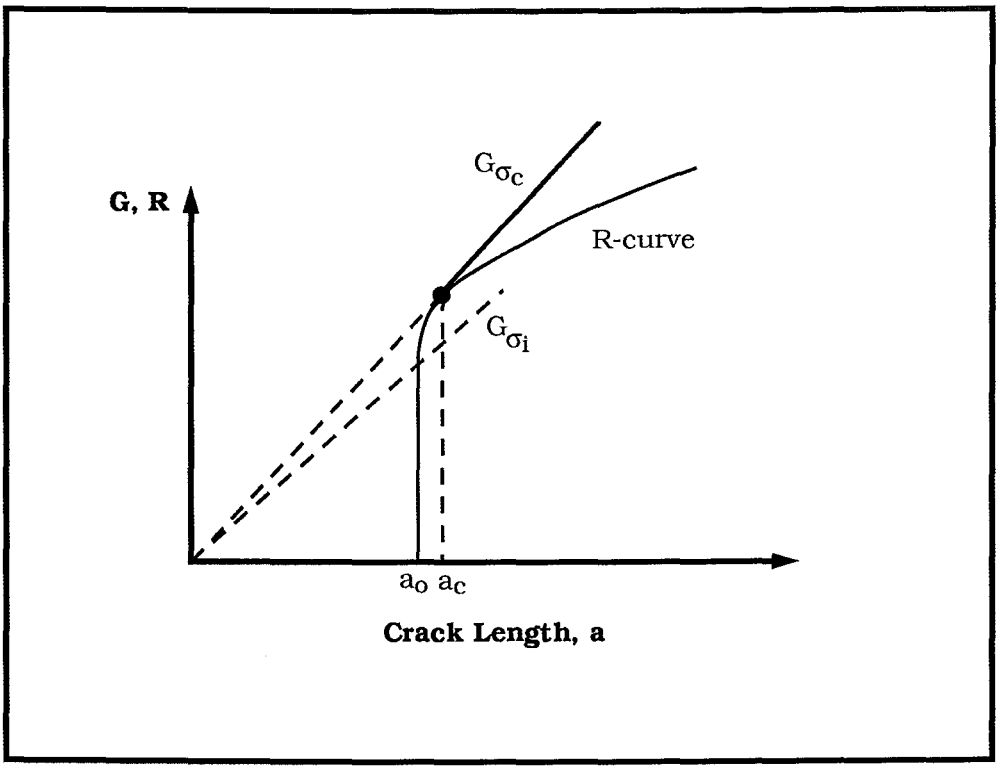

Figure 2.10a : Schematic of the rising R-curve.

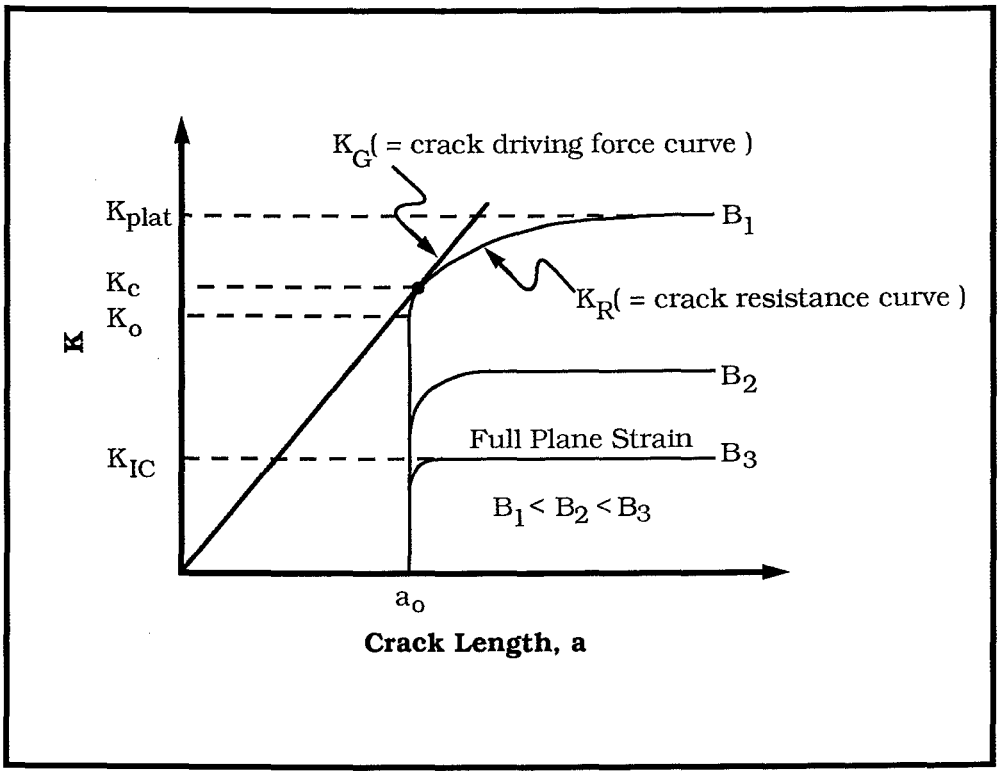

Figure 2.10b : Schematic of the R-curve in terms of the stress intensity factor.

In practice the R-curve is not considered in terms of G and R. The stress intensity factors K_c and K_R are used since the stress intensity approach is widely used in toughness testing and $K^2 = E'G$. Figure 2.10b shows three important points:

(i) K_o is the point of critical crack extension.

(ii) K_c is the critical stress intensity at instability.

(iii) K_{plat} is the plateau level of the K_R curve.

Figure 2.10b also shows the family of curves for specimens of decreasing thickness with the same initial crack length. The thinner the specimen the higher the value of K_c which Krafft *et al.* explained in terms of the model of shear lip size as [125]

$$R = \frac{dW_s}{dA}(1-S) + \frac{dW_p}{dV}\frac{BS^2}{2} \qquad (2.55)$$

where dW_s/dA = energy consumption rate for plane strain per unit surface area,

dW_p/dV = energy consumption rate for plane stress per unit volume,

S = fraction of specimen, thickness B, in plane stress,

(1-S) = fraction of specimen in plane strain.

When plane strain predominates (i.e. S = 0) then $K_c = K_o = K_{IC}$.

The American Society for Testing and Materials published a recommended practice for R-curve determination in 1976 and a standard followed in 1981 [126]. Three types of specimen are recommended: the centre-cracked tension specimen, the compact tension specimen and the crack line wedge-loaded specimen. Generally the specimens have a thickness representative of the plates considered for service application.

For the majority of situations where LEFM can be applied plane-stress fracture toughness testing (the Feddersen Method) is more simple to use and only if knowledge of slow stable crack growth is needed will the R-curve technique be used.

Many structural materials have high toughness and low yield strength and, for valid K_{IC} tests, thicknesses of up to 1 metre can be required, or else a very low test temperature. Similarly testing for K_c using plate specimens can be prohibitive; therefore a different concept is required.

2.2 *Elastic-Plastic Fracture Mechanics (EPFM)*

The methods used in elastic-plastic fracture mechanics extend the description of fracture behaviour beyond the elastic region but they too have limitations. Figure 2.11 shows the idealised ranges of applicability of LEFM and EPFM. This shows that there is some overlap between LEFM and EPFM. EPFM cannot treat general yield leading to plastic collapse, and general yield will not be dealt with since it is outside the area of interest. Using EPFM crack initiation is able to be predicted using one or two parameters. Of the concepts available to do this the most widely accepted are the J-integral and the Crack-Tip Opening Displacement (CTOD) methods, although other methods, such as the equivalent energy method, are available.

The J-integral concept has been developed primarily in the United States of America as a fracture criterion for materials used in the power generating industry. In this application the difference between material behaviour in the laboratory and actual structures will be small. The J-integral will not account for local differences in behaviour of materials, for example in welded joints. The crack-tip opening displacement was developed primarily by the Welding Institute in Britain to characterise the crack-tip region's strain field of weldments for a certain set of conditions.

The limitations of LEFM were recognised reasonably early in its development and the research and development of J-integral and CTOD test procedures has occurred from the early 1960's up to the present date. The following discussion will consider the J-integral and CTOD concepts and briefly include assessments of other methods.

2.2.1 THE J-INTEGRAL

This concept is based on an energy balance approach, first introduced by Rice [33]. Equation (2.10)

$$U = U_o + U_a + U_\gamma - F$$

remains valid as long as behaviour remains elastic, it need not be linear. Therefore nonlinear elastic behaviour can be used to model plastic behaviour of a material. If equation (2.10) is rewritten as

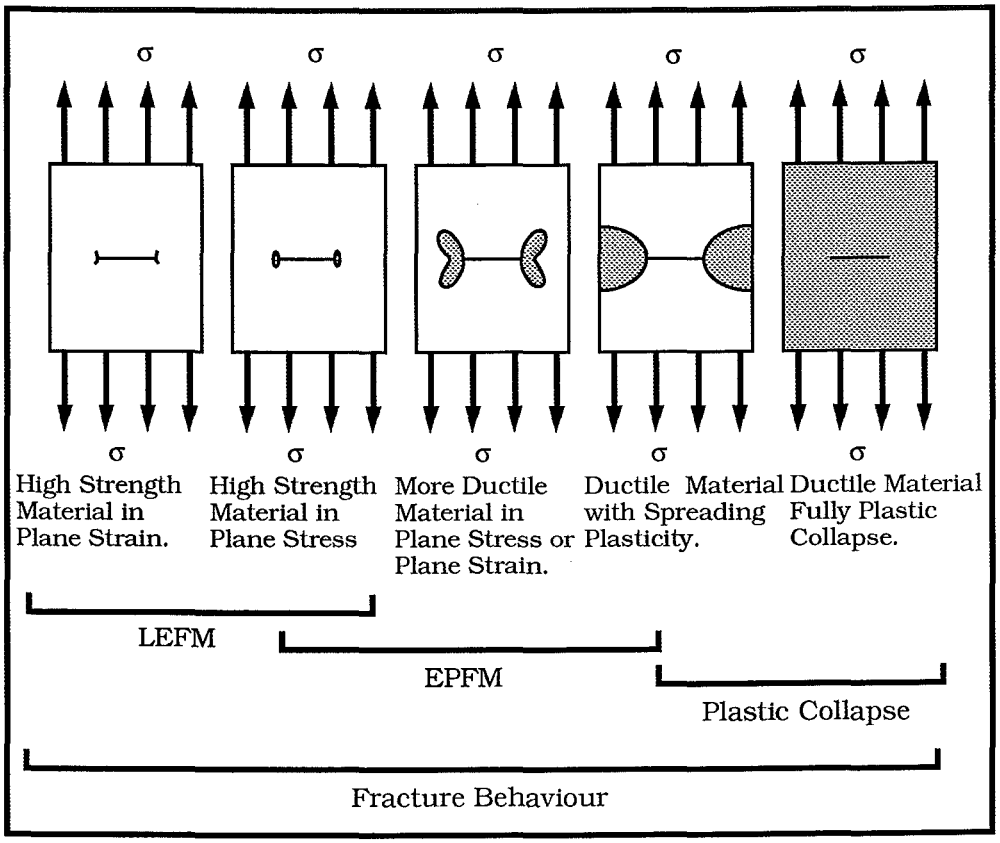

Figure 2.11 : The ranges of applicability of LEFM and EPFM to describe fracture behaviour.

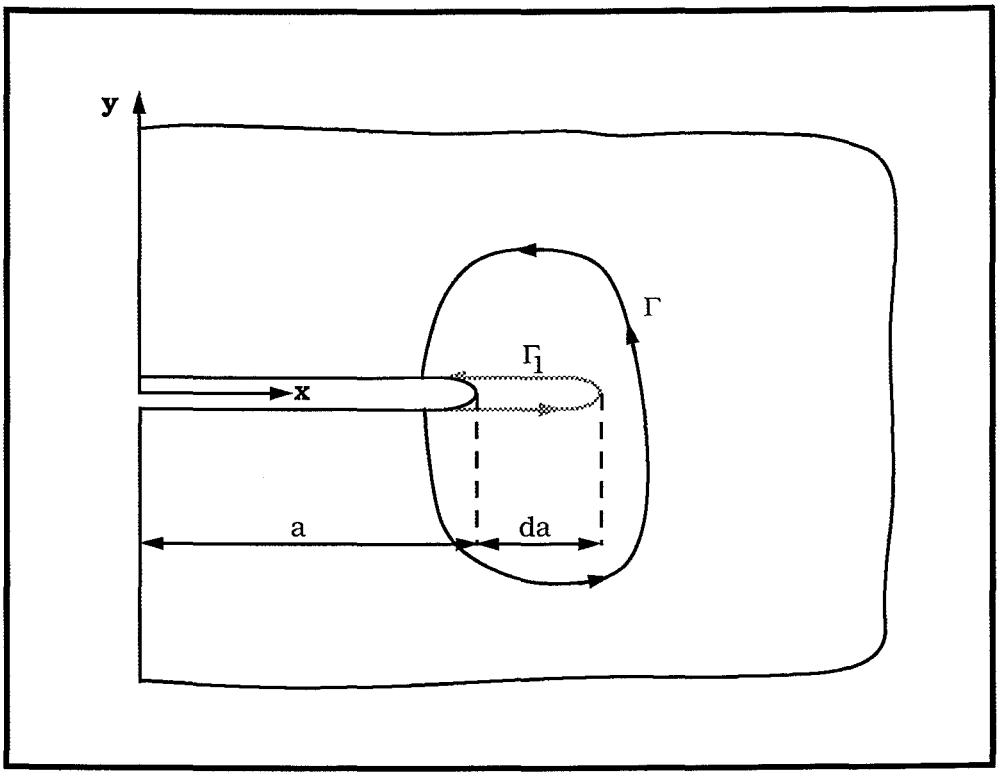

Figure 2.12 : The J-integral; the relationship between the change in potential energy and the line integral[33].

$$U = U_p + U_\gamma \tag{2.56}$$

where U_p is the potential energy containing all energy terms contributing to nonlinear elastic behaviour,i.e.

$$U_p = U_o + U_a - F, \tag{2.57}$$

then the condition for instability is

$$\frac{dU_p}{da} \geq \frac{dU_\gamma}{da} \tag{2.58}$$

and the nonlinear elastic equivalent of G is J where

$$J = \frac{-dU_p}{da}. \tag{2.59}$$

This is the rate of release of stored energy of the material and is the crack driving energy. Equation (2.59) is expressed as a path independent line integral (as shown in Figure 2.12) given by Rice as [33]

$$J = \int_\Gamma \left(W dy - \mathbf{T}\frac{\partial \mathbf{u}}{\partial x} ds \right) \tag{2.60}$$

where W is the total strain energy density, **T** is the traction vector acting on the arc length ds, and **u** is the displacement vector. Γ is any contour anti-clockwise from the lower to the upper crack face. The assumption of non-elastic behaviour is compatible with actual material behaviour only if no unloading occurs in any part of the material. When crack growth occurs the material is unloaded at the crack tip and therefore the J-integral principle is applicable only up to the beginning of crack extension; therefore it is expected that there is a critical material parameter J_c which predicts the onset of crack growth.

Since J = G for the linear elastic case then

$$J = G = K^2/E' \tag{2.61}$$

where E' = E for plane stress and E' = $E/(1-\nu^2)$ for plane strain. However J has been developed with no effects of strain in the through thickness direction taken into account and it is strictly valid only in the case of plane strain.

2.2.2 J-INTEGRAL TESTING

Testing for critical values of J involves a large amount of data analysis. ASTM introduced a standard for J_{IC} testing in 1982 as ASTM E813; a later revision is referenced [39]. ASTM has also introduced a standard for determining J-R curves (ASTM E1152), which are an analogy with R-curve testing [40]. Chipperfield summarised J estimation procedures in 1978 and these are presented in Table 2.1 [127].

Table 2.1
Summary of J Estimation Procedures

Method	J-Integral	Equation Number	Reference Number
1	$J = \frac{-1}{B}\left(\frac{\partial U}{\partial a}\right)_{\Delta}$	(2.62)	34
2	$J = \frac{-1}{B}\left[\frac{\partial(\int P d\Delta)}{\partial a}\right]_{\Delta}$	(2.63)	128
3	$J = \frac{2U}{B(W - a)}$	(2.64)	129, 130
4	$J = J_e + J_p$		35
	$= [\eta_e U_e/(W-a)B] + [\eta_p U_p/(W-a)B]$	(2.65)	
5	$J = [2/B(W-a)][(n_1 P\Delta) + (n_2 U)]$	(2.66)	133
6	$J = \frac{(P\Delta - 2U_{nc})}{B(W - a)}[1 + \alpha(P/P_{max})^2]$	(2.67)	129
7	$J = J_e + J_p$	(2.68)	
	where $J_e = (PY/BW^{1/2})^2(1/E')$	(2.69)	35
	and $J_p = \frac{2P}{B(W-a)}\left[\frac{W}{a + r(W-a) + z}\right](V-V_e)$	(2.70)	
	and $r = 0.45$ for $a/W \leq 0.45$		
	$r = 0.40$ for $a/W > 0.45$		
8	$J = [\eta_e U_e/B(W-a)] + [U_p/B(W-a)]$	(2.71)	127
9	$J = (K^2/E') + (2U_p - P\Delta_i)/B(W-2a)$	(2.72)	129
	where $K = (P/2BW)(\pi a \sec(\pi a/W))^{1/2}$	(2.73)	

(a) Method 1

Begley and Landes proposed the original method for J_{IC} determination [34]. It was a multiple-specimen technique where load-displacement diagrams are obtained for a number of specimens of different crack lengths. A graph is prepared of energy per unit thickness (U- the area under the load-displacement curve) versus the crack length at different displacements. Taking the slope of these graphs ($\partial U/\partial a = J$) then J-displacement calibration curves can be prepared for particular crack lengths. Knowing the displacement (v) at the onset of crack extension enables J_{IC} to be found from the J-v calibration curve for each initial crack length. Although there are now easier methods available this is used as a reference check for more recent methods.

(b) Method 2

A numerical technique was proposed by Bucci *et al.* [128]. The basis of the technique involved measuring the load-load point displacement curve for the specimen and then J was calculated using known compliance functions for the specimen geometry, plastic zone correction factors and slip-line field predictions for the collapse load of the specimen.

(c) Method 3

Analysis by Rice *et al.* and by Landes and Begley led to the much simpler equation (2.64), $J = 2U/B(W-a_0)$, for a specimen subject to bending [129,130]. Rice *et al.* found that in a deeply cracked bar subject to bending then

$$J = \frac{2}{B(W-a)} \int_0^{\theta_c} M d\theta_c = \frac{2}{B(W-a_0)} \int_0^{V_c} P dV_c \qquad (2.64a)$$

where θ_c is the contribution of the introduced crack to the total bending angle, M is the bending moment and V_c is the critical displacement. Effectively $J = 2U_c/B(W-a_0)$ where U_c is the area under the load-displacement curve due to the introduction of the crack. However in a J_{IC} test the total energy of the specimen is found where

$$U_t = U_c + U_{nc}, \qquad (2.64b)$$

U_t being the total energy and U_{nc} the energy of an uncracked specimen. However Landes and Begley showed that $U_{nc} << U_c$ so that

$$J = 2U_t/B(W-a_0) \tag{2.64}$$

where U_t is the total area under the load-displacement diagram [130]. Equation (2.64) applies to the single notched bend specimen but may be extended to the compact tension specimen using the compliance function f(a/W) where

$$f(a_0/W) = (1+\alpha)/(1+\alpha^2) \tag{2.74}$$

and $$\alpha = 2[(a_0/b_0)^2 + a_0/b_0 + 0.5]^{1/2} - 2(a_0/b_0 + 0.5) \tag{2.75}$$

and $b_0 = W-a_0$.

This gives for the CT specimen

$$J = 2U_t f(a_0/W)/B(W-a_0) \tag{2.76}$$

(d) Methods 4 and 7

These methods follow on from method 3. Sumpter and Turner give a more general form of equation (2.64) such that [35],

$$J = J_e + J_p \tag{2.68}$$

where $$J_e = [\eta_e U_e/(W-a_0)B] \tag{2.77}$$

and $$J_p = [\eta_p U_p/(W-a_0)B] \tag{2.78}$$

and the crack to width ratio a_0/W over which these can be used is from 0.2 to 0.7. U_p and U_e are the plastic and elastic energy components under the load-displacement curve, respectively, and η_p is approximately 2.0. The value of η_e is dependent on specimen geometry and the crack length to width ratio [127]. There is inconsistency between method 4 and method 3 in that results from method 4 can exceed those of method 3 by up to 30% [127]. Method 7, also from Sumpter and Turner, is an extension of method 4 for the

SENB specimen [35]. The method measures load versus crack mouth opening displacement and assumes rigid body rotation of the specimen after yield, thereby relating plastic clip gauge displacement to plastic load point deflection and J is given by equations (2.68) to (2.70) in Table 2.1.

(e) Methods 5, 6, 8 and 9

These methods are developments of the previously discussed methods and are relevant for a particular type of specimen. Merkle and Corten gave equation (2.66) for compact tension specimens where a_0/W is greater than 0.5 [133].

Equation (2.67) is given by Rice *et al.* in the same analysis as for method 3 [129]. It applies to the SENB specimen and if the uncracked energy of the beam is assumed to be negligible then equation (2.67) reduces to equation (2.64).

Methods 8 and 9 are the results of work by Bucci *et al.* (Method 8) and by Rice *et al.* (Method 9) on applying the J-integral to centre-cracked tension specimens [128,129].

Clarke *et al.* published a procedure in 1979 for determining the ductile fracture toughness (J_c), the value of J at the onset of crack growth [36]. Based on these methods the ASTM have adopted the formula,

$$J = J_e + J_p \tag{2.68}$$

where $$J_e = \frac{K^2(1-\nu^2)}{E} \tag{2.79}$$

and $$J_p = \frac{\eta A_p}{B(W-a)}. \tag{2.80}$$

A_p is the area under the load-displacement curve up to the plastic displacement component and represents the plastic energy of the cracked specimen and η is 2 for the SENB specimen and η is $2 + 0.522\,(W-a_0)/W$ for the CT specimen [39].

The size criteria for acceptance of J are

$$B, W-a_0 \geq 25J/\sigma_o \tag{2.81}$$

based on experience, but these criteria were originally proposed by Paris in the written discussion of Reference 34 as $B,W\text{-}a_0 > 50J/\sigma_0$. The flow stress ($\sigma_0$) is typically

$$\sigma_0 = {}^1/_2(\sigma_u + \sigma_{ys}) \tag{2.82}$$

and accounts for strain-hardening. Other restrictions on J were the number of acceptable experimental points plotted on J-crack extension diagram as shown in Figure 2.13. The 0.15 mm offset line accounts for apparent crack extension due to plastic blunting as load is applied and the 1.5 mm offset line is to limit the spread of the plastic zone in the specimen. ASTM E813-87 uses a similar method to this for determining J_{IC} [39]. The determination of the J-R curve as shown in Figure 2.13 is given by ASTM E1152-87 using a single specimen technique [40]. For J values that exceed the capacities defined by the standards then a modified version of J called J_M has been developed by Ernst [132]. The J parameter provides a lower bound for fracture mechanics and as such provides conservative values.

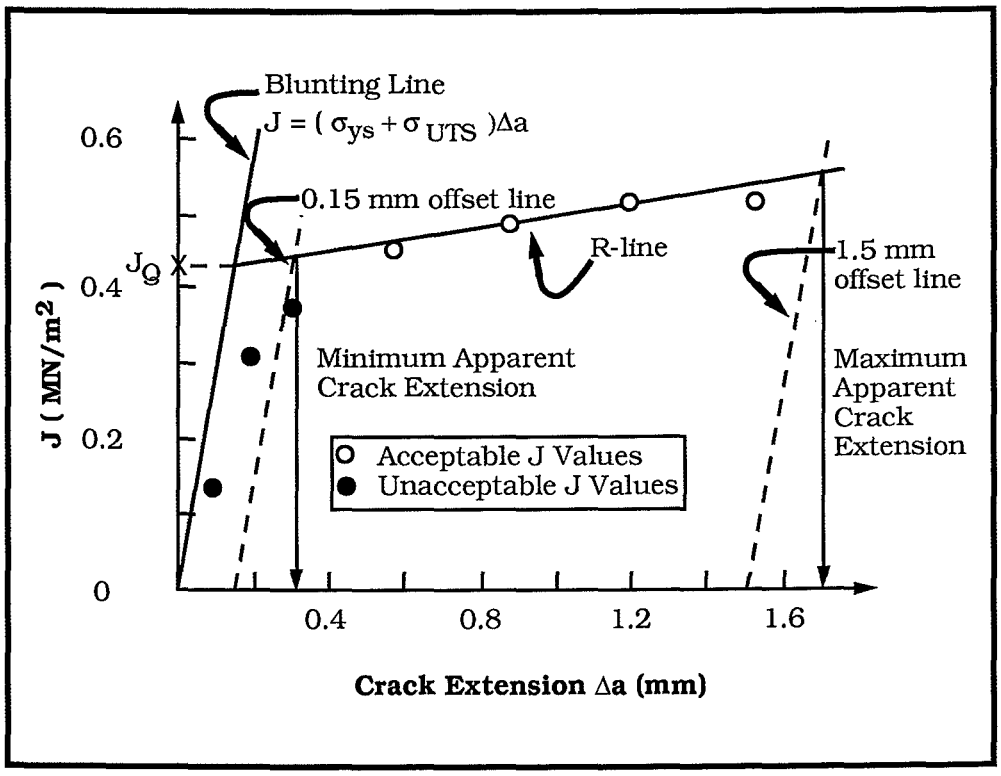

Figure 2.13 : Schematic of the J-Δa diagram showing acceptable J values and J_Q.

2.2.3 *THE CRACK-TIP OPENING DISPLACEMENT (CTOD)*

Both Wells and Cottrell considered the amount of crack opening prior to crack extension as a parameter to characterise the crack-tip region's strain field for a given set of conditions [25,26]. The crack-tip opening displacement can be found using the analysis of plastic zone size of either Irwin or Dugdale [112,114]. Wells, using Irwin's approach, showed that the CTOD is related to the critical crack extension force analogous to K_{IC}. Using equation (2.29) for crack flank displacement (developed using Westergaard's solution) in plane stress then

$$v = 2\sigma(a^2-x^2)^{1/2}/E. \tag{2.83}$$

The total displacement is $\delta=2v$, and from Figure 2.5, using Irwin's effective crack length for $x = a - r_y$ then

$$\delta_t = 4\sigma(a^2 + 2ar_y + r_y^2 - a^2)^{1/2}/E \tag{2.84a}$$

$$\approx 4\sigma(2ar_y)^{1/2}/E \tag{2.84b}$$

assuming $r_y << a$. Using equation (2.43) for r_y then

$$\delta_t = 4K_I^2/(\pi E\sigma_{ys}) = 4G/(\pi\sigma_{ys}) \tag{2.85}$$

which is an approximation for the CTOD. The fracture criterion is a critical value of the CTOD (δ_c).

Cottrell also used the CTOD concept to explain why small test specimens, cut from ship plate which had fractured by cleavage before general yield, failed in a ductile manner when tested at the same temperature [26]. Cottrell proposed that the plastic zone engulfed the whole cross-section of the small specimen before δ_c was obtained whereas in the large plate δ_c was obtained first and caused failure before general yielding.

The usual derivation of the crack opening displacement follows the analysis of Dugdale expanded on by Burdekin and Stone [27,114]. From Figure 2.6 the notional crack increment carries the yield stress of the material. The Dugdale approach uses a Westergaard-type function, which gives the final result as

$$a/(a+\Delta a_n) = \cos(\pi\sigma/2\sigma_{ys}) \tag{2.86}$$

which reduces to

$$\Delta a_n = \frac{\pi}{8}\left(\frac{K_I}{\sigma_{ys}}\right)^2 \tag{2.87}$$

The crack flank displacement between a and $a+\Delta a_n$ can be found using the stress functions used in the Dugdale analysis. Burdekin and Stone provided a solution for the crack flank displacement such that [27],

$$2v_t = \delta_t = \frac{8\sigma_{ys}a}{\pi E} \ln \sec\left(\frac{\pi\sigma}{2\sigma_{ys}}\right) \tag{2.88}$$

which is a starting point for most CTOD analyses. Hahn and Rosenfield reported similar results from their own analysis and that of Goodier and Field [133]. They also demonstrated the equivalence of the Bilby-Cottrell-Swinden model of yield around the crack tip and Dugdale's strip yield model [133]. Bilby *et al.* modelled the yield zone around the crack tip using arrays of dislocations, considering Mode III tearing by screw dislocations and Mode II shear to be by edge dislocations [134].

When $\sigma << \sigma_{ys}$ then equation (2.88) may be expanded by McClaurin's series to give

$$\delta_t = \frac{8\sigma_{ys}a}{\pi E}\left\{\frac{1}{2}\left(\frac{\pi\sigma}{2\sigma_{ys}}\right)^2 + \frac{1}{12}\left(\frac{\pi\sigma}{2\sigma_{ys}}\right)^4 + \ldots\right\} \tag{2.89a}$$

from which only the first term needs to be considered since $\sigma << \sigma_{ys}$. Therefore,

$$\delta_t\sigma_{ys} = \pi\sigma^2 a/E. \tag{2.89b}$$

When $\sigma << \sigma_{ys}$ then LEFM conditions will apply, which for a centre-cracked infinite plate in plane stress conditions gives,

$$G = \pi\sigma^2 a/E. \tag{2.40}$$

This implies

$$G = \sigma_{ys}\delta_t \tag{2.90}$$

which is usually written as

$$G = M\sigma_{ys}\delta_t. \tag{2.91}$$

M is a plastic stress intensification factor to account for different stress states, specimen geometries and work hardening. The value of M varies from 1 for conditions of plane stress and relaxation around the crack tip and non-work hardening materials, to 2 where the crack tip is highly constrained [28-31]. Sailor did show that M could reach 3.5 for material with a very high strain hardening index [85]. However theoretical treatments expect M to vary between 1 and 2 [32]. Pratap and Pandey found that M in the G-CTOD relationship appeared to be a function of the yield strength of the specimen and loading geometry under plane strain conditions of loading; their results indicated M had a range of 0.48 for high yield strength steel (σ_{ys} = 2104 MPa) to 0.84 for low yield strength steel (σ_{ys} = 404 MPa) which they felt needed further investigation [135]. They felt the failure of equation (2.91) to account for plastic zone size may explain the low values of M. A further study gave M as high as 1.61 [136].

Chew demonstrated the relationship could be written as

$$K_I = (E'M\sigma_{ys}\delta_c)^{1/2} \tag{2.92}$$

where $1 \leq M \leq 2$ and $E' = E$ for plane stress and $E' = E/(1-\nu^2)$ for plane strain [16]. Using $E = 207 \times 10^3$ MPa and $\nu = 0.3$ for steel Chew wrote equation (2.92) as

$$K_{IC} = 0.4769\ (\sigma_{ys}\delta_c)^{1/2} \tag{2.93}$$

for the conservative case of M = 1. Therefore it appears that the CTOD concept can provide an alternative to the K_{IC} test when $\sigma << \sigma_{ys}$, and can tolerate substantial yielding as well. However Lai reported that CTOD overestimated K_{IC} by as much as 2.5 times when using CTOD values as found using BS5762:1979 [41,137]. Lai

suggested that this was due to the rotational constant, used in the calculation of the critical CTOD, which would be too large when plasticity is limited [137]. Although others have used equation (2.92) successfully the relationship needs to be used with care [16,29,30].

The CTOD concept was extended to the post yield failure regime by Heald *et al.* [138]. Using miniature tensile specimens that were elements of the relaxed zone at the crack tip then Heald *et al.* reasoned that the specimens fail (and crack growth occurs) at σ_u, the ultimate tensile stress of the material. Using σ_u in equation (2.88) and assuming plane strain conditions, the fracture stress is

$$\sigma_F = \frac{2}{\pi}\sigma_u \cos^{-1} \{\exp - \left(\frac{\pi K_{IC}^2}{8\sigma_u^2 a}\right)\}. \qquad (2.94)$$

Equation (2.94) seems to describe conditions from LEFM to general yielding.

2.2.4 CTOD TESTING

The major disadvantage of the CTOD approach is that equation (2.88) is valid only for an infinite plate and it isn't possible to derive similar formulae for practical geometries. It seems, therefore, that the value of CTOD at the onset of fracture can be used to compare the fracture resistance of materials but not to calculate a critical crack length in a structure. However testing for and calculating the CTOD is relatively simple.

(a) Development of the CTOD test

Initially CTOD testing was carried out using test pieces that were notched but not fatigue cracked. Notches were prepared using a jeweller's saw or a slitting wheel and the CTOD was directly measured using a paddlemeter [27]. Another technique was to use double-notched specimens which were fatigue cracked and then fractured. The critical CTOD was found by metallographic sectioning of the pre-cracked notch that didn't fracture [139].

It was appreciated, however, that use of a fatigue crack was essential so that:

(i) the notch would match an actual crack in a structure, and

(ii) to try and maintain continuity with the K_{IC} test. Fatigue precracking means that the critical CTOD is inferred from measurements made at the crack mouth. The CTOD test was

developed primarily by the British Welding Institute, and a draft for development DD19 on CTOD testing was published in 1972 by the British Standards Institute, and a standard BS5762 followed in 1979 [41,140]. Also BS PD6493 published in 1980 gave some guidance for acceptance of defects in welds using CTOD results [54]. The British standard for the CTOD test uses the SENB specimen although the ASTM standard E1290-89 for CTOD testing gives methods of testing for SENB and CT specimens [44].

The standard technique to measure CTOD uses a clip-gauge extensometer to measure the opening at standard knife-edges mounted on a specimen; the amount of opening is called the crack mouth opening displacement (CMOD). The relationship between the CMOD and the CTOD can be found either experimentally or theoretically [141]. Figure 2.14 shows a rigid specimen rotating about a neutral axis (which is a sliding plastic hinge). The crack-tip opening displacement is then given by

$$\delta_t = \frac{V_g r b}{rb + a + z} \tag{2.95}$$

where V_g is the crack mouth opening displacement, b = (W-a), the length of uncracked ligament, r is the rotation factor, a is the total crack length and z corrects for the position of the clip gauge above the surface of the specimen. Although this equation is very simple there are two difficulties with it;

(i) the value of the rotation factor r varies significantly depending on the degree of plasticity ahead of the crack tip and on the specimen geometry. Initially r is very small and lies close to the crack tip as the specimen is loaded but the hinge point shifts away from the crack tip as yielding occurs around the crack tip and r increases. Green and Hundy gave r = 0.5 as a constant value when extensive yielding had occurred [142]. Values of r are given in Table 2.2, and these values vary from 0 to 0.654 (depending on whether it is an experimental or a theoretical result). The original draft for development DD19:1972 used the experimental value of r = 0.33 for SENB specimens but this was increased to r = 0.4 in BS5762:1979 [41,140]. Matsoukas *et al.* showed that r could be given by

$$r_p = 0.463 - 0.04\ (a/W) \tag{2.96}$$

from slip-line field theory which indicated r_p should be increased to at least 0.46 [143]. The difference in r values will give a 5 to 10 percent difference in CTOD measurements.

The ASTM standard E1290-89 recommends that

$$r_p = 0.4(1 + \alpha) \tag{2.97}$$

where for SENB specimens $\alpha = 0.1$ and $r_p = 0.44$ and for CT specimens,

$$\alpha = 2[(a_o/b_o)^2 + a_o/b_o + 0.5]^{1/2} - 2(a_o/b_o + 0.5). \tag{2.98}$$

This gives $r_p = 0.47$ for $0.45 \leq a_o/W \leq 0.50$
and $r_p = 0.46$ for $0.50 < a_o/W \leq 0.55$ [44].
The factor α is based on analysis by Merkle and Corten although their analysis would give $r = 0.5\ (1+\alpha)$ for the compact tension specimen [131]. Wu *et al.*, after theoretical analysis, showed that the errors in r could be substantial if the Ramberg-Osgood strain-hardening index of the material was less than 5 [144]. They provided slip-line field analytical solutions for the SENB and CT specimens but for $N \geq 5$ the values in the ASTM standard can be used [144].

(ii) Interpretation of the clip gauge displacement (V_g). The increase in V_g is due to elastic opening of the crack and rotation about the plastic hinge. Therefore the clip gauge displacement V_g must be separated into an elastic component V_e and a plastic component V_p as shown in Figure 2.15. The respective "elastic" CTOD and "plastic" CTOD components can then be calculated from V_e and V_p given as

$$\delta_t = \delta_e + \delta_p \tag{2.99a}$$

where $$\delta_e = K_I^2(1-\nu^2)/2\sigma_{ys}E \tag{2.99b}$$

and $$\delta_p = \frac{V_p r_p(W-a_0)}{r_p(W-a_0) + a_0 + z}. \tag{2.99c}$$

δ_t represents the displacement at the original fatigue crack tip. Included in δ_e is a plastic constraint factor M=2 as discussed for equation (2.92).

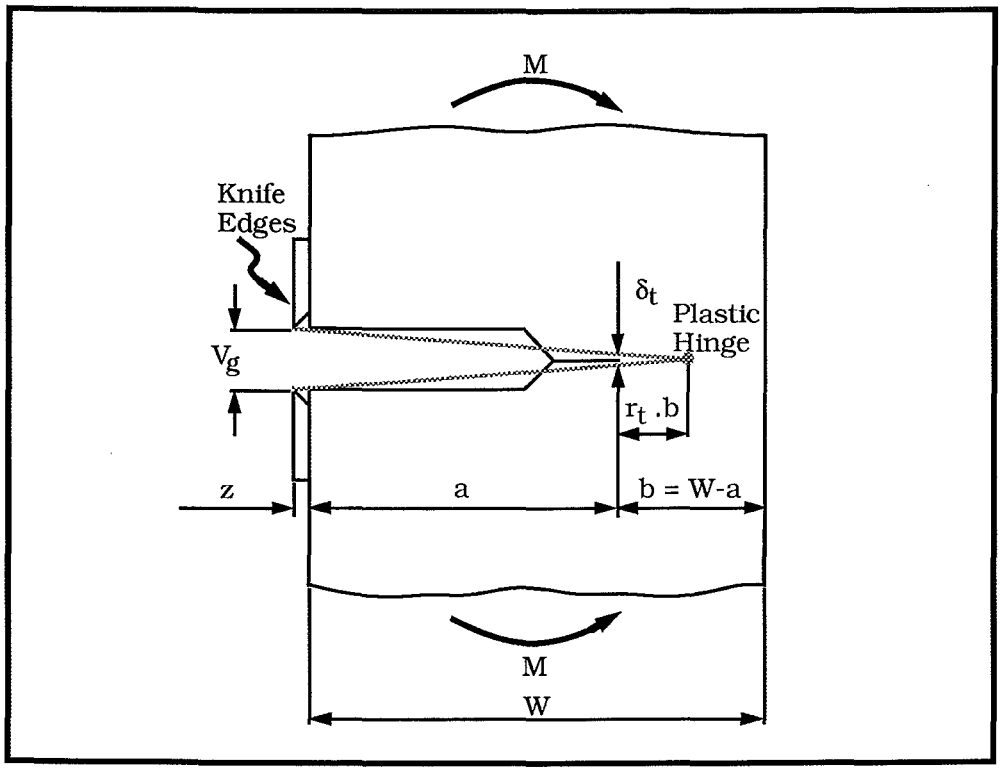

Figure 2.14 : Geometrical relationship between Clip Gauge Displacement (V_g) and CTOD (δ_t).

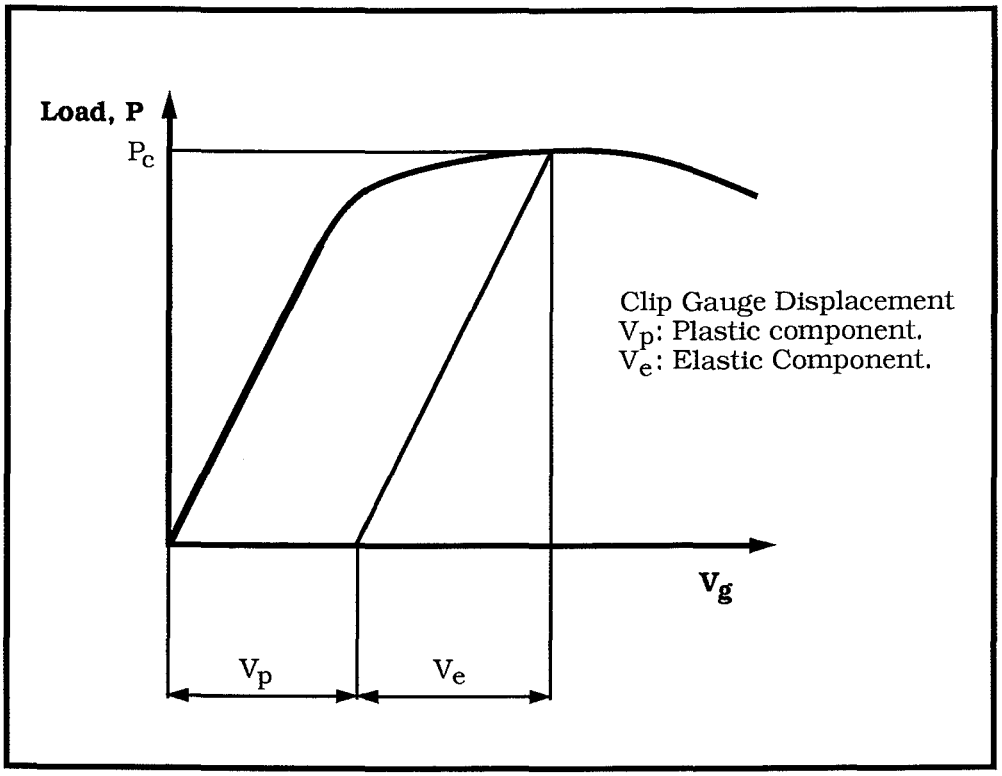

Figure 2.15 : Schematic of a load-displacement record showing elastic and plastic components of clip gauge displacement.

Table 2.2
Variation in the rotation factor, r_p

Reference	Value of r_p	Derivation	Specimen
140	0.33	Experimental	SENB
145	0.45	Slip-line Field Theory	SENB
37	0.4	Experimental	SENB
141	$0.1 < r_p < 0.4$	Experimental	SENB
	0.33	Adopted	SENB
44	0.44	Slip-line Field Theory	SENB
	0.46, 0.47		CT
29	$0.125 < r_p < 0.397$	Experimentally based $0.025 \leq \delta \leq 0.255$ $r = A_0+A_1\delta+A_2\delta^2+A_3\delta^3$	SENB
142	0.5	Slip-line Field Theory	SENB
144	$0.306 < r_p < 0.556$	Slip-line Field Theory	SENB
	$0.308 < r_p < 0.654$	$2 < n < \infty$ $^1/_4 < a/W < 7/8$	CT
135	$0 < r_p < 0.18$	Experimental	SENB
153	$0 < r_p < 0.6$	Theoretical	SENB
143	$0.455 < r_p < 0.439$	Slip-line Field Theory	SENB

In BS DD19:1972 δ_t was calculated on the basis of work by Wells [140,145]. For SENB specimens this gave

$$\delta_t = \frac{0.45(W-a_0)}{0.45\,W + 0.55a_0 + z}\left[V_g - \frac{\gamma\sigma_{ys}W}{E'}\right] \qquad (2.100)$$

for $$V_g \geq 2\,\frac{\gamma\sigma_{ys}W}{E'} \qquad (2.101)$$

and $$\delta_t = \frac{0.45(W-a_0)}{0.45\,W + 0.55a_0 + z}\left[\frac{V_g^2 E'}{4\gamma\sigma_{ys}W}\right] \qquad (2.102a)$$

for $$V_g < \frac{2\gamma\sigma_{ys}W}{E'}. \qquad (2.102b)$$

Also $E' = E/(1-\nu^2)$ and γ is a non-dimensionalised limiting value of elastic clip gauge displacement [140]. This was replaced in the standard BS5762 by the formula proposed by Dawes [37],

$$\delta = \delta_e + \delta_p = \frac{K^2}{2\sigma_{ys}E'} + \frac{0.4(W-a_0)}{0.4\,W + 0.6a_0 + z}V_p \qquad (2.103)$$

where $r_p = 0.4$ and $E' = E/(1-\nu^2)$. The general form of this equation is that of equation (2.99a-c). Although calculation of δ_t generally represents CTOD at the original crack tip as proposed by Dawes *inter alia*, Rice proposed the displacement at points subtending an angle of 90° at the current crack tip as the CTOD [33,37].

Pratap and Pandey tried to avoid using the rotational factor r_p and presented the CTOD as,

$$\delta_t = V_g/\{1+[\left(\frac{a+z}{a}\right)\left(\frac{1+R/2a}{(R/a + (R/2a)^2)^{1/2}} - 1\right)]\} \qquad (2.104)$$

where $$R = \frac{1}{\pi M'}\left(\frac{K_I}{\sigma_{ys}}\right)^2 \qquad (2.105)$$

and R represents the plastic zone size where M' is the plastic constraint factor [135]. Pratap and Pandey have shown M' to vary considerably with a/W ratio (a deeper crack induces more plastic constraint), with loading geometry (CT specimens show higher constraint) and with specimen thickness (increasing thickness increases the constraint) [136].

Kolednik also provides a different procedure for calculation of CTOD from clip gauge displacement for CT and SENB specimens [146,147]. Kolednik wrote that CTOD should be calculated from either equations (2.99b) or (2.99c) but not both, i.e. $\delta_t = \delta_e$ for no yielding or $\delta_t = \delta_p$ for yielding, when using the Dawes formula. Therefore, using the Dawes formula would give non-conservative CTOD values especially when δ_e was approximately the same as δ_p.

Kolednik presented results of his work and that of Fields and Miller to show r_p attains a value of 0.6 [146,148]. A new method for calculating CTOD using experimentally determined values of r_p found during loading is given by Kolednik [146,147]. There is, however, a misinterpretation of the definition of the factor r_p in this analysis with regard to the Dawes formula. Figure 2.16 shows the definition of the overall and plastic rotation factors as considered by Kolednik [146]. For the definition of V_p in Figure 2.16 the plastic hinge shifts towards the crack front from infinity to $r_p b$ as V_p increases and plastic collapse is approached. Therefore r_p decreases from ∞ to 0.6 as found by Kolednik [146].

Therefore, knowing r_p at a particular load, the CTOD can be calculated and the elastic component is not needed for calculation,

$$\delta_t = \frac{V_p(W-a)r_p}{r_p(W-a) + a + z} \qquad (2.106)$$

where $0.6 \leq r_p < \infty$. However both the formula of Wells and that of Dawes are based on total clip gauge displacement (V_t) where an overall rotational factor (r_t) increases from zero at $V_t = 0$ up to a constant value at plastic collapse; the plastic hinge continually moves away from the crack tip. Therefore both Wells' and Dawes' formula are based on equation (2.95),

$$\delta_t = \frac{V_g r b}{rb + a + z},$$

which can be split into elastic and plastic components.

$$\text{Therefore } V_g = V_e + V_p \qquad (2.107a)$$

as from Figure 2.15 and

$$\delta_t = \frac{V_e r_t b}{r_t b + a + z} + \frac{V_p r_t b}{r_t b + a + z}. \qquad (2.107b)$$

Provided r is known at all states of loading then equations (2.107a-b) could be used to find the CTOD. However the elastic component is given by the relationship between CTOD and LEFM so that $\delta_e = K_I^2(1-\nu^2)/2\sigma_{ys}E$ as in equation (2.99b), where K_I is found from the load of interest. The overall rotation factor therefore only applies to the

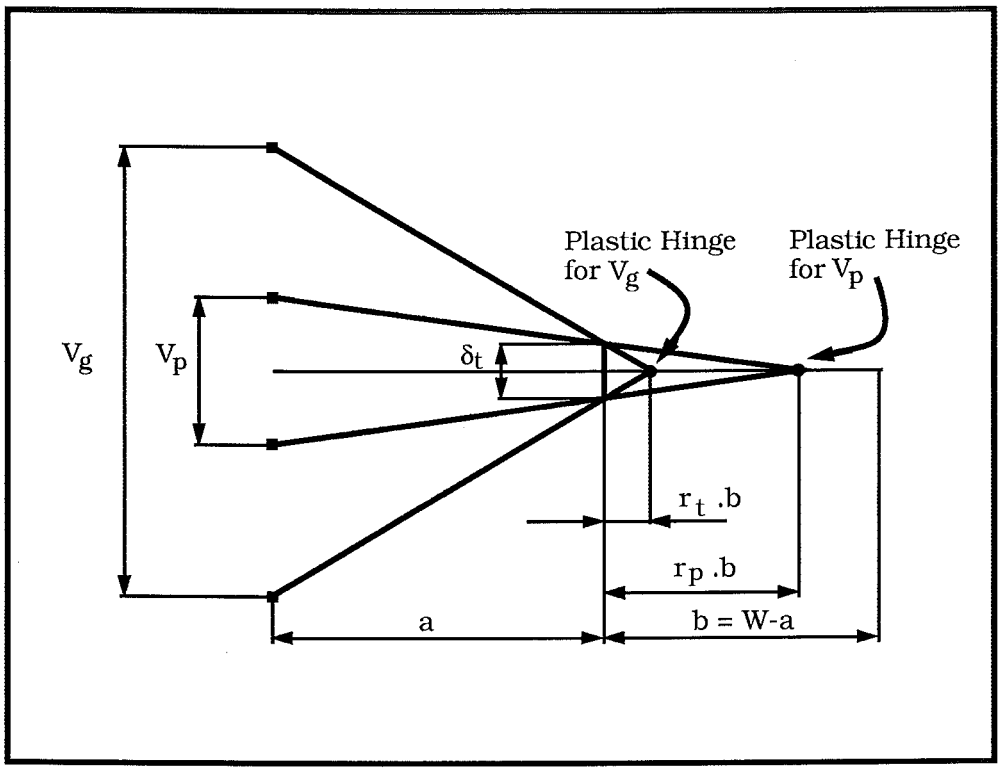

Figure 2.16 : The overall and the plastic rotation factor as discussed by Kolednik[146].

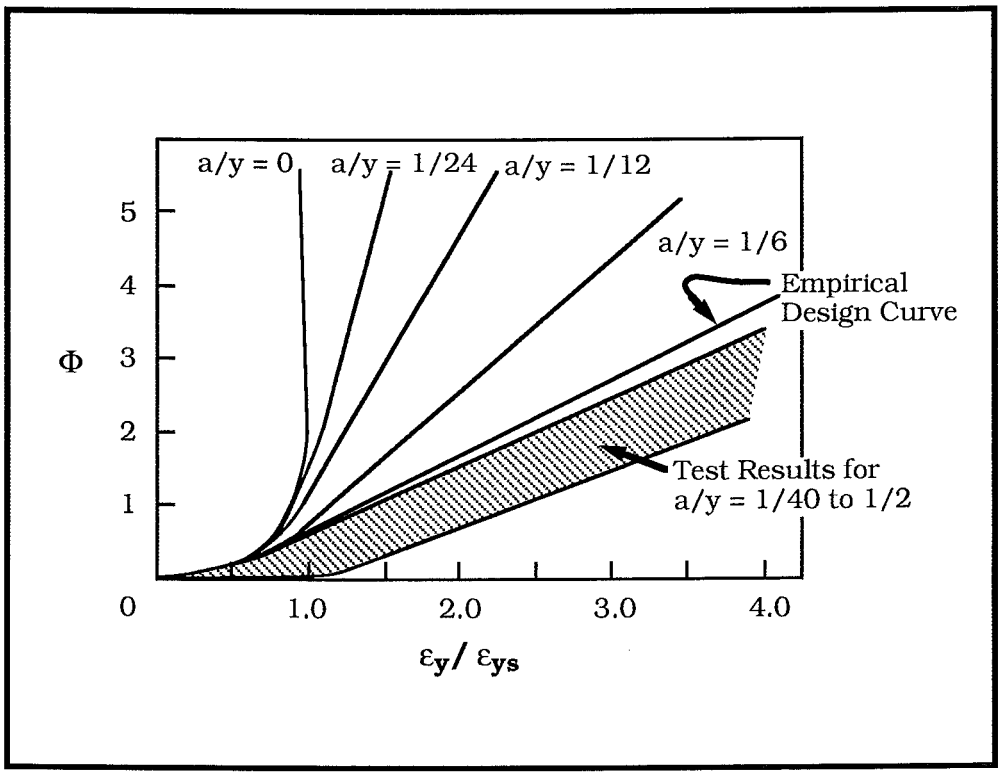

Figure 2.17 : The analytical and experimental COD design curve[63].

plastic component of clip gauge displacement. The value which r_t approaches at plastic collapse is called r_p, the rotational factor at plastic collapse [149]. Wells used a value of $r_p = 0.45$ based on slip line field theory whereas Dawes used $r_p = 0.4$ based on experimental work [37,145]. Therefore the accepted analyses and that of the Kolednik method approach a constant value of r_p but from opposite sides of the plastic collapse hinge. More importantly the approach of Dawes provides a simple formula to calculate CTOD which can be used over all materials.

(b) The CTOD Design Curve

The critical CTOD for a structure or a material can be obtained. The next step is to be able to use this information to assess defects and safety of structures. BS PD6493:1980 provides guidelines on assessments of weldments [54]. To assess the performance of a structure the COD design curve has been developed. The CTOD is made dimensionless such that

$$\Phi = \frac{\delta_t E}{2\pi\sigma_{ys}a} = \frac{\delta_t}{2\pi\varepsilon_{ys}a} \qquad (2.108)$$

where ε_{ys} is the elastic strain at yield. The strain over a certain distance in a cracked plate is determined from a non-singular stress function and a plot is made of Φ against relative strain $\varepsilon/\varepsilon_{ys}$ (Figure 2.17). The intention was to provide a design curve for each a/y value so that once the critical COD was known from specimen tests the maximum permissible strain in a cracked structure could be predicted. However empirical data showed no dependence on a/y and all data fell in a single scatterband. The analytical solution appears to hold only up to $\varepsilon/\varepsilon_{ys} \approx 0.5$. The final design curve is an empirical one which predicts conservative results. From the work of Dawes the final assessment is given by [51],

$$a_{max} = \frac{\delta_{t\ crit} E \sigma_{ys}}{2\pi\sigma_1^2} \qquad \text{for } \sigma_1/\sigma_{ys} < 0.5 \qquad (2.109a)$$

and

$$a_{max} = \frac{\delta_{t\ crit} E}{2\pi(\sigma_1 - 0.25\sigma_{ys})} \qquad \text{for } 0.5 < \sigma_1/\sigma_{ys} < 2 \qquad (2.109b)$$

where a_{max} is the maximum permissible crack size and σ_1 is the sum of all component stresses. The COD design curve was reviewed by

Dawes in 1980 [51]. A similar design curve for the J-integral was presented by Turner in 1980, who also gave a review of COD defect assessment in 1984 [52,150].

There is active development of new assessment procedures which are less restrictive and more accurate than the current COD design curve approach [151]. These include the CTOD plastic collapse modified strip yield model and a CTOD reference stress model and these are examined elsewhere [151]. Both of these models assess ductile fracture by incorporating the material's crack growth resistance (CTOD-Δa) curve.

2.2.5 *THE EFFECT OF SPECIMEN GEOMETRY ON CTOD*

It had been realised from its beginning that the CTOD test is thickness dependent which accounts for the requirement that full-thickness specimens are used in References 41 and 44. Any reduction in constraint (such as decreasing thickness) leads to an increase in CTOD. Thus Harrison reports Wells' results for constant thickness specimens which show that by varying the crack depth to width ratio (a/W) a minimum CTOD is found for a/W = 0.5 [149]. The results of the effects of specimen geometry and crack depth to width ratio can be summarised as follows:

(a) The crack depth-to-width ratio a/W

De Castro *et al.* found δ_c decreases with increasing a/W near the transition temperature but was insensitive to a/W at lower temperatures [38]. Above the transition temperature δ_c decreased with increasing a/W. Li *et al.* found that the CTOD at initiation of crack growth decreased slightly with an increase in a/W when $a/W \geq 0.2$ but increased significantly when $a/W \leq 0.15$ [152]. Ebrahimi found that the fracture mode transition temperature shifted to higher temperatures with increasing specimen thickness and a/W ratio [86]. Pratap and Pandey found that:

(i) r, the rotational factor, increases with decreasing thickness and effect of a/W on r appears to be thickness dependent [153].

(ii) The effective plastic constraint (M) increases with increasing thickness and a/W ratio [136].

(b) Specimen Geometry

Pratap and Pandey found that r_p is a maximum for the CT specimen geometry, and when extensive plastic deformation occurs the SENB specimen has a higher value of r_p than SEN tension

specimens [153]. This is contrary to the work of Matsoukas *et al.* and Wu *et al.* where r_p was less for the SENB specimen than for the CT specimen [143,144]. However it is found that the CTOD is higher for CT than SENB specimens [136].

Since CTOD is so markedly affected by changing specimen thickness then a thickness criterion is needed for a thickness independent CTOD. The criterion is derived from the J-integral thickness criterion, equation (2.81), i.e. $B,W\text{-}a_0 \geq 25J/\sigma_0$. De Castro *et al.* write this as [38],

$$B,W\text{-}a_0 \geq \frac{25M\sigma_{ys}\delta_c}{(\sigma_{ys} + \sigma_u)/2}. \qquad (2.110)$$

The more usual form is [153],

$$B > 25\delta_c. \qquad (2.111)$$

The standards for CTOD testing require full thickness specimens and usually these meet the size criterion [41,44,154].

2.2.6 *THE RELATIONSHIP BETWEEN CTOD AND J*

The relationship between CTOD and the J-integral is well established. The CTOD focuses attention on the crack-tip region and is able to be directly related to the micromechanism of fracture. J_c relates to a macroscopic work term or to crack-tip conditions, depending on the contour chosen. The load-point displacement (Δ) is proportional to J and to δ. Therefore it is logical to assume J and δ are proportional to each other. Early work gave

$$\delta_{crit}\sigma_{ys} = J \qquad (2.112)$$

for critical plane strain conditions [30,33,34,129]. This relationship is now written

$$J = m\sigma_{ys}\delta_t \qquad (2.113)$$

where m varies between 1.15 and 2.95 depending on specimen geometry, constraint and other factors [16,31,32,35-38,52]. When LEFM conditions apply then m = 1.15.

Therefore, two simple methods exist for assessing the toughness of a material and the integrity of a structure in the elastic-plastic regime. For studying the micromechanism of fracture the CTOD concept provides a better analysis.

2.2.7 THE TEARING MODULUS CONCEPT

The J-integral concept is strictly valid only up to the beginning of crack growth. Since J - Δa plots show a well-defined rise as Δa increases these are referred to as J-resistance curves. However the R-line for many materials is very steep and J after a few millimetres crack extension can be 2 or 3 times J_{IC}. Attention has centred on describing slow stable crack growth under elastic-plastic conditions of which the tearing modulus is one concept. The area of interest is ductile tearing without cleavage. For a large number of geometries and loads J can be calculated and represented on a J-a (the crack-driving force) diagram as shown in Figure 2.18a [63]. Upon the J-a diagram the material's J-resistance curve can be inserted at its initial crack length a_o from which the point of tearing instability is found (for example, P_4 in Figure 2.18a). This graphical method is not accurate and Paris has suggested calculating the slopes of both curves and then comparing them [53]. To get a temperature independent parameter Paris gave

$$T_{mat} = \frac{dJ}{da} \cdot \frac{E}{\sigma_o^2} \qquad (2.114)$$

where T_{mat} is the tearing modulus and is a material characteristic and σ_o is the flow stress typically given as $^1/_2(\sigma_{ys} + \sigma_u)$. The applied tearing modulus is

$$T_{app} = \left(\frac{dJ}{da}\right)_{app} \cdot \frac{E}{\sigma_o^2} \qquad (2.115)$$

and when $T_{app} \geq T_{mat}$ instability occurs. This concept is suitable to apply to the SENB specimen since an analytical solution is easily found. Usually, T_{app} and T_{mat} are plotted on a single J-T diagram (Figure 2.18b). Quite often the T_{mat} line has a negative slope for structural steels since the slope of the J-R line decreases as Δa increases. One of the difficulties with the tearing modulus concept is that solutions for T_{app} are very complex for most geometries.

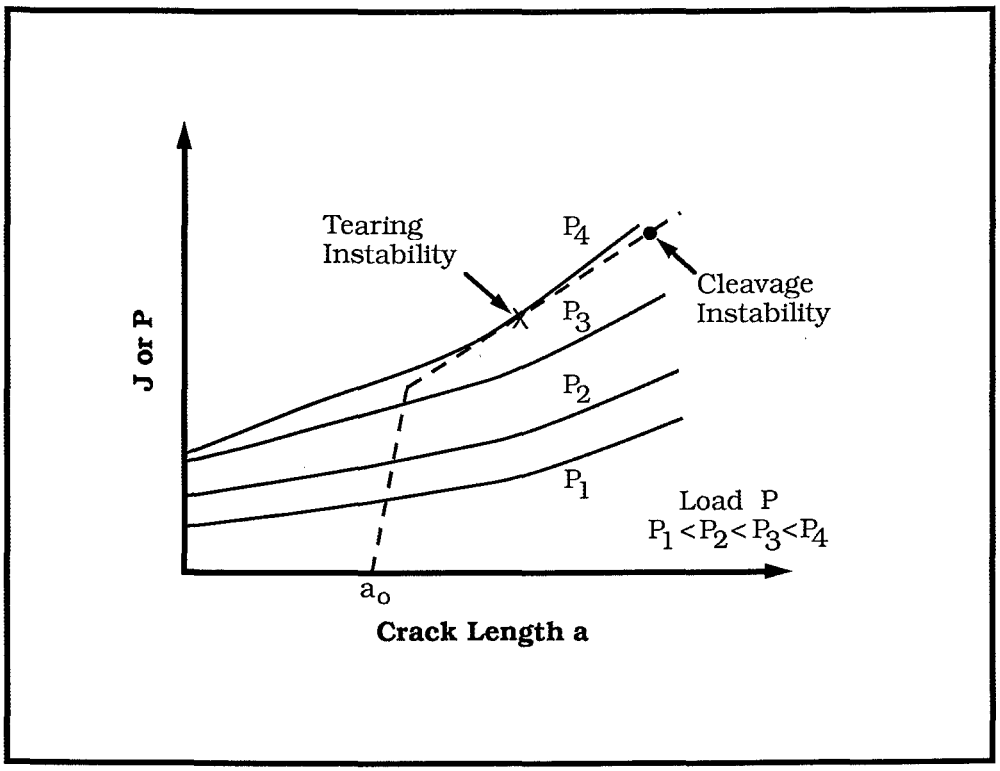

Figure 2.18a : The crack driving force diagram, J-a.

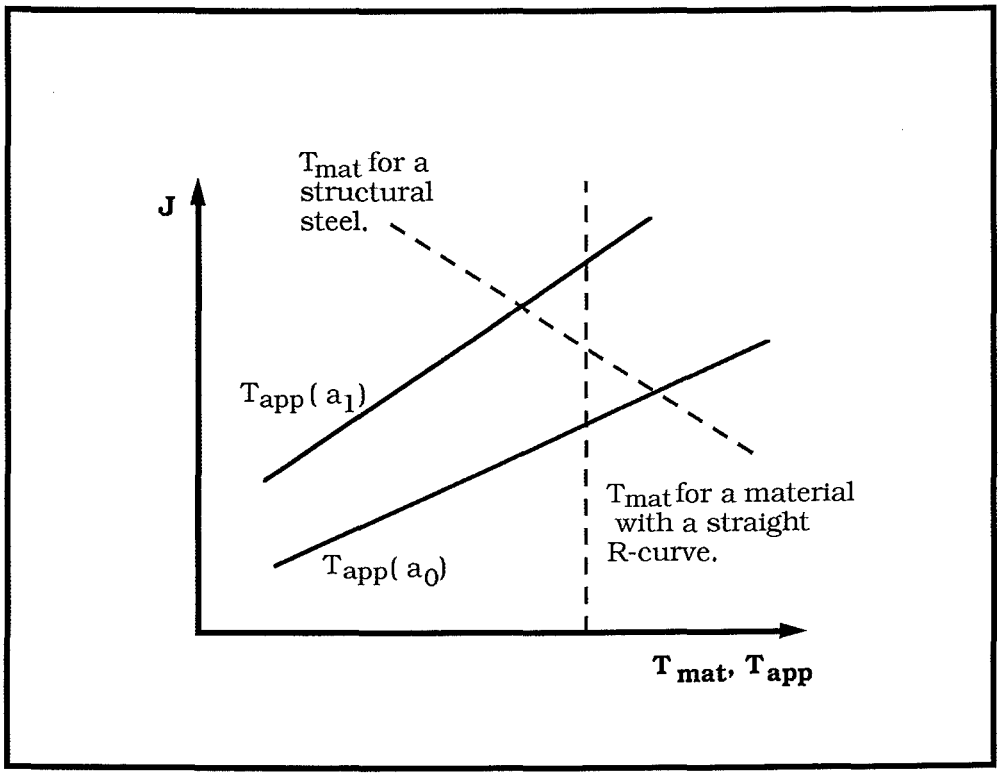

Figure 2.18b : The J-T diagram for stability assessment;
$T_{app} \geq T_{mat}$ indicates tearing instability.

2.2.8 LOAD-DISPLACEMENT CURVE ANALYSIS

There are several methods available that analyse load-displacement curves in the post-yield regime. These relate the toughness values determined to K_{IC} using test results which are invalid according to the criteria of references 23 and 24.

(a) The Equivalent Energy Method

The fracture toughness measurement K-EE provides an economical and simple method of determining fracture toughness values from specimens that are relatively small.

Witt reported a test based on the knowledge of the volumetric energy ratio of a flawed and a perfect structure or specimen [46]. Witt found that this parameter depended essentially on thickness or temperature with little dependence on geometry. Hence, a normalised load-displacement curve could be formed using a normalising parameter such as thickness B. At any point on the curve the area under the curve represents the energy input into the crack opening at that point.

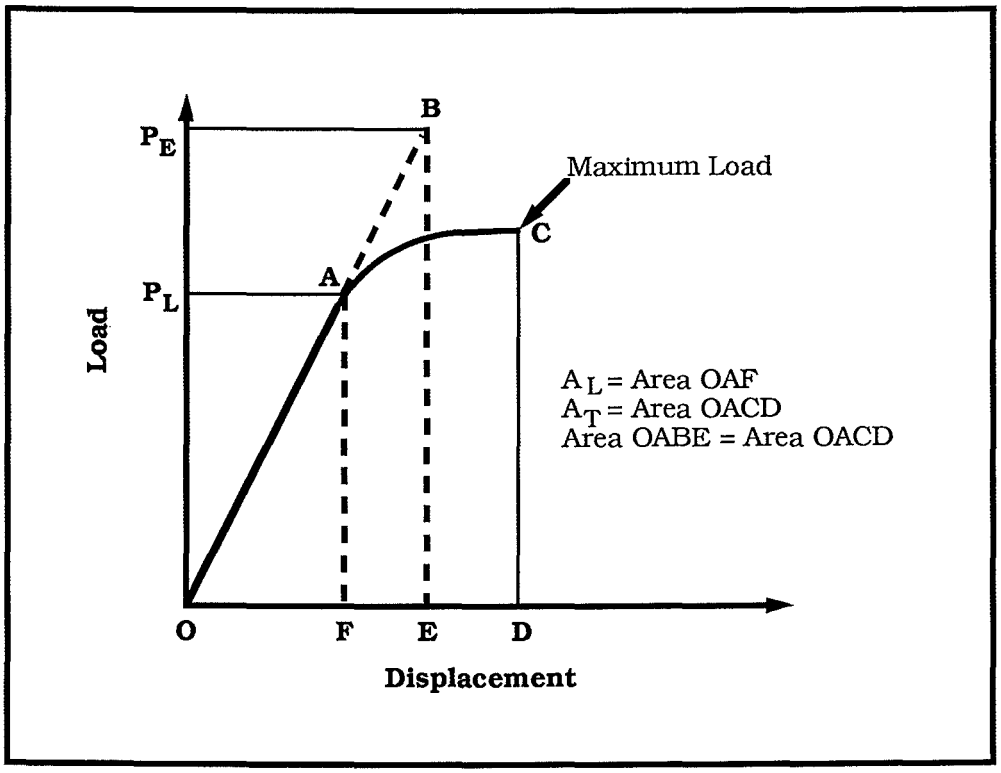

Figure 2.19 : Load-displacement diagram for Equivalent Energy method to determine fracture toughness, equation (2.117).

From the load-displacement curve (Figure 2.19) Witt gave the fracture toughness in the elastic-plastic regime as

$$K\text{-}EE = \frac{P_L f(a/W)}{BW^{1/2}} \cdot \left(\frac{A_T}{A_L}\right)^{1/2} \qquad (2.116)$$

where P_L is a selected load on the linear portion of the curve, A_L is the area under the curve to P_L, A_T is the area under the curve to maximum load and the ratio $(A_T/A_L)^{1/2}$ is the square root of the volumetric energy ratio [46].

Subsequent work showed that experimental results provided a good estimate of K_{IC} provided plastic deformation was small [47-49,155]. ASTM have published a standard using the equivalent energy method for invalid K_{IC} test results so that a fracture toughness value is still obtained [45].

(b) Load-Displacement Curve Fitting

This method was developed by Chell and Milne to estimate fracture toughness from invalid test data using the load-pin-displacement curve [50].

For a constant load test the relationship between J and the displacement at the loading pins (D_{pin}) due solely to the crack is

$$D_{pin} = B\frac{\partial}{\partial P}\int_0^a J\,da \qquad (2.117)$$

where P was the load and B the specimen thickness. J was then given by

$$J = \frac{8a}{\pi^2 E'} Y^2(a/W)\sigma_L^2(a/W)\ln\sec\left\{\frac{\pi\sigma}{2\sigma_L(a/W)}\right\} \qquad (2.118)$$

where σ is the applied stress and $E' = E$ for plane stress and $E' = E/(1-\nu^2)$ for plane strain. $Y(a/W)$ is the standard compliance function for the test specimen and $\sigma_L(a/W)$ is the plastic collapse stress under plane stress condition where

$$\sigma_L(a/W) = \alpha\sigma_1(1-a/W)^n. \qquad (2.119)$$

For CT specimens α is 0.5 and for SENB specimens α is 2. For centre-cracked specimens n = 1 and for single edge notch cracks n

= 2. The collapse stress σ_1 must be estimated, from which J and D_{pin} are obtained and then fitted to the experimental load-displacement curve by an iterative process. The fracture toughness K_{IC} is given by the relationship $J_{IC} = K_I^2(1-\nu^2)/E$ and $\sigma=\sigma_F$, the fracture stress in equation (2.118). Results of experimental investigations did show the method gave reasonable results for K_{IC} [49,50].

2.3 Summary

In order to test the fracture toughness of a material several standardised tests have been developed. In summary:

(i) Griffith developed the fracture criterion for a brittle material which was extended to more ductile materials by Irwin and Orowan, such that

$$\sigma_F = \left[\frac{2E(\gamma_p + \gamma_\varepsilon)}{\pi a}\right]^{1/2} \qquad (2.40)$$

(ii) Irwin developed the stress intensity approach which determined the elastic stress field around the crack tip and was given by

$$K_I = \sigma(\pi a)^{1/2} \qquad (2.22)$$

(iii) The fracture stress intensity reaches a constant value characteristic of the material, designated the plane-strain fracture toughness, K_{IC}. The toughness is given by

$$K_Q = \frac{P_Q}{BW^{1/2}} \cdot f(a_0/W) \qquad (2.51)$$

for the CT specimen and $K_Q = K_{IC}$ when

$$B, W-a_0, a_0 \geq 2.5(K_Q/\sigma_{ys})^2 \qquad (2.52a)$$

Testing for K_{IC} is governed by the standards ASTM E399 or BS 5447.

(iv) Linear Elastic Fracture Mechanics can only be used in limited yielding situations. Therefore Elastic-Plastic Fracture Mechanics has been developed to assess yielding situations, for which two main test methods have evolved.

(v) The CTOD test method measures the critical crack opening of the material prior to crack extension. The CTOD is given by

$$\delta_t = \frac{8\sigma_{ys}a}{\pi E} \ln \sec\left(\frac{\pi\sigma}{2\sigma_{ys}}\right) \tag{2.88}$$

(vi) Testing by BS5762 or ASTM E1290 finds δ_t by geometric consideration such that

$$\delta_t = \frac{K_I^2(1-\nu^2)}{2E\sigma_{ys}} + \frac{V_p r_p(W-a_0)}{r_p(W-a_0) + a_0 + z} \tag{2.99a-c}$$

(vii) The J-integral is based on an energy balance approach which is given by a path independent integral around the crack tip,

$$J = \frac{-\partial U_p}{\partial a} = \int_\Gamma (Wdy - \mathbf{T}\frac{\partial \mathbf{u}}{\partial x} ds) \tag{2.59}$$

(2.60)

(viii) The J-integral is governed by standards ASTM E813 and ASTM E1152. J–R curves are formed and J is given by

$$J = J_e + J_p = \frac{K^2(1-\nu^2)}{E} + \frac{\eta_p U_p}{B(W-a_0)} \tag{2.79}$$

(2.80)

where U_p is the area under the load-displacement curve for plastic deformation. The acceptance of a J value is governed by limits on the J-R curve.

(ix) The compatibility of K_{IC}, J and CTOD are shown by the relations

$$G_{IC} = M\sigma_{ys}\delta_c \tag{2.91}$$

$$J_{IC} = G_{IC} \tag{2.61}$$

and $$J = m\sigma_{ys}\delta \tag{2.113}$$

(x) Other methods exist for determining fracture toughness values, the most promising being the tearing modulus based on J-T diagrams.

(xi) The rotation factor r_p used in the CTOD varies from 0 to 0.6 depending on the plasticity developed at the crack tip. The value of 0.4 used in the British standard is too low but the values of 0.44 (SENB) and 0.45 - 0.47 (CT) used in the ASTM standard are more appropriate.

CHAPTER 3

Mechanisms of Fracture and their Influence on Fracture Toughness

3.1 *Introduction*

The study of fracture mechanics can be envisaged as covering a wide range of scales, from the atomistic up to the structural. It becomes necessary to work with a different model for each scale with boundary conditions coming from the next largest and smallest scales. The smaller the size of the model, from which larger ones can be integrated to obtain fracture load for a given geometry, the broader the range of conditions which can be predicted or correlated from experimental data. The fracture toughness of a material is influenced by the microstructure, grain size and yield strength of the material, the test temperature and strain rate and the specimen geometry and thickness among other things.

Changing these conditions influences the mode of fracture. In this chapter the mechanisms of cleavage and ductile fracture are examined for mild steel, and also the fracture mode transition temperature (FMTT).

3.2 *Cleavage Fracture*

The understanding of brittle fracture has improved considerably over the last four decades. For simple ferrite-carbide microstructures the micromechanisms of fracture are very well described. Cleavage fracture can be described as the transgranular splitting of a metal along certain low index crystallographic planes called cleavage planes. The {100} planes have been shown to be common cleavage planes in the BCC metals e.g. V, Cr, Mo, W, Fe and most steels, and the {0001} planes in the CPH metals, e.g. Mg, Zn, Sn. FCC metals do not normally exhibit cleavage fracture. The bright granular appearance of cleavage fracture in low carbon steels occurs due to light being reflected from the flat "cleaved" surface of each grain.

Cleavage fracture is controlled by the tensile stress normal to the fracture plane since cleavage is the result of pulling atom planes apart as opposed to shearing [64]. Cleavage fracture is more likely to

occur when the ratio of tensile stress (σ) to shear stress (τ) is high i.e. triaxially stressed structures are more likely to fail by cleavage than uniaxially stressed structures.

Various micromechanisms for initiation and propagation of cleavage fracture have been proposed [65-72]. The critical stress for propagation is the microscopic cleavage stress σ_F.

3.2.1 THE ZENER-STROH THEORY OF MICROFRACTURE

It was suggested by Zener that the stress levels at the head of a dislocation pile-up could be sufficient to cause cleavage fracture [65]. Dislocations pile into the crack as it widens and the surrounding material relaxes. This mechanism is slip-induced so that the following discussion considers slip-induced cleavage fracture. This view is adopted by most fracture theories. Stroh first adopted this approach in developing his theory of fracture [66,157-159]. Figure 3.1 shows dislocations piled up to form a wedge shape crack. Stroh wrote that to form a crack n dislocations piled up under the effective shear stress (τ_{eff}) are required such that

$$nb\tau_{eff} = 12\gamma \tag{3.1}$$

where b is the Burger's vector and γ is the surface energy [157]. Using the result of Eshelby *et al.* the pile-up will occupy a length L of the slip plane given by [160],

$$\tau_{eff}^2 L = 12\gamma\mu/\pi(1-\nu) \tag{3.2}$$

where μ is the shear modulus and ν is Poisson's ratio. If the dislocations pile up on the grain boundaries then L is equal to half the grain diameter (d). The critical conditions for crack nucleation are then [157],

$$\tau_{eff} \equiv \tau_{ys} - \tau_i \geq \left[\frac{24\mu\gamma}{\pi(1-\nu)d}\right]^{1/2} \tag{3.3}$$

where τ_{ys} is the shear yield stress and τ_i is the lattice friction shear stress. Crack nucleation is predicted to be the most difficult stage in cleavage fracture caused by this mechanism and if γ remains constant during the fracture process (as is assumed) then cleavage is nucleation controlled. In this analysis the effect of local shear

stresses in propagating the crack are neglected and Stroh assumed that crack formation in a non-uniform stress field was equivalent to that in a uniform stress field [161]. Allowance for these effects confirmed nucleation-controlled fracture and there is experimental evidence for cleavage fracture to be nucleation controlled in zinc polycrystals [162].

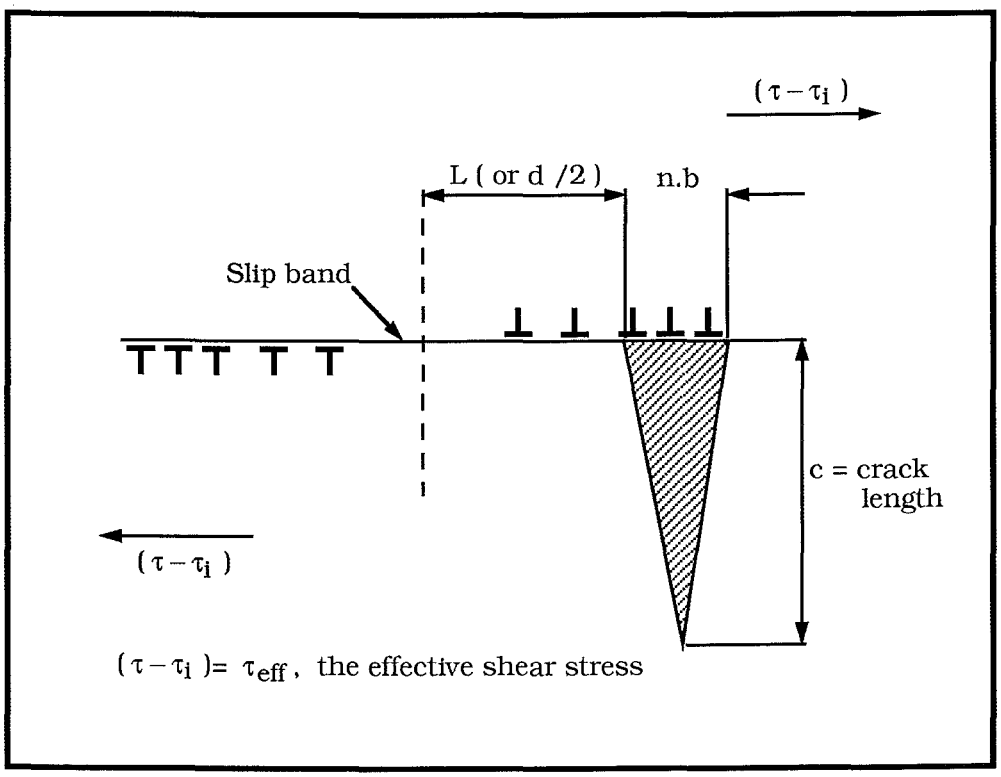

Figure 3.1 : Cleavage crack nucleation at the head of a dislocation pile-up.

3.2.2 *THE COTTRELL THEORY OF CLEAVAGE FRACTURE*

Cottrell proposed an alternative dislocation mechanism for nucleation of cleavage fracture in BCC metals such as mild steel [67,68]. In 1953 Petch found the relationship between cleavage strength and grain size for a mild steel based on dislocation pile-up on a blocked slip line at a grain boundary [163]. The results of this are shown in Figure 3.2. For zero plastic deformation,

$$\sigma_F = \sigma_{iF} + k_F d^{-1/2} \qquad (3.4)$$

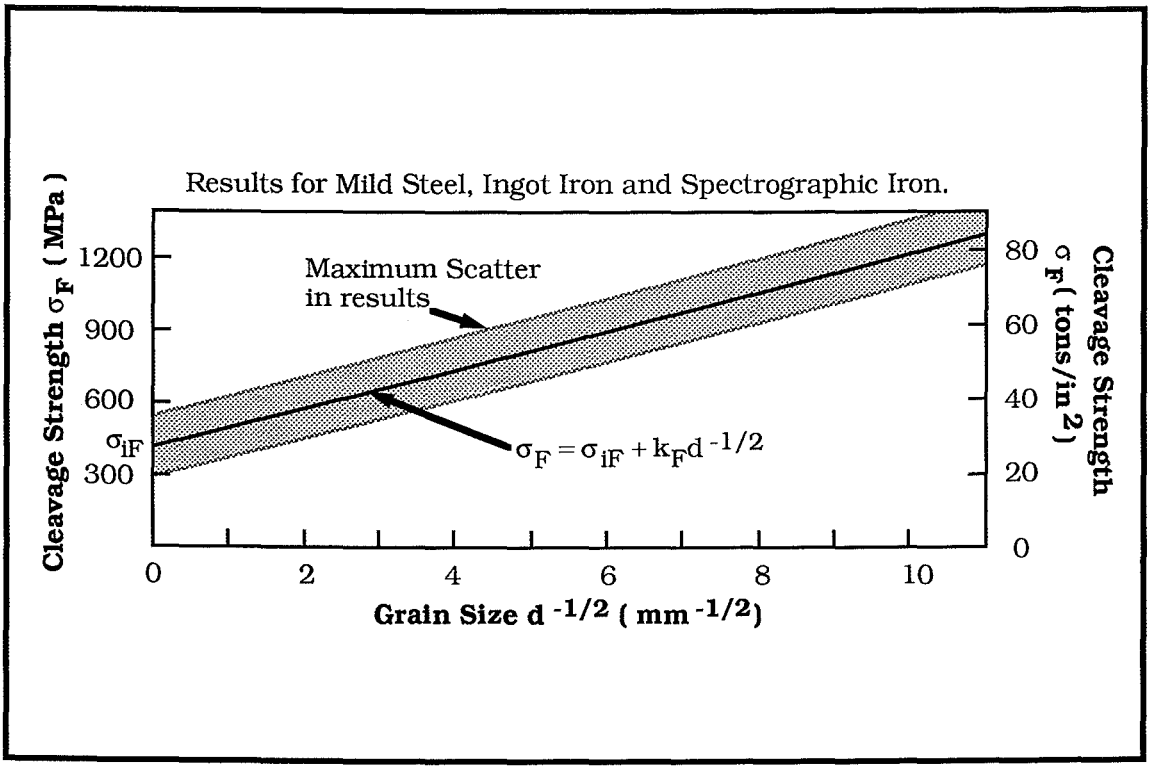

Figure 3.2 : The relationship between cleavage stress and grain diameter for mild steel at -188 °C[163].

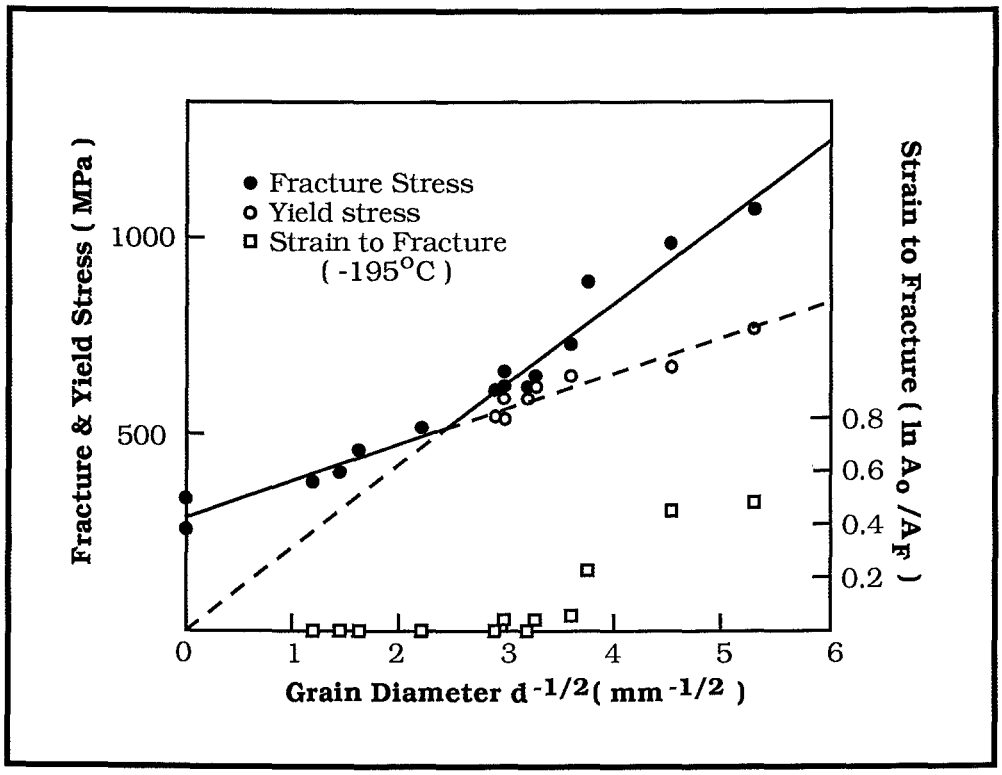

Figure 3.3 : The yield and fracture stresses at -195 °C as a function of grain size for low carbon steel[74].

where σ_F is the cleavage stress, k_F is a constant, d is the grain diameter and σ_{iF} is the friction stress opposing dislocation motion [163]. This has the same form as the grain size dependence of lower yield stress given by Hall and Petch [163,164] as,

$$\sigma_{ys} = \sigma_i + k_y d^{-1/2} \tag{3.5}$$

where σ_{ys} is the yield stress and k_y is a constant and $k_y < k_F$. Experimental results showed σ_{iF} and σ_i were common. It was concluded that the results would apply as long as no complication arose from a precipitate intruding and becoming the controlling stress concentrator [163].

Low investigated the postulation that some localised yielding must occur before cleavage fracture is initiated in steels [74]. The results are shown in Figure 3.3 from which it was concluded that the cleavage fracture stress was coincident with yield stress for coarse-grained material, and exceeded the yield stress for fine-grained material. This was interpreted to mean that microcracks did not form below the yield stress; some slip is required to provide high local stresses needed to initiate a cleavage crack. The microcracks may or may not propagate depending on their size and the applied stress when they do form. For fine-grained material the stress had to be raised above the yield stress to a value proportional to $d^{-1/2}$ before spontaneous propagation would occur [74]. The requirement of small scale plastic deformation before cleavage was confirmed by Griffiths and Oates on tests on a 3% silicon-iron [75].

Both Cottrell and Petch recognised that cleavage fracture was tensile stress controlled [67,68,87,163]. Figure 3.4 shows Cottrell's model of cleavage crack nucleation in BCC metals. Dislocations slipping on intersecting {101} planes interact to form a sessile dislocation and its Burgers vector is normal to the cleavage plane. This is accompanied by a reduction in dislocation energy so that crack nucleation is easier than if it is by the Zener-Stroh mechanism. The cleavage stress is given by

$$\sigma_F \geq \left(\frac{2\mu\gamma}{k_y{}^s d}\right)^{1/2} \tag{3.6}$$

where k_y^s is the shear Hall-Petch yielding constant [67]. This model predicts that cleavage fracture is propagation controlled and explains the effects of grain size and yielding parameters on fracture [161]. However it does neglect the influence of other microstructural variables. McMahon and Cohen showed this was important in tensile tests with mild steels that had identical yield and flow properties but different carbide particle distributions; the coarse carbides promoted cleavage fracture whereas the fine carbides allowed more ductile flow [165].

Knott investigated that influence of tensile stress (the hydrostatic stress) at cleavage fracture by testing mild steel bend specimens and varying the included angles of the notches [64]. The maximum tensile stress below the notch at fracture was estimated using slip-line field theory where

$$\sigma_{yy} \approx 3\sigma_{ys} \tag{3.7}$$

using the Von Mises yield criterion. It was found that the maximum tensile stress was independent of notched angle and temperature; so therefore cleavage follows a critical tensile stress criterion [64]. This is supported by the work of Oates and of Tetelman *et al.* [166-168]. Oates found that slip or twin bands initiated cracks in the brittle, second-phase particles (carbides) and that the critical fracture event was the growth of precipitate-size cracks into the ductile ferrite matrix [166]. In a further investigation on a mild steel and a manganese steel (the manganese altering the carbide distribution) Oates found that σ_F for the mild steel was temperature and strain-rate insensitive but the manganese steel's fracture stress was markedly temperature and strain-rate sensitive which supported the previous conclusion [167].

Since tensile stress governs the propagation of crack nuclei then this implies that the cleavage of mild steel is propagation controlled. Also, if the Zener-Stroh mechanism controls nucleation then fracture can only be propagation controlled if some brittle second phase provides a low surface energy region. The crack nucleus can be arrested at the phase boundary and generate a microcrack which subsequently propagates as a Griffith defect controlling the final fracture.

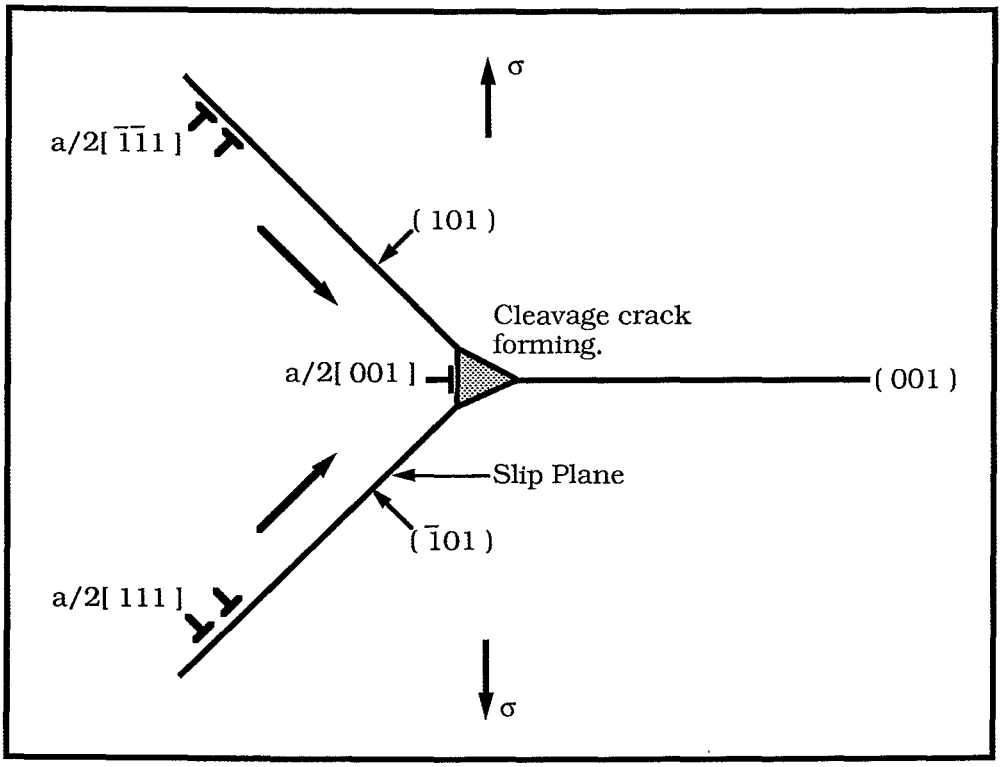

Figure 3.4 : Intersection of slip planes to form a cleavage crack (Cottrell's model)[67].

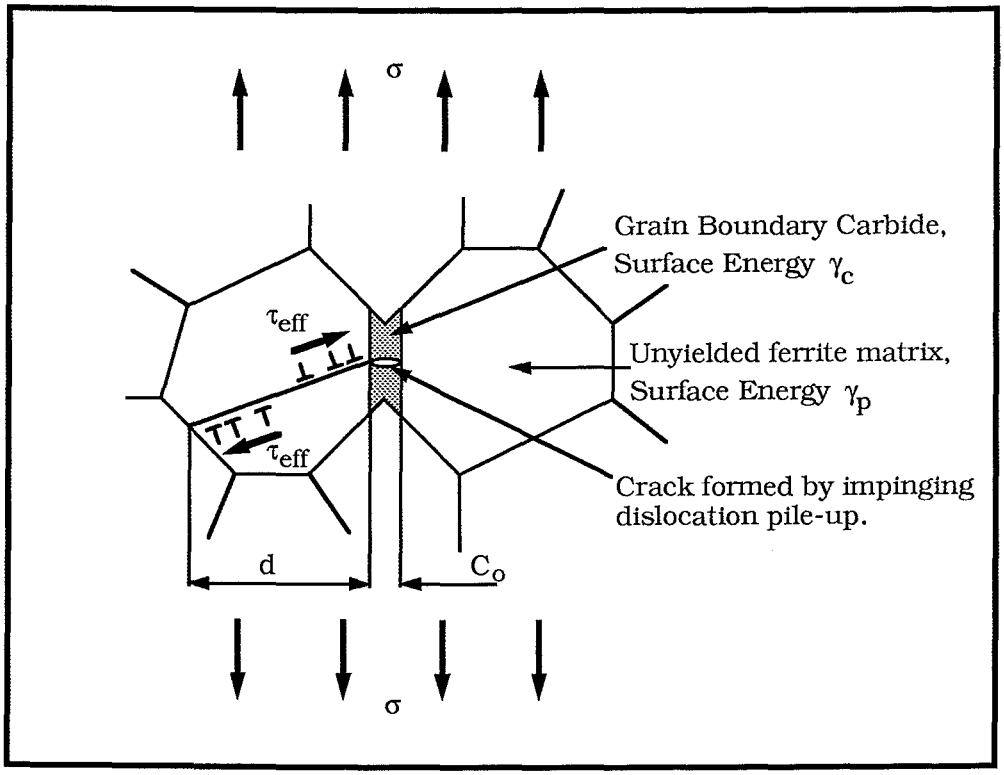

Figure 3.5 : Formation of cleavage cracks by cracked grain-boundary carbides (Smith's model)[69,70].

3.2.3 *SMITH'S MODEL OF CLEAVAGE FRACTURE*

Figure 3.5 illustrates Smith's theoretical model of cleavage fracture in mild steel. The impinging dislocation pile-up cracks the grain boundary carbide and the microcrack formed propagates as a Griffith defect under the combined action of the pile-up and the applied stress [69,70]. By considering the change in energy with crack length the critical cleavage stress is,

$$\left(\frac{C_o}{d}\right)\sigma_F^2 + \tau_{eff}^2 \left[1 + \frac{4}{\pi}\left(\frac{C_o}{d}\right)^{1/2} \frac{\tau_i}{\tau_{eff}}\right]^2 \geq \frac{4E\gamma_p}{\pi(1-\nu^2)d} \qquad (3.8)$$

where C_o is the thickness of the grain boundary carbide, E is Young's modulus and γ_p is the effective surface energy of ferrite [69]. Almond *et al.* proposed a similar model of cleavage fracture in steels and gave the cleavage fracture stress as [169],

$$\sigma_F = \left[\frac{k_y^2 d}{4C_o} + \frac{8\mu\gamma_p}{\pi(1-\nu)C_o}\right]^{1/2} - \frac{k_y d^{1/2}}{2C_o} \qquad (3.9)$$

where all terms are as previously used.

Lindley *et al.* showed that carbide cracking could occur by fibre loading. They used it to explain why the majority of carbides were cracked in the centre of their length when the dislocation pile-up model predicts a random distribution of cracks along the carbide length [71]. The model applied for specimens which had macroscopically yielded, and they felt the mechanism should be effective for 0.75% plastic strain and higher. The model also explained why cleavage fracture usually initiated well inside the plastic zone in a notched bar test and not at the elastic-plastic interface where the highest tensile stress was predicted to occur by slip-line field theory. However finite element stress analyses have shown the maximum tensile stress occurs well inside the plastic zone and the fibre-loading mechanism is not necessary to explain this [161,170]. This does highlight the statistical nature of cleavage fracture in steel.

Cleavage fracture may also be initiated by deformation twins at high strain rates and low temperatures. Twinning is commonly observed in steels below -140°C [64,71,171]. The finer the microstructure the lower the temperature that twinning occurs [161]. Intersecting twins have been observed to nucleate cleavage

fracture [73]. High strain rates at higher temperatures cause twins to be found adjacent to the fracture surface.

3.2.4 *THE EFFECTS OF MICROSTRUCTURE ON CLEAVAGE FRACTURE STRESS*

(a) Grain Size

Evensen found that Smith's model appears to contradict the experimentally observed grain size dependence of the cleavage fracture stress [74,77,163,166,172,173]. Using the Hall-Petch relationship equation (3.5) in terms of shear stress

$$\tau_{eff} \equiv \tau_{ys} - \tau_i = k_y^s d^{-1/2} \qquad (3.5a)$$

then Smith's fracture criterion reduces to,

$$\sigma_F^2 + \frac{(k_y^s)^2}{C_o}\left[1 + \frac{4\tau_i}{\pi k_y^s} C_o^{1/2}\right]^2 \geq \frac{4E\gamma_p}{\pi(1-\nu^2)C_o}. \qquad (3.10)$$

This equation predicts that the fracture stress is dependent on the carbide thickness only since k_y^s is regarded as a constant. The constant k_y^s is a measure of the ease of unpinning of dislocations and is usually considered to be independent of grain size [174]. However some researchers have found a dependence of k_y^s on grain size [Reference 43 of 174,98]. This would indicate an influence of grain size on cleavage fracture stress through k_y^s; k_y^s is essentially independent of temperature from -160 to 25°C except in lightly pinned steels (e.g. quenched steels) [97,96].

It was suggested by Knott that since the growth of both ferrite and grain boundary carbides is controlled by the same diffusion process then the ratio C_o/d will be approximately constant [77]. Curry and Knott observed that if it is assumed that the "largest observed" carbide particle gives rise to fracture then equation (3.8) can be used to predict the grain size dependence of cleavage fracture for normalised and annealed steels [175]. Results of their analysis are shown in Figure 3.6. Their line of best fit gives $\gamma_p = 14 J/m^2$ and doesn't show a linear relationship between σ_F and $d^{-1/2}$. Curry and later Gerberich *et al.* both gave an empirical relationship as [89,176],

$$\sigma_F = k_F' d^{-1/4} \qquad (3.11)$$

where k_F' is a constant and typically is 80 $MPam^{1/2}$ [89].

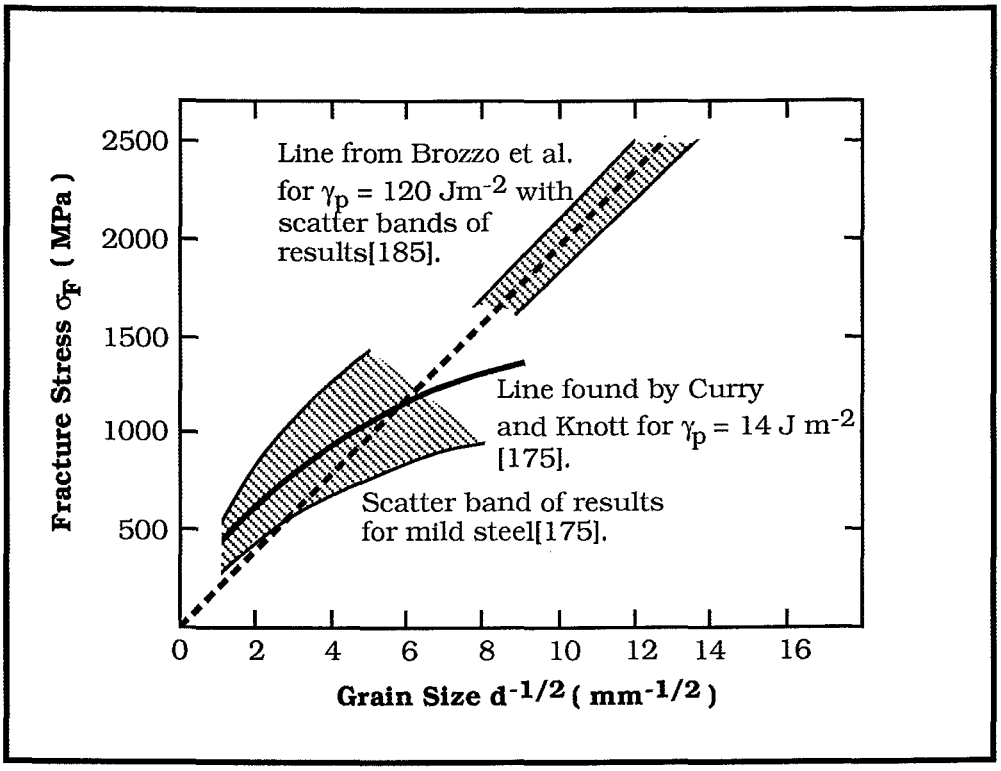

Figure 3.6 : The dependence of cleavage fracture stress on grain size as given by Curry and Knott[79,175].

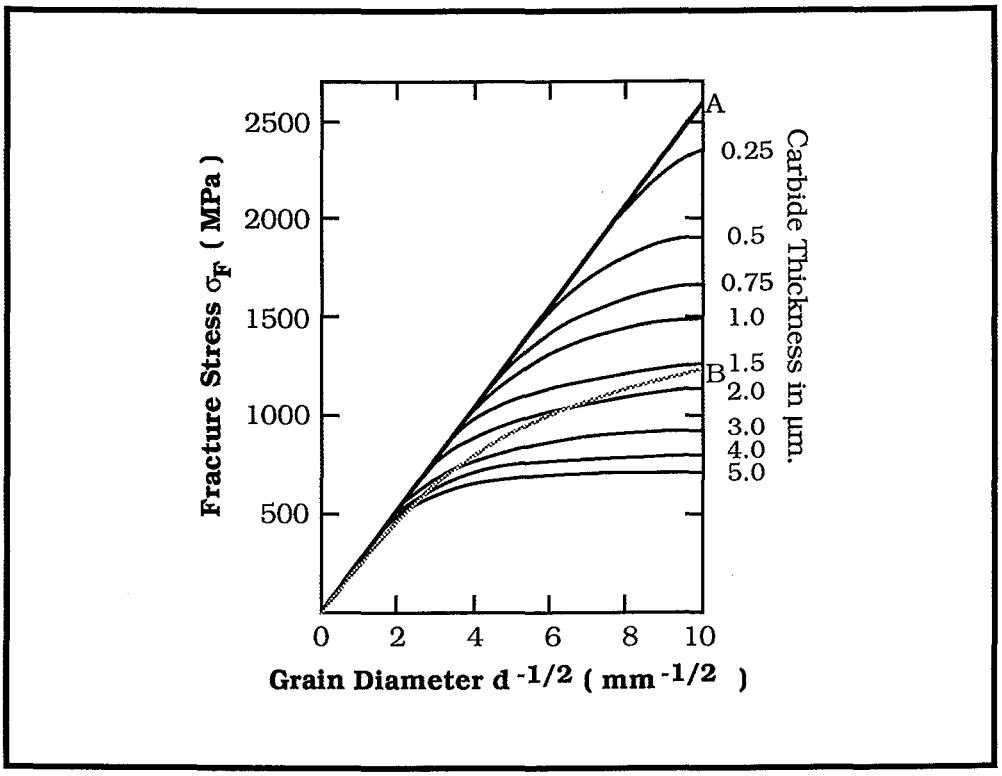

Figure 3.7 : The effect of carbide thickness on the cleavage fracture stress using equation (3.12) [180].

If cleavage fracture stress is proportional to $d^{-1/2}$ then grain-sized microcracks should be observed in mild steels and then these could act as crack nuclei. Grain-sized microcracks have been reported but the experimental results of Curry and Knott shown in Figure 3.6 do not support this proposal [175,177–179]. Prior to fracture cracked carbide particles but no grain-sized microcracks were observed by Curry and Knott [175]. McMahon and Cohen found that if a ferrite microcrack arrested at a grain boundary it would not repropagate even under an increased load [165]. However Chen *et al.* found that the critical event depended upon the notch of the specimen [179]. Their results showed that the cleavage fracture in Charpy V-notched specimens from -45 to -60°C was controlled by the propagation of a ferrite grain-sized microcrack into the neighbouring ferrite matrix (after initiation at a second-phase particle). In CTOD precracked specimens at -110°C the critical event was propagation from a second-phase particle-sized microcrack. This work used C-Mn steel where σ_F has been shown to change substantially with temperature and strain rate [166,167]. Chen *et al.* felt that the change in σ_F due to the change in the critical event was related to the different effective shear stress ahead of a notch and a crack [179].

Petch discussed the proposal that since static equilibrium conditions indicated no grain size dependence of cleavage strength when there was experimental evidence to the contrary then a dynamic calculation involving the formation of a non-equilibrium crack in a carbide should be made [180]. Petch felt that there is a possibility of a collapse of the pile-up and that the carbide crack hitting the ferrite is a non-equilibrium crack wedged open by $\approx nb$, where n is the number of dislocations in the original pile-up. In his analysis a result similar to that of Almond *et al.* is found, where

$$\sigma_F = \left[\frac{8\mu\gamma_p}{\pi(1-\nu)C_o} - \frac{k_y^2 d}{8\pi^2 C_o^2}\right]^{1/2} - \frac{k_y d^{1/2}}{2^{3/2}\pi C_o} \qquad (3.12)$$

which predicts cleavage strength depending on carbide thickness and on the grain size [180]. The calculated cleavage strengths at yield are shown in Figure 3.7 for varying carbide thicknesses. Mintz *et al.* found that with $d^{-1/2} = 13.5\ mm^{-1/2}$ an increase in carbide thickness beyond 1 μm had no effect on the fracture mode transition temperature and when $d^{-1/2} = 5.5\ mm^{-1/2}$ the limit was 2-3 μm

[181]. The curve OB in Figure 3.7 represents the limit for change to control by propagation through the ferrite grain boundaries. Therefore, over a limited range of grain size (commonly $d^{-1/2} > 3$ $mm^{-1/2}$) where variation of carbide thickness has occurred because of heat treatment to vary the grain size, then the cleavage strength may be given by $\sigma_F = \sigma_{iF} + k_F d^{-1/2}$ [180]. With coarser carbides Petch concluded microcrack propagation through the ferrite grain boundaries becomes the critical step and gives a grain size dependence.

The critical stress intensity for cleavage fracture of mild steel was given as depending on grain size by Armstrong [182]. Using equation (2.46) $K_I = (8/\pi)^{1/2}\sigma_{ys}\Delta a_n^{1/2}$ where $a >> \Delta a_n$ then Armstrong substituted for yield stress with flow stress using a Hall-Petch dependence to give,

$$K_F = c's^{1/2}[\sigma_i + k_\varepsilon d^{-1/2}] \qquad (3.13)$$

where $c' = (8/\pi)^{1/2}$ and σ_i and k_ε are the appropriate friction stress and microstructural stress intensity (constant for flow stress) for a stress value which is to be determined and $s = \Delta a_n$ is the effective length of the plastic zone. The plastic zone was estimated to decrease with decreasing grain size but not sufficiently to reverse the positive Hall-Petch dependence for σ_{ys} [182].

Petch and Armstrong showed that the effect of dislocation friction stress and of grain size on toughness was very simple by considering work-hardening [183]. Using the true stress-true strain power relationship

$$\sigma = A\varepsilon^n \qquad (3.14)$$

where σ is the true stress, ε the true strain, n the Holloman strain-hardening index and A is a constant then the work-hardening rate is,

$$\frac{d\sigma}{d\varepsilon} = nA\varepsilon^{n-1} \approx \frac{nA}{\varepsilon}. \qquad (3.15)$$

With a constant cleavage fracture stress the critical stress intensity K_C is approximately proportional to the square root of crack-opening displacement so,

$$dK_c = \frac{-K_c}{2nA} d\sigma_{ys} \qquad (3.16)$$

and $$K_c = K_c' \exp[-\sigma_{ys}/2nA] \qquad (3.17)$$

where K_c' is a constant. This equation showed good agreement with experimental results and they concluded that when fracture is by cleavage the effect on K_c of temperature, or other factors that influence the friction stress, can be accounted for by the work hardening needed to maintain a critical stress at the cleavage particles [183].

(b) Other Microstructural Influences

In spheroidised steel Hodgson and Tetelman proposed that σ_F was proportional to $D_o^{-1/2}$ (D_o being the diameter of the largest observed carbide particle) [184]. Curry and Knott showed this could be the case but it should be noted that a carbide microcrack in spheroidised steels will provide a penny-shaped nucleus which raises σ_F to $\pi/2$ greater than that for a similar through cracked grain boundary carbide [175].

Cleavage fracture can occur in steels such as lath martensites and low-carbon bainites containing no discrete carbide particles [185-191]. For such microstructures cleavage would seem to be controlled by the martensite/bainite packet size although lath width may have an influence [185-187,190]. Brozzo *et al.* present results showing σ_F to be proportional to the reciprocal square root of the packet size [183]. It is not considered proven that cleavage fracture in these steels obey a critical tensile stress criterion; cleavage fracture will be initiated by a dislocation mechanism in the absence of brittle second phase particles so fracture could be nucleation controlled. Recent work by Bowen & Knott does show a critical tensile stress criterion is obeyed, and that fracture is inclusion controlled [188,189]. They have also shown that in specimens with a coarse martensitic micro structure σ_F decreases with increasing specimen size [191].

Groom and Knott also showed that a substantial increase in dislocation density by pre-straining results in an elevation of fracture stress in mild steel and in its transition temperature [178].

3.2.5 *THE RITCHIE-KNOTT-RICE MODEL OF CLEAVAGE FRACTURE*

A major objective in micromechanical modelling is to predict values of K_{IC} from measured values of σ_F. In the presence of pre-existing sharp cracks crack-tip blunting prevents the crack from propagating when the energy balance of the Griffith criterion for fracture is satisfied. It is possible to show the stress distribution ahead of a sharp crack, as shown in Figure 3.8, by using computations of local stresses and strains to relate continuum plasticity analyses with microstructural mechanisms (σ_F) [192]. This stress distribution varies significantly from that for a notch since the stress distribution for a notch is essentially constant over microstructurally significant distances. Ritchie *et al.* formed a model where the steel's cleavage fracture stress had to be exceeded over some characteristic distance from the crack tip before fracture occurred [72]. The characteristic distance was considered to be 1 to 2 grain diameters so that,

$$\sigma_F(2\pi X_0)^{1/2} \geq K_{IC} \qquad (3.18)$$

where X_0 is the characteristic distance. This assumes that X_0 is temperature independent. Therefore, the predicted temperature dependence of fracture toughness arises solely from the temperature dependence of the yield stress [193]. Curry and Knott investigated the grain size dependence of X_0 and this is shown in Figure 3.9 [77]. No simple relationship was found to exist, the results suggested X_0 was grain-size independent for $d < 40$ μm, but Rawal and Gurland did show equation (3.18) could be used successfully with steel having a grain size from 8.3 to 13 μm [76,77]. Curry and Knott concluded that the characteristic distance should be viewed as representing the probability of finding a sufficiently large microcrack nucleus in a highly stressed region to cause cleavage fracture [77]. At a sharp crack statistical competition becomes operative and the RKR model does not consider the statistical nature of cleavage fracture nor the possibility of out of crack plane crack nucleation.

Bowen *et al.* determined X_0 at each test temperature finding X_0 generally increased with temperature. Therefore, the predicted K_{IC} values from the RKR model would give a lower bound to experimentally measured values [193]. Also they explained that the increased plastic zone size around a blunt notch compared to that of

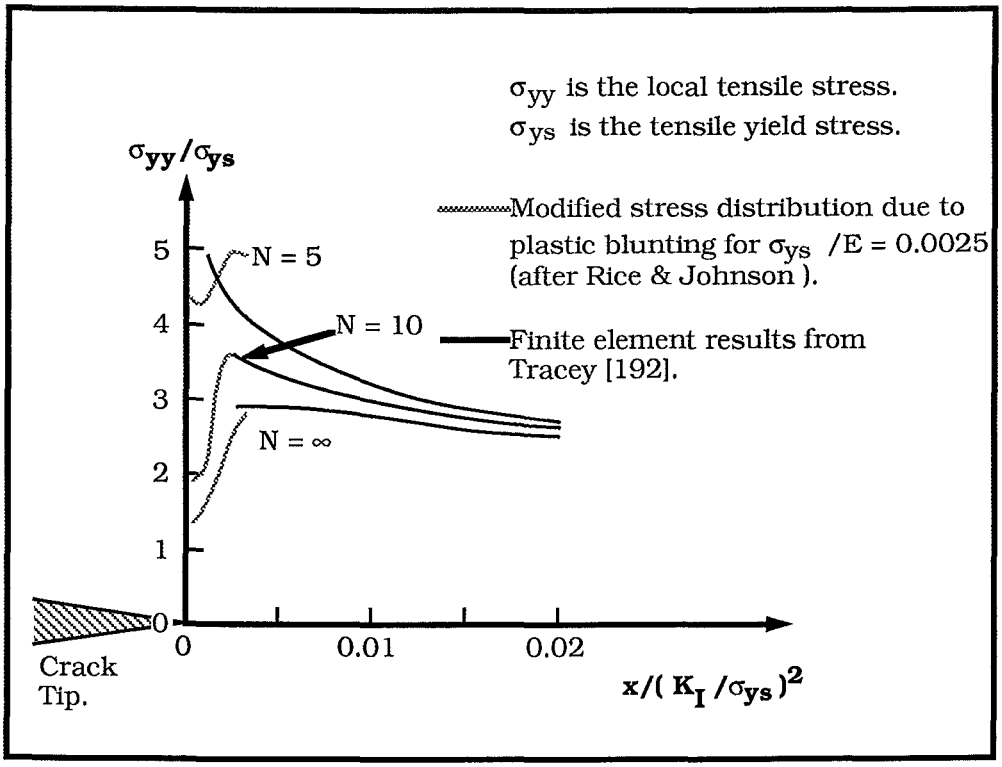

Figure 3.8 : The local tensile stress as a function of the distance x ahead of a tensile-loaded crack in plane-strain [192,201].

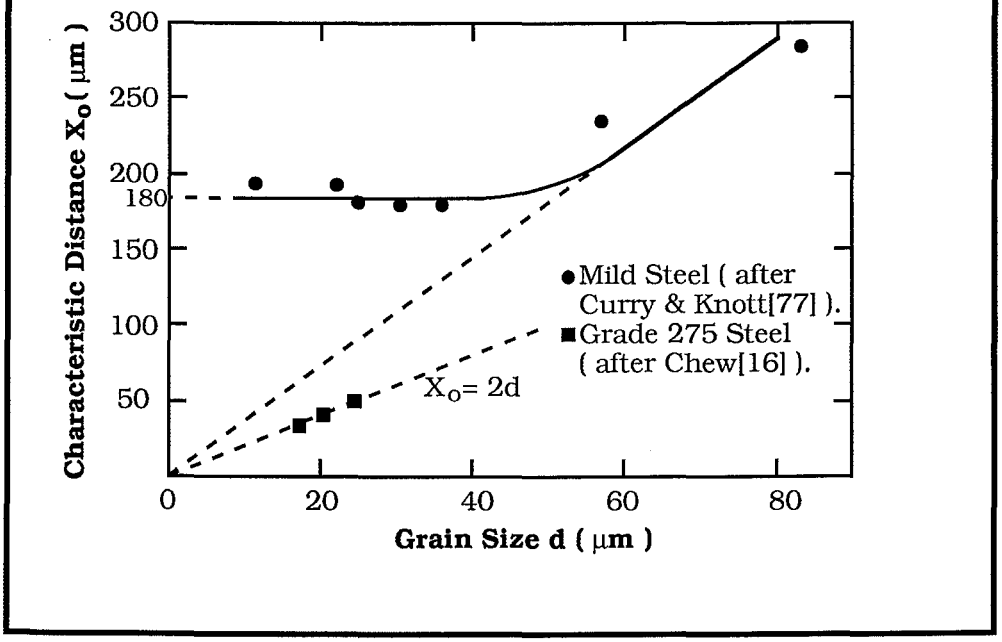

Figure 3.9 : The dependence of the characteristic distance (X_o) on grain size (d) [16,77].

a sharp crack (a ratio of 64:1 at -120°C and 116:1 at -196°C) would mean the blunt notch routinely samples coarse carbides whereas the sharp crack doesn't. Therefore the mean carbide size is important in determining σ_F and values of K_{IC} at a particular test temperature will be lower for a blunt notch.

Curry has given the grain size and temperature dependence of the cleavage fracture toughness in mild steels using the RKR model [89-91]. Curry uses an analytical description of the stress distribution ahead of a loaded crack tip in material deforming in plane strain small-scale-yielding following the Ramberg-Osgood stress-strain law [194],

$$\varepsilon/\varepsilon_{ys} = \sigma/\sigma_{ys} - \alpha(\sigma/\sigma_{ys})^N \qquad (3.19)$$

where ε is the tensile strain and σ is the tensile stress and subscript ys denotes the yield stress values, α is a numerical constant and N is the work-hardening exponent, usually between 5 and 10 for structural steels [143]. The strain hardening exponents, n from equation (3.14) and N from equation (3.19) are approximately related by $N \approx 1/n$.

The maximum principal stress $\sigma_{11}(x)$ at a point X within the plastic zone ahead of the crack tip is given by

$$\frac{\sigma_{11}(X)}{\sigma_{ys}} = \beta\left\{\frac{X}{(K/\sigma_{ys})^2}\right\}^{-1/(N+1)} \qquad (3.20)$$

where K is the stress intensity to which the crack is loaded and β is the amplitude of the stress singularity available from Hutchinson's solution of the stress distribution at the crack tip [194]. Due to crack-tip blunting in mild steels the maximum tensile stress that can be produced ahead of the crack tip is $\sigma_{11}(max)/\sigma_{ys} \approx 5$ for N = 5 and $\sigma_{11}(max)/\sigma_{ys} \approx 3.7$ for N = 10 [72]. The microscopic cleavage fracture criterion of Ritchie *et al.* can be written as

$$\sigma_{11}(X) \geq \sigma_F \text{ for } X \leq X_0. \qquad (3.21)$$

Combined with equation (3.20) this gives,

$$K_{IC} = \beta^{-(N+1)/2}\, X_0^{1/2}\, \frac{\sigma_F^{(N+1)/2}}{\sigma_{ys}^{(N-1)/2}}. \qquad (3.22)$$

Since the stress analysis applies only within the plastic zone then X_0 must be less than the plastic zone size. The dependence of K_{IC} on grain size, temperature and strain rate may now be found. Curry gave the grain size dependence of fracture stress as $\sigma_F = k_F' d^{-1/4}$ where $k_F' = 80$ MPam$^{1/4}$ [89]. From Figure 3.9 the restriction on grain size was $d < 40$ μm when X_0 is independent of grain size. Using the Hall-Petch relationship for grain size, $\sigma_{ys} = \sigma_i + k_y d^{-1/2}$, then

$$K_{IC} = [\beta^{-(N+1)} X_0 \frac{(k_F' d^{-1/4})^{(N+1)}}{(\sigma_i + k_y d^{-1/2})^{(N-1)}}]^{1/2} \qquad (3.23)$$

Curry gives typical values of $d = 20$ μm, $X_0 = 180$ μm, $\alpha = 1$, $N = 9$ and $\beta = 2.045$ which gives $K_{IC} \approx 40$ MPam$^{1/2}$ when a value of 30 MPam$^{1/2}$ would be more appropriate [89]. The value of β influences K_{IC} substantially, a 50% error in β will change K_{IC} by a factor of 8. However by taking the product $K_{IC}\beta^{(N+1)/2}$ Curry was able to show a maximum in toughness occurred when grain size ranged from 3 to 15 μm in the temperature range where cleavage typically occurs [89].

Petch suggested that the friction stress σ_i was made up of an athermal component $\sigma_i(st)$ and a temperature dependent component σ_i^* which Conrad confirmed [87,97]. Armstrong, after Petch, gave the temperature dependence of the friction stress as [99],

$$\sigma_i^* = A\exp[-(\beta_0 + \beta_1 \log\dot{\varepsilon})T] \qquad (3.24)$$

where A, β_0 and β_1 are constants, $\dot{\varepsilon}$ is the strain rate and T is the absolute temperature. Substituting for σ_i in equation (3.23) where $\sigma_i = \sigma_i^* + \sigma_i(st)$ then

$$K_{IC} = [\frac{\beta^{-(N+1)} X_0 (k_F' d^{-1/4})^{N+1}}{\{\sigma_i(st) + A\exp[-(\beta_0+\beta_1 \ln\dot{\varepsilon})T] + k_y d^{-1/2}\}^{N-1}}]^{1/2}. \qquad (3.25)$$

Equation (3.25) predicts K_{IC} as a function of strain rate, temperature and grain size. Equation (3.25) only applies to slip-induced cleavage. When the strain rate is so high that adiabatic conditions prevail at the crack tip (which raises the crack-tip temperature) then conflicting processes result and the equation fails. It could be used to predict

the fracture mode transition temperature but the stress analysis fails when significant crack-tip blunting occurs.

3.2.6 STATISTICAL MODELS OF CLEAVAGE FRACTURE

When microstructurally significant stress gradients are absent, as in notched-bar fracture tests, then the measured fracture toughness will be the lowest available value determined by the largest cracked carbide present. However in the presence of a sharp crack where the stress distribution is like that of Figure 3.8 statistical competition operates and it is likely a finer carbide particle within the plastic zone around the crack will act as the crack nucleus at a higher applied stress intensity. Watanabe *et al.* presented a fracture toughness versus temperature relationship (Figure 3.10) which shows schematically the sort of scatter expected in toughness testing; FG is approximately from -100 to -10°C [195]. A number of statistically based models of carbide-induced cleavage fracture have been developed.

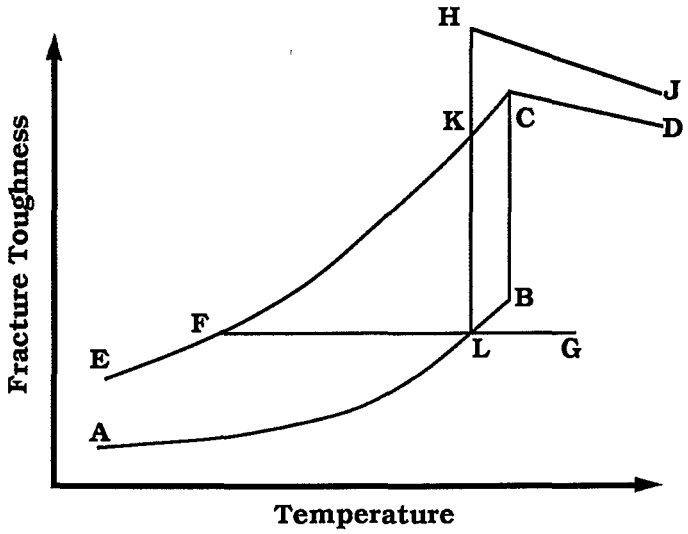

Line AB : lower bound of scatter, weakest cleavage strength.
CD : lower bound of upper shelf toughness.
EFKC : upper bound of scatter, highest cleavage strength.
FG : toughness where ductile crack extension first appears.
HJ : upper bound of upper shelf toughness.
HKL : temperature representing lower bound of the scatter in temperature where fracture mode transistion occurs.
BC : upper bound of HKL.

Figure 3.10 : Schematic of the expected scatter in toughness testing as a function of temperature[195].

(a) Curry and Knott's Model [77,196]

Curry and Knott proposed a statistical model of cleavage fracture in 1976 and subsequently developed it in 1979 [77,196]. The tensile stress σ_F required to cause fracture at a carbide particle crack of any given radius r_o, using the Griffith criterion is

$$\sigma_F = \left[\frac{\pi E \gamma_p}{2(1-\nu^2)r_o}\right]^{1/2} \tag{3.26}$$

for a penny-shape crack. The probability $P(f,r_o)$ of a cracked carbide particle being subjected to a large enough stress to cause fracture is estimated as,

$$P(f,r_o) = SP(r_o)X^2 n_a \theta \tag{3.27}$$

where $P(r_o)$ is the probability of the carbide particle having radius r_o, X is the characteristic distance associated with a particle of radius r_o, n_a is the area number density of carbide particles, S is a shape factor and θ accounts for particle orientation and the probability the particle is cracked. By summing $P(f,r_o)$ over all carbide radii and setting the sum equal to unity then the fracture criteria are defined,

$$\sum_{r_o} \{\theta SP(r_o)X^2 n_a\} = 1 \tag{3.28}$$

i.e. one carbide particle must be subjected to its critical stress for fracture to occur. For any one specimen K_{IC}, σ_{ys} and n_a are constant and since X is characterised in small-scale yielding by r_o, σ_{ys} and K_c then equation (3.28) can be rewritten

$$K_{IC} = M\sigma_{ys}(n_a\Sigma)^{-1/4} \tag{3.29}$$

where M is a constant to allow for shape and orientation effects and

$$\Sigma = \sum_{r_o} \{P(r_o) \left[\frac{X}{(K_{IC}/\sigma_{ys})^2}\right]^2\}. \tag{3.30}$$

This summation can be performed by combining the frequency distribution of the carbide particle radii and a crack-tip stress distribution using the appropriate carbide radius-fracture

stress relationship. Curry and Knott found good agreement between experimental and predicted results using this model [196].

(b) Wallin, Saario and Törrönen's Model [197]

Wallin *et al.* proposed a two dimensional statistical model of cleavage fracture in 1984 which is based on Curry and Knott's model [197]. Fracture is assumed to occur when the principal stress

$$\sigma_{yy} = f(\sigma_{ys}, X, K_I, n, E) \tag{3.31}$$

ahead of the crack tip at the site of a carbide (radius r_o) exceeds σ_F given by equation (3.26). From equations (3.26) and (3.31) the critical radius for cleavage fracture is,

$$r_o = \frac{\pi E \gamma_p}{2(1-\nu^2)\sigma^2_{yy}} \tag{3.32}$$

where $$\gamma_p = \gamma_s + W_p \tag{3.33}$$

and γ_s is the surface energy of the matrix and W_p is the plastic work necessary for crack propagation. Wallin *et al.* then express the probability P_f of fracture as [197],

$$P_f = 1 - \prod_{X=0}^{X_p} [1 - P(r \geq r_o)]^{N_a.B.dX.F} \tag{3.34}$$

where $P(r \geq r_o)$ is the probability of a carbide having a radius greater than or equal to r_o, B is the specimen thickness, F is the fraction of carbides involved in the fracture process and N_a is the number of carbides per unit area. In equation (3.34) the multiplication is performed over the plastic zone size (X_p), as shown in Figure 3.11, in small increments of distance dX. When equation (3.34) is solved for different levels of loading K_I, a K_I-P_f graph is produced from which the expectance value for stress intensity for fracture is

$$K_{1f} = \sum_{i=0}^{\infty} K_{1,i}[P_f(K_{1,i}) - P_f(K_{1,i-1})] \tag{3.35}$$

where the expectance value K_{1f} is assumed to be equal to the experimentally determined mean value of K_{IC}.

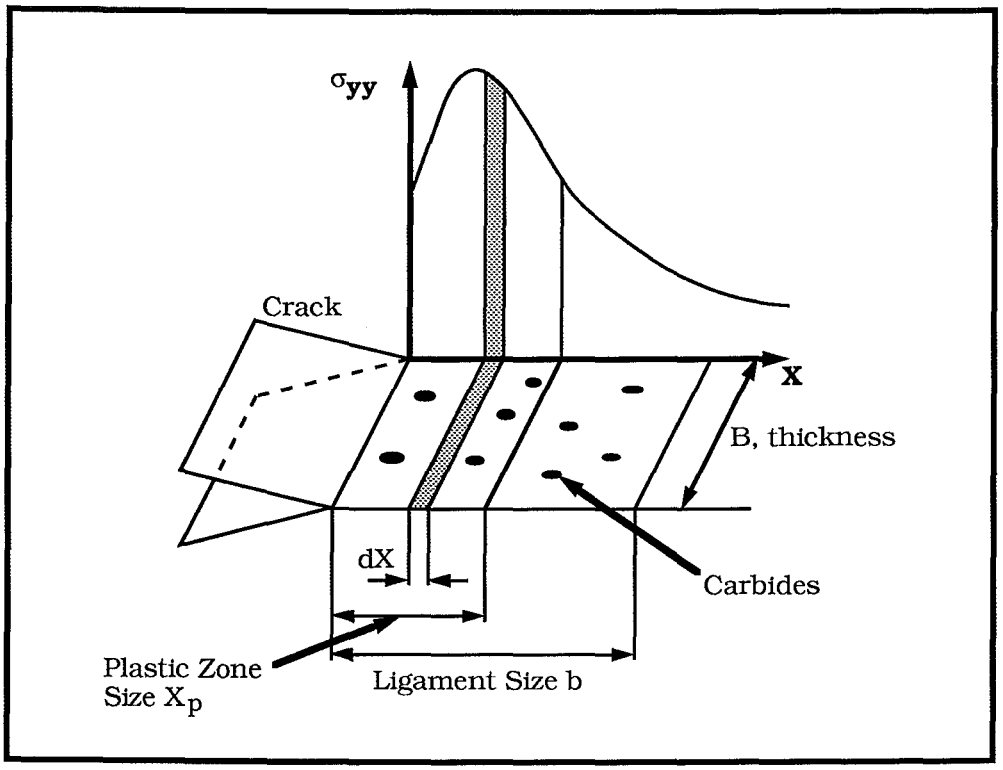

Figure 3.11 : Schematic of the boundary conditions of the WST statistical model of cleavage fracture[197].

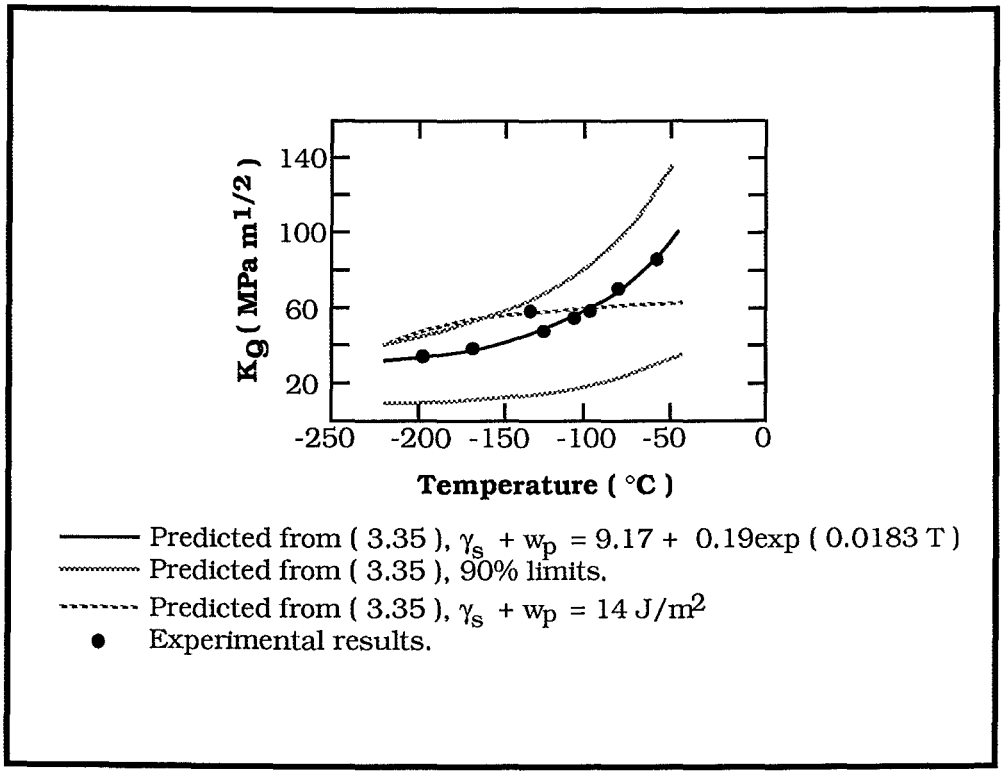

Figure 3.12 : Comparison of predicted (WST model) and experimental K_Q results for ferritic tool steel[197].

To apply the model the stress distribution ahead of the crack tip must be assumed, similar to that of Reference 192 and shown in Figure 3.8, and the carbide distribution ($P(r_o)$) is given as

$$P(r_o) = \frac{c^{a-1}}{(a-2)!}\left(\frac{r_o}{r}\right)^{-a}\exp[-c/(r_o/\bar{r})] \qquad (3.36)$$

where c and a are constants, $\bar{r}$ is the geometric mean radius of the carbides and r_o is the radius of the carbide under consideration [197]. Significantly Wallin *et al.* take γ_p as dependent on temperature. Curry and Knott gave γ_p as about 14 J/m^2 where γ_s is about 2 J/m^2 and the difference is irreversible work done in propagating the crack [77]. One feature of the term W_p is the creation of dislocations whose mobility depends on temperature and consequently W_p would be expected to have the same temperature dependence. The temperature dependent component of the force resisting dislocation movement is proportional to the Peierls-Nabarro force and hence the temperature dependence of W_p will be inversely related to the Peierls-Nabarro force (the temperature dependence of the yield stress) [197]. Using the model of yield stress temperature dependence given by Kotilainen *et al.*, W_p is

$$W_p = W_o + [W_p(o) - W_o]\exp[mT] \qquad (3.37)$$

where W_o is the athermal component of W_p, $W_p(o)$ is W_p at T = 0K and m is the exponential constant of the Peierls-Nabarro force [197,198]. With F taken as a constant equal to 10^{-2} (although it will depend on the yield stress and the strain hardening exponent of the matrix as well as the volume fraction and strength of the carbides) experimental results of Wallin *et al.* are shown in Figure 3.12 together with 90% confidence levels on K_{IC} [197]. In these results Wallin *et al.* used $\gamma_p = 9.17 + 0.19\exp(0.0183T)$ J/m^2 and also plotted are results using $\gamma_p = 14 J/m^2$ from Curry and Knott [77,197]. The experimental results and predictions show good agreement. The weakest link theory is incorporated in this model since equation (3.34) includes a thickness term.

A number of models based on weakest-link theory and using a two or three Weibull parameter distribution have been produced [199-207]. For example the two parameter model of the Weibull distribution is often

$$P_f = 1 - \exp[-(K_I/K_o)^m] \qquad (3.38)$$

where P_f is the probability of fracture, K_I is the applied stress intensity, K_o is a normalization factor and m is an exponent describing the magnitude of scatter [204]. K_o is equal to the value of K_I which stands for a failure probability of 0.63. Wallin showed that the WST model is comparable and compatible in use to the Weibull distribution for description of fracture toughness values [204]. Wallin found that the scatter in results is the same given by both models and that m is a constant and equal to 4 [204].

Results of Lin *et al.* indicated that for a fixed particle size distribution both sharp-crack and rounded-notch toughness decrease as grain size increases [206]. At a fixed grain size with increasing particle size the sharp-crack toughness increases while rounded-notch toughness decreases. The effects result mainly from the difference in the number of "activated particles" in the plastic zone.

The statistical theories of cleavage fracture provide a good estimate of the scatter in fracture toughness data below the transition temperature. Their disadvantage for engineering application is that the carbide distribution on the crack plane must be known. The region of highest scatter in K_{IC} results will be in the fracture mode transition region.

3.3 The Fracture Mode Transition Temperature

The effects of temperature on fracture behaviour can be summarised in a stress/temperature diagram as shown in Figure 3.13 [206]. The diagram contains the expected temperature dependence of the yield stress (σ_{ys}), the peak stress in the plastic zone (σ_{yy}), the carbide strength (S) and the matrix grain strength (Σ). The regions of behaviour identified are dictated by the respective stress levels. At the lowest temperatures both S and Σ are below σ_{ys} and cleavage occurs once the nucleation condition is satisfied and the fracture is nucleation controlled. When S exceeds Σ and the yield stress but not the peak stress (σ_{yy}) then the particles crack. Particles which satisfy the criterion for propagation given by equation (3.26) across the carbide/matrix interface become the source of cleavage fracture. As temperature increases $\Sigma > S > \sigma_{ys}$ and particles may crack, the crack may extend up to the first ferrite grain boundary without causing

failure (i.e. a stable grain size crack). Cleavage fracture would occur when a crack extends dynamically according to the condition that the average stress $\sigma > \Sigma$. At the highest temperatures $\Sigma > S > \sigma_{yy}$ and cleavage fracture is then impossible and the transition to ductile fracture occurs. Particles may still crack and the crack blunts acting as a nucleus for microvoid coalescence. Chen *et al.* gave the following conditions for a complete description of the ductile to brittle transition of a BCC alloy [100]. Any description must include:

(i) A mechanical equation of state including work-hardening.

(ii) Dislocation dynamics or strain-rate sensitivity parameters which account for both solid-solution strengthening or softening.

(iii) A cleavage criterion for simple stress states which includes the above as well as grain size effects.

(iv) A cleavage criterion for crack or notches incorporating all of the above.

This section will examine some of the existing models of the fracture mode transition temperature.

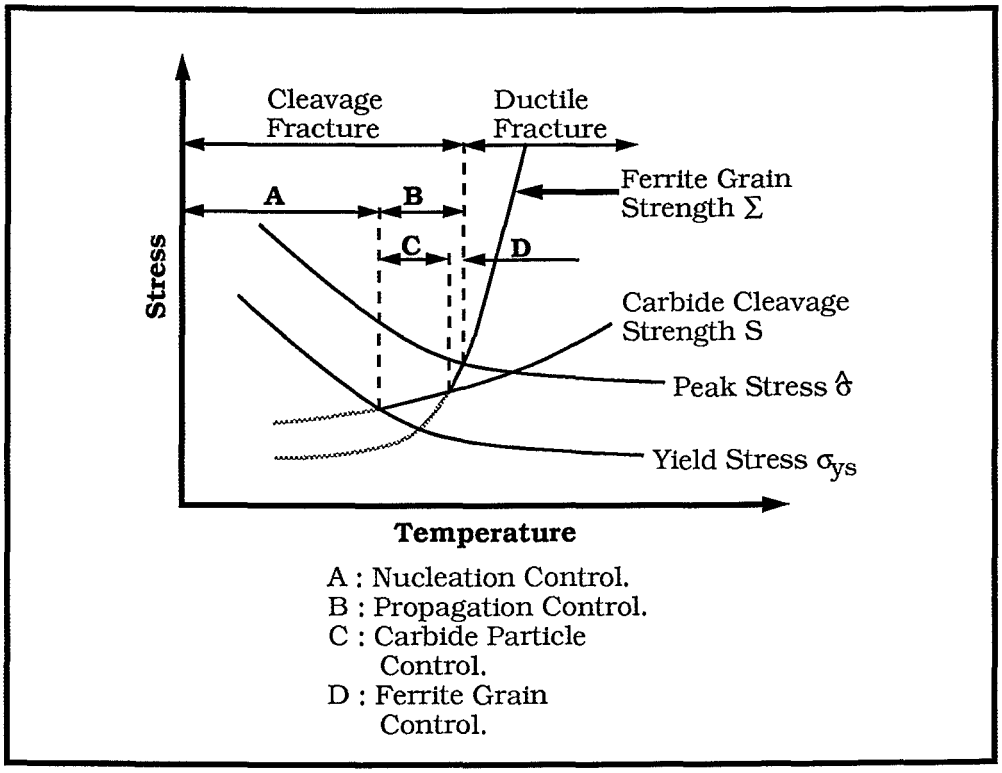

Figure 3.13 : Schematic of the temperature dependence of cleavage fracture toughness resulting from either particle or grain-sized microcracks[206].

3.3.1 *THE COTTRELL-PETCH MODEL OF TRANSITION TEMPERATURE [67,68,87,209]*

At fracture mode transition there are competing processes on load application between yielding and cleavage crack propagation. The transition can be considered on the basis of Griffith crack propagation below transition and obtain a condition for energy transition as Cottrell did [67,68]. Or it may be considered as a transition in fracture mode from ductile to cleavage fracture which Petch did [87,209]. Both Cottrell and Petch considered fracture to occur based on dislocation pile-ups as shown in Figure 3.1. Using Cottrell's approach the Griffith equation must be written so the energy of the dislocation pile-up is equated to the surface energy of the crack [67,68]. The energy of the pile-up is given by the product of the applied stress and the maximum displacement between the crack faces. Therefore

$$\sigma na = 2\gamma \tag{3.39}$$

where σ is the applied stress
$n.a$ is the maximum displacement between the crack faces,
n is the number of dislocations in the pile-up
a is the Burgers vector of each dislocation
and γ is the effective surface energy of the matrix.

The shear strain of the pile-up is

$$na/d = (\tau - \tau_i)/\mu \tag{3.40}$$

where $\tau - \tau_i$ is the effective shear stress
μ is the shear modulus
τ is the applied shear stress
τ_i is the friction shear stress
and d is the length of slip band containing the dislocations.

At yield the pile-up is assumed to occupy a length equal to half the grain diameter. Using the Hall-Petch equation, $\tau_{ys} = \tau_i + k_y{}^s d^{-1/2}$, then transition occurs when the cleavage fracture stress and yield stress are approximately equal and by substitution into equation (3.40),

$$na \approx k_y^s d^{1/2}/\mu. \qquad (3.41)$$

Yielding is shear stress controlled whereas cleavage crack propagation is tensile stress controlled. Therefore a factor β which equals $2\tau/\sigma$ is introduced where

β = 2 for torsion
= 1 for tension
$\approx$ 1/3 for notches in tension [8]

Therefore at the yield point, equating equations (3.39) and (3.41) in terms of tension,

$$\sigma_{ys} k_y d^{1/2} = \beta\mu\gamma \qquad (3.42)$$

where k_y is the contribution of grain boundaries to the strength of polycrystalline metals in tension. If $\sigma_{ys}k_y d^{1/2}$ is smaller than $\beta\mu\gamma$ then ductile yielding results but if $\sigma_{ys}k_y d^{1/2}$ is greater than $\beta\mu\gamma$ then cleavage fracture occurs. Petch presented his analysis in terms of fracture stress and k_F presented in equation (3.4) though the results are similar. Equation (3.42) makes fracture a function of grain size and the stress state β. However it is also a function of temperature and strain rate because the yield stress (σ_{ys}) is dependent on these quantities [97]. Cottrell had assumed the temperature dependence was through k_y but this is constant for steels in the normalised condition [68,96]. Petch took temperature to influence fracture through the friction stress (σ_i), given in Section 3.2.5 as $\sigma_i = \sigma_i(st) + \sigma_i^*$, where $\sigma_i(st)$ is an athermal component and σ_i^* is the temperature dependent component [87]. Using equation (3.24) with constant strain rate then

$$\sigma_i^* = A \exp(-\alpha T) \qquad (3.43)$$

where A and α are constants and T is the absolute temperature [87,209]. Provided $\sigma_i(st)$ is small then an approximation for the friction stress is

$$\sigma_i \approx A \exp(-\alpha T). \qquad (3.44)$$

Since from equation (3.5) $\sigma_{ys} = \sigma_i + k_y d^{-1/2}$ then equation (3.42) may be rewritten as

$$\sigma_i k_y d^{1/2} = \beta\mu\gamma - k_y^2 \tag{3.45}$$

and substituting for σ_i from equation (3.44) and taking natural logarithms of both sides,

$$\ln(Ak_y d^{1/2}) - \alpha T = \ln(\beta\mu\gamma - k_y^2). \tag{3.46}$$

By rearranging to find T_c, the transition temperature, then

$$\alpha T_c = \ln A - \ln\left(\frac{\beta\mu\gamma}{k_y} - k_y\right) - \ln d^{-1/2}. \tag{3.47}$$

A further approximation for the friction stress can be made since when the temperature range is small the temperature dependence of σ_i may be taken as linear [8,87]. Then,

$$\sigma_i \approx \sigma_i(st) + C - DT \tag{3.48}$$

where C and D are constants and the yield stress is

$$\sigma_{ys} \approx \sigma_i(st) + C - DT + k_y d^{-1/2}. \tag{3.49}$$

By substitution into equation (3.42) for yield stress,

$$[\sigma_i(st) + C - DT]k_y d^{1/2} = \beta\mu\gamma - k_y^2 \tag{3.50}$$

which upon dividing through by $k_y d^{1/2}$ and subtracting $(\sigma_i(st) + C)$ from each side gives the transition temperature as

$$DT_c = \sigma_i(st) + C - \left(\frac{\beta\mu\gamma}{k_y} - k_y\right) d^{-1/2}. \tag{3.51}$$

These equations [(3.47) and (3.51)] make the transition temperature a function of grain size, the Peierls-Nabarro stress, the strength of dislocation locking and the stress state. They predict a

linear dependence of T_c on ln $d^{-1/2}$ or, less accurately, $d^{-1/2}$ which researchers have found [8,87].

3.3.2 *THE TRANSITION TEMPERATURE BY ARMSTRONG [210,211]*

Armstrong writes that for experimental conditions existing at the transition temperature then equation (3.42) can be written [210],

$$(\sigma_i d^{1/2} + k_y)k_y = k_y k_F + \sigma_{iF} k_y d^{1/2} \qquad (3.52)$$

where σ_{iF} is the intercept of equation (3.4) with $d^{-1/2} = 0$ and is the friction stress associated with dislocations involved in cleavage crack formation and propagation. A comparison of equations (3.42) and (3.52) shows that

$$\beta\mu\gamma = k_y k_F + \sigma_{iF} k_y d^{1/2}. \qquad (3.53)$$

Using equation (3.44) substituted into equation (3.52) for σ_i then,

$$\alpha T_c = \ln A - \ln[(k_F - k_y) + \sigma_{iF} d^{1/2}] - \ln d^{-1/2} \qquad (3.54)$$

which gives a different dependence of T_c on grain size to that of equation (3.47) if σ_{iF} is not zero. If the athermal component of friction stress is taken into consideration then,

$$\alpha T = \ln A - \ln[(k_F - k_y) + (\sigma_{iF} - \sigma_i(st))d^{1/2}] - \ln d^{-1/2}. \qquad (3.55)$$

If the temperature dependent component of friction stress is written including strain rate (equation (3.24), $\sigma_i^* = A\exp[-(\beta_0+\beta_1 \ln\dot{\varepsilon})T]$) then the fracture mode transition temperature may be written [99,211],

$$T_c = \frac{1}{\beta_0+\beta_1 \ln\dot{\varepsilon}} \ln\left[\frac{A}{(k_F - k_y)d^{-1/2} + \sigma_{iF} - \sigma_i(st)}\right] \qquad (3.56)$$

where A is the yield stress less the grain size component at T = 0K (the Peierls stress). There is no given dependence on stress state in this model which is required to fully describe transition behaviour. Equation (3.24) may be rewritten as

$$\frac{\sigma_{ys} - \sigma_i(st)}{\sigma_p^*} = \left(\frac{\dot{\varepsilon}}{\nu}\right)^{B2T} \exp(-\alpha T) \qquad (3.57)$$

where $A = \sigma_p^*$ the Peierls stress and ν is the frequency factor defined in Section 5.3.3 [211]. This is similar to the rate equation used by Pisarenko and Krasowsky reported by Gerberich *et al.* as [176],

$$\frac{\sigma_{ys} - \sigma_i(st)}{\sigma_p^*} = \left(\frac{\dot{\varepsilon}}{\nu'}\right)^{(kT/H_o)} \qquad (3.58)$$

where H_o is the activation energy defined at $\ln(\sigma_p^*/\sigma_i) = 1$ (i.e. where the thermal component of yield stress falls off to 1/e at approximately room temperature) and k is Boltzmann's constant. This is based on the thermal activation theory of yielding by Conrad [97,98] (see Section 5.3.3).

The fracture criterion for cracks and notches is then,

$$T_c = \frac{H_o}{k} \ln[\sigma_p^* / \left(\sigma_F \left(\frac{2\pi dc}{B}\right)^{N/N+1} - \sigma_i\right)] [\frac{1}{\ln(\nu'/\dot{\varepsilon}_o)}] \qquad (3.59)$$

where d is the grain diameter, c is a constant, B is the specimen thickness, N is the strain-hardening exponent and σ_F and σ_i are the cleavage fracture and athermal stresses respectively containing grain size contributions. When α=0 and N=0 then equations (3.57) and (3.59) are identical. Gerberich *et al.* developed these models further using the conditions specified by Chen *et al.* [100,176].

3.3.3 THE FMTT IN Fe-BINARY ALLOYS [100,176]

Gerberich *et al.* modelled the ductile-brittle transition temperature of Fe-Ni and Fe-Si alloys using dislocation dynamics and particle-nucleated cleavage mechanisms. They performed their tests using slow-bend and Charpy Impact V-notch specimens. Their model showed how increasing Ni additions lead to a monotonically decreasing transition temperature due to increased cleavage fracture stress. With increasing Si content a minimum in transition temperature was found due to lowered cleavage fracture stress. They began with the simple fracture criterion from Orowan that [19]

$$M\sigma_{ys}\,|_{T,\dot{\varepsilon}_p} = \sigma_{yy}(max) \geq \sigma_F \qquad (3.60)$$

where $\sigma_{ys}\,|_{T,\dot{\varepsilon}_p}$ is the uniaxial yield stress at the temperature and strain rate of interest, $\sigma_{yy}(max)$ is the maximum stress at the discontinuity, σ_F is the cleavage fracture stress and M is the plastic constraint factor which elevates the yield stress ahead of the crack on notch. Using relationships established in reference 100 Gerberich *et al.* found that,

$$\ln(\dot{\varepsilon}/\nu) = -\frac{\theta'\Delta G_o}{kT}\left[\frac{\sigma_p^* - (\sigma_{ys}-\sigma_i)}{\sigma_p^* + (\sigma_{ys}-\sigma_i)}\right] \qquad (3.61)$$

where $\sigma_i = \sigma_i(st) + k_y d^{-1/2}$, ΔG_o is the activation free energy, and θ' is a constant used to fit theoretical ΔG_o estimates to experimental results. Combining equations (3.60) and (3.61) gives

$$T_c = \frac{\theta'\Delta G_o}{k}\left[\frac{\sigma_p^*-C_1}{\sigma_p^*+C_1}\right]\frac{1}{\ln(\nu/\dot{\varepsilon})} \qquad (3.62)$$

where $$C_1 = \sigma_F/M - \sigma_i \qquad (3.63)$$

Gerberich *et al.* found this produced satisfactory comparison between the model and observed results. Using equation (3.11) the effect of grain size on the transition temperature may be observed,

$$T_c \approx \frac{\theta'\Delta G_o}{k\ln(\nu/\dot{\varepsilon})}\left[\frac{\sigma_p^*-C_2}{\sigma_p^*+C_2}\right] \qquad (3.64)$$

where $$C_2 = \frac{k_F' d^{-1/4}}{M} - \sigma_i(st) - k_y d^{-1/2}. \qquad (3.65)$$

Figure 3.14 shows the results of transition temperature versus grain size for their experimental results, where the predicted curves are slightly non-conservative (i.e. they predict lower transition temperature values than those observed).

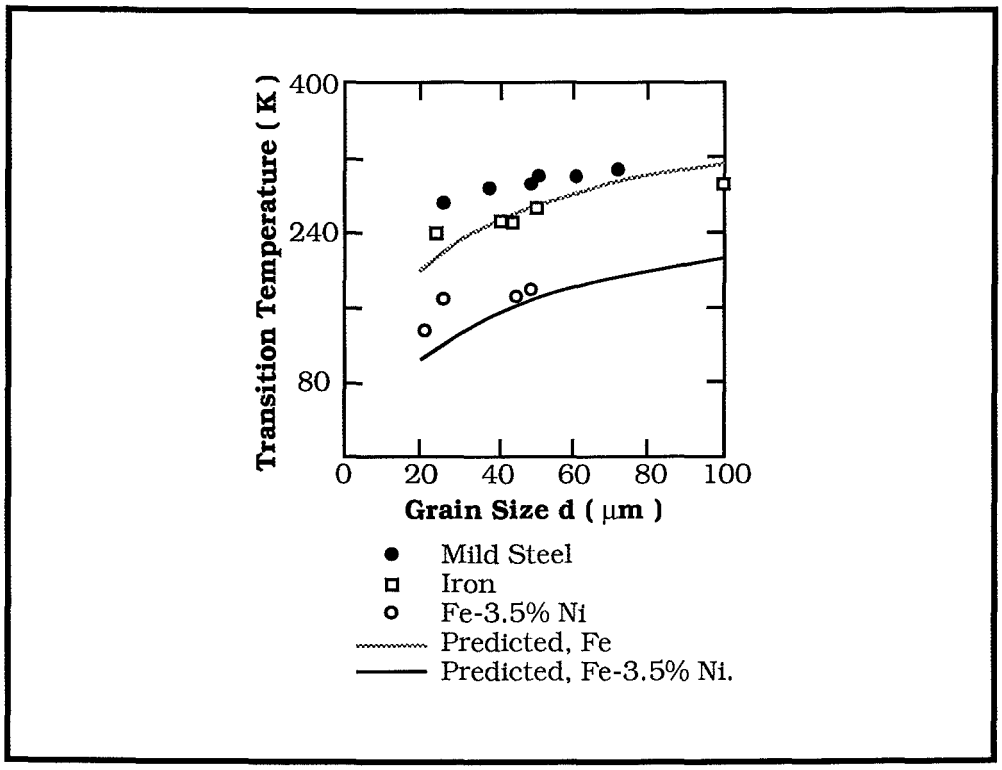

Figure 3.14 : Predicted (equation (3.64)) and experimental results of the FMTT as a function of grain size[176].

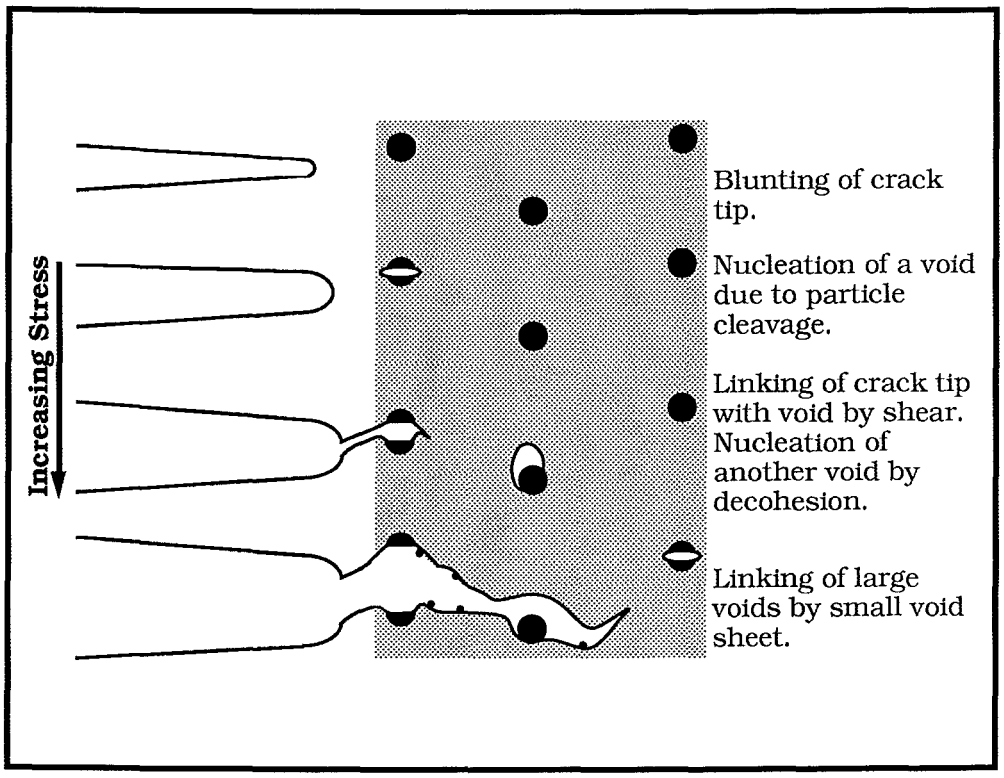

Figure 3.15 : Schematic of ductile crack extension by transgranular microvoid coalescence.

3.4 *Ductile Fracture*

The majority of models of ductile fracture usually consider fracture to occur by transgranular microvoid coalescence as shown schematically in Figure 3.15. Fracture takes place by nucleation of voids at second phase particles (either by cracking or decohesion) and growth of individual voids until the voids coalesce and join up with the crack tip. The three different states of fracture (nucleation, growth, coalescence) are commonly considered separately and a variety of models describing ductile fracture have been published.

3.4.1 NUCLEATION

If particles are strongly bonded to the matrix voids are nucleated by subjecting the particles to high stresses from dislocations tangling around them [156]. Nucleation then depends on a critical dislocation density or shear strain. For most non-metallic inclusions in steel the bonding is so weak however that voids form at almost zero strain [212]. Argon *et al.* have described the condition for void nucleation in terms of a critical interface strength (σ_i) between the second phase particles and the matrix such that the normal stress (σ_{yy}) at the interface must exceed σ_i for void formation to occur [78]. Since the critical stress usually exceeds the yield stress of the matrix then the matrix has to locally work-harden to reach the criterion for voiding. It is convenient therefore to describe the nucleation conditions in terms of a critical macroscopic strain ε_n. This model uses a continuum plasticity approach.

Ashby proposed a dislocation mechanism that accounts for the local work hardening and the increase in flow stress at the particles [213]. The macroscopic nucleation strain is related to the interface tensile stress by considering the number of dislocation loops piling up against the particle.

Although Argon *et al.* and Ashby assume void formation to be caused by interface decohesion, the cracking of second phase particles or inclusions has been observed to result in voiding. In these cases the fibre-loading model of Lindley *et al.* (Section 3.2.3) will describe the nucleation criterion [71].

3.4.2 GROWTH AND COALESCENCE

Once initiated voids grow under the influence of an applied tensile stress although a lateral stress seems necessary also if voids

are to grow sideways as well as lengthways [212]. There are several models which describe this process.

McClintock's model calculates fracture ductility as a function of the volume fraction of voids assuming they grow until they touch [79]. It describes the effects of a hydrostatic stress field on the growth of the array of cylindrical voids. The model tends to overestimate total fracture strain [172].

Thomason's model considered that localised flow is set up between the voids, so that internal necking occurs between cavities in the material [80]. The condition for coalescence is expressed in terms of the intercavity spacing or the volume fracture of cavities.

The Brown-Embury model assumes that the voids elongate along the major strain axis [81]. Unconstrained plastic flow along the planes of maximum shear stress occurs when the length of void attains the value of the average initial inter-particle spacing, therefore coalescence and failure occurs. The model apparently describes experimental results very well [172].

3.4.3 THE RELATIONSHIP TO FRACTURE TOUGHNESS

Rice and Johnson presented a two-dimensional plane strain model of the necking process [214]. The model assumed a pre-crack which had straight sides and whose tip was situated at one inclusion spacing (X_o) from the nearest particle of radius R_o. The crack-tip opening at the point where coalescence of the blunting crack and the expanding void first occurs is the initiation COD (δ_i). Variation of δ_i/X_o with X_o/R_o is usually plotted. This model is consistent with the stretch-zone-width being the length of new surface along the blunted crack tip up to the "knife-edge" separation point [212].

The void growth depends on the state of stress in terms of $\sigma_m/\bar{\sigma}$ where σ_m is the mean stress and $\bar{\sigma}$ is the equivalent stress [215]. The growth of a spherical void in a non-hardening material is given as,

$$\frac{dR}{d\bar{\varepsilon}} = 0.28R \exp(3\sigma_m/2\bar{\sigma}) \qquad (3.66)$$

where R is the radius of the void and $d\bar{\varepsilon}$ the increment of equivalent strain. The conclusions from this are that δ_i will increase if the inclusions are small and widely spaced and also specimen orientation will affect toughness due to the shape of inclusions elongated by

rolling [215]. Specimens cut in the longitudinal direction of rolling, where inclusions are elongated normal to the line of crack advance show high strains longitudinally as far as the ends of the inclusion [84].

Some materials show values of δ_i lower than those predicted by the model. This occurs when the steel loses its capacity for work-hardening at high strains. Shear fracture may then occur along localised shear bands instead of void growth [82]. The Rice and Johnson model predicts that the minimum value of δ_i/X_o is approximately 0.5 though commonly δ_i is in the range 1.0 X_o to 2.7 X_o [215]. One of the problems with these models is that they assume a uniform distribution of void nucleating particles whereas in most structural steels these will be grouped together in a non-uniform fashion resulting in a reduction in effective nucleation and in the growth strain [78,81].

Therefore, the crack-tip ductility in fibrous fracture is affected primarily on the gross non-metallic or inter-metallic inclusion content and the hardening capacity. Hahn and Rosenfield and also Garrett and Knott have shown the effects of hardening capacity on toughness [216,217]. Consider Figure 3.18 where there is a region of intense plastic deformation ahead of the crack tip. The width of this region (λ) is a function of the strain hardening exponent (n) and Hahn and Rosenfield found at the onset of fracture that

$$\lambda(n)_c \approx 0.025\ n^2 \text{ (in metres)} \qquad (3.67)$$

The maximum tensile strain at the crack at fracture ε_f^* was equal to $\varepsilon_f/3$ where ε_f was the true strain in a tensile test [216]. This gives the critical CTOD as,

$$\delta_c = 0.05\ \varepsilon_f\ n^2/3. \qquad (3.68)$$

From equation (2.92) $\delta_t \approx K_I^2/E'\sigma_{ys}$, so substituting for δ_c into equation (3.68) gives

$$K_{IC} = [0.05\ \varepsilon_f n^2 E'\sigma_{ys}/3]^{1/2}. \qquad (3.69)$$

This equation has shown good agreement with measured values of K_{IC} and δ_i in a range of commercial and pure aluminium alloys [212].

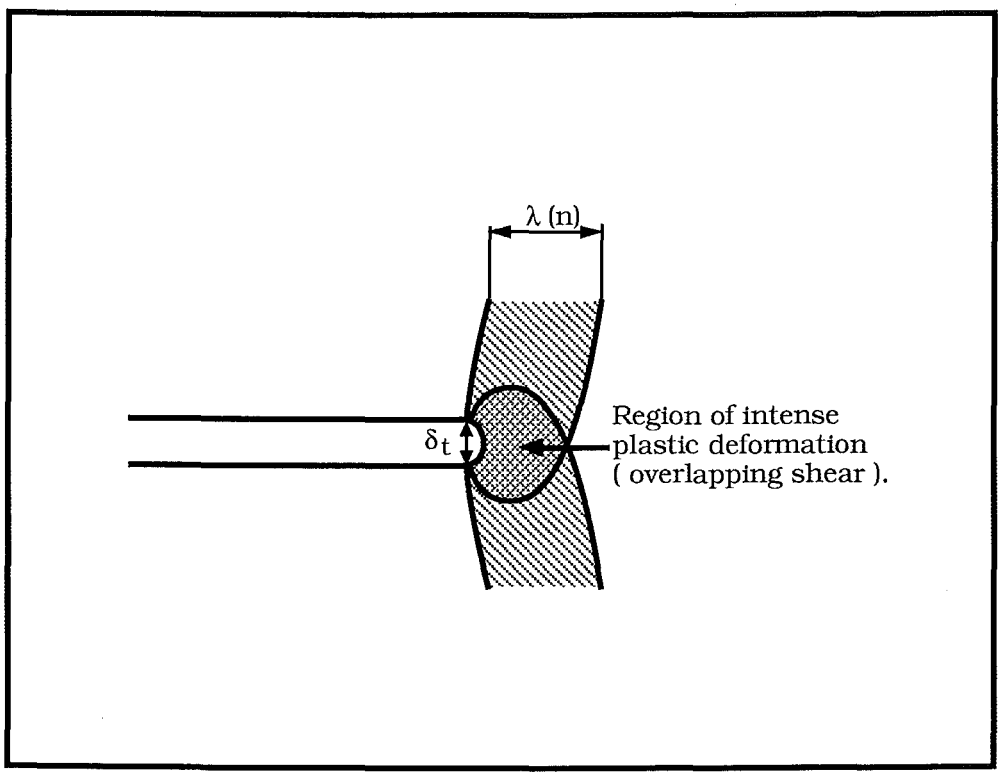

Figure 3.16 : Schematic of the plane-strain plastic zone at the onset of instability [216].

The maximum value of COD is limited by the amount of strain the material can sustain at the crack tip, and therefore by the initial radius of the notch. Smith and Knott and also Chipperfield and Knott measured the critical COD values as a function of notch root radius for steel and found a constant ratio between COD and root radius [84,218]. Below a critical notch root radius the COD is constant indicating increasing fracture strain for decreasing root radius. The slot width of the crack s is usually taken as being twice the notch root radius ρ. When $s \geq s_c$ (the critical slot width below which δ_i is constant) the ratio δ_i/s_c may be defined as the critical crack-tip strain usually known as the notched ductility ε_{fi} [83]. When ductile fracture is initiated ahead of a fatigue crack, similar values of ε_{fi} will be attained over a critical length parameter l_f of the material so that

$$\delta_i = l_f \varepsilon_{fi} \qquad (3.70)$$

Smith and Knott found l_f to be in good agreement with the initial MnS inclusion spacing [84].

Sailor showed that the critical length parameter is dependent on grain size for steels of varying strengths. In this model [85]

$$\ln(\delta_i/l_f) = \bar{\varepsilon}_p \qquad (3.72)$$

where $\bar{\varepsilon}_p$ is the plastic strain at the crack tip so that $\bar{\varepsilon}_p = 0.2\ \varepsilon_f$ and l_f is twice the grain size for ferritic steels.

3.4.4 DUCTILE FRACTURE AT TRANSITION

Ebrahimi examined fracture in the ductile to brittle transition on weld metals [86]. It has been shown that the process of microvoid coalescence is dependent on the plastic strain as well as the hydrostatic stress. In precracked specimens the effective strain is a maximum at the tip of a blunted crack and the hydrostatic stress component reaches a maximum value at a distance approximately equal to 2δ [86,214]. The void growth rate will be at maximum, therefore, at a distance between the tip of a crack and the boundary of the large strain region, given by Knott as 1.1δ [219]. Conceivably discrete ductile microcracks could form ahead of the crack tip as well as at the crack tip, which Ebrahimi observed [86]. Three types of fracture processes observed by Ebrahimi are shown schematically in Figure 3.17

(a) Type I; Fracture occurs at low temperatures when the yield stress is high. The material fails under small-scale-yielding conditions. Characteristic of the microstructure cleavage microcracks form at a small distance ahead of the crack tip and unstable brittle fracture develops.

(b) Type II; As the temperature increases the yield stress decreases and the critical fracture stress is achieved at larger plastic zone sizes and CTOD value ($\delta_c < 0.15$ mm). Cleavage microcracks form only when some strain-hardening has occurred in the plastic zone, and these form ahead of the crack tip. In areas of localised strain many small shear cracks develop from the crack tip and crack initiation is complete when shear instability is achieved between a propagating cleavage crack and a shear microcrack. Therefore a shear zone precedes unstable cleavage fracture and the shear zone width correlates with the plastic zone i.e. increasing in size from specimen mid thickness to edge. With increasing temperature shear is easier and cleavage more difficult so the shear zone width, similar

to the stretch zone width produced by elastic blunting, will increase with increasing temperature. This suggests that cleavage microcrack formation is still the controlling mechanism for Type II behaviour since stretch zone width and shear zone width would be expected to remain approximately constant with change in temperature if shear instability was the controlling mechanism. Therefore the observation of microvoid coalescence in a small region next to the crack tip would not constitute a ductile fracture criterion.

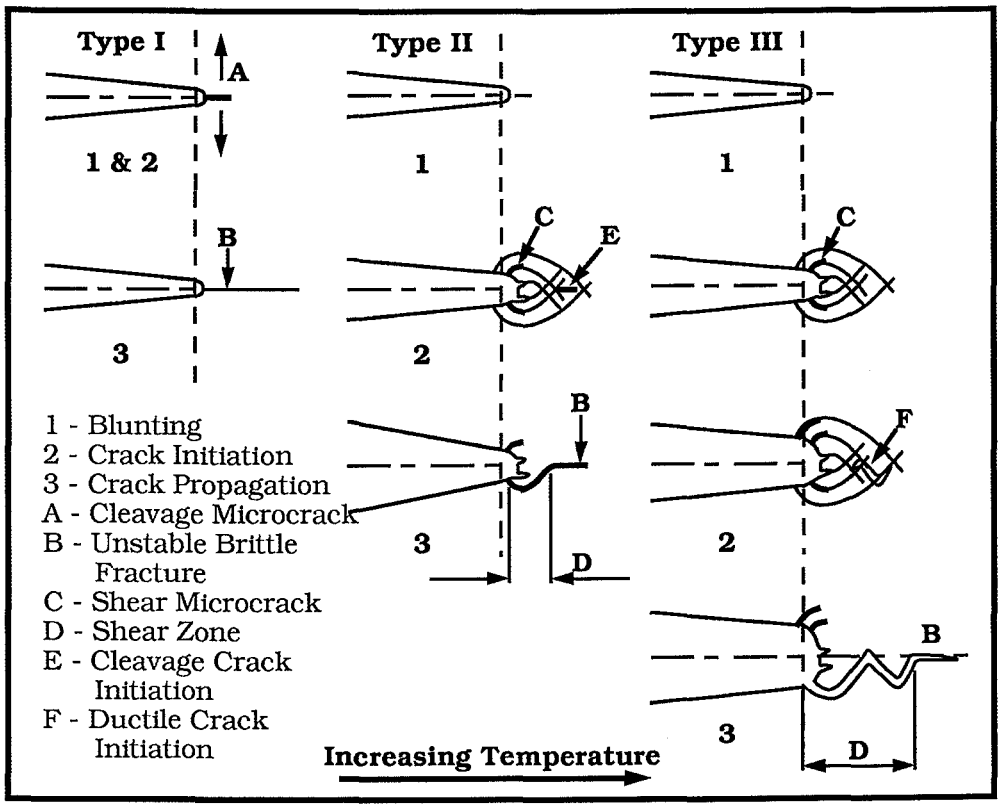

Figure 3.17 : Schematic of the process of crack initiation with increasing temperature[86].

(c) Type III; This behaviour occurs when the temperature is raised high enough into the fracture mode transition region that the combination of stresses and strains ahead of the blunted crack favour the formation of ductile microcracks ahead of the crack tip. When these link up with the shear microcracks at the crack tip then fracture initiation is complete. In this temperature region the stretch zone width remains constant consistent with the insensitivity

of δ_i. The shear zone width observed by Ebrahimi was always less than $2\delta_i$ (≈300 μm) which suggested cleavage fracture was triggered within the initial strain-hardened volume. Ebrahimi felt that since ductile crack initiation precedes unstable brittle crack propagation then the critical CTOD measured could not be classified as δ_c [86]. This behaviour occurred for $0.15 < \delta_c < 0.4$ mm in Ebrahimi's experimental work.

A Type IV behaviour can be described but is not illustrated. This is where slow stable crack growth precedes instability either by cleavage fracture or final ductile rupture, but this instability occurs outside the initial plastic zone.

Ebrahimi found that an increase in specimen thickness from 12.7 to 25.4 mm raised the fracture mode transition temperature by about 25°C. In 25.4 mm thick specimens an increase in a/W from 0.25 to 0.75 raised the FMTT by about 15°C and also the slope of the transition curve was much steeper with a/W = 0.75. The effects of thickness can be explained in terms of constraint or by statistical effects. An increase in thickness increases constraint. An increase in constraint means that plane strain conditions are maintained to a higher temperature, i.e. the FMTT increases. An increase in thickness also means there is an increased probability of finding weak spots at the tip of a crack. Ebrahimi observed stable cleavage microcracks of approximately 150 μm with a grain size of approximately 10 μm in the transition region. This observation suggests that crack propagation from a cracked carbide particle into the ferrite matrix is not the critical fracture event in this transition regime. The cleavage microcracks, approximately 15 times the grain size, may arrest at microstructural inhomogeneities or when loss of stress intensification due to a negative stress gradient in the direction of propagation occurs. The effect of an increase in a/W increases the plastic constraint hence FMTT increases.

3.5 Summary

A review of cleavage and ductile fracture and the fracture mode transition temperature has been presented. It is found that:

(i) The cleavage fracture stress is coincident with the yield stress for coarse-grained steel and exceeds the yield stress in fine-grained steel.

(ii) Cleavage fracture requires small local plastic deformation to occur at the crack tip before instability occurs.
(iii) Cottrell gave the fracture criterion for an intersecting slip-plane mechanism as

$$\sigma_F \geq \left(\frac{2\mu\gamma}{k_y{}^s d}\right)^{1/2} \tag{3.6}$$

(iv) Cleavage fracture is propagation controlled which is tensile stress dependent. Further, for mild steels the critical event is the propagation of cracks from cracked carbide into the ferrite matrix for temperatures below the fracture mode transition.
(v) Smith gave the fracture criterion for a carbide-controlled mechanism as,

$$\left(\frac{C_o}{d}\right)\sigma_F{}^2 + \tau_{eff}{}^2\left[1 + \frac{4}{\pi}\left(\frac{C_o}{d}\right)^{1/2}\frac{\tau_i}{\tau_{eff}}\right]^2 \geq \frac{4E\gamma_p}{\pi(1-\nu^2)d} \tag{3.8}$$

(vi) Although the dependence of fracture stress on grain size is usually given as,

$$\sigma_F = \sigma_{iF} + k_F d^{-1/2}, \tag{3.4}$$

Curry and Gerberich *et al.* have given it as,

$$\sigma_F = k_F' d^{-1/4} \tag{3.11}$$

(vii) The cleavage fracture stress is generally considered to be temperature independent except where the carbide distribution in the steel is low, as in C–Mn steels.
(viii) The Ritchie Knott Rice model predicts cleavage fracture will occur when the cleavage fracture stress is exceeded over some characteristic distance ahead of the crack tip,

$$\sigma_F(2\pi X_o)^{1/2} \geq K_{IC}. \tag{3.18}$$

Curry extended this to give the grain size and temperature dependence of fracture toughness as,

$$K_{IC} = \frac{\beta^{-(N+1)/2}\, X_o^{1/2}(k_F' d^{-1/4})^{(N+1)/2}}{\{\sigma_i(st) + A\exp[-(\beta_0+\beta_1 \ln\dot{\varepsilon})T] + k_y d^{-1/2}\}^{(N-1)/2}} \qquad (3.25)$$

(ix) Statistical theories of cleavage fracture explain that statistical competition in the presence of a sharp crack allows finer carbides to act as a crack nucleus at higher stress intensity. In the absence of stress gradients at a notch the toughness value will be determined by the largest cracked carbide present.

(x) The plastic constraint ahead of a notch is given as 3 using slip line theory and the Von Mises yield criterion. For a sharp crack, including strain hardening effects, the constraint may range from 3.7 to 5 times the yield stress and maximum principal stress occurs closer to the crack tip.

(xi) On the basis of an energy criterion the transition temperature may be written as

$$\alpha T_c = \ln A - \ln\left(\frac{\beta\mu\gamma}{k_y} - k_y\right) - \ln d^{-1/2} \qquad (3.47)$$

or in a simpler approximation as,

$$DT_c = \sigma_i(st) + C - \left(\frac{\beta\mu\gamma}{k_y} - k_y\right) d^{-1/2}. \qquad (3.51)$$

Therefore an increasing transition temperature is predicted with increasing grain size.

(xii) Both Chen *et al.* and Ebrahimi have shown that the fracture controlling mechanism in the transition region may not be the propagation of cracks from carbides into the ferrite matrix but grain-size microcracks. The critical event then becomes unstable fracture across a ferrite/ferrite grain boundary.

(xiii) Ductile fracture by microvoid coalescence may occur by linking of voids through necking or shear, the voids forming by decohesion of inclusions or second phase particles or by cleavage of the same particles. The ductile fracture is stress and strain controlled.

(xiv) The ductile fracture toughness has been given as depending on stress and strain as

$$K_{IC} = [0.05\ \varepsilon_f n^2 E' \sigma_{ys}/3]^{1/2} \qquad (3.69)$$

(xv) Fracture at transition may be a result of ductile and cleavage microcrack formation linked by shear to the blunted crack tip before instability occurs.

CHAPTER 4

Charpy Impact Testing and Grain-Size Measurement

4.1 Introduction to Experimental Program

The experimental program was designed to provide information on the crack nucleation and propagation process in the Crack-Tip Opening Displacement (CTOD) test by variation of grain size and chemical composition of the test material. Previous work [16], on which the present program was based, had investigated the effects of static and dynamic strain-ageing on the toughness of low-carbon steels. That investigation found that the CTOD test did not differentiate between the three steels under investigation with regard to fracture mode transition temperature (FMTT) though the Charpy Impact test showed a variation of about 20°C in FMTT [4]. A discussion of these results said that by:

(i) varying the size of the plastic zone ahead of the fatigue crack, and

(ii) by varying the degree of strain-ageing in the fatigue zone

then progress could be made towards differentiation of the crack nucleation and propagation energies in the CTOD test [4]. This may be achieved by altering the grain size rather than the fatigue amplitude, and altering the composition.

There were seven stages to the experimental program;

(i) Selection and heat treatment of experimental steels; to give an appropriate range of grain size (Section 4.2).

(ii) Manufacture of Test Specimens for Charpy Impact, Tensile and CTOD testing (Sections 4.4, 5.4 and 6.1).

(iii) Charpy Impact Testing; to find the steels' transition temperature for comparison with CTOD test results (Section 4.4).

(iv) Tensile Testing; to give the lower yield or 0.2% proof stress over a range of temperature (Section 5.4).

(v) CTOD Testing; over a range of temperature to give the fracture transition (Chapter 6).

(vi) Grain Size Measurement; Polishing, photomicrography and grain size count on specimens to find the grain size of the experimental steels (Section 4.3).

(vii) Scanning Electron Microscopy; to examine the fracture surface of the CTOD Specimens to find the mode of failure (Section 7.2.3).

Detailed discussion of these stages follows in the subsequent sections and chapters.

4.2 Experimental Steels

4.2.1 COMPOSITION

Two low-carbon steels were selected for the experimental investigation; their chemical compositions by percentage weight are given in Table 4.1.

(a) Steel L: This steel was supplied as 6 m x ϕ38 mm reinforcing bar by Pacific Steel Ltd. of Auckland, New Zealand. It is a NZ3402P/73 Grade 275 reinforcing steel with a titanium addition. Chemical composition was determined by spectrometric analysis at Pacific Steel Ltd. Using the nitrogen analysis method of the United Steel Company the nitrogen content was determined as acid soluble and acid insoluble. Details of the method of nitrogen analysis may be found in references 295 and 296.

To heat treat the steel (to achieve a range in grain size) and to manufacture test specimens the selected bars were cut to length (approximately 150 mm) and hot-rolled using the Mechanical Engineering Department's Radyne high frequency furnace and the rolling mill. This produced bars of about 40 mm width and 18 mm thickness. The process involved substantial cross rolling but final rolling was always in the longitudinal direction. The cross-rolling deforms MnS inclusions so that the approximate circular cross section of the inclusions becomes more elliptical.

(b) Steel H: This steel was cast by A.G. Price Ltd., Auckland, New Zealand and rolled by Pacific Steel Ltd. The steel was in 600 x 50 x 50 mm billets and also forged ϕ16 mm bars (used for tensile specimens). It was an alternative selection when a similar steel to Steel L (but without a titanium addition) was not available. The steel was a special cast with a high active nitrogen content. Chemical composition and nitrogen content were determined as for Steel L. The selected bars were cut to length (approximately 100 mm) and hot-rolled as for Steel L, except rolling was predominantly

Table 4.1
Chemical Composition of Experimental Steels

Elements (% W/W)	Steel	
	L [Pacific Steel 09791/9]	H [Pacific Steel S19A]
C	0.19	0.09
Mn	0.55	0.21
Si	0.17	0.06
S	0.032	0.036
P	0.032	0.037
Al	0.009	0.016
Ni	0.12	0.39
Cr	0.13	0.10
Mo	0.016	0.014
Cu	0.47	0.13
Sn	0.037	0.019
V	0.03	0.002
Ti	0.032	0.001
N Sol:	0.0017	0.0121
Insol:	0.0075	0.002
Total:	0.0092	0.0141
N Sol:	0.0018	0.0114
Insol:	0.0074	0.001
Total:	0.0092	0.0124
Al (Sol.)	–	0.005

Note: L – Identification for low nitrogen steel
H – Identification for high nitrogen steel

longitudinal. The bars produced were about 50 mm wide and 20 mm thick.

The difference in composition of the steels will not allow direct comparison of results between the two steels. However, trends will be observable using two steels of different composition.

4.2.2 HEAT TREATMENT OF THE STEELS

The experimental steels were heat treated to give a range in grain size, the heat treatments being detailed in Table 4.2. The choice of heat treatments was based on previous work by Chua, who had achieved a wide range of grain sizes in his experimental investigation [220]. The four heat treatments were chosen to give a wide range in grain size while maintaining similar microstructure.

(a) A: The double-normalizing heat treatment refines the austenite and ferrite grain size and produces a fine pearlite [221]. The soaking time of 0.5 hours at an austenitising temperature of 900°C allows the material to form a homogeneous solution without grain growth occurring. The faster cooling rate of heat treatment A will produce a smaller ferrite grain size than the slower cooling rates of heat treatments B, C and D since increasing the cooling rate decreases the ferrite grain size, as shown in Figure 4.2 [222]. The amount of pearlite produced during transformation is determined on the iron-carbon equilibrium diagram by the Lever Rule. Since Steel H has a carbon content of 0.09 wt% compared to a carbon content of 0.19 wt% for Steel L, Steel H will form less pearlite.

(b) B, C and D: These heat treatments had a fixed soak time of 2 hours, followed by slow cooling from 920 to 680°C in 20 hours. Austenitising temperature increased from 920°C (for B) to 1200°C (for D). The austenitic grain size is influenced by six factors:

(i) austenitising time
(ii) austenitising temperature
(iii) presence of small inclusions
(iv) heating rate
(v) prior microstructure
(vi) special heat treatment.

The influence of (iv) and (v) is small, being in the order of one grain size number (ASTM scale) and (vi) can have a large or small effect [223-225]. Miller showed that increasing austenitising time increases the grain size (see Figure 4.1), or with constant time, then increasing the austenitising temperature increases austenite's grain size [226]. Figure 4.2 shows that increasing austenitic grain size increases the ferrite grain size on transformation [7,222]. The slow cooling rate from 920°C produces coarse pearlite.

Table 4.2
Heat Treatment of Experimental Steels.

Batch	Annealing Temperature (°C)	Time in hours	Furnace used	Cooling Method
A	900	0.5 + 0.5	Birlec	Double Normalised - Soak 0.5 hours at 900°C - Air cool ≤ 680°C - Soak again 0.5 hours at 900°C - Air cool.
B	920	2	Birlec	Control cool from 920°C to 680°C in 20 hours, then furnace cool.
C	1060	2	Gallenkamp & Birlec	Soak in Gallenkamp, then transfer to Birlec. Control cool from 920°C to 680°C in 20 hours, then furnace cool.
D	1200	2	Gallenkamp & Birlec	Soak in Gallenkamp, then transfer to Birlec. Control cool from 920°C to 680°C in 20 hours, then furnace cool.

Notes:

1. Decarburisation of steel reduced by:

1.1 Birlec furnace has a L.P. gas curtain above 700°C.

1.2 In the Gallenkamp furnace, graphite pieces were placed by the steel and a stream of argon gas was blown over the batch.

2. Batch Size:

2.1 Heat treatment C; Material was split into two batches due to furnace size, giving batches C1 and C2 for each steel.

Therefore batches for heat treatment were:

Steel L : LA, LB, LC1, LC2, LD1, LD2

Steel H: HA, HB, HC1, HC2, HD1, HD2.

3. The following batches did not show the desired grain size and were repeated as detailed below:

Steel	Batch	Microexamination and repeat heat treatment
L	B	A mixed grain size resulted with a fine grain on the bar centre-line only. The original soak temperature of 900°C was increased to 920°C and the heat treatment repeated with the same material.
H	B	ϕ16 mm round bar showed excessive grain growth. New stock was used for the repeat heat treatment and the procedure was changed as detailed: (i) Soak at 920°C for 0.5 hours; (ii) Air cool ≤ 680°C; (iii) Follow B as given.
H	C1	A mixed grain size resulted in the first batch. The procedure was changed as follows: (i) Soak at 920°C for 0.5 hours; (ii) Air cool ≤ 680°C; (iii) Follow C as given.
4. Tensile specimens for Steel H were machined from Batch A, B(repeat), B(original), C, D. B(original) was re-designated Y. 5. Decarburisation occurred at the edges of all the bars. Specimens were machined from the bar centre.		

4.3 *Grain Size Measurement*

The grain size of the steels had to be quantitatively measured so that the effect of grain size on the fracture mode transition temperature may be studied.

4.3.1 GRAIN SIZE MEASUREMENT PROCEDURE

Microspecimens were taken from the ends of used Charpy Impact Specimens (to give longitudinal sections to the rolling direction) and from the heads of used tensile specimens (to give transverse sections to the rolling direction). The specimens were mounted in Bakelite, a thermosetting plastic, for ease of handling during polishing. Normal polishing methods were used as given in Reference [227]. After polishing the specimens were etched in 2% Nital solution for approximately 30-60 s. Photomicrographs were taken from 2 to 3 areas of the specimen, depending on the uniformity of grain size.

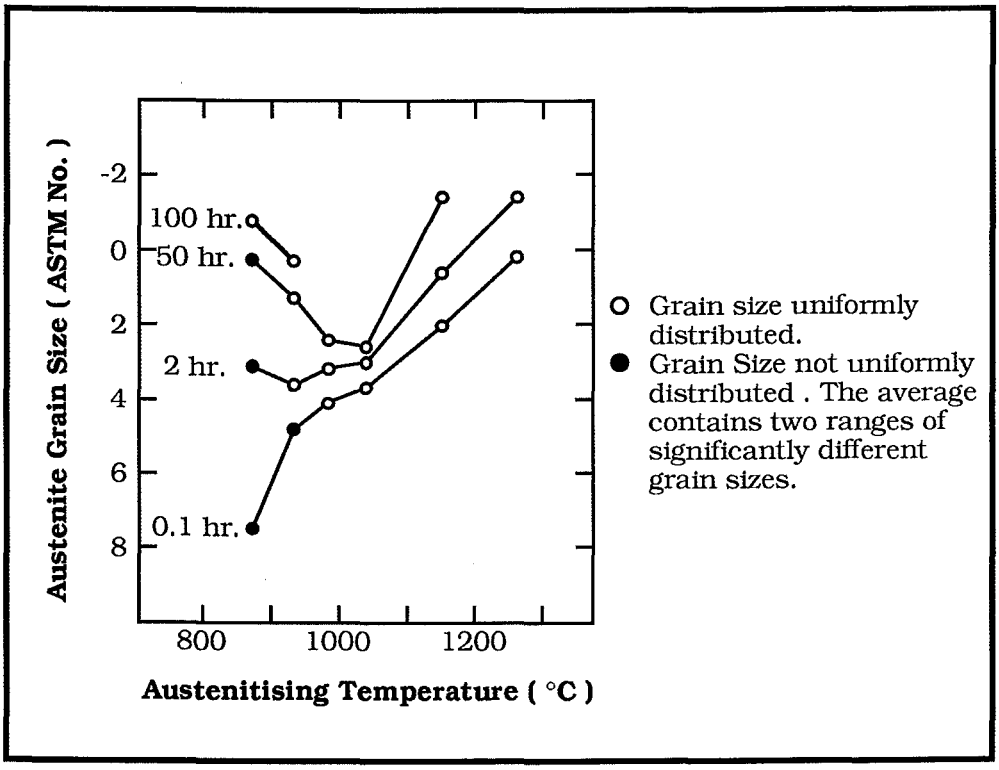

Figure 4.1 : The dependence of austenite grain size on austenitising temperature for different soak times[226].

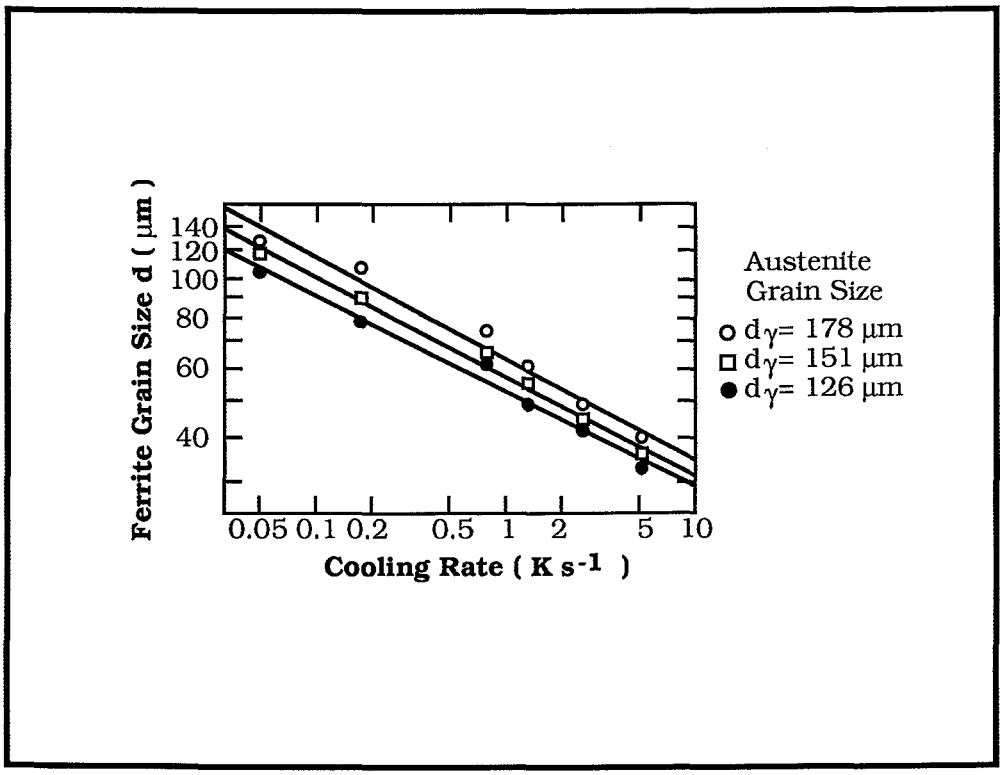

Figure 4.2 : The effect of cooling rate and austenite grain size on ferrite grain size of a mild steel[222].

Magnification varied depending on the actual size of the grains and allowing identification of pearlite grains from grain boundaries.

A modified lineal intercept method was used to determine the "effective ferrite grain size" by considering the steel to be a two phase metal (i.e. ferrite and pearlite). ASTM E112-85, "Standard Methods for Determining the Average Grain Size", was used for guidance in finding the grain size. The method followed was:

(i) A grid of straight lines, of total length L_i, is drawn on a photomicrograph of known magnification. Figure 4.3 shows an example of this.

(ii) The total length of pearlite fraction (L_p) is determined and subtracted from L_i to give the length of ferrite fraction (L_f).

(iii) The total number of intercepts made with the ferrite grain boundaries (pearlite is regarded as a grain boundary) (N_f) are counted.

(iv) The mean intercept length is given by,

$$\bar{l}_f = \frac{L_f}{N_f \times \text{Magnification}} = \frac{(L_i - L_p)}{N_f \times \text{Magnification}} \qquad (4.1)$$

(v) The pearlite fraction is

$$\% \text{ Pearlite} = \frac{L_p}{L_i} \times 100\% \qquad (4.2)$$

(vi) Total line length was approximately 1500 mm on each photomicrograph and the number of intersections was approximately 150-300 per photomicrograph.

(vii) ASTM Grain size number and its 95% confidence limits were determined from ASTM E112-85. Mean intercept length, $\bar{l}_f$, was used for subsequent work as the average grain size and for calculating the reciprocal square root of grain size.

ASTM E112-85, Section 5, Generalities of Application says

"5.1 It is important, in using these methods , to recognise that the estimation of grain size is not a precise measurement .... the grain cross sections produced by a random plane (surface of observation) through such a structure, would have a distribution of areas varying from a maximum value to zero, depending upon where the plane cuts each individual crystal. Clearly, no two fields of observation can be exactly the same."*[230]

---

* Grain Size Measurement

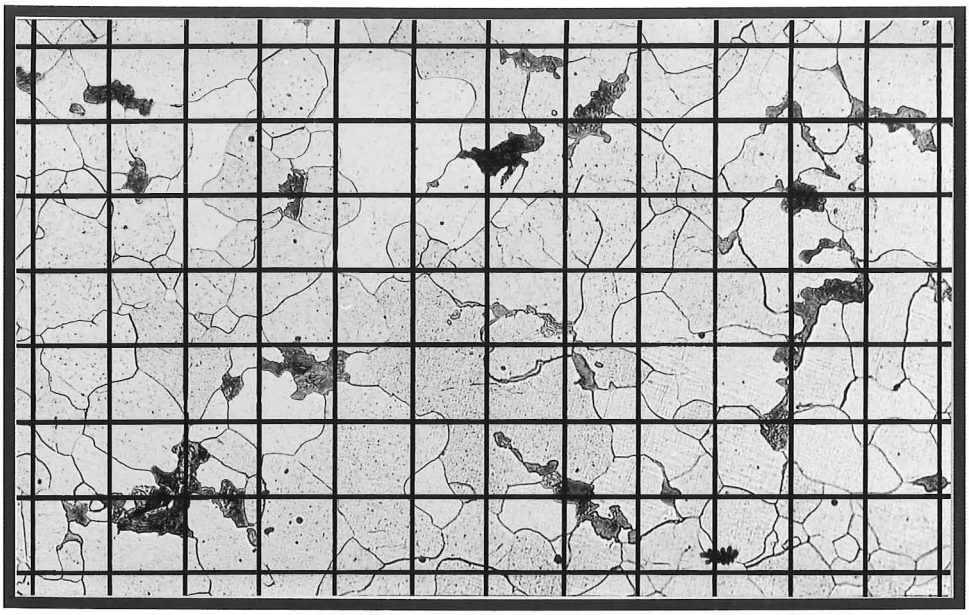

Figure 4.3 : A typical example of the linear intercept method to determine grain size. 0.1 mm

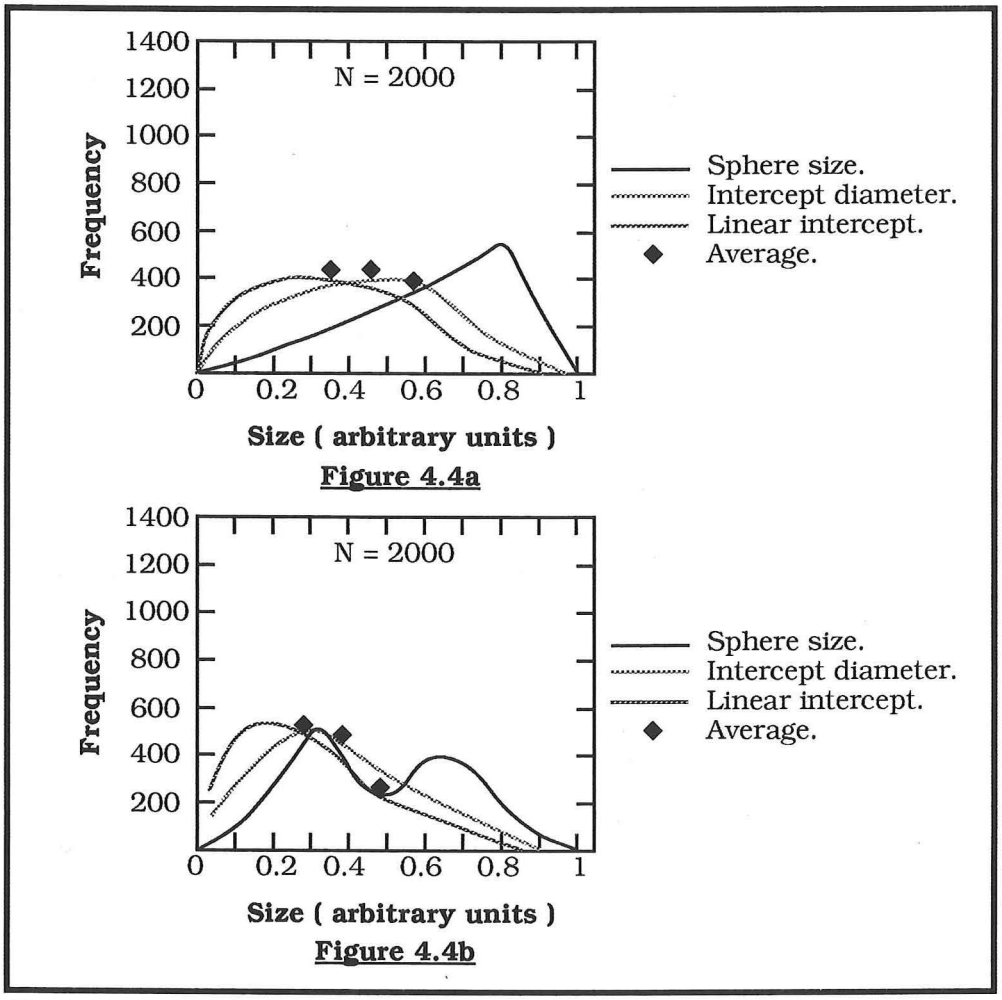

Figure 4.4 : Sectioning of spheres to simulate grain-size determination using random sampling[231].
(a) Distributions of sphere and intercept parameters for right-skewed sphere-size distribution.
(b) Distributions of sphere and intercept parameters for bimodal sphere-size distribution.

This implies that the degree of accuracy of grain size measurement is limited. The more uniform a crystal structure the more the measurement will approach the "true" average grain diameter.

Figure 4.4 shows figures from Reference 231 [15]. Hensler used a sphere to represent a grain (for mathematical convenience) and performed simulated random-sampling experiments [231]. He used a computer to investigate the relationship between the size distribution of grains and the distribution of dimensions of planar and linear intercepts of the grains. The figures show that the average intercept diameter is $\pi/4$ (0.78) and linear intercept is $\pi^2/16$ (0.61) of the average grain diameter, within experimental error. These results apply to a right-skewed and a bimodal distribution. Therefore grain size measurements underestimate the actual average grain size.

Hensler also showed that the grain size doesn't affect the error by sectioning. Therefore a small grain size will have the same error as a large grain size distribution. Dunne *et al.* found that mean intercept length, average equivalent circle diameter, geometric mean and mode are poor representations of a skewed distribution [234]. Alternative mean ferrite grain sizes, weighted in terms of grain volume and grain area, were found to be more sensitive to skewness. Skewness was pronounced in the steels investigated in Reference 234 due to low hot-rolling temperature (915-850°C) with large percentage reductions, producing a distribution of very fine ferrite with some large grains. Methods for determining the weighted diameters are adequate when the specimen number is low or automated measuring methods are available [234].

Previous investigations have used the mean intercept distance ($\bar{l}$ in ASTM E112-85) [12,16,220,228,229,232]. It can be corrected to nominal diameter by multiplying by $4/\pi$;

$$\bar{d}_n = 4\bar{l}/\pi \qquad (4.3)$$

Pussegoda [12] determined the nominal diameter as "effective ferrite grain size" but use of $\bar{d}_n$ is only representative of the particular field of view and may not be used as an average [230]. Also $\bar{d}_n$ is accurate only for spheres and in equiaxed uniform grains. ASTM E112-85 eliminates this problem by defining ASTM grain size numbers so ASTM No. 0 has a mean intercept size of precisely 32.00 mm on a field at 100x magnification for micro-size scale.

Since an absolute grain size is not determined then as long as the method of measurement is consistent between samples the use of mean intercept length as "average grain size" is justified.

4.3.2 GRAIN SIZE MEASUREMENT RESULTS

The results of grain size measurement are presented in Table 4.3. The results given are the average mean intercept in μm, the range and median of results, the standard deviation and "$d^{-1/2}$" (in $mm^{-1/2}$) found from the mean intercept. Photomicrographs of grain size are shown in Figures 4.5 to 4.13. Figures 4.5 to 4.8 show Steels LA, LB, LC and LD respectively. Figures 4.9 to 4.13 show Steels HA, HB, HC, HD and HY respectively. Photomicrographs were taken at a uniform magnification so visual comparison between grain sizes is given.

(a) Steel L

The photomicrographs for Steel L show a ferrite/pearlite matrix, the percentage pearlite ranging form 6.4 to 17.5%. There is no observable trend with increasing grain size for the percentage pearlite.

Steels LA, LB and LD show uniform equiaxed ferrite/pearlite matrices. Grain size increases with the higher austenitising temperatures and increased soaking times and also with the decreased cooling rate. Pearlite is more coarse in LB and LD; the slow cooling rate allowing time for growth of the pearlite into a coarse structure [221].

Miller showed that the growth of austenite grains is complex [226]. Figure 4.1 shows that increasing austenitising time increases austenitic grain size. The complex pattern of grain growth is;

(i) at low austenitising temperatures growth proceeds slowly.

(ii) at 925-980°C a few grains grow rapidly to a huge size producing a mixed structure of large and small grains. After a long austenitising time only large grains remain.

(iii) At about 1040°C more grains grow but the average growth rate slows. Therefore, both the maximum and average grain size is less than at 925-980°C.

(iv) Between 1150-1260°C grains grow rapidly to a large size and the maximum and average grain size are larger than those produced by any lower austenitising temperature for the same austenitising time.

Table 4.3
Grain Size for Experimental Steels.

Batch	$\bar{d}$ (μm)	σ_{n-1} (μm)	Range (μm) Low	High	ASTM Grain no.	95% C.L.	$d^{-1/2}$ ($mm^{-1/2}$)	Average % Pearlite
LA	10.132	0.897	8.343	11.585	9.962	-0.394 +0.475	9.939	10.01
LB	18.695	1.284	17.464	20.960	8.195	-0.311 +0.348	7.262	8.23
LC[1]	40.968	7.121	16.197	53.327	5.931	-0.730 +0.979	4.941	12.59
LD	56.196	8.898	45.093	76.997	5.019	-0.671 +0.874	4.218	13.42
HA	14.038	1.211	12.060	15.459	9.021	-0.385 +0.445	8.440	2.49
HB[2]	43.189	14.351	24.650	66.394	5.779	-1.265 +2.303	4.812	1.78
HC	48.710	7.695	36.872	64.834	5.432	-0.671 +0.874	4.531	2.09
HD	57.030	8.316	43.002	72.585	4.977	-0.624 +0.797	4.187	2.22
HY[3]	53.770	15.087	28.954	74.127	5.146	-1.100 +1.802	4.313	2.76
Average H[4]	50.821	12.249	24.650	74.127	5.309	-1.263 +1.469	4.436	3.17

1. LC represents the average of a duplex grain size. the results of analysis of the small and large grain size contributions are given below.
2. This average grain size for HB was used only for the regression analysis of lower yield strength versus temperature and grain size. In CTOD calculations and for the analysis of transition temperature an average Charpy test piece grain size of d = 27.823 μm was used. In tensile test pieces a duplex grain structure resulted; details of this are given below.
3. HY represents an average tensile test piece grain size only.
4. The average grain size of HB, HC, HD and HY was used in the analysis of lower yield strength versus temperature and grain size when results for these batches were grouped about the same curve.

Grain Size for LC, HB and HY								
Batch	$\bar{d}$ (μm)	σ_{n-1} (μm)	Range (μm) Low	High	ASTM Grain No.	95% C.L.	d-1/2 (mm-1/2)	Average % in steel
LC(S)	23.284	5.657	16.197	28.656	7.561	-0.975 +1.484	6.553	14
LC(L)	42.542	5.539	31.579	53.327	5.822	-0.563 +0.701	4.848	86
HB(Charpy)	27.823	4.929	24.650	38.745	7.048	-0.742 +1.001	5.995	–
HB(S)	40.562	4.370	34.016	45.526	5.960	-0.474 +0.566	4.965	43
HB(L)	58.605	6.350	47.579	66.394	4.898	-0.476 +0.570	4.131	57
HY(S)	35.525	5.827	28.954	41.375	6.342	-0.693 +0.914	5.306	36
HY(L)	63.906	5.409	57.711	74.127	4.648	-0.378 +0.436	3.956	64

Note: S = small grain size and L = large grain size.

This pattern is affected by the alloy content of the steel. Steels LB and LD follow (i) and (iv) of the pattern respectively. Steel LC has a duplex (or mixed) grain structure (Figure 4.14), the grain diameter having a range 16.20 - 53.33 μm with a standard deviation of 7.12 μm. The smaller grain size has an average mean intercept of 23.38 μm, and the larger grain size has an average mean intercept of 42.54 μm. The smaller grain size has an estimated 20-30% distribution in the microstructure, the larger grain size having 70-80% distribution. This reflects the pattern of growth in (iii) above where a majority of grains have grown rapidly to a large size but islands of finer grains remain. With longer austenitising time the finer grains would be replaced. An average grain size of the small and large grain sizes of LC is used in following work.

(b) Steel H

The lower carbon content of Steel H gives a range of 0.55-3.91% for pearlite fraction, there being no observable trend with increasing grain size. Steels HA, HC and HD show a uniform, equiaxed ferrite/pearlite matrix, their grain sizes being given in Table 4.3. The pattern of complex ferrite growth is repeated in heat treatment B, C and D.

For Steel HB, the specimens taken from Charpy test pieces have a uniform grain structure. The tensile specimens for HB show a duplex grain structure, the range being 34-66 μm in grain diameter. This structure is shown in Figure 4.15. The smaller average grain diameter of HB (Tensile) is 40.56 μm (with 43% distribution in the microstructure). The larger average grain diameter is 58.61 μm (with 57% distribution in the microstructure). The microstructure is repeated in Steel HY. HY was the same as heat treatment B. The duplex microstructure has a small grain size of 35.53 μm (with 36% distribution in the microstructure) and a large grain diameter of 63.91 μm (with 64% distribution). The duplex microstructure is repeated to a lesser extent in the tensile specimens of HC and HD. The tensile specimens were machined from forged ϕ16 mm bar rather than rolled-down billet. The size of the bar has different heating and cooling rates than the more massive rolled billet. This gives shorter austenitising times at temperature and shorter transformation times. Heat treatment B at 920°C is on the edge of the pattern of growth between 925-980°C. HB (Tensile) reflects this pattern of growth where there is roughly equal distribution of the

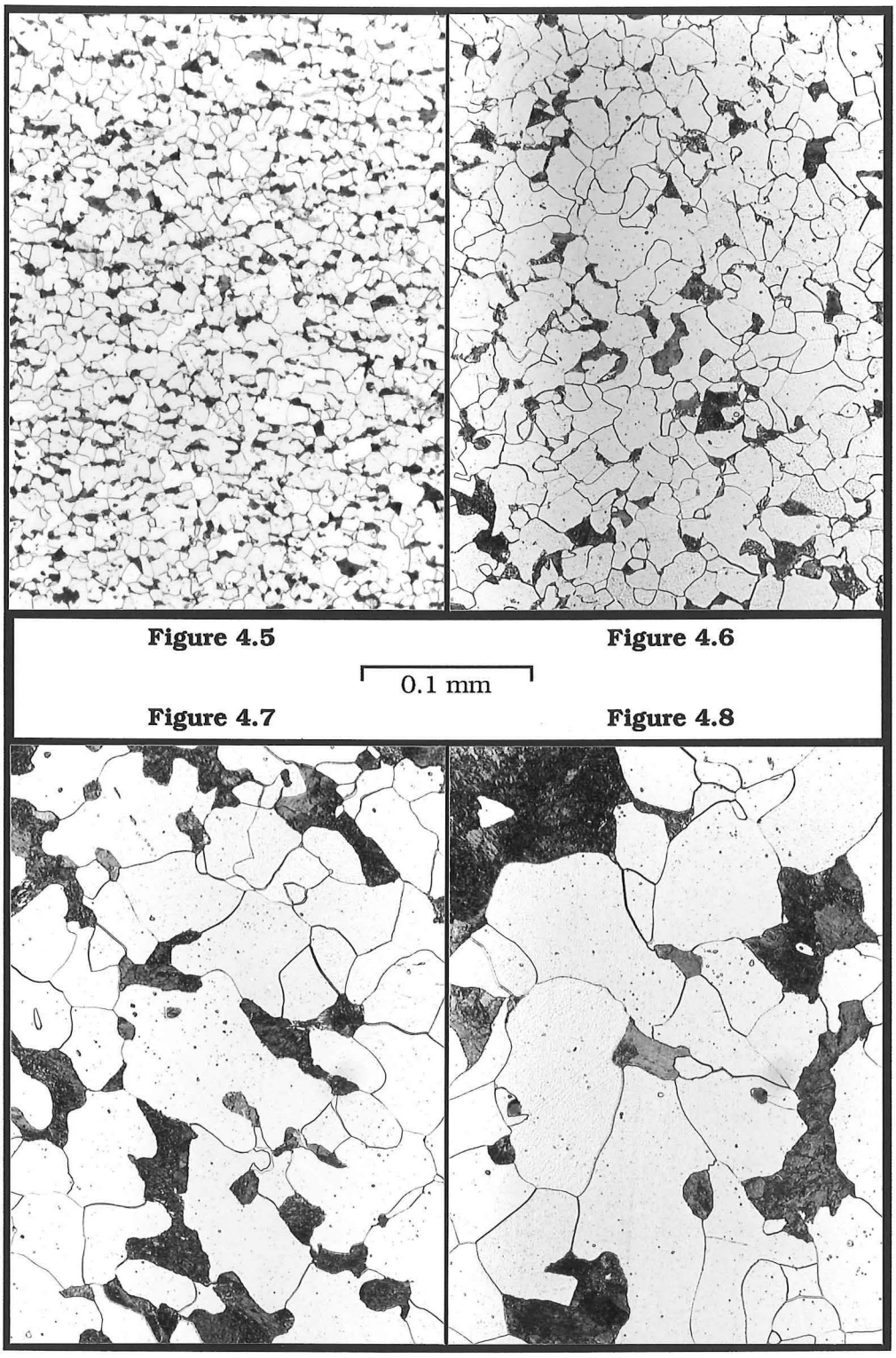

Photomicrographs of grain size for Steel L ;
Figure 4.5 : LA, ASTM grain no. 9.962
Figure 4.6 : LB, ASTM grain no. 8.195
Figure 4.7 : LC, ASTM grain no. 5.931
Figure 4.8 : LD, ASTM grain no. 5.019

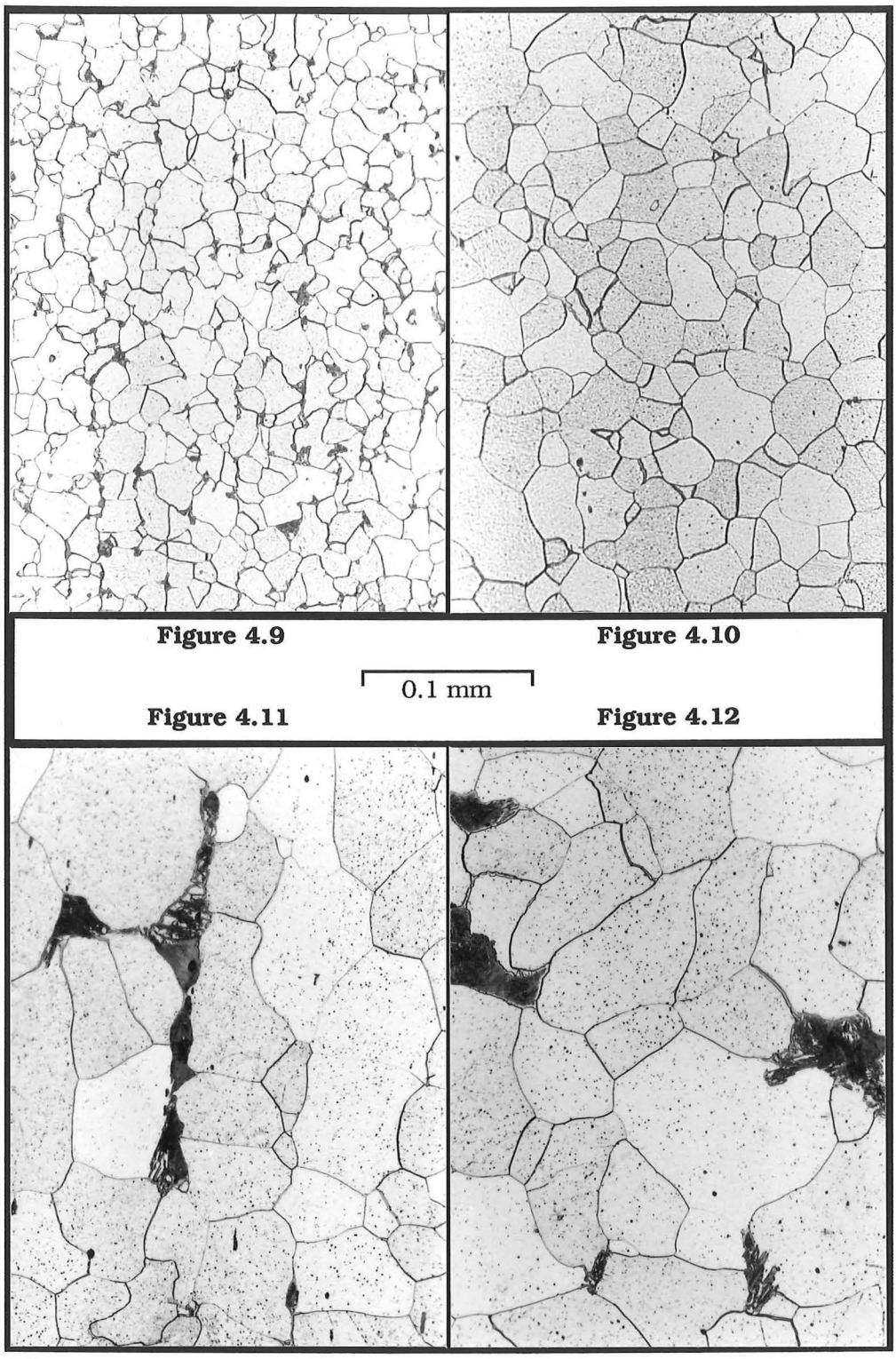

Photomicrographs of grain size for Steel H ;

Figure 4.9 : HA, ASTM grain no. 9.021.
Figure 4.10 : HB, ASTM grain no. 7.048.
Figure 4.11 : HC, ASTM grain no. 5.432.
Figure 4.12 : HD, ASTM grain no. 4.977.

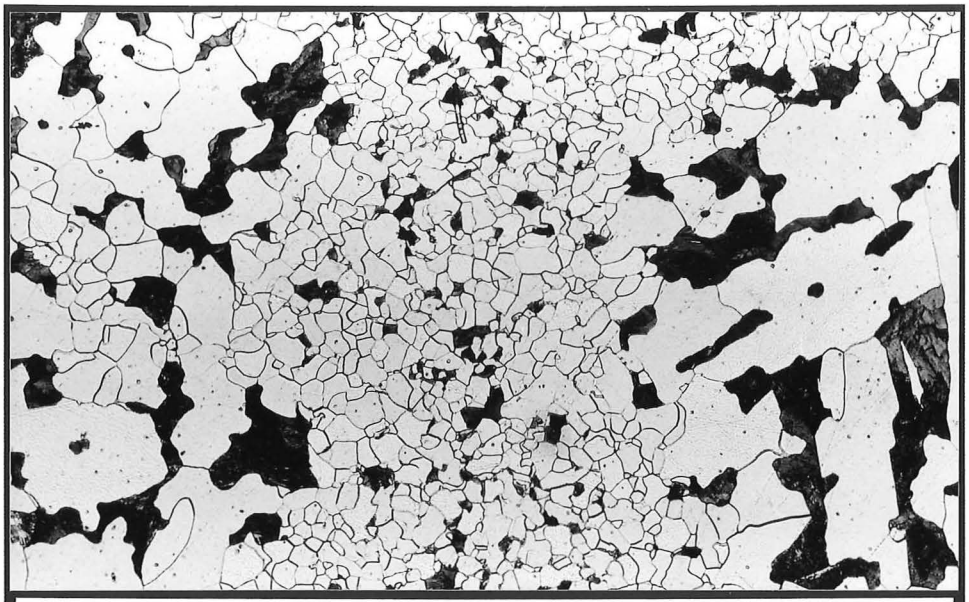

Figure 4.14

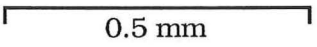

Figure 4.15

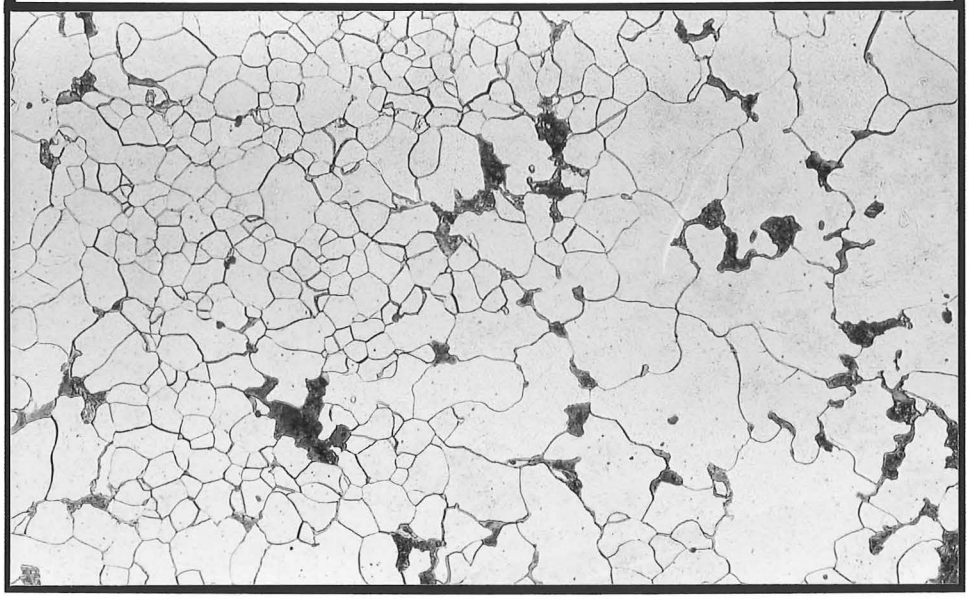

Photomicrographs to show the duplex grain structure of ;
Figure 4.14 : LC, ASTM grain no.'s 7.561 and 5.822.
Figure 4.15 : HB, ASTM grain no.'s 5.960 and 4.898.

small and large grain sizes. At the higher austenitising temperatures of HC and HD then the small volume of the ϕ16 mm bar allows replacement of the fine grains with massive ferrite.

In work on the grain size dependence of the fracture mode transition temperature the average grain size of the Charpy specimens of HB is used because of the duplex grain structure of HB (Tensile). In analysis of the temperature and grain size dependence of yield strength an average grain size of HB, HC, HD and HY is used although the final model is based on the individual grain sizes.

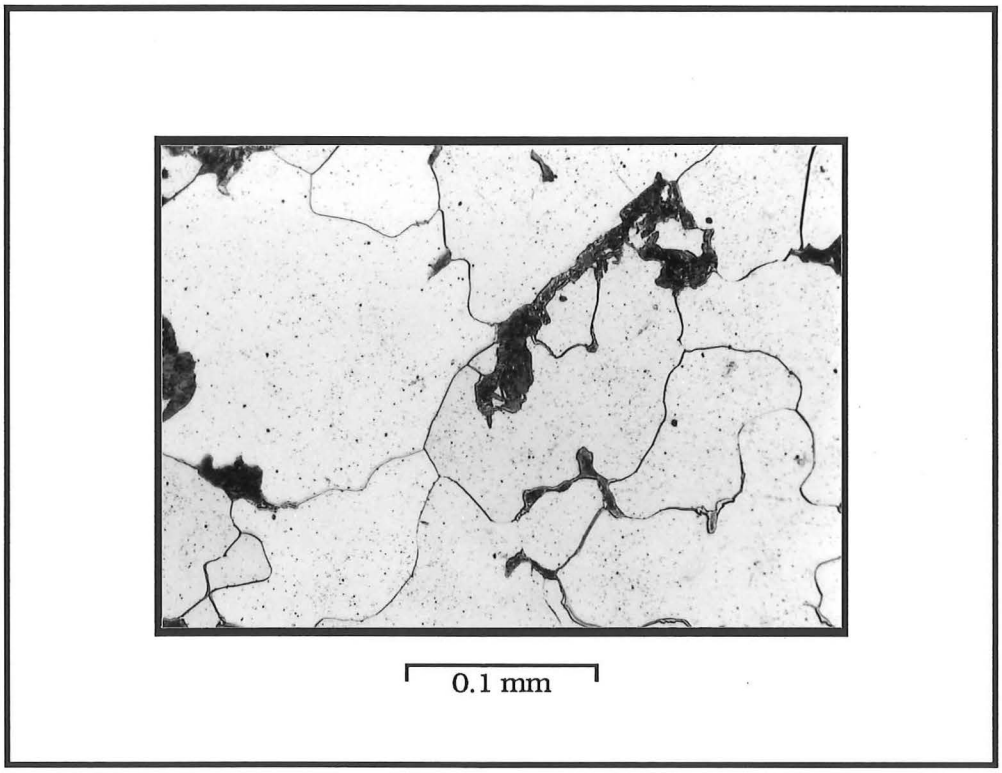

Figure 4.13 : Photomicrograph of Steel HY, ASTM grain no. 5.146.

4.4 Charpy V-notch Impact Testing

Charpy V-notch impact testing was carried out to find the fracture mode transition temperature of each experimental steel as defined by this test. It also enables a comparison to be made between the Charpy V-notch impact test and the CTOD test and to correlate this with other available experimental data.

4.4.1 FACTORS AFFECTING THE CHARPY IMPACT TEST

Originally the Charpy Impact test was used to identify which materials failed in a brittle manner at a particular temperature. It is now commonly used to find the temperature at which fracture mode

transition occurs in a particular material. From Figure 4.16 where energy for fracture is plotted against temperature there is a definite transition region for low strength materials, such as low and medium carbon steels. Below the transition failure is by cleavage fracture whereas above the transition failure is ductile by microvoid coalescence.

Figure 4.17 shows schematically the anvil striker and the Charpy test piece. Full details of the Charpy V-notch impact test are given in BS131, Part 2: 1972. Briefly, the standard Charpy specimen is a 10 mm square beam, 55 mm long, containing a 2 mm deep V-notch with a root radius of 0.25 mm at mid-length, and is supported at its ends in the horizontal position. The test specimen is cooled or heated to the test temperature and then placed on the machine supports. Within 6 seconds an impact load is applied via a striker on a swinging pendulum. The load is applied at specimen mid-span opposite the notch. The results can be expressed by:

(i) Energy absorbed by fracturing the test specimen,

(ii) Assessing the proportion of fracture surface showing granular (cleavage fracture) or fibrous (microvoid coalescence) appearance,

(iii) Measuring the lateral contraction at the root of the notch.

Figure 4.16 shows that a similar curve is obtained for each of the above criteria when the results are plotted against temperature to show the impact transition temperature. The impact transition temperature can be defined using the above criteria. Kobayashi *et al.* investigated the transition temperature using the criteria Charpy-V 15 ft-lb energy, 0% Shear and 15 mil lateral expansion, finding these to be yield point fracture criteria [233]. Also investigated were the criteria Charpy-V 30-35 ft.lb energy and 25% Shear, which were identified as the initiation ductility transition temperature. Other researchers [8,12,16] have used the Charpy-V 20ft lb (27 Joule) energy criterion which Reference 24 of [8] identified as the ductility transition temperature. Another common criterion is the 50% shear fracture appearance transition temperature (FATT) [5,9,59]. This investigation uses the 20 ft.lb (27 Joule) energy criterion as the definition for Charpy-V transition temperature, although results are included for the 50% Shear FATT. The ductility transition temperature is also used for CTOD testing i.e. where initiation of ductile crack extension first occurs.

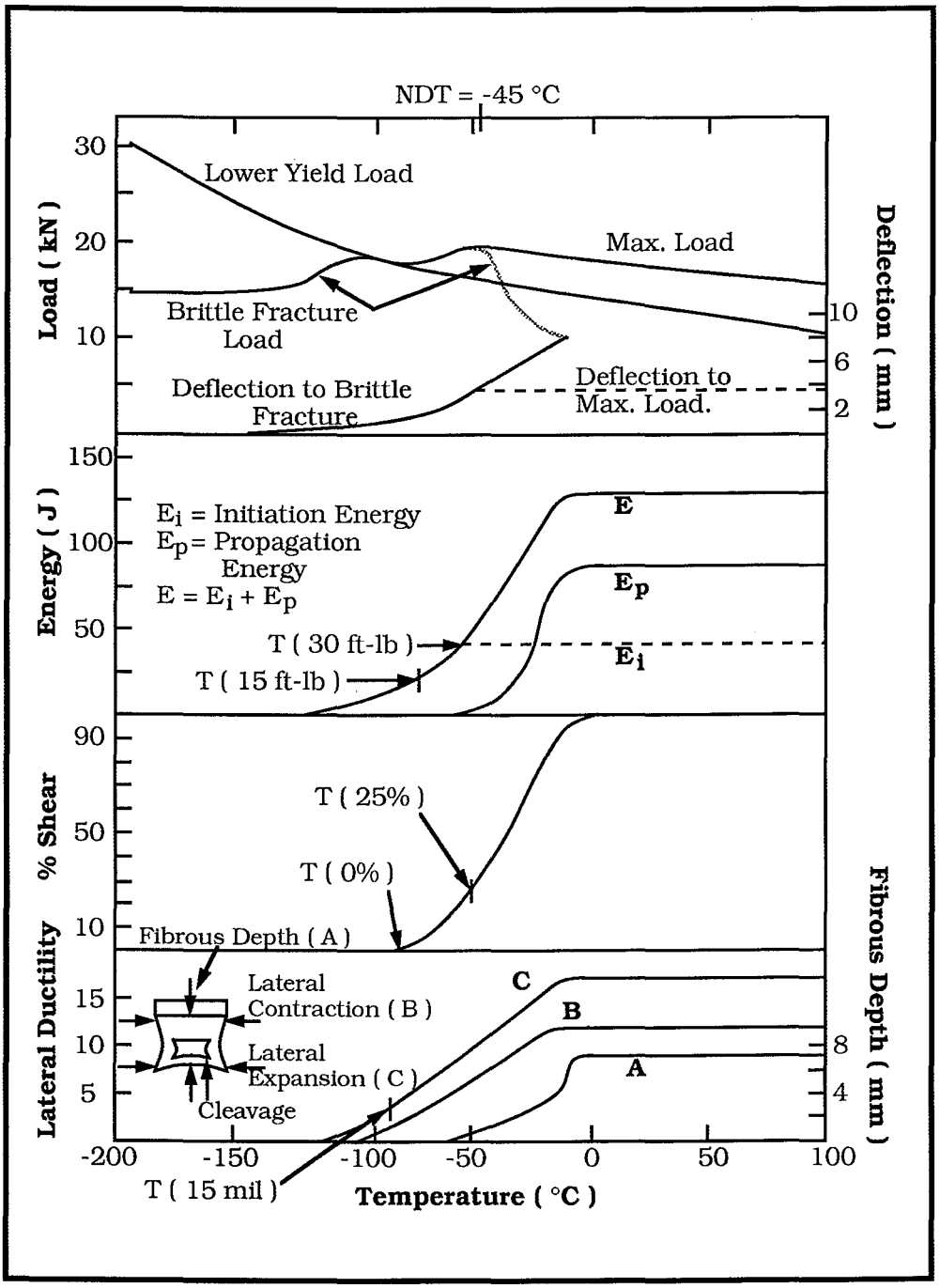

Figure 4.16 : Analysis of transition behaviour in the Charpy impact test for a low-carbon pressure vessel steel[233].

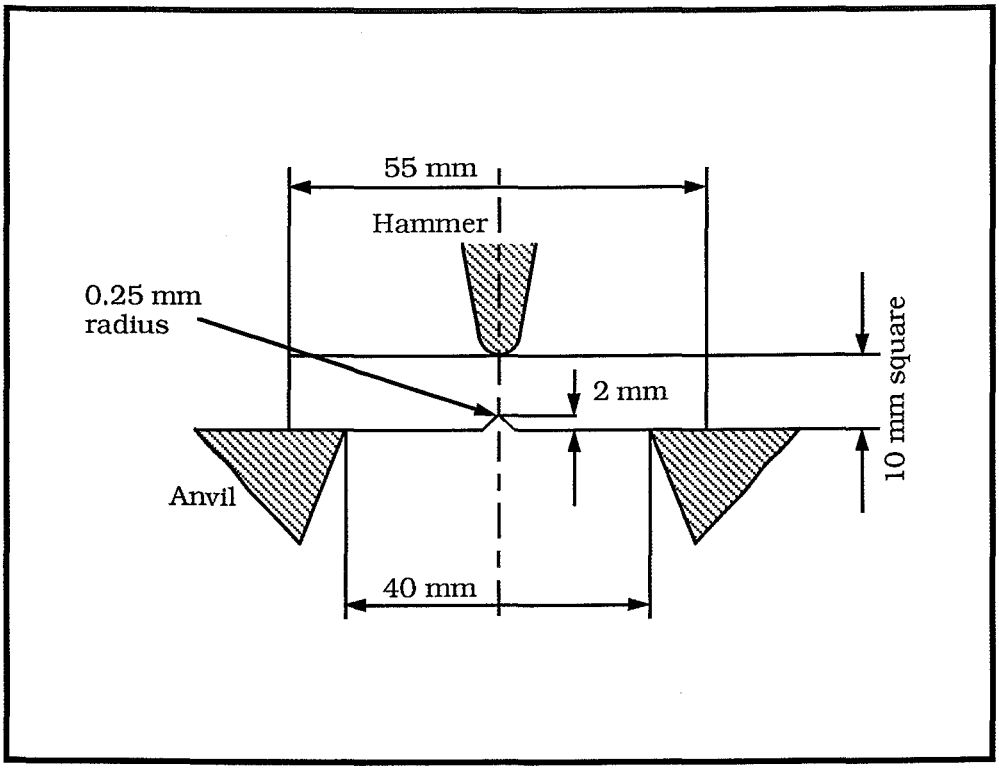

Figure 4.17 : Schematic of the Charpy V-notch Impact Test.

The transition temperature is affected by the composition of the steel, grain size, strain rate and stress state (the size of specimen and notch used).

(a) Composition

Figure 4.18 shows that the transition temperature increases for increasing carbon content of the steel. This is due to an increasing amount of pearlite in the microstructure [5]. It was suggested that this occurred because;

(i) the fracture of cementite lamallae lead to notch effects,and

(ii) the creation of voids at ferrite-pearlite interfaces results in the generation of dislocations at the interfaces thus providing nuclei for cracks.

Equation (4.16) of Reference [8] gives the transition temperature for low carbon alloy steels as,

$$T_{27} = 264(\%C) - 11.8(d^{-1/2}) + 28(\%Mn) - 140\ 000(F^1) + 3850(\%N_R) + 18(\%Cr) + 68(\%Si_T) + 50(\%Al_R) + \text{constant} \qquad (4.4)$$

where $F^1 = \dfrac{(\%Mn)(\%N_R)}{(\%Mn) + K_n(\%N_R)}$

and the constant K_n = 1500 and T_{27} is in °C. F^1 accounts for the variability of dislocation locking strength [8]. In structural steels dislocation locking is thought to be mainly by nitrogen [87] and the effectiveness of nitrogen locking is controlled by Mn content [6]. Equation (4.4) shows that increasing N content initially decreases the transition temperature but further increases result in an increase in transition temperature. Other elements increase the transition temperature although the coefficient for silicon is only significant in fully killed steels [8]. Erasmus, in eliminating the grain size term by virtue of a relationship between $d^{-1/2}$, Mn, Ni and N_{AlN}, found that the effect of nickel on the transition temperature was purely due to its effect on ferrite grain size [8].

(b) Strain Rate and Stress State

The transition temperature found by the Charpy-V impact test is influenced by the type of notch and the size of the specimen. Ferguson and Thorby found an expected 30°C increase in transition temperature by using a fatigue crack instead of the standard notch in the Charpy test [17]. However Chew found that the transition temperature determined by the CTOD test was approximately 40°C lower than those of the Charpy test [16]. Therefore, the strain rate of the test used has a large effect on the transition temperature and with increasing strain rate the transition temperature increases. Sumpter and Caudrey in their paper showed that the dynamic CTOD test has an increase in transition temperature compared to the static CTOD test [123].

Results of sub-standard Charpy specimens in Figure 4.19 show that the transition temperature increases as specimen thickness increases [235]. This is because fracture toughness is dependent on the thickness of the specimen tested,

$$K_c = \frac{P}{BW^{1/2}} \bullet f(a/W), \qquad (4.5)$$

where P = Load at instability

B = Thickness of specimen

W = Width of specimen

f(a/W) =Geometry factor of crack length(a) to width(W) ratio, which was developed in Chapter 2. With increasing thickness the stress state is changing from plane stress to plane strain.

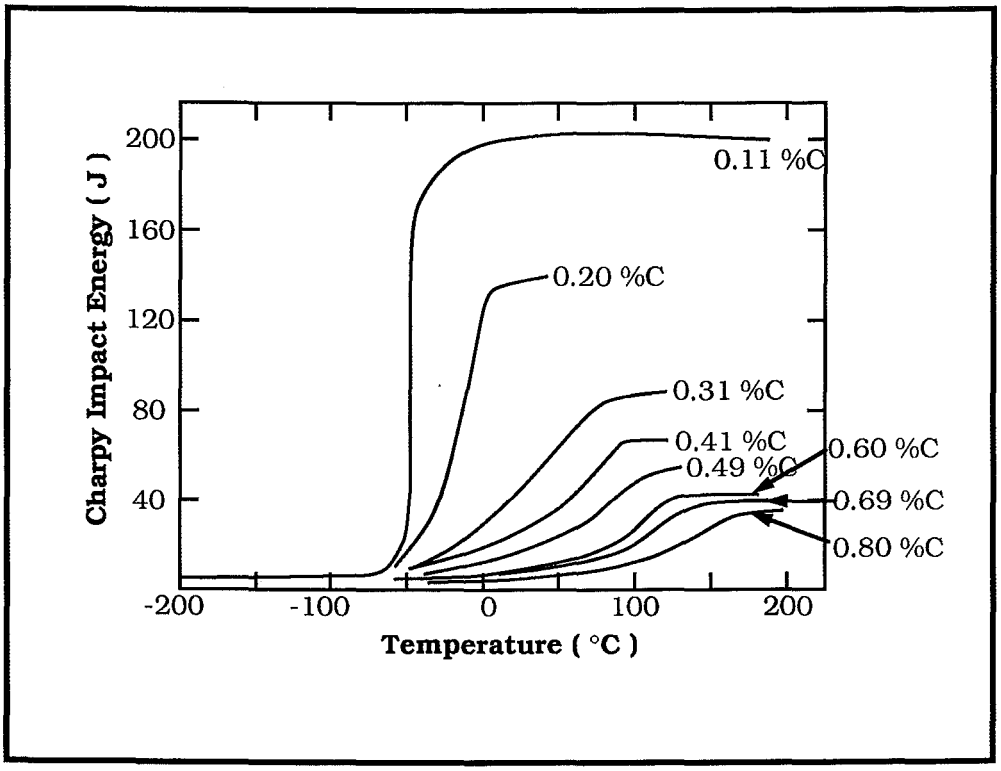

Figure 4.18 : The effect of pearlite on the transition temperature measured by the Charpy Impact test as obseved by Burns and Pickering[5].

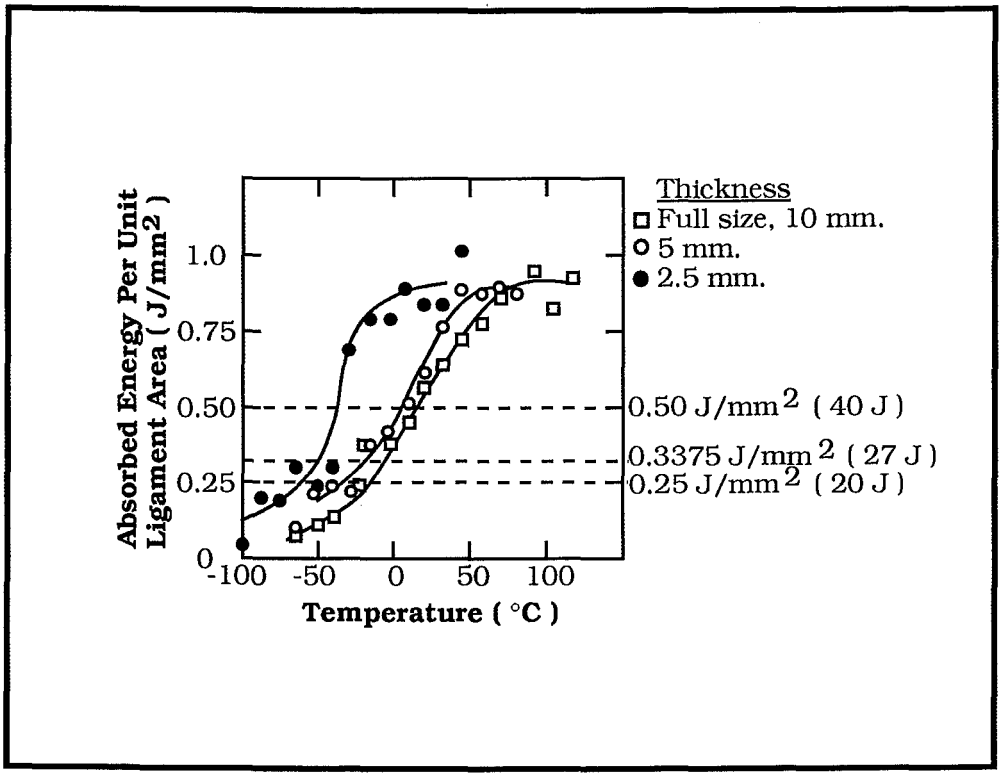

Figure 4.19 : The effect of specimen thickness on the FMTT curve using the Charpy impact test for BS 1501-281 plate[235].

(c) Grain Size

In Chapter 3 Equation (3.51) for transition temperature was developed where,

$$DT_c = \sigma_i(st) + C - \left(\frac{\beta\mu\gamma}{k_y} - k_y\right)d^{-1/2}.$$

Both equations (3.51) and equation (4.4) have negative coefficients for grain size, $d^{-1/2}$. That is, with increasing $d^{-1/2}$ (decreasing grain size) the transition temperature decreases. The coefficient for $d^{-1/2}$ as given in equation (3.51) can vary between -15.5 and -9.65 depending upon the nitrogen and manganese contents of the steel used to determine the coefficient by regression analysis [10]. This variation is due to the segregation of carbon and nitrogen to the grain boundaries and variability of dislocation locking at grain boundaries provided by these elements [10]. The gradient of equation (3.51) is -11.8°C/$mm^{-1/2}$ in Reference 8 and -11.6°C/$mm^{-1/2}$ in Reference 7.

4.4.2 EXPERIMENTAL PROCEDURE

The Charpy V-notched specimens were prepared from Steels L and H to the specifications of BS131 Part 2: 1972. Figure 4.20 gives the dimensions of the specimens used and Figure 4.21 shows the orientation of the notch crack plane to the rolled direction of the steel. This orientation is L-T; the crack front propagates normal to the rolling direction. Specimens were machined after heat treatment of the experimental steels.

(b) Test Procedure

The tests were made on an Avery Impact Testing machine with a striking velocity of 5 ms^{-1} and a striking energy of 298J. For sub-ambient temperature tests specimens were cooled by immersion in a petroleum ether/dry ice mixture and for elevated temperature tests specimens were heated using hot oil. A minimum soak time of 15 minutes at the test temperature was allowed to ensure homogeneous temperature throughout the specimen.

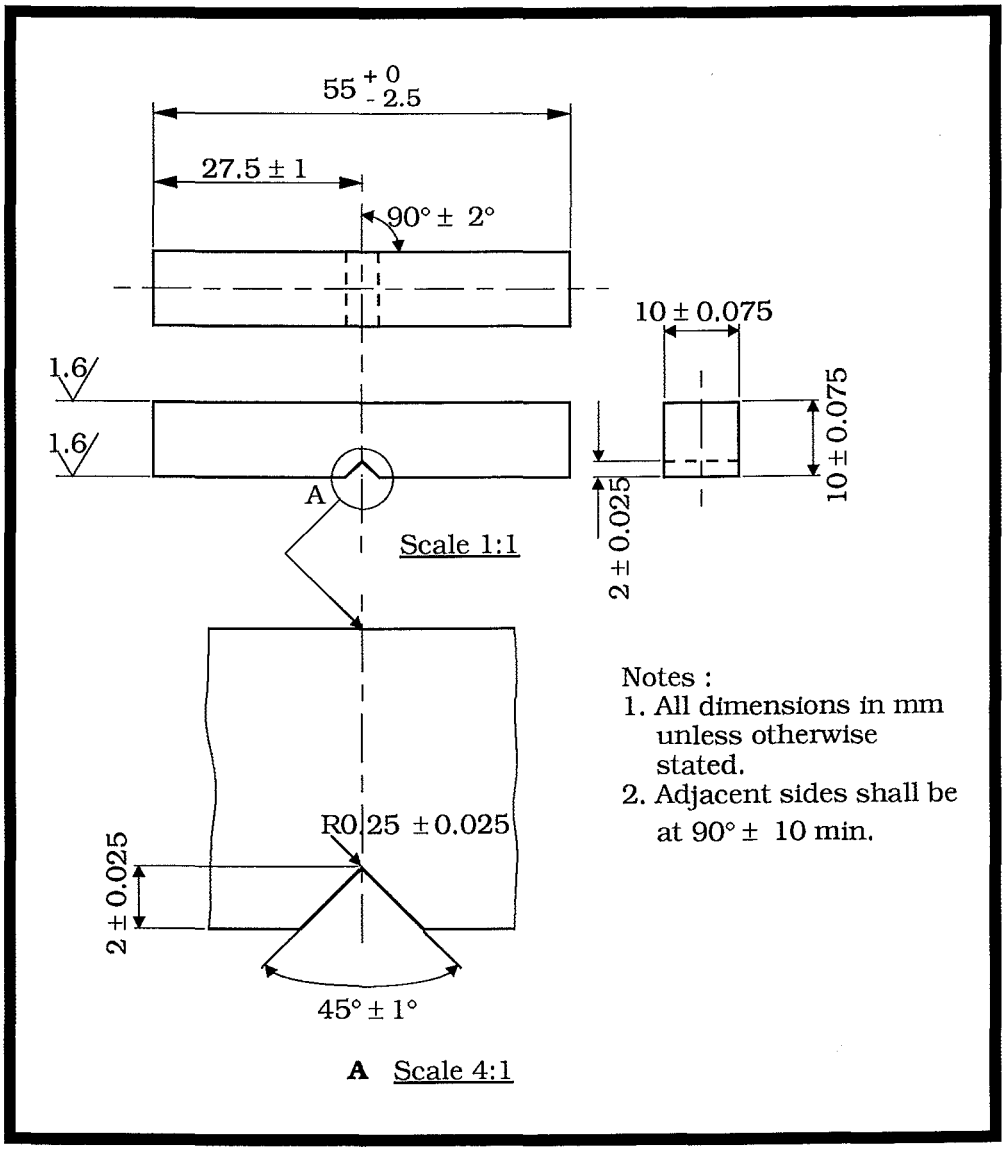

Figure 4.20 : The Charpy (Simple Beam) Impact Test Specimen, Type A.

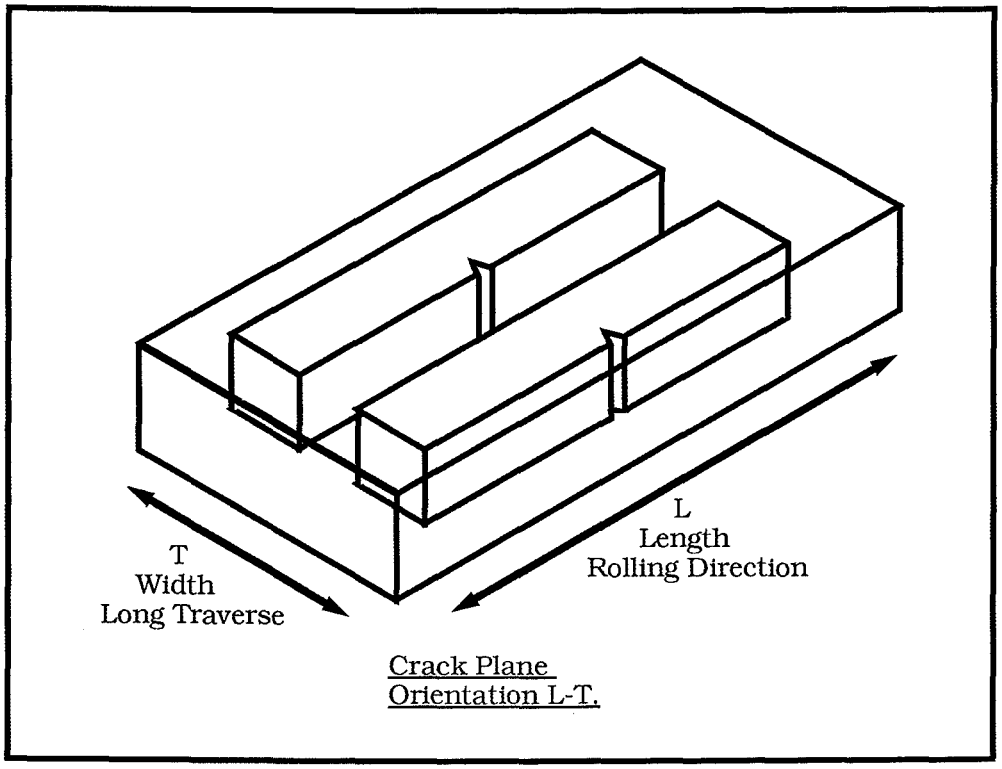

Figure 4.21 : The notch plane orientation of the Charpy specimens relative to rolling direction.

4.4.3 EXPERIMENTAL RESULTS

Tables of results for Charpy V-notch impact testing are given in Appendix A. Impact transition curves are shown in Figures 4.22 - 4.25. Figure 4.22 shows results of impact energy (J) versus temperature for Steels LA-LD respectively while Figure 4.23 shows results of percentage shear versus temperature for the same steels. Figure 4.24 shows results of impact energy (J) versus temperature for Steels HA-HD respectively while Figure 4.25 shows percentage shear versus temperature for the same steels. A line of best fit has been drawn for each set of results to give an estimated fracture mode transition curve. Table 4.4a presents the transition temperature estimated from the transition curve at 27J impact energy or 50% Shear.

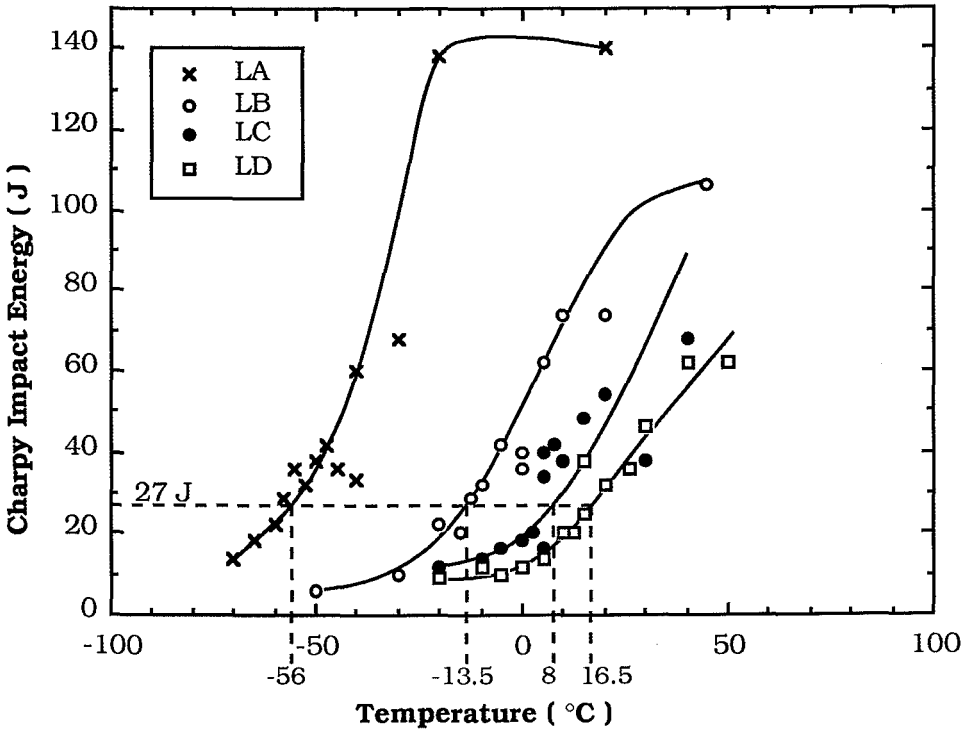

Figure 4.22

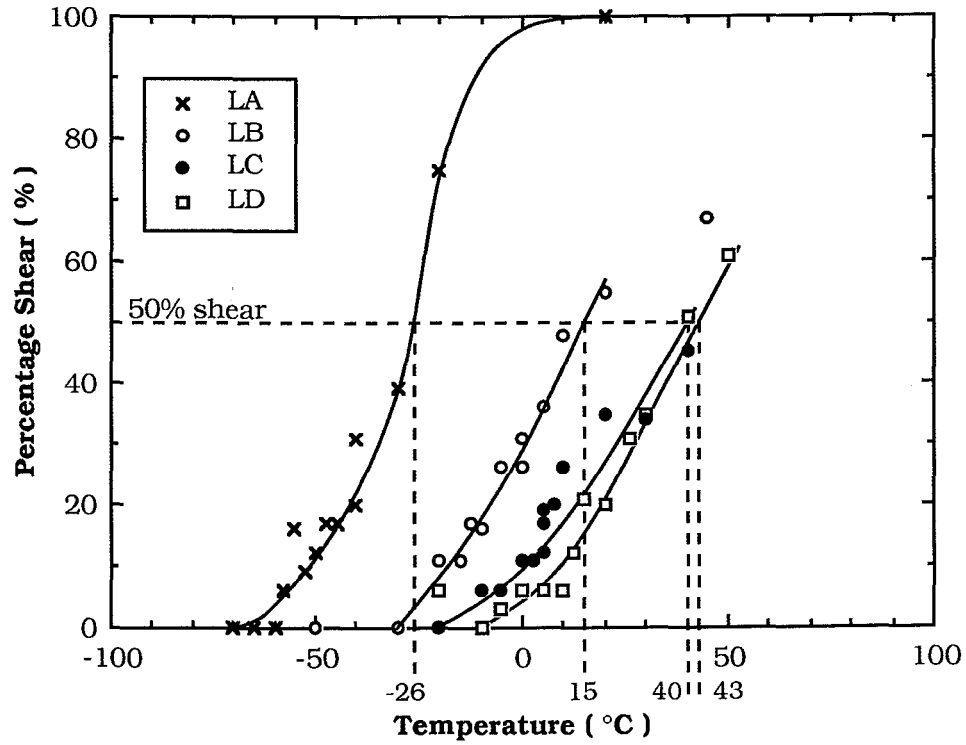

Figure 4.23

Figure 4.22 : Charpy impact energy (J) as a function of test temperature (°C) for Steel L.

Figure 4.23 : The percentage of shear fracture of the Charpy specimen as a function of test temperature (°C) for Steel L.

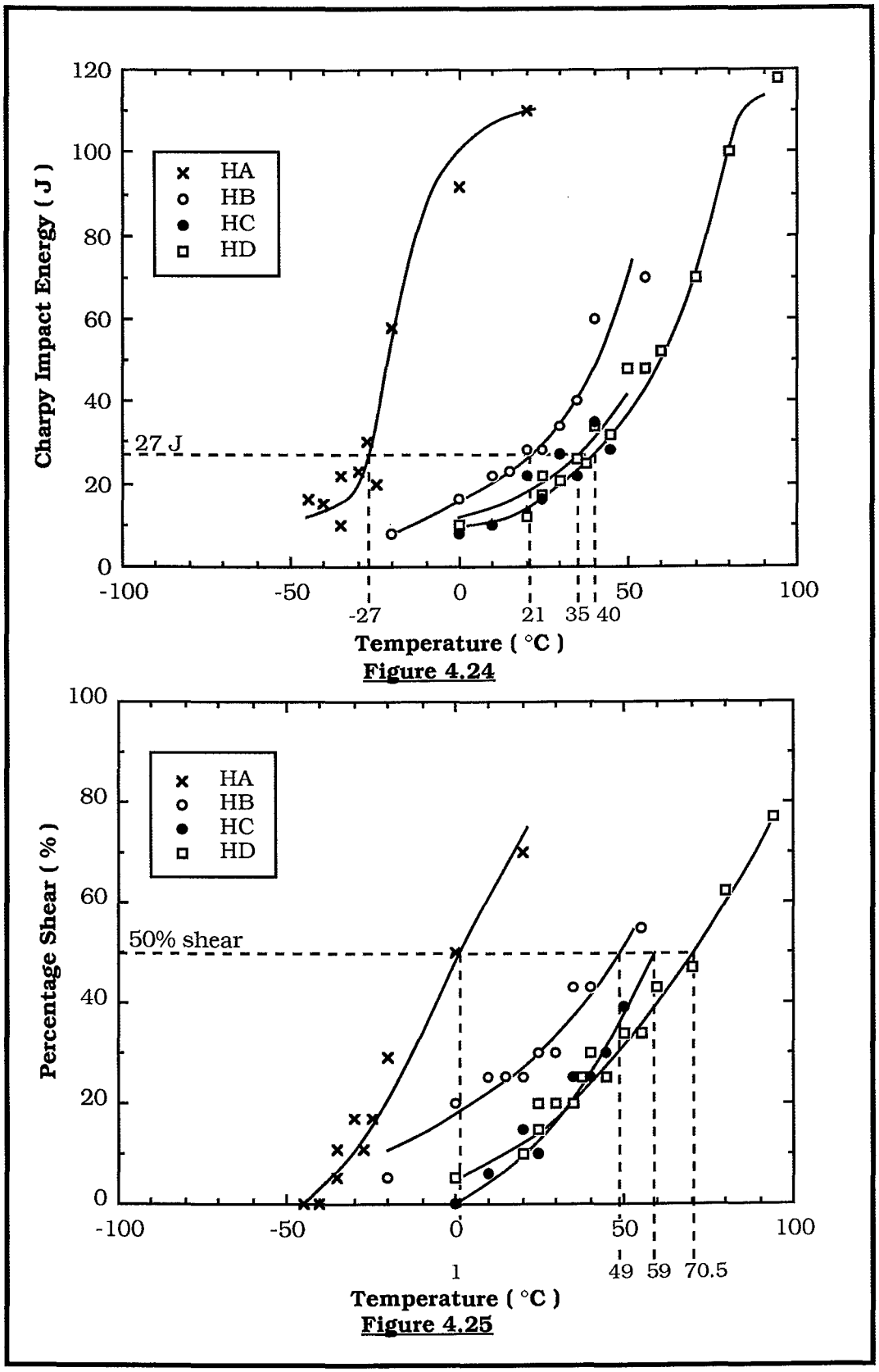

Figure 4.24 : Charpy impact energy (J) as a function of test temperature (°C) for Steel H.

Figure 4.25 : The percentage of shear fracture of the Charpy specimen as a function of test temperature (°C) for Steel H.

Table 4.4a
Estimated Transition Temperatures for Charpy Impact Tests

Steel	$d^{-1/2}$ ($mm^{-1/2}$)	T_{27} (°C)	$T_{50\%}$ (°C)
LA	9.939	-56	-26
LB	7.262	-13.5	15
LC	4.941	8	40
LD	4.218	16.5	43
HA	8.440	-27	1
HB	5.995	21	49
HC	4.531	35	59
HD	4.187	40	70.5

Table 4.4b
Linear Regression[1] Results for Transition Temperature (°C) versus Grain Size ($mm^{-1/2}$)

	L, 27J	L, 50% shear	H, 27J	H, 50% shear
Equation No.	4.7	4.8	4.9	4.10
r	0.9918	0.9908	0.9883	0.9836
Significance	99%	99%	98%	98%
B_0	70.72	98.66	107.70	134.79
B_1	-12.44	-12.24	-15.63	-15.53
95% C.L. of B_1	±4.88	±5.09	±7.35	±8.66
Significance of B_1	99%	99%	98%	98%
$\bar{y}$	-11.25	18	17.25	44.88
95% C.L. of $\bar{y}$	±10.92	±11.38	±12.30	±14.50

1. Equation of the form $T_c(°C) = B_0 + B_1 d^{-1/2}(mm^{-1/2})$
2.. For the definition of statistical symbols see Appendix B.

4.4.4 DISCUSSION OF RESULTS

(a) General: From Figures 4.22 and 4.24 the results show scatter around the fracture mode transition region although the scatter is less when percentage shear is plotted versus temperature (Figures 4.23 and 4.25). The scatter is greatest in the results for LC where the impact energy at 5°C has a range 16-40 J. Therefore T_{27} = 8°C for LC will have a large associated error. The scatter in results for heat treatment C is due to the duplex microstructure formed. Testing at the same temperature, if the crack plane contains a high distribution of small grains then the material appears tougher than the same material with a high distribution of large grains in the crack plane. A crack is expected to be more difficult to nucleate and propagate in fine-grained material. The results for the other heat treatments are uniform and with a range in transition temperature of 72.5°C for Steel L and of 67°C for Steel H then using an average grain size for heat treatment C was acceptable.

(b) Grain Size: Figures 4.22 and 4.23 show the grouped transition curves for Steel L for impact energy and percentage shear respectively and figures 4.24 and 4.25 show the same grouped data for Steel H. The results show that increasing grain size increases the fracture mode transition temperature (using either 27J or 50% FATT as transition criterion), as expected from equation (3.51). The range in T_{27} transition temperature is 72.5°C ((-56) - 16.5°C) for Steel L and is 67.0°C ((-27) - 40°C) for Steel H. Chew found that the CTOD test showed no variation in FMTT between the 3 steels he investigated yet the Charpy test had showed a variation of 19°C for T_{27} transition temperature for the 3 steels [16]. An overall range of 96°C in T_{27} transition temperature for this work should show whether the CTOD test can distinguish between the steels with regard to fracture mode transition. The average difference of 28.5°C (26 - 32°C) between T_{27} and 50% FATT transition temperatures was not considered significant.

Figures 4.26 and 4.27 show the transition temperature as a function of $d^{-1/2}$ for Steel L and Steel H respectively. Table 4.4b gives the results of a least squares linear regression analysis performed on the data to give,

$$T_c(°C) = B_0 + B_1 d^{-1/2}(mm^{-1/2}), \qquad (4.6)$$

where T_c is the transition temperature in °C,

and B_0 and B_1 are constants.

A detailed description of the regression analysis technique is given in Section 5.5. The resulting equations are,

(i) Steel L

$$T_{27} = 70.72 - 12.44\ d^{-1/2} \quad (4.7)$$

$$T(50\%) = 98.66 - 12.24\ d^{-1/2} \quad (4.8)$$

(ii) Steel H

$$T_{27} = 107.70 - 15.63\ d^{-1/2} \quad (4.9)$$

$$T(50\%) = 134.79 - 15.53\ d^{-1/2} \quad (4.10)$$

Equations (4.7) and (4.8) and their respective coefficients are significant at the 1% level, that is, the correlation will occur by chance only once in one-hundred times. The correlation coefficients of Equations (4.7) and (4.8) are such that 98.4% and 98.2% respectively of the total variation in transition temperature is explained by these equations.

Equations (4.9) and (4.10) and their respective coefficients are significant at the 2% level; such a correlation will occur by chance twice in one-hundred times. The correlation coefficients of equations (4.9) and (4.10) are such that 98% and 97% respectively of the total variation in transition temperature is explained by these equations. 95% confidence limits are plotted on Figures 4.26 and 4.27. For Steel L the confidence limits are ±10.92°C for T_{27} and ±11.38°C for T(50%). For Steel H the confidence limits are ±12.30°C for T_{27} and ±14.50°C for T(50%).

The coefficients of $d^{-1/2}$ for Steel L are -12.44°C/$mm^{-1/2}$ (for T_{27}) and -12.24°C/$mm^{-1/2}$ (for T(50%)) and for Steel H are -15.63°C/$mm^{-1/2}$ (for T_{27}) and -15.53°C/$mm^{-1/2}$ (for T(50%)). In Section 4.4.1 this coefficient was given as varying from -15.65 to -9.65°C/$mm^{-1/2}$, depending upon the composition of the steels used to determine the coefficient. From Reference 10 this coefficient varies according to the amount of carbon and nitrogen segregated at grain boundaries. The influence of interstitial content on k_y and γ_e represents a measure of dislocation locking at the grain boundaries. This is affected by the manganese content of the steel through its interaction with nitrogen. The difference in interstitial content of Steel L (0.19 wt% C, 0.002 wt% N_{sol})compared to Steel H (0.09 wt% C, 0.012 wt% N_{sol}) explains the difference in coefficients for $d^{-1/2}$.

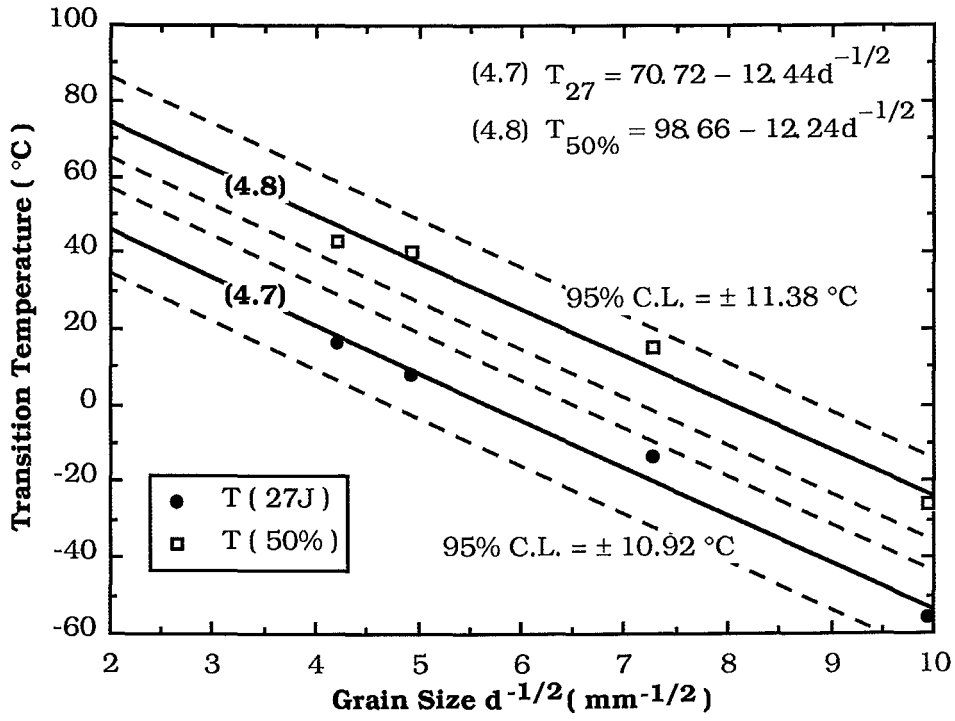

Figure 4.26

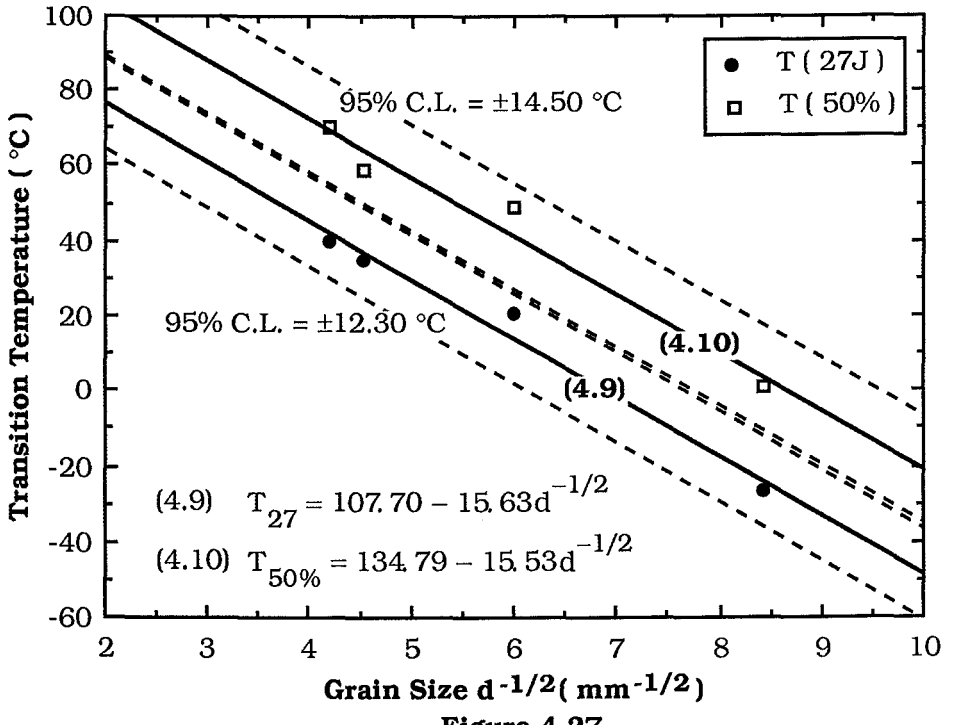

Figure 4.27

Figure 4.26 : The Charpy impact transition temperature (°C) as a function of grain size as $d^{-1/2}$ ($mm^{-1/2}$) for Steel L.

Figure 4.27 : The Charpy impact transition temperature (°C) as a function of grain size as $d^{-1/2}$ ($mm^{-1/2}$) for Steel H.

A comparison of the coefficients for Steels L and H shows that the coefficients are significantly different at the 20% level but not at the 10% level; the slopes will be significantly different two times in ten when there is no difference in slopes. For T_{27} the coefficients B_1 can be pooled to give an average coefficient, $\bar{B}_1$. For T_{27} this gives $\bar{B}_1$ = -13.59 ± 3.94°C/mm$^{-1/2}$ at the 95% confidence level. This confidence level includes the coefficients of Steel H and L in its range and those of published work i.e. -11.8°C/mm$^{-1/2}$ [8] and -11.6°C/mm$^{-1/2}$ [7]. Thus the coefficients found are similar to the results of other workers.

Also T_{27} is calculated using equation (4.4) and these results are presented in Figure 4.28 for Steel L and Steel H. These results lie within the 95% confidence limits of equations (4.7) and (4.9) for T_{27}. The equations found may be used, therefore, with certainty in further analysis.

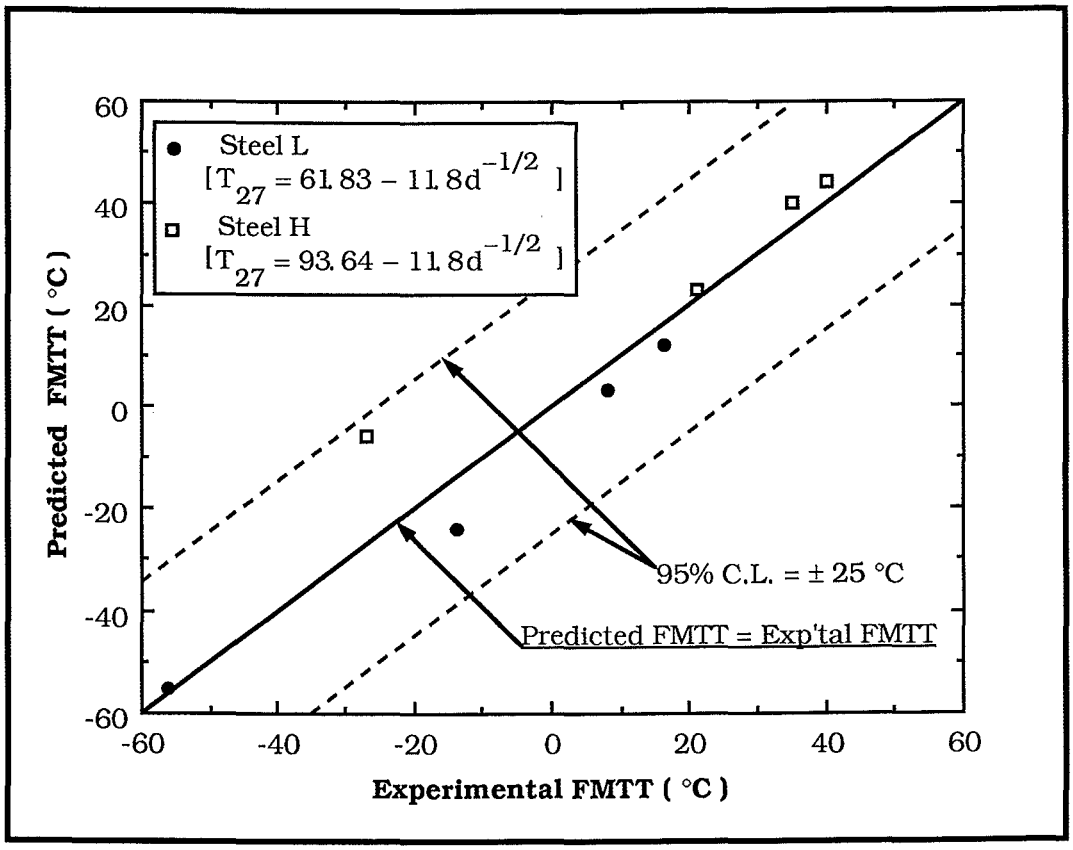

Figure 4.28 : The predicted FMTT from equation (4.4) as a function of the experimental FMTT using the 27 J transition criterion for Charpy impact testing.

4.5 *Summary*

In this chapter an outline of the experimental program has been given. The experimental steels and their heat treatment have been detailed with factors influencing the heat treatment being discussed. Grain size measurement of the steels has been presented and it was concluded;

(i) that the measurement of grain size is imprecise and that correction factors to produce a spherical grain do not effect the statistical distribution of determined grain size and,

(ii) that using mean linear intercept length as ferrite grain size is acceptable.

The Charpy V-notch impact test was described and results of experimental tests found,

(iii) that there is a range in transition temperature from -56 to +40°C for the two steels using the T_{27} criterion. This range is large enough that CTOD testing can be done to see whether it distinguishes between the grain sizes.

(iv) There is a linear relationship between transition temperature and grain size for the steel such that

$$T_{27} = B_0 + B_1 d^{-1/2} \qquad (4.6)$$

which is significant at the 1% level for Steel L and the 2% level for Steel H. This relationship is similar to that found by Petch [87].

(v) The coefficients of -12.44°C/mm$^{-1/2}$ and -15.63°C/mm$^{-1/2}$ for $d^{-1/2}$ for Steels L and H respectively are in agreement with other published data. The differences between the two coefficients are due to the different steel compositions. These results for transition temperature may be used in the CTOD-Charpy correlation.

CHAPTER 5

Yield Point and Tensile Testing

Fracture toughness testing, whether using linear elastic fracture mechanics (LEFM) to determine K_c (the stress intensity), or using elastic-plastic fracture mechanics (EPFM) to determine the critical CTOD (δ_c), requires the yield or 0.2% proof stress of the material tested at the test temperature. Since fracture toughness testing in this investigation is carried out over a wide range of temperature then tensile testing is performed over the same temperature range. A review of literature on the yield phenomena for steels suggests an empirical model can be developed of the temperature and grain size dependence of the lower yield stress. A knowledge of these dependencies is needed to be able to use micromechanical models of cleavage fracture to predict the fracture mode transition.

5.1 The Yield Point Concept

Yielding is the transformation in metals from elastic to plastic deformation. It occurs either via a gradual transformation in the load-extension curve (Figure 5.1a) or via a sudden drop in load at the start of a localised heterogeneous transition in the load-extension curve (Figure 5.1b). The former "continuous yield point" applies to the majority of metals and for engineering purposes the yield point is described by the stress needed to produce a small specific strain e.g. 0.2% and this is referred to as the 0.2% proof stress of the material. The latter "discontinuous yield point" occurs in low- and mild-carbon steels. The "upper yield stress" (σ_{uy}) corresponds to the stress at the abrupt decrease in load. It is affected by testing-machine stiffness, axiality of applied load and the geometry and surface finish of specimens [62,236].

The load-extension curve fluctuates around an approximately constant load value following upper yield. Ignoring transient values the lowest stress measured in this region is the "lower yield stress" (σ_{ly} or σ_{ys}). It is affected by test temperature, strain rate, grain size, chemical composition, prior plastic deformation and strain-ageing among other things but it is regarded as a material property and is

quoted in preference to the upper yield stress. The extension and corresponding strain value at this stress level are the "yield point elongation" and "Lüder strain" respectively.

Macroscopically the yield point can be described as a distinct band of plastically deformed metal forming on the plane of maximum principal shear stress (approximately 45° in an uniaxial tensile test) at some stress concentration. This "Lüder band" strain hardens and further yielding and band propagation occurs at uniform velocity along the specimen until plastic deformation has spread along the entire length of the specimen. Several bands are usually formed, the edge of each acting as a stress concentrator. In the following discussion and throughout the thesis the yield stress refers to the lower yield stress.

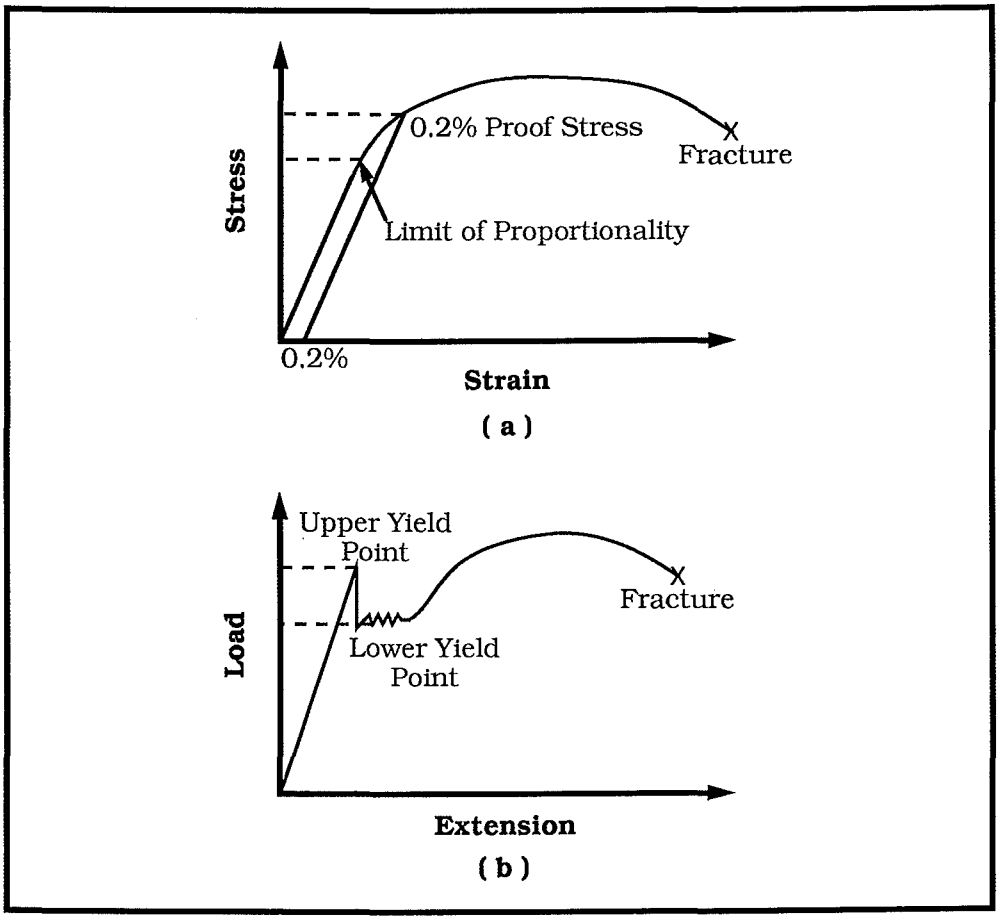

Figure 5.1 : (a) Schematic of the stress-strain curve for a material tested in tension showing a continuous yield.
(b) Schematic of the load-extension curve for a low-carbon steel tested in tension showing a discontinuous yield.

5.2 *Yield Point Models*

5.2.1 *THE GRAIN-BOUNDARY THEORY*

The dependence of the yield point of steels on carbon and nitrogen content was well known at the beginning of the twentieth century. In 1913 Dalby, when describing load-extension indicator diagrams, suggested that if steel is assumed to be constructed of large aggregates of iron (ferrite) through which was distributed a network of crystalline structure (cementite) then yield occurs when the crystalline network gives way [237]. The material continues to carry even greater load as it deforms plastically. The yield was assumed to be slip of the crystals. Kuroda independently suggested a similar model in 1938 [238] but this theory was criticised in detail by Cottrell who pointed out that since pronounced yield effects occurred with as little as 0.02 wt.% carbon present then the carbide films must be extremely thin yet these films would bear the whole load of the specimen after yield of the grains has passed [92]. Cottrell and then Cottrell and Bilby proposed a new theory based on dislocation locking by the interstitial carbon and nitrogen atoms in steel [92,93].

5.2.2 *THE COTTRELL-BILBY THEORY OF YIELD*

A successful theory of the yield point has to explain;

(i) The variation of yield stress with temperature,

(ii) the effects of strain rate,

(iii) the existence of delayed yielding,

(iv) the variation of yield stress with grain size in polycrystalline materials, and

(v) the phenomenon of serrated yielding which arises with strain-ageing.

In 1943 McAdams and Mebs suggested that both the resistance to plastic deformation and the technical cohesive strength may have a thermodynamic basis determined by values of energy rather than force [239]. This implies that yield is thermally activated. Cottrell, Cottrell and Bilby, and Nabarro argued that the yield point in iron is due to carbon or nitrogen atmospheres [92,93,240]. The cause of formation of the atmospheres is the relief of strain energy by migration of the interstitial atoms from their interstitial sites, where they cause large dilation, to the tensile

region round an edge dislocation where the lattice is itself dilated. Cottrell and Bilby estimated a concentration of 10^{-6} wt.% C is sufficient to place one carbon atom per dislocation per atom plane assuming the normally accepted dislocation density of 10^8 lines cm^{-2} in well annealed material [93]. This gives a binding energy of about 0.5 eV per atom plane. For the upper yield to occur the applied strain energy assisted by thermal activation must exceed this binding energy to tear the dislocations from their atmospheres, in which case they become highly mobile, multiply and produce rapid flow under small stresses. The difference between the upper and lower yield is that the release of dislocations (at the edge of Lüder's bands) at the lower yield is helped by the elastic disturbance of nearby plastic flow. The upper yield does not have this elastic disturbance available to help. Later measurements by internal friction or by electrical techniques revealed that the number of atoms per dislocation plane was large, usually exceeding 10 [241]. This suggested precipitation rather than atmosphere formation was important.

Cottrell and Bilby were able to explain the variation of temperature and strain rate on yielding (Section 5.3.2), as well as delayed yield. The "break-away" theory considers that dislocations break-away from their atmospheres and multiply. The critical strain rate for break-away to occur was calculated by Cottrell to be

$$\dot{\varepsilon} = 4D\rho b/l_o, \qquad (5.1)$$

where D is the solute diffusion coefficient, ρ the dislocation density, b the Burgers' vector and l_o a characteristic length taken as the radius of the atmosphere [103]. For iron l_o is about 40b or more characteristically for substitutional cases l_o is about 10b. Considering dislocations that have broken away and multiplied then the effect of grain size may be introduced.

5.2.3 *The Hall-Petch Equation*

Grain boundaries provide a barrier to the passage of dislocations and along an active slip band dislocations will pile up against the grain boundary producing very large tensile stresses. Considering Figure 5.2, a force of $(\tau - \tau_i)$ may be considered to have

been transferred from a blocked slip band of length l to the adjacent grain, where τ is the applied shear stress and τ_i is the friction stress opposing glide of the dislocation in the slip band. Zener suggested that a blocked slip line will resemble a freely slipping crack under a shear stress [65]. The stress at a distance r ahead of the blocked slip band may be found by directly summing the stresses due to the individual dislocations [66]. However, by using the analogy between the slip band and a crack then linear elastic theory gives the raised shear stress distance r ahead of the slip band as $\tau .(l/4r)^{1/2}$, where ($r << l$). Therefore, assuming the existence of τ_c (the critical shear stress value required to unlock dislocations from the locked source) and taking r as the average distance between the end of the blocked slip band and the nearest locked dislocation sources in the adjacent grain, the elevated stress caused by the dislocation pile-up gives rise to yielding in the adjacent grain when

$$\tau_c = (\tau - \tau_i).(l/4r)^{1/2} \qquad (5.2)$$

If it is assumed that;

(i) $l = R.d$ where d is the mean grain diameter and R is a statistical constant that is dependent on the orientation of the slip plane to the grain boundary such that R = constant x $(f(\theta))^2$,

(ii) the applied stress is equal to the lower yield stress and

(iii) that maximum shear stress theory applies, i.e. $\tau = \sigma/2$ then equation (5.2) may be written

$$\sigma_c = (\sigma_{ys} - \sigma_i).(Rd/4r)^{1/2}. \qquad (5.3)$$

Rearranging and assuming that σ_c is a constant material property,

$$\sigma_{ys} = \sigma_i + k_y d^{-1/2} \qquad (5.4)$$

where $k_y = 2\sigma_c(r/R)^{1/2}$, a constant. (5.5)

Equation (5.4) is known as the Hall-Petch equation after work by Hall and Petch [163,164]. For any particular material σ_i and k_y are constants, σ_i being the "friction stress" and k_y is the unpinning parameter. For the Cottrell-Bilby theory to hold k_y should be temperature-dependent. Work by Fisher found k_y was temperature-independent (as shown in Figure 5.3) [242].

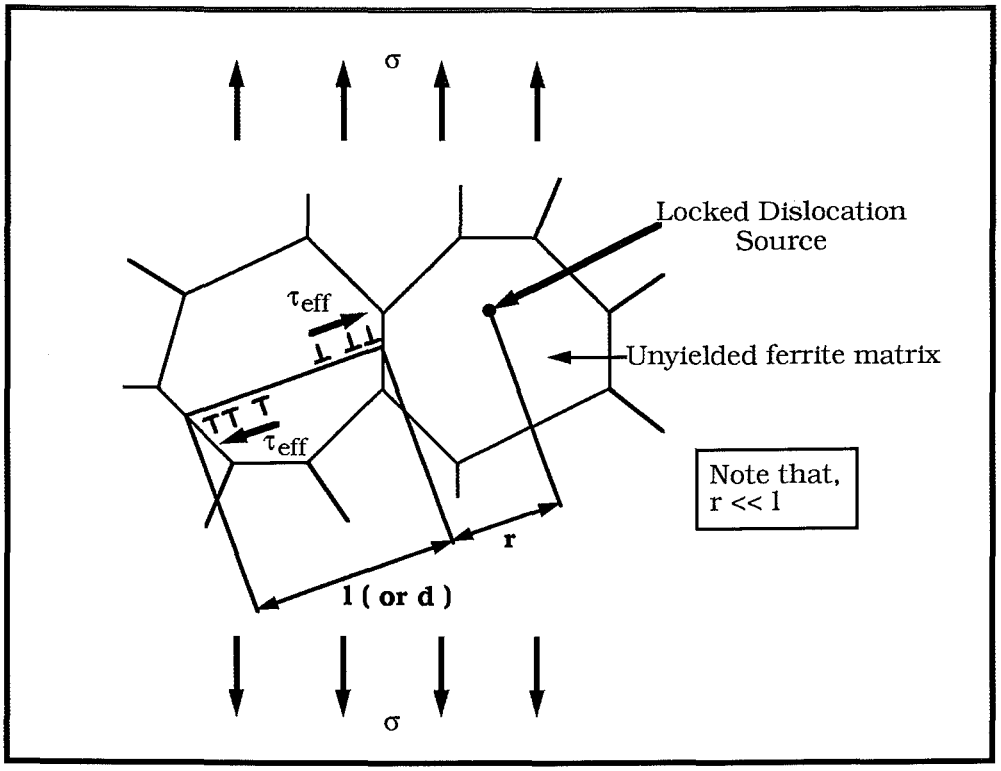

Figure 5.2 : Dislocation pile-up at the grain boundary to unlock dislocation in adjacent grain at yield.

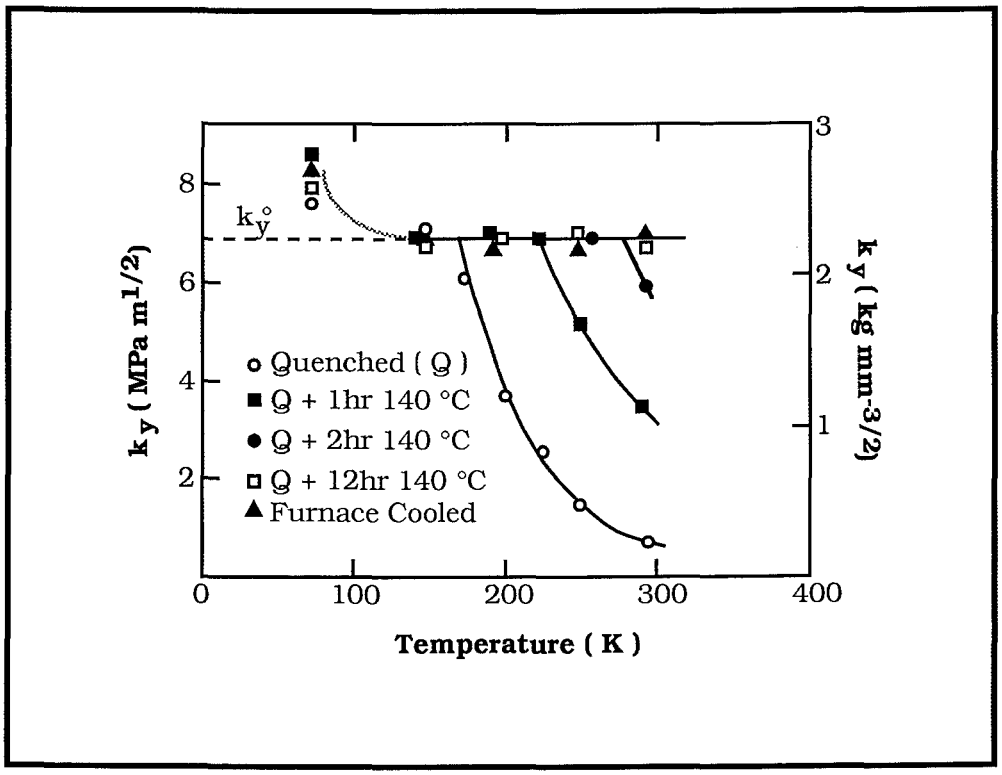

Figure 5.3 : The dependence of the strength of dislocation locking k_y on heat treatment and temperature[242].

Except for lightly aged steels, there is a limiting saturation value k_y° which is independent of continued solute segregation and changes in test temperature. Cottrell argued that when pinning was strong it was easier for the localised stress concentration at the end of the relaxed slip band to create dislocations immediately on the other side of the grain boundary than it was to unpin dislocations further away in that grain. Thus,

$$k_y = 2\sigma_c r_c^{1/2} \qquad (c = \text{creation}), \tag{5.6}$$

for strong pinning and

$$k_y = 2\sigma_p r_p^{1/2} \qquad (p = \text{pinning}), \tag{5.7}$$

for weak pinning where σ_p is an unpinning stress that is less than σ_c. It follows from standard dislocation theory that k_y is almost independent of temperature in strongly pinned polycrystals. Due to rapid segregation of carbon and nitrogen to dislocations in iron conventional annealing and normalizing heat treatments must commonly produce strong pinning. Mintz summarised known information on k_y in 1984 [174].

It was found k_y has a common range of 14-24 MN $m^{-2}mm^{1/2}$. Although k_y has been developed on the basis of dislocation pile-ups, the pile-ups have been rarely observed in practice. A number of theories have been proposed that do not rely on pile-ups, that of Li is probably the most recognised because it can relate k_y values to grain boundary segregation effects [243]. Li proposed that yield was controlled by the ability to propagate dislocations from the boundary regions, the theory being that grain boundaries contain ledges which on their removal generate dislocations in the matrix. The dislocation density is therefore controlled by the ledge density which increases with decreasing grain size. Workers have found little relationship between k_y and ledge density although a high density of unresolvable ledges observed by Cochrane could account for this [244]. The ledge density would be critically dependent on the impurity content at the boundaries since impurities would stabilize the ledges; hence increasing impurity content should increase k_y.

The summary of Mintz shows that Mn and Si decrease k_y with increasing content from 24 to 14 $MNm^{-2}mm^{1/2}$, and Al reduces k_y only at high content [174]. A faster cooling rate reduces k_y but it may be restored by annealing. Increasing carbon and nitrogen content increases k_y. The linear relationship with grain size occurs, Li suggests, when there is no equilibrium segregation of impurities to the grain boundaries or when grain boundaries are fully saturated. It has been observed that k_y is dependent on grain size [98].

When k_y is independent of temperature the delay time for yielding cannot be due to the thermally activated release of dislocations. It must therefore be the time required for mobile dislocations to glide across their grains. Observation of dislocation generation and movement gave the next development in yield theory.

5.2.4 THE HAHN THEORETICAL MODEL

It is clear that in a strongly pinned material dislocations remain permanently locked. Therefore yielding will occur by the generation of new dislocations, which will rapidly multiply under the applied stress and possibly a situation is produced whereby the new dislocations can continue to move under a lower stress.

The basis of this theory is from work by Johnston and Gilman on lithium fluoride, who noted that this material exhibited a yield point in the as-grown condition, and also that the crystals could be grown with a notably low dislocation content of only a few thousand lines per square centimetre [95]. Work by Patel and Chaudhuri on germanium found that the yield drop introduced 10^5 dislocations per square centimetre from dislocation-free material [245].

Hahn used the above observations for development of a new yield point model [246]. It assumed that most dislocations remain locked by their precipitates and that the dislocations responsible for slip are heterogeneously nucleated and multiply rapidly. The yield drop can be accounted for quantitatively in terms of the rapid multiplication of dislocations and the stress dependence of dislocation velocity.

In the model the strain rate of the machine, ($\dot{\varepsilon}$), must be matched by the elastic strain rate ($\dot{\varepsilon}_e$) and the plastic strain rate ($\dot{\varepsilon}_p$) contributions,

$$\dot{\varepsilon} = \dot{\varepsilon}_e + \dot{\varepsilon}_p \qquad (5.8)$$

The elastic strain rate can be described in terms of the rate of stress application and the modulus M, which is descriptive of the nett elastic response of the test bar, grips and testing machine,

$$\dot{\varepsilon}_e = \frac{1}{M}\frac{d\sigma}{dt} \qquad (5.9)$$

The plastic strain rate, expressed in terms of the Burger's vector (b), the dislocation density (ρ) and the average velocity of the dislocations (v), is;

$$\dot{\varepsilon}_p = 0.5bf\rho v \qquad (5.10)$$

where f is a fixed fraction of the dislocation density and 0.5b is the contribution of a single dislocation of unit length and moving with unit velocity in a direction close to the maximum resolved shear stress.

Dislocation multiplication upon straining can be described by a parabolic relation of the form,

$$\rho = \rho_o + C\varepsilon_p^a, \qquad (5.11)$$

where C and a are constants and ρ_o is the average density of unlocked dislocations nucleated heterogeneously at inclusions or other discontinuities below the nominal stress level associated with significant dislocation mobility.

The stress dependence of velocity is

$$v = (\tau/\tau_o)^{m^*}, \qquad (5.12)$$

where τ is the resolved shear stress, τ_o the resolved shear stress corresponding to unit velocity and m^* is a temperature-dependent material characteristic. If the change in macroscopic flow stress ($\Delta\sigma$) approximates the stress increment needed to maintain a given velocity then the effect of strain-hardening may be introduced via a simple linear strain-hardening law,

$$\Delta\sigma = q\varepsilon_p, \qquad (5.13)$$

such that

$$v = (2\tau_o)^{-m^*}(\sigma - q\varepsilon_p)^{m^*}, \qquad (5.14)$$

where q is the macroscopic work-hardening coefficient and σ is the tensile stress corresponding to τ. Hence, by combining equations (5.8), (5.9), (5.10), (5.11) and (5.14) an expression between flow stress, plastic strain and strain rate is obtained;

$$\dot{\varepsilon} = \frac{1}{M}\frac{d\sigma}{dt} + 0.5bf(\rho_o + C\varepsilon_p{}^a)(2\tau_o)^{-m^*}(\sigma - q\varepsilon_p)^{m^*}. \qquad (5.15)$$

If the elastic stress is neglected then the model is not elastic but totally rigid; under these conditions a finite yield stress, determined by ρ_o and $\dot{\varepsilon}$, is assumed the instant the test begins. Equation (5.15) can be rewritten as,

$$\sigma = q\varepsilon_p + 2\tau_o\left(\frac{\dot{\varepsilon}}{0.5bf(\rho_o + C\varepsilon_p{}^a)}\right)^{1/m^*} \qquad (5.16)$$

This equation makes no allowances for the effect of grain size and temperature as well as other metallurgical factors.

From the preceding discussion it follows that body-centred cubic metals will show a discontinuous yield point if:

(i) the initial density of mobile dislocations is sufficiently low, and either

(ii) the internal stress opposing dislocation motion is sensitive to dislocation velocity or

(iii) the grain boundaries are effective barriers to mobile dislocations.

Annealed polycrystalline low-carbon steels usually satisfy all three of these requirements. The yield strength of annealed low-carbon steels is dominated by the grain size effect in tests at ambient temperature and normal strain rates.

5.3 The Temperature Dependence of Yield Stress

The temperature range of most interest when looking at the temperature dependence of yield stress is where $T < 0.2\ T_m$, where T_m is the melting-point temperature in K. For iron, therefore, T is less than about 90°C. It is readily accepted that the Hall-Petch

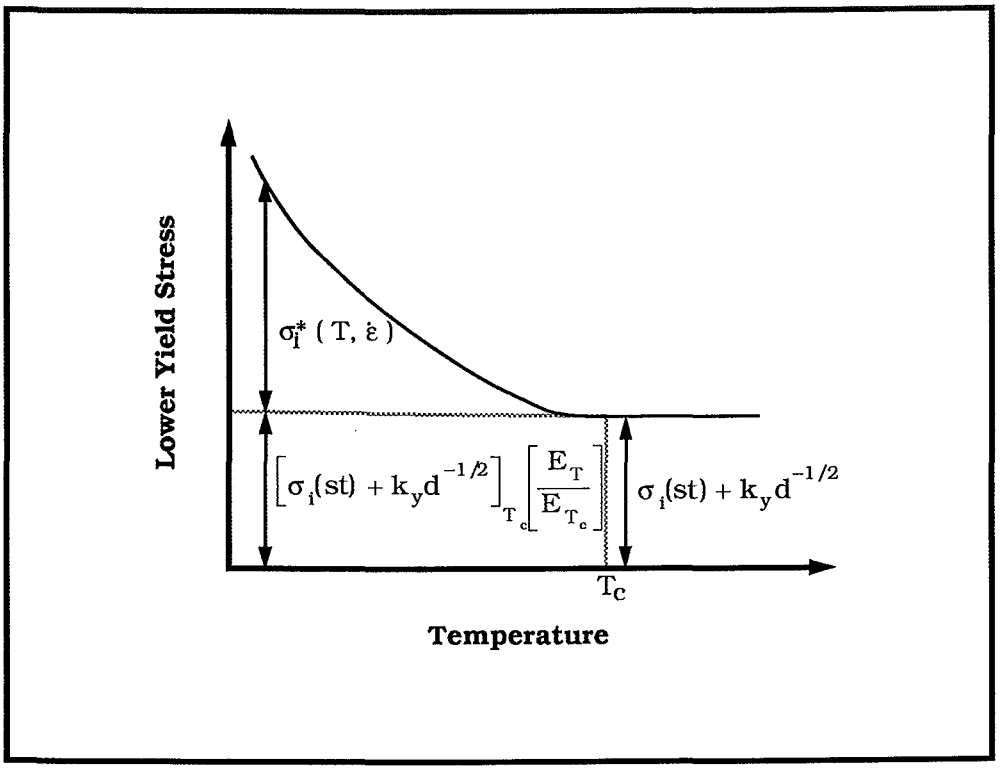

Figure 5.4 : Schematic of the temperature dependence of the lower yield stress divided into thermal and athermal components.

equation (equation (5.4)) may be written as the sum of three components for yield stress,

$$\sigma_{ys} = \sigma_i^* + \sigma_i(st) + k_y d^{-1/2}, \qquad (5.17)$$

where σ_i^* is a thermal component dependent on the temperature and strain rate of testing, $\sigma_i(st)$ is an athermal component dependent on the composition of the material, k_y is a constant and $d^{-1/2}$ is the reciprocal square root of the mean grain diameter. A similar equation exists for flow stress but k_y becomes $k_{(flow)}$ which is usually less than k_y. Figure 5.4 shows, schematically, the variation of yield stress with temperature. There is a critical temperature T_c above which σ_i^* the thermal component is nearly zero. Therefore at test temperatures above and equal to T_c equation (5.17) becomes,

$$\sigma_{ys} = \sigma_i(st) + k_y d^{-1/2}, \ \sigma_i^* = 0 \qquad (5.17a)$$

and below T_c equation (5.17) is,

$$\sigma_{ys} = \sigma_i^* + (\sigma_i(st) + k_y d^{-1/2})(E_T/E_{T_c}). \qquad (5.17b)$$

(E_T/E_{T_c}) gives the variation of the long range internal stress with temperature due to variation in the modulus of elasticity. Generally the variation is neglected since the thermal component is very large in comparison to the athermal component at low test temperatures. Therefore in the present discussion it is assumed $E_T \approx E$ at ambient temperature. Of interest is the variation of σ_i^* with temperature and the mechanism involved in this variation.

5.3.1 TIME-RATE DEPENDENT MODELS

McAdams and Mebs in their work on low-carbon steels suggested that stress be plotted against temperature on Kelvin's original thermodynamic scale [239]. This was based on equal temperature intervals being equivalent to equal thermodynamic efficiencies such that,

$$\sigma_A - \sigma = C\log(T/T_A), \tag{5.18}$$

where σ_A is the yield stress at ambient temperature T_A and σ is the yield stress at the test temperature T. At the same time Zener and Holloman, in a series of papers, described methods for determining the effect of temperature and strain rate on flow stress, fracture stress and yield stress [247-249]. They proposed that a quantitative equivalence may be derived for temperatures and rates of strain at temperatures below the blue-brittle range of steel. The general form of the functions was,

$$\sigma = \sigma(p,\dot{\varepsilon}) \tag{5.19a}$$

$$p = p(\dot{\varepsilon}, T), \tag{5.19b}$$

for true flow stress and true strain. p must be dimensionless and must be expressed as a ratio of the rate of deformation and of some other time rate connected with the material. Nearly all time rates associated with materials are governed by heats of activation and their temperature dependence is,

$$\text{time rate} = f_0\exp(-Q/RT). \tag{5.20}$$

For p to have physical significance then f_0 must have theoretical significance.

The value usually assigned to this constant in diffusion problems is that first given by Dushman and Langmuir,

$$f_o = JQ/Nh, \tag{5.21}$$

where J is the mechanical equivalent of heat, N is Avogadro's number, and h is Planck's constant [250]. Interpreting f_o as such then the time rate is essentially the number of times per second any given atom acquires the heat of activation Q and

$$p = \dot{\varepsilon}\exp(Q/RT)/f_o \tag{5.22}$$

Dushman and Langmuir note that the time rate given by equation (5.20) is a semi-empirical relation.

A study of high purity Aluminium single crystals found that between 205 to 77 K the critical shear stress necessary to cause glide to set in at a given rate in the active slip system may be expressed as $\sigma = A\exp(Q/RT)$ [251]. This assumes a constant strain rate and that the expression $\exp(Q/RT)$ provides a measure of the proportion of atoms in the lattice (probably associated with dislocations) involved in the physical change of plastic flow. Taking logarithms of $\sigma = A\exp(Q/RT)$ gives,

$$\log \sigma = \log A + Q/RT. \tag{5.23}$$

Johnston writing on the flow stress of lithium fluoride crystals uses a similar expression but these empirical relations do not provide an explanation of temperature dependence of yield [252].

5.3.2 *THE TEMPERATURE DEPENDENCE OF THE COTTRELL-BILBY YIELD POINT MODEL*

The variation of yield stress with temperature was estimated by Cottrell and Bilby [93]. First, the yield stress at -273°C (0K) was estimated. This is given as,

$$\sigma_{0K} = \frac{3\sqrt{3}A'}{4\lambda^2 r_o^2}, \tag{5.24}$$

where A' is a constant and is about 3×10^{-3} Nm^{-2}, λ is the slip distance and r_o is the equilibrium distance of the carbon atom from

the dislocation core. Extrapolating known values of yield stress to 0K gave $\sigma_{0K} \approx 1250$ MNm^{-2} and $r_o \approx 7$Å which are reasonable. Consider Figure 5.5 where thermal fluctuations are seen as pulling a loop of the dislocation line clear of its carbon atmosphere. If the stress near the dislocation lies in the range σ/σ_{0K} to $(\sigma + d\sigma)/\sigma_{0K}$ the time before a successful fluctuation occurs is proportional to $\exp(U(\sigma/\sigma_{0K})/kT)$ where U is the activation energy as a function of stress, k is Boltzmann's constant and T is the absolute temperature. However, the time spent in this stress range during a tensile test is inversely proportional to the rate of stressing $d\sigma/dt$. Yielding should occur when the quantity,

$$S = \frac{d\sigma}{dt}.\exp\left(\frac{-U(\sigma/\sigma_{0K})}{kT}\right) \qquad (5.25)$$

reaches a characteristic fixed value. Thus, at constant testing rate, the yield point should vary with temperature such that U/kT remains constant. Using the experimental data of McAdams and Mebs', Cottrell and Bilby found this agreement in their original paper [93,236].

This result has been simplified by Fisher [94]. Fisher assumed the work of formation of the critical size loop in Figure 5.5 to be,

$$U = (\gamma_o^2/b\tau).f(\gamma/\gamma_o) \qquad (5.26)$$

where $f(\gamma/\gamma_o)$ is $f(x) = \text{arc cos } x - x(1 - x^2)^{1/2}$ (5.26a)

$$\approx 2/3[2(1 - x)]^{3/2} \text{ for } x \approx 1$$

and γ_o and γ are the energies per unit length of dislocation when free from absorbed solute atoms and in the presence of them respectively. When U is supplied by a thermal fluctuation the number of loops that form in one second is proportional to $\exp(-U/kT)$ and the proportionality constant is the product of a frequency factor υ and the number of possible sites for loop formation, n_s. Substituting for U,

$$\dot{n} = n_s\upsilon\exp[-\gamma_o^2 f(\gamma/\gamma_o)/b\tau kT]. \qquad (5.27)$$

The delay time for yielding is $1/\dot{n}$, given by

$$\log(\Delta t) = -A + BG^2/\tau T \quad (5.28)$$

where $A = \log(n_s \upsilon / n_1)$ (5.28a)

and $B = \gamma_0^2 f(\gamma/\gamma_0) \log e / G^2 bk$ (5.28b)

and G is the shear modulus. If the delay time is assumed to be constant as it is during normal tensile testing then the yield stress-temperature relationship is,

$$\sigma_{ys} T/G^2 = \text{constant} \quad (5.29)$$

or $\sigma_{ys} = \text{constant}/T$ (5.29a)

This implies yield stress is inversely proportional to temperature and this was shown to fit the data of McAdams and Mebs [94]. Clough and Pavlovic used this relationship for tests on vanadium where they found it produced a closer fit than the relationship found by Zener and Holloman and described earlier [253]. Work on a flow stress of SAE 4340 Steel and other iron-based alloys by Nunes and Larson showed a relationship of the form

$$\sigma_{0.04} = M/T + \sigma_o \quad (5.30)$$

where T = absolute temperature, M = slope, σ_o = intercept at T_o and $\sigma_{0.04}$ = true stress at a true strain of 0.04. The slope M changed with change in the controlling mechanism of deformation but was essentially constant from -196°C to ambient temperature [254-256]. The relationship "σ is proportional to $1/T$" provides a good empirical description of the variation of yield stress with temperature but the theoretical derivation has been based on the break-away theory of yield. Therefore the temperature dependence of yield stress based on multiplication theory and not unpinning must be examined.

5.3.3 THE THERMAL ACTIVATION THEORY OF YIELDING

Johnston and Gilman found that the temperature dependence of the yield stress in lithium fluoride is governed by dislocation mobility and by the effect of impurities on the mobility of free dislocations [95]. Their conclusions were that the yield point was due to the rapid multiplication of dislocations and their subsequent

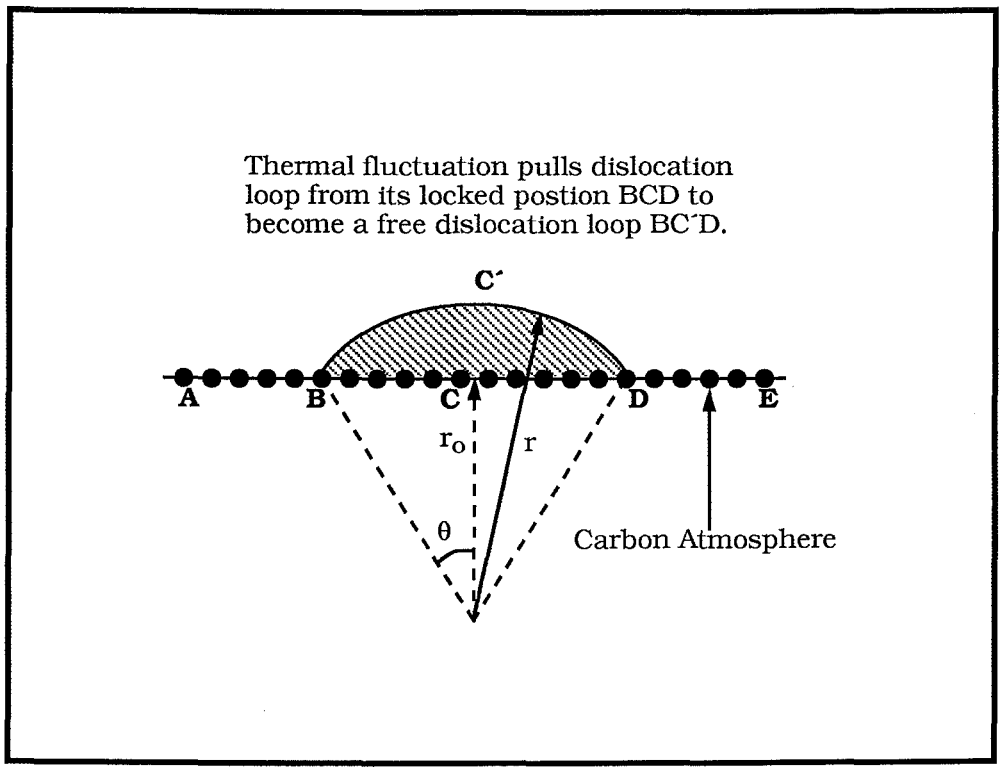

Figure 5.5 : The release of a free dislocation loop from its carbon atmosphere according to "break-away theory"[94].

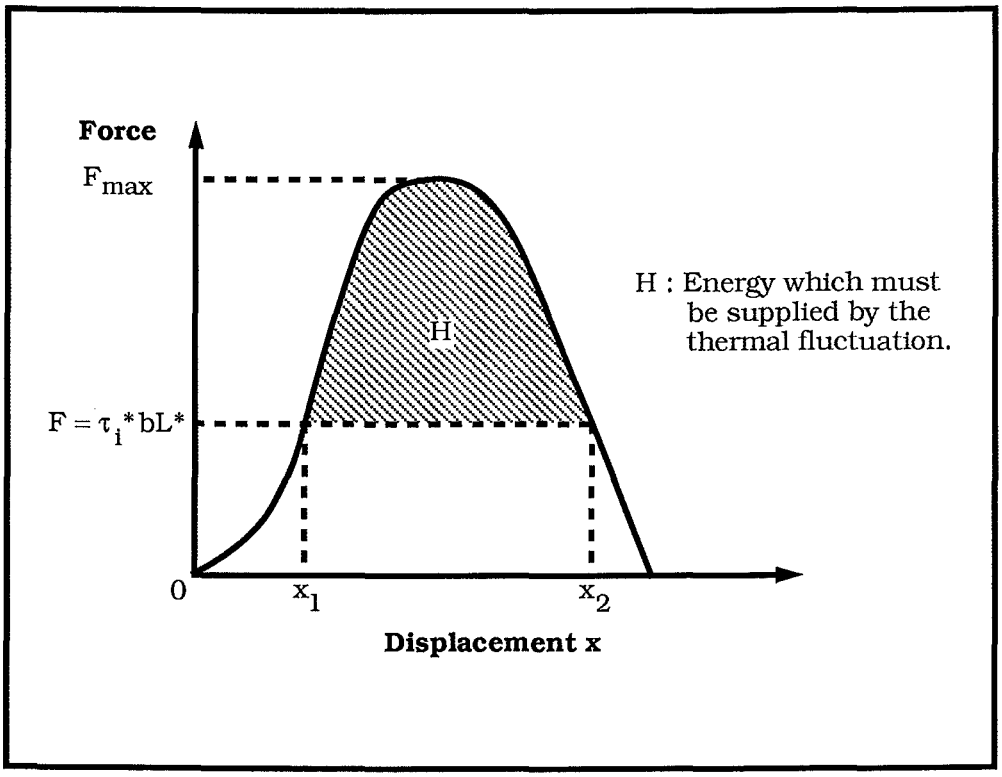

Figure 5.6 : Schematic of the force-distance relationship for thermally activated yielding of iron[97].

movement rather than the unpinning of dislocations from their atmospheres. They found dislocation velocity varied exponentially with 1/T between 25 and -50°C, that is, $v_s = f(\sigma)\exp(-U/kT)$, where $U \approx 0.7$ eV and σ = stress. U is not a function of stress and $f(\sigma) = A\sigma^m$, where m is from 15 to 25 and is characteristic of the material. A is a constant. The temperature dependence of the dislocation velocity may imply that the limiting process in dislocation movement is thermally-activated with an activation energy of about 0.7 eV. The temperature dependence of the lower yield stress is then overcoming resistance to motion in other dislocation free areas during the thermally activated process.

Heslop and Petch suggested that the variation of friction stress σ_i^* in equation (5.17) with temperature was due to resistance of dislocation motion by the Peierls-Nabarro stress and that as temperature increased so did the width of the dislocation [257]. Subsequently many workers have accepted that the temperature-dependence is due to the Peierls-Nabarro stress but the width of the dislocation does not change; it is the thermal fluctuation required by the dislocation to overcome the potential that changes, and this has been extensively investigated by Conrad and his co-workers [97,98]. If the nature of the potential barrier and the detailed manner in which it is overcome is ignored then a simple theory may be developed whereby dislocations are thermally activated over this barrier. Using equation (5.17) in terms of shear stress τ,

$$\tau = \tau_i^* + \tau_i(st) + k_y^s\, d^{-1/2}, \qquad (5.31)$$

then energy H must be supplied to the dislocation by thermal means for it to overcome the potential barrier of the Peierls-Nabarro forces. The shear strain rate is,

$$\dot{\gamma} = \rho b \dot{s} = \rho b s \nu^* \exp(-H(\tau,T)/kT) \qquad (5.32)$$

where ρ is the dislocation density, b the Burgers' vector, $\dot{s}$ is the average velocity of dislocations, s is the product of the number of places where thermal activation can occur and the area swept out per thermal fluctuation, and ν^* is the frequency of vibration of a dislocation segment. If $\nu = \rho b s \nu^*$, an overall frequency factor, then the force-distance relationship for thermally activated yielding or

flow will have the general form shown in Figure 5.6. For a given value of stress τ_i^* a dislocation will take the position x_1 and energy H which must be supplied by thermal fluctuations is given by the shaded area. Equation (5.32) can then be written,

$$\dot{\gamma} = \nu \exp\{-(H^* - v^*\tau_i^*)/kT\}, \tag{5.33}$$

where H^* is the total area under the force-distance curve between x_1 and x_2 and $v^*\tau_i^* = bL^*(x_2 - x_1)\tau_i^*$ is the work done by the stress during thermal activation, b is the Burger's vector and L^* is the length of dislocation segment involved in the activation. $v^* = bL^*(x_1 - x_2)$ is the activation volume and typically is from $5b^3$ to greater than $100b^3$ for BCC metals. H is primarily a function of the effective shear stress τ_i^* (i.e. the thermal component of yield stress) and it may be shown that

$$H = -k\left(\frac{\partial \ln \dot{\gamma}/\nu}{\partial 1/T}\right)_{\tau_i^*} \tag{5.34}$$

$$= -kT^2\left(\frac{\partial \ln \dot{\gamma}/\nu}{\partial \tau}\right)_T \left(\frac{\partial \tau_i^*}{\partial T}\right)_{\dot{\gamma}} \tag{5.34a}$$

Rearranging equation (5.32) and differentiating it, the activation volume for the deformation process may be defined as

$$v^* = \frac{-dH}{d\tau_i^*} = kT\left(\frac{\partial \ln \dot{\gamma}/\nu}{\partial \tau_i^*}\right)_T, \tag{5.35}$$

from which,

$$H \approx kT\ln(\nu/\dot{\gamma}) \tag{5.36}$$

If ν is relatively independent of temperature, stress and structure then H,v^* and ν may be found from usual mechanical testing. For polycrystalline BCC metals a reasonable assumption is that $\tau = \sigma/2$ and that $\gamma = 0.7\varepsilon$ where σ is the tensile stress and ε is the tensile strain. It is found that H is an increasing and v^* is a decreasing function of temperature but these functions in fact conceal a stress dependence of both H and v^*. H and v^* both increase with decreasing stress.

Conrad's theory allows a unified treatment of iron and the group Va and VIa metals so that low-temperature deformation may be described by a single, thermally activated process. There are five thermally-activated dislocation mechanisms that have been proposed to account for the strong temperature and strain rate dependence of the yield stress in BCC metals. In chronological order these are:

(i) Breaking away from an interstitial atmosphere.
(ii) Overcoming the Peierls-Nabarro stress.
(iii) Non-conservative motion of jogs.
(iv) Overcoming interstitial precipitates.
(v) Cross-slip.

Evidence against (i), (iii), (iv) and (v) is summarised in Table 5.1 after Conrad [98]. There are strong arguments against the motion of jogs or cross-slip being the controlling mechanisms, mainly because the parameters H and v^* are independent of structure and they are the same for yielding and flow. Jogs and cross-slip are concerned with the motion of screw dislocations yet edge dislocations have the same mobility; this is further evidence against these mechanisms.

(a) *Peierls-Nabarro stress and Double-Kink Nucleation*

When the frictional resistance to dislocation motion (the Peierls-Nabarro stress) is appreciable it is generally assumed that deformation proceeds by the thermally assisted production of kink pairs (shown in Figure 5.7) in otherwise straight dislocation lines. Following the Dorn-Rajnak model the critical length l^* of dislocation between the two kinks has an activation energy

$$H = E_K\{1 + \tfrac{1}{4}\ln(16\ \tau_p/\pi\tau_i^*)\}, \qquad (5.37)$$

where E_K is the energy of a single kink, τ_p is the Peierls' stress (the yield stress at 0K) and τ_i^* is the effective shear stress [260]. It follows that the stress exponent of the dislocation velocity m^* (Equation (5.12)) is,

$$m^* = H_K/4kT. \qquad (5.38)$$

This, as well as suggesting m^* is inversely proportional to temperature, ties the thermal activation theory of yielding of Conrad to the dislocation multiplication theory. Experimental results do not

Table 5.1
Summary of evidence against specific mechanisms proposed as rate-controlling during yield

Mechanism	*Contrary Evidence*
Breaking-away from an interstitial atmosphere.	1. All yielding and flow phenomena exhibit the same values of H and v^*. 2. H and v^* are independent of interstitial content. 3. H and v^* are the same for the mobility of dislocations as determined by etch pits as for initial yielding.
Non-conservative motion of jogs.	1. H and v^* are independent of structure. 2. H and v^* for yielding and flow are the same as for the mobility of edge dislocations, which do not move non-conservatively
Overcoming interstitial precipitates	1. H and v^* are independent of impurity content. 2. H and v^* are independent of the quantity of interstitial precipitates. 3. τ^* decreases with increase in quantity of precipitates.
Cross-slip	1. H and v^* for yielding and flow are the same as for the mobility of edge dislocations, which cannot cross-slip.

show m^* varying quite as much with temperature but this could be due to using the applied stress instead of the effective stress [259].

Conrad concluded that the good agreement between values of H_0 and H_K in his analysis indicated that the nucleation of kinks is the rate-controlling mechanism during low temperature deformation of the BCC metals due to the resistance of Peierls-Nabarro force. Also it was found that the frequency factor ν in pure single- and poly-crystals was 3 to 4 times higher than in impure material. The pure material also has a weaker temperature dependence of τ_i^*. It appears that the difference in ν is due to the increased lateral distance a kink moves in pure material as compared to the impure material. This suggests that interstitial atoms or precipitates influence the extent to which the kinks can spread before encountering an obstacle. Besides acting as obstacles to kink motion, the interstitial atoms or precipitates may induce cross-slip. Since k_y in equation (5.17) is relatively independent of temperature and the activation energy and activation volume, as a function of stress, are the same for all deformation phenomena suggests that the yield point is not due to the thermally assisted unpinning of dislocations from their interstitial atmosphere but is a result of the sudden multiplication of dislocations by the double cross-slip mechanism proposed by Johnston and Gilman [95].

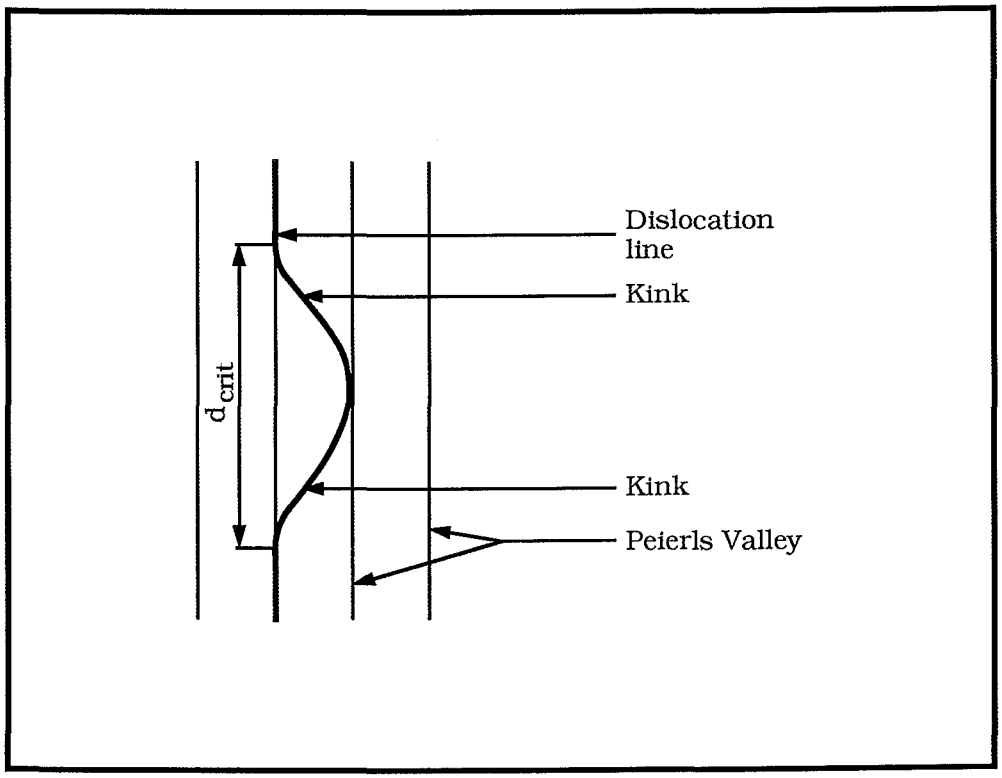

Figure 5.7 : Schematic of the thermally assisted production of kink pairs(dislocation loop spreading)[241,260].

(b) Interstitial Impurities

Evidence contrary to the Peierls-Nabarro stress being the controlling mechanism was presented by Stein *et al.* [258]. In tests on iron single crystals containing less than 5 x 10^{-3} ppm impurities (purified by ZrH_2) they found that the change in yield stress between 27 and -196°C was 76 MNm^{-2} (11 ksi). The change in yield stress for 0.003 to 0.023 wt% carbon steel over the same temperature range was 172 MNm^{-2} (25 ksi). The conclusion was that the Peierls-Nabarro stress could not be responsible for more than 76 MNm^{-2} of the temperature-dependence of the yield stress. The interstitials impurities were responsible for at least 96 MNm^{-2} of the variation of yield stress with temperature, and therefore the temperature dependence is due to the interaction of mobile dislocations with interstitial impurities in solid solution. Arguments against this conclusion were put forward by Christian and Masters [259]. They found that for 0.01 ppm of impurities the flow stress at -196°C should be about 5 MNm^{-2} higher than at room temperature, whereas for 0.005 ppm of carbon Stein *et al.* found it was 76 MNm^{-2} [258,259]. This would mean that a substantial part of temperature dependence arises from lattice interactions. Also polycrystals of the same purity iron exhibit a stress dependence similar to impure irons [259].

One theory of interaction with solute atoms is that of Fleischer given in reference 241. In this theory the important defects are those lying within one atom distance of the slip plane. This gives a force-distance curve with a maximum at x = 0. Yielding takes place by thermally activated jumps through the distortions. The variation of yield stress is then,

$$(\tau/\tau_0)^{1/2} = 1 - (T/T_0)^{1/2} \qquad (5.39)$$

where T_0 is a characteristic temperature and τ_0 is the yield stress at absolute zero.

There is debate over whether Conrad's or Fleischer's theory holds. Near room temperature when the contribution from the Peierls-Nabarro mechanism to yield stress would be low it is expected that another mechanism would be operating. A study of solid-solution softening at low temperatures found that although $(\tau_i^*)^{1/2}$ as a function of $T^{1/2}$ was linear in the region from -145 to

67°C the slopes of the lines were much larger than expected from Fleischer's theory and that solid-solution softening is contrary to the same theory [269]. This is an indication that no single mechanism is rate controlling in the yield process even at low temperatures. It is likely that the temperature-dependence of yield stress arises from the interaction of the Peierls-Nabarro stress and interstitials with the double-kink mechanism of Dorn and Rajnak.

5.3.4 EMPIRICAL MODELLING OF THE TEMPERATURE DEPENDENCE OF YIELD STRESS

Time-rate based models of the temperature-dependence of yield stress or flow stress were presented in section 5.3.1. There are a number of other models which are based on the thermal activation theory of yielding of Conrad. Petch suggested that,

$$\sigma_i^* = A\exp(-\alpha T) \tag{5.40}$$

was a possible form of the temperature dependence of σ_i (σ_i^* + $\sigma_i(st)$), A and α being constants [209]. Since $\sigma_i(st)$ is low then σ_{ys} may also be described by an equation of this form. Armstrong showed that this equation could be approximately equated to Conrad's thermal activation theory [99].

Use equation (5.33) in terms of tensile stress and strain rate such that

$$\dot{\varepsilon} = \nu\exp\{-(H_o - v^*\sigma_i^*/2)/kT\}. \tag{5.41}$$

Divide through by ν and take logarithms of both sides and rearrange so that σ_i^* is on the LHS,

$$\sigma_i^* = 2\frac{H_o}{v^*} + 2\frac{kT}{v^*}\ln\left(\frac{\dot{\varepsilon}}{\nu}\right). \tag{5.42}$$

For T = 0 K equate equations (5.40) and (5.42) which gives A,

$$A = 2H_o/v_o^* \tag{5.43}$$

where v_o^* is the value of v^* at T = 0 K. To evaluate α the RHS of equations (5.41) and (5.42) are equated,

$$\alpha = -\frac{1}{T} \cdot \ln\left(\frac{2H_o}{v^*A} + \frac{2kT}{v^*A}\ln\left(\frac{\dot{\varepsilon}}{\nu}\right)\right) \tag{5.44}$$

From Conrad typical values for steel at T = 190 K and $\dot{\varepsilon} = 10^{-4}$ s^{-1} are $v^* \approx 3.4 \times 10^{-28}$ m^3 and $\nu = 5 \times 10^8$ s^{-1} (where T = 190 K is the median temperature for the range 80-300 K) [97]. H_o is approximately 0.6 eV and A is about 1800 MNm^{-2} from Petch [209]. Using these estimates then,

$$2\frac{H_o}{v^*A} > 0, \; -\frac{2H_o}{v^*A} < 2\frac{kT}{v^*A}\ln\left(\frac{\dot{\varepsilon}}{\nu}\right) < +\infty, \tag{5.45}$$

so α may be expanded in series noting that

$$\left| 4\frac{H_o}{v^*A} \right| > \left| 2\frac{kT}{v^*A}\ln\left(\frac{\dot{\varepsilon}}{\nu}\right) \right| \tag{5.46}$$

to give

$$\alpha \approx \frac{k}{H_o}\ln\left(\frac{\nu}{\dot{\varepsilon}}\right) - \frac{1}{T}\ln\left(2\frac{H_o}{v^*A}\right). \tag{5.47}$$

Equation (5.47) will hold at higher or lower temperatures, or different strain rates due to the change in σ_i^* and v^*. Since v^* increases as temperature increases the changes will counteract each other and α will remain approximately constant. It can be shown that

$$-\frac{1}{T}.\ln\left(\frac{2H_o}{v^*A}\right) \approx \text{constant} = \beta_o. \tag{5.48}$$

Therefore equation (5.40) can be rewritten as,

$$\sigma^*_i \approx 2\frac{H_o}{v_o^*}\exp\left(-\left\{\beta_o + \frac{k}{H_o}\ln\left(\frac{\nu}{\dot{\varepsilon}}\right)\right\}T\right). \tag{5.49}$$

Equation (5.49) allows the friction stress as given by Petch to be expressed in terms of the thermal activation rate analysis parameters. Several workers have used this form of expression for σ_i^* in equation (5.17) to give an empirical relation as,

$$\sigma_{ys} = A\exp[-(\beta_0 + \beta_1 \ln\dot{\varepsilon})T] + C + k_y d^{-1/2} \qquad (5.50)$$

where A, β_0, β_1 and C are constants and $C = \sigma_i(st)$ [171,198,261,262]. Vlach *et al.* did not include a specific grain size term however [262].

Chen *et al.*, using the Dorn-Rajnak model for thermally-activated flow in BCC metals dependent on the Peierls-Nabarro stress, developed a semi-empirical model of the temperature and grain size dependence of yield stress [100]. They give the yield stress as,

$$\sigma_{ys} = \sigma_o^* \left(\frac{1 + AT\ln(\dot{\varepsilon}/\nu)}{1 - AT\ln(\dot{\varepsilon}/\nu)} \right) + \frac{\xi_m^2 c}{kT_c b^3} + k_y d^{-1/2} \qquad (5.51)$$

where $A = k/\theta 2U_K$, T_c is as defined in equation (5.17a), σ_p^* is the Peierls stress at absolute zero, θ is a parameter introduced to allow the theoretical activation energy to better approximate the activation free energy ΔG_o and equals 4/3 and $2U_K$ is the activation energy of a double kink. ξ_m is the total size interaction energy of kinks with solute atoms and c is the concentration of solute atoms. This approach offers an empirical model closely based on theory but increases the analysis and mechanical testing required since change of strain rate tests are required. If the strain rate $\dot{\varepsilon}$ is assumed to be constant then equation (5.51) may be written

$$\sigma_{ys} = \sigma_p^* \frac{(1 + BT)}{(1 - BT)} + C + k_y d^{-1/2} \qquad (5.52)$$

where B and C are constants.

5.3.5 SUMMARY

The temperature dependence of yield stress is found to be thermally-activated. The mechanism is explained by dislocation interaction with the Peierls-Nabarro stress or with interstitial impurities. The most widely accepted model is the Peierls-Nabarro

stress model, where the Dorn-Rajnak model is one of the most flexible interpretations of the Peierls stress mechanism since it allows for perturbed energy barriers. This model relies on the nucleation of double kinks.

Since yield is no longer regarded as the break-away of dislocations from the interstitial atmosphere the Cottrell-Bilby model will not apply to yield except when the material has been heat treated so that dislocations are only lightly pinned.

Empirical models of the temperature dependence of the thermal component of yield stress find σ_i^* is proportional to 1/T, $\exp[-(\beta_0 + \beta_1 \ln\dot{\varepsilon})T)$ and $\sigma_p^*(1 + BT)/(1 - BT)$. The last two models are based on thermal activation parameters of Conrad's theory and "σ_i^* proportional to 1/T" is based on Cottrell-Bilby's theory of yield.

5.4 *Experimental Tensile Testing and Results*

Tensile testing was performed to establish the temperature and grain size dependence of the lower yield stress (σ_{ys}) of the two experimental steels used in the toughness testing programme.

5.4.1 SPECIMEN PREPARATION

The tensile test specimen dimensions and its machining sequence are shown in Figure 5.8. The specimens were machined from the heat treated material, the tensile axis being in the direction of rolling (shown in Figure 5.9). This orientation is that relevant to CTOD and Charpy testing. The tensile specimens tested at -196°C were given additional polishing in the longitudinal direction, finishing with Grade 600 emery paper. This was done to eliminate the notch effects of machining marks.

5.4.2 TEST PROCEDURE

The tests were conducted over the temperature range from -196 to 65°C on an Instron Universal Testing machine. Testing was performed to BS18:1987 on tensile testing and BS3688 Part 1: 1981 on elevated temperature testing [263,264]. Except for tests at ambient temperature the specimen was tested by immersing the specimen and grips in liquid at the test temperature. Tests were performed in the Amsler Environmental Test Chamber (Model No. TV742) shown in Figure 6.9. The chamber has cooling and refrigerating wells, the specimen being in refrigerant in the

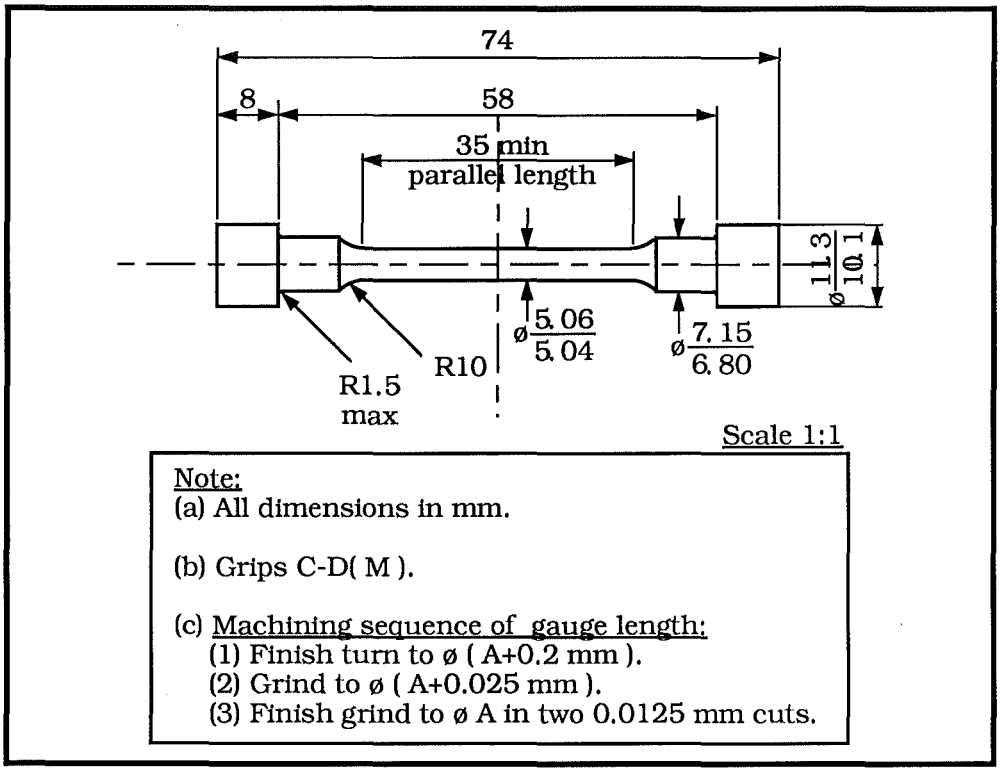

Figure 5.8 : Tensile Test Specimen Type 20.

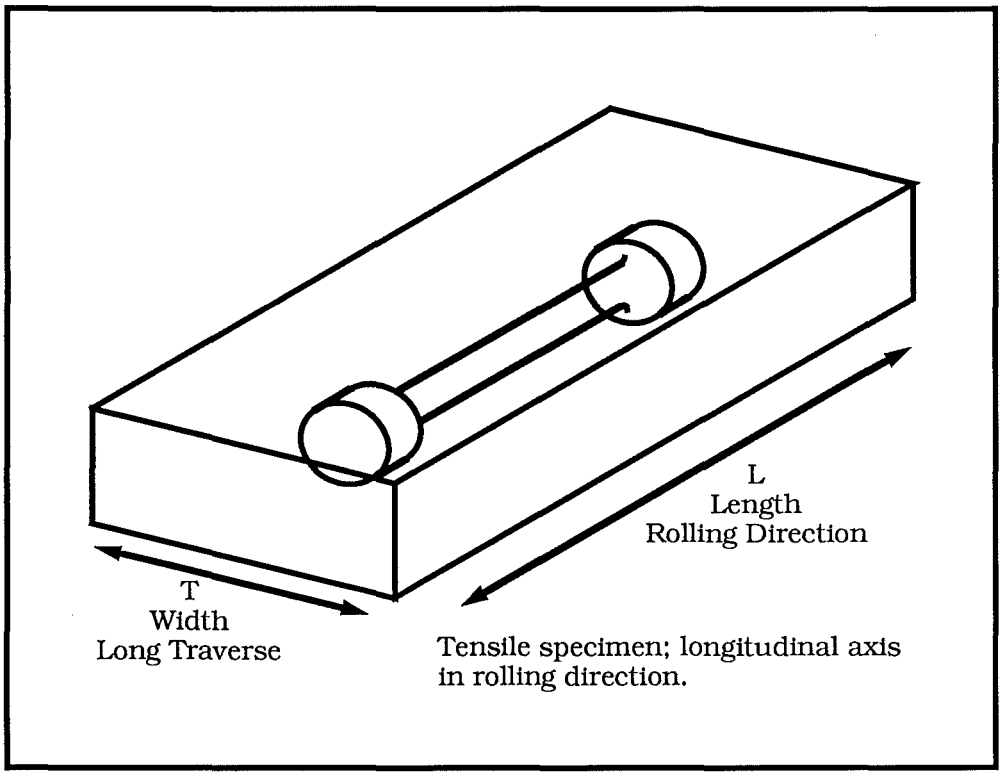

Figure 5.9 : The orientation of the tensile test specimens relative to the rolled direction of the bar.

refrigerating well. The chamber achieves test temperature by heat exchange between the coolant and the refrigerant, with no mixing of the two liquids. Table 5.2 contains a list of the different coolants and refrigerants and temperature range over which they were used. Temperature control of the chamber was ±2°C. The temperature of the specimen was monitored by a NiCr–Ni thermocouple in contact with the specimen on the gauge length. Before commencing a test the specimen was immersed in the liquid at test temperature for a minimum of 15 minutes to ensure temperature homogeneity.

The direct extension of the specimen could not be recorded because of use of the environmental chamber. Test records of applied load versus machine crosshead displacement supplied sufficient information to find the lower yield stress of the material. Figure 6.11 also shows how crosshead displacement was measured and Figure 5.10 shows a typical autographic plot of the test record. The yield point became more pronounced (a larger drop from the upper yield to lower yield point) as test temperature was lowered. The tests were performed at a crosshead speed of 0.5 mm min^{-1} to give an approximate strain rate of 3.33×10^{-4} s^{-1}.

Table 5.2
Coolants and Refrigerants used for Tensile and Fracture Toughness testing.

Temperature Range (°C)	Refrigerant[1]	Coolant[2]
20 - 65	Oil	Oil
20	Air[3]	–
20 - (-60)	Petroleum Ether	Petroleum Ether/ Dry Ice
-60 - (-140)	Petroleum Ether	Liquid Nitrogen
-196	Liquid Nitrogen[3]	–

1. Specimen was immersed in the refrigerant.
2. Coolant cooled refrigerant by heat exchange with no mixing of the liquids.
3. Specimen tested directly in "refrigerant" with no coolant needed.

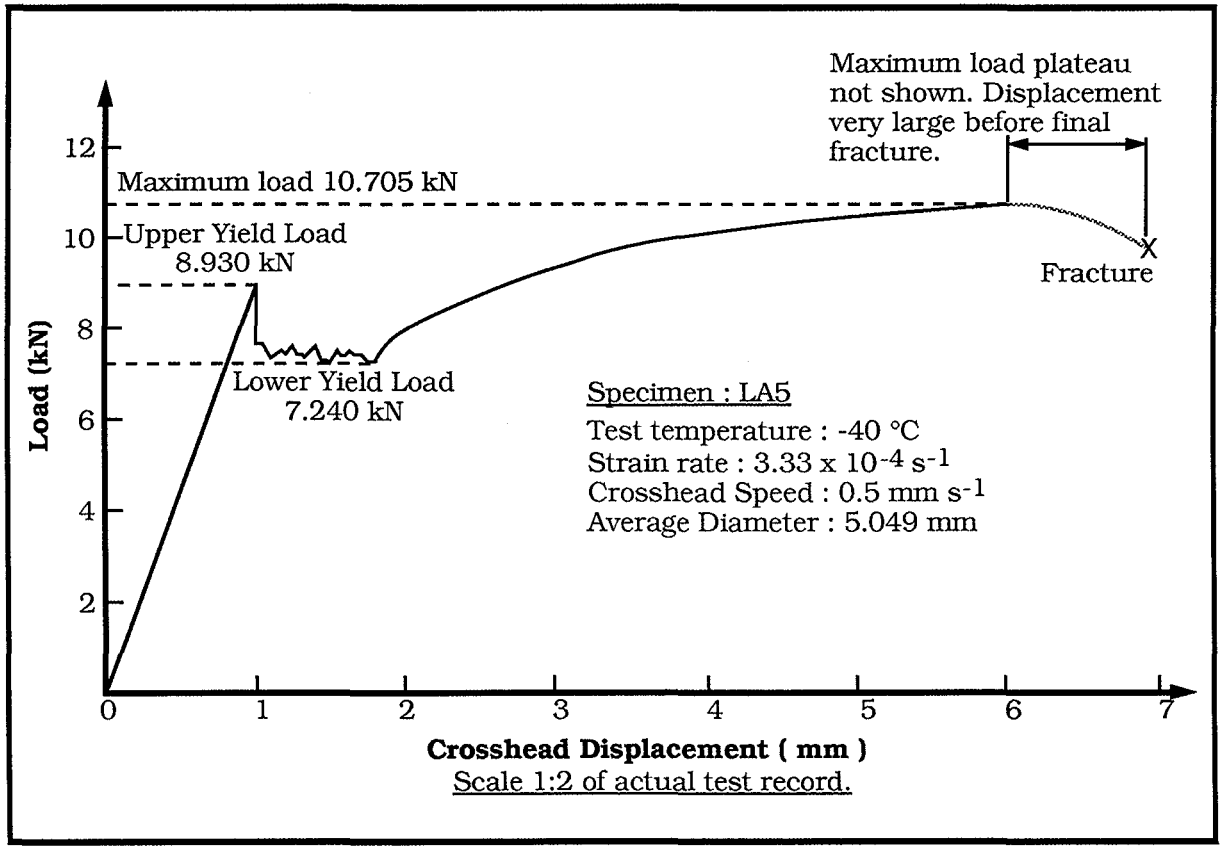

Figure 5.10 : A typical load-displacement record from tensile testing to find the lower yield stress of the experimental steels.

5.4.3 LOWER YIELD STRESS RESULTS

The results of lower yield stress for both steels are given in Table 5.3. Figure 5.11 shows results of lower yield stress versus temperature for Steel L and Figure 5.12 shows results of lower yield stress versus temperature for Steel H. These figures show that as temperature decreases the yield stress increases, the rate of change in yield stress increasing as well. The results also show that the yield stress decreases with increasing grain size.

At -196°C specimens for LA, LB, LC, LD and HA showed upper and lower yield points, and twinning was not observed. The specimens strain-hardened and failed by brittle fracture. Steels HB, HC, HD and HY showed an observable upper yield point at -196°C. As strain moved into the Lüder strain region the specimens failed by brittle fracture. Low has investigated the effects of yielding on cleavage stress [74]. It was found that at -195°C the cleavage fracture stress was coincident with the yield stress for coarse-grained materials and exceeded the yield stress for fine-grained materials. HB, HC, HD and HY may be considered to be coarse-grained; therefore the fracture load and stress were assumed to be the yield load and stress of the material.

At the elevated temperature of +45 and +65°C Steel H exhibited some dynamic strain-ageing. This is ageing which occurs almost simultaneously with plastic straining. Figure 5.13 displays the results of tensile tests at 100°C from reference 265. Chew summarised the effects of dynamic strain-ageing shown in Figure 5.13 as:

(i) Serrations of the stress-strain curve.

(ii) Increase in the rate of work-hardening.

(iii) Decrease in ductility [16].

With increasing active nitrogen content (from Steels 1 to 3, figure 5.13) the effects are more pronounced. Below 150°C strain-ageing is predominantly due to nitrogen hence any dynamic strain-ageing will be due to high active nitrogen content.

Wilson for a rimmed low carbon steel found that, with reference to equation (5.4), $\sigma_{ys} = \sigma_i + k_y d^{-1/2}$;

(i) k_y decreased from 20 to 100°C and from 160 to 200°C, while remaining constant in the intermediate temperature range.

(ii) σ_i increased slightly from 75 to 150°C and fell slightly at higher temperatures [266].

Table 5.3
Lower Yield Strength versus Temperature for Tensile Testing.

Temperature (°C)	Lower Yield Strength (MPa) of Steel/Batch.								
	LA	LB	LC	LD	HA	HB	HC	HD	HY
+65	319	265	213	203	280	197	209	199	193
+45	322	263	222	200	286	206	207	197	198
+20	330 331	268 275	231	207	289	206 211	198	214 206	207
0	338	281	226 234	211	301	207	212	209	211
-20	350	294	255	220	319	224	229	221	212 215
-40	362	304	271	244	325	224 233	234	225	234
-60	383	318	262 270	257	350	241	256	260	245
-80	413	351	301	275	382	279	281	281	277
-100	437	380	316	306	417	304	313	311	321
-120	471	416	370	352	462	357	358	354	363
-140	529	467	426	421	511	426	429	418	435
-196	773	720	691 693	677	779	683 693	704	681	705

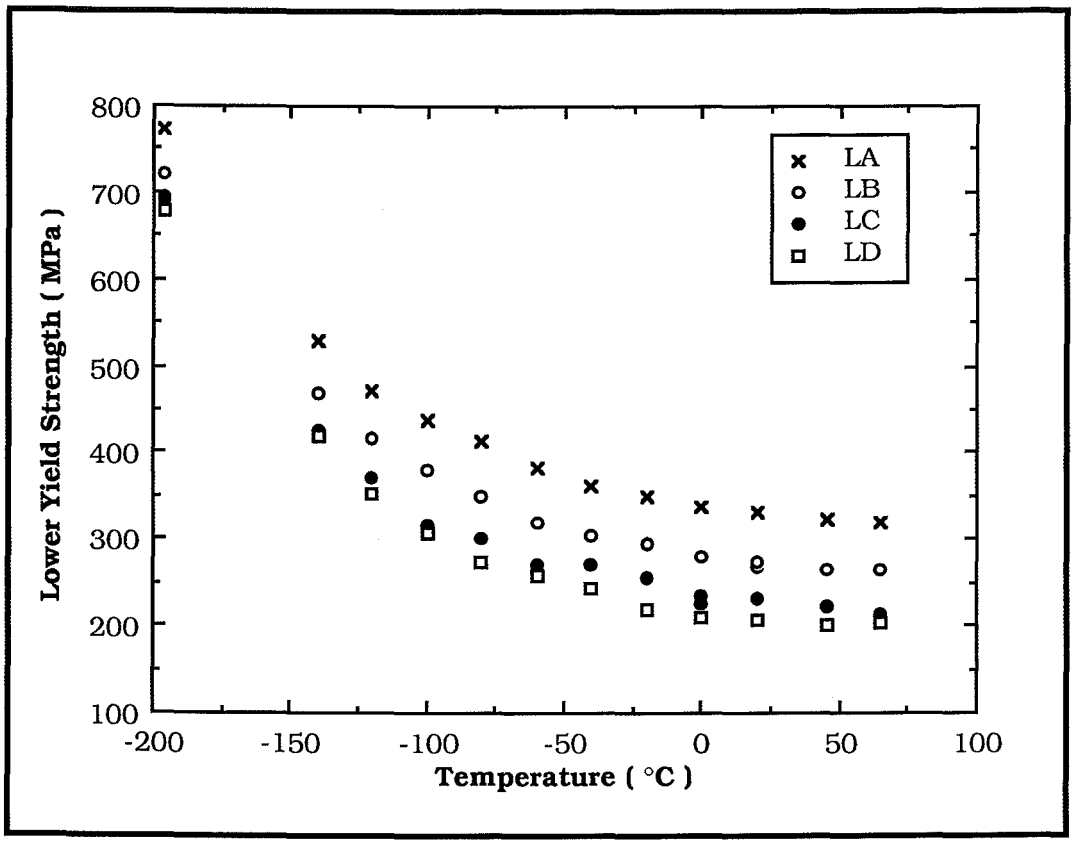

Figure 5.11 : Lower Yield Strength (MPa) as a function of test temperature (°C) for Steels LA-LD.

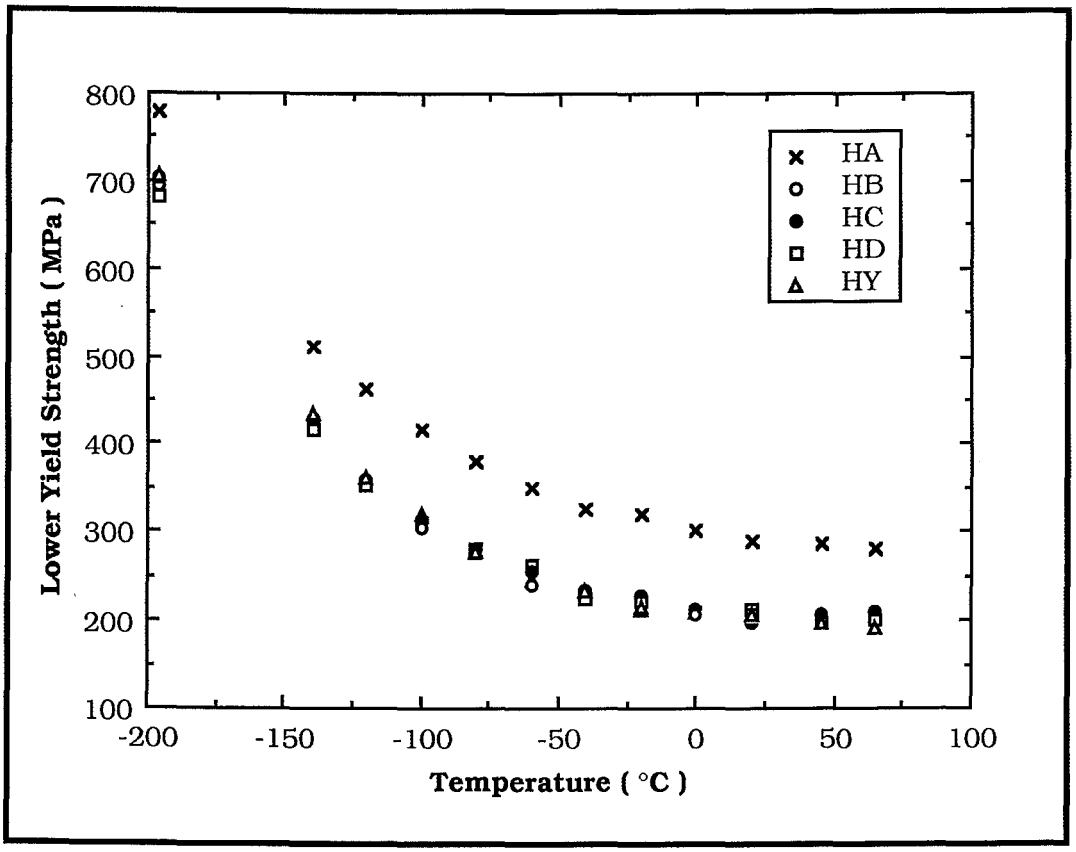

Figure 5.12 : Lower Yield Strength (MPa) as a function of test temperature (°C) for Steels HA-HD and HY.

In the absence of carbon and nitrogen σ_i would be expected to fall smoothly above 20°C. The slight rise at the beginning of the "blue-brittle" temperature range probably indicates increased frictional drag on the dislocations in this temperature range.

The test records for Steel H exhibited a yield point at +45°C and +65°C and, as the specimens strain-hardened, the curves showed some serrations or "jerky-flow" whereas Steel L did not show this. Steel H has a high active nitrogen content and it can be expected to show dynamic strain-ageing. However the nitrogen in Steel L is combined as the precipitate TiN giving a low active nitrogen content. The effect on k_y is assumed to be insignificant and k_y is taken as constant over the test temperature range.

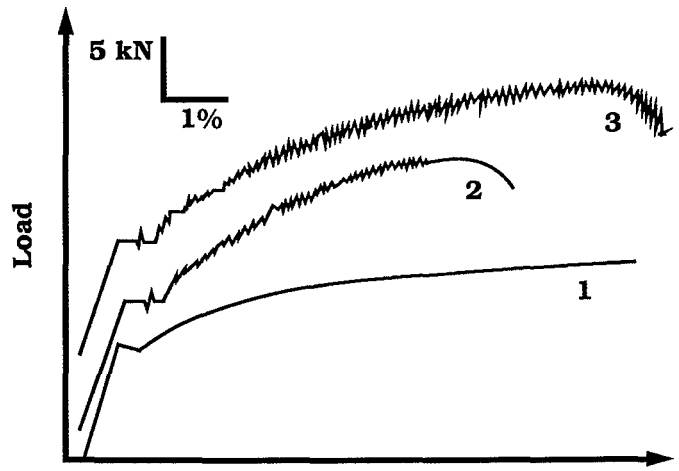

Chemical compostion of steels.

Steels	1	2	3
C %	0.23	0.23	0.08
Mn %	0.45	0.46	0.21
Ti %	0.036	Nil	Nil
Al_{sol} %	–	–	0.005
N_{sol} %	0.0004	0.0051	0.0121
N_{insol} %	0.0061	0.0009	0.0020
N_{total} %	0.0065	0.0060	0.0141
N_{AlN} %	0.0001	0.0002	Nil

Figure 5.13 : Tensile tests at 100 °C showing dynamic strain-ageing[265].

5.5 *Modelling the Temperature and Grain Size Dependence of Yield Strength*

There are a number of forms of curve to consider when trying to model the yield stress results. The final form of equation should be similar to

$$\sigma_{ys} = \sigma_i^* + \sigma_i(st) + k_y d^{-1/2}. \qquad (5.17)$$

Using linear regression techniques the form of the equation obtained is,

$$\sigma_{ys} = \sigma(T) + k_y d^{-1/2} \qquad (5.53)$$

where $\sigma(T)$ is a function of temperature and

$$\sigma(T) = \sigma_i^* + \sigma_i(st). \qquad (5.54)$$

The different equation forms for $\sigma(T)$ are summarised in Table 5.4. The results of Section 5.4.3 were analysed using a curve fitting technique applied to the equations in Table 5.4. This uses multiple-linear regression techniques to determine the least squares line. This form of analysis assumes that the data can be correlated by a straight line, and that the least squares line is the straight line from which the sum of squares of deviations of one of the variables is a minimum. This technique is not restricted to variables having a dependent-independent relationship, but merely describes in mathematical terms the nature of the relationship between the variables. In evaluating the degree of the relationship, all error or inaccuracy is assumed to be in the measurements of one of the variables, and that the other variables are precisely known. Therefore, the imprecision is associated with the dependent variable and the independent variable is assumed to be precise.

In the analysis performed the imprecision is associated with the yield stress (that is, it is the dependent variable) and the temperature and grain size are assumed to be precisely known (that is, temperature and grain size are independent variables).

A detailed description of linear regression techniques is given by Volk [267]. The analyses reported here were carried out using a Multiple-Linear Regression (MLR) program on an IBM Compatible XT

Table 5.4
Summary of the functions used to model the yield stress.

Reference	Equation[1,2,3]	Equation No.
Petch [87]	$\sigma_{ys} = B_1\exp(-B_2T) + B_3 + k_y d^{-1/2}$	(5.54a)
Fleischer [241]	$\sigma_{ys}^{1/2} = A_1 - A_2T^{1/2} + k_y d^{-1/2}$	(5.54b)
Mott & Nabarro [241]	$\sigma_{ys} = A_1 + A_2T^{2/3} + k_y d^{-1/2}$	(5.54c)
Fisher [94]	$\sigma_{ys} = A_1 + A_2/T + k_y d^{-1/2}$	(5.54d)
Power Curve	$\sigma_{ys} = A_1T^{A2} + k_y d^{-1/2}$	(5.54e)
Logarithmic curve	$\sigma_{ys} = \log A_1 + A_2\log T + k_y d^{-1/2}$	(5.54f)
Polynomial curve	$\sigma_{ys} = A_1 + A_2T + A_3T^2 + \ldots + A_nT^n + k_y d^{-1/2}$	(5.54g)
Chen *et al.* [100]	$\sigma_{ys} = B_1\left(\frac{1 + B_2T}{1 - B_2T}\right) + B_3 + k_y d^{-1/2}$	(5.54h)
Power curve (Revised)	$\log \sigma_{ys} = \log A_1 + A_2T + k_yX$	(5.56c)
	$X = [\frac{d^{-1/2}}{\sigma_{ys}} + \frac{k_y'}{2}\left(\frac{d^{-1/2}}{\sigma_{ys}}\right)^2 + \frac{k_y'^2}{6}\left(\frac{d^{-1/2}}{\sigma_{ys}}\right)^3 + \ldots]$	(5.56d)
Chen *et al.* [100] (Revised)	$\sigma_{ys} = A_2/T + A_3d^{-1/2}/T + k_y d^{-1/2} + A_1$	(5.57a)

1. Strain rate ($\dot{\varepsilon}$) is assumed to be constant.
2. B_1, B_2, B_3, k_y, $A_1 - A_n$ are constants.
3. Temperature is in Kelvin, σ_{ys} is in MPa and $d^{-1/2}$ is in $mm^{-1/2}$

Personal Computer. For the analyses equations (5.54a), (5.54e) and (5.54h) needed rearranging so that the result was similar to equation (5.53).

(a) Equation (5.54a): For the exponential curve the equation is,

$$\sigma_{ys} = B_1\exp(-B_2T) + k_y d^{-1/2} + B_3, \qquad (5.55)$$

where B_1, B_2 and B_3 are constants. To give a linear form for regression analysis it would be normal to take logarithms of both sides to give,

$$\log \sigma_{ys} = \log(B_1 \exp(-B_2 T) + B_3 + k_y d^{-1/2}) \qquad (5.55a)$$

To continue with the equation in this form values must be assumed for the constants B_1, B_2, B_3 and k_y. However, an alternative method is to expand $\exp(-B_2 T)$ in equation (5.55) by an infinite power series to give,

$$\sigma_{ys} = B_1\left(1 - B_2 T + \frac{B_2^2}{2!} - \frac{B_2^3 T^3}{3!} + \ldots + \frac{(-1)^{n+1}}{(n-1)!} B_2^n T^n + \ldots\right) + B_3 + k_y d^{-1/2} \qquad (5.55b)$$

which upon combining constants together can be written

$$\sigma_{ys} = A_1 + A_2 T + A_3 T^2 + \ldots + A_n T^n + \ldots + k_y d^{-1\backslash 2}$$

which is the same as equation (5.54g). That is, the exponential equation may be represented by an infinite polynomial. The MLR program regards T, T^2, T^3, ..., T^n as n separate independent variables.

(b) Equation (5.54e): The power curve equation may be written,

$$\sigma_{ys} = A_1 T^{A2} + k_y d^{-1/2}, \qquad (5.56)$$

and taking logarithms of both sides to give a linear equation,

$$\log \sigma_{ys} = \log(A_1 T^{A2} + k_y d^{-1/2}). \qquad (5.56a)$$

Again the values of the constants A_1, A_2 and k_y would have to be assumed to perform a linear regression on this equation. However, if $k_y d^{-1/2}$ is subtracted from both sides of equation (5.56) and logarithms taken of both sides then,

$$\log(\sigma_{ys} - k_y d^{-1/2}) = \log A_1 T^{A2}. \qquad (5.56b)$$

The LHS expression may be normalised by dividing (σ_{ys} - $k_y d^{-1/2}$) through by σ_{ys}. Then the LHS may be expanded by a logarithmic series where the series is valid for $-1 < k_y d^{-1/2}/\sigma_{ys} \leq 1$ to give

$$\log \sigma_{ys} = \log A_1 + A_2 T + k_y X \qquad (5.56c)$$

$$\text{where } X = \left(\frac{d^{-1/2}}{\sigma_{ys}} + \frac{k_y'}{2}\left(\frac{d^{-1/2}}{\sigma_{ys}}\right)^2 + \frac{k_y'^2}{6}\left(\frac{d^{-1/2}}{\sigma_{ys}}\right)^3 + \ldots\right) \qquad (5.56d)$$

This assumes X is a known independent variable using a previously found value of k_y'. The solution is found by iterating towards the solution of k_y. Once k_y is found (i.e. unchanging between iterations) then the next term in the series expansion is checked to ensure that it is insignificant i.e. $\frac{k_y'^3}{4!}\left(\frac{d^{-1/2}}{\sigma_{ys}}\right)^4$ for equation (5.56d).

(c) Equation (5.54h): The equation from Chen *et al.* can be written in an alternative form as well. By multiplying both sides by (1 - B_2T) then the equation is,

$$B_2 T\sigma_{ys} = 1 - B_1(1 + B_2T) - B_3(1 - B_2T) - k_y d^{-1/2}(1 - B_2T). \qquad (5.57)$$

Dividing through by B_2T and collecting like terms equation (5.57) becomes,

$$\sigma_{ys} = A_2/T + A_3 d^{-1/2}/T + k_y d^{-1/2} + A_1, \qquad (5.57a)$$

where A_1, A_2, A_3 and k_y are constants, and ($d^{-1/2}/T$) is assumed to be a third independent variable.

5.5.1 RESULTS OF MULTIPLE-LINEAR REGRESSION ANALYSIS

The experimental model had to model the yield stress of the experimental steels over the temperature range -196 to +65°C. This is a limitation for most of the models described since their range is -196°C to ambient temperature. Using results from Table 5.3 as the data input the results of the regression analysis are given in Appendix B, in Table B.1 for Steel L, Table B.2 for Steel H-combined grain size and Table B.3 for Steel H-individual grain size. There are two tables of results for Steel H since the grain sizes of HB, HC, HD and HY are

about the same. Therefore two analyses were made of each equation for Steel H;

(i) The results of HB, HC, HD and HY were pooled using an average grain size for HB, HC, HD and HY of 4.4 $mm^{-1/2}$.

(ii) The results of HB, HC, HD and HY were separated into their respective grain sizes.

Appendix B also contains Figures B.1 - B.24 which allow comparison of the regression results with the experimental points. Figures 5.14, 5.15 and 5.16 show the chosen models for Steels L, H (Combined) and H (Individual) respectively (these are Figures B.1, B.9 and B.17 respectively of Appendix B). The chosen model is a cubic polynomial with respect to temperature,

$$\sigma_{ys} = A_1 + A_2T + A_3T^2 + A_4T^3 + k_yd^{-1/2} \qquad (5.58)$$

where A_1, A_2, A_3, A_4 and k_y are constants. Table 5.5 contains the values of the constants for each steel. All the constants have a significance of greater than 99.9%. Equations (5.59), (5.60) and (5.61) have a significance much greater than 99.9%, that is, the probability that the correlations will occur by chance are much less than 1 in 1000 times. However this result also applies to all the other regression results. The F-values of 5083, 8297 and 4802 for equations (5.59), (5.60) and (5.61) respectively are considerably higher than those of most of the other regression results, and the significance of the equation is found from the F-value. Other correlations with high F-values[+] were; equations (B.3), (B.11) and (B.19) where σ_{ys} is proportional to 1/T; equations (B.2), (B.10) and (B.18) where σ_{ys} is proportional to T^4; and equations (B.4), (B.12) and (B.20) based on Chen *et al.*'s model.

The equations based on 1/T show a high degree of correlation, for example, equation (B.3) has r = 0.9976, F = 5273. However its overall error is greater than equation B.1 and from figure B.3 the deviation between experimental and the predicted result is significant above room temperature. Therefore these equations (B.3), (B.11), (B.19), (B.4), (B.12) and (B.20) based on 1/T could be used in the temperature range from -196 to 20°C.

The models based on the polynomial $A_1 + A_2T + A_3T^2 + A_4T^3 + A_5T^4$ have a high degree of correlation as well, for example

---

[+] See Appendix B for definition of symbols.

Table 5.5
Results of Multiple-Linear Regression Analysis of Selected Yield Stress Model for Experimental Steels.

Steel	L	H(Combined)	H(Individual)
Equation No.	5.59	5.60	5.61
Figure No.	5.14	5.15	5.16
DF	48	60	60
R	0.9988	0.9991	0.9984
$s(\hat{y})$	7.09	6.47	8.50
F-value	5083	8297	4802
Equation Significance	> 99.9%	>99.9%	>99.9%
Coefficients:			
A_1	1124.3	1149.0	1144.6
A_2	-9.57	-9.71	-9.63
A_3	3.14×10^{-2}	3.05×10^{-2}	3.01×10^{-2}
A_4	-3.55×10^{-5}	-3.25×10^{-5}	-3.19×10^{-5}
k_y	20.85	23.16	22.89
$\bar{y}$	349.2	317	317
95% C.L. of $\bar{y}$	± 1.96	± 1.60	± 2.11

1.. Equation used is,

$$\sigma_{ys} = A_1 + A_2T + A_3T^2 + A_4T^3 + k_y d^{-1/2} \qquad (5.58)$$

where σ_{ys} is the lower yield stress (MPa), T is the temperature (K) and $d^{-1/2}$ is the grain size ($mm^{-1/2}$). $A_1 - A_4$ and k_y are constants.

2. For the definition of statistical abbreviations see Appendix B.

3. The significance of all coefficients is greater than 99.9%.

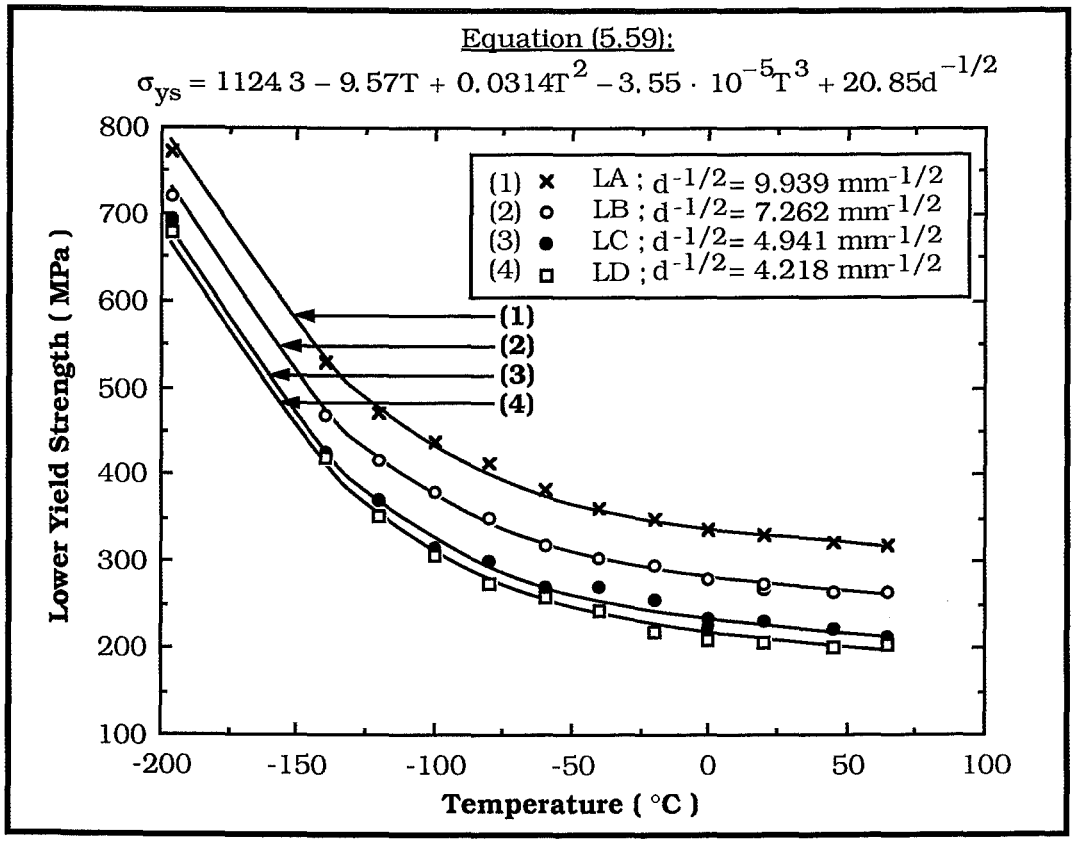

Figure 5.14 : Lower yield strength (MPa) as a function of temperature (°C) and grain size ($mm^{-1/2}$) for Steel L using equation (5.59).

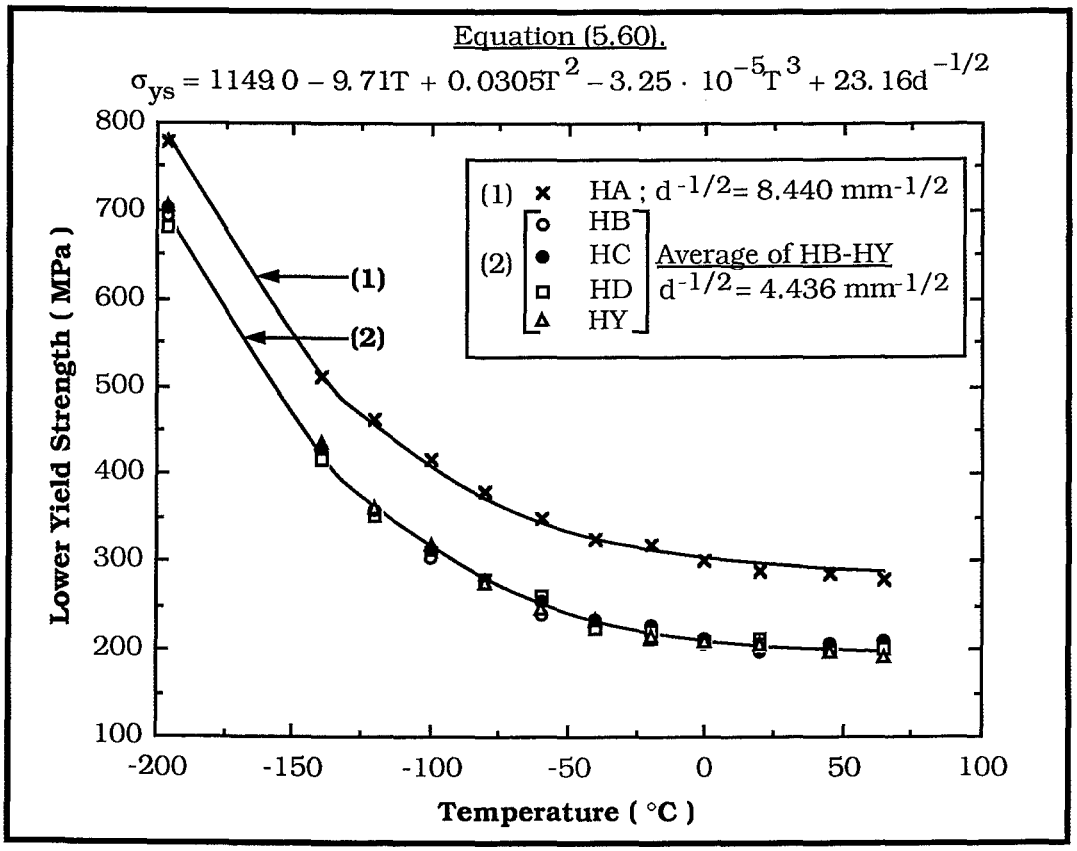

Figure 5.15 : Lower yield strength (MPa) as a function of temperature (°C) and grain size ($mm^{-1/2}$) for Steel H using equation (5.60).

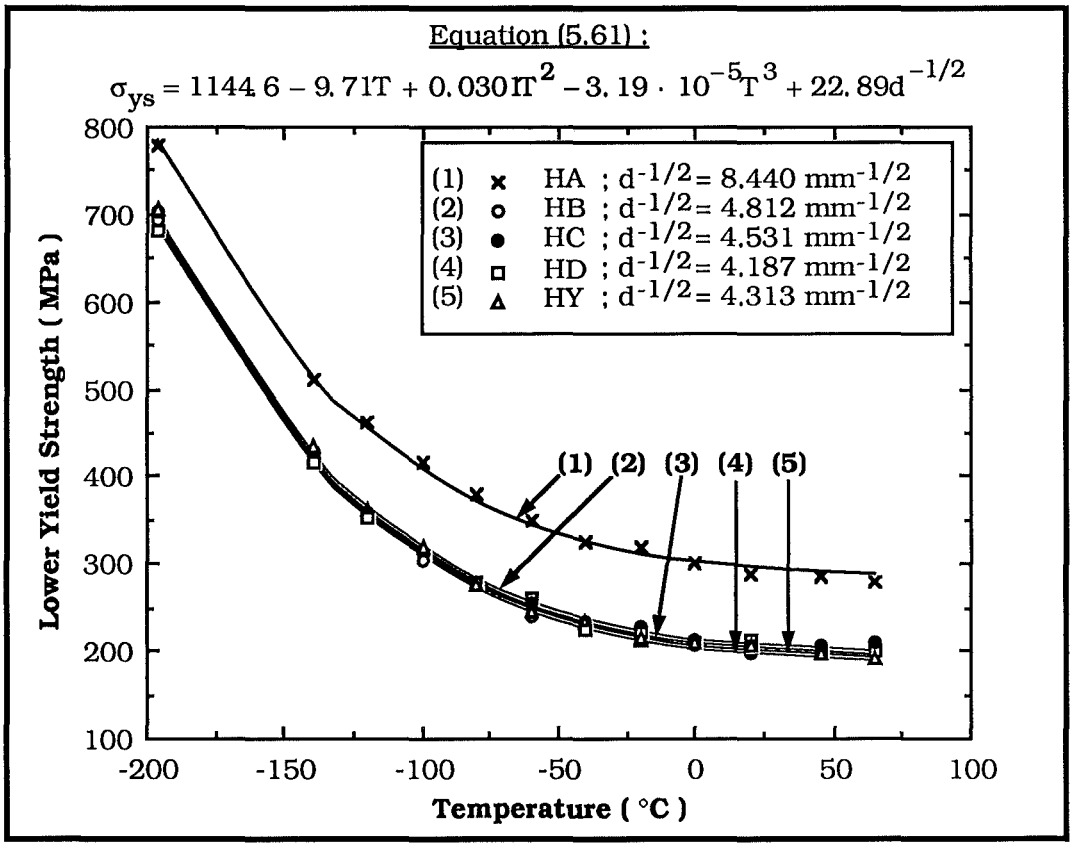

Figure 5.16 : Lower yield strength (MPa) as a function of temperature (°C) and grain size ($mm^{-1/2}$) for Steel H using equation (5.61).

equation (B.2) has r = 0.9989, F = 4360. Its 95% confidence limits of $\bar{y}$ are ±1.896 MNm^{-2} compared to ±1.962 MNm^{-2} for equation (5.59) but the constants A_4 and A_5 have lost significance. The significance is 99.8% for A_4 and 90% for A_5 in equation (B.2) compared to the significance of all constants in equation (5.59) being greater than 99.9%. Therefore the T^4 term is not significant and the model may be reduced to a cubic polynomial. The comparison is similar for Steel H; for equation (B.18), A_4 has a significance of 80% and A_5 has a significance of between 50-80%.

For equation (5.59) 99.76% of the total variation in yield strength is explained by the equation. For equation (5.60) 99.91% of the total variation in yield strength is explained while 99.8% of the total variation in yield strength is explained in equation (5.61) by their respective correlation coefficients.

Equation (5.61) is used for calculating the yield stress of Steel H at test temperature since it was correlated using 5 grain sizes as opposed to 2 grain sizes used in equation (5.60). Equation (5.61) is as significant as equation (5.60) when there is no significant difference in the grain size of HB, HC, HD and HY.

5.5.2 *DISCUSSION OF EMPIRICAL MODEL*

The model of the temperature and grain size dependence of lower yield stress has been found as a cubic polynomial of temperature. The model has a very good correlation with experimental results but to have more than a specific application in this case the coefficients should agree with previous observations on yield strength.

(a) k_y

In reference 174 the common range for k_y was 14-24 $MNm^{-2}mm^{1/2}$. In the experimental models the coefficient k_y is 20.85 $MNm^{-2}mm^{1/2}$ for Steel L and 22.89 $MNm^{-2}mm^{1/2}$ for Steel H. It is expected that the higher the carbon content then the higher k_y will be [174]. This accounts for the high value of k_y for Steel L which has a carbon content 0.19 wt%. Increasing active nitrogen content also increases k_y, which would account for Steel H having a higher value of k_y than Steel L since Steel H has a high active nitrogen content; 0.012 wt% compared to 0.0017 wt% for Steel L. There is variation to these trends. Table 2 of reference 174 reports k_y as 25.5 $MNm^{-2}mm^{1/2}$ for a 0.004 wt% carbon 0.0005 wt% nitrogen steel and k_y as

21.6 $MNm^{-2}mm^{1/2}$ for a 0.014 wt% carbon, 0.003 wt% nitrogen steel. Figures 5.17 and 5.18 show that the Hall-Petch equation, $\sigma_{ys} = \sigma_i + k_y d^{-1/2}$, applies to these results. These figures of yield strength versus the reciprocal square root of grain size show a linear relationship between the two variables. The predicted slopes are 20.85 $MNm^{-2}mm^{1/2}$ for Steel L and 22.89 $MNm^{-2}mm^{1/2}$ for Steel H. It is possible that these slopes and hence k_y would change with a wider range in grain size. The significance of k_y in equations (5.59) and (5.61) is greater than 99.9%. It may be concluded that the values of k_y are in agreement with other work and are acceptable.

(b) Athermal Stress Component

An approximate athermal stress can be found for the steels considered. This stress varies with temperature only through the temperature variation of the modulus, E. It is independent of strain rate and is associated with long-range stress fields; thus it is dependent upon composition. It can be found by extrapolating $d\sigma_{ys}/dT$ versus temperature curves to zero. This gives the critical temperature T_c above which σ_i^*, the thermally-dependent component is zero. By plotting yield stress versus grain size for this temperature the friction stress is given at $d^{-1/2} = 0$ $mm^{-1/2}$ (i.e. infinite grain size). Figures 5.19 and 5.20 show plots of $d\sigma_{ys}/dT$ versus temperature for Steels L and H respectively. To find where $d\sigma_{ys}/dT$ is about zero linear regression analysis has been performed on each set of results to give the equations shown on Figures 5.19 and 5.20. Results for T = 318K (45°C) and T = 338 K (65°C) were not included in these analyses. It was found that $(\Delta\sigma_{ys}/\Delta T)_{\dot{\varepsilon}} = 0$ when T_c = 280K for Steel L and T_c = 276 K for Steel H. On Figures 5.17 and 5.18 the yield stress at these temperatures is plotted versus grain size. Extrapolating the curves to $d^{-1/2} = 0$ $mm^{-1/2}$ gives the athermal friction stress (σ_i(st)) as 129 MNm^{-2} for Steel L and 108 MNm^{-2} for Steel H.

A summary of athermal stress components found in other research is given in Table 5.6. The athermal stress component is found to vary from about 31 MNm^{-2} found by Petch to 525 MNm^{-2} found by Vinogradov *et al.* [209,268]. From Table 5.6 σ_i(st) is dependent upon composition and increases with increasing alloy content. Vinogradov *et al.* felt the very high values of σ_i(st) could be discounted because the low concentrations of alloying elements in solid solution in their steels should not give such a high result [268].

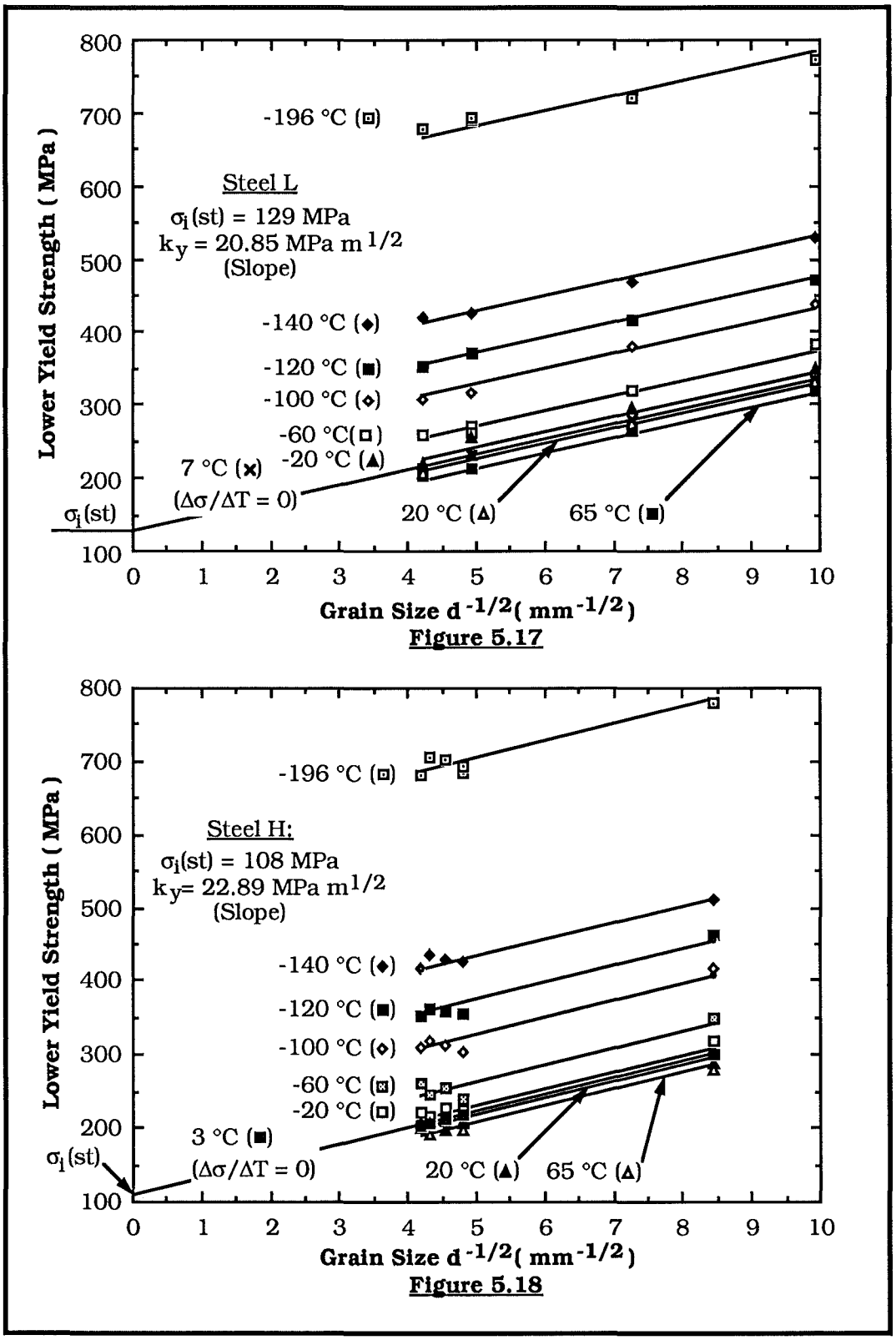

Figure 5.17 : Lower yield strength (MPa) as a function of grain size ($mm^{-1/2}$) at various test temperatures for Steel L. Line shows predicted results.

Figure 5.18 : Lower yield strength (MPa) as a function of grain size ($mm^{-1/2}$) at various test temperatures for Steel H. Line shows predicted results.

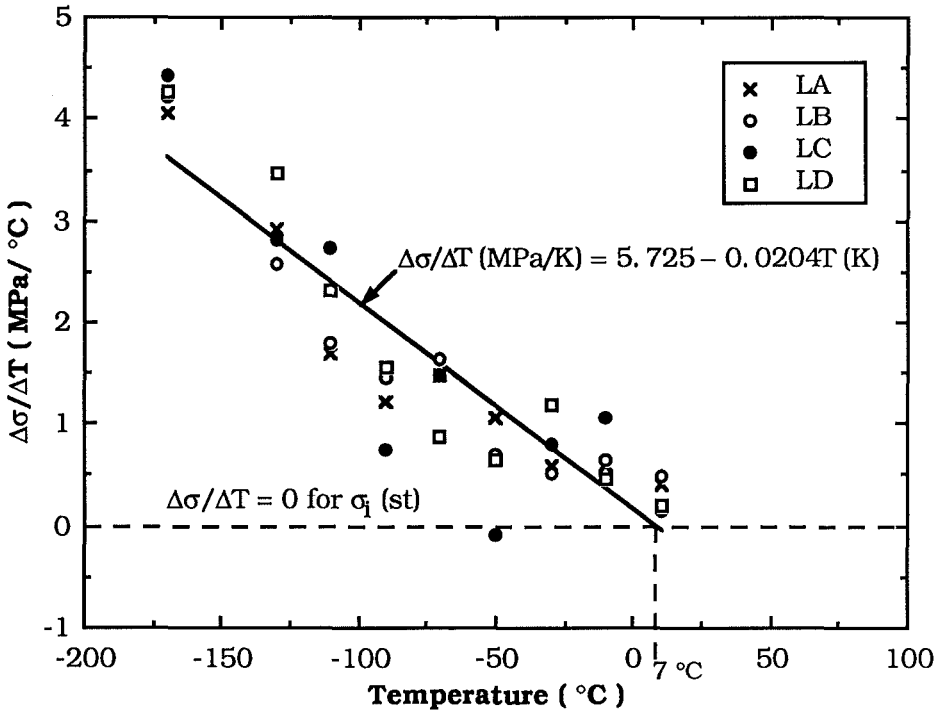

Figure 5.19

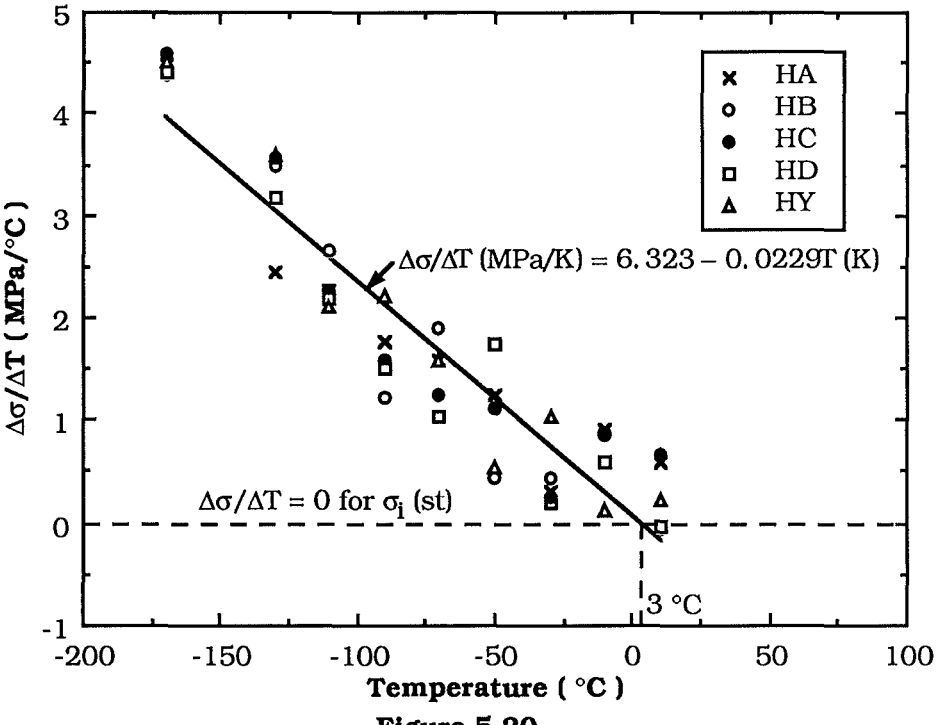

Figure 5.20

Figure 5.19 : The change in lower yield strength with respect to the change in test temperature (MPa/°C) as a function of temperature (°C) for Steel L.

Figure 5.20 : The change in lower yield strength with respect to the change in test temperature (MPa/°C) as a function of temperature (°C) for Steel H.

Table 5.6
Summary of Athermal Stress Components of Yield Stress.

Material	σ_i(st) (MPa)	Reference
L, Mild Steel, 0.19%C	129	Present work
H, Mild Steel, 0.09%C, 0.012%N	108	Present work
Mild Steel, 0.06%C	41	Hall [164]
Mild Steel, 0.12%C	71	Armstrong et al. [270]
Swedish Iron, 0.02%C	47	Cracknell & Petch [271]
Mild Steel, 0.11%C	31	Petch [209]
Fe	69	Chen et al. [100]
Fe-1%Si	121	"
Fe-2.5%Si	167	"
Fe-4%Si	222	"
Fe-1%Ni	108	"
Fe-2.5%Ni	134	"
Fe-4%Ni	175	"
0.16%C, 2.8%Cr, 0.6%Mo,0.3%V, Pressure vessel steel (Bainitic).	500	Kotilainen et al. [198]
0.42%C, 0.74%Mn, 1%Si	525	Vinogradov et al. [268]
0.42%C, 0.55%Mn, 2.01%Ni	160	"
0.43%C, 0.82%Mn, 2.5% Cr	88	"

Even allowing for this, the estimated values of $\sigma_i(st)$ for steels L and H are in the right range for a low-carbon steel. $\sigma_i(st)$ will be higher than Petch's result since Steel L has 0.19 wt% carbon, and Steel H has 0.012 wt% active nitrogen compared to the 0.11 wt% carbon steel used by Petch [209].

The results are probably an overestimate of the athermal component, relying on $(\Delta\sigma_{ys}/\Delta T)_{\dot{\varepsilon}}$ which asymptotically approaches zero. If, for example, T_c = 318 K as in reference 269 then $\sigma_i(st)$ = 116 MNm^{-2} for Steel L and $\sigma_i(st)$ = 98 MNm^{-2} for Steel H. $\sigma_i(st)$ as found is of the same order of magnitude as these results. Therefore, although the results must be treated with caution, $\sigma_i(st)$ is similar to the results of other work and may be used as an approximate value of athermal stress.

(c) Coefficients of $\sigma(T)$

The form of $\sigma(T)$ is a cubic polynomial, $A_1 + A_2T + A_3T^2 + A_4T^3$, derived from equation (5.54a), $\sigma(T) = B_1\exp(-B_2T) + B_3$. The power series expansion of equation 5.54a to T^3 is,

$$B_1\exp(-B_2T) + B_3 = B_1(1 - B_2T + B_2^2T^2/2 - B_2^3T^3/6) + B_3. \qquad (5.62)$$

The coefficient A_1 in equation (5.58) contains the athermal stress component $\sigma_i(st) = B_3$. If coefficients are equated then

$$B_1 = A_1 - B_3 \qquad (5.62a)$$
$$-B_1B_2 = A_2 \qquad (5.62b)$$
$$B_2^2B_1/2 = A_3 \qquad (5.62c)$$
$$B_2^3B_1/6 = A_4 \qquad (5.62d)$$

from which B_1 and B_2 can be found. Table 5.7 gives the results for B_1 and B_2 from equations (5.59) and (5.61). The constant B_1 is not the extrapolated yield stress at T = 0 K. The grain size and athermal stress components must be added to B_1. This estimated yield stress at T = 0 K is given in Table 5.8, which also summarizes some other values of yield stress at T = 0 K. The range of yield stress is from about 751 to 2002 MNm^{-2}, depending on the composition and the grain size of the material. The range in yield stress from 1212 to 1332 MNm^{-2} for Steel L and from 1240 to 1338 MNm^{-2} for Steel H lies in the middle of the values of other published work. The values also depend upon the form of extrapolation of yield stress to T = 0 K.

Table 5.7
Coefficients of Yield Stress Model Exponential Equation.

Steel		L	H
Model Equation No.		5.59	5.61
Coefficient	Equation		
B_1 (MNm^{-2})	5.62a	955.3	1036.6
B_2 (K^{-1})	5.62b	0.010	9.29×10^{-3}
	5.62c	8.11×10^{-3}	7.62×10^{-3}
	5.62d	6.06×10^{-3}	5.69×10^{-3}
β_0 (K^{-1})	5.64	3.23×10^{-3}	3.66×10^{-3}
B_2 (K^{-1})	5.63	7.63×10^{-3}	8.06×10^{-3}

For example equation (B.6) (the logarithmic equation) at T = 1 K gives σ_{ys} = 2023 MNm^{-2} for LA, which is higher than any yield stress in Table 5.8.

By calculating B_2 from A_2, A_3 or A_4 a different value of B_2 will be found but these should be of the same order of magnitude. Also B_2 should be of a similar order of magnitude to that predicted by the thermal activation theory of Conrad. From reference 99

$$-B_2T = -(\beta_o + \frac{k}{H_o}\ln(v/\dot{\varepsilon})T, \qquad (5.63)$$

$$\text{where } \beta_o = \frac{1}{T}\ln\left(\frac{2H_o}{v^*B_1}\right) \qquad (5.64)$$

If the median values of temperature and activation volume are used from Conrad's paper then T = 190 K, $v^* = 3.4 \times 10^{-28}$ m^3 and $H_o = 8.8 \times 10^{-20}$ J [97]. Using these values and B_1 from equations (5.59) and (5.61) then β_o is found as shown in Table 5.7. The testing strain rate was 3.33×10^{-4} s^{-1}. Using this in equation (5.63) gives B_2 as shown in Table 5.7, 7.63×10^{-3} K^{-1} for Steel L and 8.06×10^{-3} K^{-1} for

Table 5.8
Estimated Yield Stress at Absolute Zero (0 K).

Material	σ_{ys} at T = 0 K (MPa)	B_1 (MPa)	Reference
LA	1331.5	955.3	Present work
LB	1275.7	955.3	Present work
LC	1227.3	955.3	Present work
LD	1212.3	955.3	Present work
HA	1337.7	1036.6	Present work
HB	1254.7	1036.6	Present work
HC	1248.3	1036.6	Present work
HD	1240.4	1036.6	Present work
HY	1243.3	1036.6	Present work
Annealed ingot iron	1250	-	Cottrell & Bilby [93]
Mild Steel, 0.15%C.	1800	1800	Armstrong [99]
Pressure vessel steel, 0.16%C, 2.8%Cr, 0.6% Mo, 0.3%V	1755	1255	Kotilainen et al. [198]
Mild Steel, 0.10%C	1825	1670	Okumura [171]
Mild Steel, 0.10%C	2002	1670	Okumura [171]

Steel H. Comparing these results with B_2 found from coefficients A_2, A_3 and A_4, it is found that these are very similar. Thus the cubic polynomial form of temperature dependence finds similar values to those predicted by thermal activation theory.

Values for B_2 given by other workers are: 1.1×10^{-2} K^{-1} [99], 1.4×10^{-2} K^{-1} [171] and 1.04×10^{-2} K^{-1} [198]. The difference between the values of B_2 is mainly in the different values of B_1 found (i.e. the Peierls stress) and also the different strain rates used for testing, 10^{-4} s^{-1} in reference 99 and 2.6×10^{-3} in reference 171. It should be noted that the yield stress measured in reference 171 was found by compression testing and not tensile testing.

Although it has been shown that the yield stress temperature dependence can be represented as an exponential equation, for yield stress calculations equations (5.59) and (5.61) will be used. This is since the polynomial is a truncated form of an infinite power series expansion of the exponential equation. Since there are missing higher order terms the resulting exponential equation does not predict the experimental results with accuracy. As more higher order terms are used to calculate the coefficients of equation (5.54a) then the equation approaches the accuracy of the polynomial. With more experimental points higher order polynomials could be used since the coefficients would have more significance.

(d) Comparison of $\sigma(T)$ with published work

For the model to apply generally it must apply to other experimental data. In reference 171 results are given of lower yield stress versus temperature and grain size for 0.11 wt% carbon steels. Table 5.9 contains results of estimated yield stress from the figures of reference 171 although there is variation in the results plotted. For example the yield stress of Steel PQ1 at 17°C may be read as 482 MNm^{-2} from Figure 1 of reference 171 or as 455 MNm^{-2} from Figure 2 of reference 171. Figure 5.21 shows the experimental points of yield stress versus temperature for Steels PQ1, PQ2 and PQ3. Also plotted are an estimated curve using the empirical equation of reference 171 and the estimated curve of a multi-linear regression analysis to give an equation similar to equation (5.58). The results of this analysis are given in Table 5.10, which also includes results of the analysis using equation (5.54c) where yield stress is proportional to 1/T.

Table 5.9
Estimated Lower Yield Stress Results from Reference 171.

Steel	PQ1	PQ2	PQ3
Grain Size ($mm^{-1/2}$)	16.8	12.0	6.5
Temperature (°C)	Lower Yield Strength (MPa)		
+17	482	400	276
-40	486	448	-
-70	-	-	350
-90	550	497	393
	-	511	-
-120	616	582	465
-150	711	682	548
	719	-	591
-196	1111	1011	811
	1117	1041	845

The empirical equation of reference 171 is

$$\sigma_{ys} = 45 + 0.54d^{-1/2} + 1670 \exp[-(\beta_0 + \beta_1 \log\dot{\varepsilon})T] \quad (5.65)$$

where σ_{ys} is the yield stress (MNm^{-2}), $\dot{\varepsilon}$ the strain rate, T the temperature (K), $\beta_0 = 8.9 \times 10^{-3}\ K^{-1}$ and $\beta_1 = -7.9 \times 10^{-4}\ K^{-1}$. Strain rate was taken as $2.56 \times 10^{-3}\ s^{-1}$. Figure 5.21 shows that the fit of a cubic polynomial to the experimental data is better than the given empirical equation. Equation (5.66),

$$\sigma_{ys} = 1695.4 - 17.2T + 6.83.10^{-3}T^2 - 9.36.10^{-5}T^3 + 18.8d^{-1/2},$$

is much more significant than 99.9%. The coefficients are more significant than 99.9% except A_4 ($-9.36.10^{-5}\ MNm^{-2}K^{-3}$) which is significant at the 99.5% level. With more data points the significance would increase. The correlation coefficient is 0.9916 and explains 98.33% of the observable error in yield stress.

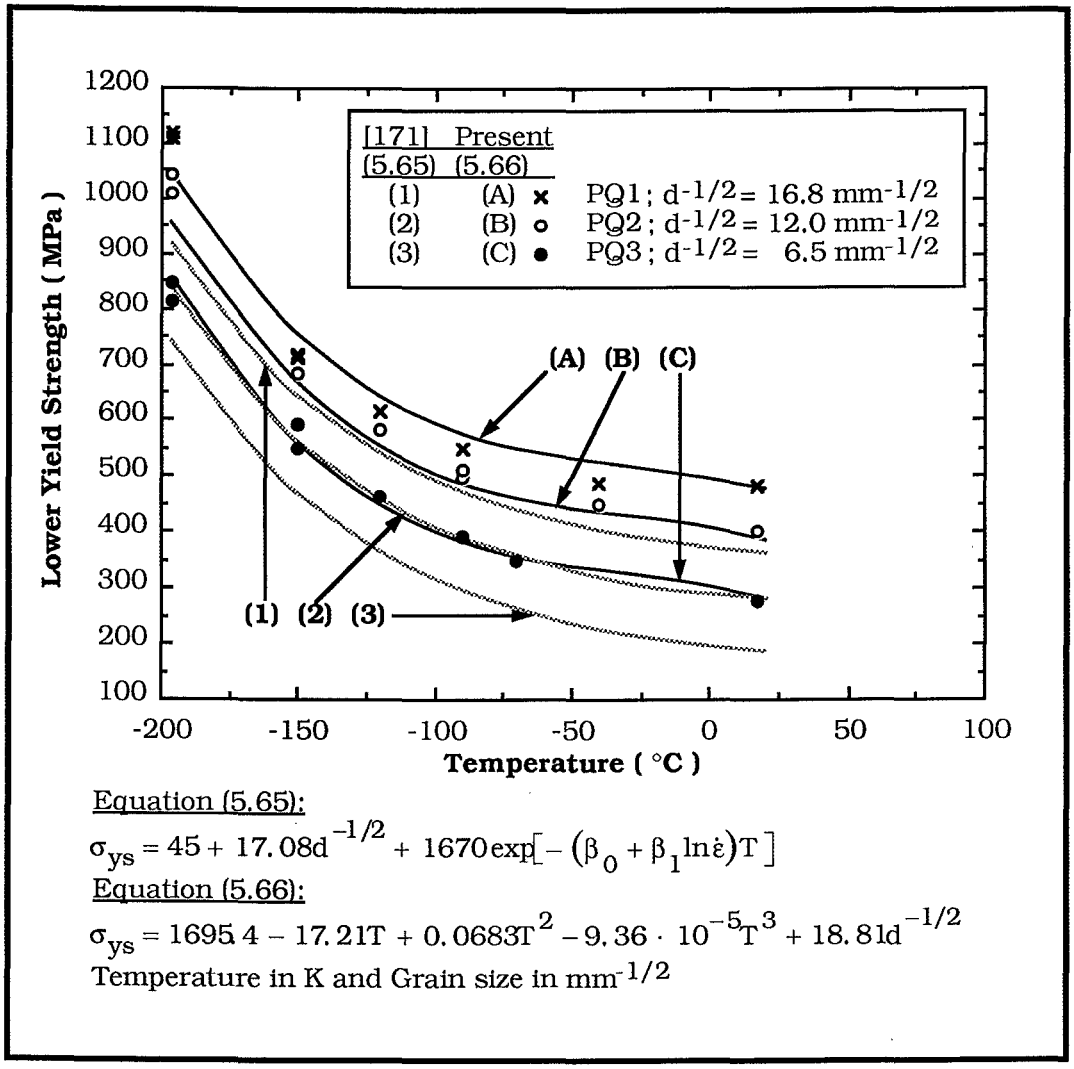

Equation (5.65):

$$\sigma_{ys} = 45 + 17.08d^{-1/2} + 1670\exp\left[-\left(\beta_0 + \beta_1 \ln\dot{\varepsilon}\right)T\right]$$

Equation (5.66):

$$\sigma_{ys} = 1695.4 - 17.21T + 0.0683T^2 - 9.36 \cdot 10^{-5}T^3 + 18.81d^{-1/2}$$

Temperature in K and Grain size in $mm^{-1/2}$

Figure 5.21 : Lower yield strength (MPa) as a function of temperature (°C) for 0.11 wt% C steel; results from reference 171.

The results of equations (5.67) where yield stress is proportional to 1/T show similar significance.

The coefficients may be examined using the same analysis as used on the coefficients of equations (5.59) and (5.61). For equation (5.66) k_y = 18.8 MNm^{-2} $mm^{1/2}$ whereas reference 171 gives k_y = 17.1 $MNm^{-2}mm^{1/2}$ (0.54 $MNm^{-3/2}$). The 95% confidence limits of k_y are ±3.50 $MNm^{-2}mm^{1/2}$; therefore k_y = 17.1 $MNm^{-2}mm^{1/2}$ lies within the expected range of k_y. Equating coefficients of equation (5.66) and (5.62), where $\sigma(T) = B_1\exp(-B_2T) + B_3$, it is found B_1 = 1650 ± 250 MNm^{-2} at the 95% confidence level (having subtracted B_3 = 45 MNm^{-2} as the solution hardening term of Mn and Si, the athermal stress component). From reference 171 B_1 = 1670 MNm^{-2} and this is included in the range of B_1 from equation (5.66).

Using B_1 = 1650 MNm^{-2} gives B_2 = 0.01043 K^{-1} and the value of B_2 = 0.01043 K^{-1} is of the same order of magnitude as B_2 = 0.011 K^{-1} from reference 99 and B_2 = 0.0104 K^{-1} from reference 198.From equation (5.64) $\beta_0 = (1/T)\ln(2H_0/v^*B_1)$ which gives β_0 = 6.1 x 10^{-3} K^{-1} when T = 190 K, H_0 = 8.8 x 10^{-20} J, v^* = 3.4 x 10^{-28} m^3 and B_1 = 1650 MNm^{-2}. Using the experimental value of β_0 and the assumed strain rate of 2.56 x 10^{-3} s^{-1} then β_1 in equation (5.65) is found as -7.23 x 10^{-4} K^{-1} which is very close to β_1 = -7.9 x 10^{-4} K^{-1} from reference 171.

The similarity of the constant implies that the exponential form of the temperature dependence of yield stress may be represented as a cubic polynomial and for the results of reference 171 the model curve as given by the polynomial predicts more closely the experimental results than the original empirical equation of reference 171. The values of the constants of the model are similar to those predicted by the thermal activation theory of Conrad.

The regression analysis results show that $\sigma(T)$ may be any best fit function and that with sufficient data the coefficients of $\sigma(T)$ will agree with theoretically predicted values. The type of function used will depend on the temperature range of the testing. Furthermore, the developed model need not show explicitly the controlling mechanism of the yield point.

Table 5.10
Results of Multiple-Linear Regression Analysis on Yield Stress Results of Reference 171.

Model	Cubic Polynomial	1/T
Equation No.	5.66	5.67
Figure No.	5.21	-
r	0.9916	0.9916
$s(\hat{y})$	34.44	32.80
D.F.	19	21
F-value	278	614
Significance of Equation	>99.9%	>99.9%
Coefficients		
A_1	1695.4	-59.36
A_2	-17.21	60113
A_3	6.83×10^{-2}	-
A_4	-9.36×10^{-5}	-
k_y	18.81	18.97
Significance of Coefficients		
A_1	>99.9%	98%
A_2	>99.9%	>99.9%
A_3	>99.9%	-
A_4	99.5%	-
k_y	>99.9%	>99.9%
$\bar{y}$	635.1	635.1
95% C.L. of $\bar{y}$	±14.7	±13.9

1. Equation (5.66) is

$$\sigma_{ys} = A_1 + A_2T + A_3T^2 + A_4T^3 + k_yd^{-1/2},$$

where σ_{ys} is the yield stress (MPa), T is the temperature (K) and $d^{-1/2}$ is the grain size ($mm^{-1/2}$). $A_1 - A_4$ and k_y are constants.

2. Equation (5.67) is

$$\sigma_{ys} = A_1 + A_2/T + k_yd^{-1/2},$$

where σ_{ys}, T and $d^{-1/2}$ are as above.

3. For the definition of statistical constants see Appendix B.

5.6 *Summary*

In this chapter a number of yield point models have been examined and it may be concluded that a discontinuous yield point will occur in steel or other BCC metals if,

(i) the initial number of mobile dislocations is low, and either,

(ii) the internal stress opposing dislocation motion is sensitive to dislocation velocity, or

(iii) the grain boundaries are effective barriers to mobile dislocations.

Previous work has also shown that;

(iv) The grain boundary barrier theory gives yield stress as $\sigma_{ys} = \sigma_i + k_y d^{-1/2}$ (Equation (5.4)), known as the Hall-Petch equation. This theory does not allow for dislocation velocity effects.

(v) The Cottrell-Bilby theory of yield by the break-away of dislocations from their pinning atmosphere applies only to lightly pinned material produced by rapid cooling rates.

(vi) The unpinning constant k_y has a range of about 14-24 $MNm^{-2}mm^{1/2}$ for steel and is independent of temperature.

(vii) The Hahn dislocation multiplication theory (equation (5.16)) does not include grain size effects which is an important omission at room temperature where the grain size effect is dominant.

(viii) The yield stress may be written as the sum of an athermal stress component, a temperature-dependent stress component and a grain-size dependent stress component (equation (5.17)).

(ix) The temperature-dependent stress component is dependent on the Peierls-Nabarro stress as given by the thermal activation theory of yielding of Conrad, although it was shown interstitial impurities have an important effect as well.

(x) Empirically the temperature-dependent stress component may be represented as $\sigma_i^* = A\exp(-\alpha T)$ (equation (5.40)).

From experimental work and analysis it was found that;

(xi) Experimental tensile testing and a multiple-linear regression analysis gave the yield stress as $\sigma_{ys} = A_1 + A_2T + A_3T^2 + A_4T^3 + k_y d^{-1/2}$ (equation (5.58)) where A_1, A_2, A_3, A_4 and k_y are constants. The temperature dependent part of the model, $\sigma(T) = A_1 + A_2T + A_3T^2 + A_4T^3$, is a truncated power series expansion of equation (5.40) and the coefficients A_1, A_2, A_3 and A_4 gives values of A and α in equation (5.40) in agreement with those predicted by thermal activation theory and those values found by other workers.

(xii) The model (equation (5.58)) was applied to another worker's experimental results and it successfully modelled the temperature and grain size dependence of yield stress whereas the original empirical equation did not.

Finally, the equations (5.59) and (5.61) may be used to calculate the yield stress of the steels used in CTOD testing.

CHAPTER 6

Fracture Toughness Testing

6.1 *Experimental Procedure*

This chapter presents the experimental procedure, results and discussion of results for fracture toughness testing of the two experimental steels, L & H. The chemical composition of the steels is given in Table 4.1 and the heat treatment and resulting grain sizes are given in Tables 4.2 and 4.3 respectively. The experimental techniques used for fracture toughness testing were:

(i) The plane strain fracture toughness test using standards ASTM E399-83 and BS5447:1977 [23,24].

(ii) The crack-tip opening displacement (CTOD) test for determining the temperature dependence of fracture toughness using standard BS5762:1979 and with reference to standard ASTM E1290-89 when it became available [41,44].

(iii) Optical and scanning electron microscope examination of the fracture surface of broken fracture toughness specimens.

Fracture toughness testing was performed to both plane-strain fracture toughness and crack-tip opening displacement test standards so toughness results using these methods could be compared and since the CTOD test can give valid K_{IC} results. The fracture mode transition temperature was estimated from the determined temperature dependence of fracture toughness for each set of specimens and then the grain size dependence of the transition temperature was found.

6.1.1 SPECIMEN PREPARATION

The compact tension (CT) specimen was used in the investigation to maintain continuity with a previous investigation [16]. Harrison, on discussion on the types of specimens used in CTOD testing, says that there is no reason why the CT specimen can't be used since similar results to those for SENB specimens are achieved [149]. However the large amount of machining required to produce a CT specimen could be a deterrent. The specimen dimensions are given with respect to the specimen width (W) as shown in Figure 6.1. The specimen width (W) for the CT specimen is the distance

between the load-line and the back face of the specimen. The specimen thickness (B) is half of the specimen width. The specimen thickness selected was 15 mm since Chew found that equation (2.111)

$$B \geq 25\delta_c$$

gave thickness independent toughness results for upper-shelf CTOD values of Grade 275 Steel (Steel L) when B = 11.25 mm [16]. At initiation of stable crack extension the minimum thickness value for thickness independent values was given by Chew as B = 7 mm. B = 15 mm was also the maximum thickness able to be machined from the hot-rolled and heat-treated bar for Steel L.

The crack-plane orientation in relation to the rolling direction of the raw stock is shown in Figure 6.2 and specimen specifications are given in Table 6.1. The crack-plane orientation of L-T means the direction of crack propagation is normal to the rolling direction.

Table 6.1
Fracture Toughness Specimens

Material	Specimen Type[1]	Thickness (mm)	Crack Plane Orientation[2]
L	CT	15	L-T
H	CT	15	L-T

1. See Figures 6.1 and 6.3
2. See Figure 6.2

To help nucleate the fatigue crack a chevron notch was used, shown in Figure 6.3. The fatigue pre-cracking was conducted on an Amsler High Frequency Vibrophore (Figure 6.4) and the progress of crack propagation visible on the specimen faces was monitored using an optical microscope and pencil lines marked on the specimen face at minimum and maximum permissible crack lengths (Figures 6.5 and 6.6).

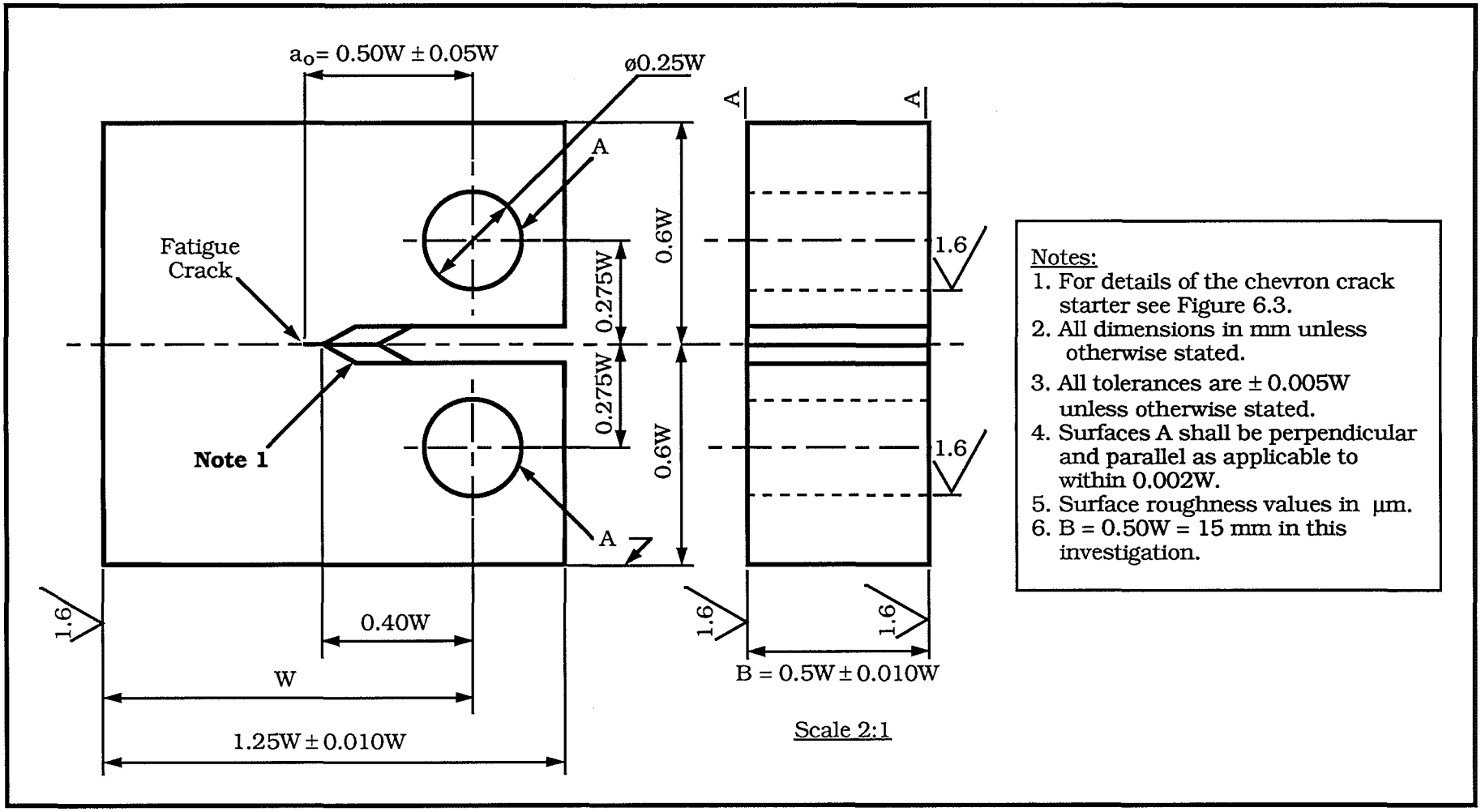

Figure 6.1 : The Compact Tension (CT) Specimen[23,24,44].

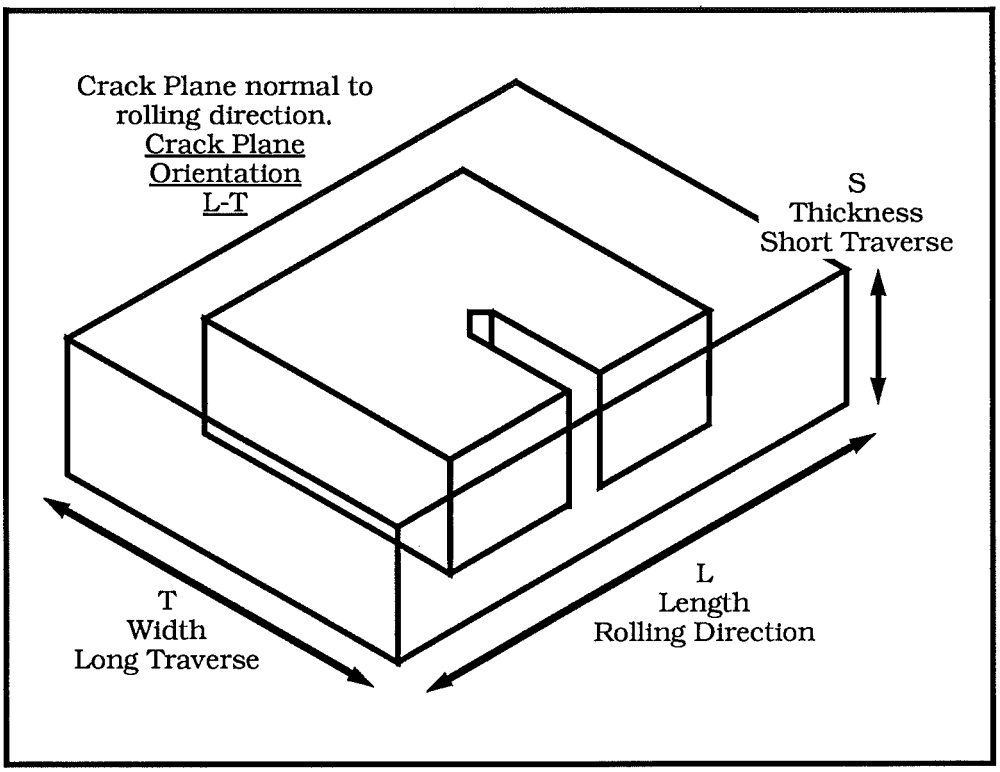

Figure 6.2 : The orientation of the crack plane of the compact tension toughness specimens relative to the rolling direction.

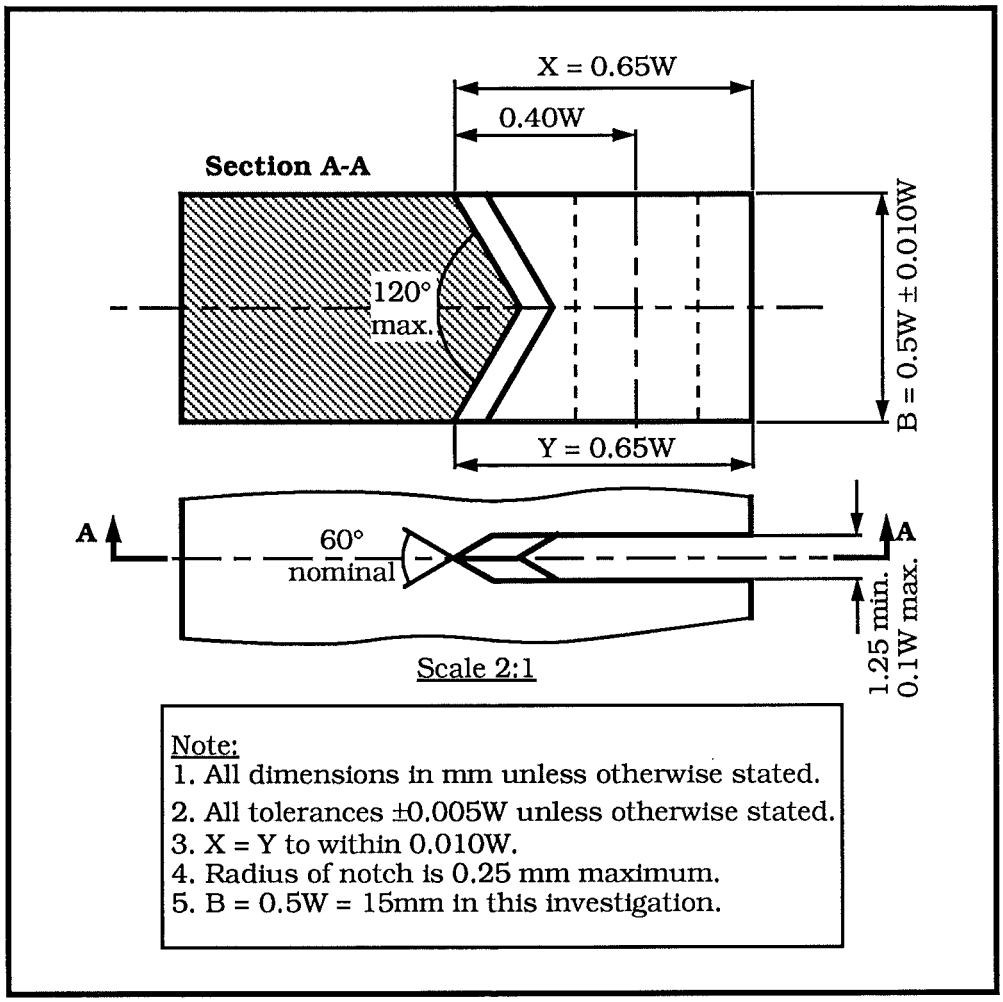

Figure 6.3 : The Chevron Notch fatigue crack starter[23,24,44].

Figure 6.4 : Fatigue cracking a CT specimen on the Amsler Vibrophore.

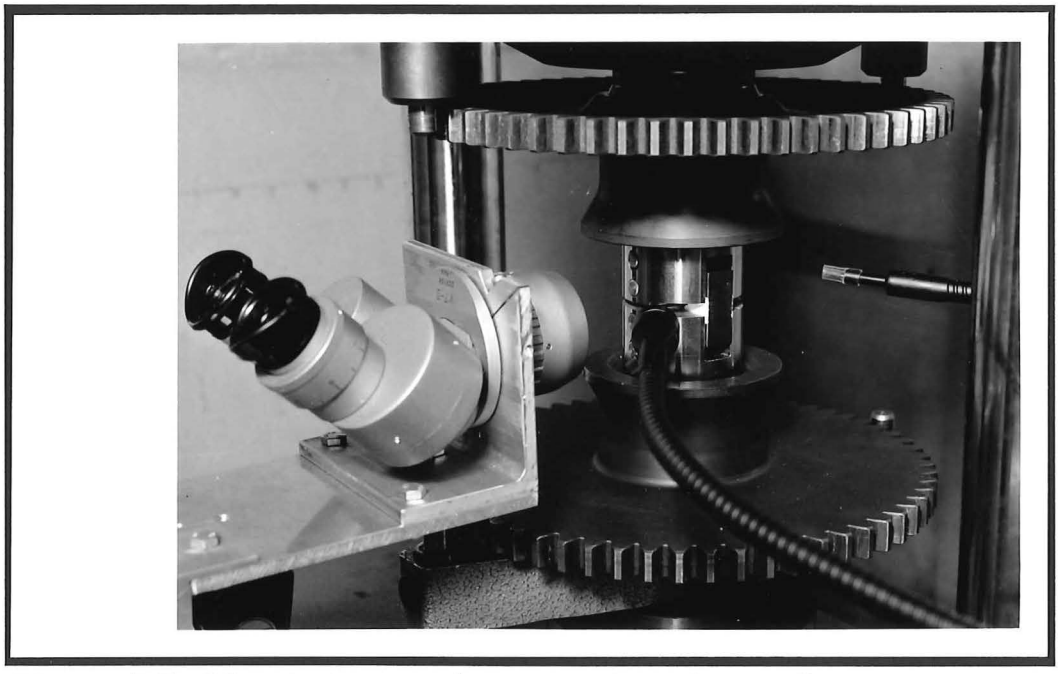

Figure 6.5 : Monitoring crack propagation during fatigue cracking using an optical microscope.

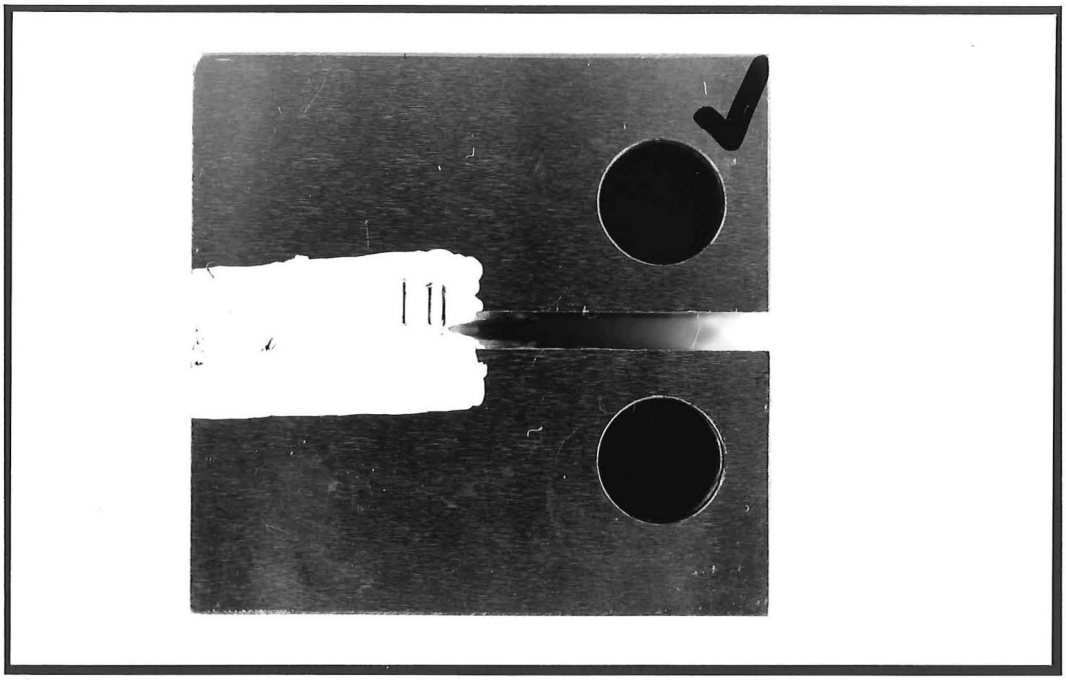

Figure 6.6 : A CT toughness specimen marked prior to fatigue cracking. 10 mm

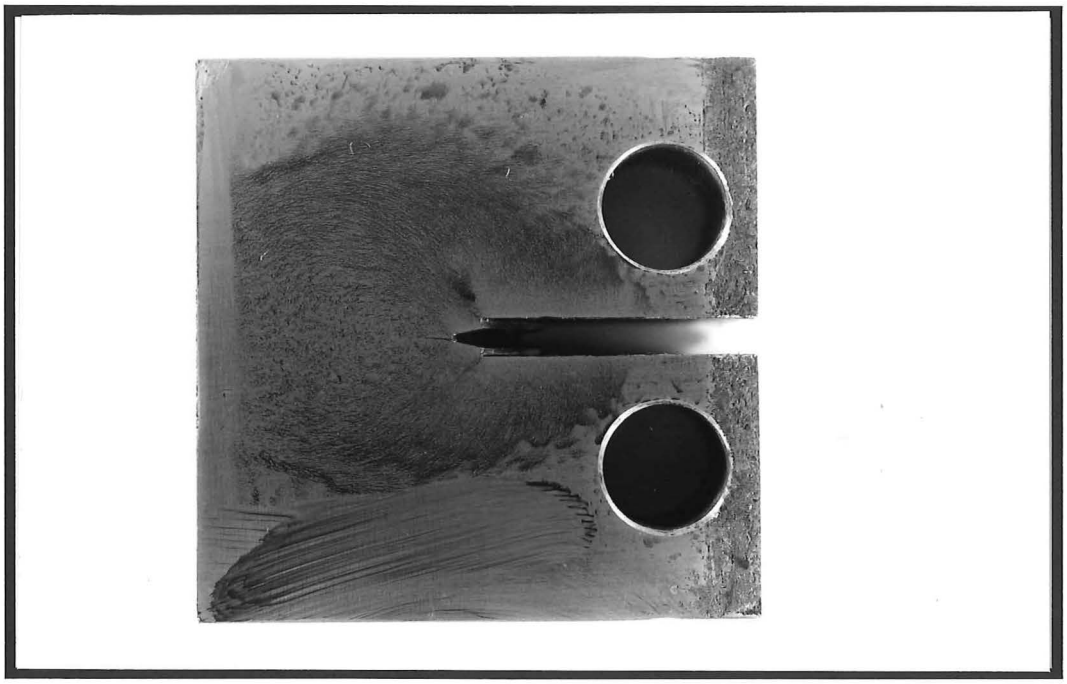

Figure 6.7 : A CT specimen after fatigue cracking showing a crack from the root of the notch. 10 mm

The maximum load of the alternating stress was kept low so that the maximum stress intensity (K_f) during the final 2.5% extension of the crack length by fatigue cracking would meet the requirement

$$K_f \leq 0.6 \left(\frac{\sigma_{y1}}{\sigma_{y2}}\right) K_Q \qquad (6.1)$$

where K_Q is the calculated apparent fracture toughness of the specimen in $MNm^{-3/2}$ after testing, σ_{y1} is the yield stress of the material at the temperature of fatigue cracking and σ_{y2} is the yield stress of the material at the temperature of fracture toughness testing [23,24,41]. ASTM E1290-89 recommends that the maximum load during fatigue cracking for the CT specimen is,

$$P_f = 0.4\, Bb_o\sigma_f/(2W-a_o) \qquad (6.2)$$

where $b_o = (W-a_o)$, a_o is the length of the original fatigue crack and B is the specimen thickness and σ_f is the average of the material's yield stress σ_{ys} and ultimate tensile stress σ_{uts} [44]. This is the same load level recommended for fatigue cracking in ASTM E813-87 for J_{IC} testing [39]. A summary of the fatigue cracking history is given in Table 6.2 and the fatigue cracking history of all specimens is given in Appendix C.

Table 6.2
The Fatigue Cracking History of CT Specimens

Material	Initial Maximum Load Amplitude (kN)	Final Maximum Load Amplitude (kN)	Approximate Number of Stress Cycles(10^3)
LA	4.3	3.1	220-633
LB	4.3	3.1	241-502
LC	4.3	3.1	266-454
LD	4.5	3.1	285-425
HA	3.9	2.7	202-487
HB	3.9	2.7	281-393
HC	3.9	2.7	330-489
HD	3.9	2.7	371-412
LZ	4.5-5.9	3.1-3.9	344-722
HZ	5.5	3.8-3.9	276-523

The length of fatigue crack was monitored to ensure that the ratio of crack length/specimen width (a_0/W) was 0.50 ± 0.05. After testing the specimens measurement of the crack length showed that a_0/W was met adequately. To ensure all specimens were cracked a non-destructive test using dye-penetrant was carried out on each specimen. An example of such a crack is shown in Figure 6.7.

After fatigue cracking specimens were given an ageing heat treatment of 100°C for 3 hours in an air circulating oven. The time for ageing heat-treatments at a particular temperature is given using Hundy's equation for strain-ageing

$$\log_{10}\left(\frac{t_r}{t}\right) = 4400\left(\frac{1}{T_r} - \frac{1}{T}\right) - \log_{10}\left(\frac{T}{T_r}\right) \qquad (6.3)$$

where t_r is the ageing time at ambient temperature T_r (K) and t is the ageing time at the elevated ageing temperature T(K) [265,297]. This heat treatment was done since it was not possible to test the specimens immediately after fatigue cracking and a previous investigation had found that strain-ageing in the plastic zone around the crack tip raised the FMTT as given by the CTOD test [16]. Figure 6.8a shows the results from the thesis of Chew for a Grade 275 steel with 0.0049 wt % active nitrogen content [16]. After the ageing treatment the FMTT has increased by about 6.5°C. When no active nitrogen is present there is no noticeable increase in FMTT after the ageing treatment. This is shown in Figure 6.8b where the results are for a Grade 275 steel with 0.0003 wt % active nitrogen content after a titanium alloy addition. Therefore it is known that the FMTT will increase slightly due to strain ageing of the fatigue damaged zone ahead of the crack tip if the steel has a high active nitrogen content.

6.1.2 TENSION TESTING

The CTOD tests were conducted in a similar manner to the tensile tests to find the temperature dependence of the lower yield stress. The tests were performed over the temperature range from -196 to +65°C on an Instron Universal Testing Machine. Except for tests at ambient temperature the specimen was tested by immersing the specimen and grips in liquid at the test temperature. Tests were performed in the Amsler Environmental Test Chamber (Model No. TV742) shown in Figure 6.9, the operation of the chamber being covered in Section 5.4.2. Table 5.2 contains a list of the different

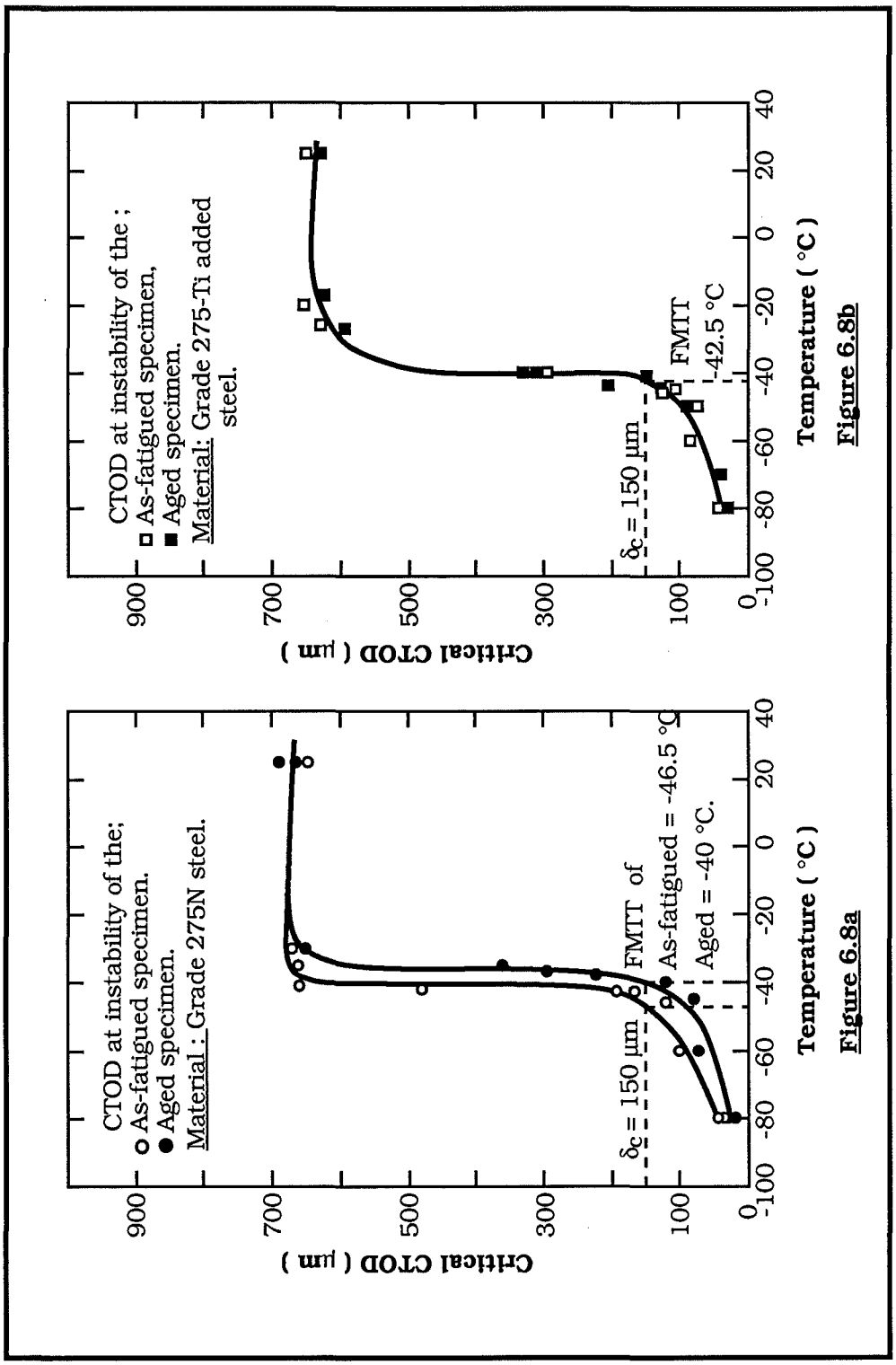

Figure 6.8(a) : The temperature dependence of critical CTOD of normal grade 275 steel; showing the effect of strain-ageing.

Figure 6.8(b) : The temperature dependence of critical CTOD of Ti-alloyed grade 275 steel; showing the effect of strain-ageing [16].

coolants and refrigerants used and the temperature range over which they are used. Temperature control of the chamber was ±2°C. The temperature of the specimen was monitored using a NiCr–Ni thermocouple attached to the crack-tip region of the specimen. Before commencing a test the specimen and grips were immersed in the liquid at test temperature for a minimum of 15 minutes to ensure temperature homogeneity. The tests were performed at a crosshead speed of 0.5 mm min^{-1} to give an approximate loading rate of 0.5 to 0.6 MPa $m^{1/2}$ s^{-1}.

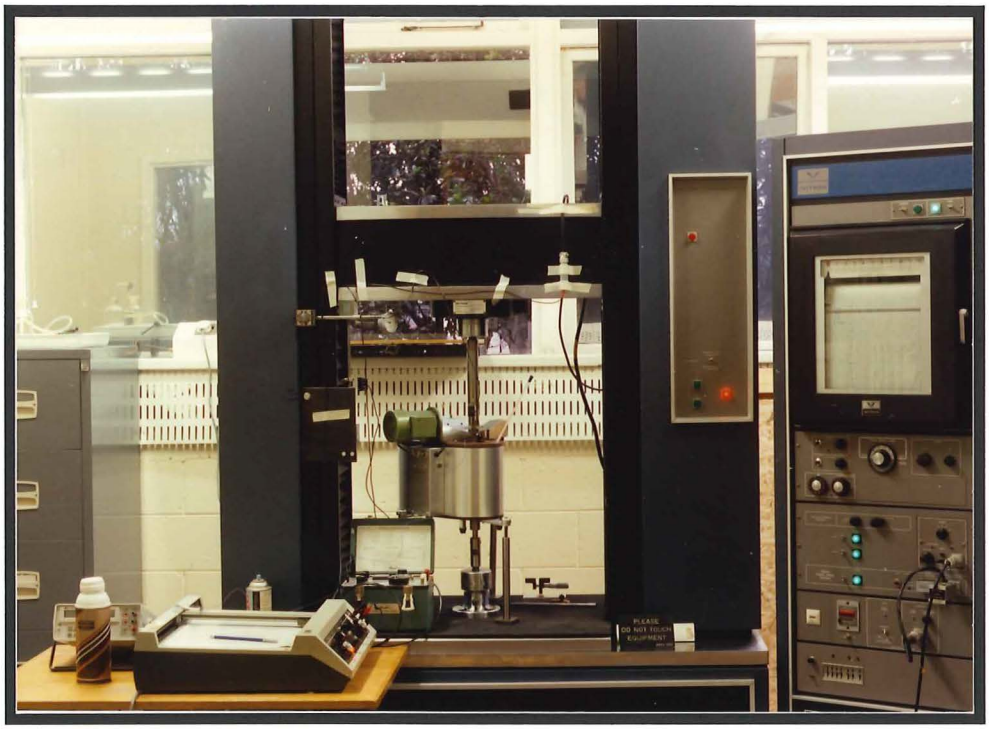

Figure 6.9 : The experimental set-up showing the Instron testing machine and the environmental chamber.

6.1.3 MEASUREMENT OF CRACK-TIP OPENING DISPLACEMENT

The crack-tip opening displacement was measured indirectly with an Instron A384-1B clip gauge extensometer. It was not possible to attach the clip gauge across knife edges mounted directly on the specimen in elevated or sub-ambient temperature tests. Therefore the clip gauge was mounted on knife edges attached to two Nilo low expansion extension arms, as Chew used, raising the clip gauge out of the test chamber [16]. The system is shown schematically in Figure 6.10. The correlation between CTOD and clip gauge displacement V_g was found using a silicone rubber crack-tip replication technique [16,29,148,272,273]. The determination of

this correlation is given in Section 6.2. The recording system is shown in Figure 6.11.

The extensometers were calibrated against the displacement recorder-pen of the Instron testing machine prior to every test or daily when more than one test was performed per day.

The typical CTOD test record was in the form of autographic plots of applied load (P) versus crosshead displacement (V_{CH}) and clip gauge displacement (V_g) versus time. By measuring the time to complete the test then applied load (P) versus clip gauge displacement (V_g) records were formed. A typical test record is shown in Figure 6.12.

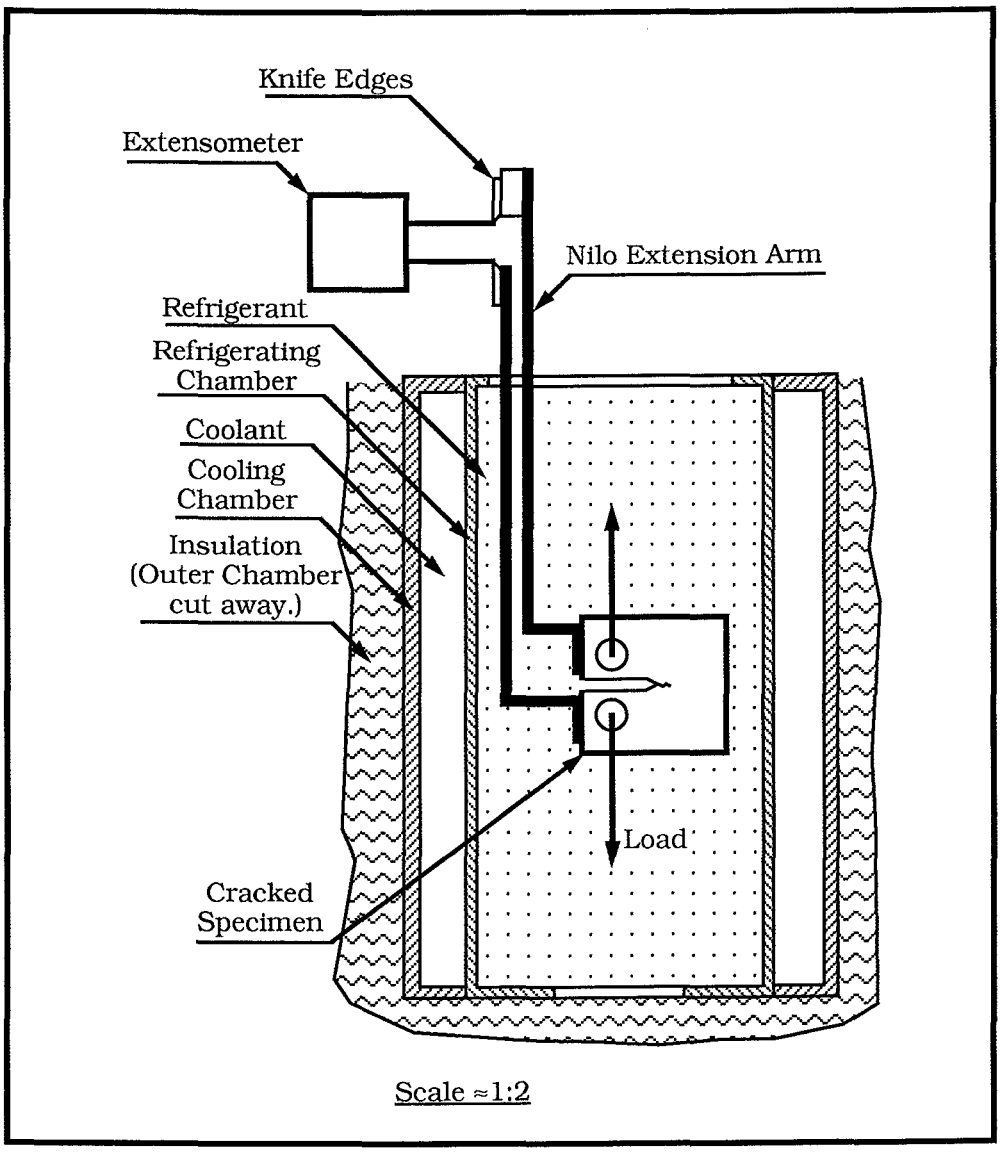

Figure 6.10 : Schematic of the clip gauge extensometer mounted on Nilo extension arms on specimen.

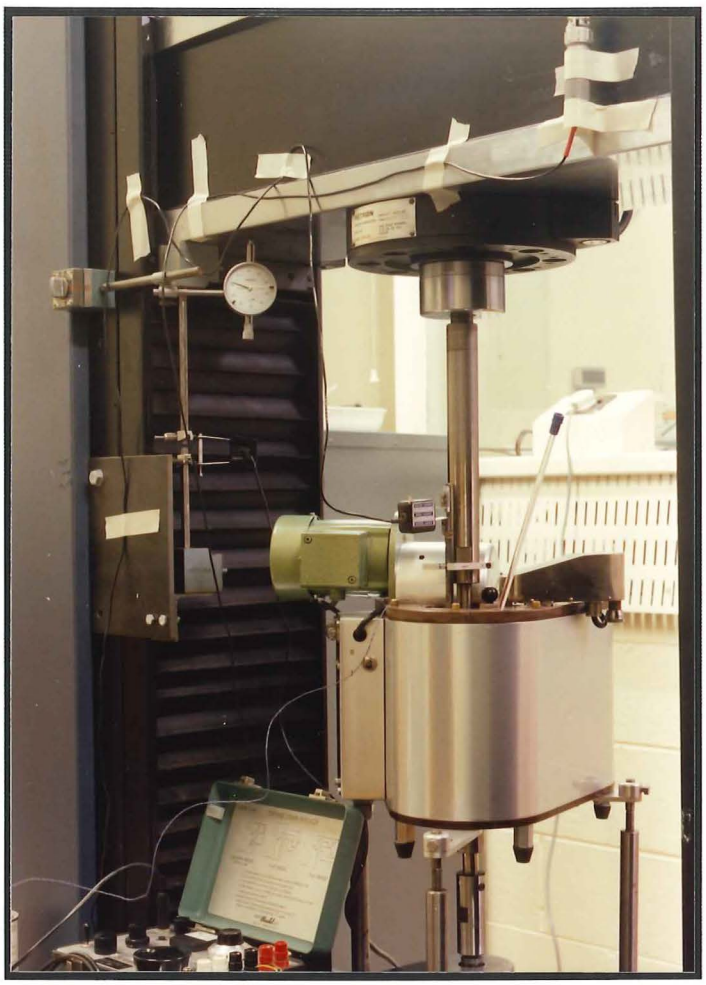

Figure 6.11 : The mounting of the clip gauge extensometer and the crosshead displacement extensometer.

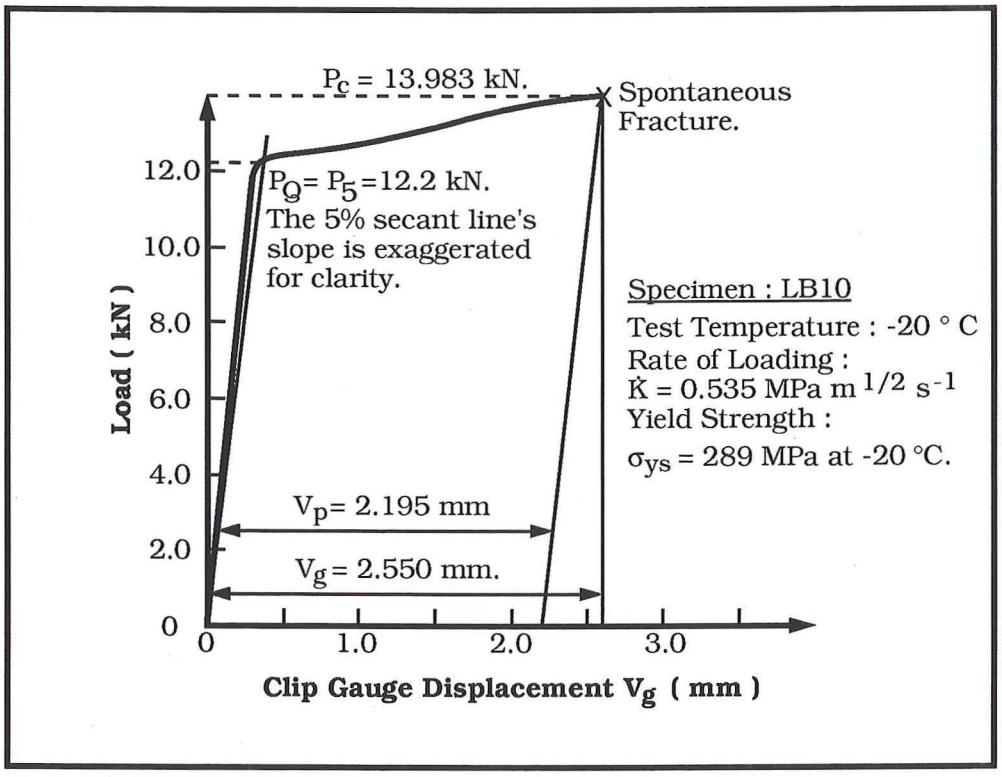

Figure 6.12 : A typical load-clip gauge displacement test record.

After completing the test the specimen fracture surface was examined under an optical microscope and the crack length to the tip of the original fatigue crack was measured at 0%, 25%, 50%, 75% and 100% of B, the specimen thickness. The average of 25%, 50% and 75% B were taken as the final crack length a_o. The method of analysis of test records is given in Section 6.3.

6.2 Correlation between CTOD and Clip-Gauge Displacement

It was decided to use a silicone rubber crack-tip replication technique to give a correlation between CTOD and Clip-gauge displacement V_g. The reasons for this were:

(i) The uncertainty in mounting the clip gauge on the Nilo extension arm system, especially as the equation

$$\delta = \delta_e + \delta_p = \frac{K^2(1-\nu^2)}{2\sigma_{ys}E} + \frac{r_p V_p (W-a_o)}{r_p(W-a_o) + a_o + z} \qquad (2.99)$$

might be affected by the large "z" value in the system used, i.e. the magnitude of rotation will be greater if z is large.

(ii) Figure 6.13 shows the results of a similar calibration from Chew for B = 10, 20 and 30 mm [16]. With B = 15 mm in the present investigation a comparison between the two correlations in the two investigations could be made, to see if the line for B = 15 mm lies between the correlation lines for B = 10 mm and B = 20 mm.

(iii) If equation (2.99) is used there is uncertainty in the value of the rotation factor r_p and at the beginning of experimental work values of r_p were not available for the CT specimen. BS5762:1979 uses $r_p = 0.4$ for the SENB specimen but discussion in Section 2.2.4 shows r_p may vary significantly depending on the amount of plastic deformation at the crack tip and the variation in the Ramberg-Osgood strain-hardening index N. During the course of the present investigation ASTM E1290-89 on CTOD testing was published and it recommended values of

$r_p = 0.47$ for $a_o/W < 0.50$

and $r_p = 0.46$ for $a_o/W \geq 0.50$ [44].

Therefore, a comparison can be made between the correlation found by this study and CTOD values found using equation (2.99) and the r_p values recommended by ASTM E1290-89.

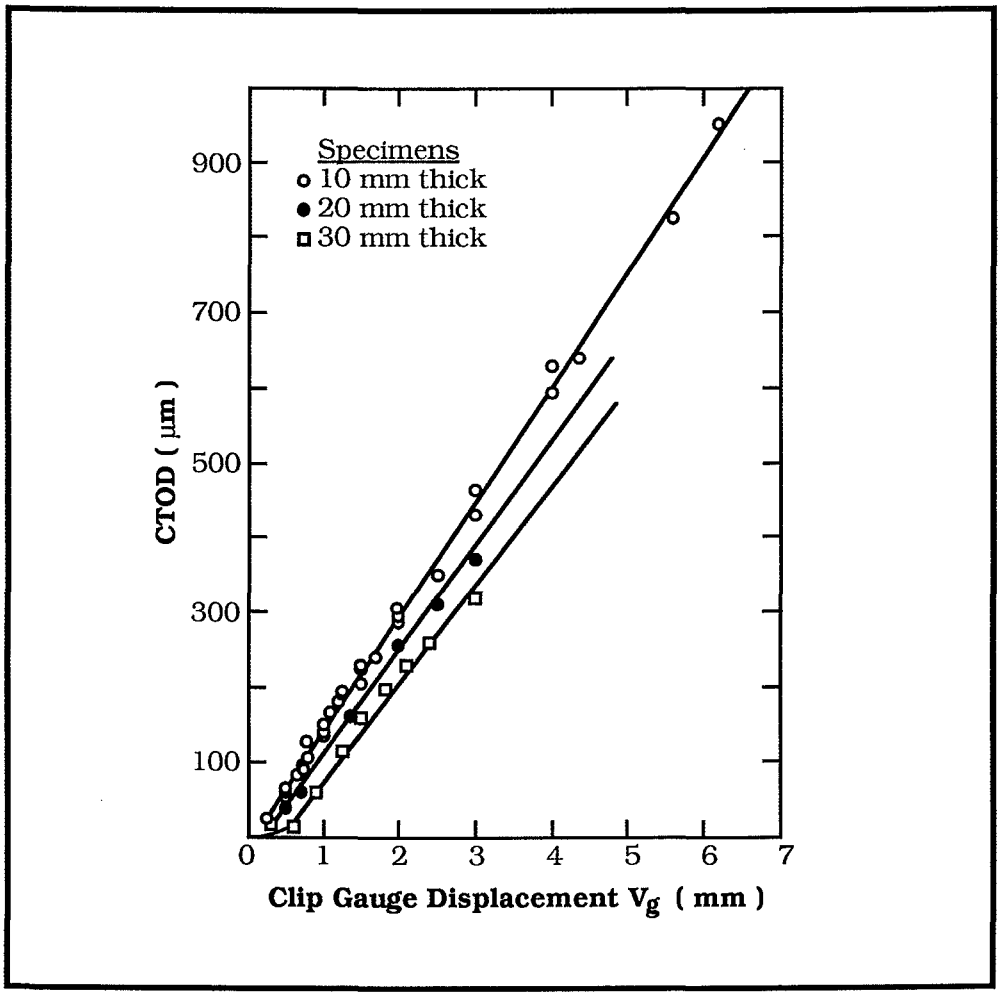

Figure 6.13 : Calibration of CTOD as a function of clip gauge displacement for CT pre-cracked specimens [16].

6.2.1 EXPERIMENTAL PROCEDURE

There are a number of investigations which have used silicone rubber to produce a replica of the crack-tip profile [16,29,148,272-274]. The technique involves loading the specimen to a pre-determined clip gauge displacement and then producing the crack-tip replica with the silicone hardening rubber. The experimental procedure is summarised below:

(a) *Preparation of Specimens:* For the CTOD-V_g correlation a total of 30 CT specimens were used. To cover the range of experimental grain size Steel L specimens were machined from bar heat-treated to Heat Treatment A, and were designated LZ. Steel H

specimens were machined from bar heat-treated to Heat Treatment D, designated as HZ. Also the toughness specimens tested at ambient temperature from LA to HD were used for the correlation. Details of the specimen and material properties are given in Table 6.3. Specimens were fatigue cracked (summarised in Table 6.2) and then the ageing heat treatment at 100°C for 3 hours was carried out.

Table 6.3
Properties of Specimens used in CTOD-V_g correlation

Steel	LZ	HZ
Specimen Type	CT	CT
Crack Plane Orientation	L-T	L-T
Nominal Thickness	15	15
Lower Yield Stress, 20°C (MPa)	330	205
T_{27} (°C)	-48	+47
Grain Size, $d^{-1/2}$ ($mm^{-1/2}$)	9.939	4.187

(b) *Tension Testing:* The specimens were tested at 0.5 mm min^{-1} constant crosshead displacement on the Instron Universal Testing Machine at ambient temperature. The experimental set-up is shown in Figure 6.14. The specimen was loaded to either a pre-determined clip gauge displacement or crosshead displacement. The time to reach the displacement was recorded. The test was halted and the rubber was injected in to the crack and left to cure. During the time of curing the load relaxed by about 5% but from previous work this is not expected to affect the replica results [16,273]. The silicone rubber used was Kerr's Light Bodied Permlastic Elastic Impression Material Type III (Polysulphide Base, Low Viscosity). Once the rubber had cured the test was continued until the specimen was broken. The replica was peeled off the half of the specimen on which it remained and sectioned along its mid-section. Figure 6.15 shows the replicas before sectioning.

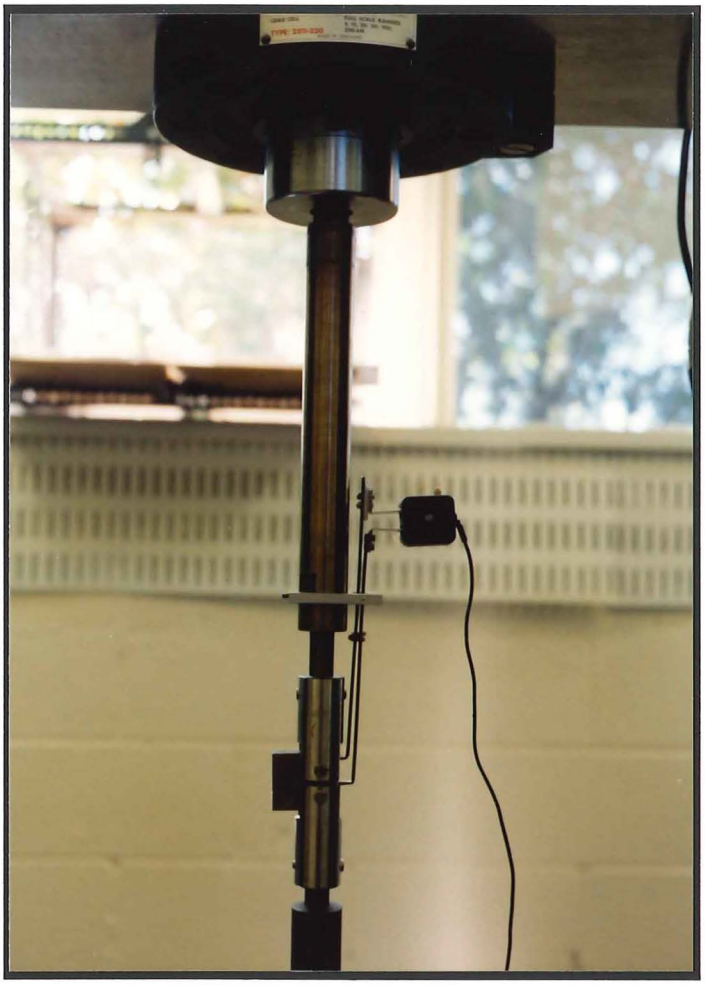

Figure 6.14 : The measurement of clip gauge displacement (V_g) for the CTOD-V_g correlation.

Figure 6.15 : Silicone-rubber replicas of cracks prior to sectioning.

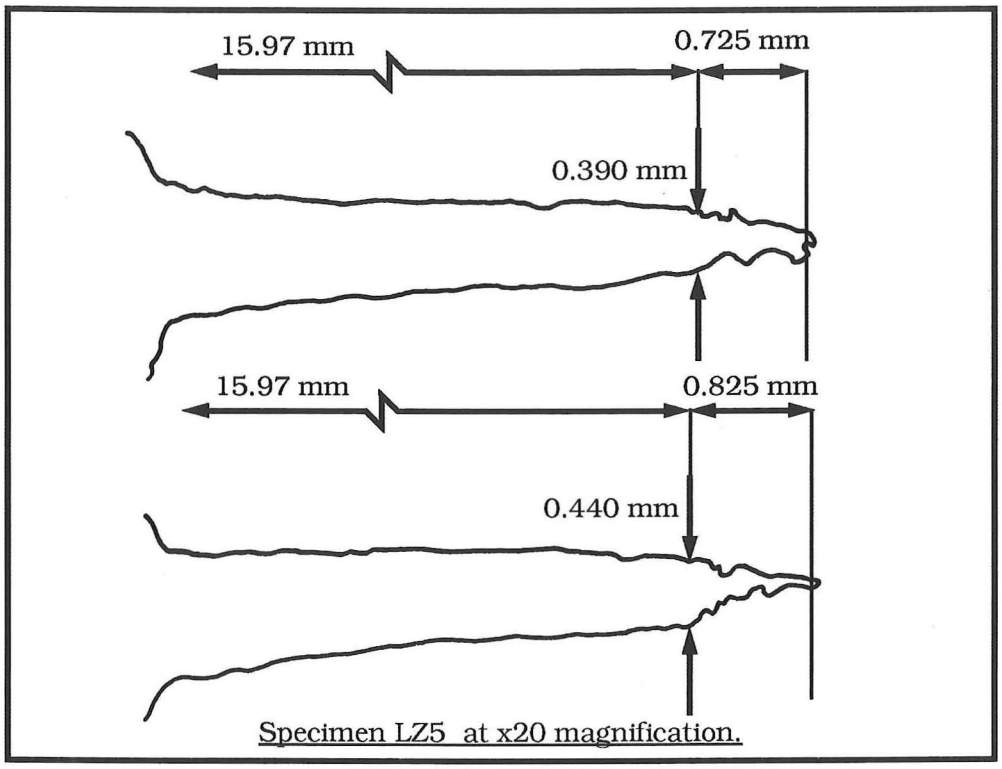

Figure 6.16 : An example of a shadowgraph tracing of a crack-tip replica (x20).

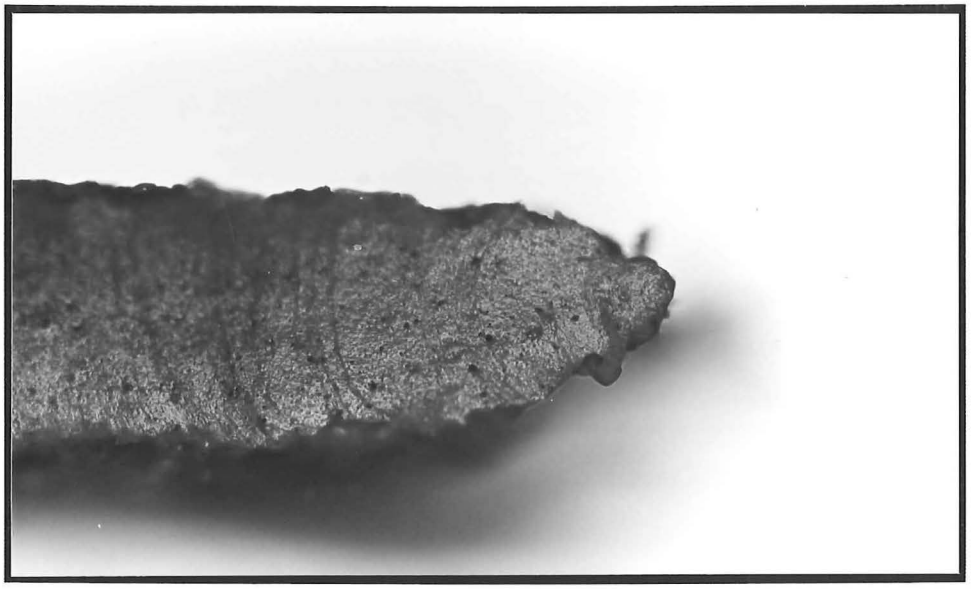

Figure 6.17 : A sectioned silicone-rubber crack replica (x120).

0.1 mm

(c) *Measuring the CTOD:* The records obtained were applied load (P) versus crosshead displacement (V_{CH}) and clip gauge displacement (V_g) versus time, and the time of the test. From these V_g against V_{CH} plots and applied load (P) against V_g plots could be formed.

The CTOD was measured at the position of the original fatigue crack tip as recommended by Dawes and used by Davies [37,273]. A tracing of each half of the replica was made on a shadowgraph (Nikon Model 6C) at x20 magnification. An example of a tracing is shown in Figure 6.16. The CTOD and ductile crack extension could be measured from the tracing. The position of the original crack tip could be determined by measuring the distance between the fatigue crack-tip and a reference point, usually the tip of chevron crack starter vee, on the fracture surface of the broken specimen.

Photomicrographs were taken of the replicas. By photographing a scale at the same magnification the CTOD could be measured from the photomicrograph, an example of this is shown in Figure 6.17. Using a filar eyepiece on the microscope the ductile crack extension was measured as well. The results were tabulated and an average CTOD was calculated for each clip gauge and crosshead displacement.

The crack length to the tip of the original fatigue crack was measured using the optical microscope and the filar eyepiece at 0, 25, 50, 75 and 100% of the thickness B. The average crack length was calculated as the average of the readings at 25, 50 and 75% B.

Since measurements of the replica were made within 24 hours of the cast being taken shrinkage of the replica is considered negligible since Robinson and Tetelman in their experimental investigation found the rubber shrank only 0.5 percent after 250 hours [29].

6.2.2 RESULTS OF CTOD FROM SILICONE RUBBER REPLICAS

For clip gauge displacement greater than 1.5 mm a graph of V_g versus V_{CH} was plotted from V_g versus time records and the time of the test for a constant crosshead speed of 0.5 mm min^{-1}. A typical example of V_g versus V_{CH} is shown in Figure 6.18. After plastic deformation has occurred V_g is directly proportional to time which suggests it is directly proportional to V_{CH} as well. This is similar to the method used by Chew [16]. The results for V_g, V_{CH} and CTOD are

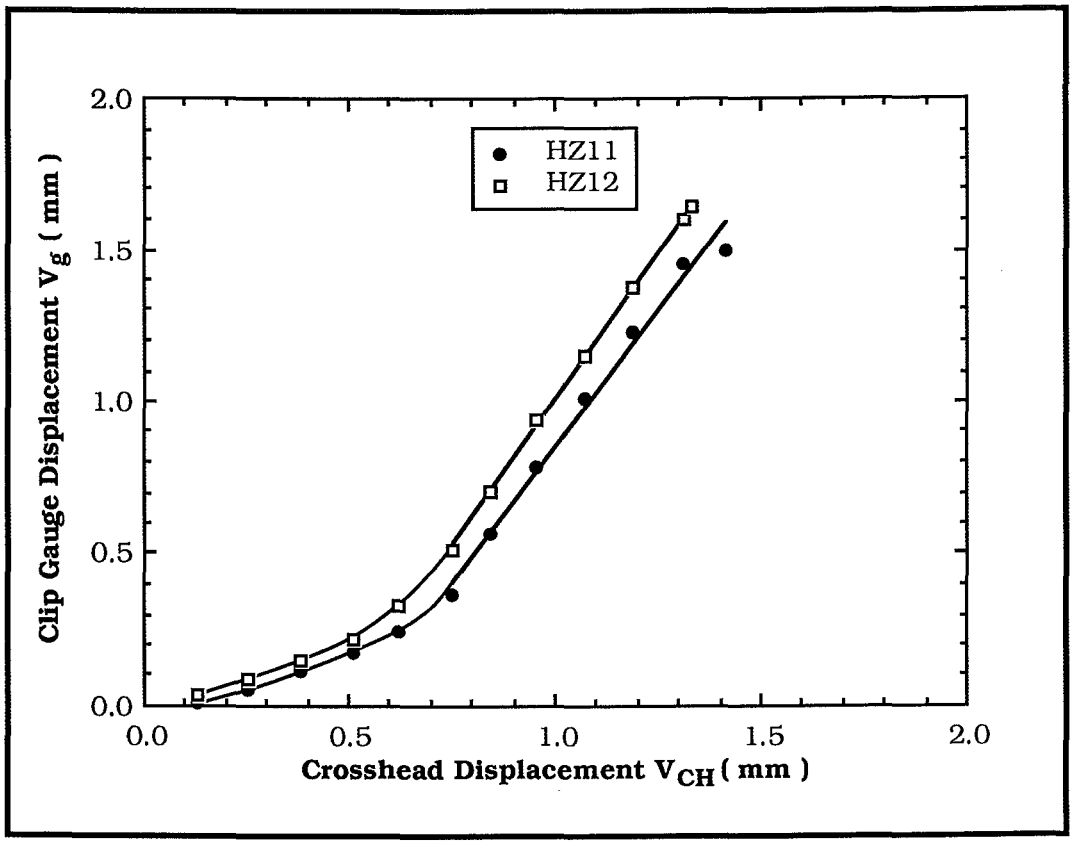

Figure 6.18 : Typical record of clip gauge displacement V_g (mm) as a function of crosshead displacement V_{CH} (mm).

given in Table E.1 and are shown in Figure 6.19 (a-b). The fatigue history of the specimens is given in Appendix C and critical CTOD results are given in Appendix D.

6.2.3 CORRELATION OF CTOD AGAINST V_g AND V_{CH}

Examination of Figure 6.19(a-b) suggests that;

(i) The correlation for both V_g and V_{CH} will be linear and

(ii) The correlation is different for the two steels LZ and HZ.

(iii) The position of the rotation point initially varies as the specimen is loaded, before becoming constant as yielding occurs around the crack tip. This was shown by Robinson and Tetelman and by Chew *inter alia* [16,29]. Robinson and Tetelman gave the variation in the rotation factor as,

$$r_p = A_0 + A_1COD + A_2COD^2 + A_3COD^3 \qquad (6.4)$$

where A_0, A_1, A_2 and A_3 are constants [29]. The rotation factor varies from 0 when CTOD is zero to $r_p \approx 0.5$ at high values of CTOD.

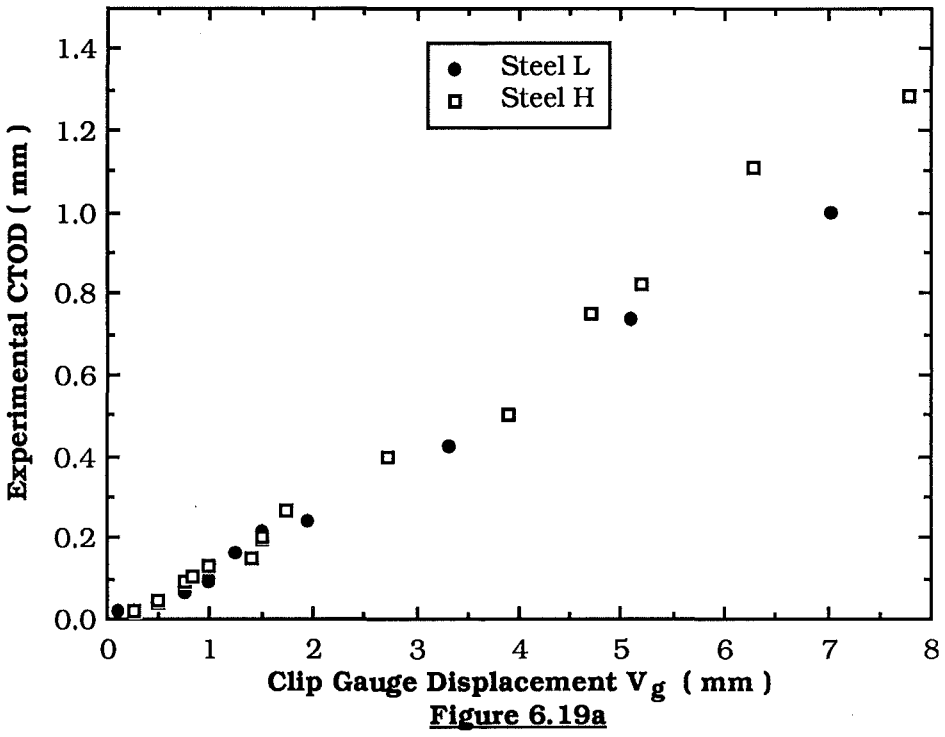

Figure 6.19a

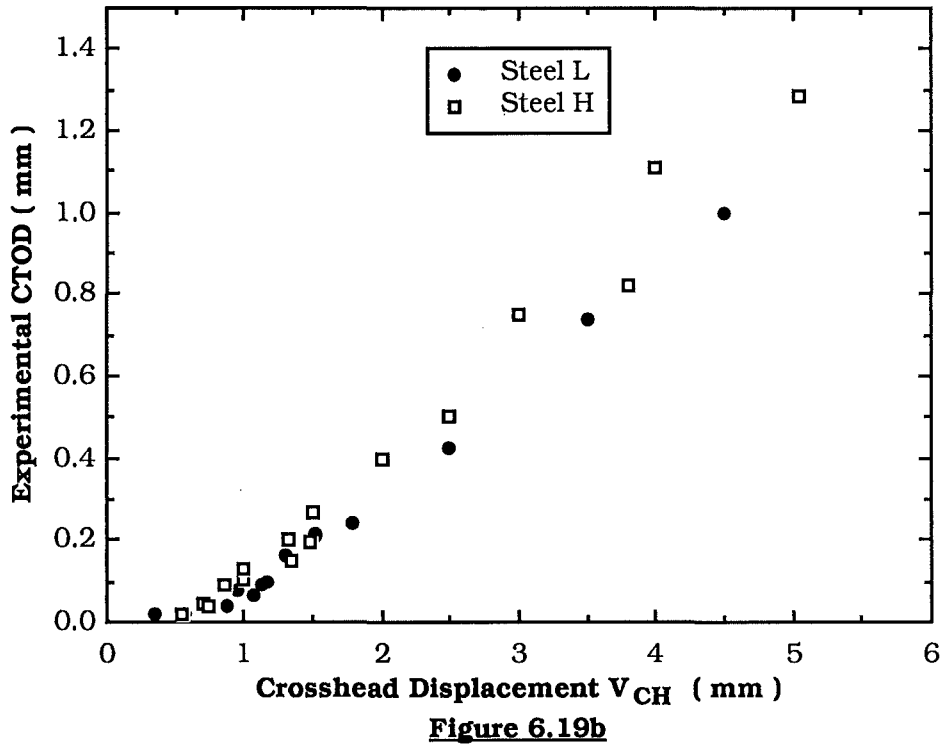

Figure 6.19b

Figure 6.19 : (a) Experimental CTOD (mm) as a function of clip gauge displacement V_g (mm) for CTOD correlation. (b) Experimental CTOD (mm) as a function of crosshead displacement V_{CH}(mm) for CTOD correlation.

Figure 6.12 indicates that before general yielding occurs the clip gauge displacement is directly proportional to the load and therefore to the stress intensity factor,

$$V_g = \alpha K \tag{6.5}$$

where α is constant [29]. From equation (2.61)

$$G = K^2(1-\nu^2)/E$$

for plane strain and equation (2.90)

$$G = \sigma_{ys}\delta$$

then for small scale yielding

$$\delta = \frac{K^2(1 - \nu^2)}{\sigma_{ys}E} \tag{6.6}$$

where σ_{ys} is the yield strength of the material. Substituting equation (6.5) into equation (6.6) gives,

$$\delta = \frac{V_g^2(1 - \nu^2)}{\alpha^2\sigma_{ys}E} \tag{6.7}$$

Therefore for small scale yielding CTOD is dependent on the square of clip gauge displacement and also the yield stress of the material.

However at large CTOD values when r_p is constant the dependence of CTOD on V_g will change. From equation (2.99 a-c)

$$\delta_t = \frac{K^2(1-\nu^2)}{2\sigma_{ys}E} + \frac{V_p r_p b_o}{(r_p b_o + a_o + z)}$$

the CTOD still has a slight dependence on V_g^2 and σ_{ys} but will be dominated by the plastic term of the equation, $V_p r_p b_o/(r_p b_o + a_o + z)$. When the CTOD is large then r_p is constant and CTOD is linearly dependent on the plastic component of clip gauge displacement V_p.

Taking these factors into account the CTOD-V_g and CTOD-V_{CH} correlations were initially modelled as,

$$\delta = A_0 + A_1X \tag{6.8}$$

and $$\delta = A_0 + A_1X + A_2X^2 \tag{6.9}$$

where A_0, A_1 and A_2 are constants and $X = V_g$ for clip gauge displacement and $X = V_{CH}$ for crosshead displacement.

These analyses used multiple-linear regression techniques using Lotus 123 and Basic MLR software on an IBM-compatible XT personal computer. The same assumptions applied in Section 5.5 on modelling the temperature and grain size dependence of yield stress are also applied here. Therefore the independent variable (V_g or V_{CH}) is assumed to be precisely known and all error is assumed to be with the imprecision of the dependent variable (the CTOD).

For each equation two analyses were performed, the first where the intercept A_0 was computed and the second where the intercept A_0 was set at zero. Intuitively, when the specimen is unloaded then V_g is zero and the CTOD is also zero. This is not obvious when V_{CH} is measured. Due to elastic loading of the grips and pins as the specimen is loaded then the crosshead displacement may be positive before any crack opening occurs; therefore the intercept need not pass through zero.

6.2.4 MODEL FOR CLIP GAUGE DISPLACEMENT, V_g

The model of CTOD against V_g was considered in several stages. The model was first formed considering the results for Steels L and H separately, then as a combined set of results, and finally as a combined set of results including a grain size dependence.

(a) Separate Models

Table 6.4(a-b) contains the regression results for the CTOD-V_g correlation for Steels L and H considered separately. The results show that all the equations based on equations (6.8) and (6.9) have a significance greater than 99.9% with F-values from 808 for equation (6.17) to 2444 for equation (6.10). The correlation coefficient is from 0.9911 for equation (6.15) to 0.9977 for equation (6.12) which means that the total variation in CTOD explained by the regression ranges from 98.2% for equation (6.15) to 99.54% for equation (6.12). The predicted results for equations (6.10) and (6.14) (the linear model with computed intercept) are plotted on Figure 6.20.

This also has the predicted curves from Chew plotted on it, for B = 10, 20 and 30 mm [16]. The predicted result for Steel L lies between the predicted lines for B = 10 mm and B = 20 mm. This would confirm Chew's calibration since specimen thickness was B = 15 mm. Chew's correlation is not affected by chemical composition given the data available. The experimental data from the present investigation does show two separate curves for Steels L and H; the linear model for Steel H (equation (6.14)) lies above the correlation for B = 10 mm, with a steeper slope.

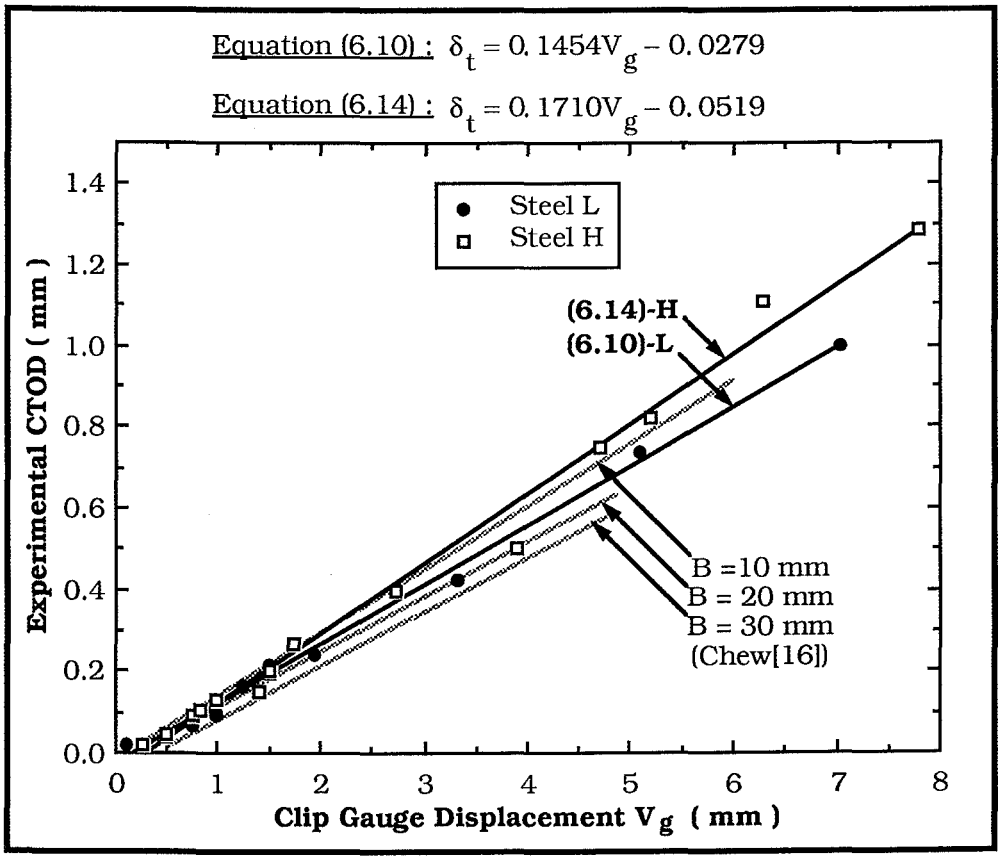

Figure 6.20 : Experimental CTOD (mm) as a function of clip gauge displacement V_g (mm) for equations (6.10) and (6.14).

Table 6.4a
Results of Multi-Linear Regression Analysis of CTOD-V_g Model for Steel L

Equation No.	6.10	6.11	6.12	6.13
Figure No.	6.20	-	-	6.21
N	14	14	14	14
D.F.	12	13	11	12
R	0.9976	0.9950	0.9977	0.9972
$s(\hat{y})$	0.0211	0.0290	0.0213	0.0227
F-value	2444	1290	1205	1053
Equation Significance	>99.9%	>99.9%	>99.9%	99.9%
Coefficients				
A_0	-0.0279	0	-0.0196	0
A_1	0.1454	0.1382	0.1354	0.1196
A_2	-	-	0.00147	0.00346
Coefficients' Significance				
A_1	>99.9999%	>99.9999%	>99.9999%	>99.9999%
A_2	-	-	50%	98%
$\bar{y}$	0.2425	0.2425	0.2425	0.2425
95% C.L. of $\bar{y}$	±0.0123	±0.0167	±0.0125	±0.0132

Note: 1. For definition of statistical abbreviations see Appendix B.
2. V_g and δ are in mm.

Table 6.4b
Results of Multi-Linear Regression Analysis of CTOD-V_g model for Steel H

Equation No.	6.14	6.15	6.16	6.17
Figure No.	6.20	-	-	6.21
N	16	16	16	16
D.F.	14	15	13	14
R	0.9951	0.9911	0.9961	0.9960
$s(\hat{y})$	0.0408	0.053	0.0379	0.0384
F-value	1431	836	831	808
Equation Significance	>99.9%	>99.9%	>99.9%	>99.9%
Coefficients				
A_0	-0.0519	0	-0.0245	0
A_1	0.1710	0.1596	0.1425	0.1264
A_2	-	-	0.003896	0.005756
Coefficients' Significance				
A_1	>99.9999%	>99.9999%	>99.9999%	>99.9999%
A_2	-	-	90%	99.8%
$\bar{y}$	0.3816	0.3816	0.3816	0.3816
95% C.L. of $\bar{y}$	±0.0219	±0.0283	±0.0205	±0.0206

Note: 1. For definition of statistical abbreviations see Appendix B.
2. V_g and δ are in mm.

The main differences between the specimens used in the CTOD-V_g correlation are the grain size and chemical composition between Steels L and H. The linear models for Steels L and H with a computed intercept (equations (6.10) and (6.14)) show good correlation coefficients of R = 0.9976 and R = 0.9951 respectively but where experimental results and Chew's work show a non-linear relationship at low CTOD values then prediction by these models is poor. At low CTOD values the CTOD is proportional to V_g^2 as discussed in Section 6.2.3 so deviation of the linear model is expected.

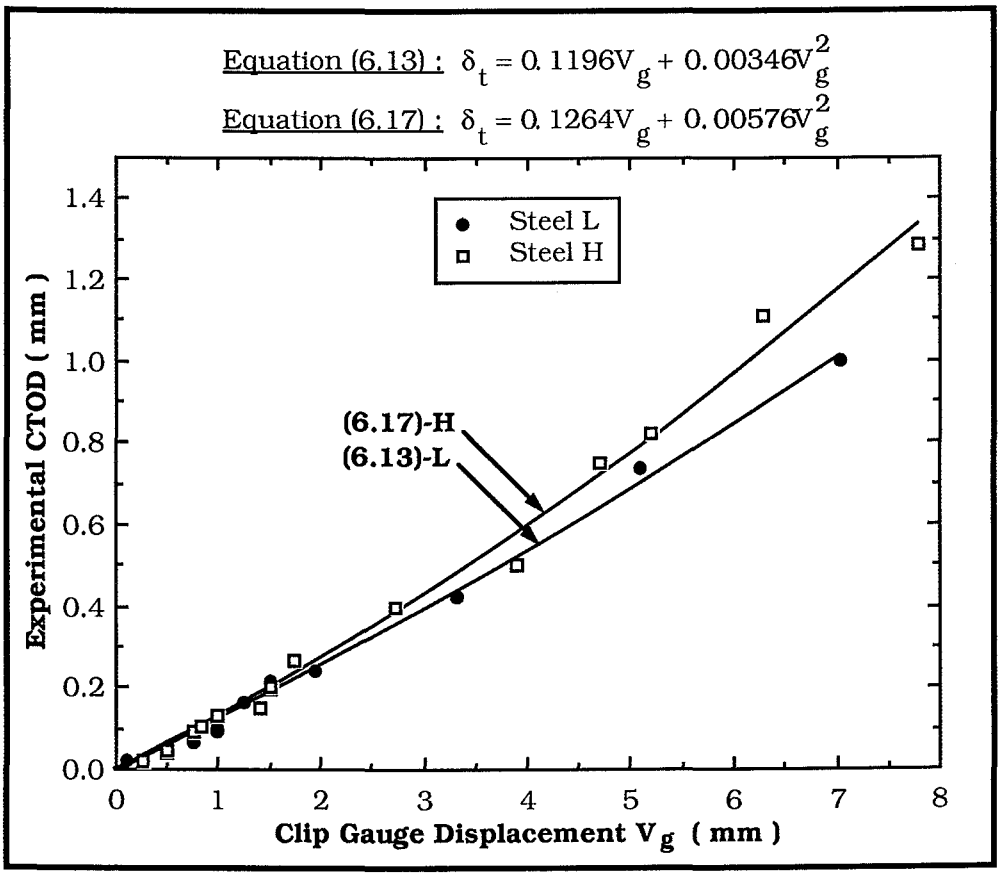

Figure 6.21 : Experimental CTOD (mm) as a function of clip gauge displacement V_g (mm) for Steels L & H; using a quadratic model through the origin.

From Table 6.4, examination of equation (6.12) for Steel L,

$$\delta = -0.0196 + 0.1354V_g + 0.00147V_g^2, \qquad (6.12)$$

and of equation (6.16) for Steel H,

$$\delta = -0.0245 + 0.1425V_g + 0.003896V_g^2, \qquad (6.16)$$

it is clear that the fit of the model to the experimental results is improved using the quadratic relationship with correlation coefficients of R = 0.9977 for equation (6.12) and R = 0.9961 for equation (6.16) but the improvement is only slight. The linear term dominates the equation. The significance of the linear coefficient A_1 in equations (6.10) to (6.17) is greater than 99.9999%. The significance of the V_g^2 coefficient A_2 in equation (6.12) is only 50% and in equation (6.16) is only 90%; therefore over the range of clip gauge displacement considered the V_g^2 term appears to be insignificant even though at low clip gauge displacements CTOD has an expected dependence on it.

If the condition that $\delta = 0$ when $V_g = 0$ is applied to the regression analysis then the significance of the coefficient A_2 changes without any significant change in the value of the correlation coefficient. The results of equation (6.13) for Steel L,

$$\delta = 0.1196V_g + 0.00346V_g^2, \qquad (6.13)$$

and equation (6.17) for Steel H,

$$\delta = 0.1264V_g + 0.005756V_g^2, \qquad (6.17)$$

are shown in Figure 6.21 where the resulting quadratic has been forced through zero. The respective correlation coefficients are R = 0.9972 and R = 0.9957. Although the coefficient A_1 is still significant at the 99.9999% level in both cases the coefficient A_2 is now significant at the 98% level for equation (6.13) and at the 99.8% level for equation (6.17). Although the significance of A_2 is still much less than that of A_1 it indicates that the V_g^2 term is important when the model is forced through zero.

To test whether the experimental results for L & H were significantly different the slopes of equations (6.10) and (6.14) were compared. To compare two slopes for regressions of one independent variable a pooled variance of estimate $\bar{s}^2(\hat{y})$ is calculated which is weighted according to the respective regressions' degrees of freedom,

$$\bar{s}^2(\hat{y}) = \frac{(N_1-2)s^2(\hat{y}_1) + (N_2-2)s^2(\hat{y}_2)}{(N_1-2) + (N_2-2)} \qquad (6.18)$$

where N_1 and N_2 are the number of data points for equations (6.10) and (6.14) respectively, and $s^2(\hat{y}_1)$ and $s^2(\hat{y}_2)$ are the variance of estimates for equations (6.10) and (6.14) respectively [267]. The t test for the difference between two slopes is

$$t = b_1-b_2/\overline{s}(\hat{y})\left(\frac{1}{\Sigma' x_{12}} + \frac{1}{\Sigma' x_{22}}\right)^{1/2} \qquad (6.19)$$

with $N_1 + N_2 - 4$ degrees of freedom. The slopes are b_1 and b_2 respectively and $\Sigma' x = \Sigma x^2 - (\Sigma x)^2/N$, and $s(\hat{y})$ is the pooled standard error of estimate. For equations (6.10) and (6.14) the information from Table 6.4 gives $\overline{s}^2(\hat{y}) = 1.10168$ and $t = 4.288$ for 26 degrees of freedom. From appropriate tables of the t-distribution $t_{0.001,26} = 3.707$ and $t_{0.0001,26} = 4.587$ [287]. Therefore the difference between the two slopes is significant at the 99.9% level. This may be stated as "the difference between the slopes observed would be expected to occur once in 1000 times from data with the variance of estimate calculated for these results when there was no difference between the slopes". Therefore, the slopes are significantly different and explanation for the different curves between the two steels may be investigated.

(b) Combined Data Sets

The results of the multi-linear regression for the pooled data of Steels L and H are given in Table 6.5. The significance of equations (6.20) to (6.23) is greater than 99.9% in each case with F-values from 959 for equation (6.23) to 1797 for equation (6.20). The significance of the linear coefficient A_1 is again greater than 99.9999% for each equation indicating its dominance on the correlation.

Table 6.5
Results of Multiple-Linear Regression Analysis of CTOD-V_g Model for Steels L and H.

Model	Linear	Linear	Quadratic	Quadratic
Equation No.	6.20	6.21	6.22	6.23
Figure No.	-	-	6.22	6.22
N	30	30	30	30
D.F	28	29	27	28
R	0.9923	0.9886	0.9932	0.9928
$s(\hat{y})$	0.0447	0.0535	0.0429	0.0433
F-value	1797	1245	978	959
Equation Significance	>99.9%	>99.9%	>99.9%	>99.9%
Coefficients				
A_0	-0.0433	0	-0.0207	0
A_1	0.1622	0.1520	0.1367	0.1219
A_2	-	-	0.003588	0.005359
Coefficients' Significance				
A_1	>99.9999%	>99.9999%	>99.9999%	>99.9999%
A_2	-	-	90%	99.9%
$\overline{y}$	0.3167	0.3167	0.3167	0.3167
95% C.L. of $\overline{y}$	±0.0167	±0.0200	±0.0161	±0.0162

Note: 1. For definition of statistical symbols see Appendix B.
2. V_g and δ in mm.

Although the results for the linear and quadratic models with computed intercepts (equations (6.20) and (6.22)) are similar when the condition of a zero intercept is applied the quadratic model (equation (6.23)) is superior to the linear model (equation (6.21)). Equation (6.23) compared to equation (6.21) has a correlation coefficient R = 0.9928 compared to R = 0.9886 and a standard error of estimate $s(\hat{y})$ = 0.0433 compared to $s(\hat{y})$ = 0.0535. The significance of the V_g^2 coefficient A_2 is 90% for equation (6.22) and 99.9% for equation (6.23). The quadratic model through the origin shows a large improvement over the other models.

Figure 6.22 shows CTOD against V_g for equations (6.22) and (6.23). Figure 6.23 shows the predicted CTOD results against experimental CTOD results for equation (6.22) and Figure 6.24 shows the predicted CTOD results against experimental CTOD results for equation (6.23).

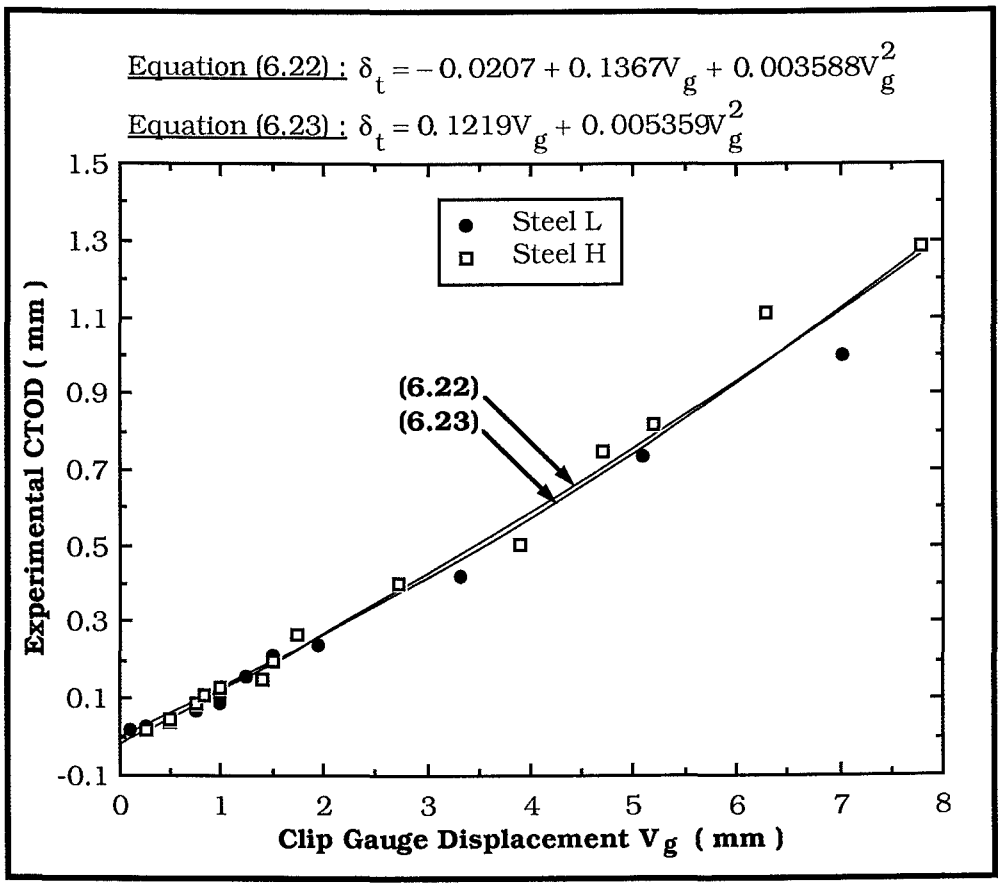

Figure 6.22 : Experimental CTOD (mm) as a function of clip gauge displacement V_g (mm) for the pooled data of Steels L & H using a quadratic model.

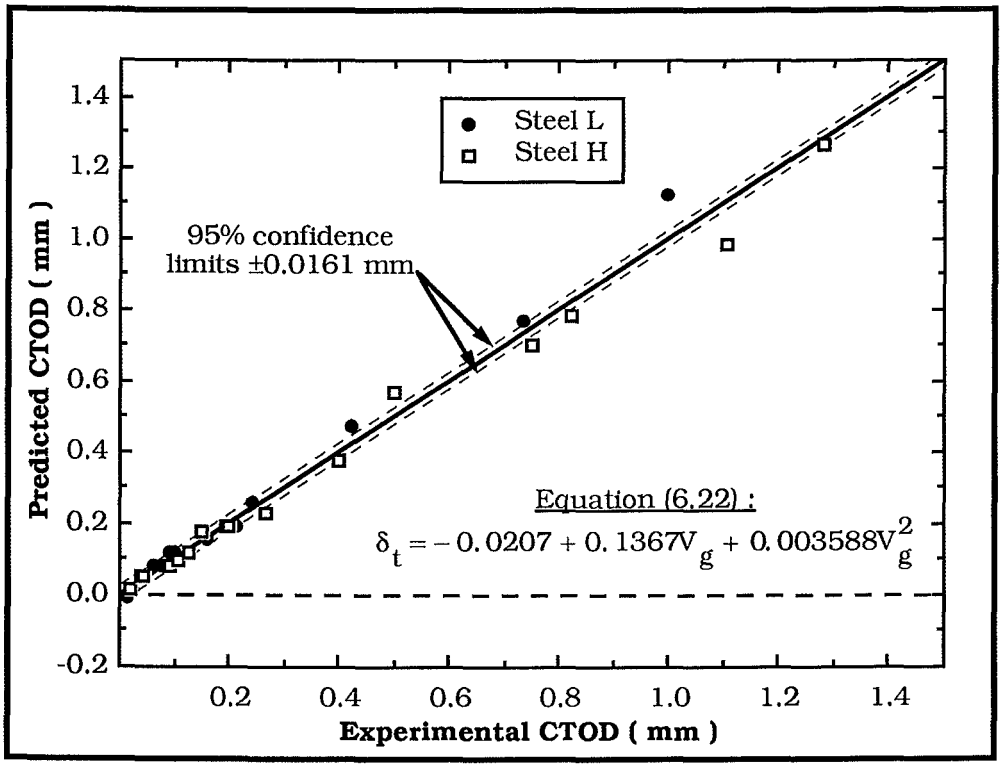

Figure 6.23 : Predicted CTOD (mm) as a function of experimental CTOD (mm) for equation (6.22)

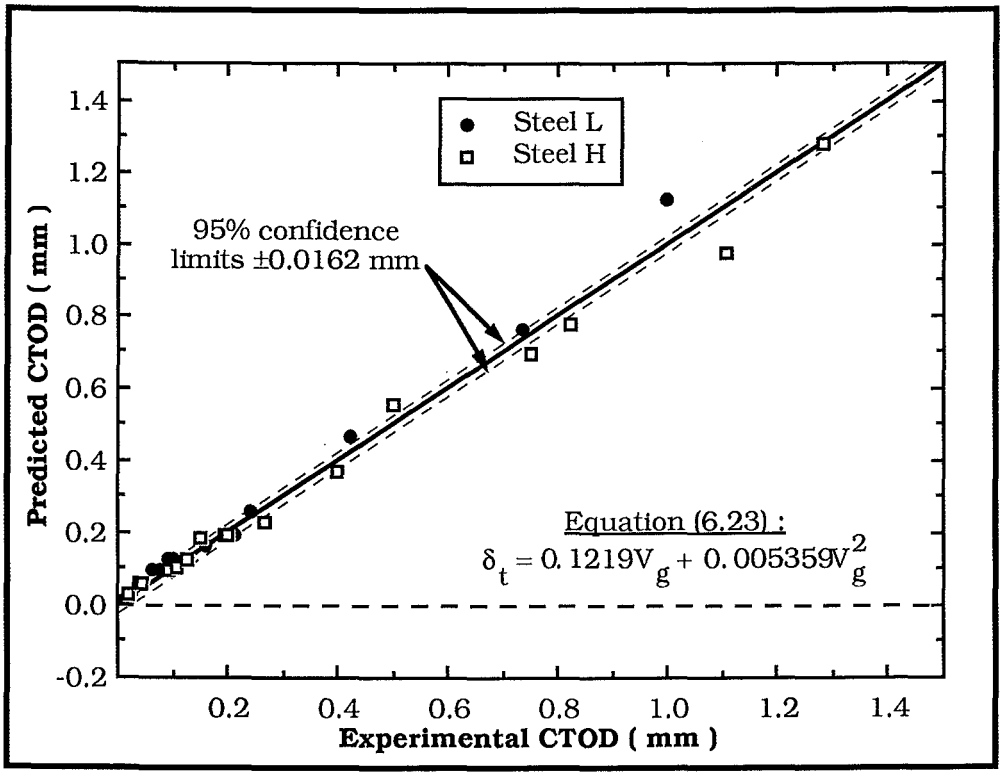

Figure 6.24 : Predicted CTOD (mm) as a function of experimental CTOD (mm) for equation (6.23) ; a quadratic model through the origin.

From Figure 6.22 when the CTOD is large then there is not much difference between the quadratic models using either a computed or zero intercept. When the CTOD is low ($\delta < 0.200$ mm) then there is a divergence with the model with the zero intercept lying higher than the model with a computed intercept. When the residuals of predicted CTOD results against experimental CTOD are examined, as in Figures 6.23 and 6.24 then the results of equation (6.22) show that the points are more evenly distributed about the line "predicted CTOD equals experimental CTOD" when $\delta<0.200$ mm. For equation (6.23), the predicted CTOD results are larger than the experimental values when $\delta<0.200$ mm which could be an indication that the form of the model is incorrect for a zero intercept or that the results will not have a zero intercept. However, it might reflect the difficulty in directly measuring small CTOD values.

From Figures 6.23 and 6.24 the predicted results for Steel H lie below the experimental results at large CTOD values. Such a pattern is not so clear at low CTOD values. For Steel L the predicted results are greater than the experimental results at large and small CTOD values.

The observed trend that there are separate curves for Steel L and H could be due to several factors:

(i) the difference in composition, due to differences in carbon and nitrogen content or

(ii) the difference in grain size of the specimens used for the calibration or

(iii) experimental error, arising mainly from the position of measurement and the measurement of values of CTOD.

Equation (2.91),

$$G = M\sigma_{ys}\delta,$$

contains a plastic stress intensification factor M to account for different stress states, specimen geometries and work hardening. In Section 2.2.3 M was shown to vary from 1 for plane stress to 2 for plane strain. If equation (2.91) is rewritten as

$$\delta = G/M\sigma_{ys} \qquad (6.24)$$

then the dependence of the CTOD on yield strength and work hardening is seen. This does not relate the dependence to the clip gauge displacement however. If equation (2.99a-c) which gives CTOD as a function of V_g is examined the influence of yield strength and work hardening on CTOD can be found.

Equation (2.99a-c),

$$\delta_t = \frac{K^2(1-\nu^2)}{2\sigma_{ys}E} + \frac{V_p r_p b_0}{(r_p b_0 + a_0 + z)}$$

contains the elastic term

$$\delta_e = K^2(1-\nu^2)/2\sigma_{ys}E \qquad (2.99b)$$

and the plastic term

$$\delta_p = V_p r_p b_0/(r_p b_0 + a_0 + z). \qquad (2.99c)$$

Between Steels L and H it is assumed that, geometrically, b_0, a_0 and z are unchanged and that ν and E have the same value i.e. ν = 0.3 and E = 210 GPa as used by Chew [16]. Therefore the values which can influence the CTOD are K^2, V_p, r_p and σ_{ys} but it has been shown that K^2 is directly proportional to V_g^2 and V_g is the independent variable under investigation. The plastic component of clip gauge displacement V_p is related to V_g; therefore the variation between the two steels occurs by variation in the yield strength (σ_{ys}) and in the rotation factor (r_p).

(b.1) The effect of grain size

The effect of grain size on the lower yield stress is given by the Hall-Petch model described in Section 5.2.3 where equation (5.4),

$$\sigma_{ys} = \sigma_i + k_y d^{-1/2},$$

σ_i being the friction stress and k_y a constant, shows that refining the grain structure will increase yield stress. This effect was found in the experimental results described in Section 5.4.3. Therefore, from equation (6.7)

$$\delta_t \propto V_g^2/\sigma_{ys} \tag{6.25}$$

and substituting for yield stress with equation (5.4) then

$$\delta_t \propto V_g^2/(\sigma_i + k_y d^{-1/2}) \tag{6.26a}$$

or approximately,

$$\delta_t \propto V_g^2 d^{1/2}. \tag{6.26b}$$

This gives an expected grain size dependence of CTOD where decreasing the grain size decreases the expected CTOD for a given clip gauge displacement.

This could be expected since decreasing the grain size increases the yield strength of the material. Increasing the yield strength will reduce the size of the plastic zone; this would be expected to reduce the CTOD for a given applied stress intensity. This is shown by using Dugdale's analysis of plastic zone size where the notional crack increment Δa_n is given by equation (2.46) as

$$\Delta a_n = \frac{\pi}{8}\left(\frac{K_I}{\sigma_{ys}}\right)^2,$$

K_I is the applied stress intensity [114]. Increasing σ_{ys} by decreasing the grain size reduces Δa_n and the size of the plastic zone.

Figure 6.25 shows a schematic of the stress distribution ahead of the crack tip for two different levels of yield stress assuming elastic-perfectly plastic behaviour. If work hardening is included then the stress ahead of the crack tip will increase and the size of the plastic zone will decrease; the higher the rate of work hardening the smaller the resultant plastic zone.

By grain refinement the rate of work hardening is increased [275,276]. Therefore the material with the smaller grain size will have a small plastic zone. The rate of work hardening will also affect the rotation factor r_p.

If the energy input into deformation around the crack tip is considered then the amount of energy put into plastic deformation around the crack tip increases with increase in plastic zone size.

The energy may be regarded as the product of strain energy per unit volume and the volume of the plastic zone. For similar loading conditions (i.e. the same clip gauge displacement) then an increase in volume of plastically deformed material will increase the energy input. The increase in volume is associated with the material of lower yield strength, i.e. the larger grain size, and the energy input is proportional to the CTOD (from equation (2.91)). Therefore for the same clip gauge displacement the lower yield strength material (the larger grain size in this case) will be expected to have a higher value of CTOD providing all other testing conditions are similar.

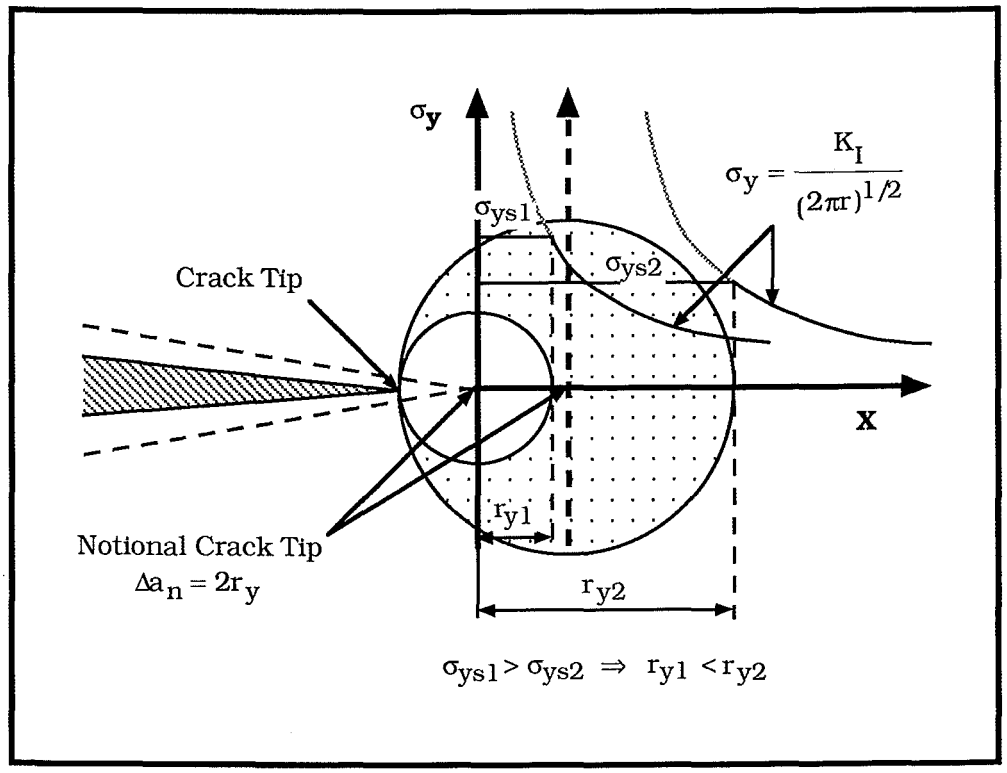

Figure 6.25 : Schematic of the stress distribution and plastic zone ahead of the crack tip for two different values of yield stress.

(b.2) The plastic rotation factor, r_p

Green and Hundy gave $r_p = 0.5$ based on slip line field theory when extensive yielding had occurred and r_p was a constant [142]. BS 5762:1979 uses $r_p = 0.4$ whereas ASTM E1290-89 varies r_p from 0.44 to 0.47 depending on specimen geometry and a_o/W ratio [41,44].

When r_p is constant then from equation (2.95),

$$\delta_t = \frac{V_g r_p b}{(r_p b+a+z)},$$

the CTOD is directly proportional to the clip gauge displacement i.e.

$$\delta_t = R_p V_g \tag{6.27}$$

where R_p is constant, δ_t is the total CTOD and V_g is the total clip gauge displacement. It has been shown experimentally that r_p could be material dependent, affected by the rate at which plastic collapse occurs [29,135]. Theoretically r_p has been shown to be independent of strain hardening providing the Ramberg-Osgood strain hardening exponent N is greater than 5 [144].

However Wu *et al.* did show that when a/W = 0.5 for the bend specimen r_p has a range from 0.438 for N = 5 to 0.431 for N = 10. For the compact tension specimen when a/W = 0.5 r_p has a range from 0.400 for N = 5 to 0.428 for N = 10. Typical structural steels have a Ramberg-Osgood strain-hardening index N from 5 to 10 [144]. In Section 3.2.5 N was given as $N \approx 1/n$ where n is the Holloman strain-hardening exponent. The Holloman strain-hardening exponent n shows a grain size dependence given by Erasmus and Soh as

$$n = n_o - k_n d^{-1/2} \tag{6.28}$$

where n_o and k_n are constants [275,276]. An increase in grain size will increase the strain-hardening exponent n, and therefore N will show a grain size dependence as well. From the dependence of r_p on N discussed previously it would be expected r_p would show a grain size dependence as well.

For the compact tension specimen

$$r_p \propto N \tag{6.29a}$$

which upon substituting for N with equation (6.28) gives

$$r_p \propto 1/(n_o - k_n d^{-1/2}). \tag{6.29b}$$

Pratap and Pandey found that r_p was dependent on the yield strength of the material, the lower the yield stress of the material the higher the value of r_p [135,153]. From the dependence of yield strength on grain size there is an implied dependence of the plastic rotation factor r_p on grain size where

$$r_p \propto 1/\sigma_{ys}. \tag{6.30a}$$

From equation (5.4), the Hall-Petch equation

$$\sigma_{ys} = \sigma_i + k_y d^{-1/2}$$

then

$$r_p \propto 1/(\sigma_i + k_y d^{-1/2}). \tag{6.30b}$$

Having established that the rotation factor will show a dependence on grain size the form of this dependence can be established. One possible solution would be that r_p is proportional to the products of equations (6.29b) and (6.30b), that is,

$$r_p \propto \frac{1}{(n_o - k_n d^{-1/2})(\sigma_i + k_y d^{-1/2})}. \tag{6.31}$$

By normalising both bracketed terms this gives

$$r_p \propto 1/n_o\sigma_i \left(1 - \frac{k_n d^{-1/2}}{n_o}\right)\left(1 + \frac{k_y d^{-1/2}}{\sigma_i}\right). \tag{6.32}$$

The bracketed terms may be expanded by a power series expansion of $(1 + x)^{-1}$ [287],

$$(1+x)^{-1} = 1-x+x^2-x^3+\ldots+(-1)^{n-1}x^{n-1}. \tag{6.33}$$

If this power series expansion is applied to both $(1-k_n d^{-1/2}/n_o)^{-1}$ and $(1+k_y d^{-1/2}/\sigma_i)^{-1}$ then the dependence of r_p on grain size can be given mathematically. However the similarity of expressions for the grain size dependence of N and σ_{ys} would indicate a cross correlation between N, σ_{ys} and grain size. Therefore an investigation into the

effect of grain size on the plastic rotation factor appears to be necessary, which is beyond the scope of this investigation.

(b.3) Chemical Composition

A change in chemical composition of the material tested will affect the yield stress, the strain-hardening index and the rate of strain hardening of the material.

The lower yield stress of the material has been give in Section 5.3, equation (5.17), as

$$\sigma_{ys} = \sigma_i^* + \sigma_i(st) + k_y d^{-1/2}$$

where σ_i^* is the temperature component of yield stress, $\sigma_i(st)$ is the athermal component and k_y is a constant. Table 5.6 presented a summary of the magnitudes of athermal stress components. For this investigation it was found Steel L (0.19 wt%C) had $\sigma_i(st)$ equal to 129 MNm^{-2} and Steel H (0.09 wt%C, 0.012 wt%N) had $\sigma_i(st)$ equal to 108 MNm^{-2}. From the discussion of (b.1) in this section this would imply that Steel H would have a larger plastic zone due to the lower yield stress and hence a larger CTOD. From Section 5.2.3 it is known that k_y has a range from 14 to 24 $MNm^{-2}\ mm^{1/2}$ and that k_y increases with increasing carbon and nitrogen content [174]. For the steels used k_y is 20.85 $MNm^{-2}\ mm^{1/2}$ for Steel L and k_y is 22.89 $MNm^{-2}\ mm^{1/2}$ for Steel H. The yield stress will increase at a faster rate for increasing grain size for Steel H. So k_y will also influence the size of the plastic zone.

The relationship between true stress and true strain for work-hardening materials was given by equation (3.14) in Chapter 3 as

$$\sigma = K_n \varepsilon^n$$

where K_n is a constant and n is the Holloman strain-hardening exponent. The rate of strain-hardening was given by equation (3.15),

$$\frac{d\sigma}{d\varepsilon} = nK_n\varepsilon^{n-1}.$$

It was discussed in (b.1) of this section that a higher rate of work-hardening will decrease the size of the plastic zone and hence give a lower CTOD. Equation (6.24),

$$n = n_o - k_n d^{-1/2},$$

shows the influence of grain size on the strain-hardening index. Morrison reported that carbon content had little influence on "n" [277]. However the constant K_n is influenced by grain size and carbon content. Morrison gave these influences as,

$$K_n = A_1 + B_1 d^{-1/2} \qquad (6.34)$$

where A_1 and B_1 are constants and

$$K_n = A_2 + B_2(\%C) \qquad (6.35)$$

where A_2 and B_2 are constants [277]. Therefore K_n increases with decreasing grain size or increasing carbon content. It would be expected that steels with a larger grain size and lower carbon content will have a higher strain-hardening index and a lower rate of work hardening than a fine grained, higher carbon content steel (Steel HZ compared to Steel LZ). So a larger plastic zone will form and a larger CTOD result for a given clip gauge displacement for Steel HZ compared to Steel LZ.

Determining the influence of nitrogen content and carbon content on the mechanical properties of the steel must also consider their interaction with other elements in the steel; for example nitrogen is partitioned by manganese and forms precipitates with titanium. The interaction between nitrogen and manganese influenced the given model of the Charpy Impact transition temperature given in Chapter 4 as

$$F' = \frac{(\%Mn)(\%N_R)}{(\%Mn) + K_n(\%N_R)}$$

from Erasmus [8]. Also steels microalloyed with titanium show an increase in strength due to the precipitate TiN, which also prevents strain-ageing in the steel [11]. Any influence of the chemical composition on the properties of the material should initially include

the influence of such interactions though these may be found to be statistically insignificant. It was considered that with only two experimental steels there was insufficient data to explain variation in properties due to differences in composition.

It was decided that the model of CTOD against clip gauge displacement would include a grain size dependence only. Using equations (6.9) and (6.26b) the model was written as

$$\delta_t = A_0 + A_1 V_g + A_2 V_g^2 d^{1/2} + A_3 V_g d^{1/2} \qquad (6.36)$$

where A_0, A_1, A_2 and A_3 are constants. The term $A_3 V_g d^{1/2}$ is an estimate of the influence of grain size on the plastic rotation factor r_p.

(c) Combined Data Sets with a Grain Size Dependence

The results of the multiple-linear regression analysis using equation (6.36) are given in Table 6.6. There are four cases presented; equation (6.37) where $A_3 = 0$ and the intercept is computed, equation (6.38) where $A_3 = 0$ and the intercept is zero, equation (6.39) where the y-axis intercept and A_3 are computed and equation (6.40) where the y-axis intercept is zero and A_3 is computed. The correlation coefficient R has a range from 0.9964 for equation (6.38) to 0.9968 for equation (6.39). All equations have a significance greater than 99.9% with F-values from 1326 for equation (6.40) to 2054 for equation (6.37).

When the significance of the coefficients is examined there is a significant difference from the results for the combined data sets. The significance of the linear coefficient A_1 is still greater than 99.9999% for each equation. However the significance of the coefficient A_2 for the term $V_g^2 d^{1/2}$ ranges from 99.9% for equation (6.39) to 99.9999% for equations (6.38) and (6.40). The V_g^2 term, by incorporating a grain size dependence, has increased its significance. The significance level of the coefficient A_3 is 80% for equation (6.39) and 50% for equation (6.40). The lack of significance for this coefficient implies that there is either no grain size dependence for the linear term or other factors cancel out the expected grain size dependence expected of the plastic rotation factor.

Table 6.6
Results of Multiple-Linear Regression Analysis of CTOD-V_g model for L and H including grain size

Model Equation (6.36)		$\delta_t = A_0 + A_1V_g + A_2V_g^2d^{1/2} + A_3V_gd^{1/2}$		
Equation No.	6.37	6.38	6.39	6.40
Figure No.	6.26	6.27, 6.28	-	-
N	30	30	30	30
D.F.	27	28	26	27
R	0.9967	0.9964	0.9968	0.9966
$s(\hat{y})$	0.0300	0.0305	0.0301	0.0302
F-value	2054	1939	1329	1326
Equation Significance	>99.9%	>99.9%	>99.9%	>99.9%
Coefficients				
A_0	-0.0148	0	-0.01180	0
A_1	0.1284	0.12113	0.1288	0.1255
A_2	0.03005	0.034222	0.03269	0.03839
A_3	-	-	-0.02129	-0.04964
Coefficients' Significance				
A_1	>99.9999%	>99.9999%	>99.9999%	>99.9999%
A_2	99.999%	99.9999%	99.9%	99.9999%
A_3	-	-	80%	50%
$\overline{y}$	0.3167	0.3167	0.3167	0.3167
95% C.L. of $\overline{y}$	±0.0111	±0.0114	±0.0113	±0.0113

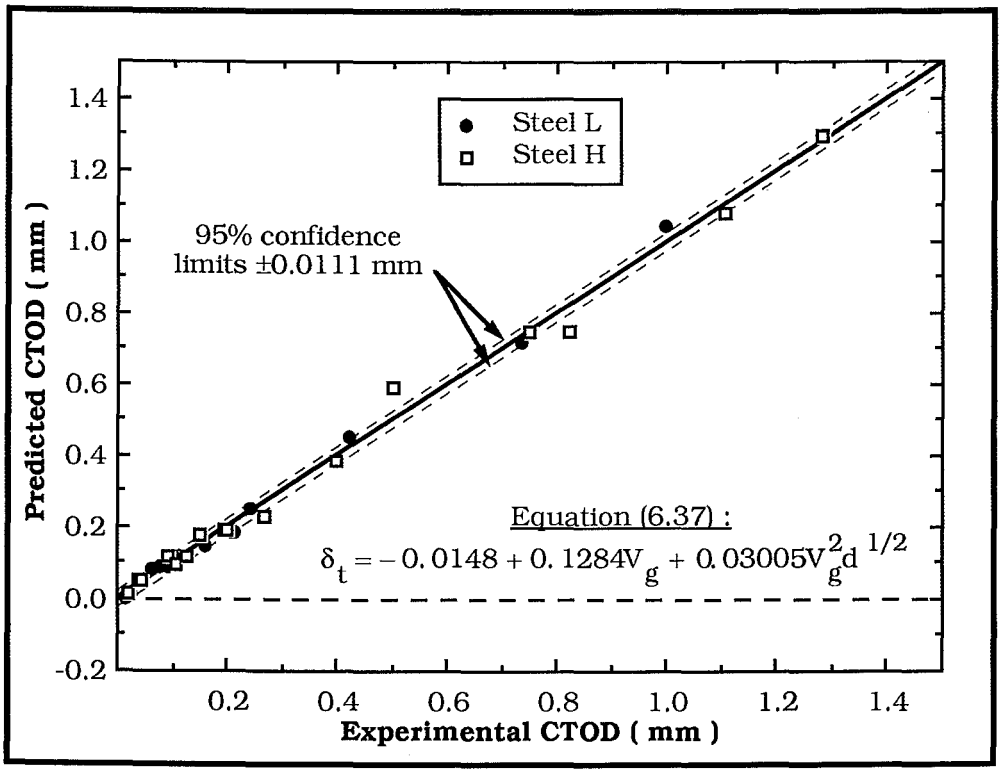

Figure 6.26 : Predicted CTOD (mm) as a function of experimental CTOD (mm) equation (6.37) ; the quadratic model including grain size.

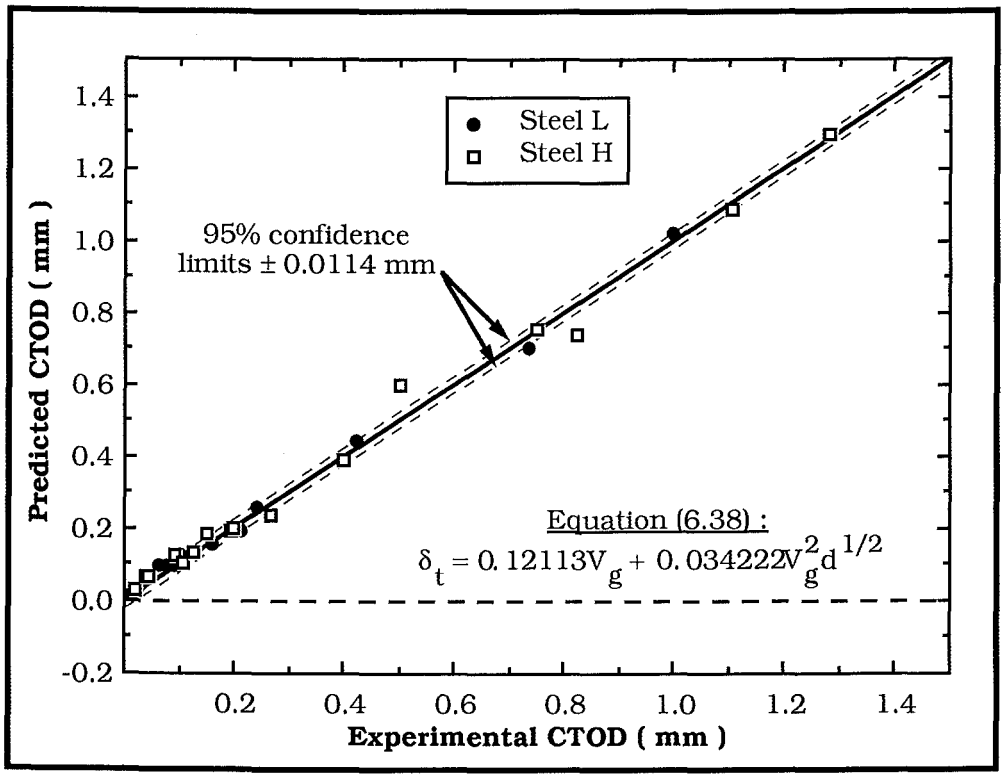

Figure 6.27 : Predicted CTOD (mm) as a function of experimental CTOD (mm) for equation (6.38); the quadratic model through the origin and including grain size.

Figures 6.26 and 6.27 show the results of predicted CTOD against the experimental CTOD for equations (6.37) and (6.38) respectively. The "fit" of equation (6.37) with a computed y-axis intercept is better than that of equation (6.38) with a zero intercept, especially when the CTOD is low ($\delta_t < 0.20$ mm). When the CTOD is less than 0.20 mm equation (6.38) predicts results larger than the experimental results although this is probably due to the few large CTOD results unduly influencing the regression. At larger CTOD values experimental error is more likely due to excessive rotation of the clip gauge knife edges. 95% confidence limits are plotted on Figures 6.26 and 6.27. The total variation in CTOD explained by equation (6.37) is 99.35% and by equation (6.38) is 99.28%. The result of equation (6.37) suggests that the use of the model with the term $V_g^2 d^{1/2}$ is acceptable. By applying the condition that the model must pass through the origin then equation (6.38),

$$\delta = 0.121113\ V_g + 0.034222\ V_g^2 d^{1/2},$$

V_g in mm is chosen as the acceptable model.

Figure 6.28 shows CTOD against clip gauge displacement for equation (6.38) for $d^{-1/2} = 4.187$ mm$^{-1/2}$ (HZ) and $d^{-1/2} = 9.939$ mm$^{-1/2}$ (LZ) overlying the experimental results.

At low values of V_g then the curves for individual grain sizes overlap which would be expected since the product $V_g^2 d^{1/2}$ will be small. The model is acceptable compared to the experimental results.

A relationship has been established between clip gauge displacement, grain size and CTOD. The model could be improved and further developed by including the effect of composition on CTOD through yield strength and the plastic rotation factor. Figure 6.18 shows the relationship between clip gauge displacement and crosshead displacement. It has been assumed that V_g is proportional to V_{CH} above the range of the clip gauge. Therefore a model can also be formed of the dependence of CTOD on crosshead displacement.

6.2.5 CROSSHEAD DISPLACEMENT, V_{CH}

The relationship between V_{CH} and V_g is initially non-linear, then as time increases the relationship is linear so that V_g is directly proportional to V_{CH}. The relationship for a CT specimen will depend

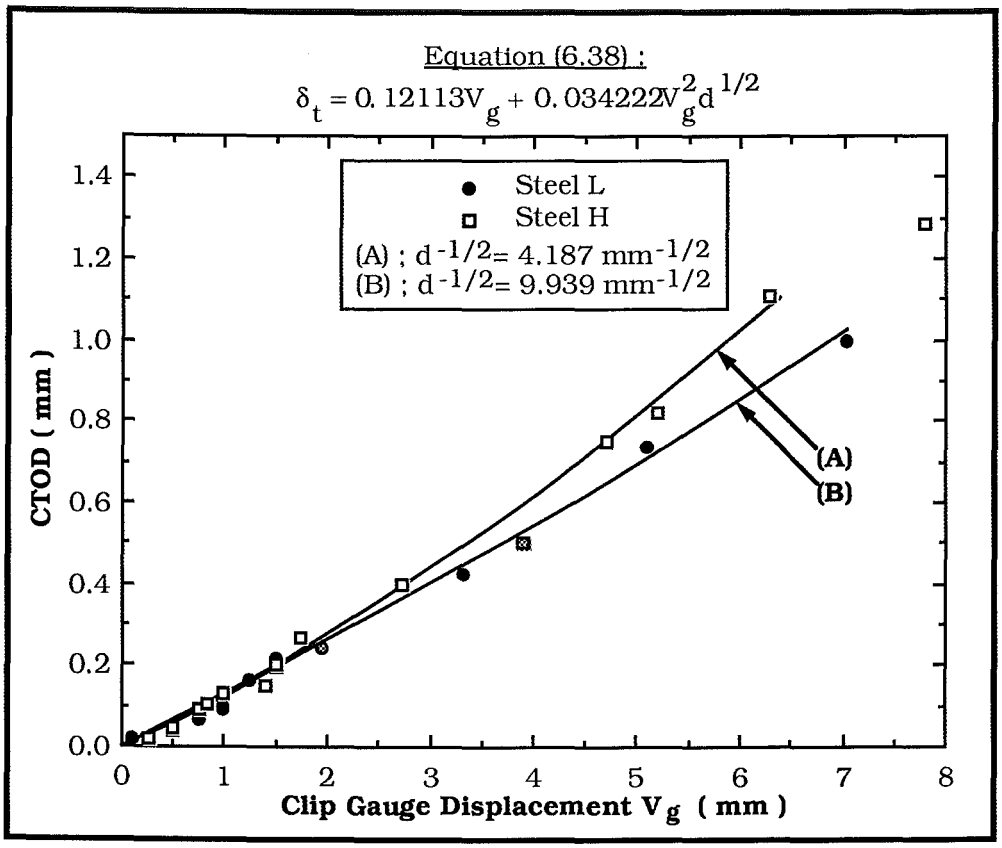

Figure 6.28 : Experimental CTOD (mm) as a function of clip gauge displacement V_g (mm) showing the predicted results using equation (6.38).

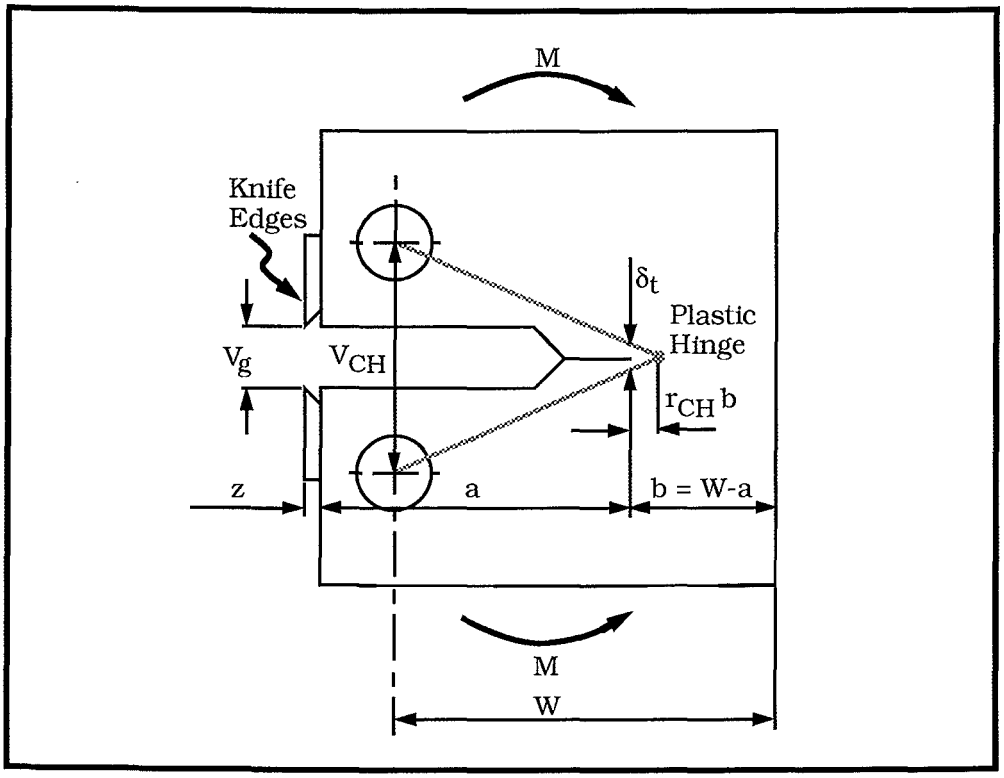

Figure 6.29 : Schematic of the geometric relationship between crosshead displacement (V_{CH}) and CTOD for the CT specimen.

on different aspects than for a SENB specimen. For a bend specimen it could be expected that the non-linear region will be smaller compared to the CT specimen. Using the CT specimen the initial non-linear region may vary depending upon the experimental set-up, mainly how much crosshead movement is needed until any crack opening takes place. This will depend on the elastic extension of the grips and elastic bending of the pins holding the specimen. Therefore there may be some crosshead displacement before any clip gauge displacement and hence before any crack-opening displacement.

When forming the correlation between CTOD and crosshead displacement two factors were considered. The first is that since clip gauge displacement and crosshead displacement are directly proportional to each other then the model developed of CTOD versus V_{CH} will have the same form as the model of CTOD against clip gauge displacement. This might be expected since the displacement at the pins can be related geometrically to CTOD in the same manner as clip gauge displacement. This is shown in Figure 6.29 which gives for the CT specimen,

$$\delta_t = \frac{V_{CH} r_{CH} b_0}{(r_{CH} b_0 + a_0)} \qquad (6.41)$$

where b_0 and a_0 are as defined before and r_{CH} is a rotation factor which will be less than the plastic rotation factor associated with clip gauge displacement, but will behave in a similar manner increasing from zero when CTOD is zero up to a constant value as plastic collapse is approached.

The other factor to consider is that since the y-axis intercept need not be zero when V_{CH} is zero then the intercept is computed and not forced through the origin.

Multiple-linear regression techniques were used on the results shown in Figure 6.19b. Similar equation forms to those used to model clip gauge displacement were considered, based on

$$\delta_t = A_0 + A_1 X + A_2 X^2 \qquad (6.8)$$

where A_0, A_1 and A_2 are constants. The cases presented are for: Steels L and H considered individually (equations (6.42) and (6.43)), Steels L and H considered as a combined data set with a computed

intercept (equation (6.44)) and Steels L and H considered as a combined data set with a grain size dependence of the V_{CH}^2 term given as

$$\delta_t = A_0 + A_1 V_{CH} + A_2 V_{CH}^2 d^{1/2} \qquad (6.45)$$

where A_0, A_1 and A_2 are constants. These results are presented in Table 6.7. Equation (6.42) for Steel L has a correlation coefficient R = 0.9964 and equation (6.43) for Steel H has a correlation coefficient R = 0.9918. Their respective F-values are 760 and 390 giving each equation a significance level greater than 99.9%. Again the linear term is dominant since its coefficient has a significance of 99.9% for each case whereas for the quadratic term the coefficient A_2 has a significance of 99.5% for equation (6.42) and of only 20% for equation (6.43). If the data is pooled the significance of A_2 should increase similarly to the CTOD-V_g correlation.

With the results for L and H combined the fit of the equation is not as good as for the individual curves. The correlation coefficient drops to 0.9879 for equation (6.44). With the larger number of degrees of freedom the significance A_1 has 99.999% significance while A_2 is 95% significant. The significance of A_2 may be less than for Steel L (99.5% significance) but it is a considerable improvement over the equation for Steel H (20% significance). Figure 6.30 shows the predicted CTOD against experimental CTOD for

$$\delta_t = A_0 + A_1 V_{CH} + A_2 V_{CH}^2 \qquad (6.44)$$

where A_0 = -0.1165 mm, A_1 = 0.2030 and A_2 = 0.01494 mm^{-2}. The predicted results are evenly distributed around the line of experimental results with the smallest CTOD result giving a negative prediction. At large CTOD values there is a large difference between predicted CTOD values and the experimental results.

When the regression analysis is performed including a grain size dependence with the V_{CH}^2 term then the difference between predicted CTOD values and experimental values is considerably reduced. The predicted results are from

$$\delta_t = A_0 + A_1 V_{CH} + A_2 V_{CH} d^{1/2} \qquad (6.45)$$

Table 6.7
Results of the Multiple-Linear Regression Analysis of CTOD-V_{CH} Model for Steels L and H.

Type	L	H	Combined L & H	Combined with grain size
Equation No.	6.42	6.43	6.44	6.45
Figure No.	-	-	6.30	6.31,6.32
N	14	16	30	30
D.F.	11	13	27	27
R	0.9964	0.9918	0.9879	0.9967
$s(\hat{y})$	0.02675	0.05506	0.05686	0.02995
F-value	760	390	550	2017
Equation Significance	>99.9%	>99.9%	>99.9%	>99.9%
Coefficients				
A_0	-0.07817	-0.1522	-0.1165	-0.1108
A_1	0.1448	0.2597	0.2030	0.190806
A_2	0.02195	0.006102	0.01494	0.113386
Coefficients' Significance				
A_1	99.9%	99.9%	99.999%	>99.9999%
A_2	99.5%	20%	95%	99.9999%
$\overline{y}$	0.2425	0.3816	0.3167	0.3167
95% C.L. of $\overline{y}$	±0.0157	±0.0297	±0.0213	±0.0112

Note: 1. For definition of statistical abbreviations see Appendix B.

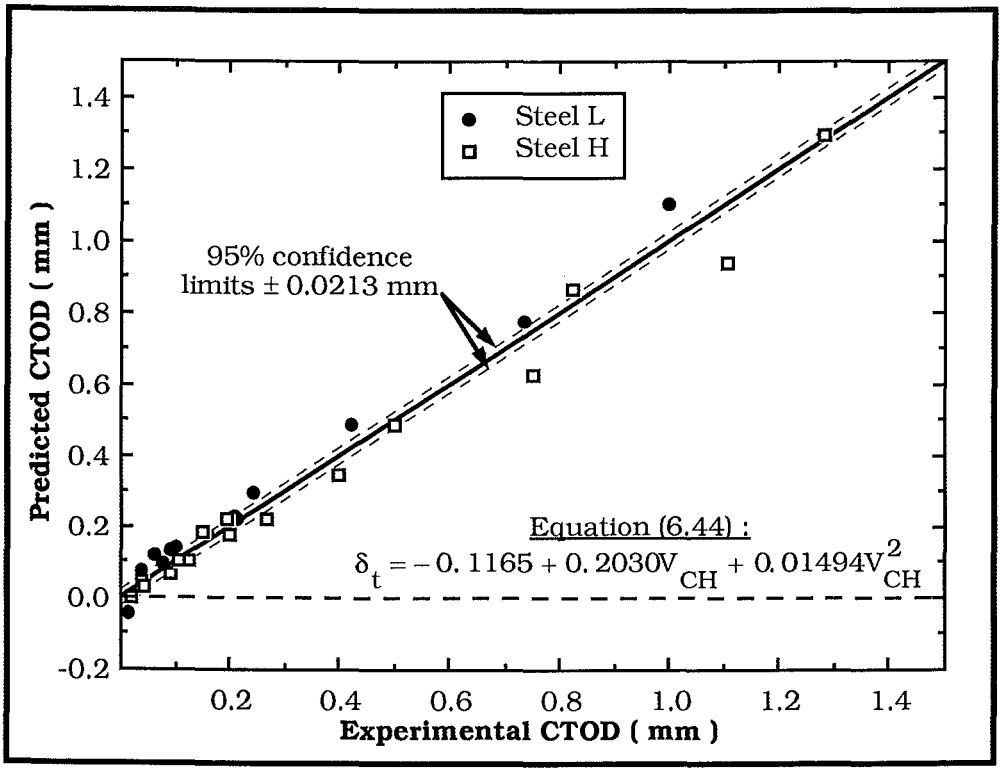

Figure 6.30 : Predicted CTOD (mm) as a function of experimental CTOD (mm) for crosshead displacement using equation (6.44).

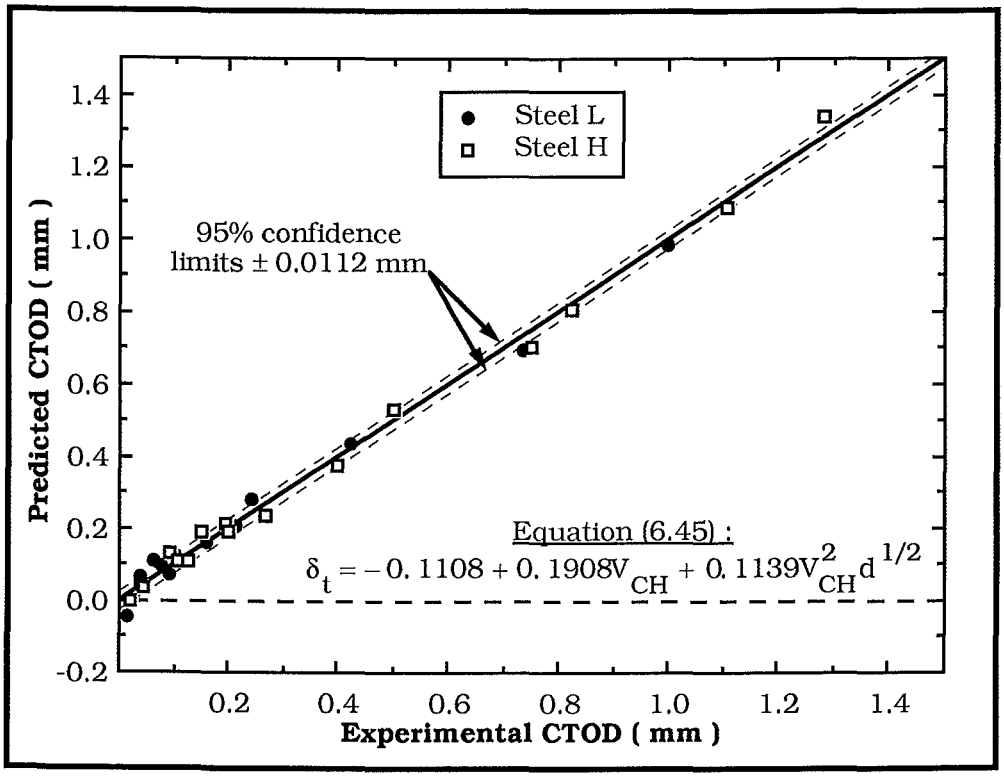

Figure 6.31 : Predicted CTOD (mm) as a function of experimental CTOD (mm) for equation (6.45); a quadratic model including a grain size term.

where A_0 = -0.11077 mm, A_1 = 0.190806, A_2 = 0.113386 $m^{-3/2}$ and V_{CH} is in mm and $d^{1/2}$ in $mm^{1/2}$. This, again, gives a negative predicted CTOD at small crosshead displacements. The "fit" of this model is considerably better than the previous equations with a correlation coefficient of R = 0.9967 and a F-value of 2017, which is larger than those of equations (6.42) to (6.44). This implies the model is more significant than the other equations considered. The significance of the coefficients is improved as well. The coefficient A_1 has a level of significance greater than 99.9999% and A_2 has a level of significance of 99.9999%. 95% confidence limits are plotted on Figure 6.31. On the basis of favourable statistical results and from the expected form of the model

$$\delta_t = -0.1107 + 0.190806V_{CH} + 0.113386V_{CH}^2 d^{1/2} \quad (6.45)$$

would be chosen for the CTOD-Crosshead Displacement correlation. The standard error of estimate $s(\hat{y})$ is 0.02995 which is very good, since when Steel H is considered by itself then $s(\hat{y})$ = 0.05506.

Figure 6.32 shows a plot of the experimental CTOD results as a function of crosshead displacement with predicted curves using equation (6.45) drawn for $d^{-1/2}$ = 4.187 $mm^{-1/2}$ and $d^{-1/2}$ = 9.939 $mm^{-1/2}$ (the two limits in grain size tested). When crosshead displacement is zero the 95% confidence limits are ± 0.0251 mm but the origin is not included in this range. Therefore, a positive crosshead displacement before any crack opening will indicate elastic extension of the grips.

If clip gauge displacement cannot be measured then crosshead displacement may be used to measure the crack-tip opening displacement. Chew has said that measurement of crosshead displacement using SENB specimens would be preferable to using CT specimens with extension arms for mounting the clip gauge [278]. This is since the greater rotation of the extension arms amplifies movement of the clip gauge.

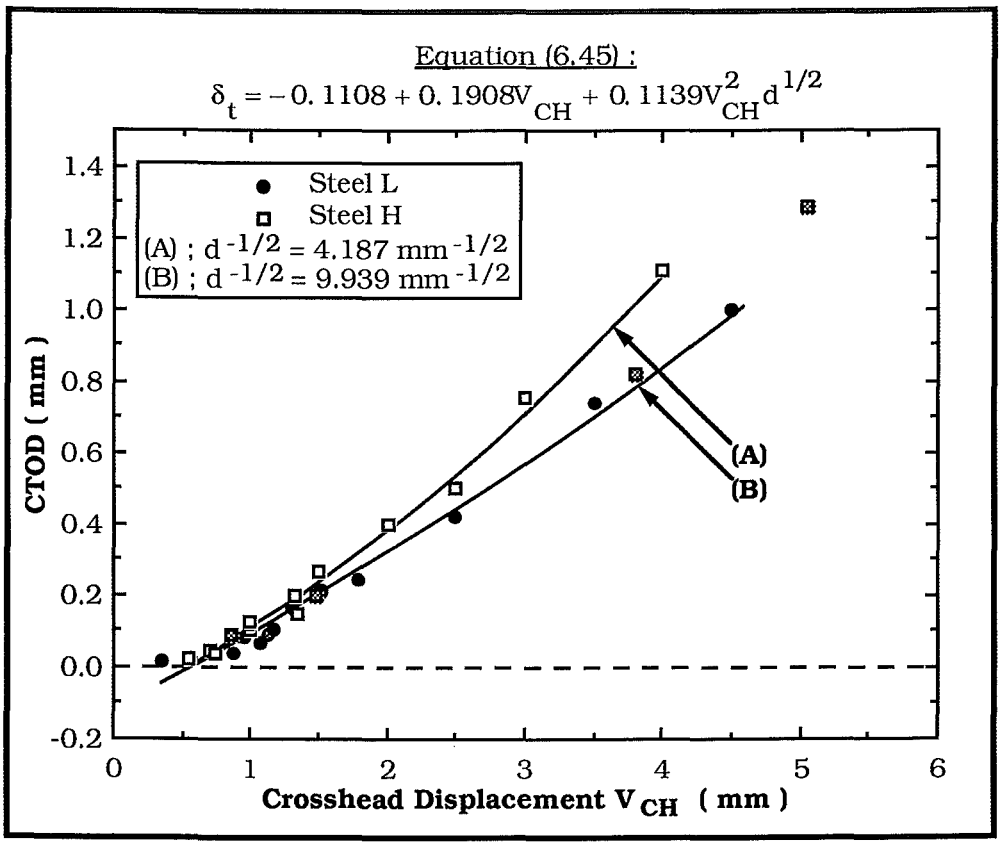

Figure 6.32 : Experimental CTOD (mm) as a function of crosshead displacement V_{CH}(mm) showing the predicted results using equation (6.45)

6.2.6 COMPARISON OF CTOD CALCULATIONS

A method has been presented where the crack-tip opening displacement may be calculated for the CT specimen as

$$\delta_t(mm) = A_1 V_g + A_2 V_g^2 d^{1/2} \qquad (6.38)$$

where V_g is the clip gauge displacement in millimetres, $d^{1/2}$ is the square root of grain size in $mm^{1/2}$ and for thickness B = 15 mm, A_1 = 0.121113 and A_2 = 0.034222 $mm^{-3/2}$.

The equation for calculating CTOD given by ASTM E1290-89 for the CT specimen is

$$\delta_t = \frac{K^2(1-\nu^2)}{2\sigma_{ys}E} + \frac{V_p r_p b_0}{(r_p b_0 + a_0 + z)} \qquad (6.46)$$

where $K = YP/(BW^{1/2})$ (6.47)

σ_{ys} = yield or 0.2% proof stress at test temperature.

E = Young's modulus at test temperature.

P = Load at the critical event

ν = Poisson's ratio

V_p = Plastic component of clip gauge displacement at the critical event.

z = distance of the knife edges from the load line in CT specimens.

r_p = plastic rotation factor

= 0.47 for $0.45 \leq a_0/W \leq 0.50$ or

0.46 for $0.50 < a_0/W \leq 0.55$

b_0 = $(W - a_0)$

and $Y = (2 + a_0/W)(0.886+4.64\ a_0/W-13.32(a_0/W)^2 +14.72(a_0/W)^3-5.6(a_0/W)^4) / (1-a_0/W)^{3/2}$ (6.48)

for the CT specimen. Values of Y are tabled in the standard for different values of a_0/W [44]. If equation (6.38) is used for calculating experimental CTOD then the predicted results using this equation should compare favourably with those predicted using equation (6.46).

It would be expected that the standard equation should give conservative values of CTOD. When the clip gauge displacement is small V_p is very small and the term

$$\delta_p = V_p r_p b_0/(r_p b_0 + a_0 + z) \tag{6.49}$$

is negligible or zero. The elastic term δ_e given by

$$\delta_e = K^2(1-\nu^2)/2\sigma_{ys}E \tag{6.50}$$

uses the plastic constraint factor M = 2 for the case of plain strain. The value of δ_t at small clip gauge displacement is conservative.

As the specimen is opened r_p increases from zero up to a constant value as plastic collapse is approached. Since a constant value of r_p is used in equation (6.46) before plastic collapse is reached i.e. where r_p is still increasing then there would be a "middle range" where the CTOD will be less conservative.

When the clip gauge displacement is very large the elastic term δ_e is negligible. Ductile crack extension will have occurred so

that the compliance of the specimen will have changed. Consequently V_p as found by the standard will be greater than the true value of plastic clip gauge displacement. The error caused by this has been shown to be less than 5% from CTOD values determined using the changed compliance [149]. It means these results will be less conservative.

Using equation (6.46) the crack-tip opening displacement was calculated from the load-clip gauge displacement records of the specimens used for the CTOD-V_g calibration. The CTOD was calculated at the same load and clip gauge displacement as where the silicone-rubber replicas were taken of the crack tip. These results are presented in Table E.2 with the corresponding experimental and predicted CTOD results. Figure 6.33 shows the calculated ASTM CTOD against experimental CTOD measured from the silicone rubber replicas. At lower values of CTOD there are a mixture of conservative and non-conservative results before the CTOD using equation (6.46) diverges from the experimentally measured CTOD. Similarly Figure 6.34 shows the calculated ASTM CTOD against predicted CTOD using equation (6.38). Except for one result all ASTM values are less than the predicted results. This is expected since the predicted CTOD from equation (6.38) is greater than the experimental CTOD at low values of δ_t due to forcing the regression equation through the origin. At larger CTOD values the predicted and experimental CTOD are similar so if the ASTM CTOD values are conservative compared to experimental results then they will be conservative compared to the predicted CTOD.

Although there is divergence between the ASTM CTOD values and the predicted and experimental CTOD results at large values ($\delta_t \gtrsim 0.500$ mm) there is good agreement at low values of CTOD ($\delta_t \lesssim 0.500$ mm). It is important that when δ_t is small that there is good agreement since this includes the range of CTOD used to define the transition criteria for ductile to brittle transition. Over the range of conditions and the material considered the use of equation (6.38) appears to be justified.

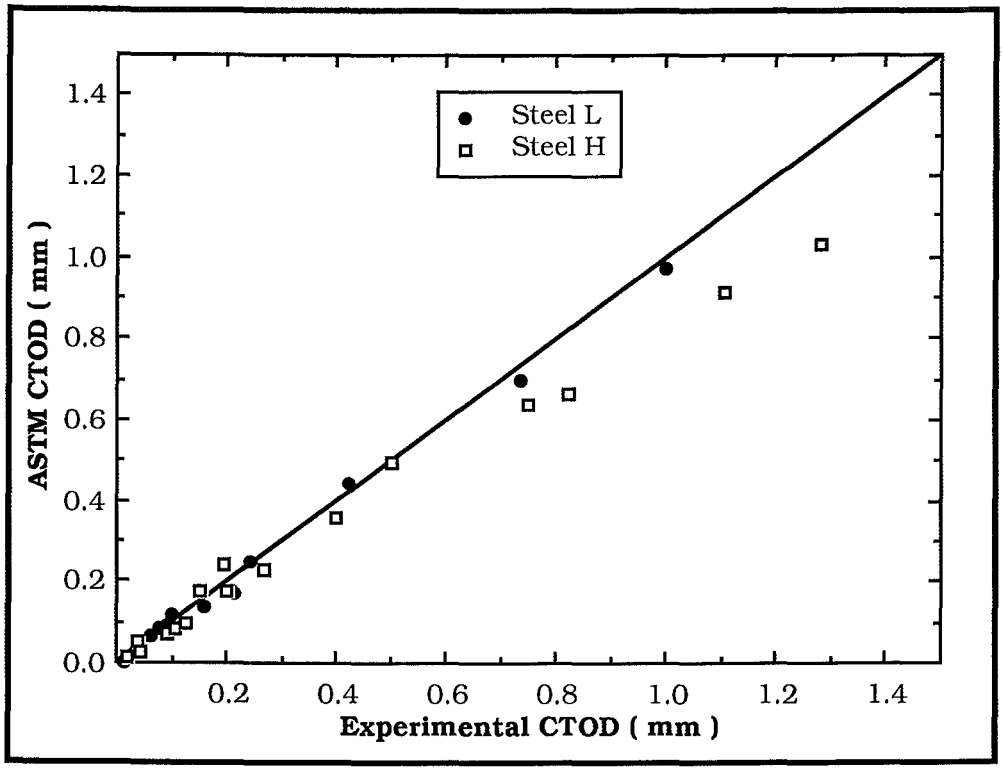

Figure 6.33 : ASTM CTOD (mm) [Equation (6.46)] as a function of experimental CTOD (mm) for Steels L and H.

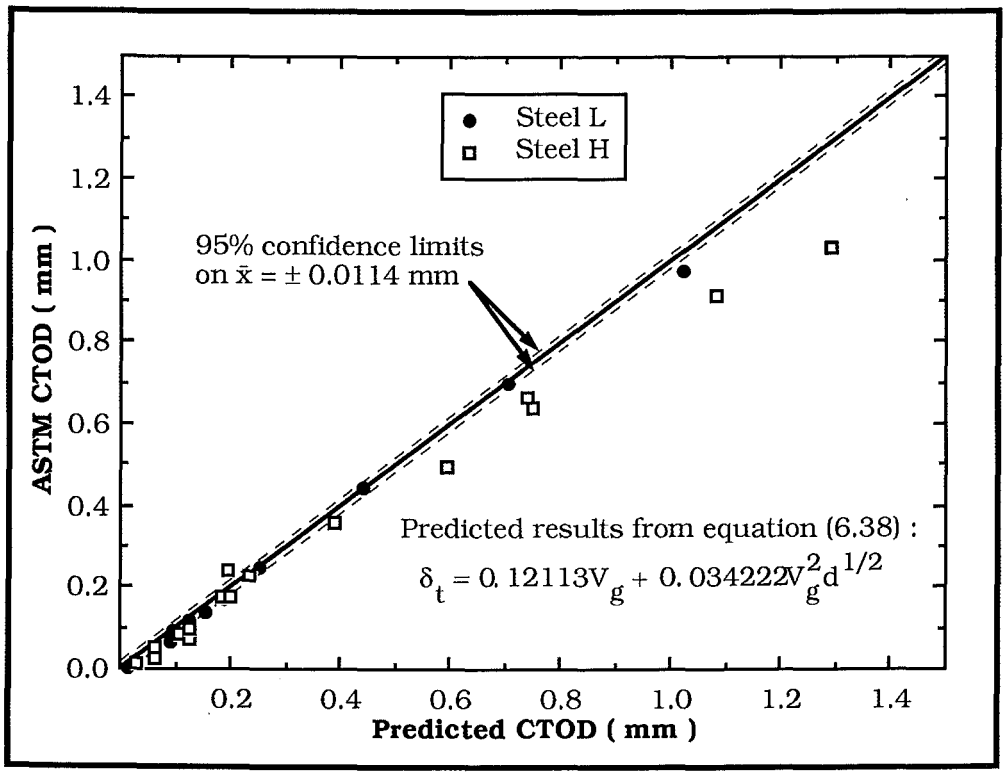

Figure 6.34 : ASTM CTOD (mm) [Equation (6.46)] as a function of predicted CTOD (mm) [Equation (6.38)] for Steels L and H.

6.2.7 *CTOD TRANSITION TEMPERATURE CRITERION (Initiation of Ductile Crack Extension)*

Slow stable crack extension often precedes either unstable brittle crack extension (pop-in) or a maximum load plateau [149]. Figure 6.15 shows silicone-rubber replicas on specimens exhibiting stable crack extension. The value of CTOD at initiation of ductile crack extension (under essentially plane-strain conditions) is regarded as being a "material property" [16,29,148,273,37,84]. Therefore, it is independent of geometry type and loading and Ebrahimi has found it to be independent of temperature above the ductile-brittle transition temperature [86].

Figure 4.16 showed results for Charpy V-Notch impact testing and the different criteria used to assess the transition temperature for ductile to brittle behaviour. For the present investigation the transition criterion used for Charpy V-Notch Impact testing was 27 Joules (20 ft lb) as discussed in Section 4.4.1. This was identified as the ductility transition temperature where ductile crack extension first appears. Therefore the same transition criterion will be used for CTOD testing, that is, where ductile crack extension first occurs.

The criterion for transition temperature in CTOD testing is commonly taken as the initiation value of stable crack extension [16,84,57,59,148]. Oda took this value as $\delta_i = 0.16$ mm, Ebrahimi used $\delta_i \approx 0.15$ mm and the Welding Institute's correlation of COD and Charpy V test data gave this as $0.10 \leq \delta_i \leq 0.20$ mm [57,59,84]. Other reference levels have been set for transition in CTOD or K_{IC} testing. Pisarski gave a review of correlations relating Charpy energy to K_{IC} in 1978 [55]. In his review Pisarski reported transition criteria of 100 MPa $m^{1/2}$ for K_{IC} tests on carbon-manganese and low alloy steels and of 28J for Charpy tests on the same steels. Thaulow used fracture appearance of both the COD and Charpy tests for transition [279]. It is logical though, if a comparison is to be made between Charpy and CTOD transition temperatures, that both are found from the same criterion, i.e. the ductility transition temperature.

A number of methods to determine the value of δ_i have been proposed and are referred to in BS5762:1979 but one method which is commonly used is the multi-specimen R-curve method. This method loads specimens to different amounts of crack growth, unloads the specimen and then the specimen is broken open, in liquid nitrogen for example. A curve of CTOD against crack extension

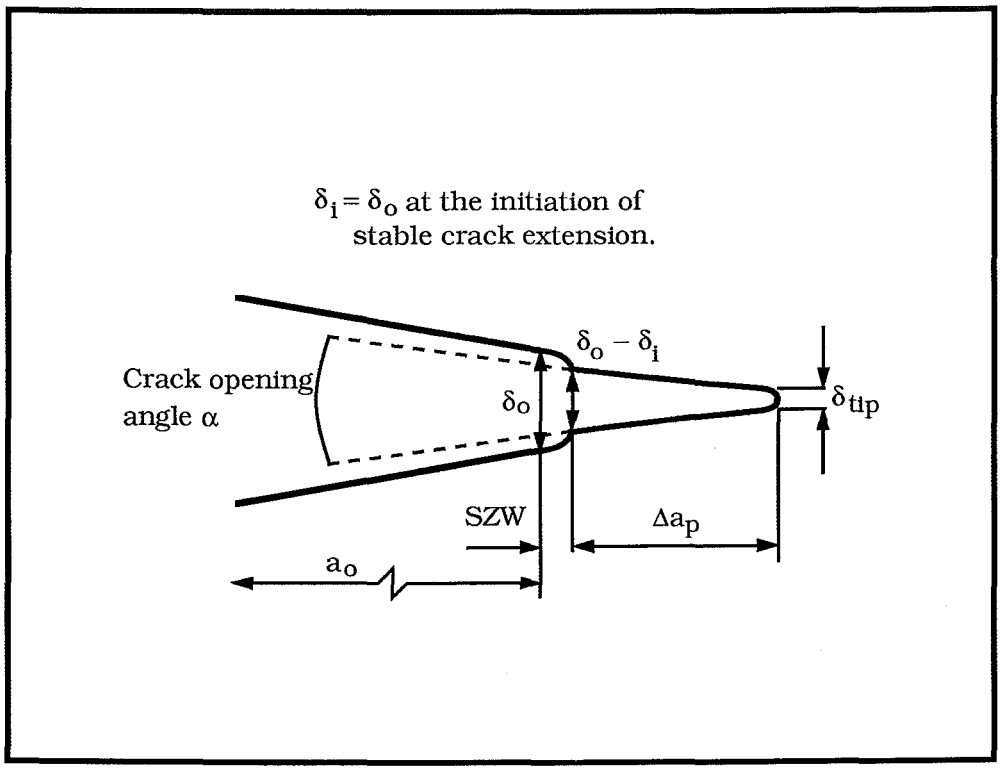

Figure 6.35 : The geometry of a growing ductile tear showing δ_i and the SZW [149].

is plotted and a regression line formed through these points. This is projected back to zero crack growth to give the initiation CTOD δ_i.

However BS5762:1979 and ASTM E1290-89 interpret crack extension differently. Consider Figure 6.35 which shows the definition of δ_i. The crack has opened and the tip of the crack has shifted due to plastic blunting. The width of the zone due to blunting at ductile crack initiation is the stretch zone width (SZW) which is usually taken as

$$\delta = 2SZW \tag{6.51}$$

from workers such as Fields and Miller [148,149]. Therefore the total crack length comprises

$$a_p = a_0 + SZW + \Delta a_p \tag{6.52}$$

where a_p is the total physical crack size, a_0 is the original crack length prior to testing and Δa_p is the length of stable crack growth (averaged over the specimen width). BS5762:1979 excludes the

stretch zone width in its measurement of crack extension. Therefore, when CTOD is plotted against Δa_p, δ_i is found at $\Delta a_p = 0$. Exclusion of the stretch zone width from the stable crack extension measurement can be very difficult and the width of the zone measured depends on the viewing angle [149].

ASTM E1290-89 includes the SZW in its measurement of crack extension following the procedure adopted in ASTM E813-87 for determining J_{IC} from J-Δa_p diagrams. The diagram formed from crack extension measurement (including SZW) has exclusion lines at $\Delta a_p = 0.15$ mm and $\Delta a_p = 1.5$ mm. The exclusion line at $\Delta a_p = 0.15$ mm is used to ensure Δa_p can be measured accurately [63]. The exclusion line at $\Delta a_p = 1.5$ mm is used to ensure Δa_p is generally less than 6% of the remaining uncracked ligament of the specimen tested. It means that the requirement $B>25\delta_c$ is met and net section yield does not occur i.e. plane-strain conditions prevail. If crack extension is large then curvature along the crack front is significant and the average crack length measurement has no physical significance.

A minimum of six points are used, one of which must lie between $1.0 \leq \Delta a_p \leq 1.5$ mm and one must be between $0.15 \text{ mm} \leq \Delta a_p < 0.5$ mm. ASTM E1290-89 forms a regression line through these points of the form

$$\delta = C_1.(C_2 + \Delta a_p)^{C3} \qquad (6.53)$$

where C_1, C_2 and C_3 are constants and Δa_p includes the SZW. If C_3 is not zero (i.e. the regression is a power curve) then this indicates plane strain conditions were not met. The intersection of the regression line with a 0.2 mm offset line determines the CTOD at the onset of ductile crack extension. The 0.2 mm offset was adopted for J_{IC} testing by the nuclear power industry, given as $J_{0.2}$ [282].

A graph of CTOD against crack extension was able to be plotted using results from:

(i) The correlation of CTOD against V_g using silicone-rubber replicas. On replicas which showed ductile crack extension the extension at mid-section was measured using optical microscopy and the shadowgraph tracings. The measured crack extension was correlated with the measured CTOD.

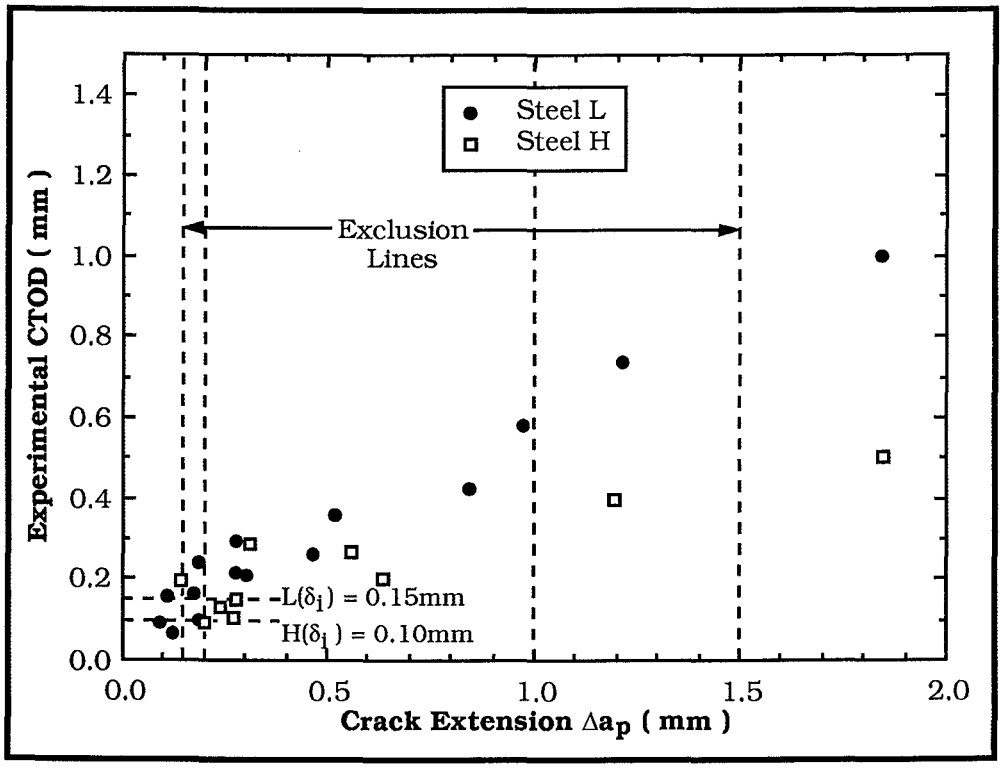

Figure 6.36 : CTOD (mm) as a function of stable crack extension, Δa_p ,(mm) for Steels L & H.

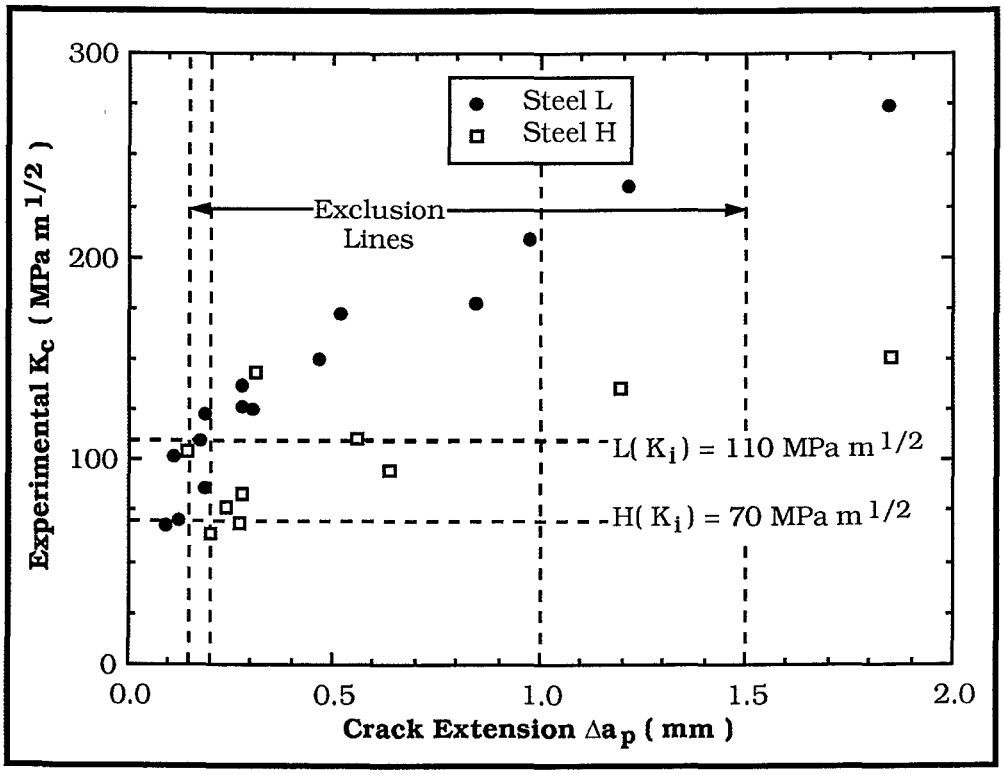

Figure 6.37 : K_c (MPa $m^{1/2}$) as a function of stable crack extension, Δa_p ,(mm) for Steels L & H.

(ii) Fracture Toughness Tests to find the temperature dependence of CTOD for the material tested. Specimens whose test record showed a maximum load plateau could not be used. However, where a test record showed some yielding (and possible stable crack extension) before either a significant "pop-in" or failure by cleavage then the CTOD and crack extension at the instability could be found due to the change in mode of failure.

The results of CTOD, K_c and crack extension are given in Table E.3. Figure 6.36 shows CTOD against crack extension up to Δa_p = 2.0 mm and Figure 6.37 shows K_c against crack extension up to Δa_p = 2.0 mm. Smith and Knott found that δ_i appeared to be unaffected by grain size [84]. Therefore results for the same steel but different grain sizes may be grouped together. The results for Steels L and H appear to diverge as crack extension increases so the results for each steel were analysed separately.

ASTM E1290-89 provides a simple BASIC program to find the regression line $\delta = C_1.(C_2 + \Delta a_p)^{C3}$. However since a multi-linear regression program had been used previously the analysis was done using this program. Several data sets were used since a number of points were close to but outside the exclusion lines or else some points were not representative of the trends of the data and could be excluded. The results of the CTOD regression analysis and the estimated δ_i at Δa_p = 0.2 mm are given in Table 6.8(a-b).

For Steel H the correlation coefficient is from 0.9026 to 0.9746 for equations (6.54a) to (6.54e) while each equation is significant at the 99.9% level. The standard error of estimate ranges from 0.032 for equation (6.54d) to 0.177 for equation (6.54e). The results for Steel L are similar with a correlation coefficient from 0.9348 to 0.9895 for equation (6.54f) to (6.54j) while each equation is significant at the 99.9% level. The standard error of estimate is from 0.0431 for equation (6.54g) to 0.275 for equation (6.54j).

For Steel H, δ_i has a range from 0.099 to 0.152 mm. The result at δ_i = 0.152 mm appears to be an exception however and δ_i for Steel H is about 0.100 mm. Due to the errors associated in measuring crack extension a more accurate figure is not necessary. For Steel L, δ_i has a range from 0.149 to 0.168 mm. From the regression analyses δ_i is about 0.150 mm for Steel L. These results are similar to other transition criteria found [57,59.84].

Table 6.8a
Results of Multiple-Linear Regression Analysis for CTOD-Δa_p correlation for Steel H

Type	Linear[1]	Linear[1]	Power[2]	Linear[1]	Power[2]
Δa_p (mm) Points excluded	–	0.141, 0.380	0.141, 0.380	0.141, 0.380, 1.85	0.141, 0.380, 1.85
Equation No.	6.54a	6.54b	6.54c	6.54d	6.54e
N	10	8	8	7	7
D.F.	8	6	6	5	5
R	0.0903	0.9746	0.9699	0.9610	0.9521
s($\hat{y}$)	0.0613	0.0363	0.1637	0.0332	0.1767
F-value	35	113	95	60	48
Equation Sig.	99.9%	99.9%	99.9%	99.9%	99.9%
Coefficients					
C_1	0.1074	0.0669	-	0.0481	-
C_2	0.2212	0.2502	-	0.2967	-
C_3	-	-	0.7470	-	0.7764
C_4	-	-	0.3340	-	0.3455
δ_i(mm)	0.152	0.117	0.100	0.107	0.099

1. Equation used is $\delta = C_1 + C_2\Delta a_p$
2. Equation used is $\delta = C_4\Delta a_p{}^{C_3}$
3. C_1, C_2, C_3 and C_4 are constants.

Table 6.8b
Results of Multiple-Linear Regression Analysis for CTOD-Δa_p correlation for Steel L

Type	Linear[1]	Linear[1]	Power[2]	Linear[1]	Power[2]
Δa_p(mm) Points excluded	–	0.094, 0.191, 0.280	0.094, 0.191, 0.280	0.094, 0.191, 0.280, 1.842	0.094, 0.191, 0.280, 1.842
Equation No.	6.54f	6.54g	6.54h	6.54i	6.54j
N	15	12	12	11	11
D.F.	13	10	10	9	9
R	0.9822	0.9895	0.9520	0.9798	0.9348
s($\hat{y}$)	0.0512	0.0431	0.2615	0.0443	0.2748
F-value	355	470	97	216	62
Equation Sig.	99.9%	99.9%	99.9%	99.9%	99.9%
Coefficients					
C_1	0.0659	0.0462	-	0.0392	-
C_2	0.5120	0.5262	-	0.5447	-
C_3	-	-	0.8319	-	0.8194
C_4	-	-	0.5685	-	0.5584
δ_i(mm)	0.168	0.151	0.149	0.148	0.149

1. Equation used is $\delta = C_1 + C_2\Delta a_p$.
2. Equation used is $\delta = C_4\Delta a_p{}^{C_3}$
   (Regression equation was $\log\delta = \log C_4 + C_3\log\Delta a_p$).
3. C_1, C_2, C_3 and C_4 are constants.

A transition temperature criterion must also be defined for K_c fracture toughness results found using

$$K_c = 0.4769\ (\sigma_{ys}\delta_c)^{1/2}\ \text{MPa m}^{1/2}. \qquad (2.93)$$

François and Krasowsky defined the transition of K_{IC} using the relationship between the thickness B of the specimen and $(K_{IC}/\sigma_{ys})^2$ [280]. They gave this as

$$B = \beta(K_{IC}/\sigma_{ys})^2 \qquad (6.55)$$

where β is a constant. When β is taken as 2.5 then equation (6.55) corresponds to the ASTM limit of validity for the thickness of K_{IC} specimens given by

$$B \geq 2.5(K_{IC}/\sigma_{ys})^2. \qquad (2.53)$$

However since K_c is found using the CTOD then the same method used to find δ_i can be used to find the value of K_C at initiation of stable crack extension, although this will be affected by grain size due to the dependence of K_c on yield strength. For Steel H, for example, δ_i = 0.100 mm gives K_c = 67.1 MPa $m^{1/2}$ for HD and K_c = 82.3 MPa $m^{1/2}$ for HA. This variation is considered insignificant for the purpose of defining the transition criterion.

Results of K_c and crack extension are given in Table E.3 and K_c against crack extension are plotted on Figure 6.37. The regression analysis was calculated separately for Steels L and H.

The data used for equation (6.54f) was used for Steel L's analysis and the data used for equation (6.54b) was used for Steel H's analysis. A regression analysis was made of each data set based on

$$K_c = A_0 + A_1\Delta a_p \qquad (6.56)$$

where A_0 and A_1 are constants and

$$K_c = A_0 + A_1 \ln\Delta a_p \qquad (6.57)$$

where A_0 and A_1 are constants. These results are given in Table 6.9. Similarly to the results for CTOD versus Δa_p each equation is

significant at the 99.9% level and the correlation coefficient R has a range between 0.9514 for equation (6.56a) to 0.9748 for equation (6.57a). At Δa_p = 0.2 mm these results give an initiation value of fracture toughness K_i from 109 to 112 MPam$^{1/2}$ for Steel L and from 65 to 75 MPa m$^{1/2}$ for Steel H. From these results the initiation fracture toughness was set at 110 MPa m$^{1/2}$ for Steel L and at 70 MPa m$^{1/2}$ for Steel H.

Table 6.9
Results for Steels L and H of the Multiple-Linear Regression Analysis on K_c-Δa_p Correlation.

Steel	H		L	
Type	Linear[1]	Log[2]	Linear[1]	Log[2]
Δa_p (mm) Points excluded	0.141, 0.310	0.141, 0.310	-	-
Equation No.	6.56a	6.57a	6.56b	6.57b
N	8	8	15	15
D.F.	6	6	13	13
R	0.9514	0.9748	0.9538	0.9669
s($\hat{y}$)	10.53	7.63	18.63	15.81
F-value	57	114	131	187
Equation Sig. Coefficients	99.9%	99.9%	99.9%	99.9%
A_0	64.70	126.28	86.95	212.40
A_1	51.57	38.19	113.21	62.65
K_i (MPa m$^{1/2}$)	75.02	64.81	109.60	111.57

1. Equation used is $K_c = A_0 + A_1\Delta a_p$, A_0 and A_1 are constants.
2. Equation used is $K_c = A_0 + A_1 \ln\Delta a_p$, A_0 and A_1 are constants.

The transition criteria for fracture toughness testing are given in Table 6.10.

Table 6.10
Transition Temperature Criteria for Fracture Toughness Testing

Steel	CTOD (mm)	K_c (MPa $m^{1/2}$)
L	0.150	110
H	0.100	70

Having established the CTOD-V_g correlation and the fracture mode transition criteria it is now possible to examine the temperature dependence of the fracture toughness of the experimental steels.

6.3 Fracture Toughness Test Results

Fracture toughness testing was performed as described in Section 6.1 to give the temperature dependence of K_{IC} and CTOD for Steels L and H. The critical events for toughness values were assessed using standard interpretations.

6.3.1 ANALYSIS OF LOAD-DISPLACEMENT RECORDS

The test record provided data to assess a number of results for each specimen. Results were assessed at the original crack tip length as recommended by Dawes [37]. The results assessed were:

(a) Apparent Fracture Toughness, K_Q

Using ASTM E399-83 the apparent fracture toughness at the instability load P_Q for CT specimens is given by

$$K_Q = P_Q Y / BW^{1/2} \qquad (6.58)$$

where B is the specimen thickness

W is the specimen width

a_0 is the original crack length to the tip of the fatigue crack

and $$Y = (2+a_0/W)(0.886+4.64a_0/W-13.32(a_0/W)^2 + \frac{+14.72(a_0/W)^3-5.6(a_0/W)^4)}{(1-a_0/W)^{3/2}} . \quad (6.48)$$

Values of Y are tabled in ASTM E399-83 (and also ASTM in E1290-89) for $0.45 \leq a_0/W \leq 0.55$. The series expansion for Y was given by Srawley as accurate to within ±0.4% over the range of a_0/W from 0.2 to 1 [281].

The thickness dependence of K_Q was assessed using

$$a_0, b_0, B \geq 2.5(K_Q/\sigma_{ys})^2 \quad (6.59)$$

where $b_0 = W-a_0$ is the uncracked ligament length and σ_{ys} is the yield strength of the material at test temperature. If this was satisfied the apparent fracture toughness K_Q was accepted as the valid thickness independent plane-strain fracture toughness K_{IC}.

(b) Critical Crack-Tip Opening Displacement, δ_c

The critical CTOD was evaluated using two different equations. CTOD was found using

$$\delta_c = A_1V_g + A_2V_g^2d^{1/2} \quad (6.38)$$

where δ_c is the critical CTOD in mm, $A_1 = 0.121113$, $A_2 = 0.034222$ $m^{-3/2}$, $d^{1/2}$ is the square root of grain size in $mm^{1/2}$ and V_g is the total clip gauge displacement in mm at the point of instability.

The critical CTOD was also found using

$$\delta_c = \frac{K^2(1-\nu^2)}{2\sigma_{ys}E} + \frac{r_pb_0V_p}{(r_pb_0 + a_0 + z)} \quad (6.46)$$

where K, σ_{ys}, E, P, ν, V_p, z, r_p, b_0 and Y are as defined in Section 6.2.6. This is the assessment used by ASTM E1290-89 to find the critical CTOD.

(c) Apparent Fracture Toughness K_c using δ_c

In Section 2.2.3 it was shown that the fracture toughness for limited yielding around the crack tip could be written as

$$K_c = (E'M\sigma_{ys}\delta_c)^{1/2} \quad (2.92)$$

where $1 \leq M \leq 2$ and $E' = E$ for plane stress and $E' = E/(1-\nu^2)$ for plane strain. Using $E = 207 \times 10^3$ MPa and $\nu = 0.3$ for steel Chew wrote this as

$$K_c = 0.4769(\sigma_{ys}\delta_c)^{1/2} \qquad (6.60)$$

for $M = 1$, σ_{ys} is in MN m^{-2} and δ_c is in μm [16]. The fracture toughness was also found using critical values of δ_c and the yield stress at the test temperature substituted into equation (6.60).

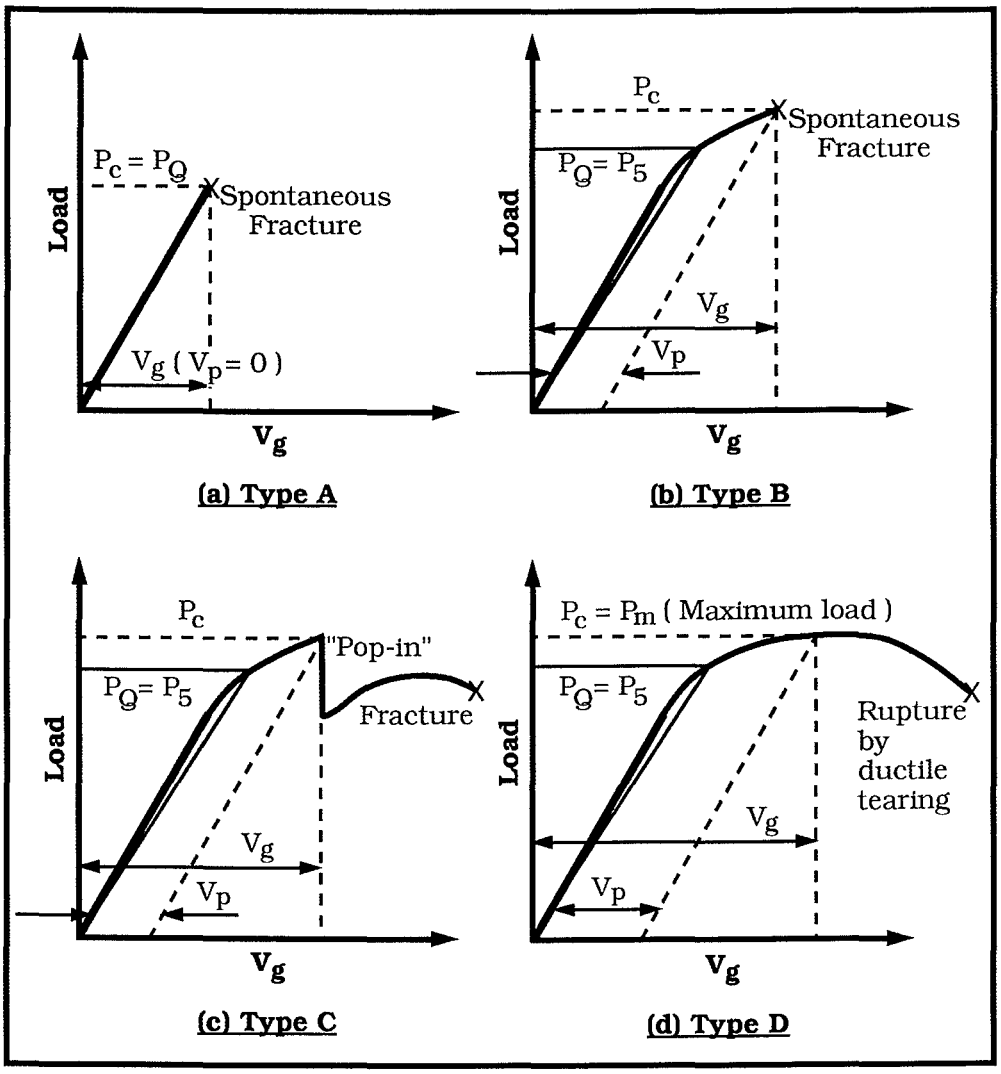

Figure 6.38 : Schematics of load-clip gauge displacement records.
(a) Type A; spontaneous fracture in elastic region.
(b) Type B; yielding before spontaneous fracture.
(c) Type C; "pop-in" with stable crack extension.
(d) Type D; stable crack extension with maximum load plateau.

(d) Critical values of CTOD and Load

Typical test records are shown in Figures 6.38(a-d). Figure 6.38a shows a test where unstable brittle fracture of the specimen has occurred in the linear region of the test record. For tests of this type the critical instability occurs at $P_Q = P_C$ and there is little or no plastic yielding in the material so $V_p = 0$. Therefore K_Q and δ_c are calculated from the same position.

Figure 6.38b shows a test where yielding has occurred around the crack tip. Depending on how far the test proceeds stable crack extension may or may not have occurred. While the load is still rising spontaneous brittle fracture occurs and the specimen fails. The critical CTOD is calculated at the point of spontaneous fracture as shown in Figure 6.38b. The apparent fracture toughness K_Q is calculated from the load $P_Q = P_5$. The load P_5 comes from the intersection of the secant line OP_5 with the load-displacement record. The secant line is drawn through the origin of the test record with the slope $(P/V_g)_5 = 0.95(P/V_g)$ where (P/V_g) is the slope of the initial elastic part of the record i.e. OP_5 has a slope 5% less than the initial linear part of the record. If every load preceding P_5 is lower than P_5 then $P_Q = P_5$ otherwise the higher load preceding P_5 is P_Q (this happens if "pop-in" occurs). This follows the procedure established by ASTM E399-83 [23]. In this case K_Q and δ_c are calculated at different events.

Figure 6.38c shows a test record which is an extension of Figure 6.38b. In this case the test record shows a "pop-in" after some yielding and possible crack extension have occurred at the crack tip but the load curve is still rising. The unstable brittle fracture has then arrested and stable crack extension continues. Maximum load after "pop-in" may or may not exceed the load at "pop-in" depending on the size of the "pop-in". If it does not exceed the load at "pop-in" then the critical instability is taken as the clip gauge displacement and load at "pop-in". When "pop-in" is followed by a rising load curve then "pop-in" may be ignored on the basis of a method given by ASTM E1290-89; the drop in load has to be small and recovery is rapid [44]. In this case maximum load is the critical event. However the crack may arrest for a number of reasons but one may be that the crack driving force drops since the response of the machine is not fast enough [149]. Some consider that without exception "pop-in" may not be ignored. It is likely that for

inhomogeneous materials (e.g. weld metals) small "pop-ins" may occur due to fortuitous positioning of the fatigue crack. In homogeneous material the "pop-in" is likely to be a material characteristic. $\delta_c = \delta_u$ if the critical event is at "pop-in" or $\delta_c = \delta_m$ if it is at maximum load. The apparent fracture toughness K_Q will be found using the 5% offset secant line.

Figure 6.38d shows a test record where the specimen has reached a maximum load plateau and substantial yielding and stable crack extension have occurred. The apparent fracture toughness K_Q is again found using the 5% offset secant line. The critical CTOD value is found at the clip gauge displacement where load first reaches maximum load and then $\delta_c = \delta_m$. To calculate δ_m the crack length used is a_0, the length of the initial fatigue crack, which means δ_m has physical significance. It is a practical alternative to use since the ductile tear will grow rapidly after maximum load is reached and it is not possible to distinguish between tearing before and after maximum load.

To use δ_m as the critical CTOD follows the practice of the British Welding Institute since δ_i is regarded as being too conservative [149]. It is argued that since δ_i represents a point low down on the R-curve and the specimen remains intact well beyond δ_i, then the structure will behave similarly. Chipperfield argued against using δ_m since it is geometry and thickness dependent whereas δ_i represented a constant value [283]. However Towers and Garwood have shown that, although maximum load toughness parameters (δ_m or J_m) are test-piece geometry dependent, conservative estimates of the toughness at which structural ductile instability occurs will be predicted [282,284]. Towers and Garwood used the R-curve to demonstrate that under load control maximum load corresponds to the point of instability for sustained loading.

Under displacement control loading can be continued past maximum load with no instability occurring, with a corresponding reduction in load level. Hence the maximum load point will occur at a lower displacement than ductile instability irrespective of the system energy for displacement control and conservative toughness values result [284].

The standards specify testing with full thickness specimen of the structure under investigation [41,44]. Chew assessed critical values of CTOD in the same manner for the load-displacement

records represented by Types A-D but concluded that the behaviour represented by Figures 6.38(c-d) did not provide meaningful data on the instability of the crack-tip material if $\delta_c = \delta_m$ or δ_u was significantly greater than δ_i [16]. However if δ_m or δ_u is found from the original crack-tip length then it will have physical significance. If the size criterion given by

$$B > 25\delta_c \tag{6.61}$$

is met then the critical CTOD will provide information on the instability of the material and not just for the specimen size concerned. For a nominal thickness of B = 15 mm then δ_c must be less than 0.600 mm.

(e) Rate of Loading

From the initial linear portion of the graph the rate of increase of the stress intensity factor was found from the slope and the crosshead speed. Crosshead speed was set at 0.5 mm/min which gave a rate of loading between 0.463 and 0.689 MPa $m^{1/2}$ s^{-1}.

6.3.2 THE TEMPERATURE DEPENDENCE OF δ_c RESULTS

The material properties and constants used to calculate toughness results are given in Table 6.11. Equations (5.59) and (5.61) were used to calculate lower yield stress at test temperature for steels L and H respectively. The values of E and ν were taken from "The Mechanical and Physical Properties of the British Standard En Steels" by Woolman and Mottram [285]. The results for CTOD and K_{IC} testing are given in Appendix D. These include specimen identification, test temperature, yield strength, type of critical CTOD, critical CTOD load P_c, critical apparent fracture toughness load P_Q, critical CTOD found using equations (6.38) and (6.46), K_c found using equation (6.60) and K_Q found using equation (6.58) and whether or not this is a valid K_{IC} result.

Figures 6.39 and 6.40 show critical CTOD against temperature and critical CTOD against yield stress respectively for Steel L. Figures 6.41 and 6.42 show critical CTOD against temperature and critical CTOD against yield stress respectively for Steel H. Critical CTOD is δ_c calculated by equation (6.38). Graphs of δ_c versus σ_{ys} were plotted following the investigation of work-hardening on fracture toughness by Petch and Armstrong [183].

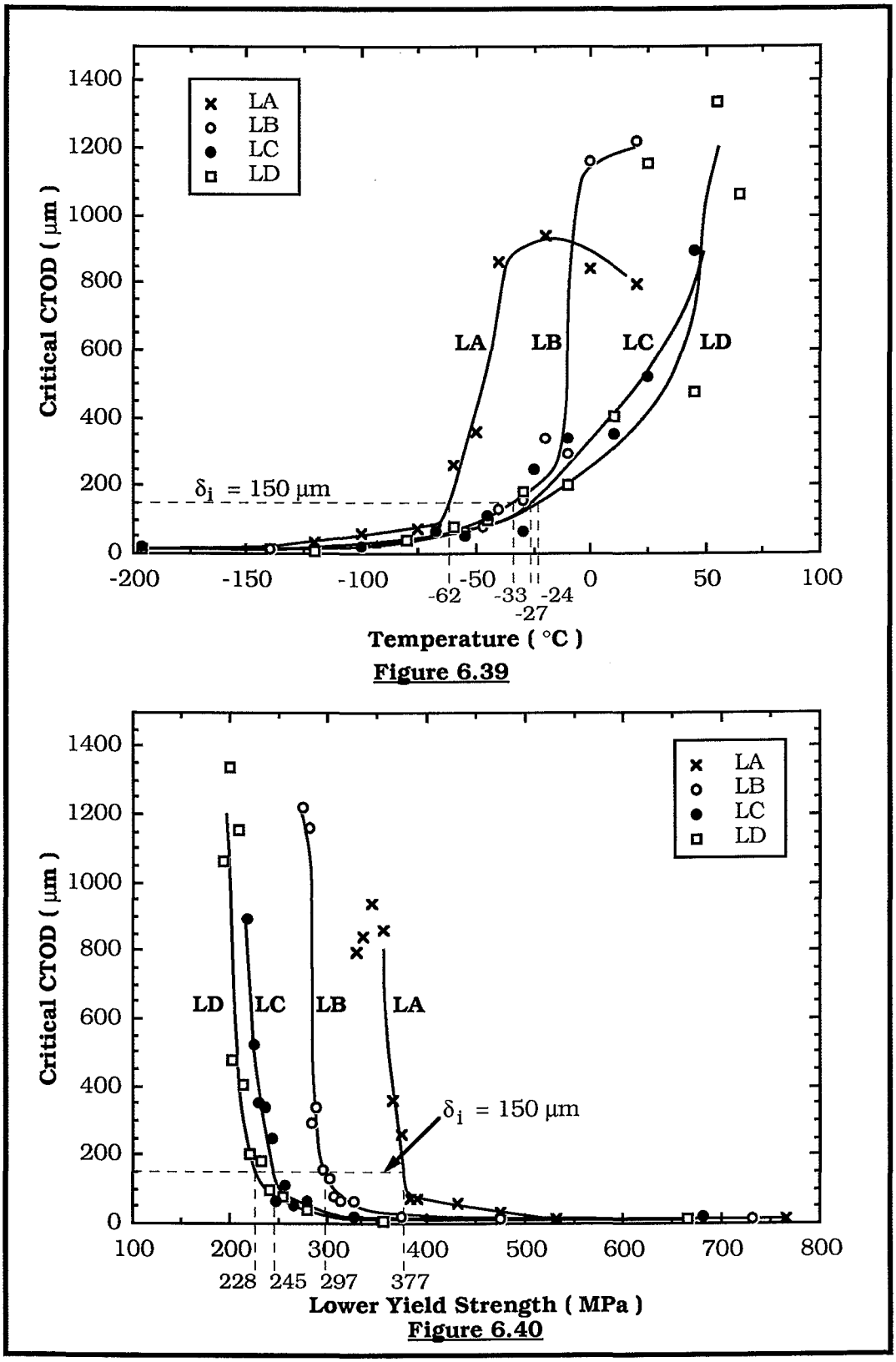

Figure 6.39 : Critical CTOD (μm) as a function of test temperature (°C) for Steel L.

Figure 6.40 : Critical CTOD (μm) as a function of lower yield strength (MPa) for Steel L.

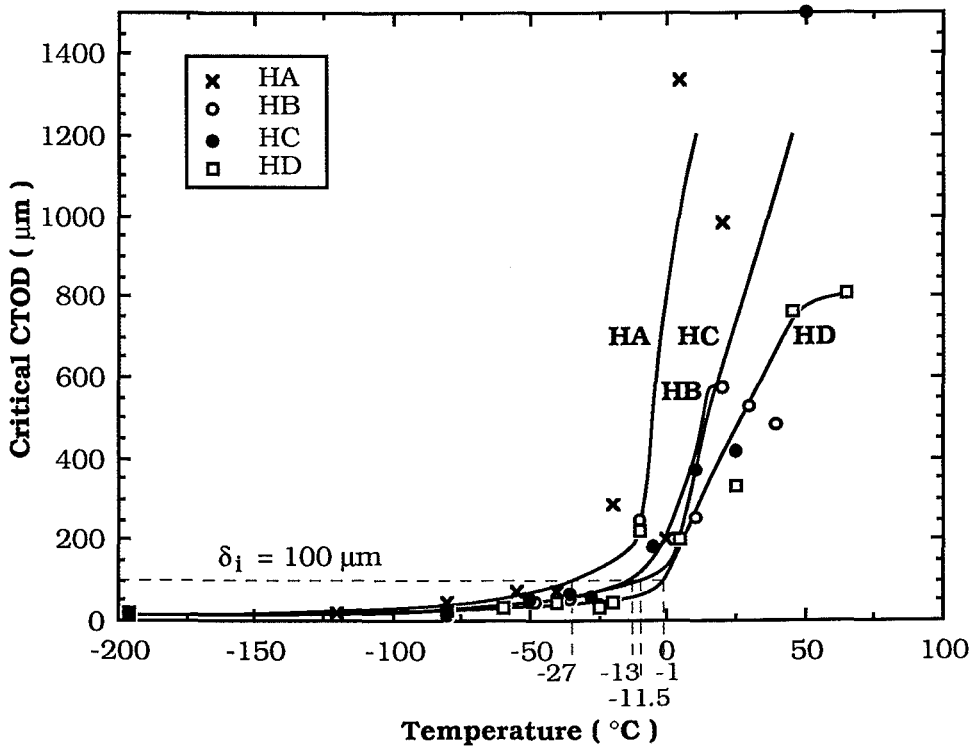

Figure 6.41

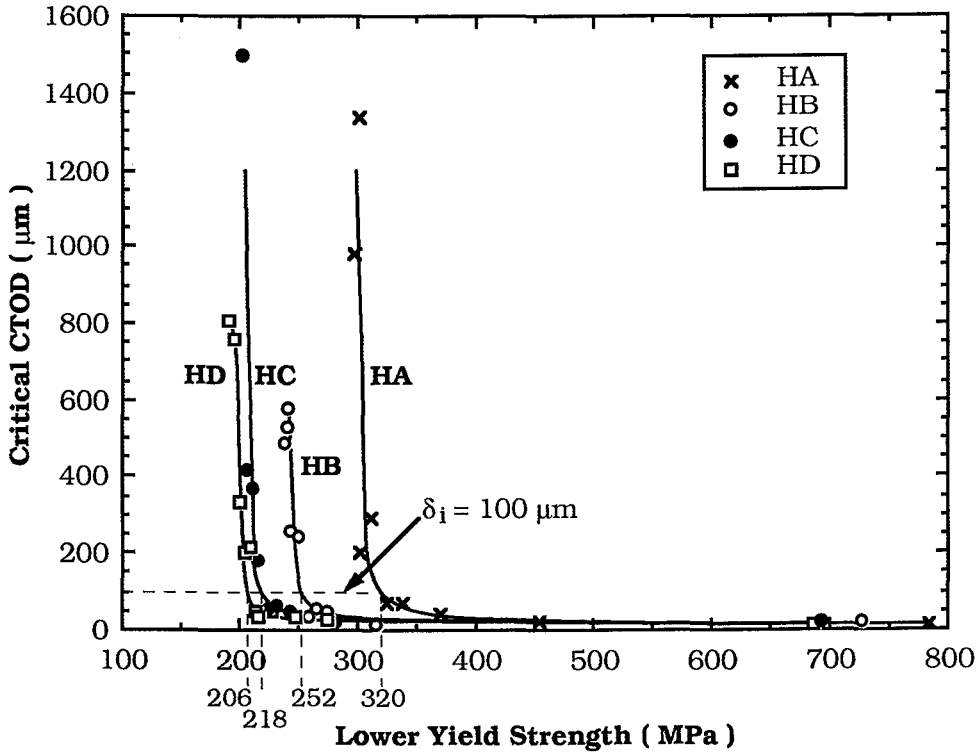

Figure 6.42

Figure 6.41 : Critical CTOD (μm) as a function of test temperature (°C) for Steel H.

Figure 6.42 : Critical CTOD (μm) as a function of lower yield strength (MPa) for Steel H.

Table 6.11
Material Properties and Constants used for Calculating CTOD and K_Q

Steel	L	H
E(GPa)	210	210
ν	0.3	0.3
$d^{-1/2}$ ($mm^{-1/2}$)		
A	9.939	8.440
B	7.262	5.995
C	4.941	4.531
D	4.218	4.187
σ_{ys}(MPa)	Equation (5.59)	Equation (5.61)
r_p		
$a_0/W \leq 0.5$	0.47	0.47
> 0.5	0.46	0.46

The results for Steel L and Steel H show that with increasing temperature (or decreasing yield stress) there is a rapid transition from low to high CTOD values. For example the toughness for LA increases from δ_c = 71.5 μm at -67.5°C to δ_c = 863 μm at -40°C. For HB toughness increases from δ_c = 38.2 μm at -25°C to δ_c = 256 μm at 10°C, up to δ_c = 575 μm at +20°C. The transition occurred with a change in fracture mode from cleavage to microvoid coalescence with increasing temperature. This indicates that the fracture resistance was sensitive to the type of microfracture mechanism in both CTOD and impact testing of low strength steels, similar to results from Chew and Ebrahimi [16,86].

Figures 6.40 and 6.42 show the dependence of critical CTOD on the yield strength of the material. There is a large increase in critical CTOD for only a small decrease in yield strength of the material. For example for LA toughness increases from δ_c = 71.5 μm at σ_{ys} = 383 MNm^{-2} (-67.5°C) to δ_c = 863 μm at σ_{ys} = 357 MNm^{-2} (-40°C). For HB toughness increases from δ_c = 38.2 μm at σ_{ys} = 258 MNm^{-2} (-25°C) to δ_c = 575 μm at σ_{ys} = 242 MNm^{-2} (+20°C). The yield stress results do not include an increase in yield stress due to strain-ageing in the plastic zone around the crack tip caused by

fatigue. This would affect Steel H, and would shift its transition curves.

The fracture mode transition curves plotted on Figures 6.39 and 6.41 were drawn with the help of "lines of best fit" drawn through the experimental results of Figures 6.40 and 6.42 for Steels L and H respectively. From the temperature dependence of yield strength then the temperature dependence of the critical CTOD can be found and fracture mode transition curves may be plotted.

Both Steels L and H showed separate transition curves for each of the grain sizes. Therefore, the CTOD test could distinguish between grain size. With increasing grain size the transition temperature was generally increasing. The transition temperatures at δ_i = 0.15 mm for Steel L and at δ_i = 0.10 mm for Steel H are identified and given in Table 6.12. To compare the different transition criteria transition temperatures were also found at δ_i = 0.10 mm for Steel L and at δ_i = 0.15 mm for Steel H. Discussion of these results is given in Section 7.2.

The size criterion means that when $\delta_c \geq 0.600$ mm the results are not size independent. Since a, B, W-a $\geq 25\delta_i$ is clearly met for δ_i = 0.15 mm or δ_i = 0.10 mm and nominal dimensions of a = B = W/2 = 15 mm then the transition temperature results are thickness independent. The transition temperature will be affected by a change in constraint such as an increase in the crack length to width ratio (a_0/W) which increases constraint and therefore the transition temperature [86].

6.3.3 THE TEMPERATURE DEPENDENCE OF K_c RESULTS

Figures 6.43 and 6.44 show the dependence of K_c (from equation (6.60)) on temperature and yield strength respectively for Steel L. Figures 6.45 and 6.46 show the dependence of K_c (from equation (6.60)) on temperature and yield strength respectively for Steel H.

Similarly to the critical CTOD fracture toughness, K_c shows a rapid transition over a small temperature range for increasing temperature or decreasing yield strength. For example the toughness of LA increases from K_c = 78.9 MPa $m^{1/2}$ at -67.5°C to K_c = 265 MPa $m^{1/2}$ at -40°C.

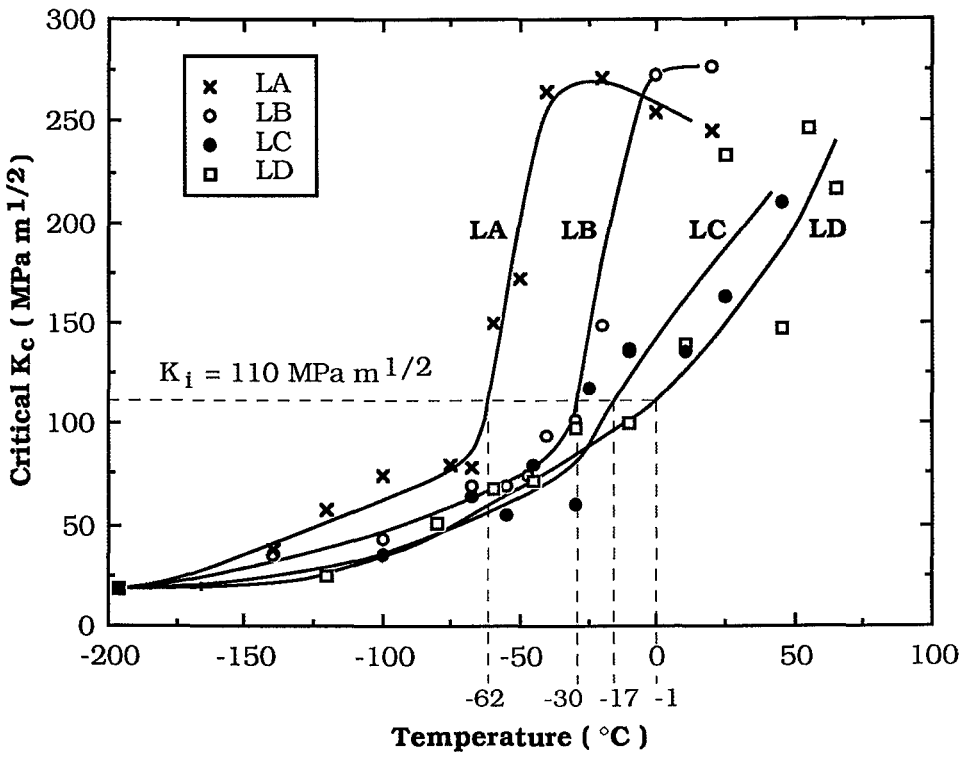

Figure 6.43

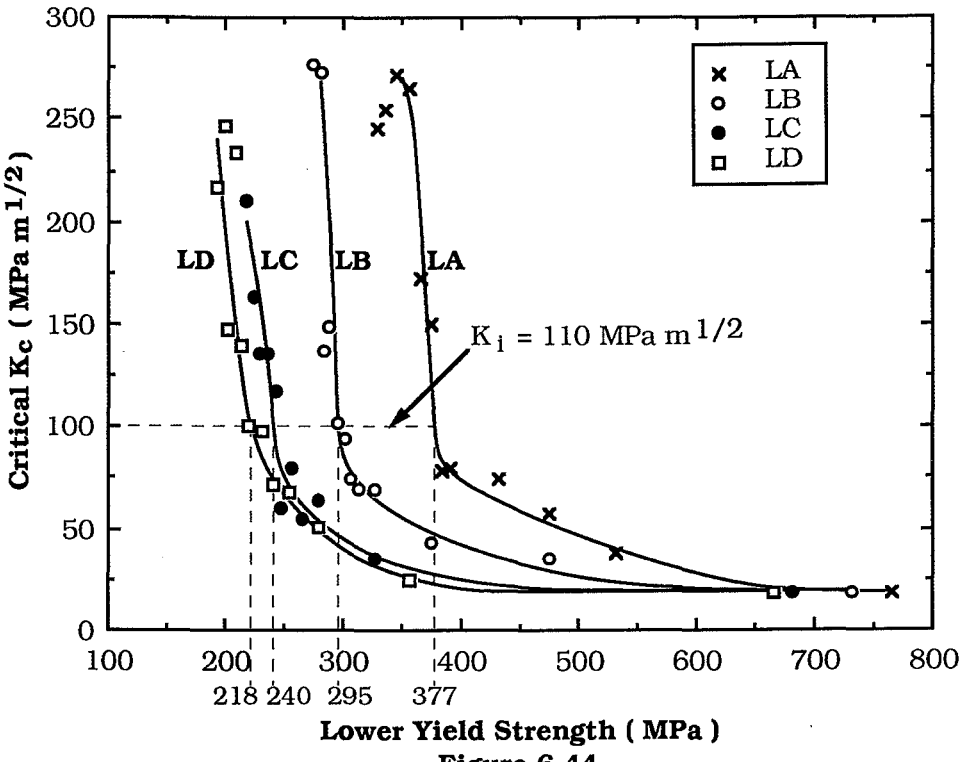

Figure 6.44

Figure 6.43 : Critical K_c (MPa m$^{1/2}$) [Equation (6.60)] as a function of test temperature (°C) for Steel L.

Figure 6.44 : Critical K_c (MPa m$^{1/2}$) [Equation (6.60)] as a function of lower yield strength (MPa) for Steel L.

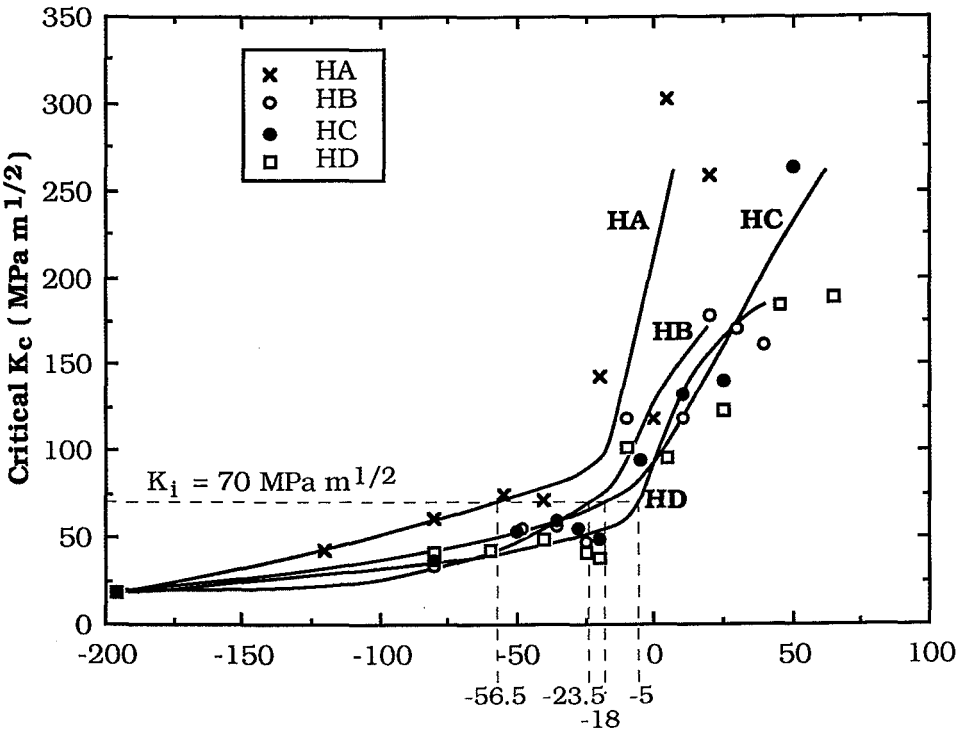

Figure 6.45

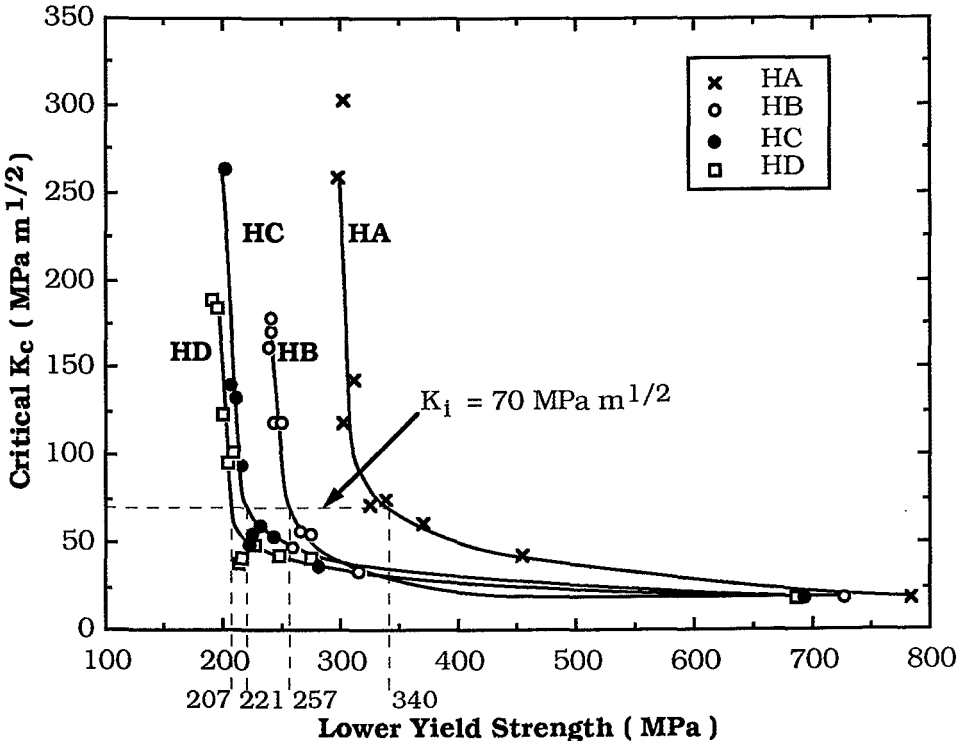

Figure 6.46

Figure 6.45 : Critical K_c (MPa $m^{1/2}$) [Equation (6.60)] as a function of test temperature (°C) for Steel H.

Figure 6.46 : Critical K_c (MPa $m^{1/2}$) [Equation (6.60)] as a function of lower yield strength (MPa) for Steel H.

This represents a change in fracture mode from cleavage to ductile fracture and indicates the sensitivity of fracture toughness to fracture mechanism. The change in fracture mode also occurs for a small change in yield strength.

Again the fracture mode transition curves of Figures 6.43 and 6.45 were drawn with the help of "lines of best fit" drawn through the K_c-σ_{ys} experimental results of Figures 6.44 and 6.46 for Steels L and H respectively.

The transition temperatures at K_i = 110 MPa $m^{1/2}$ for Steel L and K_i = 70 MPa $m^{1/2}$ for Steel H from Figures 6.43 and 6.45 respectively are given in Table 6.12. Again to compare transition criteria transition temperatures were also found at K_i = 70 MPa $m^{1/2}$ for Steel L and at K_i = 110 MPa $m^{1/2}$ for Steel H. These results are discussed in Section 7.2.

Table 6.12
Transition Temperatures for Fracture Toughness Testing.

Transition Temperature	$\delta_{0.15}$ (°C)	$\delta_{0.10}$ (°C)	K_i(110) (°C)	K_i (70) (°C)
Steel				
LA	-62	-65	-62	-86
LB	-33	-47.5	-30	-57
LC	-27	-35.5	-17	-37
LD	-24	-37	-1	-49
HA	-20	-34	-15	-56.5
HB	-5.5	-13	-8	-23.5
HC	+3	-11.5	+3.5	-18
HD	+2	-1	-1	-5

6.3.4 MODE OF FRACTURE FOR δ_c AND K_c

The transition curves given in Figures 6.39, 6.41, 6.43 and 6.45 are drawn through experimental data which show scatter about these lines. The lines represent an approximation to an average expected value of toughness over the temperature range considered.

The transition for both steels is accompanied by a change in fracture mode. Figure 6.47 shows the fracture appearance from LA and LD against test temperature and the corresponding fracture mode transition curves for critical CTOD.

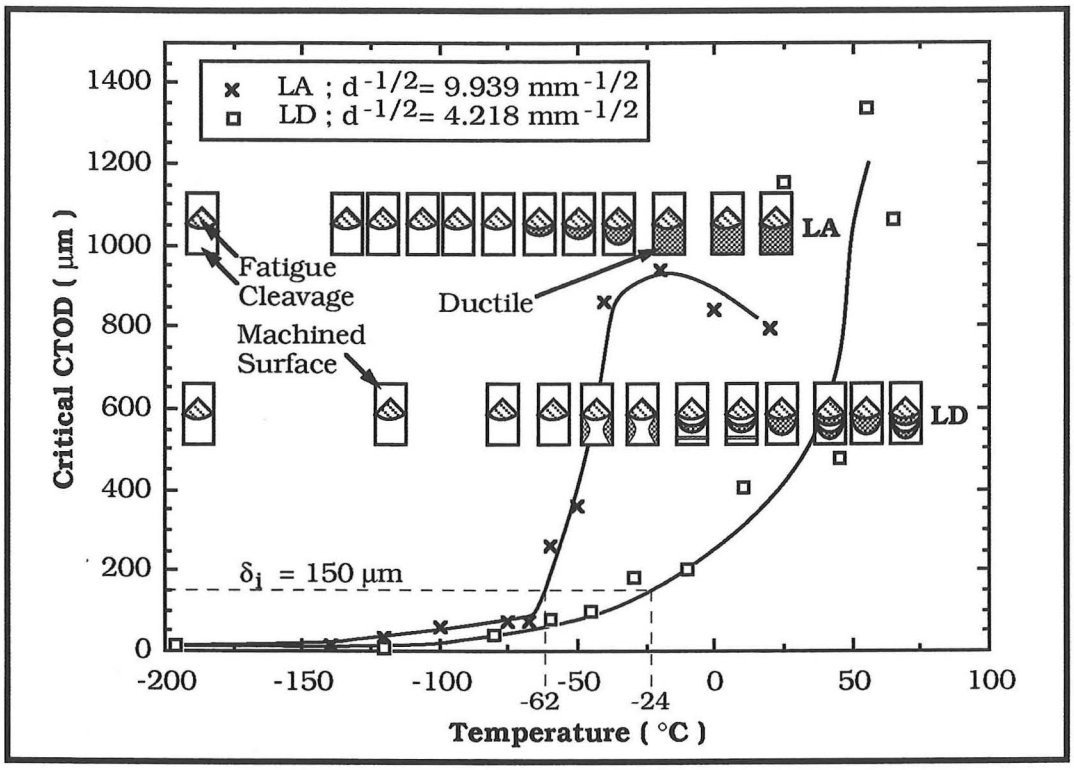

Figure 6.47 : Schematic of fracture appearance for LA & LD as a function of test temperature (°C).

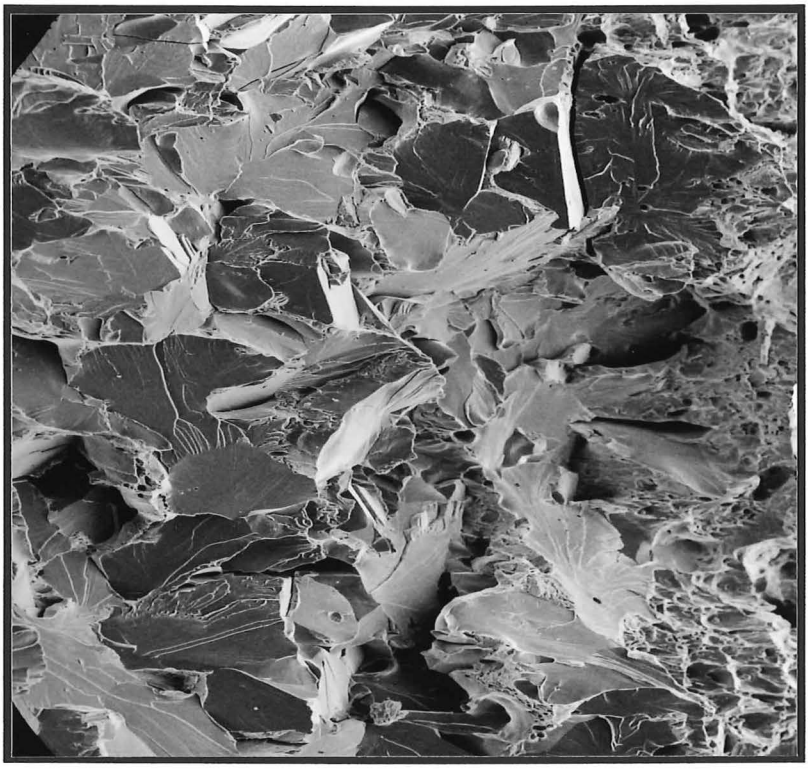

Figure 6.48 : Cleavage fracture (x210).

0.1 mm

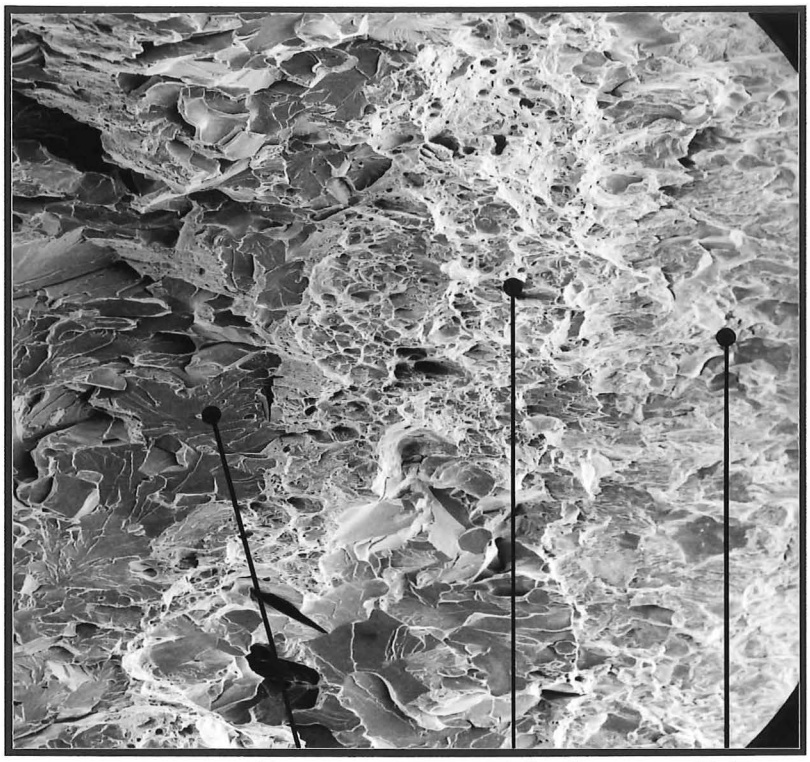

Figure 6.49 : Transitional behaviour; a mixture of cleavage fracture and microvoid coalescence (x140).

0.1 mm

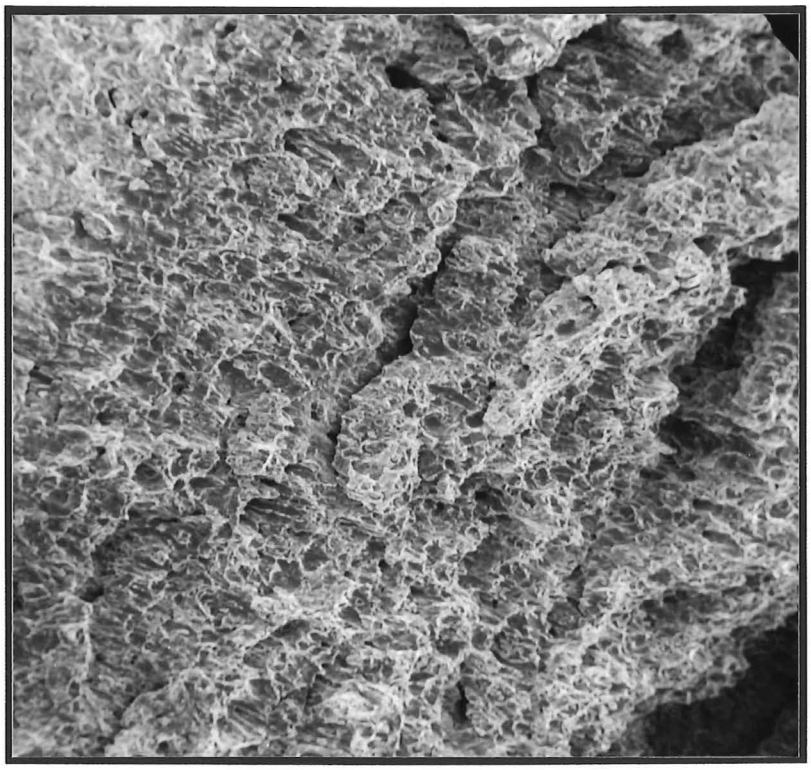

Figure 6.50 : Ductile fracture by microvoid coalescence (x136).

0.1 mm

There are three distinct regions using the fracture appearance as a guide; (I) lower shelf CTOD where failure is 100% brittle, (II) a transition where failure is mixed brittle and ductile and (III) upper shelf CTOD where failure is 100% ductile.

(a) Region I

Up to -67.5°C for LA and -60°C for LD the fracture appearance is 100% brittle fracture. Failure is by cleavage as shown in Figure 6.48 by scanning electron microscopy. The load-displacement record is linear up to spontaneous fracture (Type A - Figure 6.38a) although with increasing temperature more yielding will occur at the crack tip and the load-displacement record will show deviation from linearity at fracture (Type B - Figure 6.38b).

Figure 3.17 showed three types of fracture behaviour described in Section 3.4.4. Type I fracture occurred at low temperature when the yield stress is high, greater than the ferrite matrix strength and the carbide strength (shown in Figure 3.13). Cleavage microcracks form at a small distance ahead of the crack tip and once the nucleation condition

$$\tau_{ys} - \tau_i \geq [24\mu\gamma/\pi(1-\nu)d]^{1/2} \qquad (3.3)$$

is satisfied unstable cleavage fracture develops. Fracture is then nucleation controlled.

With increasing temperature and decreasing yield strength Type II fracture occurs. The carbide strength exceeds the yield strength and the ferrite matrix strength. Cleavage microcracks form only after some strain-hardening has occurred in the plastic zone ahead of the crack tip. Cracks (whether cracked particles or by intersecting slip planes) which satisfy the dynamic criterion for propagation (Equations (3.6) or (3.26)) become the source for cleavage fracture. Statistical competition, described in Section 3.2.6, between nucleation sites will determine the level of toughness found. Fracture is propagation controlled.

(b) Region II

From -60 to -40°C LA shows some stable ductile crack extension before failure by cleavage. This occurs in the transition region from cleavage to ductile behaviour. The transition region for LD is much larger, from -45°C up to the limit tested at +65°C. Petch showed that a smaller grain size would have a steeper transition

curve than a larger grain size [180]. Failure is a mixture of cleavage and microvoid coalescence as shown in Figure 6.49 from scanning electron microscopy. The percentage of microvoid coalescence increases with increasing temperature.

The load-displacement record changes with increasing temperature. For LA the region of yielding and stable crack extension increases before failure by cleavage fracture from -60 to -40°C (Type B - Figure 6.38b). However at -40°C the load reaches a maximum before failure occurs by cleavage. The area of ductile fracture increases and CTOD increases rapidly in this transition. Steel LA did not show any evidence of "pop-ins" although other sets of steel did.

For Steel LD the fracture appearance in the transition region is more complicated. At -45 and -30°C shear lips have formed on the edges of the specimen although failure is by cleavage fracture. This would indicate that plane-strain conditions are not met by the thickness of the specimen at these temperatures. At -10 and +10°C there is evidence of a brittle thumbnail surrounded by ductile fracture. This is evidence of decreasing constraint on the specimen. After stable crack extension final failure is by spontaneous cleavage fracture. The load-displacement record shows an increasing plastic region (Type B - Figure 6.38b) though above +25°C the load-displacement record shows a maximum plateau (Type D - Figure 6.38d). One test at +45°C shows a "pop-in" (Type C - Figure 6.38c) where stable crack extension is followed by cleavage fracture which is arrested. The "pop-in" could not be ignored even though the crack extended in a stable manner after "pop-in".

Around the transition temperature failure is by Type III behaviour. The ferrite matrix strength is greater than the carbide strength which is greater than the yield strength. Stable grain size cracks are possible and failure by cleavage occurs when the crack extends dynamically across the grain boundary. Ductile microcracks form in the initial plastic zone at the crack tip and failure is propagation controlled.

At higher temperatures cleavage fracture occurs after ductile crack extension by microvoid coalescence has extended the crack beyond the initial plastic zone. This is Type IV behaviour described by Ebrahimi [86].

(c) Region III

Most sets of specimens from LA to HD did not show fully ductile behaviour. For LA specimens at -20, 0 and +20°C the failure was 100% ductile fracture by microvoid coalescence (shown in Figure 6.50). This gave upper shelf values of CTOD. The load-displacement record shows a maximum load plateau and the specimen remains stable after maximum load (Type D - Figure 6.38d). This is still described as Type IV behaviour where slow stable crack growth precedes instability by final ductile rupture and this instability occurs outside the initial plastic zone.

6.3.5 THE TEMPERATURE DEPENDENCE OF K_Q (K_{IC})

Figures 6.51 and 6.52 show the temperature dependence of plane strain fracture toughness K_{IC} (calculated as K_Q). There is a general increase in toughness as temperature increases for both Steels L and H. For example LB's toughness increases from 24.5 MPa $m^{1/2}$ at -196°C to 56.4 MPa $m^{1/2}$ at -67.5°C. With increasing grain size the increase in toughness is smaller, for example LC shows an increase in toughness from 27.1 MPa $m^{1/2}$ at -196°C to 49.1 MPa $m^{1/2}$ at -67.5°C. For Steel H this effect was not as well defined. Steel HA showed an increase in toughness from 25.4 MPa $m^{1/2}$ at -196°C to 61.1 MPa $m^{1/2}$ at -80°C. For HB there was an increase from 25.0 MPa $m^{1/2}$ at -196°C to 45.2 MPa $m^{1/2}$ at -55°C while HC and HD showed similar increases; from 25.1 MPa $m^{1/2}$ at -196°C to 44.4 MPa $m^{1/2}$ at -50°C for HC, and from 24.5 MPa $m^{1/2}$ at -196°C to 42.7 MPa $m^{1/2}$ at -40°C for HD.

There was a rapid rise in fracture toughness over a small change in temperature for Steel L and for Steel HA although this did not represent the change in fracture mode. For Steels HB, HC and HD the slope of the transition curve with increasing temperature was low although the maximum toughness reached did not represent a change in fracture mode. This is shown in Figure 6.53 where K_{IC} for LA and LD are plotted against temperature with schematics of the fracture appearance at the corresponding test temperatures.The fracture appearance is 100% brittle for LA from -196 to -67.5°C and for LD from -196 to -60°C.

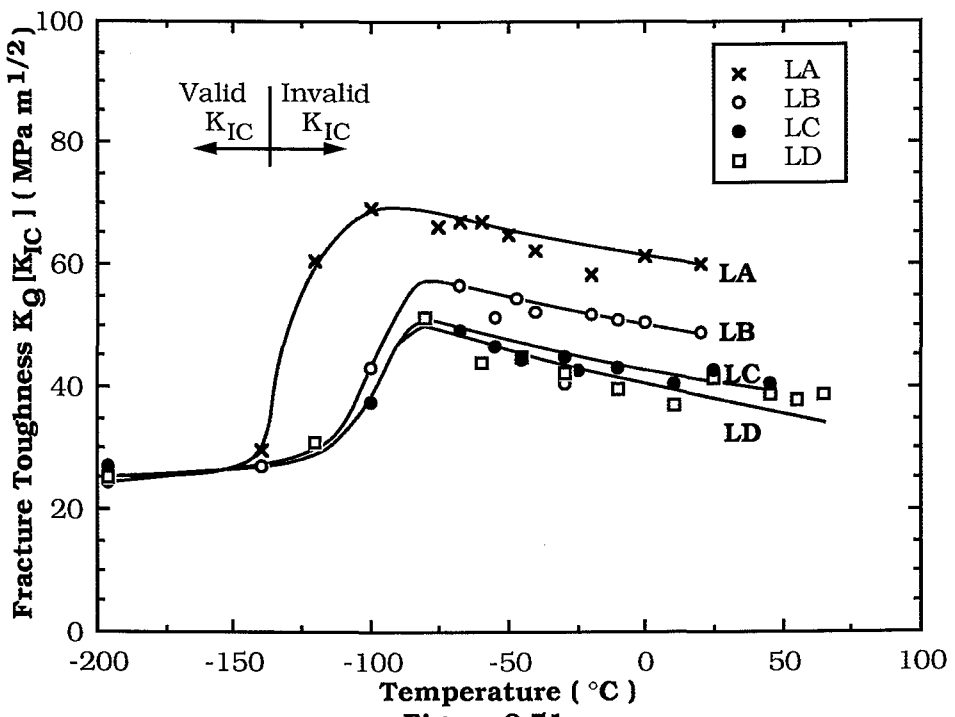

Figure 6.51

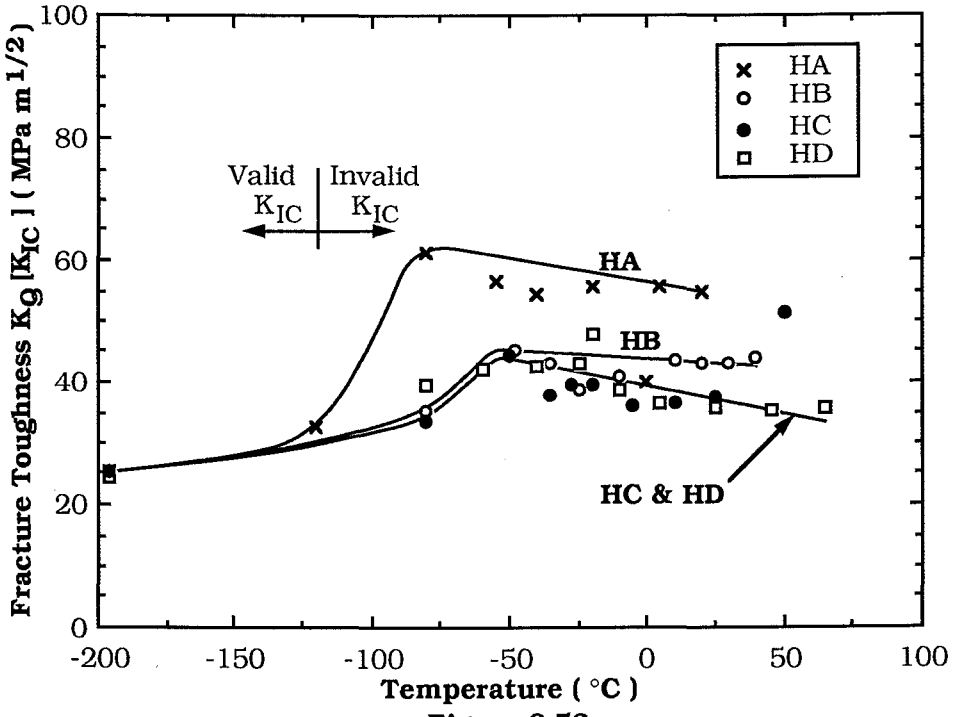

Figure 6.52

Figure 6.51 : Fracture toughness K_Q [K_{IC}] (MPa $m^{1/2}$) as a function of test temperature (°C) for Steel L.

Figure 6.52 : Fracture toughness K_Q [K_{IC}] (MPa $m^{1/2}$) as a function of test temperature (°C) for Steel H.

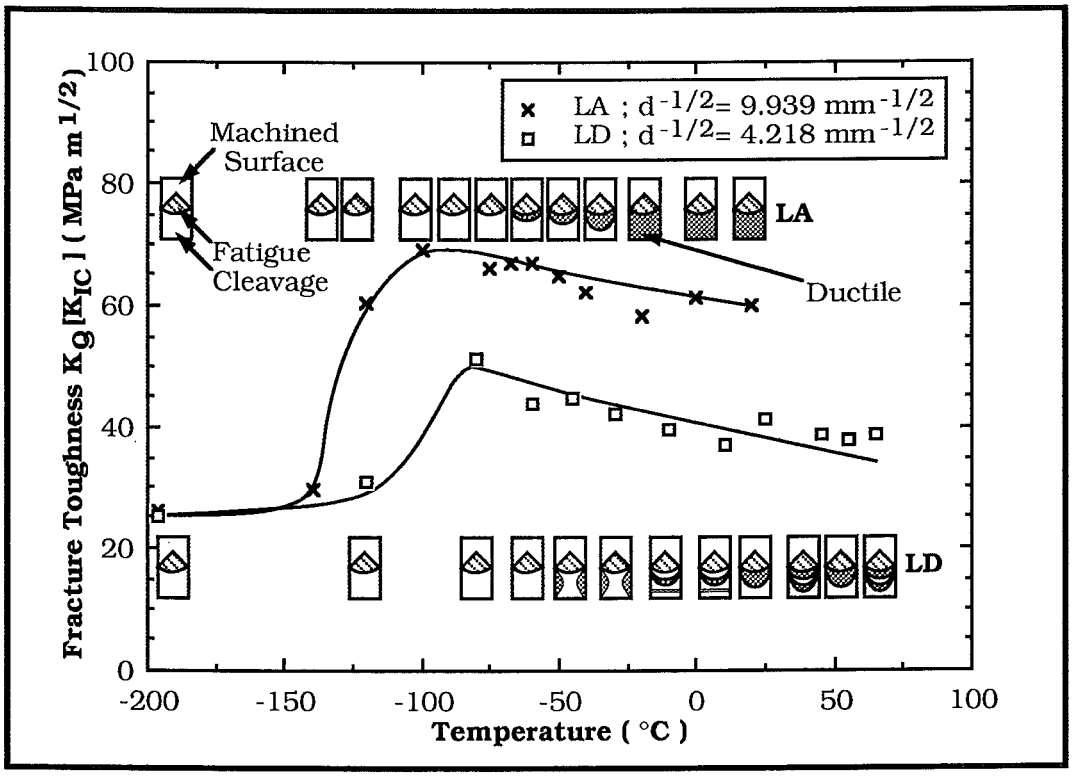

Figure 6.53 : Schematic of fracture appearance for LA & LD as a function of test temperature (°C) for K_Q .

As temperature increases the fracture becomes increasingly ductile as toughness given by the CTOD test increases. The plane-strain fracture toughness test gives a transition in toughness for LA between -140 to -100°C and for LD between -120 and -80°C. In both cases failure is still 100% cleavage fracture.

This increase in toughness represents the limit where fracture toughness values given by the plane strain fracture toughness test are no longer valid; that is, the results do not meet the criteria given by

$$a_o,\ b_o,\ B \geq 2.5\ (K_Q/\sigma_{ys})^2. \qquad (6.59)$$

Therefore the constraint from a specimen of thickness B = 15 mm or a crack length a_o = 15 mm is not sufficient to meet the imposed plane strain conditions. The increase in toughness in this temperature range may be due to several factors:

(i) At low temperatures (below about -140°C) twinning is known to occur which would make cleavage fracture easier [64,71,171].

This means fracture is nucleation controlled. Above this region cleavage is propagation controlled and toughness increases.

(ii) In section 5.3 the temperature dependence of yield strength was explained using the thermal activation theory of Conrad. The temperature dependence friction stress component of yield stress depended on the Peierls-Nabarro stress and interstitial content. As temperature increases there is more dependence on the interstitial content, the Peierls mechanism is less dominant above about -120°C. This is perhaps shown from Figures 5.19 and 5.20 showing the rate of change of yield stress for change in temperature against temperature for Steels L and H respectively. Below -80°C there is a large increase in the rate of change of yield stress with respect to temperature i.e. yield stress is increasing rapidly with decrease in temperature. This coincides with the change in controlling mechanism for yield strength. Therefore it is possible that the rise in plane-strain fracture toughness occurs with the change in controlling mechanism for yield strength.

Above the transition for plane-strain fracture toughness the experimental results show slowly decreasing values of fracture toughness. For example LB's toughness decreases from 66.9 MPa $m^{1/2}$ at -67.5°C to 48.3 MPa $m^{1/2}$ at +20°C. Similarly HB's toughness decreases from 45.2 MPa $m^{1/2}$ at -48°C to 43.7 MPa $m^{1/2}$ at +40°C. Constant or decreasing toughness values above the range of linear elastic fracture mechanics are well recognised [286]. It is argued that the size criterion for thickness given by

$$a_o, b_o, B \geq 2.5 (K_Q/\sigma_{ys})^2 \qquad (6.59)$$

should be relaxed since it produces unnecessarily conservative results [286]. Some results are found to be invalid plane-strain fracture toughness values when the load-displacement record shows no deviation from linearity. The 5% offset secant line, used on test records (Figures 6.38c-d) which show yielding and possible stable crack extension, represents a crack extension of 2%. When the fracture is a fully ductile shear mechanism the 5% offset load is related to the yield stress rather than the fracture toughness of the material. Therefore it would be expected that toughness above the plane-strain fracture toughness transition would show a constant or

decreasing value of toughness for decreasing yield strength (or increasing temperature).

6.3.6 *THE RELATIONSHIP BETWEEN K_c AND K_Q (K_{IC})*

Valid plane strain fracture toughness values were found up to -120°C. As discussed in Section 6.3.5 above this temperature toughness results did not meet the thickness criterion. François and Krasowsky defined the transition temperature in plane-strain fracture toughness from

$$B = \beta(K_{IC}/\sigma_{ys})^2 \tag{6.55}$$

where $\beta = 2.5$ for the ASTM K_{IC} limit of validity and the temperature dependence of fracture toughness is given by

$$K_{IC} = A\exp\ (T/T_o) \tag{6.62}$$

where A and T_o are constants, T_o being a reference temperature [280]. Equations (6.55) and (6.62) may be combined to give the transition temperature as

$$2T_c/T_o = Ln[(B/\beta)(\sigma_{ys}/A)^2] \tag{6.62a}$$

which gives a linear relationship between the transition temperature T_c and log B. This relationship depends primarily on experimental results and François and Krasowsky found the model gave a good representation of the transition temperature.

If plane-strain conditions are no longer valid above -120°C then it is expected that this region is an overlap between linear elastic fracture mechanics (K_{IC}) and elastic-plastic fracture mechanics (CTOD). Figures 6.54 and 6.55 show the transition curves of fracture toughness K_c and $K_Q(K_{IC})$ against temperature for Steels L and H respectively. With decreasing temperature there is an intersection between the two curves for each grain size. An approximation of the temperature at which the intersection occurs is given in Table 6.13 together with fracture toughness results in this temperature range

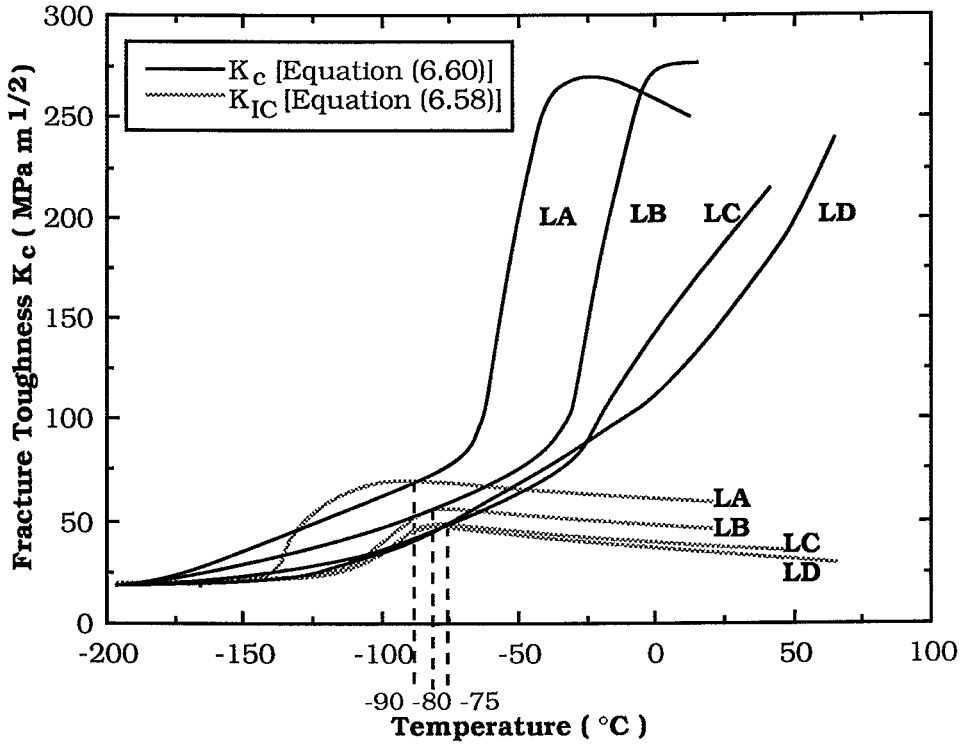

Figure 6.54

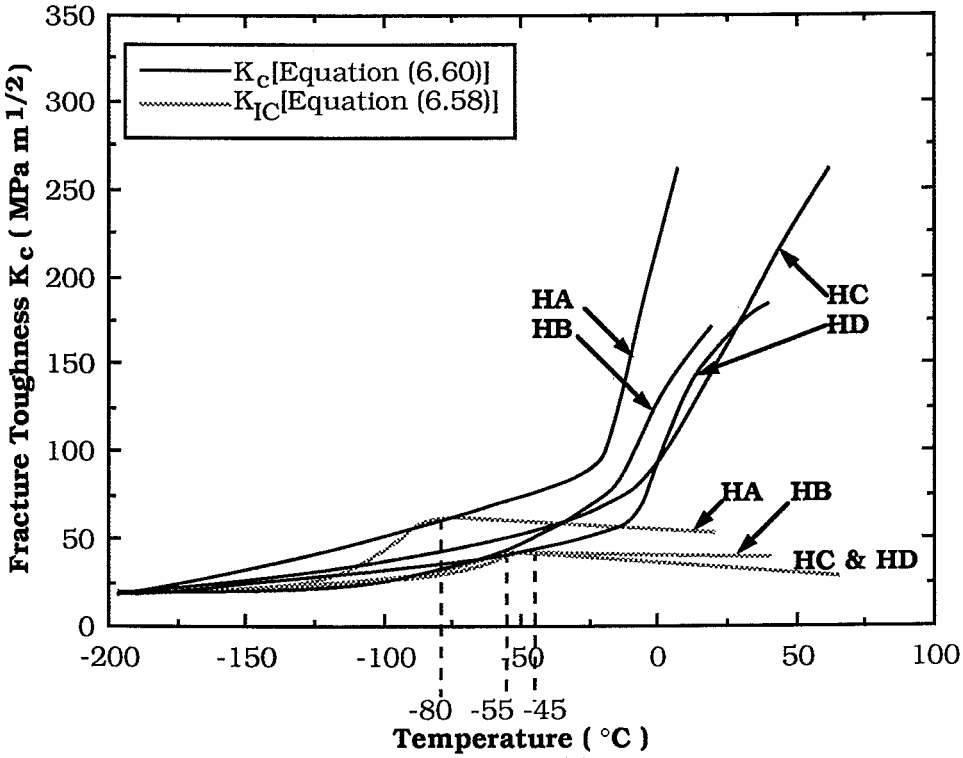

Figure 6.55

Fracture Toughness (MPa $m^{1/2}$) as a function of test temperature (°C) showing the intersection of results of LEFM & CTOD testing for ;

Figure 6.54 : Steel L.
Figure 6.55 : Steel H.

Table 6.13
Comparison of Fracture Toughness Results from Equations (6.60) and (6.58).

Specimen I.D.	Test temperature (°C)	σ_{ys} (MN m^{-2})	K_Q (6.58) (MPa $m^{1/2}$)	$B \geq 2.5(K/\sigma_{ys})$ (6.59) (mm)	K_c (6.60) (MPa $m^{1/2}$)
LA9	-196	765	26.2[1]	2.9	18.7[2]
LA2	-140	531	29.7[1]	7.8	37.3
LA1	-120	475	60.6	40.7	57.0
LA6	-100	432	69.0	63.8	74.2
LB8	-196	731	24.5[1]	2.8	18.2[2]
LB1	-140	475	27.1[1]	8.1	35.2
LB3	-100	376	42.9	60.4	43.4
LB4	-67.5	327	56.4	74.4	69.0
LC11	-196	682	27.1[1]	3.9	18.9[2]
LC8	-100	328	37.4	32.5	35.3
LC9	-67.5	279	49.1	77.4	63.7
LD9	-196	667	25.3[1]	3.6	17.8[2]
LD8	-120	356	30.9	18.8	25.0
LD4	-80	280	51.1	83.3	50.5
HA3	-196	783	25.4[1]	2.6	18.9[2]
HA1	-120	455	32.8[1]	13.0	43.0
HA5	-80	371	61.1	67.8	61.1
HA10	-55	338	56.5	69.9	74.8
HB10	-196	727	25.0[1]	3.0	18.2[2]
HB11	-80	315	35.3	31.4	32.8
HB8	-48	276	45.2	67.0	54.9
HB4	-35	265	43.1	66.1	57.0
HC3	-196	693	25.1[1]	3.3	17.8[2]
HC8	-80	282	33.3	34.9	47.4
HC10	-50	244	44.4	82.8	52.7
HC4	-35	231	37.9	67.3	58.9
HD5	-196	686	24.5[1]	3.2	17.7[2]
HD7	-80	274	39.6	52.2	41.8
HD2	-60	247	42.2	73.0	42.7
HD1	-40	227	42.7	88.5	48.7

Note: 1. Valid K_{IC} plane-strain fracture toughness results.
2. K_c calculated from critical CTOD values found using equation (6.46).
3. Intersection Temperatures are:

Grain Size	I.T. (°C)
LA	-90
LB	-80
LC	-75
LD	-80
HA	-80
HB	-55
HC	-60
HD	-45

For Steel L the intersection occurs between -90 and -75°C and for Steel H the intersection occurs between -80 and -45°C. This is higher than the temperature where the plane-strain fracture toughness becomes invalid, given as approximately -120°C.

A valid plane strain fracture toughness value can be regarded as one where the load-displacement record shows no significant deviation from linearity (which is given by the criterion $P_{max}/P_Q < 1.1$) as suggested by Priest [286]. The thickness transition for K_{IC} is then raised to the same temperature range where LEFM and CTOD intersect. If values of B, σ_{ys} and K_Q are substituted into equation (6.55) then β is approximately 0.5 at these temperatures. François and Krasowsky found $\beta \approx 0.5$ for the transition temperature (T_i) for the K_{IC} test corresponding to initiation of some stable tearing [280]. The thickness criterion can be given as

$$B \geq 0.5(K_Q/\sigma_{ys})^2. \qquad (6.63)$$

Therefore the overlap between the CTOD and K_{IC} tests gives an upper bound to plane-strain fracture toughness if the criterion $P_{max}/P_Q < 1.1$ is taken as the criterion for a valid test.

6.3.7 THE RELATIONSHIP BETWEEN FRACTURE TOUGHNESS AND MICROPARAMETERS

In Section 3.2.5 the Ritchie-Knott-Rice (RKR) model of cleavage fracture was given where the steel's cleavage fracture stress had to be exceeded over some characteristic distance from the crack tip before fracture occurred [72]. The characteristic distance X_o was considered to be 1 to 2 grain diameters so that

$$\sigma_F(2\pi X_o)^{1/2} \geq K_{IC} \qquad (6.64)$$

where σ_F is the cleavage fracture stress.

This model can be compared to the plane strain fracture toughness values found experimentally in this investigation. Ritchie *et al.* originally gave the relationship as being valid for $d_g \geq 40$ μm and $d_g \leq X_o \leq 2d_g$ where d_g is the grain diameter. Curry and Knott found X_o was independent of grain size for $d_g < 40$ μm [77]. In contrast Rawal and Gurland found that $d_g \leq X_o \leq 2d_g$ was valid for d_g from 8.3 to 13 μm for spheroidised steel [76]. Chew found that there was good agreement between experimental and predicted results using the RKR model with $X_o = 2d_g$ for grain sizes between 17.2 and 24.6 μm [16].

Chew explained that the σ_F - K_{IC} relationship had been explained using Smith's cleavage mechanism where suitable grain boundary carbides were needed [16,69]. It was considered that the existence of such carbides was reduced in fine grained materials [16]. The Cottrell mechanism of cleavage fracture (Section 3.2.2) does not require grain boundary carbides to nucleate microcracks and this model has been applied to fracture in conventional low carbon steels [172]. Chew concluded that the limit on grain size is not necessarily needed since an alternative micro-crack nucleation mechanism dependent on grain size is available [16]. Therefore Chew's results are also presented for comparison.

The fracture stress σ_F was assumed to be temperature independent [64,166,167]. The data for calculation of fracture stress at -196°C is given in Table 6.14. The fracture stress at -196°C for HB, HC and HD coincided with the lower yield stress.

Table 6.14
Tensile Properties of Experimental Steels at -196°C

Steel	Initial Diameter D_O (mm)	Fracture Diameter D_F (mm)	Fracture Load P_F (kN)	σ_{ys} (-196°C) (MNm^{-2})	σ_F (MNm^{-2})
LA	5.051	4.50	16.927	773	1064
LB	5.043	4.48	15.864	720	1006
LC	5.050, 5.037	4.85, 4.88	15.586, 15.301	691, 693	844, 818
LD	5.059	4.88	15.012	677	803
HA	5.050	4.46	15.158	779	970
HB	5.054, 5.052	5.04, 4.99	13.696, 13.882	683, 693	687, 710
HC	5.050	4.98	14.100	704	724
HD	5.047	4.96	13.632	682	706

For tests at -196°C the results are presented in two forms. Using experimental values of σ_F and d_g and with $X_o = 2d_g$ a predicted fracture toughness is calculated. Chew's results are also presented for this calculation. These results are given in Table 6.15.

Also, using the experimentally found values of K_{IC} the characteristic distance X_o is calculated. This calculation is also performed using Chew's results. These results are given in Table 6.16.

The results of Table 6.15 show that the Ritchie-Knott-Rice model of cleavage fracture toughness predicts values of fracture toughness less than the experimental values for the present investigation. Bowen *et al.* determined that the RKR model would give a lower bound to experimentally determined K_{IC} results [193].

Table 6.15
Fracture Toughness predicted using the Ritchie-Knott-Rice Model at -196°C [72].

Steel	Fracture Stress σ_F (MNm^{-2})	Average Grain diameter, d_g^3 (μm)	$X_o = 2d_g$ (μm)	K_{IC} Predicted ($MPam^{1/2}$)	K_{IC} Exp'tal ($MPam^{1/2}$)
P.V. Steel	1143	24.6	49.2	20.1	19.7
275N	1164	20.5	41.0	18.7	19.8
275T[16]	1170	17.2	34.2	17.2	18.8
LA	1064	12.9	25.8	13.5	26.2
LB	1006	24.1	48.2	17.5	24.2
LC	831[1]	52.2	104.4	21.3	27.1
LD	803	71.6	143.2	24.1	25.3
HA	970	17.9	35.8	14.5	25.4
HB	802[2]	35.4	70.8	16.9	25
HC	724	62.0	124.0	20.2	25.1
HD	706	72.6	145.6	21.3	24.5

1. Average value of fracture stress used.
2. Fracture stress calculated from $\sigma_F = 403.5 + 66.45d^{-1/2}$.
3. Average grain diameter $d_g = 4/\pi$ x (Grain Size).

The characteristic distance was calculated from experimental toughness values. For Chew's results X_o is approximately $2d_g$. However, for Steel L, X_o varies from 2.64 d_g for d_g = 71.6 μm to 7.48 d_g for d_g = 12.9 μm. For Steel H, X_o varies from 2.64 d_g for d_g = 72.6 μm to 6.09 d_g = 17.9 μm. No simple relationship is found to exist between the characteristic distance X_o and grain size which is, perhaps, an indication of the statistical nature of cleavage fracture; $X_o = 2d_g$ will give a lower bound to fracture toughness in agreement with Bowen *et al.* [193]. Curry predicted that X_o should not be influenced by temperature or strain rate since it is determined by the crack-tip stress distribution and the carbide particle distribution [91]. Bowen *et al.* found X_o increased with temperature [193].

Table 6.16
The Characteristic distance (X_o) determined from experimental K_{IC} at -196°C.

Steel	Exp'tal K_{IC} (MPa $m^{1/2}$)	Fracture stress σ_F (MN m^{-2})	X_o (μm)	$X_o = 2d_g$ [3] (μm)
P.V.	19.7	1143	47.3	49.2
275N	19.8	1164	46.1	41.0
275T [16]	18.8	1170	41.1	34.2
LA	26.2	1064	96.5	25.8
LB	24.2	1006	92.1	48.2
LC	27.1	831[1]	169.3	104.4
LD	25.3	801	158.8	143.2
HA	25.4	970	109.1	35.8
HB	25	802[2]	154.7	70.8
HC	25.1	724	191.3	124.0
HD	24.5	706	191.7	145.6

1. Average value of fracture stress used.
2. Fracture stress calculated from $\sigma_F = 403.5 + 66.45d^{-1/2}$.
3. Average grain diameter $d_g = 4/\pi$ x (Grain Size).

Table 6.17
The characteristic distance X_o calculated from experimental K_{IC}.

Specimen	Test Temp. (°C)	K_{IC} (MPam$^{1/2}$)	σ_F (MN m^{-2})	X_o (μm)
LA2	-140	29.7	1064	124.0
LB1	-140	27.1	1006	115.5
LD8	-120	30.9	801	236.8
HA1	-120	32.8	970	182.0
LA1	-120	60.6	1064	516.3

Using plane-strain fracture toughness results at other test temperatures the characteristic distance may be calculated assuming the fracture stress is temperature independent. These results are given in Table 6.17.

The results show that X_o increases with increase in temperature, for example for LA X_o = 124.0 μm at -140°C and X_o = 516.3 μm at -120°C. However it may be that the fracture stress is not temperature independent and due to increasing plastic deformation at the crack tip the fracture stress may rise [16]. The Ritchie Knott Rice model appears to predict lower bound fracture toughness values due to the statistical nature of X_o.

6.4 Summary

Fracture toughness testing was performed to find the critical crack-opening displacement and apparent fracture toughness of the experimental steels under investigation.

(i) Testing was over the temperature range -196 to +65°C using 15 mm thick compact tension specimens.

(ii) Testing was performed to standards ASTM E399-83 for plane-strain fracture toughness, and to BS5762:1979 and ASTM E1290-89 for crack-tip opening displacement.

(iii) A thickness B = 15 mm was chosen since previous work had shown that this thickness would give thickness independent toughness results [16].

(iv) A correlation was made between clip gauge displacement and crack-tip opening displacement using silicone-rubber replicas. The correlation found that CTOD found from clip gauge displacement was affected by plastic zone size. The plastic zone size is affected by yield stress and strain hardening. This gave a CTOD dependent on grain size and composition.

(v) The resulting model of CTOD calculated from clip gauge displacement included a grain size dependent term such that

$$\delta_t = A_1 V_g + A_2 V_g^2 d^{1/2} \qquad (6.38)$$

where A_1 = 0.121113 and A_2 = 0.034222 $mm^{-3/2}$.

(vi) From the linear relationship between clip gauge displacement and crosshead displacement a similar model was proposed for CTOD against crosshead displacement;

$$\delta_t = A_0 + A_1 V_{CH} + A_2 V_{CH}^2 d^{1/2} \qquad (6.45)$$

where A_0 = -0.11077 mm, A_1 = 0.190806 and A_2 = 0.113386 $mm^{-3/2}$.

(vii) CTOD was also calculated using the standard equation

$$\delta_t = \frac{K^2(1-\nu^2)}{2\sigma_{ys}E} + \frac{V_p r_p b_o}{(r_p b_o + a_o + z)}. \qquad (6.46)$$

(viii) The transition temperature criterion was defined as the CTOD where ductile crack extension initiates. From measurements of CTOD against crack extension δ_i = 0.15 mm for Steel L and δ_i = 0.10 mm for Steel H. Similarly for fracture toughness, the initiation values were K_i = 110 MPa $m^{1/2}$ for Steel L and K_i = 70 MPa $m^{1/2}$ for Steel H.

(ix) Fracture toughness (either CTOD or K_c) for Steel L and Steel H shows a rapid transition from low to high values with increasing temperature or decreasing yield strength. This shows the sensitivity of fracture toughness to mode of microfracture. Below the transition temperature failure is by cleavage fracture. Fracture is then propagation controlled by carbide cracking or Cottrell's intersecting slip planes. Near the transition fracture is thought to be propagation controlled by ferrite grain size cracks. Just above the transition failure is by some stable ductile tearing followed by cleavage fracture. Cleavage fracture initiates outside the initial strain-hardened plastic zone. At higher temperatures fracture is ductile by microvoid coalescence.

(x) Plane-strain fracture toughness increased with increasing temperature to a maximum and then remained constant or decreased slowly. The increase to a maximum toughness was a transition where the thickness criterion $B \geq 2.5(K_Q/\sigma_{ys})^2$ was not longer met. The increase in toughness was matched by a decrease in yield strength and possibly was caused by a change in yielding mechanism. From work by Priest valid plane-strain fracture toughness could be given by $P_{max}/P_Q < 1.1$ which gives $B \geq 0.5(K_{IC}/\sigma_{ys})^2$ for this investigation. This represented the maximum on the K_{IC} versus temperature curve.

(xi) There was a region of overlap between CTOD and K_{IC} results. With decreasing test temperature intersection between the two sets of toughness results occurred near the limit $B = 0.5\ (K_{IC}/\sigma_{ys})^2$.

It shows that the restriction on valid plane-strain toughness is perhaps too strict and the CTOD test gives a good estimate of an upper bound of K_{IC}. The intersection occurs after yielding has occurred at the crack tip but before initiation of stable crack extension. Therefore the intersection occurs below the transition temperature.

(xii) The Ritchie-Knott-Rice model of fracture toughness appears to give a lower bound to toughness value when $X_o = 2\ d_g$. Experimental results found $2.22\ d_g \leq X_o \leq 7.48\ d_g$ and that no simple relationship exists between grain size and the characteristic distance. If fracture stress is temperature independent then X_o increases with increasing temperature.

The experimental results show that the fracture mode transition temperature varies with grain size. This is examined in the next chapter.

CHAPTER 7

The Dependence of the Fracture Mode Transition Temperature on Grain Size

---

7.1 Introduction

In this chapter the transition temperature results of toughness testing presented in Chapter 6 are discussed with reference to grain size. These experimental results are compared to predicted FMTT results made using the Ritchie-Knott-Rice model of cleavage fracture toughness. Examination of the fracture surface by scanning electron microscopy is discussed with respect to fracture initiation. From the results presented fracture initiation and crack propagation are discussed.

A brief review of Charpy V-notch impact - CTOD (or K_{IC}) correlations is presented and from this a correlation between experimental Charpy and CTOD results is made. This correlation could be compared to other work and final conclusions made.

7.2 The Grain Size Dependence of FMTT

7.2.1 THE DEPENDENCE OF FMTT ON $d^{-1/2}$

In Section 3.3.1 the fracture mode transition was considered on the basis of dislocation pile-ups where the energy of a dislocation pile-up is equated to the surface energy of the crack [67,68].

From this analysis the transition temperature is given as a function of grain size, the Peierls-Nabarro stress, the strength of dislocation locking and the stress state. The transition temperature was given as

$$\alpha T_c = \ln A - \ln\left(\frac{\beta\mu\gamma}{k_y} - k_y\right) - \ln d^{-1/2} \qquad (7.1)$$

where α is a constant

A is a constant

$\beta = 2\tau/\sigma$ and accounts for stress state

μ is the shear modulus

γ is the effective surface energy of the matrix,

and k_y is a constant that accounts for dislocation locking.

This predicts a linear dependence of T_c on $\ln d^{-1/2}$. Less accurately a linear dependence of T_c on $d^{-1/2}$ is given if the friction stress component of yield stress is assumed to have a linear temperature dependence so that

$$DT_c = \sigma_i(st) + C - \left(\frac{\beta\mu\gamma}{k_y} - k_y\right)d^{-1/2} \qquad (7.2)$$

where D and C are constants and $\sigma_i(st)$ is the athermal stress component of friction stress. A linear dependence of T_c on $d^{-1/2}$ has been shown by a number of researchers [7,8,87]. However, it can be shown that the yield stress (and therefore the transition temperature) can be given as being dependent on d^{-1} or $d^{-1/3}$ although Morrison demonstrated that these dependencies were not as good as $d^{-1/2}$ [277,2888].

A limitation on these analyses is that the steels are not tested over a large range of grain size. For example in this investigation $d^{-1/2}$ is from 4.187 to 9.939 $mm^{-1/2}$ whereas a more desirable range could be from 2 to 16 $mm^{-1/2}$.

While recognising that other forms of grain size dependence are possible the results of the transition temperature are given as dependent on $d^{-1/2}$. In Section 4.4 the fracture mode transition temperature for Charpy V-notch impact testing was given as depending on $d^{-1/2}$. To preserve continuity the results for CTOD and K_c testing are presented in a similar manner.

The transition temperature was determined at the ductility transition temperature. In Charpy V-notch impact testing this is given by the 27 Joule criterion. For CTOD testing this is given by the initiation CTOD δ_i where stable crack extension first occurs. Experimental results of transition temperature at δ_i = 0.10 and 0.15 mm, K_i = 110 MPa $m^{1/2}$ (for L) and K_i = 70 MPa $m^{1/2}$ (for H) and also grain size are given in Table 7.1. Figures 7.1 and 7.2 show transition temperature versus $d^{-1/2}$ at δ_i = 0.10 mm and δ_i = 0.15 mm respectively. Figure 7.3 shows transition temperature versus $d^{-1/2}$ at K_i = 110 MPa $m^{1/2}$ for Steel L and at K_i = 70 MPa $m^{1/2}$ for Steel H. The transition temperatures of Chew's results are included in Figures 7.1 and 7.3.

Table 7.1
Fracture Mode Transition Temperature for Toughness testing

Steel	Grain Size ($mm^{-1/2}$)	Transition Temperature (°C)		
		$\delta_{0.15}$	$\delta_{0.10}$	K_i
LA	9.939	-62	-65	-62
LB	7.262	-33	-47.5	-30
LC	4.941	-27	-35.5	-17
LD	4.218	-24	-37	-1
HA	8.440	-20	-34	-56.5
HB	5.995	-5.5	-13	-23.5
HC	4.531	+3	-11.5	-18
HD	4.187	+2	-1	-5
275N[1]	6.984	-47	-	-43
275T[1]	7.625	-43	-	-41
PV[1]	6.376	-49	-	-43

1. Estimated from Chew's experimental results [16].

(a) Correlation of T_c against grain size

The results show that transition temperature decreases as $d^{-1/2}$ increases (or grain size decreases). At δ_i = 0.10 mm and 0.15 mm the transition temperature of Steel H is higher than that of L which is due to the different composition as well as the effects of strain ageing in the fatigue damaged zone around the crack tip [16].

The results were analysed using a least squares linear regression on an IBM compatible XT computer as previously. Grain size as $d^{-1/2}$ was taken as the independent variable assumed to be precisely known.

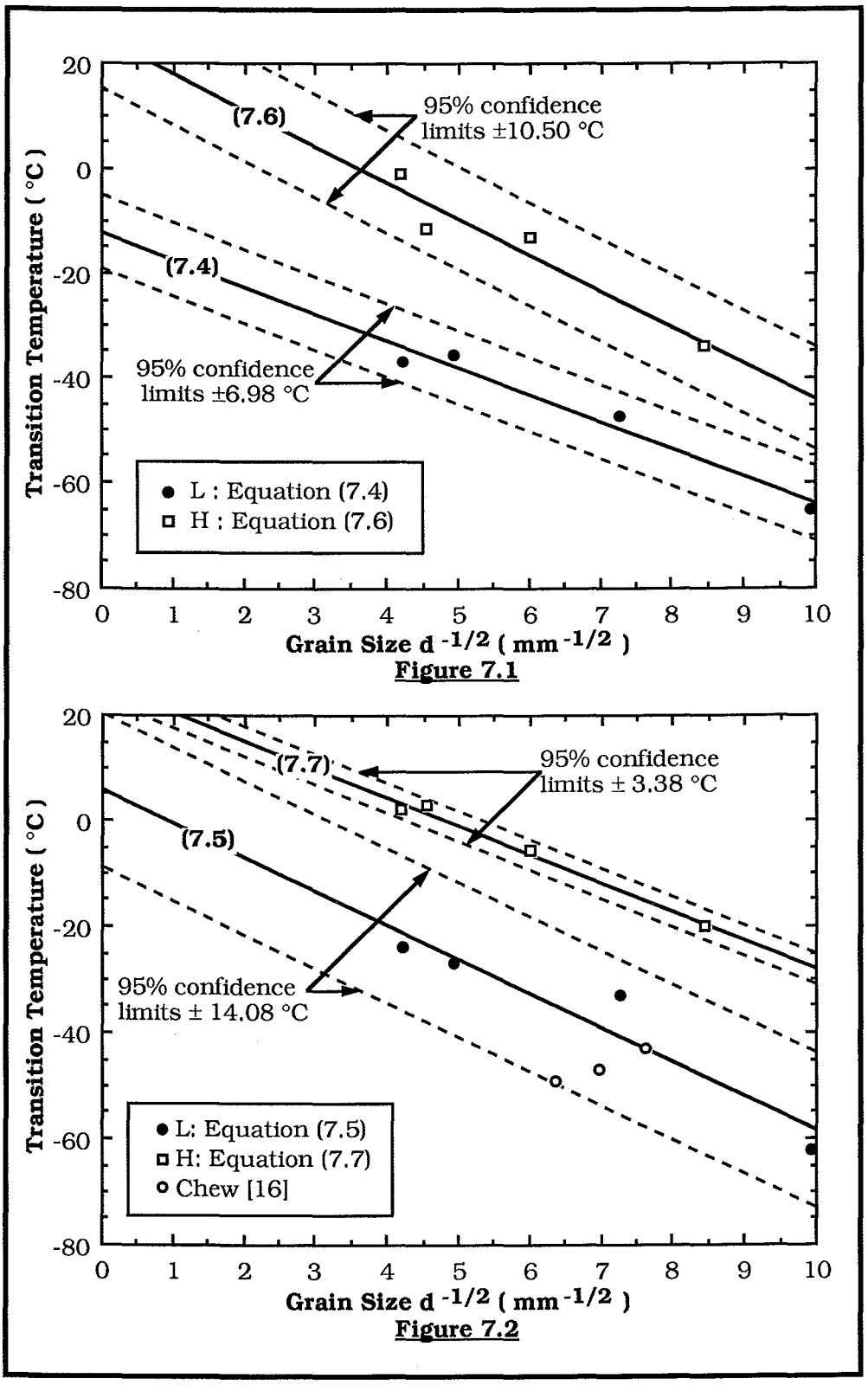

The fracture mode transition temperature (°C) as a function of grain size $d^{-1/2}(mm^{-1/2})$ for Steels L & H for transition criteria;

Figure 7.1 : δ_i = 0.10 mm.

Figure 7.2 : δ_i = 0.15 mm.

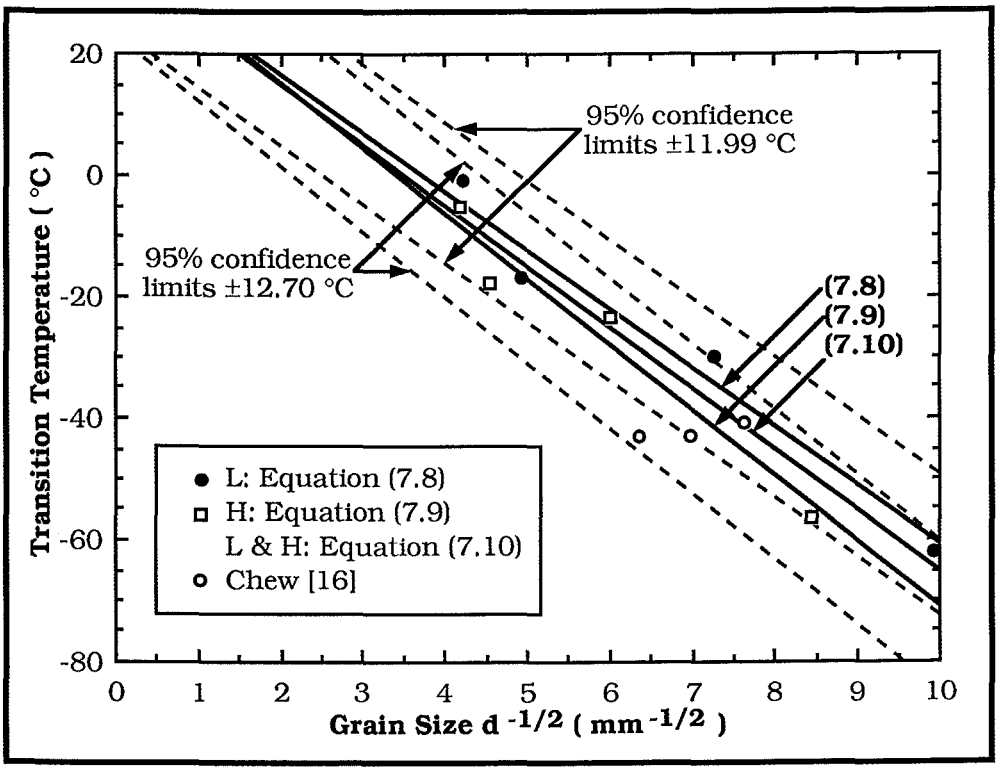

Figure 7.3 : The fracture mode transition temperature (°C) as a function of grain size $d^{-1/2}(mm^{-1/2})$ for Steels L & H using the transition criteria K_i = 70,110 MPa $m^{1/2}$

All error was assumed to be with the dependent variable, the transition temperature (T_c). The regression equation was

$$T_c = B_0 + B_1 d^{-1/2} \qquad (7.3)$$

where T_c is the transition temperature in °C, and B_0 and B_1 are constants. Table 7.2 contains the results of the regression at δ_i = 0.10 mm and 0.15 mm for L and H. Table 7.3 contains the regression results for L at K_i = 110 MPa $m^{1/2}$ and for H at K_i = 70 MPa $m^{1/2}$. Also the data for L and H at K_i was pooled and an analysis performed on this combined data.

The resulting equations are:

(i) Steel L

$$T(\delta_{0.10}) = -12.23 - 5.16\ d^{-1/2} \qquad (7.4)$$

$$T(\delta_{0.15}) = 5.77 - 6.41\ d^{-1/2} \qquad (7.5)$$

Table 7.2
Results of Multiple-Linear Regression Analysis for CTOD transition temperature against $d^{-1/2}$

Steel	L		H	
Transition Criterion	$\delta_{0.10}$	$\delta_{0.15}$	$\delta_{0.10}$	$\delta_{0.15}$
Equation No.	7.4	7.5	7.6	7.7
Figure No.	7.1	7.2	7.1	7.2
N[1]	4	4	4	4
D.F.	2	2	2	2
R	0.9808	0.9617	0.9576	0.9927
$s(\hat{y})$	3.2431	6.5453	4.8800	1.5700
F-value	51	19	22	135
Equation Sig. Coefficients	97.5%	95%	95%	99%
B_0	-12.23	5.77	24.74	26.42
B_1	-5.16	-6.41	-6.84	-5.45
95% C.L. of B_1	±3.12	±6.30	±6.27	±2.02
Significance of B_1	98%	95%	95%	99%
$\bar{y}$	-46.25	-36.5	-14.88	-5.13
95% C.L. of $\bar{y}$	±6.98	±14.08	±10.50	±3.38

1. See Appendix B for definition of statistical abbreviations

Table 7.3
Results of MLR analysis
for K_c transition temperature versus $d^{-1/2}$

Steel	L	H	Combined
Transition Criteria	K_i = 110 MPa $m^{1/2}$	K_i = 70 MPa $m^{1/2}$	-
Equation No.	7.8	7.9	7.10
Figure No.	7.3	7.3	7.3
N^1	4	4	8
D.F.	2	2	6
R	0.9844	0.9755	0.9672
$s(\hat{y})$	5.5706	5.9047	6.0996
F-value	63	39	87
Equation Sig.	97.5%	97.5%	99.95%
Coefficients			
B_0	37.50	38.25	35.09
B_1	-9.86	-11.06	-9.97
95% C.L. of B_1	±5.36	±7.59	±2.62
Significance of B_1	98%	95%	99.99%
$\bar{y}$	-27.5	-25.75	-26.63
95% C.L. of $\bar{y}$	±11.99	±12.70	±5.28

1. See Appendix B for definition of statistical abbreviations.

(ii) Steel H

$$T(\delta_{0.10}) = 24.74 - 6.84\ d^{-1/2} \quad (7.6)$$

$$T(\delta_{0.15}) = 26.42 - 5.45\ d^{-1/2} \quad (7.7)$$

(iii) Steels L and H

$$T(K_{110},L) = 37.50 - 9.86\ d^{-1/2} \quad (7.8)$$

$$T(K_{70},H) = 38.25 - 11.06\ d^{-1/2} \quad (7.9)$$

$$T(K_{70,110}) = 35.09 - 9.97\ d^{-1/2} \quad (7.10)$$

where T is in °C, $d^{-1/2}$ in $mm^{-1/2}$, B_0 in °C and B_1 in °C $mm^{1/2}$.

Equations (7.4) and (7.6) give transition temperature as a function of $d^{-1/2}$ at δ_i = 0.10 mm for L and H respectively. The correlation coefficients of equations (7.4) and (7.6) are such that 96.2% and 91.7% respectively of the total variation in transition temperature is explained by these equations. Equation (7.4) and its coefficient of $d^{-1/2}$ (B_1) are significant at the 98% level; that is, the correlation will occur by chance only twice in one-hundred times. However equation (7.6) and the coefficient B_1 are significant at the 95% level; that is, the correlation will occur by chance five out of one-hundred times. The predicted results from equations (7.4) and (7.6) are plotted on Figure 7.1 together with 95% confidence limits over the range of grain size considered.

Similarly equations (7.5) and (7.7) give T_c as a function of $d^{-1/2}$ at δ_i = 0.15 mm for L and H respectively. For equation (7.5) the correlation coefficient is such that 90.6% of the total variation in transition temperature is explained by this equation at a significance level of 95%. Equation (7.7) for H has a correlation coefficient such that 98.5% of the total variation in transition temperature is explained by this equation at a level of significance of 99%. The coefficient B_1 is significant at the 95% level for L and at the 99% level for H. These equations are plotted on Figure 7.2 with 95% confidence limits over the range of grain size considered.

Equation (7.8) gives T_c as a function of $d^{-1/2}$ at K_i = 110 MPa $m^{1/2}$ for L and equation (7.9) gives T_c as a function of $d^{-1/2}$ at K_i = 70 MPa $m^{1/2}$ for H. These equations are plotted on Figure 7.3 with 95% confidence limits. Equation (7.10) gives T_c as a function of $d^{-1/2}$ for the combined K_i data of L and H. This equation is also plotted on Figure 7.3. The correlation coefficient has a range from 0.9672 for equation (7.10) to 0.9844 for equation (7.8). Equations (7.8) and

(7.9) are significant at the 97.5% level but by increasing the number of degrees of freedom of the regression equation (7.10) is significant at the 99.95% level. The coefficient B_1 has a level of significance of 98% for equation (7.8), 95% for equation (7.9) and 99.99% for equation (7.10).

The coefficient B_1 gives the slope of the regression lines. In Section 4.4.4 the slope of "transition temperature versus $d^{-1/2}$" plots for Charpy Impact testing was found to vary between -12.24 and -15.63°C $mm^{1/2}$ and when the slopes for the T_{27} criterion were pooled a common slope of $B_1 = -13.59 \pm 3.94$°C $mm^{1/2}$ was found at the 95% confidence level. The 95% confidence level included other reported slopes of -11.6°$C^{1/2}$ and -11.8°C $mm^{1/2}$ [7,8]. At $\delta_i = 0.10$ mm and $\delta = 0.15$ mm the coefficient B_1 varies from -5.16 to -6.84°C $mm^{1/2}$.

In Section 6.2.4 statistical formulae were given to compare the slopes of two regression lines. Using this technique the slopes of:

(i) Equations (7.4) and (7.6)
(ii) Equations (7.5) and (7.7) and
(iii) Equations (7.5) and (7.6)

were compared. It was found that at $\delta_i = 0.10$ mm the slopes between L and H were significantly different at the 99.99% level. At $\delta_i = 0.15$ mm the slopes between L and H were significantly different at the 99.9% level. At the ductility transition temperature for $\delta_i = 0.10$ mm for H and for $\delta_i = 0.15$ mm for L the slopes are still significantly different at the 98% level.

The coefficient B_1 is equal to

$$B_1 = \frac{1}{D}\left(\frac{\beta\mu\gamma}{k_y} - k_y\right) \qquad (7.11)$$

from equation (7.2). The factor β accounts for stress state and will be dependent on specimen geometry, loading and notch sharpness but it is independent of composition. The shear modulus (μ) is equal to $E/2(1+\nu)$. Therefore μ will be approximately independent of composition. The effective surface energy of the matrix γ varies according to the amount of carbon and nitrogen segregated at grain boundaries and is, therefore, influenced by composition [10]. However the effective surface energy of ferrite has been given as γ_p =

14 Jm^{-2} for mild steels by Curry and Knott and as γ_p = 120 Jm^{-2} by Brozzo *et al.* for low C bainitic steels [175,185]. Therefore, γ is also dependent on microstructure. The contribution of grain boundaries to strength in tension is given by k_y which as discussed in Section 5.2 is composition dependent. In this investigation k_y was found as k_y = 20.85 MPa $mm^{1/2}$ for L and k_y = 22.89 MPa $mm^{1/2}$ for H. The constant D is the coefficient of temperature for the temperature dependent component of yield stress. It is dependent on composition and the strain rate; therefore B_1 becomes dependent on composition, strain rate and stress state. When strain rate and stress state are similar the coefficient B_1 will change for different compositions, as occurs here.

Volk gives a method to compare several regression slopes [267]. The statistical method involves finding the sum of squares of deviations for regression lines through

(i) all the data

(ii) individual sets of data with a pooled estimate of the slope and

(iii) individual sets of data each with its own slope.

To find the significance of the pooled slope compared to the individual slopes then $\Sigma\Sigma'\hat{y}^2$, the sum of the sum of squares of deviation from (iii), is found. Also $\Sigma'\hat{y}_w^2$, the sum of squares of deviation from (ii), is found. The variance ratio tested by the F test is tested at the appropriate number of degrees of freedom where the ratio is given by

$$\frac{(\Sigma'\hat{y}_w^2 - \Sigma\Sigma'\hat{y}^2)/(k-1)}{\Sigma\Sigma'\hat{y}^2/\Sigma(n_i-2)} \qquad (7.12)$$

where (k-1) is the number of degrees of freedom for the difference between the slopes where k is the number of data sets. $\Sigma(n_1-2)$ is the number of degrees of freedom of the error and n_i is the number of data points per set of data. For the slopes of equations (7.4) to (7.7) $\Sigma\Sigma'\hat{y}^2$ = 159.28 with 8 degrees of freedom, and $\Sigma'\hat{y}_w^2$ = 187.73. The sum $(\Sigma'\hat{y}_w^2 - \Sigma\Sigma'\hat{y}2)$ has 3 degrees of freedom. The F test gives $F_{3,8}$ = 0.4763 which has a significance of less than 50%. Therefore the difference in slopes would be expected to occur more than 5 times in 10 when there was no difference in slopes over the range of data tested. The pooled slope is $\bar{B}_1$ = -5.92°C $mm^{1/2}$.

The slopes of equations (7.8) and (7.9) are -9.86°C $mm^{1/2}$ and -11.06°C $mm^{1/2}$ respectively. The slope for T_c versus $d^{-1/2}$ has

decreased when using the transition criteria K_i = 110 MPa $m^{1/2}$ or 70 MPa $m^{1/2}$ compared to CTODi transition criteria. K_c has been calculated from yield strength and critical CTOD. Since yield strength is temperature dependent it is probable that the change in slope of the transition curve is due to the inclusion of the yield strength term.

Figure 7.2 includes the estimated transition temperatures at δ_i = 0.15 mm for Chew's experimental work. The results are included in Table 7.1. The results are distributed about the results for Steel L with an increasing transition temperature for decreasing grain size although each steel has a different composition. Figure 7.3 includes the estimated transition temperatures at K_i = 110 MPa $m^{1/2}$ from Chew's experimental work. The results of 275 N and 275 T lie either side of the line given by equation (7.8) for Steel L (equivalent to 275 T) and the results are distributed about the regression line given by equation (7.10). These results support the conclusion that T_c is directly proportional to $d^{-1/2}$.

(b) Comparison of CTOD, K_c and Charpy Transition Slopes

The slope of T_c versus $d^{-1/2}$ is given as

$$B_1 = \frac{1}{D}\left(\frac{\beta\mu\gamma}{k_y} - k_y\right). \qquad (7.11)$$

It was discussed that this slope will change for a change in composition affecting γ, k_y and D. Table 7.4 gives the slopes of the different correlations for T_c versus $d^{-1/2}$. From this table it is seen that the steepness of the slope increases negatively from CTODi up to the T_{27} criteria. For example, the slopes for Steel L are B_1 = -6.41°C/$mm^{-1/2}$ at δ_i = 0.15 mm, B_1 = -9.86°C/$mm^{-1/2}$ at K_i = 110 MPa $m^{1/2}$ and B_1 = -12.44°C/$mm^{-1/2}$ at T_{27}.

Table 7.4
Comparison of slopes from
T_c versus $d^{-1/2}$ correlations

Steel	B_1(°C/$mm^{-1/2}$)		
	δ_i	K_i	T_{27}
L	-6.41	-9.86	-12.44
H	-6.84	-11.06	-15.63

The difference in slope between fracture toughness testing and Charpy Impact testing will arise from differences in specimen geometry, loading, notch configuration and strain rate. The factor β accounts for stress state, specimen geometry and notch configuration. There is an expected increase in transition temperature of about 30°C when using a fatigue crack compared to a blunt vee-notch at the same strain rate [17]. The strain rate has an important effect on transition temperature therefore. The strain rate affects the material's yield stress. The constant D includes a strain rate term such that

$$DT = B_1 B_2 T \tag{7.13}$$

from equation (5.62) where B_1 is the Peierls-Nabarro stress and is constant and

$$B_2 = -[\beta_0 + \frac{k}{H_0}\ln(\nu/\dot{\varepsilon})] \tag{7.14}$$

from equation (5.63). The factors β_0, k, H_0 and ν are all approximately constant, as given in Section 5.5.1. Therefore D depends on $-\ln(1/\dot{\varepsilon})$. Typically the strain rate for a CTOD test is about $10^{-5}s^{-1}$ and for a Charpy test the strain rate is about 10^3 s^{-1} which is a difference of 8 orders of magnitude [90]. An increase in strain rate means a decrease in $-\ln(1/\dot{\varepsilon})$. Consequently, 1/D will increase resulting in a larger negative slope for T_c versus $d^{-1/2}$.

For example, in Section 5.5.2 and Tables 5.7 and 5.8 values were given for B_1, β_0, k, H_0 and ν.

Using these values gives $D \approx -7.8$ MPa/°C for $\dot{\varepsilon} = 10^{-5}s^{-1}$ and $D \approx -5.1$ MPa/°C for $\dot{\varepsilon} = 10^3 s^{-1}$ for Steel L. For Steel H, $D \approx -8.9$ MPa/°C for $\dot{\varepsilon} = 10^{-5}s^{-1}$ and $D \approx -5.92$ for $\dot{\varepsilon} = 10^3 s^{-1}$. Therefore the increase in strain rate represents a decrease in D by approximately 1/3. The slope B_1 would be expected to increase by 1/(2/3) or 3/2. When this is applied,for example, to B_1 from equation (7.5) for Steel L the expected slope is -9.62°C $mm^{1/2}$ for $\dot{\varepsilon} = 10^3 s^{-1}$ (i.e. the Charpy test). When corrected for yield strength, as in equation (7.8) for Steel L, the expected slope is -14.79°C $mm^{1/2}$ for $\dot{\varepsilon} = 10^3 s^{-1}$. This example shows the effect changing the strain rate does have and that there are other factors between the two tests unaccounted for. The

sensitivity of yield stress to a change in strain rate is significant. Work has shown that yield stress slowly increases between a strain rate of 10^{-6} to about 10^{-1} s^{-1} and then increases rapidly as strain rate increases to 10^{3} s^{-1} [97].

The higher strain rate test i.e. the Charpy Impact test, is expected to have the steeper negative slope. It implies that strain rate has a greater effect than notch acuity which supports Chew's results where a lower transition temperature is found for the CTOD test than for the Charpy test [16]. It also supports the conclusions of Sailors and Corten [60]. The effects of strain rate will to a certain extent be counteracted by adiabatic effects due to plastic deformation at the crack tip at high strain rates, as discussed in Chapter 2. The adiabatic effect could account for the difference in the observed and calculated slopes for the example discussed.

7.2.2 PREDICTION OF TRANSITION TEMPERATURE

In Section 4.4.1 the Charpy transition temperature for low carbon alloy steels was given as

$$\begin{aligned} T_{27}(^\circ) &= 264(\%C) - 11.8(d^{-1/2}) + 28(\%Mn) - 140\ 000\ F^1 \\ &+ 3850(\%N_R) + 18(\%Cr) + 68(\%Si_T) + 50(\%Al_R) \\ &+ \text{constant} \end{aligned} \qquad (4.4)$$

from Reference [8] where

$$F^1 = \frac{(\%Mn)(\%N_R)}{(\%Mn) + K_n(\%N_R)}$$

and $K_n \approx 1500$. For Steel L this gives

$$T_{27}(^\circ C) = 61.83 - 11.8\ d^{-1/2} \qquad (7.15)$$

and for Steel H

$$T_{27}(^\circ C) = 93.64 - 11.8\ d^{-1/2} \qquad (7.16)$$

Figure 4.28 shows predicted transition temperature against experimental transition temperature and it was found that there was good agreement between equations (4.7), (4.9), (7.15) and (7.16). No similar empirical equation is available to predict transition

temperature of toughness testing on the basis of composition and grain size.

The transition temperature may be found using the Ritchie-Knott-Rice model of cleavage fracture toughness. In Section 3.2.5 the dependence of K_{IC} on grain size, temperature and strain rate using the RKR model was given as

$$K_{IC} = \beta^{-(N+1)/2} X_0^{1/2} \sigma_F^{(N+1)/2} / \sigma_{ys}^{(N-1)/2} \qquad (3.22)$$

where β is the amplitude of the stress singularity at the crack tip, N is the Ramberg-Osgood strain hardening index, X_0 is the characteristic distance, σ_F is the fracture stress and σ_{ys} is the yield stress at the test temperature and strain rate [89].

For small scale yielding it has been found that fracture toughness is given by

$$K_{IC} = 0.4769(\sigma_{ys}\delta_c)^{1/2} \qquad (2.93)$$

where σ_{ys} is the yield stress in MNm^{-2} and δ_c is the critical CTOD in μm [16].

Curry has suggested that by setting $\delta_c = \delta_i$ the fracture mode transition temperature can be estimated by combining equations (3.22) and (2.93) for a steel of known δ_i [90]. The initiation CTOD must be assumed to be independent of grain size and temperature [82,84]. Temperature independence has been found until the onset of dynamic strain ageing [84]. In this investigation this sets a temperature limit of about +45°C found during tensile testing for Steel H.

The characteristic distance X_0 must be assumed to be temperature and grain size independent but there is conflicting evidence about this. Curry and Knott have shown that X_0 is grain size independent if d is less than 40 μm and X_0 is temperature independent since it is determined by the crack-tip stress distribution and the carbide particle distribution [91,162]. As discussed in Section 6.3.7 the grain size dependence of X_0 was found by Chew, and Rawal & Gurland to be $X_0 = 2\ d_g$ [16,76]. A temperature dependence of X_0 was found by Bowen *et al.* and also in this investigation but this could be due to an increase in fracture

stress with increasing temperature due to increasing plastic deformation at the crack tip rather than an increase in X_o [193].

The cleavage fracture stress is assumed to be temperature independent [64,166]. The grain size dependence of cleavage fracture stress has been given in two forms, either

$$\sigma_F = \sigma_{iF} + k_F d^{-1/2} \tag{7.17}$$

where $\sigma_{iF} = \sigma_F$ at $d^{-1/2} = 0$ and k_F is a constant or

$$\sigma_F = k_F d^{-1/4} \tag{7.18}$$

where k_F is a constant [162,163,176,210]. For ease of mathematical calculation and to be consistent with Curry's interpretation of the RKR model $\sigma_F = k_F d^{-1/4}$ will be used. The fracture toughness is given by

$$K_{IC} = \beta^{-(N+1)/2} X_0^{1/2} \sigma_F^{(N+1)/2} / \sigma_{ys}^{(N-1)/2} \tag{7.19}$$

and

$$K_{IC} = 0.4769(\sigma_{ys}\delta_c)^{1/2}. \tag{7.20}$$

The transition temperature may then be found by equating equations (7.19) and (7.20) and using the grain size dependence of fracture stress and the grain size and temperature dependence (at constant strain rate) of yield stress. The case considered is where the characteristic distance X_o is independent of grain size. Substituting $\delta_c = \delta_i$ at fracture mode transition and equating equations (7.19) and (7.20) gives

$$0.4769(\sigma_{ys}\delta_i)^{1/2} = C_1(k_F d^{-1/4})^{(N+1)/2} / \sigma_{ys}^{(N-1)/2} \tag{7.21a}$$

where $C_1 = \beta^{-(N+1)/2} X_0^{1/2}$ = constant and substituting for σ_F. Then multiply through by $\sigma_{ys}^{(N-1)/2}$ to give

$$0.4769(\sigma_{ys}\delta_i)^{1/2} \sigma_{ys}^{(N-1)/2} = C_2 d^{-(N+1)/8} \tag{7.21b}$$

where C_2 is a constant and $C_2 = C_1 k_F^{(N+1)/2}$. Combine the yield stress terms and rearrange the equation to leave only yield stress on the LHS i.e.

$$\sigma_{ys}^{N/2} = C_3 d^{-(N+1)/8} \qquad (7.21c)$$

where C_3 is a constant and $C_3 = C_2/(0.4769\delta_i^{1/2})$. By taking the 2/N root of each side the yield stress at fracture mode transition is

$$\sigma_{ys} = [C_3 d^{-(N+1)/8}]^{2/N} \qquad (7.21d)$$

which reduces to

$$\sigma_{ys} = C_4 d^{-(N+1)/4N} \qquad (7.22)$$

where C_4 is a constant and

$$C_4 = [\beta^{-(N+1)/2} X_0^{1/2} k_F^{(N+1)/2}/(0.4769\delta_i^{1/2})]^{2/N} \qquad (7.23)$$

with units of MPa $m^{+(N+1)/4N}$, all variables are in MN m^{-2} and m except δ_i is in μm. In Chapter 5 the grain size and temperature dependence of yield stress was given as

$$\sigma_{ys} = \sigma_i^* + \sigma_i(st) + k_y d^{-1/2} \qquad (5.17)$$

where σ_i^* is the temperature dependent component of yield stress, $\sigma_i(st)$ is the athermal structural component and $k_y d^{-1/2}$ is the grain size contribution. Substituting for yield stress in equation (7.22) and subtracting $(\sigma_i(st) + k_y d^{-1/2})$ from each side then

$$\sigma_i^* = C_4 d^{-(N+1)/4N} - \sigma_i(st) - k_y d^{-1/2}. \qquad (7.24)$$

The assumed form of the temperature dependence of yield stress in Section 3.3.1 for the Cottrell-Petch model of fracture mode transition was

$$\sigma_i^* = A\exp(-\alpha T) \qquad (3.44)$$

where A and α are constants for a constant strain rate. The constant $\alpha = \beta_0 + \beta_1 \ln\dot{\varepsilon}$ where β_0 and β_1 are constants and their value and significance are discussed in Sections 5.3.4 and 5.5.2. Substituting

for σ_i^* in equation (7.24) and taking natural logarithms of both sides gives

$$LnA - (\beta_0 + \beta_1 ln\dot{\varepsilon})T = ln(C_4 d^{-(N+1)/4N} - \sigma_i(st) - k_y d^{-1/2}) \quad (7.25)$$

or by subtracting ln A from both sides and multiplying through by -1 the transition temperature is

$$(\beta_0 + \beta_1 ln\dot{\varepsilon})T_c = lnA - ln(C_4 d^{-(N+1)/4N} - \sigma_i(st) - k_y d^{-1/2}) \quad (7.26)$$

where β_0, β_1, A, C_4 and k_y are constants. Less accurately the temperature dependence of yield stress may be assumed to be linear over a small temperature range. Then

$$\sigma_i^* = A_0 - A_1(\beta_0 + \beta_1 ln\dot{\varepsilon})\,T \quad (7.27)$$

and substituting for σ_i^* in equation (7.24) the transition temperature is

$$A_1(\beta_0 + \beta_1 ln\dot{\varepsilon})T_c = A_0 + \sigma_i(st) + k_y d^{-1/2} - C_4 d^{-(N+1)/4N}. \quad (7.28)$$

Equations (7.26) and (7.28) make the transition temperature a function of grain size and composition, strain rate, the Peierls-Nabarro stress, the strength of dislocation locking, the stress state (through the coefficient C_4) and the strain-hardening index. There is a limit to equation (7.26). The term $(C_4 d^{-(N+1)/4N} - \sigma_i(st) - k_y d^{-1/2})$ must be greater than or equal to zero so that for a given Ramberg-Osgood strain-hardening index there will be a maximum permissible grain size.

The dependence of equations (7.26) and (7.28) are similar to those of equations (7.1) and (7.2) which make the transition temperature a function of grain size, the Peierls-Nabarro stress, the strength of dislocation locking and the stress state. However the dependence of transition temperature on grain size is not linear with $ln d^{-1/2}$ or $d^{-1/2}$ but transition temperature will increase with increasing grain size. For a linear dependence on ln $d^{-1/2}$ or $d^{-1/2}$,

only, to exist the Ramberg-Osgood strain-hardening index must approach 1 so that $d^{-(N+1)/4N}$ approaches $d^{-1/2}$. This would mean that the material's stress-strain curve would show little yielding and strain-hardening would be very large.

Since the derivations of equations (7.1), (7.2), (7.26) and (7.28) have similar dependencies then they may be expected to be equivalent. Whether cleavage fracture is considered to be initiated by carbide cracking over a characteristic distance or by intersecting slip planes the transition temperature will depend on grain size.

The prediction of transition temperature using equations (7.26) and (7.28) may be compared to the experimental results. Not all properties needed for calculation of the coefficients in equations (7.26) and (7.28) were found experimentally. The values of k_F = 80 MPa $m^{1/4}$, X_0 = 0.180 mm and N = 9 for mild steel are given by Curry and are used in this investigation [89,90]. The strain rate in a fracture toughness test was estimated by Irwin as

$$\dot{\varepsilon} = 2\sigma_{ys}/tE, \qquad (7.29)$$

where t is the time of the test in seconds, which Curry gave as typically 5 x 10^{-5} s^{-1} [90,289]. This is an order of magnitude lower than the strain rate of the tensile test which was 3.33 x 10^{-4} s^{-1}. If the tensile test strain rate is used for calculation of β_1 in equations (7.26) or (7.28) then there is a difference of 4% in β_1 which is not considered significant. Therefore, the experimental values $B_2 = (\beta_0 + \beta_1 \ln\dot{\varepsilon})$ given in Table 5.7 may be used.

In the preceding analysis the assumed temperature dependent form of yield stress was taken as $\sigma_i = A\exp(-\alpha T)$ or $\sigma_i^* = A_0 - A_1\alpha T$. However in Chapter 5 the temperature dependence of yield stress was given as a power series expansion of $\sigma_i^* = A\exp(-\alpha T)$ assuming a constant strain rate. This gave $\sigma(T) = A_1 + A_2T + A_3T^2 + A_4T^3$ where A_1, A_2, A_3 and A_4 are constants. This model was found to have good accuracy over the temperature range from -196 to +65°C. It is mathematically difficult to express the transition temperature in terms of this function but using

$$\sigma_{ys} = C_4 d^{-(N+1)/4N} \qquad (7.22)$$

and

$$C_4 = [\beta^{-(N+1)/2} X_0^{1/2} k_F^{(N+1)/2}/(0.4769\delta_i^{1/2})]^{2/N} \qquad (7.23)$$

then the yield stress at fracture mode transition for a particular grain size may be calculated. The transition temperature can be found from yield stress versus temperature plots for that grain size, composition and strain rate, for example Figures 5.14 and 5.16, or from equations (5.59) and (5.61).

The transition temperature is calculated using equations (7.26), (7.28) and (7.22) and (7.23). These results are presented in Table 7.5. From the results it is observed that an accurate form of the temperature dependence of yield stress must be used to predict transition temperature results.

Table 7.5
Predicted Transition Temperature Results Using the Ritchie-Knott-Rice Model of Cleavage Fracture

Steel	Transition Temperature (°C)			
	Eqn. (7.26)	Eqn. (7.28)	Eqn. (7.22)[1]	Exp'tal
LA	55	-177	-58	-62
LB	67	-176	-53	-30
LC	113	-175	-38.5	-17
LD	149	-174	-29	-1
HA	45	-171	-69	-56.5
HB	56	-170.5	-65	-23.5
HC	78	-169.5	-57	-18
HD	86	-169	-55	-5
275N[2]	70	-176.4	-37.5	-43
275T	64	-176.6	-32	-41
PV	78	-176.2	-31.5	-43

1. Yield stress found using equation (7.22). Equations (5.59) and (5.61) used to find transition temperature from calculated yield stress.
2. Results from Reference [16].

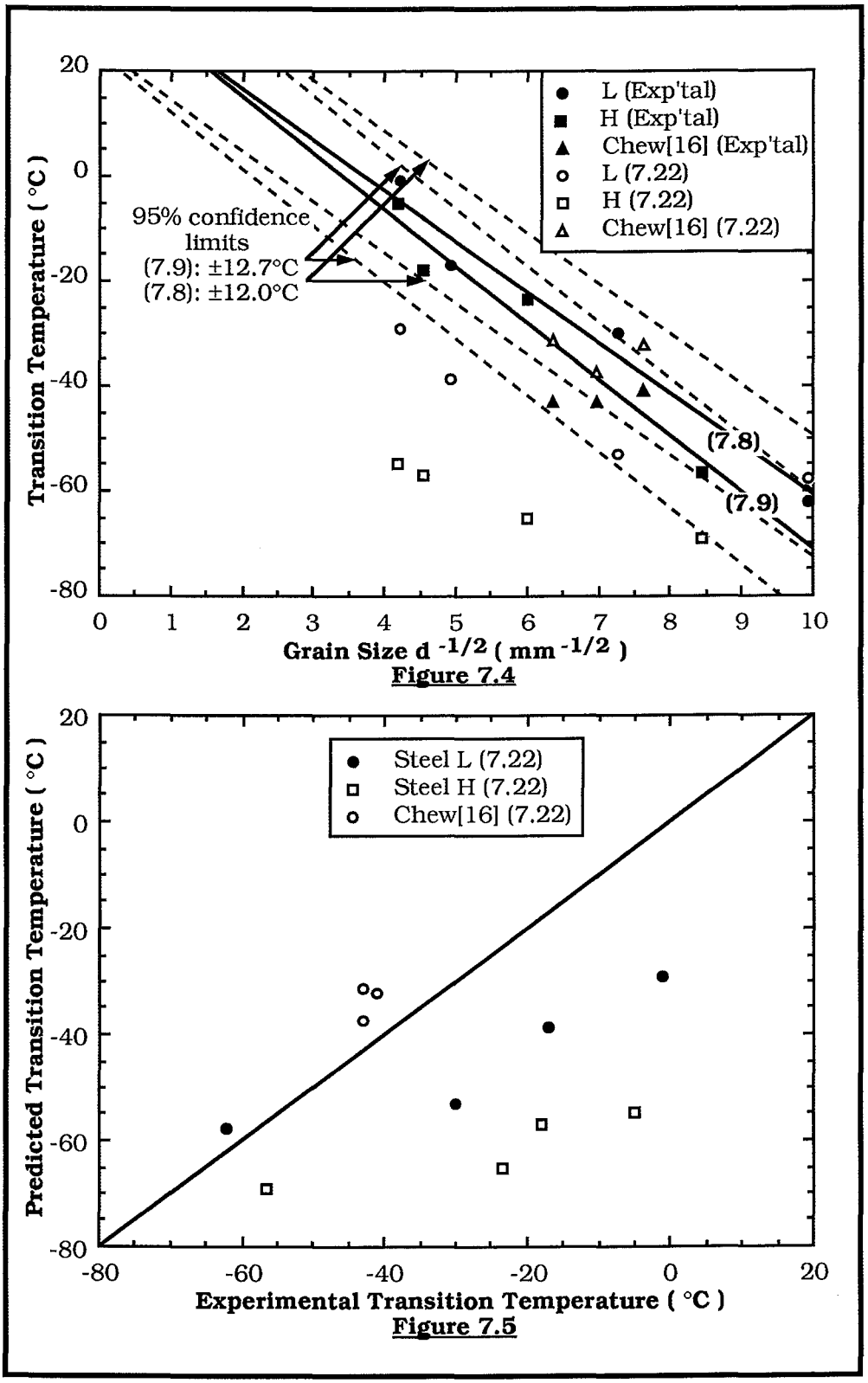

Figure 7.4 : Predicted transition temperature (°C) [Equation (7.22)] as a function of grain size $d^{-1/2}(mm^{-1/2})$ for Steels L & H.

Figure 7.5 : Predicted transition temperature (°C) [Equation (7.22)] as a function of experimental transition temperature (°C) for Steels L & H.

Using equation (7.26) the predicted transition temperature is much larger than the experimentally found transition temperature and using equation (7.28) the predicted transition is much lower than the experimental transition temperature. When the predicted transition temperature is found using equation (7.22) with equations (5.59) and (5.61) then the prediction is much closer to the experimentally determined transition temperature. Figure 7.4 shows predicted (equation (7.22)) and experimental transition temperature versus $d^{-1/2}$. The predicted transition temperature is not linear with $d^{-1/2}$ due to the influence of the term $d^{-(N+1)/4N}$.

When the strain-hardening index (N) is about 9 then $d^{-(N+1)/4N} = d^{-5/18}$ or approximately $d^{-1/4}$. Therefore, the transition temperature predicted by the micromechanical model of fracture toughness is approximately a function of $D_1d^{-1/2} + D_2d^{-1/4}$ where D_1 and D_2 are constants. However an analysis of this type in the present study is not made since the low number of data points for transition temperature against grain size means the resulting equation and coefficients will have little significance (<20%). Figure 7.5 shows the predicted transition temperature against experimental transition temperature. The results from Chew's work are higher than the experimental results in contrast to the predicted results for L and H. The predicted results from Chew's work lie very close to the predicted line for transition temperature from equation (7.5) on Figure (7.4). The results for H are between 12.5 and 50°C lower than the experimental transition temperature.These differences are greater than the differences for Steel L.

The difference between experimental and predicted transition temperature results is probably due to the assumed material properties (either N, k_F or X_0) being different to the actual material properties. If the properties change a different value of C_4 is found and d is raised to a different power. If

$$\sigma_{ys} = C_4d^{-(N+1)/4N} \qquad (7.22)$$

is used with the value of yield strength at the experimentally found transition temperature then C_4 may be calculated assuming N does not change.

The constant C_4 was calculated to be from 15.44 to 14.50 MPa $m^{5/18}$ for L, from 14.35 to 13.64 MPa $m^{5/18}$ for H and from

15.75 to 16.78 MPa $m^{5/18}$ for Chew's experimental steels. These values are compared to calculated values of 15.24 MPa $m^{5/18}$ for L at δ_i = 0.15 mm and of 15.94 MPa $m^{5/18}$ for H at δ_i = 0.10 mm. The value of C_4 = 15.24 MPa $m^{5/18}$ used to predict transition temperature for Steel lies in the range of the experimental values of C_4. Therefore when C_4 = 15.44 MPa $m^{5/18}$ for LA the predicted transition temperature will be higher than the experimental transition temperature. When the experimental value of C_4 is less than 15.24 MPa $m^{5/18}$ the predicted transition temperature will be lower than the experimental transition temperature.

For Steel H C_4 = 15.94 MPa $m^{5/18}$, which is larger than the experimental values of C_4 so the predicted results will be lower than the experimental results of transition temperature. It is likely that the assumed values of N, k_F and X_0 do not apply to Steel H. For example, if the fracture stress data of Table 6.14 is used to find the relationship $\sigma_F = k_F d^{-1/4}$ for H then k_F is found to be 59 MPa $m^{1/4}$ compared to the assumed value of 80 MPa $m^{1/4}$.

If the temperature dependence of yield stress for a particular material is known, as well as its fracture properties, then equations (7.22) and (7.23) may be used to predict a lower bound of the fracture mode transition temperature. The predicted FMTT will increase with increasing grain size. This demonstrates that the fracture mode transition temperature may be described from a micromechanical model of cleavage fracture toughness.

7.2.3 EXAMINATION OF FRACTURE INITIATION

In Section 3.4.4 fracture at transition was described using the results of Ebrahimi [86]. Four types of fracture behaviour were described. The fracture surface of broken specimens were examined using a JEOL JSM35 scanning electron microscope with the objective of determining the mode of separation at the instance of initial crack extension.

In the transition region fracture initiation can be considered to be complete when microcracks (either cleavage or ductile) in the initial strain-hardened plastic zone and shear cracks from the crack tip achieve instability [86]. The shear zone width formed increases with increasing temperature and the shape is similar to the plastic zone in the fracture plane.

The fracture surface was examined near the centre of the specimen at the tip of the fatigue crack under the scanning electron microscope. The fracture was examined for stretch zone width, shear zone width and final mode of fracture. The SEM photographs were taken in stereographic pairs at 30° and 45° tilt although only one half of the pair is presented in this thesis. Specimens were examined from toughness tests at -196°C, in the lower transition region, in the middle of the transition and from the upper shelf toughness. Evidence of either a stretch zone or shear zone was very difficult to find in most cases.

Figures 7.6 to 7.9 show the results for LD from -196 to +45°C. Figure 7.6 shows the fracture surface of specimen LD9 tested at -196°C. The fatigue crack is marked on the plate and failure is by cleavage fracture. There is no evidence of stretching as described by Beachem and Meyn so fracture has occurred with little plastic deformation [290]. The cleavage facets show typical river markings [291]. This is typical of Type I behaviour described by Ebrahimi. Cleavage fracture occurs after formation of cleavage microcracks ahead of the crack tip. At -196°C it is likely fracture is nucleation controlled.

At -30°C test temperature the fracture surface of LD1 shows three distinct regions (Figure 7.7). These are the fatigue crack, the stretch zone and the region of cleavage fracture. The estimated width of the stretch zone from Figure 7.7 and its stereo pair is 0.049 mm (the SZW marked on the figures are the SZW at the angle of tilt the photomicrograph was taken at, i.e. correcting for the angle of tilt reduces the size of the SZW). There is a distinct lip between the stretch zone and the cleavage fracture, indicating plastic deformation at the crack tip is still limited.

Figure 7.8 of specimen LD11 at +10°C again shows the fatigue crack and the stretch zone. The estimated stretch zone width is 0.062 mm so the stretch zone width has increased with an increase in temperature which is expected [86]. Final failure is by cleavage fracture although there is some evidence of microvoid coalescence at the tip of the stretch zone. This would correspond to Type II fracture behaviour described by Ebrahimi [86].

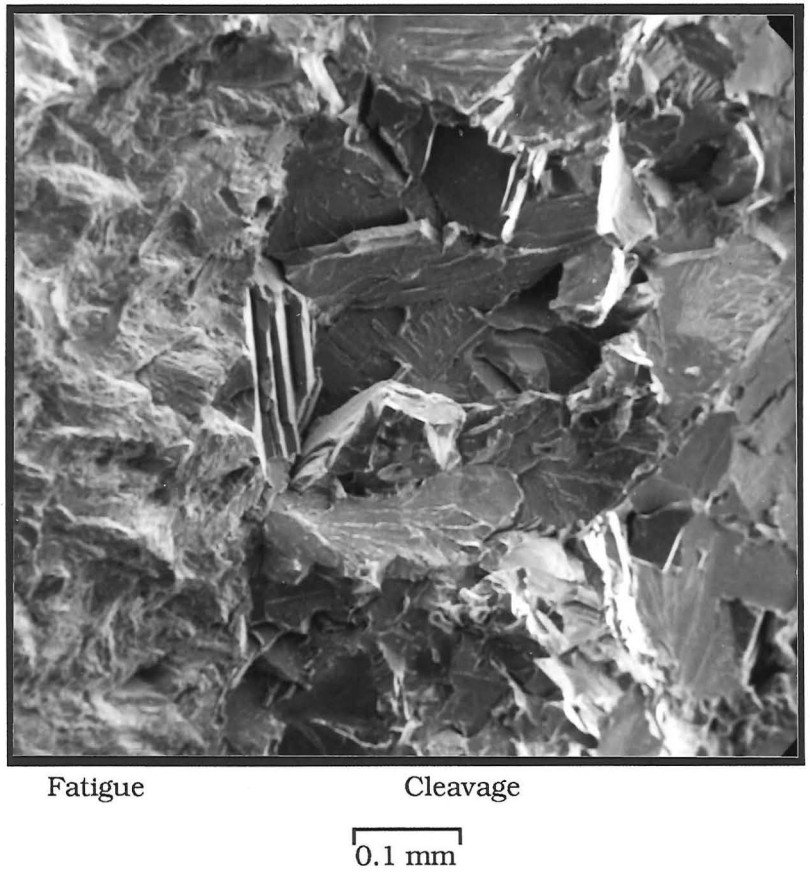

Figure 7.6 : Fracture surface of LD9 tested at -196 °C (x140, tilt45°).

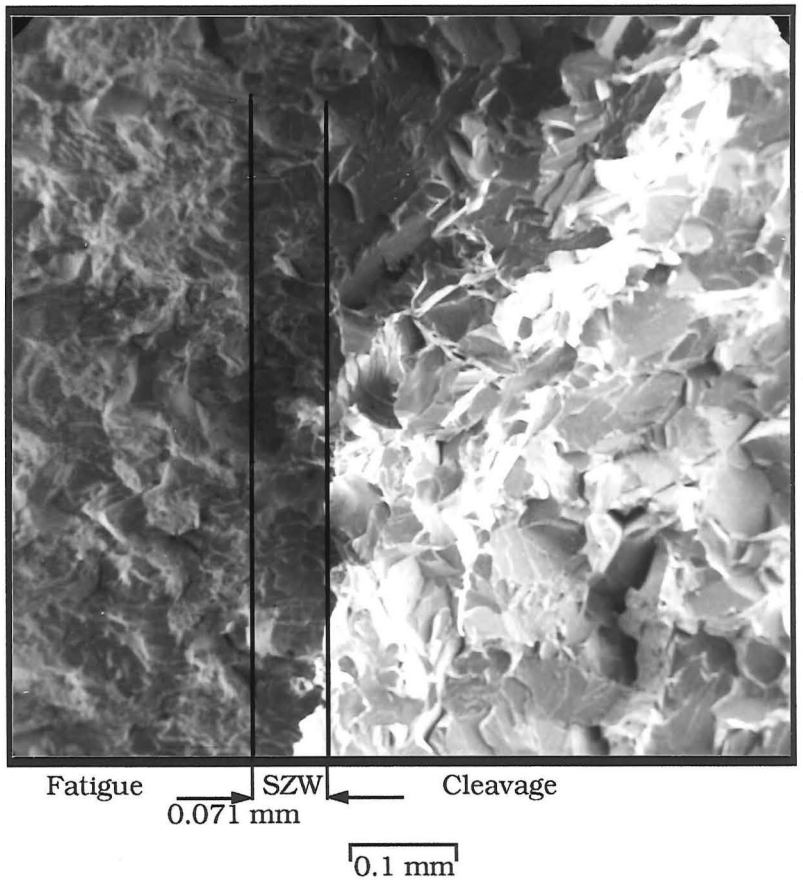

Figure 7.7 : Fracture surface of LD1 tested at -30 °C (x140, tilt 30°).

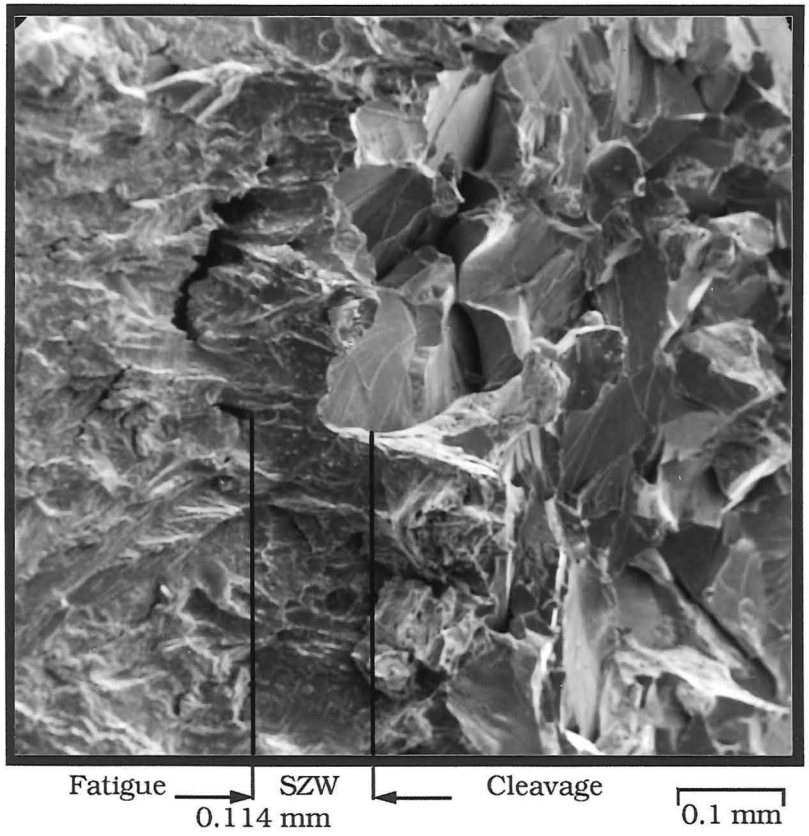

Figure 7.8 : Fracture surface of LD11 tested at +10 °C (x140, tilt 30°).

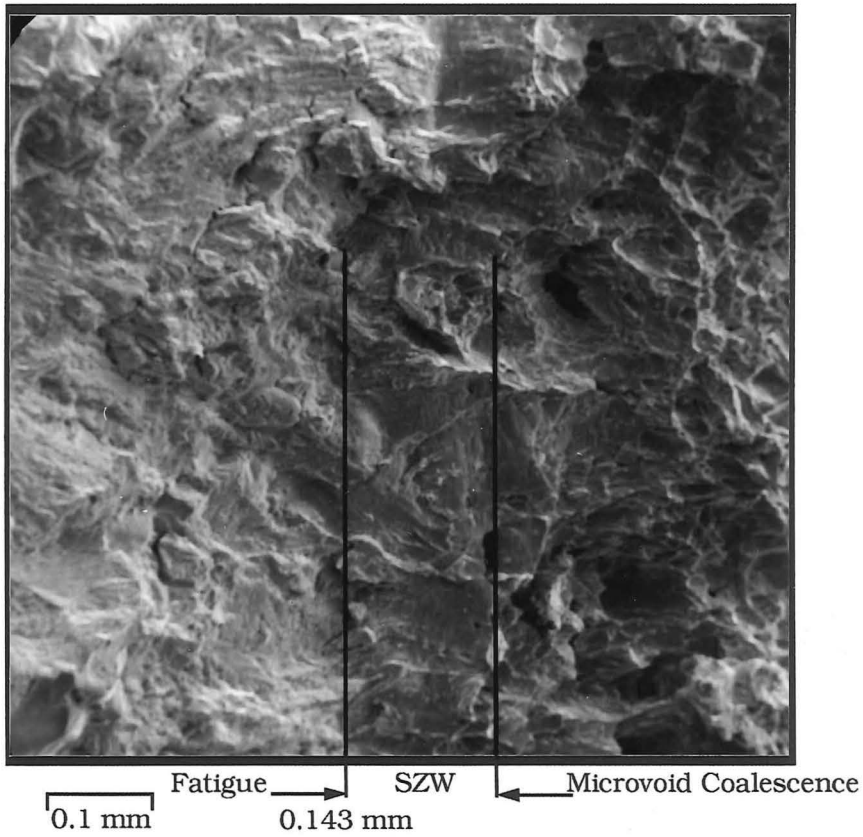

Figure 7.9 : Fracture surface of LD10 tested at +45 °C (x140, tilt 45°).

At 45°C specimen LD10 shows a stretch zone which is 0.095 mm wide (Figure 7.9). Beachem and Meyn described the stretched zone as often featureless and flat and there is some evidence of this shown in Figure 7.9 [290]. Any shear zone present is not distinguishable from the microvoid coalescence resulting from stable crack extension. The stable crack extension continues beyond the initial plastic zone and cleavage fracture occurs after 1-2 mm of stable crack extension. This is evidence of Type IV fracture behaviour described by Ebrahimi where final instability has occurred outside the initial strain-hardened volume of material around the crack tip [86].

The stretch zone width has increased with the increase in temperature. At +45°C the critical CTOD is 0.476 mm which is much larger than δ_i = 0.15 mm. After transition the SZW is expected to be temperature insensitive. It is possible that the SZW (and therefore δ_i) is not temperature independent but slowly increases with increase in temperature after transition [86,219].

The results of LD show no distinguishable shear zone. However examination of other specimens shows the presence of a small region of microvoid coalescence near the original crack tip. Figure 7.10 shows specimen LC3 tested at -30°C. There is a region of fatigue cracking before a region of microvoid coalescence followed by cleavage fracture.

This is evidence of Type II behaviour described by Ebrahimi where cleavage microcracks develop ahead of the crack tip and instability occurs when these link with ductile shear at the fatigue crack tip. There is also some microvoid coalescence distributed in the cleavage region. It indicates that the fracture process in the transition region is complex.

Figure 7.11 shows specimen HC6 tested at -5°C. At x110 magnification the fracture surface is a mixture of cleavage fracture and microvoid coalescence even though the macrofracture appearance is cleavage with ductile shear lips on the specimen's edges. Some of the cleavage facets show slip line markings. Figure 7.12 shows two facets containing river lines and slip lines. These facets are identified as A and B on Figure 7.11.

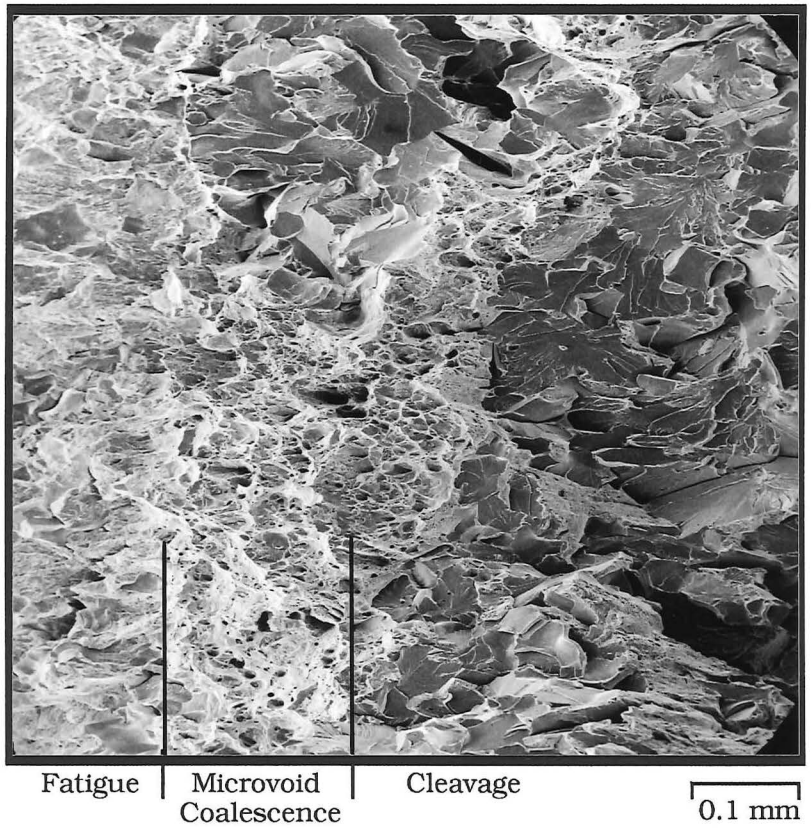

Figure 7.10 : Fracture surface of LC3 tested at -30 °C showing Type II fracture behaviour (x140, tilt 30°).

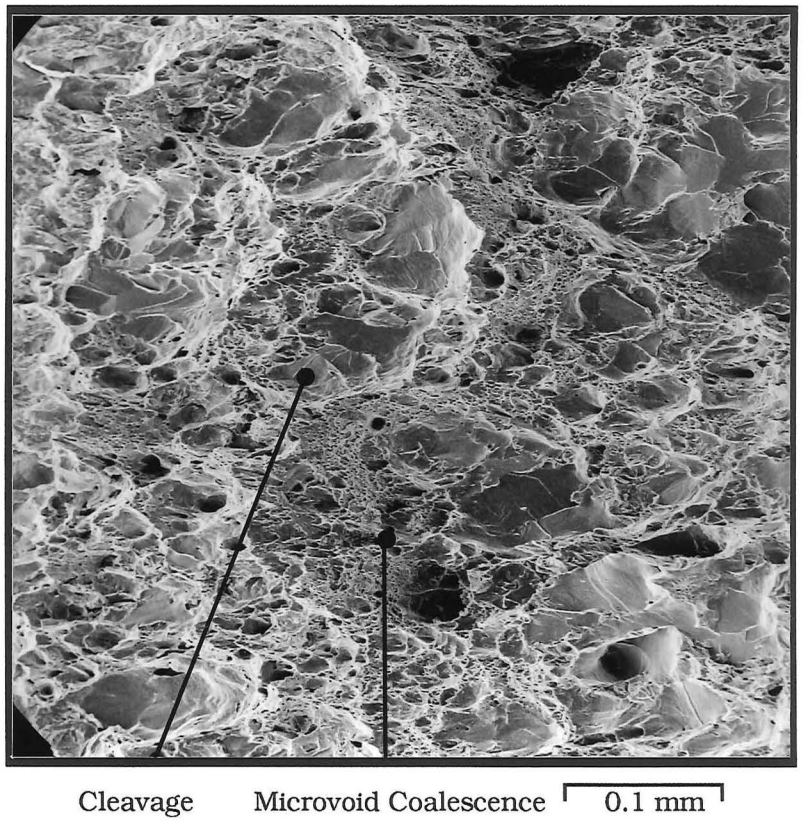

Figure 7.13 : Fracture surface of HB2 tested at +40 °C showing plastically deformed cleavage facets (x210, tilt 30°).

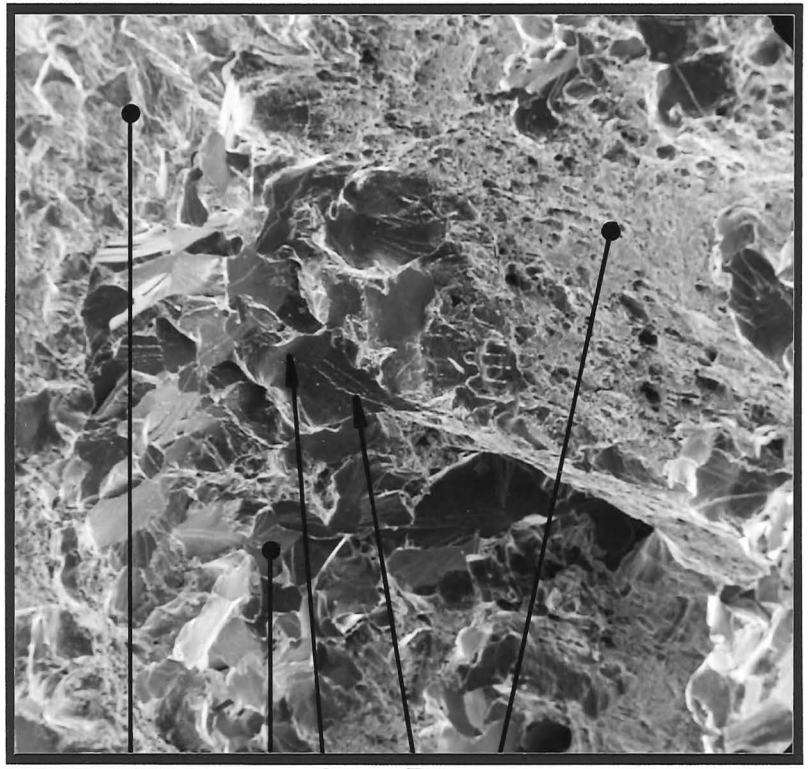

Figure 7.11 : Fracture surface of HC6 tested at -5 °C showing a mixed mode of failure (x110, tilt 30°).

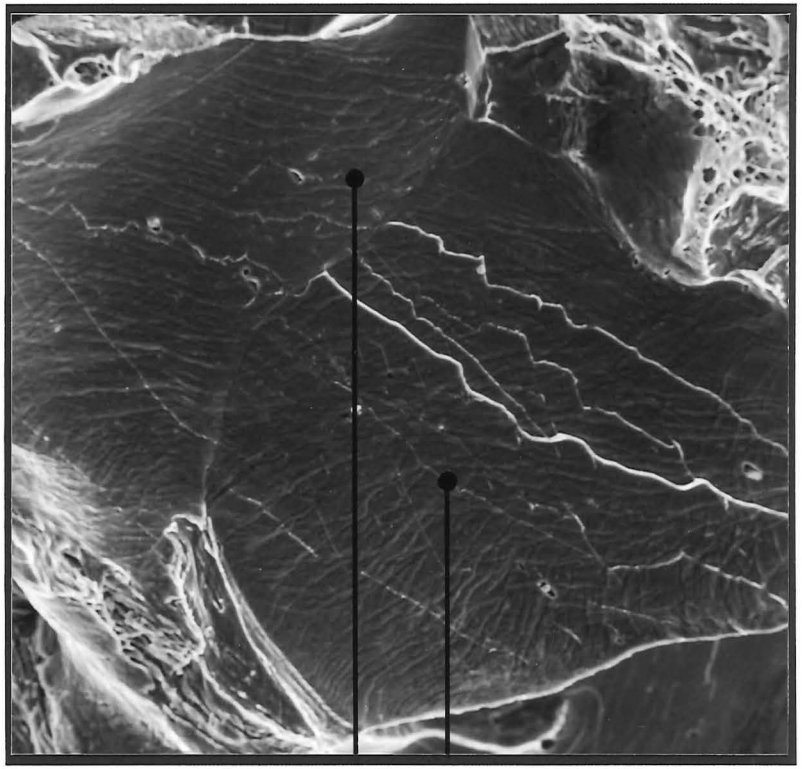

Figure 7.12 : Cleavage facets showing slip-line markings (x815, tilt 45°).

Metallic crystals are subject to a definite amount of plastic deformation in the vicinity of the cleavage crack [291]. The slip lines on the cleavage facets are similar to those shown by Beachem & Meyn on Armco iron [290]. These are produced by irregular slip where slip intersects the surface in irregular fashion [290]. It is likely some cross- and multiple-slip is involved.

The direction of macroscopic crack propagation is indicated in Figures 7.11 and 7.12. However the direction of microscopic crack propagation does not necessarily correspond to the macroscopic direction [291]. This indicates cleavage fracture propagation occurs by simultaneous or near simultaneous fracture of several individual grains each with an individual direction of propagation. The cracks join to form a general macroscopic crack front.

The mixed mode of fracture in the transition region is an indication of the more complex nature of fracture in this region. The slope of the transition curve between the lower and upper shelf values of toughness may be steep as for finer grain sizes or spread out over a wider temperature range as for larger grain sizes. As temperature increases the percentage of microvoid coalescence appearing in the fracture surface increases. This could lead to grain size cleavage cracks. Figure 7.13 shows specimen HB2 tested at +40°C at x150 magnification. The CTOD for HB2 was 0.484 mm meaning it lies in the upper regions of transition behaviour. The fracture shows areas of cleavage fracture surrounded by microvoid coalescence. The cleavage facets show slip lines indicating plastic deformation of the facet. It seems likely that the deformed facets indicate the existence of stable grain-sized or larger cleavage cracks in the material as has been observed by other workers [86,179,292].

The plastic deformation of the cleavage facets would then occur during stable crack extension by microvoid coalescence in the upper transition region. In the lower transition region the grain size microcracks could control crack propagation.

The shear zone discussed by Ebrahimi would then appear to be the first appearance of ductile fracture. The increase in shear zone width with temperature would be expected as size of the plastic zone increases and the percentage shear of the fracture increases.

7.2.4 CRACK INITIATION AND PROPAGATION

By varying the size of the plastic zone ahead of the crack tip it has been suggested that progress could be made towards differentiating between the energy required for crack initiation and crack propagation [4]. Ferguson and Thorby did suggest that the fracture toughness measured only the energy required for crack propagation [17]. This was based on Chipperfield and Knott finding that the COD for crack initiation (δ_i) in mild steel is a linear function of the notch root radius down to a radius approximately equal to the material's inclusion spacing, below which it remains constant at its minimum value [218]. For a blunt notch, as is used for Charpy V-notch specimens, δ_i will be greater than for a "sharp" fatigue crack and the energy absorbed in initiating a crack is much greater [293]. However a CTOD can be measured because plastic blunting of the fatigue crack occurs as the specimen is loaded. Therefore, energy is required for crack initiation from a blunted crack and it is expected that the CTOD measures energy required for crack initiation and crack propagation.

In Section 7.2.1 the influence of strain rate on the slope of T_c versus $d^{-1/2}$ curves was discussed. It was concluded that the effect of increasing the strain rate was to elevate the local yield stress ahead of the crack. This produced an increasing negative slope of the T_c versus $d^{-1/2}$ plot. The same assessment applies to the transition temperature for a given grain size. By elevating the yield stress fracture mode transition will occur at a higher temperature since there is a greater chance that the fracture stress is exceeded and cleavage fracture may occur. This will be offset by the lack of constraint of the Charpy specimen.

The effect of strain rate on the FMTT showed that notch acuity has only a small influence over the transition temperature. When the strain rate for fatigue cracked and blunt notch specimens is the same the transition temperature for the fatigue cracked specimen was found to be 30°C higher than for the blunt notched specimen [293]. Although this indicates that notch sharpness is significant Thorby and Ferguson felt that this shift in transition temperature was only due to a reduction in statistical scatter of results by use of the fatigue cracked specimen since the 50% FATT coincided for both types of specimens [293].

By varying the grain size of the material tested the size of the plastic zone ahead of the crack tip varies. This was discussed in Section 6.2.4 where the increase in yield strength due to grain refinement reduced the size of the plastic zone.

The size of the plastically deformed lobes produced by fatigue crack extension were found by Chew to extend 1 to 2 grains ahead and approximately 4 grains to either side of the crack tip [16]. Chew found that strain-ageing in this zone increased the fracture mode transition temperature by about 10°C in a steel of high active nitrogen content. In a similar steel, microalloyed with titanium to give a low active nitrogen content, no shift in FMTT was found after a similar ageing treatment.

The effect of strain ageing on the CTOD obtained by the notched bend test was investigated by Burdekin [88]. A series of 76 mm square notched bend specimens were given a pre-strain treatment by opening the root of the notch by 0.15 mm and closing it again with a reverse bend to the original dimensions. This was followed by a standard ageing treatment of 250°C for half an hour. This treatment resulted in an approximate increase in transition temperature of 60-70°C from the original material's FMTT. This data does not indicate how much the FMTT has increased due to plastic damage alone.

A study of strain ageing on the Charpy transition temperature has shown that a significant change in FMTT results from plastic deformation in the absence of ageing [13]. From the work of Chew a pre-strain of 5% caused a shift of 8°C in the transition temperature from Charpy Impact testing in the low active nitrogen content steel [16]. Since the amount of pre-strain caused by fatiguing will be small then any shift in transition temperature due to plastic damage will be negligible when measured by the CTOD test.

The temperature dependence of yield stress has a large influence on fracture toughness and the fracture mode transition. Figure 7.14 shows transition temperature versus yield stress for CTOD and K_c results and also includes the CTOD results from Chew's work. The transition temperature decreases rapidly with increase in yield stress. The influence of grain size on this decrease may be demonstrated by subtracting the grain size component $k_y d^{-1/2}$ from yield stress at $\delta_{0.15}$ for L and $\delta_{0.10}$ for H.

The change in yield stress over the range of transition

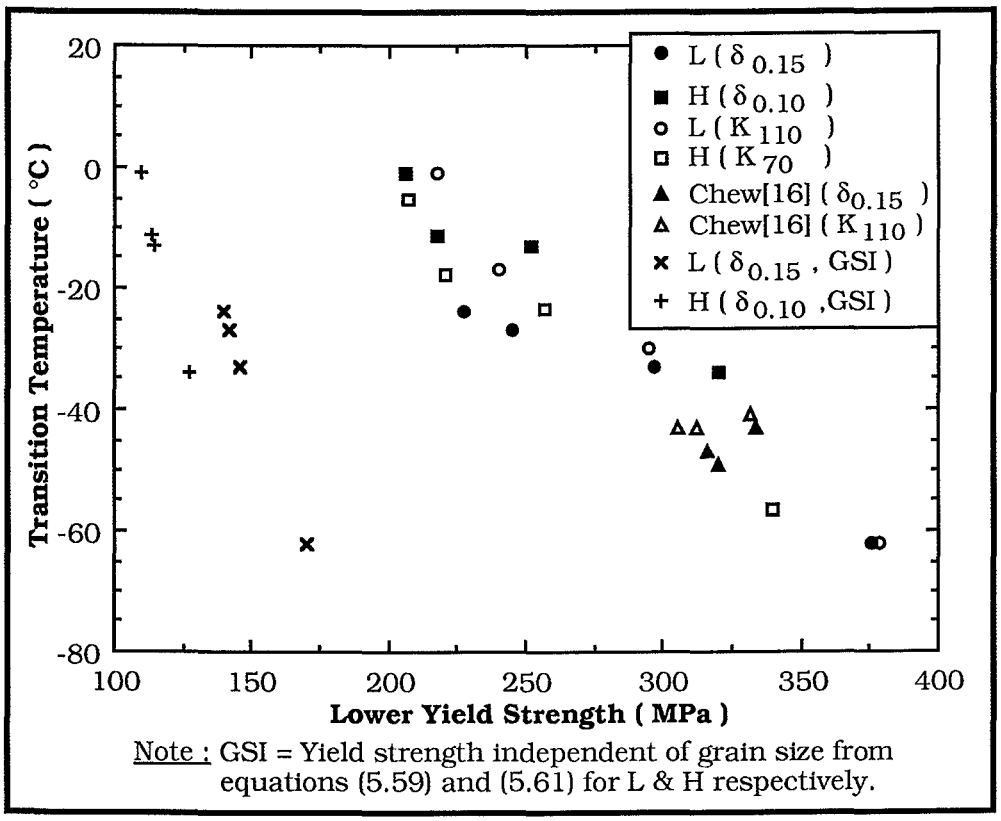

Figure 7.14 : Transition temperature (°C) as a function of lower yield strength (MPa) at transition.

temperature is 149 MN m^{-2} for L when grain size is included and only 30 MN m^{-2} when the grain size component is removed. Similarly for H the respective figures are 114 MN m^{-2} and 17 MN m^{-2}. This implies that the temperature dependence of toughness and the grain size dependence of the transition temperature arises almost solely through the grain size and temperature dependence of the yield stress.

Decreasing the grain size affects the transition temperature through a number of factors:

(i) It has been given that the ratio of carbide thickness to grain size is constant on slow cooling from austenitising temperature since both carbide thickness and grain size depend on similar diffusion phenomena [212]. A finer carbide produced by grain refinement produces a much sharper transition curve [180,181]. Therefore cleavage fracture is more difficult to initiate and propagate in the finer grain size.

(ii) In the transition region fracture is likely to be controlled by propagation of grain-size microcracks through the next grain boundary. This occurs when the ferrite matrix strength (Σ) is greater than the carbide strength (S), both of which are greater than the yield stress. This region is shown in Figure 3.13. Cleavage fracture occurs when the local peak stress exceeds the ferrite grain strength such that

$$\sigma_{local} \geq \Sigma = [\pi E G_{ff}/(1-\nu^2)d]^{1/2} \qquad (7.30)$$

where G_{ff} is the dynamic critical strain energy release rate at the first ferrite/ferrite interface [206]. At this stage particles may crack and the crack can extend to the first ferrite grain boundary without causing failure. Stable grain size cracks would then be possible and cleavage fracture occurs when the crack can extend dynamically across the grain boundary. From equation (7.30) this makes transition a function of $d^{-1/2}$.

Ebrahimi observed that cleavage crack propagation from a cracked carbide particle into the ferrite matrix was not necessarily the critical fracture event in the transition region from observation of stable grain sized cleavage microcracks [86]. Stable grain-sized microcracks have been observed by others [178,179,292]. Observation of cleavage facets surrounded by microvoid coalescence from specimens tested in the transition region (Figures 7.11 and 7.13) support this conclusion.

(iii) The effects of statistical competition will affect the transition temperature. The yield stress and fracture stress decrease with increasing grain size as discussed in Sections 3.2.2 and 5.2.3. The size of the plastic zone surrounding the crack tip increases with decrease in yield stress and consequently there is a larger probability of finding weak spots at the crack tip.

Micromechanical models of cleavage fracture predict a variation in transition temperature with grain size as discussed in Section 7.2.2. It was assumed that the characteristic distance X_0 was temperature and grain size independent and equal to 180 μm. In Section 6.3.7 X_0 was shown to vary from 92.1 μm to 191.7 μm at -196°C for the experimental steels which indicates the statistical nature of X_0 found by Curry and Knott [175]. X_0 was not found to be temperature independent which means a larger plastic zone size is

needed for cleavage fracture than if X_0 was temperature independent. The variation in X_0 was from $7.48d_g$ for the smallest grain size to $2.64\ d_g$ for the largest grain size. Therefore grain refinement will make crack initiation and propagation more difficult; due to the increased energy needed to overcome the grain boundaries.

The Ritchie-Knott-Rice model of cleavage fracture predicts that

$$\sigma_{ys} = C_4 d^{-(N+1)/4N} \tag{7.22}$$

where $C_4 = [\beta^{-(N+1)} X_0 k_F^{(N+1)}/(0.4769^2 \delta_i)]^{1/N}$ (7.23)

at the fracture mode transition. It implies that for increasing grain size the yield stress at transition will decrease provided that the characteristic distance X_0 is grain size independent. The experimental transition temperature results show that the constant C_4 differed by 6% for Steel L and by 5% for Steel H over the range of grain size tested. Therefore, under the experimental conditions possible variation in X_0 was not significant.

The decrease in yield stress will mean a larger plastic zone exists at the crack tip for the same level of stress intensity from

$$\Delta a_n = \frac{\pi}{8}\left(\frac{K_I}{\sigma_{ys}}\right)^2 \tag{2.87}$$

where Δa_n is the notional crack increment. The lower yield stress and larger plastic zone size means that the degree of plastic strain at the crack tip is larger for the coarse-grained steel at transition. In Section 3.4.3 it was discussed that fracture mode would change from cleavage to microvoid coalescence when a critical crack-tip plastic strain ε_{fi} was exceeded.

In Chew's experimental investigation strain-ageing of the plastic zone around the fatigue crack-tip produced an increase in the fracture mode transition temperature of a high active nitrogen content steel since

(i) $\sigma_{ys(aged)} > \sigma_{ys(as\text{-}fatigued)}$ (7.31)

(ii) $\varepsilon_{F(aged)} < \varepsilon_{F(as\text{-}fatigued)}$ (7.32)

where $\varepsilon_{F(aged)}$ and $\varepsilon_{F(as\text{-}fatigued)}$ are the fracture strains of the aged and as-fatigued specimens respectively [16]. Since the critical crack-tip plastic strain (ε_{fi}) was the same for the aged and as-fatigued specimens it was concluded that the specimen with the higher crack-tip strain (and lower yield stress) would attain ε_{fi} at a lower temperature i.e. the as-fatigued specimen will have a lower experimental fracture mode transition temperature.

The RKR model predicts that ε_{fi} increases with increasing grain size due to the reduction in yield stress. Due to the temperature dependence of yield stress an increasing fracture mode transition temperature with increasing grain size is predicted. Sailor's model given in Section 3.4.3 as

$$\ln(\delta_i/2d) = \bar{\varepsilon}_p \tag{3.71}$$

predicts a decreasing plastic strain with increasing grain size. Therefore the FMTT would decrease with increase in grain size but the experimental observations presented in Section 7.2 support the RKR model. The results show that the FMTT increases with increasing grain size; therefore, the critical crack-tip strain increases with increasing grain size.

These results mean that the effect of increasing the size of the fatigue damaged plastic zone (by increasing the fatigue load amplitude) should be to increase the fracture mode transition temperature. If the critical plastic strain ε_{fi} of the crack tip is unchanged by the pre-strain then the increase in yield stress caused by the pre-strain will produce an increase in fracture mode transition temperature. If the critical plastic strain ε_{fi} of the crack tip is reduced by pre-strain then the increase in yield stress can be offset by the reduction in ε_{fi} and little or no change in FMTT will occur. This can be the subject of further investigation.

It must be remembered that the standards for fracture toughness testing impose limits on the fatigue load amplitude in fatigue pre-cracking to minimise plastic damage at the crack tip. The limits

$$K_f \leq 0.6(\sigma_{y1}/\sigma_{y2})K_Q \tag{6.1}$$

where σ_{y1} and σ_{y2} are the yield stress of the material at the temperature of fatigue cracking and the temperature of the toughness testing respectively, or

$$P_f = 0.4\, Bb_0\sigma_f/(2W-a_0) \tag{6.2}$$

where P_f is the fatigue load and $\sigma_f = 0.5(\sigma_{ys} + \sigma_{uts})$ are very strict. At low temperatures σ_{ys} is large and fatigue loads must be kept very low.

In the lower transition region a specimen fractures when shear instability is reached in the ligament between the stationary blunted crack tip and a propagating cleavage microcrack before the cleavage microcrack can arrest. Therefore the probability of unstable fracture depends on the position of cleavage microcracks relative to the stress distribution ahead of the stationary crack tip. This position controls how far a cleavage microcrack could grow before it would arrest.

If the distance between the possible arrest point of a microcrack and the crack tip is less than the maximum ligament in which shear instability can occur, then the cleavage microcrack would join the blunted crack-tip and the specimen as a whole would become unstable.

Assuming that cleavage occurs as discrete microcracking across the thickness of the specimen an increase in grain size increases the probability of finding a propagating cleavage microcrack that can join the crack tip (due to increased plastic zone size). The characteristic distance X_0 decreases with respect to grain size indicating less energy is required for fracture.

In Section 6.2.4 on modelling CTOD from clip gauge displacement it was explained using

$$G_c = M\sigma_{ys}\delta_c \tag{2.91}$$

that for the same loading condition (i.e. the same clip gauge displacement) the CTOD would be larger for a material of lower yield stress. Figure 6.25 showed the stress distribution ahead of the fatigue crack for two values of σ_{ys}. For a lower yield stress material it was concluded that due to the larger volume of plastically deformed material at the crack-tip the strain energy input and therefore the

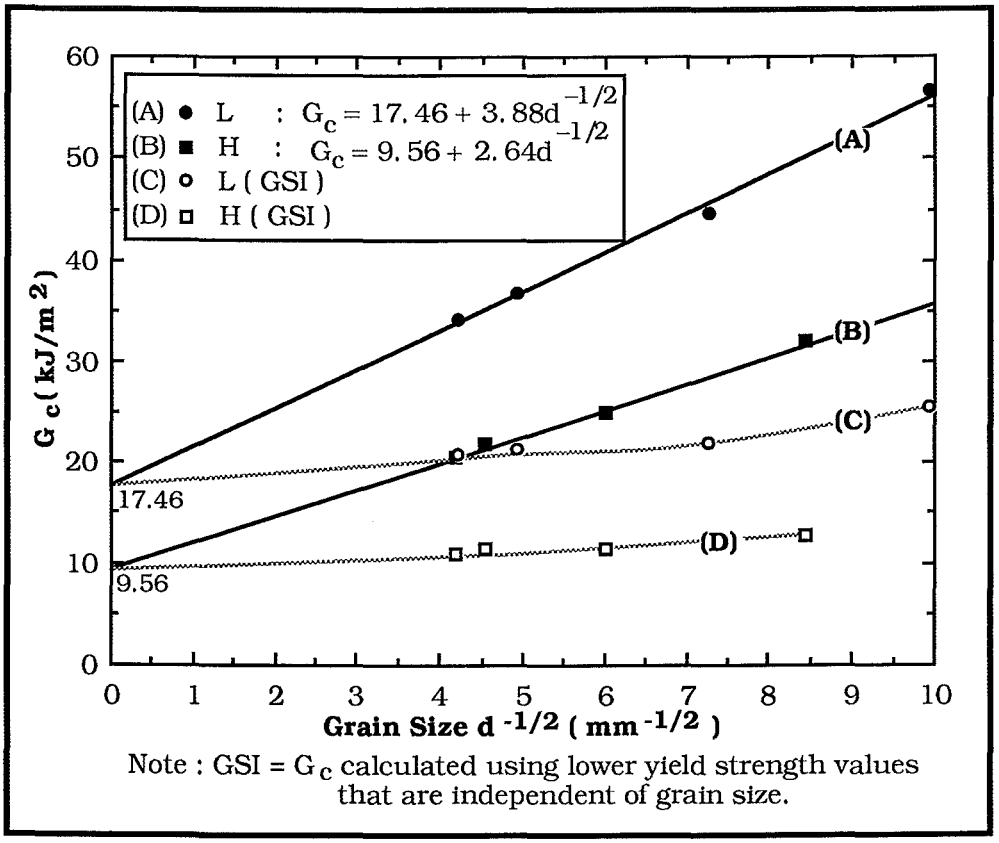

Figure 7.15 : The critical energy release rate G_c (kJ/m^2) at transition as a function of grain size, $d^{-1/2}$, ($mm^{-1/2}$).

CTOD would be higher than it is for the higher yield stress (fine-grained) material.

At transition the level of crack opening displacement is taken as a constant. Therefore energy input (G_c) will be expected to increase as grain size decreases, which represents the energy devoted to overcoming the resistance of the grain boundaries to fracture. Using $G_c = M\sigma_{ys}\delta_c$ with M = 1 and δ_c = 0.15 mm for Steel L and δ_c = 0.10 mm for Steel H the critical energy release rate at fracture mode transition may be calculated.

Figure 7.15 shows the critical energy release rate (G_c) versus $d^{-1/2}$ for Steels L and H. For Steel L, G_c increases from 34.20 kJ/m^2 at $d^{-1/2}$ = 4.218 $mm^{-1/2}$ to 56.55 kJ/m^2 at $d^{-1/2}$ = 9.939 $mm^{-1/2}$. For Steel H, G_c increases from 20.6 kJ/m^2 at $d^{-1/2}$ = 4.187 $mm^{-1/2}$ to 32.0 kJ/m^2 at $d^{-1/2}$ = 8.440 $mm^{-1/2}$.

The increase in energy due to grain refinement may be found if G_c is calculated using the yield stress at transition independent of grain size. Using these yield stress results shown in Figure 7.14, the

critical energy release rate independent of grain size is almost constant. For Steel L, G_c varies from 21.0 kJ/m^2 at 4.218 mm$^{-1/2}$ to 25.5 kJ/m^2 at 9.939 mm$^{-1/2}$. Similarly for Steel H, G_c varies from 11.0 kJ/m^2 at 3.187 mm$^{-1/2}$ to 12.7 kJ/m^2 at 8.440 mm$^{-1/2}$. From the difference between these results and the overall energy release rate the amount of energy required for crack initiation and crack propagation to overcome grain boundary resistance at fracture mode transition varies from 39% for LD($d^{-1/2}$ = 4.218 mm$^{-1/2}$) to 55% for LA($d^{-1/2}$ = 9.939 mm$^{-1/2}$) and from 47% for HD($d^{-1/2}$ = 4.187 mm$^{-1/2}$) to 60% for HA($d^{-1/2}$ = 8.440 mm$^{-1/2}$) of the total energy released at fracture.

From a "line of best fit" plotted through the results of L and H respectively on Figure 7.7 the intersection at $d^{-1/2} = 0$ gives the energy required for crack initiation and propagation through a single crystal. For Steel L this is 17.5 kJ/m^2 and 9.6 kJ/m^2 for Steel H. It appears that more information on crack nucleation and crack propagation energy would be possible if the toughness of single iron crystals was investigated. Present experimental results show that by grain refinement an increased amount of energy is required for crack initiation and propagation provided the initiation CTOD is grain size and size independent. It implies that one of the reasons the fracture mode transition occurs at a lower temperature for finer grain sizes is due to the increased energy required to overcome grain boundary resistance to crack propagation.

7.3 Correlation between the Charpy V-Notch Impact Energy and the Critical CTOD

Reliable correlations between Charpy V-notch impact energy and CTOD or K_{IC} are attractive since fracture toughness testing would cost less and be simplified. The Charpy test result is a measure of energy required to initiate fracture and propagate the crack through the specimen, which is of little use to the design engineer. The use of fracture mechanics allows the calculation of the defect size that will cause fracture in a structure or the calculation of the safe working stress in a structure assuming a permissible defect size. The two tests differ in the manner of execution and in the properties they measure. Some of the main differences are:

(a) Strain Rate

The CTOD and K_{IC} tests are carried out under "static loading" conditions with an approximate strain rate of 10^{-5} - 10^{-4} s^{-1}. The Charpy test is carried out under impact loading with an approximate strain rate of 10^3 s^{-1}. The shear yield stress has been shown to increase substantially with a large increase in strain rate [97]. The fracture mode transition temperature will therefore increase. Radon and Turner found that when the strain rate was varied from 10^{-2} s^{-1} to 10^7 s^{-1} there was a significant change in fracture toughness [122].

The toughness of most carbon-manganese and low-alloy steels is sensitive to strain rate. It would be expected that changes in Charpy toughness arising from differences in strain-rate sensitivity will not be apparent in the standard CTOD or K_{IC} test [55].

(b) Triaxiality

CTOD testing is usually carried out on specimens with the same thickness as the structure or material to be tested. K_{IC} specimens usually have sufficient thickness to ensure plane strain conditions. In Section 6.3.2 the CTOD test specimen thickness was found to give size independent results for $\delta_c \leq 0.600$ mm. Therefore the degree of crack-tip triaxiality obtained by the CTOD test could be expected to be consistent.

With Charpy tests performed using standard 10 mm thick specimens the conditions of triaxiality at the crack-tip could vary in materials of different flow stress levels. The elevation of yield stress due to dynamic loading means triaxiality can be maintained to a higher temperature compared to a slowly loaded specimen.

(c) Notch Size

The Charpy test specimen has a machined V-notch which has a root radius of 0.25 mm. The CTOD or K_{IC} specimen has a fatigue crack. The difference in root radius will modify the transition temperature measured by the two tests [293].

The positioning of the notch or crack will affect the test results. The fatigue crack will sample a range of microstructures and the toughness measured will initiate at a position representing the microstructure with the lowest toughness. The machined notch will measure the properties in a different region.

Apart from these different conditions the concepts of the tests are different. The energy measured in the Charpy test is the sum of the energy required to initiate fracture and to propagate the

crack through the specimen. The energy required to propagate the crack becomes a greater proportion of the total energy as the upper shelf of the transition curve is approached.

The CTOD test measures the energy required to cause instability of the crack-tip material regardless of the mechanism of final fracture. Therefore a successful correlation is more likely in the lower shelf of the transition curve where the differences between the tests are minimised especially energy to fracture initiation and propagation. It means that any correlation between CTOD/K_{IC} test results and Charpy V-notch test results will be empirical. A number of correlations between K_{IC} and Charpy Impact Energy (C_v) and between CTOD and Charpy Impact Energy have been published.

7.3.1 CORRELATIONS BETWEEN K_{IC} AND CHARPY IMPACT ENERGY

It is generally accepted that the form of the correlation is one of the following:

$$\left(\frac{K_{IC}}{\sigma_{ys}}\right)^2 = A\left(\frac{C_v}{\sigma_{ys}}\right) + B \qquad (7.33)$$

$$\frac{(K_{IC})^2}{E} = C(C_v)^m \qquad (7.34)$$

$$K_{IC} = D(C_v)^m \qquad (7.35)$$

where C_v is the Charpy Impact Energy in J, E is Young's modulus, σ_{ys} is the yield strength of the material and the constants A, B, C, D, m and n are found by a least-squares linear regression through the relevant data [294]. Rao and Acharya suggest that these equations should be presented in a non-dimensional form to give a more accurate description of K_{IC}.

Pisarski summarised a number of these correlations in 1978 and some of these are presented in Table 7.6 [55]. The correlations presented are for the calculation of static plane-strain fracture toughness; dynamic plane strain fracture toughness correlations have been excluded. Most of these correlations are for specific materials and their range of use is limited.

Table 7.6
Summary of Fracture Toughness-Charpy V-notch Correlations

Correlation by	Equation	Material	σ_{ys} (MN m^{-2})	Restrictions
Marandet & Sanz 4 of [55].	(7.36) $TK_{IC}(100) = 9+1.37TC_V(28)$ (7.37) $K_{IC} = 19(C_V)^{0.5}$	E36 A533b A517F St. E70	215-1100	Fracture appearance ≥ 80% crystalline.
Rolfe & Novak 6 of [55].	(7.38) $\left(\frac{K_{IC}}{\sigma_{ys}}\right)^2 = 0.127\left(\frac{5.083}{\sigma_{ys}}-0.05\right)$	A517 4147 HY130 4130 12Ni-5Cr-3Mo 18Ni-8Co-3Mo	760 945 1025 1090 1207-1330 1290-1700	Not all results valid K_{IC}.Upper Shelf of transition curve tests at 27°C.
Barsom 10 of [55].	(7.39) $K_{IC} = 30.2(C_V)^{1/2}$ (7.40) $T_{shift} = 119 - 0.12\ \sigma_{ys}$	ABS C A032 B A517 F	270 386 760	(7.39) includes data from other steels.
Chirogas & Meyer 33 of [16].	(7.41) $K_{IC} = 3.08\ \exp[0.036(T-T_{40J}) + 100] + 36.4$	–	–	–
Sailors & Corten [60].	(7.42) $K_{IC} = 14.6(C_V)^{0.5}$	A533B A517F A542	480 814 –	Primarily for A533B steel
Chew [16].	(7.43) $K_{IC} = 16(C_V)^{0.5}$ (7.44) $TK_{IC}(60) = TC_V(20)-58$	P.V.	240	Pressure Vessel Steel

Table 7.6 continued.
Summary of Fracture Toughness-Charpy V-notch Correlations

Correlation by	Equation	Material	σ_{ys} (MN m^{-2})	Restrictions
Chew [16].	(7.45) $K_{IC} = 19(C_V)^{0.5}$ (7.46) $TK_{IC}(80) = -(TC_V(20)+55)$	275N 275T	290 310	Grade 275 Structural Steel
Tsukada *et al.* [55].	(7.47) $\left(\frac{K_{IC}}{\sigma_{ys}}\right)^2 = 0.65\left(\frac{C_V}{\sigma_{ys}} - 0.0098\right)$	A508 Cl.2 A508 Cl.3 A533B	443 448 460	From round C.T. specimens
Chaudhuri *et al.* [58].	(7.50) $\log\delta_C = 2.33 - 1.14 \log C_V$ (7.51) $\log\delta_C = 2.58 - 1.30 \log C_V$ (7.52) $\log\delta_C = 1.06 \log C_V - 2.24$	API X52	520	Line pipe steel. (7.55) for weld, others for HAZ.
Oda [59].	(7.53) $\delta_C = f\sigma_{ys}\{\ln(EC_V/\sigma_{ys}^2)\}/E$ (7.54) $\delta_C = hC_V/\sigma_{ys} + k\sigma_{ys}/E$	SS41 HT80(1) HT80(2)	276 786 834	–

Chew considered the correlations of Marandet and Sanz, Barsom and also Chirogas and Meyer [16]. Chew found that by modifying Marandet and Sanz's correlation equations (7.36) and (7.37) could be made to give a reasonable estimate of K_{IC} experimental results. The other correlations gave a poor estimate of Chew's experimental K_{IC} results. The equations of Chew are also given in Table 7.6. The correlation of Marandet and Sanz could be expected to give a good fit since it was derived from a series of low alloy carbon-manganese steels with a range of yield stress from 215 to 1100 MN m^{-2} which had a similar chemical composition to Chew's experimental steels [16]. In Table 7.6 K_{IC} is in MPa $m^{1/2}$ and C_V is in Joules.

Tsukada *et al.* developed a prediction method of static and dynamic fracture toughness of nuclear pressure vessel steels from Charpy V-notch test results [56]. They based the relationship on the results of Barsom and Rolfe and Novak, and their correlation is also given in Table 7.6. Their method to determine the K_{IC}-C_v correlation is:

(i) Obtain the temperature versus energy and fracture appearance curves using the Charpy V-notch impact test.

(ii) Determine the 50% FATT and 100% shear fracture appearance temperatures (the upper shelf temperature).

(iii) At the upper shelf temperature obtain the yield strength from the static tension test.

(iv) Obtain K_{IC} from equation (7.47).

(v) Draw predicted K_{IC} versus temperature curves using the master curves given in their paper and FATT and K_{IC}. Although this method is for a specific pressure vessel grade steels its main points may be used for any correlation.

From the correlations of K_{IC} versus C_v it is concluded that these correlations may be used for quality control and material development since K_{IC} test procedures are difficult to follow during production [55,294]. The correlation may not replace the K_{IC} test where specific design data is needed [16,55].

7.3.2 CORRELATIONS BETWEEN CTOD AND CHARPY IMPACT ENERGY

A number of correlations have been given for K_{IC} versus Charpy Impact Energy. The Welding Institute of England published a correlation between CTOD and Charpy V-notch test results for ferritic steel weld metals in 1981 [57]. Correlations were established between either 40J Charpy transition temperature and CTOD = 0.2 mm or 27J Charpy transition temperature and CTOD = 0.1 mm.

Chaudhuri *et al.* gave an empirical relationship between CTOD and C_v for weldments of API X52 grade line-pipe steel as

$$\log \delta_c = D + n\log C_v \qquad (7.48)$$

where D and n are constants. The actual equations for the heat affected zone and weld metal are given in Table 7.6. Equation (7.48) is a power relationship like equation (7.35) i.e.

$$\delta_c = D(C_v)^n \qquad (7.49)$$

which is not unexpected since K_{IC}, CTOD and Charpy impact transition curves are similar in shape. These relationships were claimed to predict CTOD with 95% accuracy [58].

Oda presented a one-to-one correlation between CTOD and Charpy impact energy as

$$\delta_c = f\sigma_{ys}\{\ln(EC_v/\sigma_{ys}^2)\}/E \qquad (7.53)$$

for 100% cleavage fracture and

$$\delta_c = hC_v/\sigma_{ys} + k\sigma_{ys}/E \qquad (7.54)$$

for a mixed fracture where E is Young's modulus, f = 10, h = 1.67, k = -21.7 and σ_{ys} is the yield stress at the temperature T where critical CTOD is to be found [59]. The temperature of the Charpy test is T + ΔT where ΔT is the difference between the CTOD transition temperature at δ_c = 0.16 mm and the 50% FATT of the Charpy test.

This correlation was successful for a mild steel (σ_{ys} = 276 MPa) and a high strength steel (σ_{ys} = 786 MPa). The inclusion of the yield strength term is related to $G_c = M\sigma_{ys}\delta_c$ which gives the energy required for crack instability.

7.3.3 EXPERIMENTAL CORRELATION OF CTOD, K_c VERSUS CHARPY IMPACT ENERGY

The correlation of experimental results must consider:

(i) the temperature shift between the Charpy impact test results and CTOD or K_{IC} test data.

(ii) the form of the equation to model CTOD or K_c results from the Charpy test data and the range of the transition curve over which it is applied.

(a) The Transition Temperature Shift

Since the correlations are empirical a given temperature shift will apply specifically to the material (in its final heat-treated condition) it was developed for. In other experimental tests if the material is similar then the empirical correlation developed may also

apply for the present experimental conditions. For example, Marandet and Sanz gave the transition temperature shift as

$$T(K_{IC} = 100) = 9+1.37T(C_v = 28) \quad (7.36)$$

where the temperature (T) was in Kelvin and the transition criteria, K_{IC} = 100 MPa $m^{1/2}$ and C_v = 28J, were based on where the rapid upswing in the transition curve occurred.

Chew applied equation (7.36) to his experimental results. Equation (7.36) predicts an increase in transition temperature for K_{IC} compared to the Charpy test whereas Chew's results showed a decrease in transition temperature from the Charpy transition temperature [16]. Chew changed the transition criteria to K_{IC} = 60 MPa $m^{1/2}$ for the pressure vessel steel, K_{IC} = 80 MPa $m^{1/2}$ for the Grade 275 structural steel and C_v = 20J. The temperature shift for the pressure vessel steel was then

$$T(K_{IC}60) = T(C_v20) - 58 \quad (7.44)$$

and for the Grade 275 structural steel the temperature shift was

$$T(K_{IC}80) = -(T(C_v20) + 55) \quad (7.46)$$

where the temperature (T) was in °C. The change in prediction of transition temperature between equations (7.36), (7.44) and (7.46) is significant even though the materials tested were similar.

The transition temperature criteria used by Oda were δ_i = 0.16 mm and 50% FATT for the Charpy test [59]. The temperature shift (ΔT) was given by the difference in transition temperature found from these criteria. Therefore the difference in transition temperatures may be considered to give the temperature shift between Charpy and CTOD results. Table 7.7 gives the differences between T_{27} and $T_c(\delta_i)$ or $T_c(K_i)$ and between T(50% FATT) and $T_c(\delta_i)$ or $T_c(K_i)$ for Steels L and H.

The ductility transition temperature has been used in this investigation for definition of transition temperature given by T_{27} for the Charpy test, $T_c(\delta_i)$ for the CTOD test and $T_c(K_i)$ for the K_{IC} test. The temperature shift will be defined using these criteria. Figure 7.16 shows the transition temperature at δ_i or K_i against the Charpy

Impact transition temperature at 27 Joules. This figure shows that as the Charpy impact transition temperature increases there is an increasing difference between T_{27} and $T_c(\delta_i$ or $K_i)$.

The fracture toughness transition temperature may be given as a linear function of the Charpy impact transition temperature,

$$T_c(\delta_i \text{ or } K_i) = A_0 + A_1 T_{27} \qquad (7.55)$$

where A_0 and A_1 are constants. From a least-squares linear regression analysis on the transition temperatures then the fracture toughness transition temperature may be predicted from the Charpy impact transition temperature. Table 7.8 presents results of a regression analysis on the transition temperature results shown in Figure 7.16. Equations (7.56) and (7.57) give $T_c(\delta_i)$ as a function of T_{27} for Steels L and H respectively. Equations (7.58) and (7.59) give $T_c(K_i)$ as a function of T_{27} for Steels L and H respectively. The predicted results from these equations are plotted on Figure 7.16.

Table 7.7
Differences in Fracture Mode Transition Temperature

Steel	$T(\delta_i)$	$T(K_i)$	T_{27}	T(50%)	ΔT $(\delta_i - T_{27})$	ΔT $(\delta_i - T_{50\%})$	ΔT $(K_i - T_{27})$	ΔT $(K_i - T_{50\%})$
LA	-62	-62	-56	-26	6	36	6	36
LB	-33	-30	-13.5	15	19.5	48	16.5	45
LC	-27	-17	8	40	35	67	25	57
LD	-24	-1	16.5	43	40.5	67	17.5	44
HA	-34	-56.5	-27	1	7	35	29.5	57.5
HB	-13	-23.5	21	49	34	62	44.5	72.5
HC	-11.5	-18	35	59	46.5	70.5	53	77
HD	-1	-5	40	70.9	41	71.5	45	75.5
275N	-46.5	-43	-2	-	44.5	-	41	-
275T	-42.5	-41	-12	-	30.5	-	29	-
P.V.	-49	-42.5	7	-	56	-	49.5	-

1. All temperatures and differences in °C.

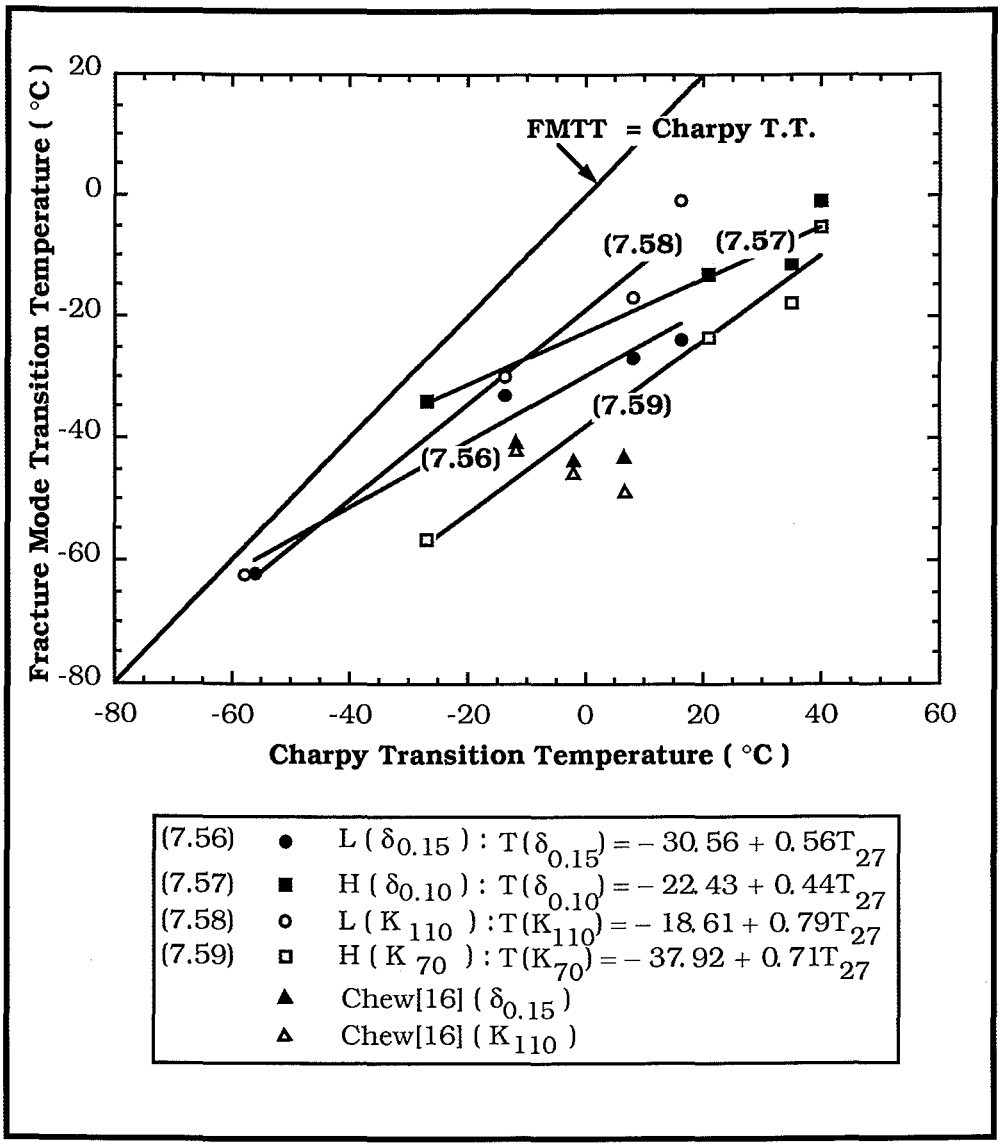

Figure 7.16 : Fracture mode transition temperature (°C) for CTOD & LEFM testing as a function of Charpy impact transition temperature (°C).

Table 7.8
$T(\delta_j)$ - T_{27} and $T(K_j)$ - T_{27} Correlation Results

Correlation	$T(\delta_j)$ - T_{27}		$T(K_j)$ - T_{27}	
Steel	L	H	L	H
Equation No.	7.56	7.57	7.58	7.59
N[1]	4	4	4	4
D.F.	2	2	2	2
R	0.9830	0.9692	0.9889	0.9842
$s(\hat{y})$	3.9086	4.1694	4.7097	4.7562
t-value	7.583	5.565	9.411	7.856
Equation Sig. Coefficients	98%	95%	98%	98%
A_0	-30.56	-22.43	-18.61	-37.92
A_1	0.53	0.44	0.79	0.71
95% C.L. of A_1	±0.30	±0.34	±0.36	±0.39
Significance of A_1	98%	95%	98%	98%
$\bar{y}$	-36.5	-14.9	-27.5	-25.8
95% C.L. of $\bar{y}$	±8.4	±9.0	±10.1	±10.2

1. See Appendix B for definition of statistical abbreviations.
2. $T(\delta_j)$, $T(K_j)$ and T_{27} in °C.

Statistically the significance of these equations is between 95 and 98%, with correlation coefficients from 0.9692 to 0.9889. It has been found that an increasing grain size results in an increasing transition temperature and that this may be given as

$$T_c = B_0 + B_1 d^{-1/2} \tag{7.3}$$

where B_0 and B_1 constants. This equation applied to both Charpy Impact testing and CTOD testing. Therefore the shift in transition temperature may be given as the difference between equation (7.3) applied to Charpy V-notch testing and applied to CTOD testing as

$$\Delta T = T_c(C_v = 27J) - T_c(\delta_i \text{ or } K_j) \tag{7.60}$$

which gives

$$\Delta T = \Delta B_0 + \Delta B_1 d^{-1/2} \tag{7.61}$$

where $\Delta B_0 = B_0(C_v) - B_0(\delta_i \text{ or } K_j)$ and $\Delta B_1 = B_1(C_v) - B_1(\delta_i \text{ or } K_j)$. If equation (7.61) is applied to the experimental results, then the resulting equations are

(i) For CTOD testing

$$\Delta T_c = 64.95 - 6.03 d^{-1/2} \text{ for Steel L} \tag{7.62}$$

and

$$\Delta T_c = 82.96 - 8.79 d^{-1/2} \text{ for Steel H} \tag{7.63}$$

(ii) For K_c testing,

$$\Delta T_c = 33.22 - 2.58 d^{-1/2} \text{ for Steel L} \tag{7.64}$$

and

$$\Delta T_c = 69.46 - 4.57 d^{-1/2} \text{ for Steel H} \tag{7.65}$$

The predicted transition temperatures using the above equations are the same as or very similar to those predicted results found using equations (7.56) to (7.59).

(b) Predicted Fracture Toughness from Charpy V-notch Test Results

For similar types of material to the experimental steels one of the more successful correlations is

$$K_{IC}(\text{or } \delta_c) = D(C_v)^n \qquad (7.35)$$

where D and n are constants [16,55,58,60]. Taking logarithms of both sides gives

$$\log K_{IC}(\text{or } \log \delta_c) = \log D + n\log C_v. \qquad (7.66)$$

The form of equation (7.66) is suitable for a least-squares linear regression and this was used to correlate fracture toughness and Charpy V-notch test results. Values of Charpy V-notch impact energy were read from fracture mode transition curves at 10°C intervals. The temperature shift was calculated from equations (7.62) to (7.65) and values of δ_c and K_c read from the appropriate fracture mode transition curve after allowance for the temperature shift. Since CTOD testing allows for plastic deformation at the crack tip upper shelf values of C_v were included in the analysis although most Charpy transition curves did not include the upper shelf region.

Variation of toughness results due to grain size was not considered and the results of each grain size for each steel were pooled to give as large a number of degrees of freedom as possible. The results of HA were not included in the analysis for Steel H since some grain size dependence in toughness results was evident. The results of the regression analysis are given in Table 7.9. The correlation coefficient is from 0.9568 for equation (7.69) to 0.9826 for equation (7.70). Each of the equations is significant at the 99.9999% level, and the coefficient n is also significant at the 99.9999% level for each correlation.

The predicted results from the CTOD-C_v are shown in Figure 7.17 for Steel L and in Figure 7.18 for Steel H, together with the experimental results. The predicted results for the K_c-C_v correlation are shown in Figure 7.19 for Steel L and in Figure 7.20 for Steel H, together with the experimental results.

Table 7.9
CTOD-C_v and K_c-C_v Correlation Results

Steel	L	H	L	H
Correlation	CTOD-C_v	CTOD-C_v	K_c-C_v	K_c-C_v
Equation No.	7.67	7.68	7.69	7.70
Figure No.	7.17	7.18	7.19	7.20
N[1]	35	24	34	24
D.F.	33	22	32	22
R	0.9585	0.9816	0.9568	0.9826
s(ŷ)	0.2945	0.1994	0.1490	0.0889
t-value	19.32	24.11	18.62	24.78
Equation Sig. Coefficients	>99.9999%	>99.9999%	>99.9999%	>99.9999%
log D	-5.0361	-6.4981	3.1601	2.3347
n	0.9950	1.3379	0.4938	0.6132
95% C.L. of n	±0.1046	±0.1151	±0.0541	±0.05132
Significance of n	>99.9999%	>99.9999%	>99.9999%	>99.9999%

1. See Appendix B for definition of statistical abbreviations.
2. δ_c in μm, K_{IC} in MPam$^{1/2}$ and C_v in J.

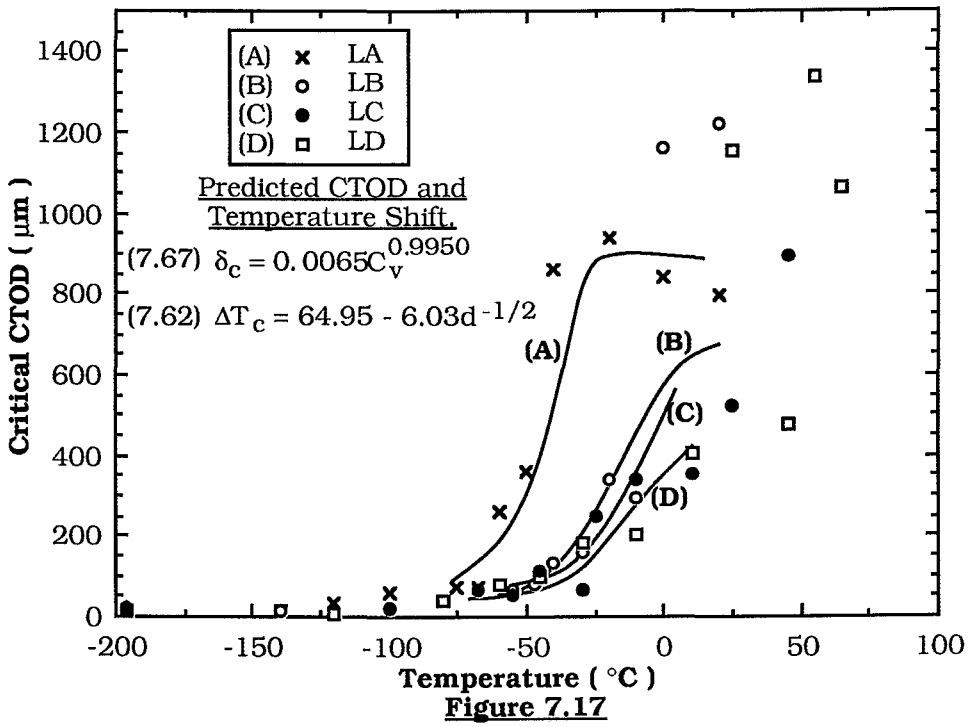

Figure 7.17

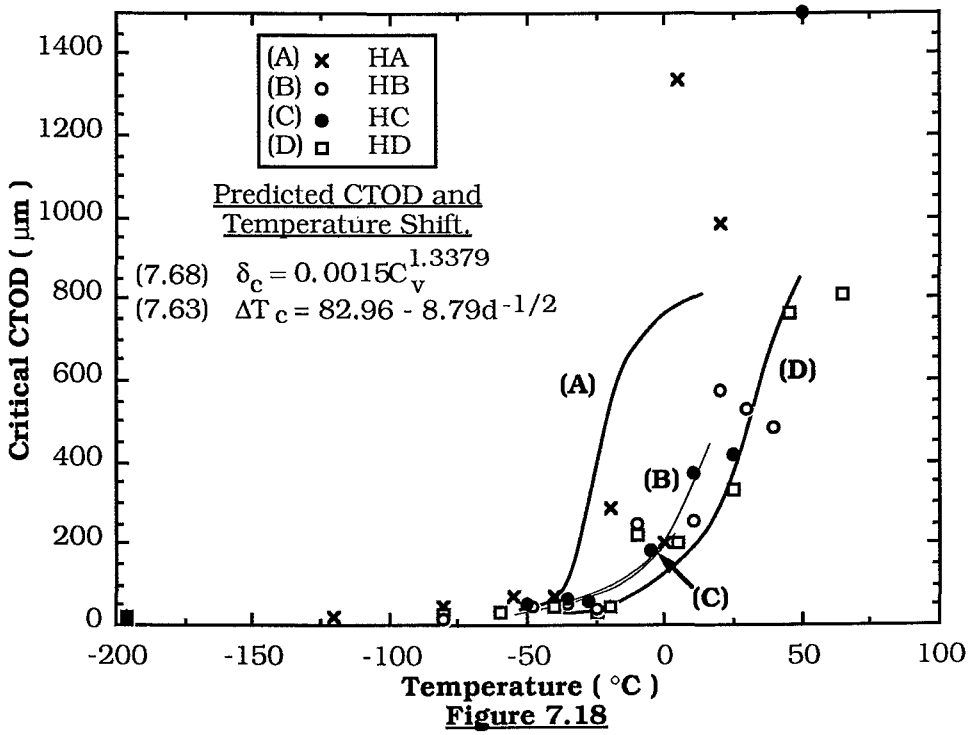

Figure 7.18

Predicted CTOD (μm) from CTOD-C_v correlation as a function of test temperature (°C) for ;

Figure 7.17 : Steel L (7.67).

Figure 7.18 : Steel H (7.68).

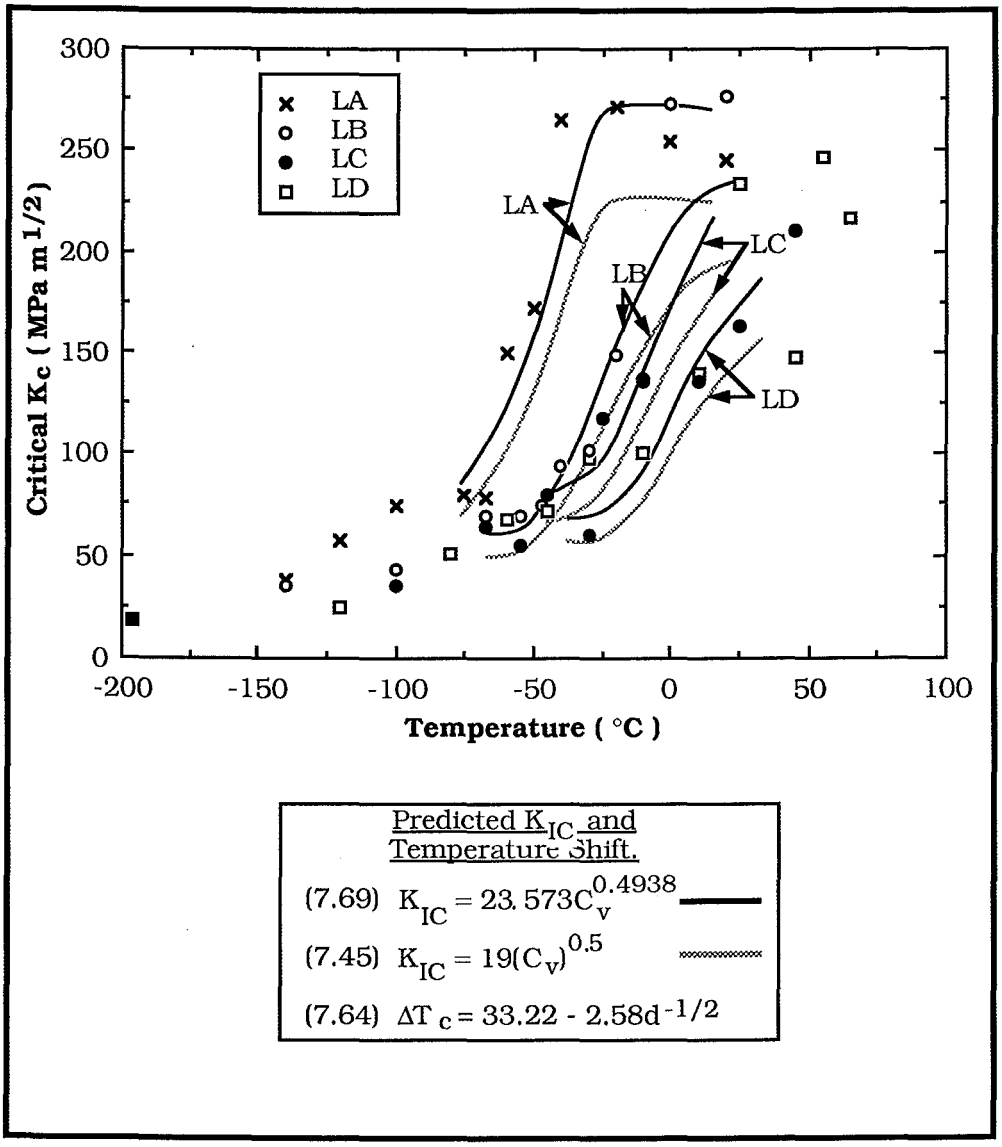

Figure 7.19 : Predicted K_{IC} (MPa $m^{1/2}$) from K_{IC} -C_v correlation as a function of test temperature (°C) for Steel L.

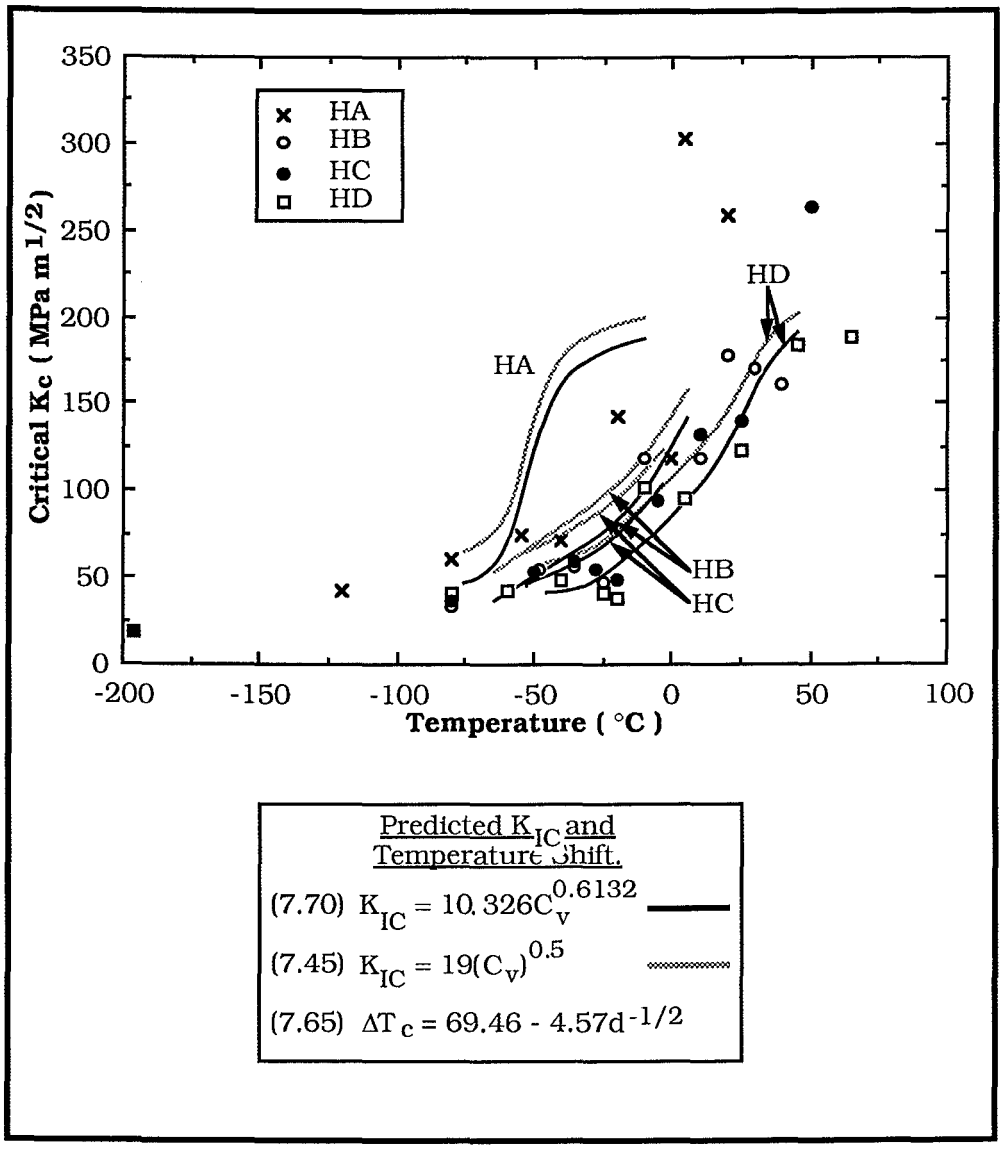

Figure 7.20 : Predicted K_{IC} (MPa $m^{1/2}$) from K_{IC}-C_v correlation as a function of test temperature (°C) for Steel H.

The predicted results describe the fracture mode transition curve well. In the transition region the results are generally conservative but at high toughness values some of the predicted results are non-conservative. In Figure 7.18 there is very little difference between the CTOD results for HB, HC and HD although equation (7.63) predicts a temperature shift between the steels. This is due to underestimation of the HB results and slight overestimation of results for HD indicating a possible grain size dependence in the toughness results which is not accounted for.

To compare these correlations with other published correlations CTOD or K_c was calculated from Charpy Impact energy using equations (7.52), (7.53), (7.54) and (7.45). Figures 7.19 and 7.20 show the predicted results from equation (7.45) for Steels L and H respectively using the temperature shift given by Chew and also equations (7.64) and (7.65). The temperature shift given by Chew does not apply to these experimental results, the shift is too large. Using the temperature shift given by equations (7.64) and (7.65) the prediction of fracture toughness is reasonably good. Since K_c is found by

$$K_c = 23.57(C_v)^{0.494} \tag{7.71}$$

for Steel L and

$$K_c = 10.33(C_v)^{0.613} \tag{7.72}$$

for Steel H, then

$$K_c = 19(C_v)^{0.5} \tag{7.45}$$

gives conservative results of fracture toughness for Steel L and non-conservative results for Steel H. The similarity of equations (7.45) and (7.71) occurs since they were developed for similar materials. This implies that the constants D and n from

$$K_{IC} = D(C_v)^n \tag{7.35}$$

depend on material composition.

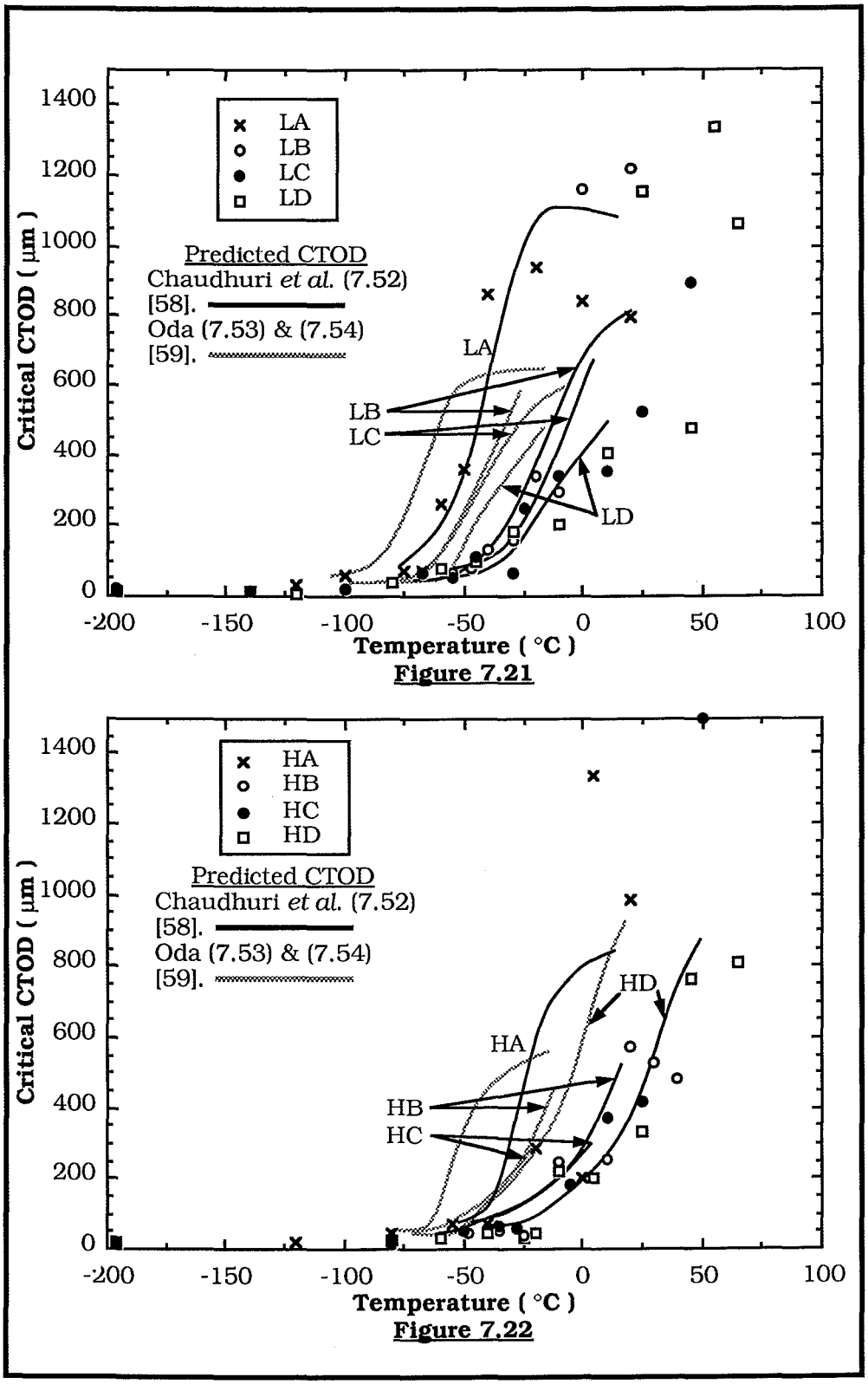

Predicted CTOD (μm) as a function of test temperature (°C) using equations of Chaudhuri *et al.* and Oda[58,59];

Figure 7.21 : Steel L.

Figure 7.22 : Steel H.

Figures 7.21 and 7.22 show the predicted results of CTOD versus temperature from equations (7.53) and (7.54) and (7.52) for Steels L and H respectively. The correlation from Oda (equations (7.53) and (7.54)) gives a transition curve similar to other transition curves but the temperature shift given by the difference between $T(\delta_i)$ and the 50% FATT is too large and the resulting transition curves are not conservative. The other set of predicted curves from equation (7.52) show good agreement with the experimental results. The form of the correlation is

$$\delta_c = DC_v^n \tag{7.49}$$

which is the same as equations (7.67) and (7.68) for the experimental steels. Chaudhuri *et al.* did not give a temperature shift for their correlation of CTOD and C_v. The temperature shift of the predicted results was calculated using equations (7.62) and (7.63) for Steels L and H respectively so it is expected that there is good agreement between the experimental and predicted results.

The correlations show that in the transition region the predicted toughness results are usually conservative, and that the toughness may be predicted by

$$K_c = D(C_v)^n \tag{7.35}$$

where D and n are constants or

$$\delta_c = \log D + n\log C_v \tag{7.48}$$

where D and n are constants. The transition temperature is given by

$$T_c = A_0 + A_1 T_{27} \tag{7.55}$$

where A_0 and A_1 are constants or the temperature shift may be given as a function of grain size as

$$\Delta T_c = \Delta B_0 + \Delta B_1 d^{-1/2} \tag{7.61}$$

where ΔB_0 and ΔB_1 are constants. The correlations are not suitable for providing fracture toughness values for fracture mechanics

calculations since their estimate of toughness or transition temperature is not always conservative. The CTOD-C_v and K_{IC}-C_v correlations will be useful as a quality control tools since the Charpy test is faster and cheaper than the standard toughness tests. A steel could have its toughness assessed during production by using the Charpy test and a CTOD-C_v correlation based on experimental data from previous experimental steels.

7.4 Summary

The results of toughness testing of the experimental steels found that there was a variation in transition temperature with variation in grain size. It was observed that:

(i) The transition temperature increased with increasing grain size and that there was a linear relationship between transition temperature and $d^{-1/2}$ for CTOD testing such that

$$T_c(°C) = B_0 + B_1 d^{-1/2} \qquad (7.3)$$

where B_0 and B_1 are constants.

(ii) The slope B_1 of this relationship depends on the composition of the material tested, notch acuity and strain rate of the test. The difference in the slope B_1 between the Charpy and CTOD tests was found to depend largely on the strain rate of the test. The increasing strain rate elevates the yield stress ahead of the crack tip.

(iii) The variation in transition temperature with grain size can be explained by the Ritchie-Knott-Rice model of cleavage fracture, which predicts an increasing transition temperature with increasing grain size. The accuracy of these predictions depended on the equation form of the temperature dependence of yield stress used as well as the material constants.

(iv) Examination of the fracture surface by scanning electron microscopy showed an increasing stretch zone width with increasing temperature.

(v) SEM examination showed that in the transition region failure occurs by a mixture of microvoid coalescence and cleavage fracture, with some cleavage facets showing signs of plastic deformation. It is possible stable grain size microcracks exist at transition.

(vi) It is found that the dependence of transition temperature on grain size is largely due to the dependence of toughness on yield

stress. An increase in grain size increases the size of the plastic zone at the crack tip. Therefore, there is a higher probability of cleavage fracture occurring and this can be maintained to a higher temperature. The increased size of plastic zone at the crack tip also means a higher critical plastic strain must be achieved at the crack tip before transition occurs. Therefore, the steel with the larger grain size will have a higher FMTT. This conclusion is supported by the micromechanical model of fracture showing an increasing FMTT with increasing grain size.

(vii) The amount of energy at transition required to overcome the resistance of grain boundaries for crack initiation and propagation increases as grain size decreases. For example, the proportion of this energy for Steel L was 33% at $d^{-1/2} = 4.218$ $mm^{-1/2}$ and 55% at $d^{-1/2} = 9.939$ $mm^{-1/2}$ of the total energy required for crack initiation and propagation. This explains why the RKR model predicts a decreasing transition temperature with grain refinement.

(viii) The correlations between Charpy V-notch impact energy and fracture toughness are likely to remain empirical. An acceptable general form seems to be

$$K_{IC}(\text{or } \delta_c) = D(C_v)^n \tag{7.35}$$

where D and n are constants. For structural steels n is approximately 0.5, but the constants will vary with composition.

(ix) The temperature shift for these correlations may be found as

$$T_c(\delta_c \text{ or } K_c) = A_0 + A_1 T_{27} \tag{7.55}$$

where A_0 and A_1 are constants, for the ductility transition temperature, or as a function of grain size as

$$\Delta T_c = \Delta B_0 + \Delta B_1 d^{-1/2} \tag{7.61}$$

where ΔB_0 and ΔB_1 are constants.

(x) The CTOD-C_v and K_c-C_v correlations are suitable as quality control tools where a quick and cheap test such as the Charpy test is required but they should not be used for specific design purposes to replace standard toughness tests.

CHAPTER 8

Conclusions and Recommendations

The fracture toughness of the two experimental steels was assessed by the CTOD test method using the compact tension specimen geometry. This test method also allowed the plane-strain fracture toughness K_{IC} of the steels to be assessed. By testing over the temperature range -196 to +65°C it is concluded from the experimental data for the structural steels that:

(i) The transition in fracture mode is accompanied by a rapid change in fracture toughness.

(ii) Satisfactory prediction of the fracture toughness results associated with cleavage fracture can be made by microfracture models. The microfracture model of cleavage implies that the fatigue crack-tip of the toughness specimen acts as a stress concentration and that microcracks need to be nucleated ahead of the crack tip before spontaneous fracture occurs.

(iii) Toughness values predicted by the microfracture model of cleavage represent a lower bound to fracture toughness when the characteristic distance is taken as twice the grain diameter. The characteristic distance ahead of the crack tip should be viewed as representing the probability of finding a sufficiently large microcrack nucleus in a highly stressed region to cause cleavage fracture. This is especially applicable to small grain sizes.

(iv) The transition temperature for the toughness test may be predicted using the microfracture model of cleavage. The predicted transition temperature is a lower bound and an increasing transition temperature is predicted with increasing grain size. The accuracy depends on the knowledge of the temperature dependence of the yield stress.

(v) Plane-strain fracture toughness increased with increasing temperature to a maximum where the thickness criterion $B \geq 2.5 (K_{IC}/\sigma_{ys})^2$ was no longer met. Load-displacement curves showed no significant deviation from linearity and the fracture mode was still cleavage. It was suggested that valid plane-strain fracture toughness values can be given by $P_{max}/P_Q \leq 1.1$ which gives a thickness criterion $B \geq 0.5 (K_{IC}/\sigma_{ys})^2$. This represented the maximum on the

K_{IC} toughness curve. It is also considered to be the region of intersection of CTOD and K_{IC} test results. Therefore the restriction on valid K_{IC} results is perhaps too strict.

By variation in the grain size of the experimental steels it was shown that there is a linear dependence of the ductility transition temperature on the reciprocal square root of grain size for CTOD and Charpy Impact testing. This dependence was given as

$$T_c(°C) = B_0 + B_1 d^{-1/2}(mm^{-1/2}) \qquad (4.6),\ (7.3)$$

where B_0 and B_1 are constants. For the Charpy Impact test, using the 27 Joule transition criterion, B_0 = 70.72°C and B_1 = -12.44°C $mm^{1/2}$ for Steel L and B_0 = 107.70°C and B_1 = -15.63°C $mm^{1/2}$ for Steel H. The coefficient B_1 for $d^{-1/2}$ was found to be in agreement with other work. The difference between the two coefficients is because of the different steel compositions.

The ductility transition criterion used for CTOD testing was the value of CTOD at initiation of stable crack extension (δ_i). This criterion gave B_0 = -5.77°C and B_1 = -6.41°C $mm^{1/2}$ for Steel L at δ_i = 0.15 mm and gave B_0 = 24.74°C and B_1 = -6.84°C $mm^{1/2}$ for Steel H at δ_i = 0.10 mm. The difference in B_1 results from differences in composition. Since a linear dependence of FMTT on $d^{-1/2}$ was observed for CTOD testing it was concluded that:

(vi) The slope B_1 depends on the composition of the material tested, notch acuity and the strain rate of the test.

(vii) Notch acuity had only a small influence on B_1. The difference in slopes between the Charpy Impact and CTOD test results depended largely on the large difference in strain rates of the two tests. The strain rate significantly affects the localised yield stress ahead of the crack tip or notch. The fracture mode transition and the temperature dependence of toughness is largely affected by the level of yield stress.

(viii) The dependence of transition temperature on grain size is due to the increase in energy needed to overcome any grain boundary resistance to crack propagation by grain refinement and the dependence of toughness on yield stress. An increase in grain size increases the size of the plastic zone at the crack tip. Therefore, there is an increased chance of cleavage fracture occurring. Also it appears that an increasing grain size and decreasing yield stress

means that a higher critical crack-tip strain must be achieved before transition occurs.

(xi) Grain refinement increases the amount of energy required for crack nucleation and crack propagation necessary to overcome the resistance of grain boundaries. This was shown using the critical energy release rate at fracture mode transition. It implies that the CTOD test measures the energy required for crack nucleation and crack propagation. It also suggests that fracture is propagation controlled by ferrite grain size and grain-size cracks in the transition region. This is supported by the observation of grain size cleavage facets in specimens tested in the transition region.

(x) The CTOD test has enough sensitivity to distinguish between different grain sizes, and different steel compositions. If a material's properties are strain-rate sensitive at high strain rates then this will not be apparent at the low strain rates of the CTOD test. Therefore in steels of similar composition and yield stress the Charpy test may show a difference in FMTT whereas the CTOD test may not.

From these results it is recommended that a study be made of the grain size dependence of critical crack-tip strain in CTOD testing using the notched ductility test to observe whether it increases with increasing grain size or not.

The results between CTOD or K_{IC} were correlated with Charpy Impact Energy (C_v) test results. An acceptable form of correlation the between Charpy impact energy and CTOD or K_{IC} appears to be

$$\delta_c \text{ (or } K_{IC}) = D(C_v)^n. \tag{7.35}$$

The constants D and n are composition dependent but grain size independent. The transition temperature shift is grain size dependent given as

$$\Delta T_c = \Delta B_0 + \Delta B_1 d^{-1/2} \tag{7.61}$$

where ΔB_0 and ΔB_1 are constants. These correlations will remain empirical relationships and therefore are suitable for quality control where a quick and cheap test such as the Charpy test is required. The correlations should not be used for specific design purposes to replace standard toughness tests.

The grain size and temperature dependence of the yield stress of the experimental steels were found from tensile testing. From the theories of yield in steel it was concluded that:

(xi) The yield stress may be written as the sum of an athermal stress component $\sigma_i(st)$ dependent on composition, a temperature (and strain rate) dependent stress component σ_i^* and a grain-size dependent stress component $k_y d^{-1/2}$, thus

$$\sigma_{ys} = \sigma_i^* + \sigma_i(st) + k_y d^{-1/2} \qquad (5.17)$$

(xii) The temperature-dependent stress component depends on the Peierls-Nabarro stress as given by the thermal activation theory of yielding by Conrad. However, the interactions of the Peierls-Nabarro stress and interstitial impurities with the movement of the double kink mechanism of yield are important.

(xiii) Over the temperature range considered several mechanisms may be operating and the temperature-dependent stress component is then described using a "best-fit" mathematical function.

The experimental results of tensile testing were analysed using multiple-linear regression analysis techniques. This analysis gave the yield stress as a function of temperature and grain size as

$$\sigma_{ys} = A_1 + A_2T + A_3T^2 + A_4T^3 + k_y d^{-1/2} \qquad (5.58)$$

where A_1, A_2, A_3, A_4 and k_y are constants. The temperature-dependent component of the model $\sigma(T) = A_1 + A_2T + A_3T^2 + A_4T^3$ is a truncated power series expansion of $\sigma_i^* = A\exp(-\alpha T)$ which other workers have shown to be in agreement with the thermal activation theory of yielding. The constants A_1, A_2, A_3 and A_4 are found to give values of the constants A and α consistent with the results of other workers. The values of k_y are consistent with other published work.

The yield stress model is then a function of temperature, grain size, the Peierls-Nabarro stress, composition (affecting the interstitial content) and the strength of dislocation locking. Further work might extend the range of the model to higher temperatures above the -196 to +65°C range and also include strain rate effects.

In CTOD testing a correlation was made between clip-gauge displacement and crack-tip opening displacement using silicone-rubber replicas of the crack tip. It was shown that the CTOD

measured from clip gauge displacement is dependent on grain size. This is due to the effect of grain size on the yield stress and rate of strain-hardening of the material which, in turn, affects the plastic-zone size at the crack tip. The CTOD is dependent on the size of the plastic zone at the crack tip. For the CT specimens tested a model was developed to give the calculated CTOD as

$$\delta_t(\text{mm}) = 0.121113\ V_g + 0.034222\ V_g^2 d^{1/2}. \qquad (6.38)$$

From the linear relationship between cross-head displacement and clip-gauge displacement a similar model of CTOD against cross-head displacement is proposed,

$$\delta_t(\text{mm}) = -0.11077 + 0.190806\ V_{CH} + 0.113386\ V_{CH}^2 d^{1/2}. \qquad (6.45)$$

These equations give comparable results to those calculated using the standard equation,

$$\delta_t = \frac{K^2(1-\nu^2)}{2\sigma_{ys}E} + \frac{V_p r_p b_0}{(r_p b_0 + a_0 + z)}. \qquad (6.46)$$

The dependence of CTOD on composition was examined and this can be the subject of further work. The influence of grain size and composition on the plastic rotation factor r_p is also worth investigation.

The investigation shows that the CTOD test may be used to select a structural material based on the fracture mode transition criterion. Modern steel-making practice regularly produces fine-grained steels so that a fracture mode transition criterion can be met for most applications. The CTOD test is sensitive to changes in grain size of the material due to the increase in energy required for crack nucleation and crack propagation.

REFERENCES

[1] Parker, E.R. (1957) "Brittle Behaviour of Engineering Structures." John Wiley & Sons Inc., N.Y.

[2] Tipper, C.F. (1962) "The Brittle Fracture Story." University Press, Cambridge.

[3] Place, A.T. (1977) "Fracture Mechanics in Engineering Design." Presentation at the Autumn Meeting, Australasian Institute of Metals, Christchurch, New Zealand.

[4] Erasmus, L.A. & Chew, C.N. (1984) in Proc. Ninth Australasian Conference on the Mechanics of Structures and Materials, Christchurch, New Zealand, pp338-343.

[5] Burns, K.W. & Pickering, F.B. (1964) *J.I.S.I.*, **202**, pp899-906.

[6] Gladman, T. & Pickering, F.B. (1965) *J.I.S.I.*, **203**, pp1212-1217.

[7] Irvine, K.J., Gladman, T. & Pickering, F.B. (1967) *J.I.S.I.*, **205**, pp161-182.

[8] Erasmus, L.A. (1971) "The Effect of Chemical Composition Variations on the Brittle-Ductile Transition Temperature of Steels." University of Cape Town, Cape Town, South Africa (Thesis: M.Sc.: Engineering).

[9] Mintz, B. (1973) *J.I.S.I.*, **211**, pp433-439.

[10] Erasmus, L.A. (1974) *J. Aust. Inst. Met.*, **19**, pp116-127.

[11] Smaill, J.S., Keown, S.R. & Erasmus, L.A. (1976) *Met. Tech.*, **3**, pp194-201.

[12] Pussegoda, L.N. (1978) "Strain-age embrittlement in reinforcing steels." University of Canterbury, Christchurch, New Zealand (Thesis: Ph.D.: Engineering).

[13] Pussegoda, L.N. & Erasmus, L.A. (1977) in Proc. Sixth Australasian Conf. on the Mechanics of Structures and Materials, Christchurch, New Zealand, pp445-451.

[14] Mintz, B. & Turner, P.J. (1978) *Metall. Trans. A*, **9A**, pp1611-1617.

[15] Erasmus, L.A. & Pussegoda, L.N. (1980) *Metall. Trans. A*, **11A**, pp231-237.

[16] Chew, C.N. (1979) "The Effects of Static and Dynamic Strain Ageing on the Fracture Toughness of Low Carbon Steels", University of Canterbury, Christchurch, New Zealand (Thesis: Ph.D.: Engineering).

[17] Ferguson, W.G. & Thorby, P.N. (1975) *Trans. N.Z. Inst. Engineers*, **3**, pp185-203.

[18] Griffith, A.A. (1920) *Phil. Trans. Roy. Soc. (London)*, **221A**, pp163-198.

[19] Orowan, E. (1945) *Trans. Inst. Eng. Ship. (Scotland)*, **89**, pp165-215.

[20] Irwin, G.R. (1948) "Fracture Dynamics." In "Fracturing of Metals." A.S.M., Cleveland, pp147-166.

[21] Irwin, G.R. (1957) *Trans. ASME, J. App. Mech.*, **24**, pp361-364.

[22] Brown, Jr., W.F. & Srawley, J.E. (1966) "Plane Strain Crack Toughness Testing of High Strength Metallic Materials, ASTM STP 410", ASTM, Philadelphia, 66p.

[23] ASTM E399-83 "Standard Test Methods for Plane-Strain Fracture Toughness of Metallic Materials," Annual Book of ASTM Standards, 03.01. ASTM Philadelphia.

[24] BS5447:1977 "Methods of Testing for Plane-Strain Fracture Toughness (K_{IC}) of Metallic Materials." British Standards Institution.

[25] Wells, A.A. (1962) in Proc. of the Crack Propagation Symposium, College of Aeronautics, Cranfield, England, **1**, pp210-230.

[26] Cottrell, A.H. (1961) ISI Special Report 69, Iron and Steel Institute, p281.

[27] Burdekin, F.M. & Stone, D.E.W. (1966) *J. Strain. Analysis*, **1**, pp145-153.

[28] Turner, C.E. (1975), J. Strain Analysis, **10**, pp207-216.

[29] Robinson, J.N. & Tetelman, A.S. (1974) in "Fracture Toughness and Slow Stable Cracking, ASTM STP 559," ASTM, Philadelphia, pp139-158.

[30] Egan, G.R. (1973) *Eng. Fract. Mech.*, **5**, pp167-185.

[31] Robinson, J.N. (1976) *Int. J. Fract.*, **12**,pp723-737.

[32] Sumpter, J.D.G. & Turner, C.E. (1976) *J. Mech. Eng. Sci.*, **18**, pp97-112.

[33] Rice, J.R. (1968) *J. App. Mech.*, **35**, pp379-386.

[34] Begley, J.A. & Landes, J.D. (1972) in "Fracture Toughness, Proceedings of 1971 National Symposium on Fracture Mechanics, Part II, ASTM STP 514," ASTM, Philadelphia, pp1-20.

[35] Sumpter, J.D.G. & Turner, C.E. (1976) in "Cracks and Fracture, ASTM STP 601", ASTM, Philadelphia, pp3-18.

[36] Clarke, G.A., *et al.* (1979) *J.T.E.V.A.*, **7**, pp49-56.

[37] Dawes, M.G. (1979) in "Elastic-Plastic Fracture, ASTM STP 668," J.D. Landes *et al.*, Ed's., ASTM, Philadelphia, pp307-333.

[38] De Castro, P.M.S.T., Spurrier, J. & Hancock, P. (1979) "Fracture Mechanics, ASTM STP 677", C.W. Smith, Ed., ASTM, Philadelphia, pp486-497.

[39] ASTM E813-87 "Standard Test Method for J_{IC}, a Measure of Fracture Toughness," Annual Book of ASTM Standards, 03.01, ASTM, Philadelphia.

[40] ASTM E1152-87 "Standard Test Method for Determining J-R Curves," Annual Book of ASTM Standards, 03.01, ASTM, Philadelphia.

[41] BS 5762:1979 "Methods for Crack Opening Displacement (COD) testing," British Standards Institution.

[42] AS 2205-7.3, 1983, "Crack Opening Displacement (COD) Test", Australian Standards Association.

[43] GB 2358-80, 1980, "Crack Opening Displacement (COD) Testing Method," Chinese Standards Association.

[44] ASTM E1290-89 "Standard Test Method for Crack-Tip Opening Displacement (CTOD) Fracture Toughness Measurement," Annual Book of ASTM Standards, 03.01, ASTM, Philadelphia.

[45] ASTM E992-84 "Standard Practice for Determination of a Fracture Toughness of Steels using Equivalent Energy Methodology," Annual Book of ASTM Standards, 03.01, ASTM, Philadelphia.

[46] Witt, F.J. (1971) U.S.A.E.C. Report ORNL-TM-3172, Oak Ridge National Laboratory, U.S.A.

[47] Witt, F.J. & Mager, T.R. (1971) *Nuclear Engineering and Design*, **17**, pp91-102.

[48] Chell, G.G., Milne, I. & Kirby, J.H. (1975) *Met. Tech.*, **2**, pp549-553.

[49] Chell, G.G. & Worthington, P.J. (1976) *Mat. Sci. Eng.*, **26**, pp95-103.

[50] Chell, G.G. & Milne, I. (1976) *Mat. Sci. Eng.*, **22**, pp249-253.

[51] Dawes, M.G. (1980) in "Advances in Elasto-Plastic Fracture Mechanics," L.H. Larsson, Ed., Applied Science Publishers, London, pp279-300.

[52] Turner, C.E. (1980) *ibid*, pp301-317.

[53] Paris, P.C., Tada, H., Zahoor, A. & Ernst, H. (1979) in "Elastic-Plastic Fracture, ASTM STP 668," J.D. Landes *et al.*, Ed.'s, ASTM, Philadelphia, pp5-36.

[54] PD 6493:1980 "Guidance on Some Methods for the Derivation of Acceptance Levels for Defects in Fusion Welded Joints," British Standards Institution.

[55] Pisarski, H.G. (1978) *The Welding Research Institute Research Bulletin*, **19**, pp362-367.

[56] Tsukada, H., Iwadate, T., Tanaka, Y & Ono, S. (1980) in "Materials, Fracture and Fatigue," Volume 1 of "Pressure Vessel Technology," *I. Mech. E.*, London. Paper C55/80, pp369-374.

[57] Dolby, R.E. (1981) "COD and Charpy V Test Data Correlation:Ferritic Steel Weld Metals" The Welding Institute, Cambridge.

[58] Chaudhuri, S.K., Ojha, S.N. & Ramaswamy, V. (1986) *Int. J. Pres. Ves. & Piping*, **22**, pp23-30.

[59] Oda, Isamu (1988) *Eng. Fract. Mech.*, **29**, pp663-671.

[60] Sailors, R.H. & Corten, H.T. (1972) in "Fracture Toughness. Proceedings of the 1971 National Symposium on Fracture Mechanics, Part II, ASTM STP 514," ASTM, Philadelphia, pp164-191.

[61] Laird, C. (1967) in "Fatigue Crack Propagation, ASTM STP 415," ASTM, Philadelphia, pp131-168.

[62] Fahy, F.W. *et al.* (1980) "Engineering Metallurgy." 2nd. ed. University of Canterbury, Christchurch.

[63] Ewalds, H.L. & Wanhill, R.J.H. (1984) "Fracture Mechanics," Edward Arnold (Publishers) Ltd., London.

[64] Knott, J.F. (1966) *J.I.S.I.*, **204**, pp104-111.

[65] Zener, C.M. (1948) "The Micro-mechanism of Fracture." In "Fracturing of Metals," ASM, Cleveland, pp3-31.

[66] Stroh, A.N. (1954) *Proc. Roy. Soc.*, **A223**, pp404-414.

[67] Cottrell, A.H. (1958) *Trans. Metall. Soc. AIME*, **212**, pp192-203.

[68] Cottrell, A.H. (1959) in "Fracture," B.L. Averbach *et al.*, Eds., M.I.T. & John Wiley & Sons, Inc., N.Y., pp20-53.

[69] Smith, E. (1966) in "Physical Basis of Yield and Fracture," Conf. Series 1, *Int. Physics and Phys. Soc.*, Oxford, pp36-46.

[70] Smith, E. (1968) *Int. J. Fract. Mech.*, **4**, pp131-145.

[71] Lindley, T.C., Oates, G. & Richards, C.E. (1970) *Acta Metall.*, **18**, pp1127-1136.

[72] Ritchie, R.O., Knott, J.F. & Rice, J.R. (1973) *J. Mech. Phys. Solids*, **21**, pp395-410.

[73] Knott, J.F. & Cottrell, A.H. (1963), *J.I.S.I.*, **201**, pp249-260.

[74] Low, J.R. (1954) in "Relations of Properties to Microstructure," A.S.M., Novelty, Ohio, pp163-179.

[75] Griffiths, J.R. & Oates, G. (1969) in "Fracture 1969," P.L. Pratt, Ed., Chapman and Hall Ltd., London. Paper 19, pp229-240.

[76] Rawal, S.P. & Gurland, J. (1977) *Metall. Trans. A*, **8A**, pp691-698.

[77] Curry, D.A. & Knott, J.F. (1976) *Met. Sci.*, 10, pp1-6.

[78] Argon, A.S., Im, J. & Needleman, A. (1975) *Metall. Trans. A*, **6A**, pp815-824.

[79] McClintock, F.A. (1968) *Int. J. Fract. Mech.*, **4**, pp101-130.

[80] Thomason, P.F. (1968) *J.I.M.*, **96**, pp360-365.

[81] Brown, L.M. & Embury, J.D. (1973) in Proc. Int. Conf. on "Strengthening of Metals and Alloys," Cambridge, p164.

[82] Clayton, J.Q. & Knott, J.F. (1976) *Met. Sci.*, **10**, pp63-71.

[83] Hahn, G.T., Hoagland, R.G. & Rosenfield, A.R. (1976) *Metall. Trans. A*, **7A**, pp49-54.

[84] Smith, R.F. & Knott, J.F. (1971) in "Conference on Practical Application of Fracture Mechanics to Pressure Vessel Technology," *I. Mech. E.*, London. Paper C9/71, pp65-75.

[85] Sailor, R.H. (1975) in "ASTM STP 605", ASTM, Philadelphia, p34.

[86] Ebrahimi, Fereshteh.(1988) in "Fracture Mechanics: Eighteenth Symposium, ASTM STP 945," D.T. Read & R.P. Reed, Eds., ASTM, Philadelphia, pp555-580.

[87] Petch, N.J. (1959) in "Fracture," B.L. Averbach *et al.*, Eds., The Technology Press, M.I.T. and John Wiley & Sons, Inc., N.Y. pp54-68.

[88] Burdekin, F.M. (1967) *British Welding Journal*, **14**, pp649-659.

[89] Curry, D.A. (1978) *Nature*, **276**, pp50-51.

[90] Curry. D.A. (1979) "The Relationship between Fracture Toughness and Charpy Impact Transition Temperatures in Mild Steel," Central Electricity Research Laboratories Laboratory Note RD/L/N109/79, C.E.R.L., Leatherhead, Surrey.

[91] Curry, D.A. (1980) *Mat. Sci. Eng.*, **43**, pp135-144.

[92] Cottrell, A.H. (1948) in "Report on the Strength of Solids," Physical Society, London, pp30-37.

[93] Cottrell, A.H. & Bilby, B.A. (1949) *Proc. Phys. Soc.* London, **62A**, pp49-62.

[94] Fisher, J.C. (1955) *Trans. Am. Soc. Metals*, **47**, pp451-462.

[95] Johnston, W.G. & Gilman, J.J. (1959) *J. Applied Physics*, **30**, pp129-144.

[96] Cottrell, A.H. (1963) in "The Relation between the Structure and Mechanical Properties of Metals," National Physical Laboratories Symposium No. 15, Volume II, HMSO, London, pp455-473.

[97] Conrad, Hans (1961) *J.I.S.I.*, **198**, pp364-375.

[98] Conrad, Hans (1963) in "The Relation between the Structure and Mechanical Properties of Metals," National Physical Laboratories Symposium No. 15, Volume II, HMSO, London, pp475-516.

[99] Armstrong, R.W. (1967) *Acta Metall.*, **15**, pp667-668.

[100] Chen, Y.T., Atteridge, D.G. & Gerberich, W.W. (1981) *Acta Metall.*, **29**, pp1171-1185.

[101] Sih, G.C. (1973) *Eng. Frac. Mech.*, **5**, pp365-377.

[102] Gilman, J.J. (1963) in "Mechanical Behaviour of Crystalline Solids," National Bureau of Standards Monograph 59, NBS, Dept. of U.S. Commerce, pp79-102.

[103] Cottrell, A.H. (1953) "Dislocations and Plastic Flow in Crystals," Oxford University Press, Oxford, p5, p9 and p137.

[104] Cottrell, A.H. (1963) in "Tewksbury Symposium on Fracture (1963)", Eng. Faculty, University of Melbourne (1965), Melbourne. C.J. Osborne, Ed. pp1-27.

[105] Inglis, C.E. (1913) *Trans. Inst. Naval Architects*, **55**, pp219-241.

[106] Westergaard, H.M. (1939) *Trans. ASME, J. Applied Mech.*, **6**, ppA49-A53.

[107] Creager, M. & Paris, P.C. (1967) *Int. J. Fract. Mech.*, **3**, pp247-252.

[108] Rooke, D.P. & Cartwright, D.J. (1976) "Compendium of Stress Intensity Factors," HSMO, London.

[109] Irwin, G.R., Kies, J.A. & Smith, H.L. (1958) *Proc. A.S.T.M.*, **58**, pp640-657.

[110] Orowan, E. (1948-49) *Reports on Progress of Physics*, **12**, pp214-232.

[111] Irwin, G.R. (1956) in "9th International Congress of Applied Mechanics," Brussels, University of Brussels (1957), **8**, pp245-251.

[112] Irwin, G.R. (1964) *Applied Materials Research*, **3**, p65-81.

[113] Irwin, G.R. & Wells, A.A. (1965) *Metall. Reviews*, **10**, pp223-270.

[114] Dugdale, D.S. (1960) *J. Mech. Phys. Solids*, **8**, pp100-104.

[115] Irwin, G.R. & Kies, J.A. (1952) *Welding Research Supplement of the Welding Journal*, **31**, pp95-s-100-s.

[116] Srawley, J.E. & Brown, W.F. (1965) "Fracture Toughness Testing Methods" in ASTM STP 381, ASTM, Philadelphia, pp133-198.

[117] Knott, J.F. (1971) *Mat. Sci. Eng.*, **7**, pp1-36.

[118] Gurumoorthy, B., Kirchner, H.O.K., Prinz, F.B. & Sinclair, G.B. (1988) *Eng. Frac. Mech.*, **29**, pp637-640.

[119] Ingham, T., Knee, N., Milne, I. & Morland, E. (1989) in "Fracture Mechanics: Perspectives and Directions (20th Symposium) ASTM STP 1020," R.P. Wei and R.P. Gangloff, Eds., ASTM, Philadelphia, pp369-389.

[120] Srawley, J.E., Jones, M.H. & Brown, W.F. (1967) *Materials Research and Standards*, **7**, pp262-266.

[121] BS DD3:1971 "Draft for Development. Method for Plane Strain Fracture Toughness (K_{IC}) Testing," British Standards Institution.

[122] Radon, J.C. & Turner, C.E. (1966) *J.I.S.I.*, **204**, pp842-845.

[123] Sumpter, J.D.G. & Caudrey, A.J. (1987) in "Fracture Toughness Testing - Methods, Interpretation and Applications," The Welding Institute, Cambridge, pp145-154.

[124] Feddersen, C.E. (1971) in "Damage Tolerance in Aircraft Structures, ASTM STP 486," ASTM, Philadelphia, pp50-78.

[125] Krafft, J.M., Sullivan, A.M. & Boyle, R.W. (1962) in Proceedings of the Crack Propagation Symposium, College of Aeronautics, Cranfield, England, **1**, pp8-28.

[126] ASTM E561-85 "Standard Practice for R-Curve Determination," Annual book of ASTM Standards, 03.01, ASTM, Philadelphia.

[127] Chipperfield, C.G. (1978) *J.T.E.V.A.*, **6**, pp253-259.

[128] Bucci, R.J., Paris, P.C., Landes, J.D. & Rice, J.R. (1971) in "Fracture Toughness. Proceedings of the 1971 National Symposium on Fracture Mechanics, Part II, ASTM STP 514," ASTM (1972), Philadelphia, pp40-69.

[129] Rice, J.R., Paris, P.C. & Merkle, J.G. (1973) in "Progress in Flaw Growth and Fracture Toughness Testing, ASTM STP 536," ASTM, Philadelphia, pp231-245.

[130] Begley, J.A. & Landes, J.D. (1973) *ibid.*, pp246-263.

[131] Merkle, J.G. & Corten, H.T. (1974) *Trans. ASME, J. Pres. Vessel Tech.*, **96**, pp286-292.

[132] Ernst, H.A. (1983) in "Elastic-Plastic Fracture: Second Symposium, Vol I - Inelastic Crack Analysis, ASTM STP 803," C.F. Shih & J.P. Gudas, Eds., ASTM, Philadelphia, ppI-191-I-213.

[133] Hahn, G.T. & Rosenfield, A.R. (1965) *Acta Metall.*, **13**, pp293-306.

[134] Bilby, B.A., Cottrell, A.H. & Swinden, K.H. (1963) *Proc. Roy. Soc.*, **272A**, pp304-314.

[135] Pratap, C.R. & Pandey, R.K. (1984) *Eng. Fract. Mech.*, **19**, pp1139-1150.

[136] Pratap, C.R. & Pandey, R.K. (1989) *Eng. Fract. Mech.*, **34**, pp233-243.

[137] Lai, M.O. (1986) *Eng. Fract. Mech.*, **24**, pp307-313.

[138] Heald, P.T., Spink, G.M. & Worthington, P.J. (1972) *Mat. Sci. Eng.*, 10, pp129-138.

[139] Knott, J.F. (1966) *J.I.S.I.*, **204**, pp1014-1021.

[140] BS DD19:1972, "Draft for Development. Methods for Crack Opening Displacement (COD) Testing, "British Standards Institution.

[141] Ingham, T., Egan, G.R., Elliott, D. & Harrison, T.C. (1971) in "Practical Applications of Fracture Mechanics to Pressure-Vessel Technology," *I. Mech. E.*, London, Paper C54/71, pp200-208.

[142] Green, A.P. & Hundy, B.B. (1956) *J. Mech. Phys. Solids*, **4**, pp128-144.

[143] Matsoukas, G., Cotterell, B. & Mai, Y.W. (1984) *Int. J. Fract.*, **26**, ppR49-R53.

[144] Wu, S.X., Mai, Y.W. & Cotterell, B. (1988) *J.T.E.V.A.*, **16**, pp555-557.

[145] Wells, A.A. (1971) in Canadian Congress of Applied Mechanics, Calgary, Canada, pp59-77.

[146] Kolednik, O. (1988) *Eng. Fract. Mech.*, **29**, pp173-188.

[147] Kolednik, O. (1989) *Eng. Fract. Mech.*, **33**, pp813-826.

[148] Fields, B.A. & Miller, K.J. (1977) *Eng. Fract. Mech.*, **9**, pp137-146.

[149] Harrison, J.D. (1981) "COD Testing and Analysis: The Present State of the Art," The Welding Institute, Cambridge.

[150] Turner, C.E. (1983) in "Elastic-Plastic Fracture Mechanics," L.H. Larsson, Ed., D. Reidel Publishing Co., (1985), pp397-410.

[151] Gordon, J.R. & Garwood, S.J. (1989) in "Fracture Mechanics Perspectives and Directions (20th Symposium), ASTM STP 1020," R.P. Wei & R.P. Gangloff, Eds., ASTM, Philadelphia, pp410-430.

[152] Qingfen Li, Limin Zhou & Shouren Li (1986) *Eng. Frac. Mech.*, **23**, pp925-928.

[153] Pratap, C.R., Pandey, R.K. & Chinadurai, R. (1988) *Eng. Fract. Mech.*, **31**, pp105-118.

[154] Wu, S.X. Cotterell, B. & Mai, Y.W. (1988) *Int. J. Fract.*, **37**, pp13-29.

[155] Buchalet, C. & Mager, T.R. (1973) in "Progress in Flaw Growth and Fracture Toughness Testing, ASTM STP 536," ASTM, Philadelphia, pp281-296.

[156] Broek, D. (1987) "Elementary Engineering Fracture Mechanics," 4th Revised Ed., Martinus Nijhoff Publishers, Dordrecht.

[157] Stroh, A.N. (1955) *Proc. Roy. Soc.*, **232A**, pp548-560.

[158] Stroh, A.N. (1955) *Phil. Mag.*, **s7**, **46**, pp968-973.

[159] Stroh, A.N. (1957) *Advances in Physics*, **6**, pp418-465.

[160] Eshelby, J.D., Frank, F.C. & Nabarro, F.R.N. (1951) *Phil. Mag.*, **s7**, **42**, pp351-364.

[161] Curry, D.A. (1980) *Met. Sci.*, **14**, pp319-336.

[162] Curry, D.A., King, J.E. & Knott, J.F. (1978), *Met. Sci.*, **12**, pp247-250.

[163] Petch, N.J. (1953) *J.I.S.I.*, **174**, pp25-28.

[164] Hall, E.O. (1951) *Proc. Phys. Soc. London*, **B64**, pp742-753.

[165] McMahon, C.J. & Cohen, M. (1965) *Acta Metall.*, **13**, pp591-604.

[166] Oates, G. (1968) *J.I.S.I.*, **206**, pp930-935.

[167] Oates, G. (1969) *J.I.S.I.*, **207**, pp353-357.

[168] Tetelman, A.S. & Wilshaw, T.R. (1969) in "Fracture 1969," P.L. Pratt, Ed., Chapman and Hall Ltd., London. Paper 18, pp219-228.

[169] Almond, E.A., Timbres, D.H. & Embury, J.D. (1969) *ibid.*, Paper 21, pp253-265.

[170] Griffiths, J.R. & Owen, D.R.J. (1971) *J. Mech. Phys. Solids*, **19**, pp419-431.

[171] Okumura, N. (1983) *Met. Sci.*, **17**, pp581-589.

[172] Evensen, J.D. (1978) "Microstructural Aspects of the Fracture Parameters of Controlled Rolled HSLA Steels," McMaster University, Hamilton, Ontario, Canada. (Thesis: Ph.D.: Metallurgy and Materials Science).

[173] Wilshaw, T.R. (1966) *J.I.S.I.*, **204**, pp936-938.

[174] Mintz, B. (1984) *Met. Tech.*, **11**, pp265-272.

[175] Curry, D.A. & Knott, J.F. (1978) *Met. Sci.*, **12**, pp511-514.

[176] Gerberich, W.W., Chen, Y.T., Atteridge, D.G. & Johnson, T. (1981) *Acta Metall.*, **29**, pp1187-1201.

[177] Owen, W.S., Averbach, B.L. & Cohen, M. (1958) *Trans. Am. Soc. Metals*, **50**, pp634-655.

[178] Groom, J.D.G. & Knott, J.F. (1975) *Met. Sci.*, **9**, pp390-400.
[179] Chen, J.H., Ma, H. & Wang, G.Z. (1990) *Metall. Trans. A.*, **21A**, pp313-320 (Part I), pp321-330 (Part II).
[180] Petch, N.J. (1986) *Acta Metall.*, **34**, pp1387-1393.
[181] Mintz, B., Morrison, W.B. & Jones, A. (1979) *Met. Tech.*, **6**, pp252-260.
[182] Armstrong, R.W. (1987) *Eng. Frac. Mech.*, **28**, pp529-538.
[183] Petch, N.J. & Armstrong, R.W. (1989) *Acta Metall.*, **37**, pp2279-2285.
[184] Hodgson, D.E. & Tetelman, A.S. (1969) in "Fracture 1969," P.L. Pratt, Ed., Chapman and Hall, London. Paper 22, pp266-277.
[185] Brozzo, P. *et al.* (1977) *Met. Sci.*, **11**, pp123-129.
[186] Curry, D.A. (1982), *Met. Sci.*, **16**, pp435-440.
[187] Curry, D.A. (1984), *Met. Sci.*, **18**, pp67-76.
[188] Bowen, P. & Knott, J.F. (1984), *Met. Sci.*, **18**, pp225-235.
[189] Bowen, P., Druce, S.G. & Knott, J.F. (1986) *Acta Metall.*, **34**, pp1121-1131.
[190] Yoshiyuki Tomita (1988) *Metall. Trans. A*, **19A**, pp2513-2521.
[191] Bowen, P. & Knott, J.F. (1986) *Metall. Trans. A*, **17A**, pp231-241.
[192] Tracey, D.M. (1976) *Trans. ASME, J. Engineering Materials and Technology*, **98**, pp147-151.
[193] Bowen, P., Druce, S.G. & Knott, J.F. (1987) *Acta Metall.*, **35**, pp1735-1746.
[194] Hutchinson, J.W. (1968) *J. Mech. Phys. Solids*, **16**, pp13-31.
[195] Juro Watanabe *et al.* (1987) *Eng. Fract. Mech*, **28**, pp589-600.
[196] Curry, D.A. & Knott, J.F. (1979) *Met. Sci.*, **13**, pp341-345.
[197] Wallin, K., Saario, T. & Törrönen, K. (1984) *Met. Sci.*, **18**, pp13-16.
[198] Kotilainen, H., Törrönen, K. & Nenonen, P. (1979) in "Strength of Metals and Alloys," Pergamon Press, Toronto, **2**, pp1431-1435.
[199] Evans, A.G. (1983) *Metall. Trans. A.*, **14A**, pp1349-1355.
[200] Mudry, F. (1986) in "Elastic-Plastic Fracture Mechanics," L.H. Larsson, Ed., D. Reidel Publishing Co., pp303-325.
[201] Tsann Lin, Evans, A.G. & Ritchie, R.O. (1986) *J. Mech. Phys. Solids*, **34**, pp477-497.

[202] Tyson, W.R. & Marandet, B. (1988) in "Fracture Mechanics: 18th Symposium, ASTM STP 945," D.T. Read & R.P. Reed, Eds., ASTM, Philadelphia, pp19-32.

[203] Anderson, T.L. & Stienstra, D. (1989) *J.T.E.V.A.*, **17**, pp46-53.

[204] Wallin, K. (1984) *Eng. Fract. Mech.*, **19**, pp1085-1093.

[205] Zurek, A.K., Follansbee, P.S. & Hack, J. (1990) *Metall. Trans. A*, **21A**, pp431-439.

[206] Tsann Lin, Evans, A.G. & Ritchie, R.O. (1987) *Metall. Trans. A*, **18A**, pp641-651.

[207] Tyson, W.R. (1989) *Metall. Trans. A*, **20A**, pp2860-2862.

[208] Couque, H., Asaro, R.J., Duffy, J. & Lee, S.H. (1988) *Metall. Trans. A*, **19A**, pp2179-2206.

[209] Petch, N.J. (1958) *Phil. Mag.*, **s8**, **3**, pp1089-1097.

[210] Armstrong, R.W. (1964) *Phil. Mag.*, **s8**, **9**, pp1063-1067.

[211] Armstrong, R.W. (1969) in "Fracture 1969," P.L. Pratt, Ed., Chapman and Hall, London. Paper 26, pp314-326.

[212] Knott, J.F. (1977) in "Advances in Research on the Strength and Fracture of Materials. Fracture 1977," D.M.R. Taplin, Ed., Pergamon Press, N.Y., **1**, pp61-92.

[213] Ashby, M.F. (1966) *Phil. Mag.*, **s8**, **14**, pp1157-1178.

[214] Rice, J.R. & Johnson, M.D. (1970) in "Inelastic Behaviour of Solids," Kanninen *et al.*, Eds., McGraw-Hill Inc., N.Y. pp641-661.

[215] Dahl, W. & Dormagen, D. (1986) in "Elastic-Plastic Fracture Mechanics," L.H. Larsson, Ed., D. Reidel Publishing Co., Dordrecht., pp203-225.

[216] Hahn, G.T. & Rosenfield, A.R. (1968) in "Applications Related Phenomena in Titanium Alloys, ASTM STP 432," ASTM, Philadelphia, pp5-32.

[217] Garrett, G.G. & Knott, J.F. (1978) *Metall. Trans A*, **9A**, pp1187-1201.

[218] Chipperfield, C.G. & Knott, J.F. (1975) *Met. Tech.*, **2**, pp45-51.

[219] Knott, J.F. (1980) *Met. Sci.*, **14**, pp327-336.

[220] Chua, C.E. (1976) "The Effect of Manganese and Nitrogen on the Lower Yield Strength of Low Carbon Steel," University of Canterbury, Christchurch, New Zealand. (Thesis: M.E: Engineering).

[221] Honeycombe, R.W.K. (1981) "Steels: Microstructure and Properties," Edward Arnold (Publishers) Ltd., London.

[222] Umemoto, M., Zing Hai Guo & Tamura, I. (1987) *Mat. Sci. Tech.*, **3**, pp249-255.

[223] Pickering, F.B. & Gladman, T. (1963) "Metallurgical Developments in Carbon Steel," ISI Special Report 81, London, p10.

[224] Digges, T.G. (1941) *Trans. Am. Soc. Metals*, **29**, pp285-316.

[225] Whiteley, J.H. (1943) *J.I.S.I.*, **148**, pp513-578.

[226] Miller, O.O. (1951) *Trans. Am. Soc. Metals*, **43**, pp260-289.

[227] Kehl, G.L. (1943) "The Principles of Metallographic Laboratory Practice," McGraw-Hill Book Co., N.Y.

[228] Liew, S.V. (1973) "The Effect of Manganese and Nitrogen on the Lower Yield Stress of Low Carbon Steels," University of Canterbury, Christchurch, New Zealand. (Thesis: M.E.: Engineering).

[229] Koh, T.P. (1974) "The Effect of Manganese and Nitrogen on the Lower Yield Stress of Low Carbon Steels," University of Canterbury, Christchurch, New Zealand. (Thesis: M.E.: Engineering).

[230] ASTM E112-85 "Standard Methods for Determining the Average Grain Size," Annual Book of ASTM Standards, 03.01, ASTM, Philadelphia.

[231] Hensler, J.H. (1968) *J.I.M.*, **96**, pp190-193.

[232] Chong Chon Jim (1980) "The Effects of Strain Ageing and Grain Size on Fatigue in Low Carbon Steels." University of Canterbury, Christchurch, New Zealand. (Thesis: Ph.D.: Engineering).

[233] Toshiro Kobayashi, Koichi Takai & Hideyo Maniwa (1967), *Trans. I.S.I.J.*, **7**, pp115-125.

[234] Dunne, D.P., Smith, R.M. & Chandra, T. (1985) in "HSLA Steels. Metallurgy and Applications," J.M. Gray *et al.*, Eds., A.S.M., Ohio, pp141-149.

[235] Towers, O.L. (1986) Metal Construction, **18**, pp171-176(I), pp254-258(II) and pp319-325(III).

[236] MacGregor, C.W. (1931) *Trans ASME, A.P.M.*, **53**, pp187-200.

[237] Dalby, W.E. (1913) *Proc. Roy. Soc.*, **88A**, pp281-289.

[238] Kuroda, M. (1938) *Sci. Pap. Inst. Phys. Chem. Research*, **38**, p1528.

[239] McAdams, D.J. & Mebs, R.W. (1943) *Proc. A.S.T.M.*, **43**, pp661-706.

[240] Nabarro, F.R.N. (1948) in "Report on the Strength of Solids," Physical Society of London, p38.

[241] Hall, E.O. (1970) "Yield Point Phenomena in Metals and Alloys," MacMillan, London, pp38-40, 70, 150-152.

[242] Fisher, R.M. (1962) Reference 27 from [96]. "Deformation of Iron," University of Cambridge, Cambridge, England. (Thesis: Ph.D.).

[243] Li, J.C.M. (1963) *Trans. Metall. Soc. AIME*, **227**, pp239-247.

[244] Cochrane, R.C. (1972) Reference 49 from [174]. Internal Report Ex 40/1/71D, British Steel Corporation, Sheffield Laboratories, Moorgate.

[245] Patel, J.R. & Chaudhuri, A.R. (1960) *Journal of Metals*, **12**, p76 (Abstract).

[246] Hahn, G.T. (1962) *Acta Metall.*, **10**, pp727-738.

[247] Zener, C. & Holloman, J.H. (1944) *J. Applied Physics*, **15**, pp23-32.

[248] Holloman, J.H. & Zener, C. (1944) *Trans. Am. Inst. Mining and Metallurgical Engineers*, **158**, pp283-297.

[249] Zener, C. & Holloman, J.H. (1944) *Trans. Am. Soc. Metals*, **33**, pp163-235.

[250] Dushman, S. & Langmuir, I. (1922) *Physical Review*, **20**, p113.

[251] Rosi, F.D. & Mathewson, C.H. (1950) *Trans. AIME, Journal of Metals*, **180**, pp1159-1167.

[252] Johnston, W.G. (1962) *J. Applied Physics*, **33**, pp2050-2058.

[253] Clough, W.R. & Pavlovic, A.S. (1960) *Trans. Am. Soc. Metals*, **52**, pp948-970.

[254] Larson, F.R. & Nunes, J. (1961) *Trans. Am. Soc. Metals*, **53**, pp663-682.

[255] Nunes, J. & Larson, F.R. (1962) *J.I.M.*, **91**, pp114-117.

[256] Nunes, J. & Larson, F.R. (1963) *Trans. Metall. Soc. AIME*, **227**, pp1369-1376.

[257] Heslop, J. & Petch, N.J. (1956) *Phil. Mag*, **s8**, **1**, pp866-873.

[258] Stein, D.F., Low, J.R. & Seybolt, A.U. (1963) *Acta Metall.*, **11**, pp1253-1263.

[259] Christian, J.W. & Masters, B.C. (1964) *Proc. Roy. Soc.*, **A281**, pp223-239(I), pp240-257(II).

[260] Dorn, J.E. & Rajnak, S. (1964) *Trans. Metall. Soc. AIME*, **230**, pp1052-1064.

[261] Aróztegui, J.J., Urcola, J.J. & Fuentes, M. (1989) *Metall. Trans. A*, **20A**, pp1657-1668.

[262] Vlach, B., Holzmann, M. & Man, J. (1986) *Metallic Materials*, **24**, pp320-325. (Translation from *Kovove Materialy*, **24**, 1986, pp654-665).

[263] BS 18:1987, "Method for tensile testing of metals (including aerospace materials)," British Standards Institution.

[264] BS 3688 Part I: 1963 (1981), "Methods for mechanical testing of metals at elevated temperatures," British Standards Institution.

[265] Erasmus, L.A. (1987) in Proc. Australasian Conf. Materials for Industrial Development, I.M.M.A., Christchurch, New Zealand, pp357-364.

[266] Wilson, D.V. (1961) *Acta Metall.*, **9**, pp618-620.

[267] Volk, W. (1969) "Applied Statistics for Engineers," 2nd Ed., McGraw-Hill, Inc., N.Y.

[268] Vinogradov, V.E., Khudenko, M.A. & Baranov, V. Ya. (1986) Izvestiya Akademii Nauk SSSR. *Metally*, **5**, pp164-168. (Translation pp161-164).

[269] Tanaka, T. & Watanabe, S. (1971) *Acta Metall.*, **19**, pp991-1000.

[270] Armstrong, R., Codd, I., Douthwaite, R.M. & Petch, N.J. (1962) *Phil. Mag.*, **s8**, **7**, pp45-58.

[271] Cracknell, A. & Petch, N.J. (1955) *Acta Metall.*, **3**, pp186-189.

[272] Lereim, J. & Embury, J.D. (1979) *Eng. Fract. Mech.*, **11**, pp161-164.

[273] Davies, P.H. (1983) in "Elastic-Plastic Fracture: Second Symposium, Volume II - Fracture Resistance Curves and Engineering Applications, ASTM STP 803," C.F. Shih & J.P. Gudas, Eds., ASTM, Philadelphia. ppII611-II631.

[274] Lereim, J. (1978) "Small Scale Fracture Toughness Testing." McMaster University, Hamilton, Ontario, Canada. (Thesis: Masters: Metallurgy).

[275] Erasmus, L.A. (1969) in Proceedings of the Second Australian Conference on the Mechanics of Structures and Materials. Adelaide, South Australia. Paper 16, pp16.1-16.27.

[276] Soh, K.S. (1970) "The Effect of Grain Size on the Tensile Flow Curve of Low Carbon Steel," University of Canterbury, Christchurch, New Zealand. (Thesis: M.E.: Engineering).

[277] Morrison, W.B. (1966) *Trans. Am. Soc. Metals*, **59**, pp824-845.

[278] Chew, C.N. (1988) Private Communication on silicone-rubber crack-tip replicas. Dr. C.N. Chew, Westralian Technical Consultants Pty, Ltd., 204 High Road, Riverton, WA6155, Australia.

[279] Thaulow, C. (1978) *Metal Construction*, **10**, pp588-589.

[280] François D. & Krasowsky, A. (1986) *Eng. Fract. Mech.*, **23**, pp455-465.

[281] Srawley, J.E. (1976) *Int. J. Fract.*, **12**, pp475-476.

[282] Garwood, S.J. (1986) in "Elastic-Plastic Fracture Mechanics," L.H. Larsson, Ed., D. Reidel Publishing Co., Dordrecht., pp85-115.

[283] Chipperfield, C.G. (1976) *Int. J. Fract.*, **12**, pp873-886.

[284] Towers, O.L. & Garwood, S.J. (1981) in "Advances in Fracture Research, Fracture 81," Pergamon Press Ltd., Oxford, **4**, pp1731-1739.

[285] Woolman, J. & Mottram, R.A. (1964) "The Mechanical and Physical Properties of the British Standard En Steels BS970:1955 (Vol. 1 En1-En20)," BISRA, Pergamon Press Ltd., Oxford.

[286] Priest, A.H. (1986) in "Size Effects in Fracture," Mechanical Engineering Publication Ltd. for I. Mech. E., London, pp53-61.

[287] Abramowitz, M. & Stegun, I.A. Editors (1965) "Handbook of Mathematical Functions with Formula, Graphs and Mathematical Tables," Dover Publications, Inc., N.Y.

[288] Baldwin, W.M. (1958) *Acta Metall*, **6**, pp139-141.

[289] Irwin, G.R. (1964) *Trans. ASME, J. Engineering for Power*, **A86**, pp444-450.

[290] Beachem, C.D. & Meyn, D.A. (1968) in "Electron Fractography, ASTM STP 436," ASTM, Philadelphia, pp59-88.

[291] Burghard, H.C. & Stoloff, N.S. (1968) in "Electron Fractography ASTM STP 436," ASTM, Philadelphia, pp32-58.

[292] Hahn, G.T., Averbach, B.L., Owen, W.S. & Cohen, M. (1959) in "Fracture," B.L. Averbach *et al.*, Eds., M.I.T. & John Wiley and Sons, Inc., N.Y., pp91-116.

[293] Thorby, P.N. & Ferguson, W.G. (1976) *Mat. Sci. Eng.*, **22**, pp177-184.

[294] Nageswara Rao, B. & Acharya, A.R. (1989) *Eng. Fract. Mech.*, **32**, pp39-42.

[295] Ratnaraj, R. (1989) "Nitrogen in HSLA and Dual Phase Steels," University of Canterbury, Christchurch, New Zealand. (Thesis: Ph.D: Engineering).

[296] The United Steel Companies Ltd. Research and Development Department, Swinden Labs, Moorgate, Rotherham, England, (1962) Report No. A3763/-/62.

[297] Hundy, B.B. (1954) *J.I.S.I.*, **178**, pp34-38.

Periodical Title Abbreviations

Acta Metall. - Acta Metallurgica
Eng. Fract. Mech. - Engineering Fracture Mechanics
Int. J. Fract. - International Journal of Fracture
Int. J. Fract. Mech. - International Journal of Fracture Mechanics
J. Applied Physics - Journal of Applied Physics
J. Aust. Inst. Met. - Journal of the Australian Institute of Metals.
J.I.M. - Journal of the Institute of Metals
J.I.S.I. - Journal of the Iron and Steel Institute
J. Mech. Phys. Solids - Journal of the Mechanics and Physics of Solids
J. Strain Analysis - Journal of Strain Analysis
J.T.E.V.A. - Journal of Testing and Evaluation
Mat. Sci. Eng. - Materials Science and Engineering
Mat. Sci. Tech. - Materials Science and Technology
Metall. Trans. A. - Metallurgical Transactions A
Met. Sci. - Metals Science
Met. Tech. - Metals Technology
Phil. Mag. - Philosophical Magazine of the Royal Society
Phil. Trans. Roy. Soc. - Philosophical Transactions of the Royal Society of London
Proc. A.S.T.M. - Proceedings of the American Society of Testing and Materials.
Proc. Phys. Soc. - Proceedings of the Physical Society, London
Proc. Roy. Soc. - Proceedings of the Royal Society, London
Trans. ASME, J. Applied Mech. - Transactions of ASME, Journal of Applied Mechanics.
Trans. ASME, J. Mech. Eng. Sci. - Journal of Mechanical Engineering and Science
Trans. ASME, J. Pres. Vessel Tech. - Journal of Pressure Vessel Technology
Trans. Am. Soc. Metals - Transactions of the American Society of Metals.
Trans. Inst. Eng. Ship. - Transactions of the Institute of Engineers and Shipbuilders (Scotland)
Trans. Inst. Naval Architects - Transactions of the Institute of Naval Architects.
Trans. Metall. Soc. AIME - Transactions of the Metallurgical Society of A.I.M.E.

APPENDIX A

Results of Charpy V-Notch Impact Tests.

Table A.1
Results of Charpy V-Notch Impact Tests for Steel L.
(Striking Energy: 298J)

Batch	Temperature (°C)	Specimen I.D.	Energy Absorbed (J)	Percentage of Shear Fracture (%)
A	-70	LA9	14	0
	-65	LA10	18	0
	-60	LA4	22	0
	-57.5	LA11	29	6
	-55	LA7	36	16
	-52.5	LA12	32	9
	-50	LA3	38	12
	-47.5	LA13	42	17
	-45	LA8	36	17
	-40	LA14	60	31
	-40	LA6	33	20
	-30	LA5	68	39
	-20	LA1	138	75
	+20	LA2	140	100
B	-50	LB4	6	0
	-30	LB10	10	0
	-20	LB1	22	11
	-15	LB7	20	11
	-12.5	LB11	29	17
	-10	LB3	32	16
	-5	LB12	42	26
	0	LB6	36	31
	0	LB13	40	26
	+5	LB9	62	36
	+10	LB5	74	48
	+20	LB2	74	55
	+45	LB8	106	67

Table A.1 continued.
Results of Charpy V-Notch Impact Tests for Steel L.
(Striking Energy: 298J)

Batch	Temperature (°C)	Specimen I.D.	Energy Absorbed (J)	Percentage of Shear Fracture (%)
C	-20	LC1	12	0
	-10	LC3	14	6
	-5	LC13	16	6
	0	LC5	18	11
	+2.5	LC14	20	11
	+5	LC8	16	12
	+5	LC9	40	17
	+5	LC12	34	19
	+7.5	LC10	42	20
	+10	LC4	38	26
	+15	LC11	48	21
	+20	LC2	54	35
	+30	LC7	48	34
	+40	LC6	68	45
D	-20	LD1	9	6
	-10	LD4	12	0
	-5	LD12	10	3
	0	LD6	12	6
	+5	LD10	14	6
	+10	LD5	20	6
	+12.5	LD11	20	12
	+15	LD9	38	21
	+15	LD14	25	21
	+20	LD2	32	20
	+26	LD13	36	31
	+30	LD8	46	35
	+40	LD7	62	51
	+50	LD3	62	61

Table A.2
Results of Charpy V-Notch Impact Tests for Steel H.
(Striking Energy: 298J)

Batch	Temperature (°C)	Specimen I.D.	Energy Absorbed (J)	Percentage of Shear Fracture (%)
A	-45	HA4	16	0
	-40	HA7	15	0
	-35	HA6	10	5
	-35	HA9	22	11
	-30	HA5	23	17
	-27.5	HA10	30	11
	-25	HA8	20	17
	-20	HA3	58	29
	0	HA2	92	50
	+18	HA1	110	70
B	-20	HB3	8	5
	0	HB1	16	20
	+10	HB4	22	25
	+15	HB9	23	25
	+20	HB2	28	25
	+25	HB5	28	30
	+30	HB6	34	30
	+35	HB10	40	43
	+40	HB7	60	43
	+55	HB8	70	55

Table A.2 continued.
Results of Charpy V-Notch Impact Tests for Steel H.
(Striking Energy: 298J)

Batch	Temperature (°C)	Specimen I.D.	Energy Absorbed (J)	Percentage of Shear Fracture (%)
C	0	HC2	8	0
	+10	HC3	10	6
	+20	HC1	22	15
	+25	HC4	16	10
	+30	HC5	27	20
	+35	HC6	22	25
	+35	HC9	22	20
	+40	HC7	35	25
	+45	HC10	28	30
	+50	HC8	48	39
D	0	HD15	10	5
	+20	HD16	12	10
	+25	HD13	22	20
	+25	HD7	17	15
	+30	HD12	21	20
	+35	HD11	26	20
	+37.5	HD2	25	25
	+40	HD10	34	30
	+45	HD6	32	25
	+50	HD9	48	34
	+55	HD5	48	34
	+60	HD4	52	43
	+70	HD8	70	47
	+80	HD3	100	62
	+94	HD1	118	77

APPENDIX B

Statistical Analysis of Lower Yield Strength as a Function of Temperature and Grain Size

---

B.1 Statistical Abbreviations

The statistical symbols and equations used are those given by Volk [267]. The mathematical tables used to assess the significance of equations and constants by either the variance ratio F or by the t-test are given in Reference 287.

Definition	Symbol
The independent variable	x
The dependent variable	y
The mean of independent variables	$\bar{x}$
The mean of dependent variables	$\bar{y}$
The slope of the regression line	b
The constant intercept with y = 0	a
The linear correlation coefficient	r
The multiple-linear regression coefficient	R
The number of data sets	N
The number of independent variables	k
The number of degrees of freedom	D.F.
The variance ratio	F-value
The t-test value	t
The sum of squares of deviation of y from $\bar{y}$	$\Sigma' y^2$
The sum of squares of deviation of x from $\bar{x}$	$\Sigma' x^2$
The sum of squares of deviation of y from the correlation line $\hat{y}$	$\Sigma' \hat{y}^2$
The sum of squares of deviation removed by the correlation	$\Sigma' c^2$
The variance of the slope	$s^2(b)$
The variance removed by the correlation	$s^2(c)$
The variance of estimate	$s^2(\hat{y})$
The standard error of the slope	s(b)
The standard error of estimate	$s(\hat{y})$
The percentage of error explained by the correlation	r^2, R^2

Symbol	Equation
(a) For Linear Regression	
D.F.	$N-2$
r^2	$r^2 = \Sigma'c^2/\Sigma'y^2$
$\Sigma'c^2$	$\Sigma'c^2 = b^2\Sigma'x^2$
b	$b = \Sigma'xy/\Sigma'x^2$
$\Sigma'x^2$	$\Sigma'x^2 = \Sigma x^2 - (\Sigma x)^2/N$
$\Sigma'y^2$	$\Sigma'y^2 = \Sigma'y^2 - (\Sigma y)^2/N$
$\Sigma'xy$	$\Sigma'xy = \Sigma xy - \Sigma x\Sigma y/N$
$\Sigma'\hat{y}^2$	$\Sigma'\hat{y}^2 = \Sigma'y^2 - b\Sigma'xy$
F	$F = s^2(c)/s^2(\hat{y})$
r	$r = \Sigma'xy/(\Sigma'x^2\Sigma'y^2)^{1/2}$
$s^2(\hat{y})$	$s^2(\hat{y}) = \dfrac{\Sigma'y^2 - b\Sigma'xy}{N-2}$
$s^2(b)$	$s^2(b) = s^2(\hat{y})/\Sigma'x^2$
$s^2(\bar{y})$	$s^2(\bar{y}) = s^2(\hat{y})/N$
(b) For Multiple-Linear Regression	
D.F.	$D.F. = N - k - 1$
R^2	$R^2 = \Sigma'c^2/\Sigma'y^2$
$\Sigma'c^2$	$\Sigma'c^2 = b_1\Sigma'x_1y + b_2\Sigma'x_2y + \ldots$
$\Sigma'\hat{y}^2$	$\Sigma'\hat{y}^2 = \Sigma'y^2 - \Sigma'c^2$
$s^2(\hat{y})$	$s^2(\hat{y}) = \Sigma'\hat{y}^2/(N - k - 1)$
F	$F = \dfrac{R^2(N - k - 1)}{(1 - R^2)k}$
95% confidence limits of b	$\pm$ t.s(b)
95% confidence limits of $\bar{y}$	$\pm$ t.s($\hat{y}$)/N
where $t = t_{0.05,\ N - k - 1}$	

B.2 *The Dependence of Yield Stress on Temperature and Grain Size.*

The results of the multiple linear regression on the yield stress data are given in Tables B.1, B.2 and B.3 for Steels L, H (combined) and H (individual) respectively. These results are based on the equations given in Table 5.4. The predicted results of these equations compared to experimental results are shown in Figures B.1 - B.8 for Steel L, Figures B.9 - B.16 for Steel H (combined) and in Figures B.17 - B.24 for Steel H (individual). The method and results of these regression analyses are discussed in Section 5.4.

Table B.1
Lower Yield Strength versus temperature and $d^{-1/2}$.
Results of MLR analysis for Steel L.

Model	x^3	x^4	Fisher	Chen *et al.*	Power	Log.	Fleisch-er	Mott
Eq'n	5.54g	5.54g	5.54d	5.57b	5.56c	5.54f	5.54b	5.54c
Figure	B.1	B.2	B.3	B.4	B.5	B.6	B.7	B.8
D.F.	48	47	50	49	50	50	50	50
R	0.9988	0.9989	0.9976	0.9979	0.9892	0.9706	0.9567	0.9233
$s(\hat{y})$	7.0946	9.4648	9.8395	9.4648	0.0518	34.4943	1.0157	55.02
F- value	5083	4360	5273	3801	1137	406	270	144
Sig.	>99.9%	>99.9%	>99.9%	>99.9%	>99.9%	>99.9%	>99.9%	>99.9%
Coefficients								
A_1	1124.3	1199.4	-32.792	-48.584	11.28	1814.6	30.467	708
A_2	-9.5719	-11.532	44858	47778	-1.1474	-301.27	-1.088	-13.753
A_3	0.0314	0.0482	-	-458.57	-	-	-	-
$A_4(10^{-5})$	-3.55	-9.33	-	-	-	-	-	-
$A_5(10^{-8})$	-	6.97	-	-	-	-	-	-
k_y	20.85	20.90	21.00	23.46	22.73	20.98	0.579	20.81
±95% C.L. of Coefficients								
A_2	0.512	1.969	917	2761	0.0538	22.25	0.100	1.711
A_3	0.0027	0.016	-	411	-	-	-	-
$A_4(10^{-5})$	0.441	5.639	-	-	-	-	-	-
$A_5(10^{-8})$	-	6.778	-	-	-	-	-	-
k_y	0.89	0.86	1.23	2.50	2.20	4.31	0.127	6.87
Significance of coefficients.								
A_1	>99.9%	>99.9%	>99.9%	>99.9%	>99.9%	>99.9%	>99.9%	>99.9%
A_2	>99.9%	>99.9%	>99.9%	>99.9%	>99.9%	>99.9%	>99.9%	>99.9%
A_3	>99.9%	>99.9%	-	95%	-	-	-	-
$A_4(10^{-5})$	>99.9%	99.8%	-	-	-	-	-	-
$A_5(10^{-8})$	>99.9%	90%	-	-	-	-	-	-
k_y	>99.9%	>99.9%	>99.9%	>99.9%	>99.9%	>99.9%	>99.9%	>99.9%
$\bar{y}$	349.19	349.19	349.19	349.19	5.792	349.19	18.38	349.19
95% C.L. of $\bar{y}$	±1.96	±1.90	±2.72	±2.62	±0.014	±9.53	±0.28	±15.20

Table B.2
Lower Yield Strength versus temperature and $d^{-1/2}$.
Results of MLR analysis for Steel H-combined.

Model	x^3	x^4	Fisher	Chen *et al.*	Power	Log.	Fleisch-er	Mott
Eq'n	5.54g	5.54g	5.54d	5.57b	5.56c	5.54f	5.54b	5.54c
Figure	B.9	B.10	B.11	B.12	B.13	B.14	B.15	B.16
D.F.	60	59	62	61	62	62	62	62
R	0.9991	0.9991	0.9961	0.9961	0.9806	0.9684	0.9562	0.9192
$s(\hat{y})$	6.4672	6.4134	13.133	13.241	0.07611	37.326	1.0936	58.983
F- value	8297	6750	4000	2623	774	468	331	169
Sig.	>99.9%	>99.9%	>99.9%	>99.9%	>99.9%	>99.9%	>99.9%	>99.9%
Coefficients								
A_1	1149.0	1201	-64.08	-64.07	11.756	1910	31.608	727.38
A_2	-9.714	-11.063	47994	47994	-1.244	-321.67	-1.199	-14.65
A_3	0.03048	0.0420	-	0.0996	-	-	-	-
$A_4(10^{-5})$	-3.25	-7.22	-	-	-	-	-	-
$A_5(10^{-8})$	-	4.78	-	-	-	-	-	-
k_y	23.16	23.16	23.28	23.28	22.76	22.83	0.644	22.62
±95% C.L. of Coefficients								
A_2	0.42	2.01	1107	3947	0.0843	21.72	0.0974	1.65
A_3	0.0022	0.0169	-	739	-	-	-	-
$A_4(10^{-5})$	0.36	5.80	-	-	-	-	-	-
$A_5(10^{-8})$	-	7.00	-	-	-	-	-	-
k_y	1.03	1.03	2.10	4.52	3.99	5.96	0.175	9.42
Significance of coefficients.								
A_1	>99.9%	>99.9%	>99.9%	>99.9%	>99.9%	>99.9%	>99.9%	>99.9%
A_2	>99.9%	>99.9%	>99.9%	>99.9%	>99.9%	>99.9%	>99.9%	>99.9%
A_3	>99.9%	>99.9%	-	<80%	-	-	-	-
$A_4(10^{-5})$	>99.9%	98%	-	-	-	-	-	-
$A_5(10^{-8})$	>99.9%	80%	-	-	-	-	-	-
k_y	>99.9%	>99.9%	>99.9%	>99.9%	>99.9%	>99.9%	>99.9%	>99.9%
$\bar{y}$	317	317	317	317	292	317	304	317
95% C.L. of $\bar{y}$	±1.60	±1.59	±3.26	±3.29	+5.58 -5.46	±9.26	+9.52 -9.37	±14.63

Table B.3
Lower Yield Strength versus temperature and $d^{-1/2}$.
Results of MLR analysis for Steel H-individual.

Model	x^3	x^4	Fisher	Chen *et al.*	Power	Log.	Fleisch-er	Mott
Eq'n	5.54g	5.54g	5.54d	5.57b	5.56c	5.54f	5.54b	5.54c
Figure	B.17	B.18	B.19	B.20	B.21	B.22	B.23	B.24
D.F.	60	59	62	61	62	62	62	62
R	0.9984	0.9984	0.9954	0.9954	0.9762	0.9680	0.9558	0.9191
$s(\hat{y})$	8.4956	8.5487	14.3319	14.4482	0.0840	37.5614	1.0986	59.017
F- value	4802	3794	3354	2200	629	462	328	169
Sig.	>99.9%	>99.9%	>99.9%	>99.9%	>99.9%	>99.9%	>99.9%	>99.9%
Coefficients								
A_1	1145	1166	-62.62	-62.53	11.637	1907.3	31.5749	726.07
A_2	-9.634	-10.200	47888	47871	-1.215	-321.0	-1.1964	-14.622
A_3	3.010	3.493	-	3.433	-	-	-	-
$A_4(10^{-5})$	-3.19	-4.86	-	-	-	-	-	-
$A_5(10^{-8})$	-	2.01	-	-	-	-	-	-
k_y	22.89	22.88	22.98	22.96	21.57	22.66	0.640	22.56
±95% C.L. of Coefficients								
A_2	0.553	2.379	1208	4387	0.092	21.86	0.098	1.65
A_3	0.003	0.020	-	813	-	-	-	-
$A_4(10^{-5})$	0.47	6.84	-	-	-	-	-	-
$A_5(10^{-8})$	-	8.23	-	-	-	-	-	-
k_y	1.36	1.37	2.29	4.95	4.40	5.99	0.18	9.42
Significance of coefficients.								
A_1	>99.9%	>99.9%	>99.9%	>99.9%	>99.9%	>99.9%	>99.9%	>99.9%
A_2	>99.9%	>99.9%	>99.9%	>99.9%	>99.9%	>99.9%	>99.9%	>99.9%
A_3	>99.9%	99.9%	-	0	-	-	-	-
$A_4(10^{-5})$	>99.9%	80%	-	-	-	-	-	-
$A_5(10^{-8})$	>99.9%	<80%	-	-	-	-	-	-
k_y	>99.9%	>99.9%	>99.9%	>99.9%	>99.9%	>99.9%	>99.9%	>99.9%
$\bar{y}$	317	317	317	317	292	317	304	317
95% C.L. of $\bar{y}$	±1.60	±1.59	±3.26	±3.29	+5.58 -5.46	±9.26	+9.52 -9.37	±14.63

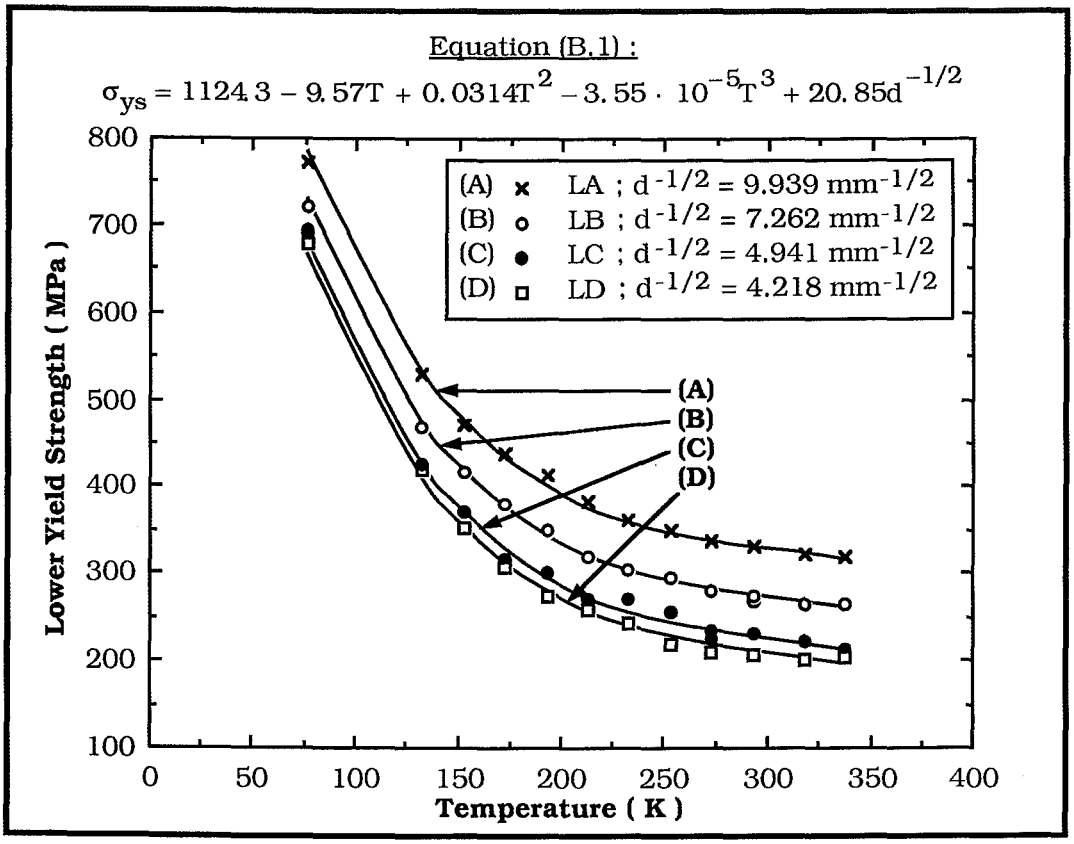

Figure B.1 : Lower yield strength (MPa) as a function of temperature (K) for Steel L; showing predicted curves for equation (B.1).

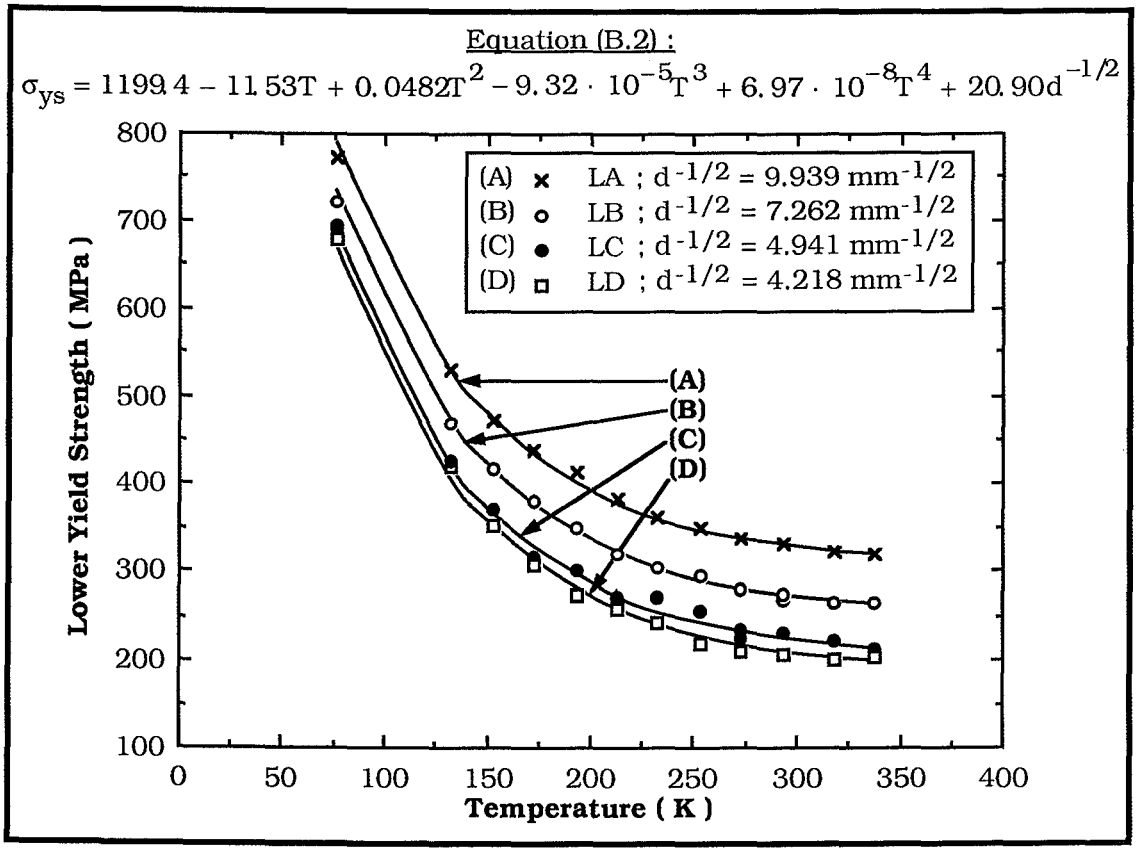

Figure B.2 : Lower yield strength (MPa) as a function of temperature (K) for Steel L; showing predicted curves for equation (B.2).

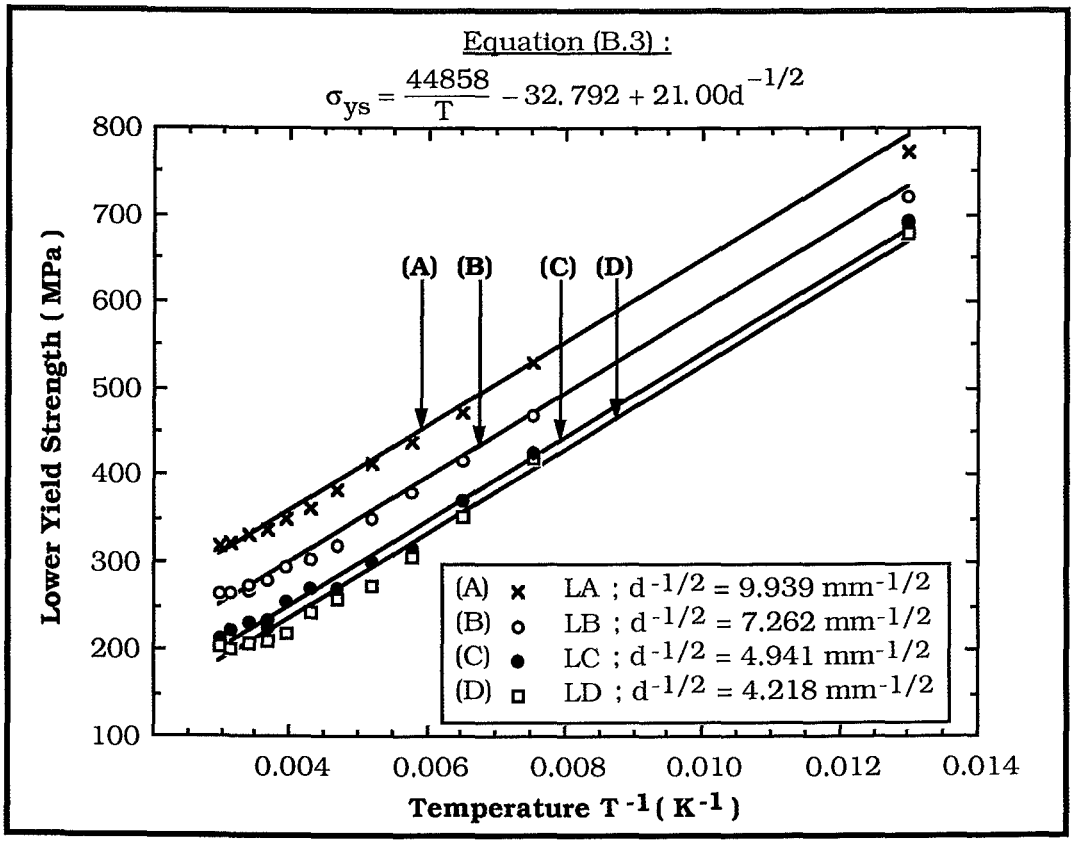

Figure B.3 : Lower yield strength (MPa) as a function of inverse temperature (K^{-1}) for Steel L; showing predicted curves for equation (B.3).

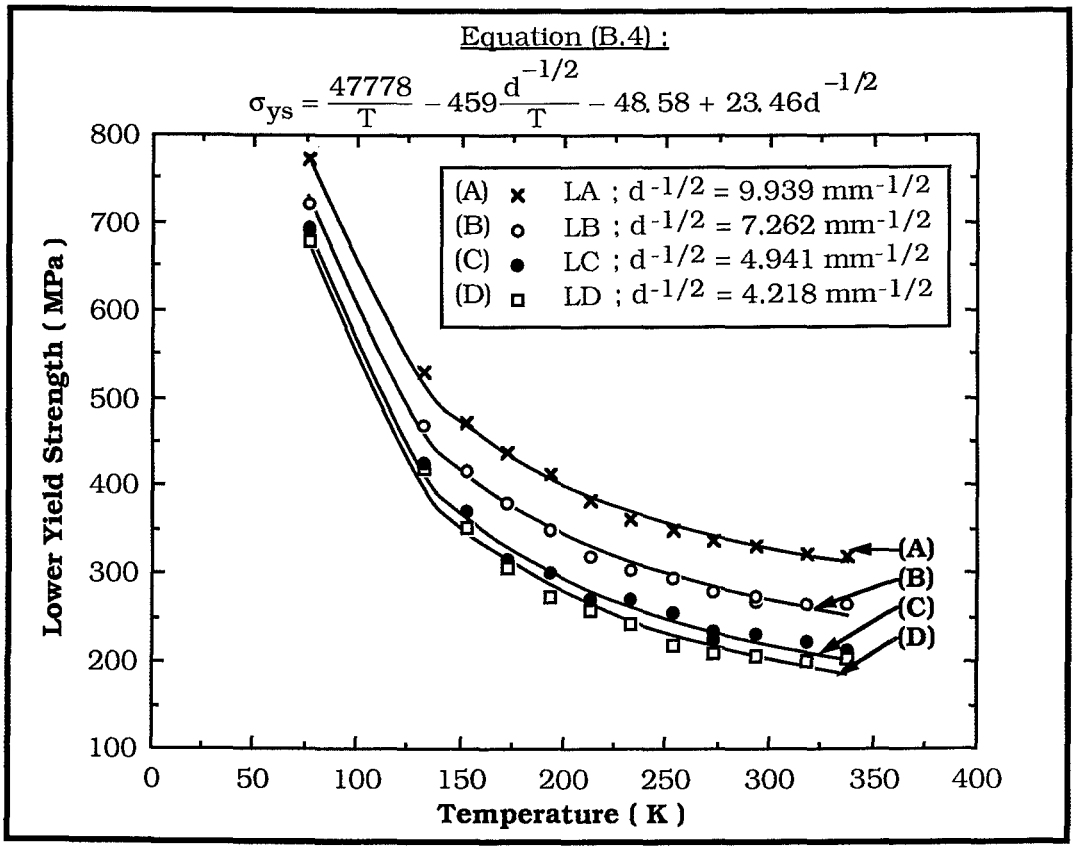

Figure B.4 : Lower yield strength (MPa) as a function of temperature (K) for Steel L; showing predicted curves for equation (B.4).

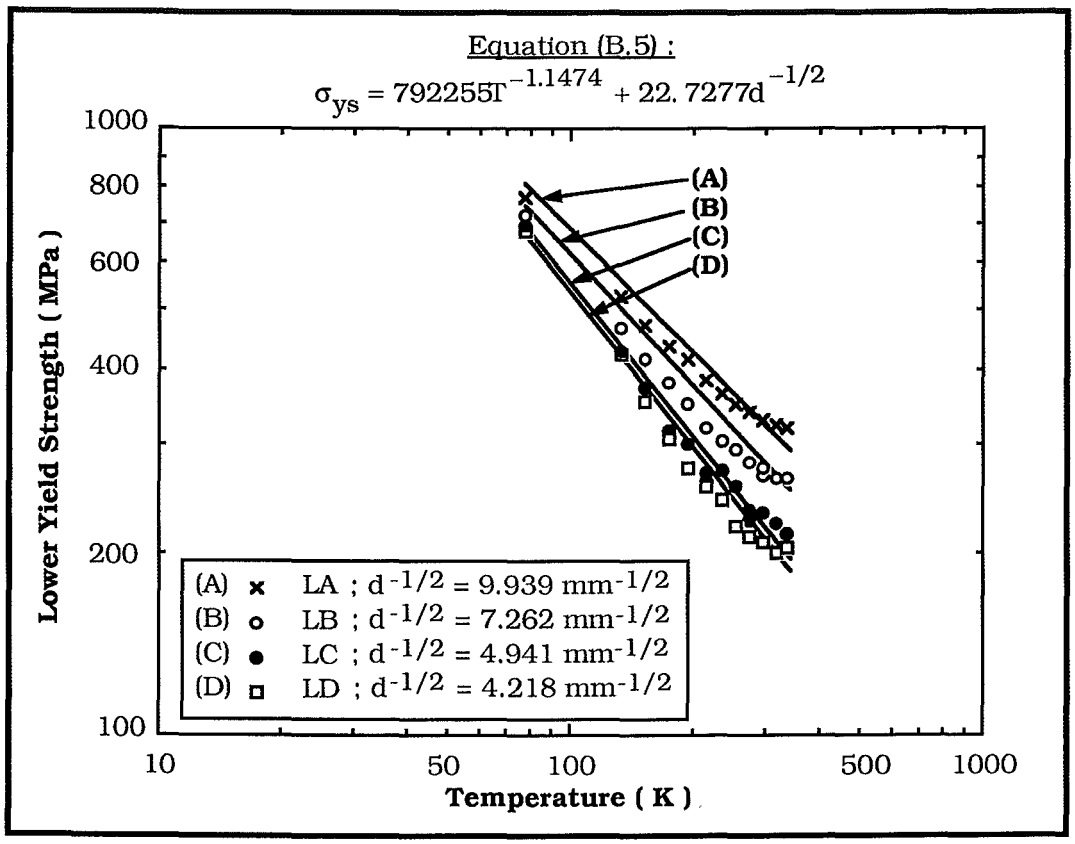

Figure B.5 : Lower yield strength (MPa) as a function of temperature (K) for Steel L on log-log axes; showing predicted curve for equation (B.5).

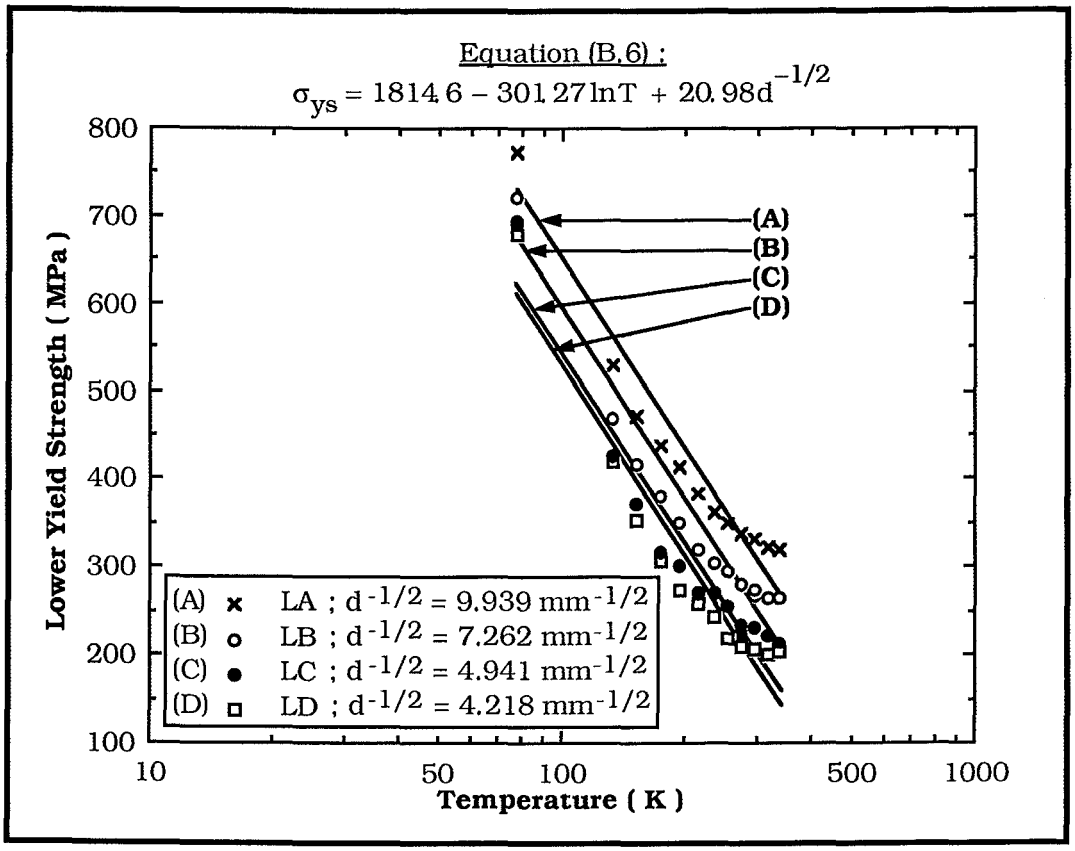

Figure B.6 : Lower yield strength (MPa) as a function of temperature (K) for Steel L on linear-log axes; showing predicted curves for equation (B.6).

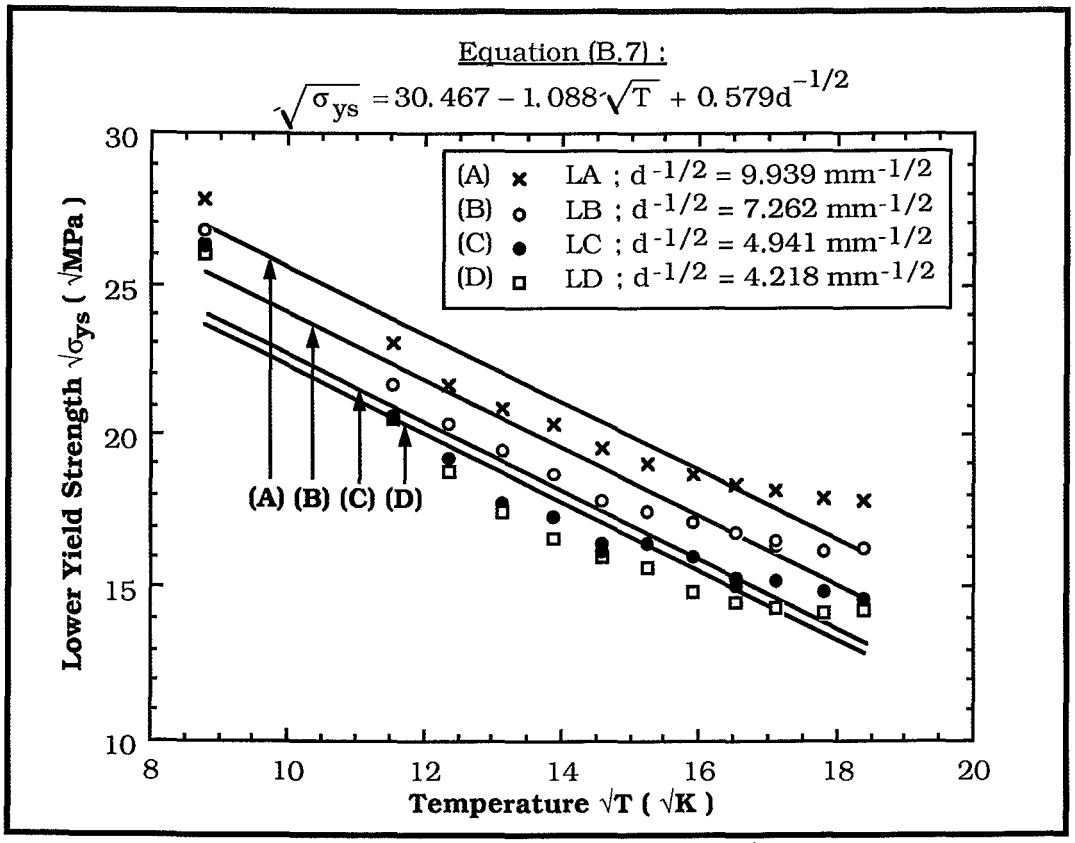

Figure B.7 : The square root of yield strength ($\sqrt{MPa}$) as a function of the square root of temperature ($\sqrt{K}$) for Steel L; showing predicted results for equation (B.7).

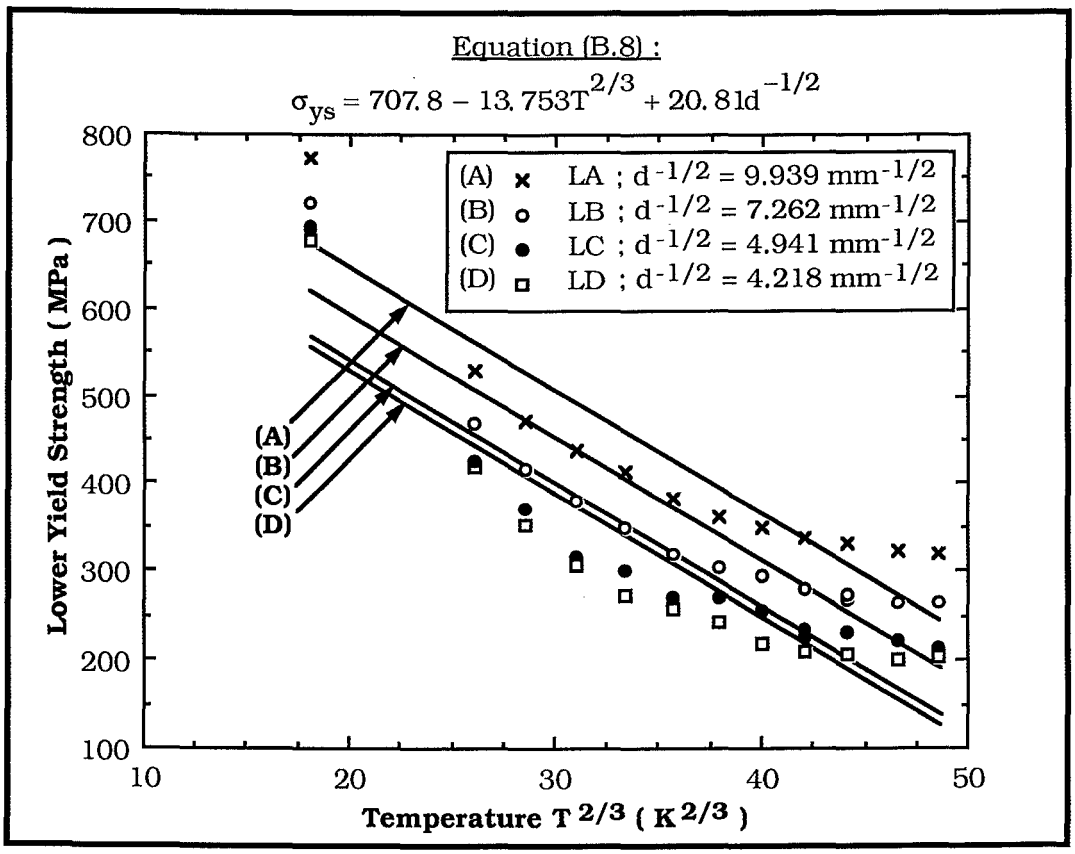

Figure B.8 : Lower yield strength (MPa) as a function of the 2/3 root of temperature ($K^{2/3}$) for Steel L; showing the predicted results using equation (B.8).

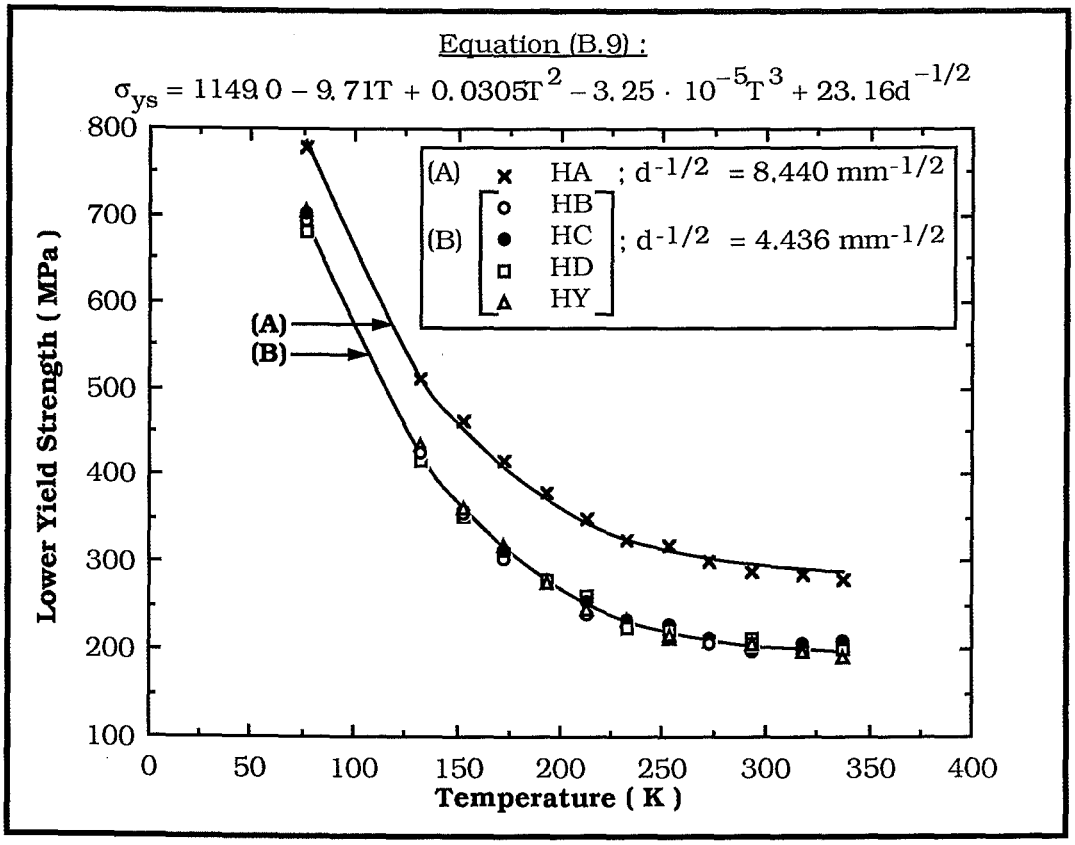

Figure B.9 : Lower yield strength (MPa) as a function of temperature (K) for Steel H; showing the predicted results for equation (B.9).

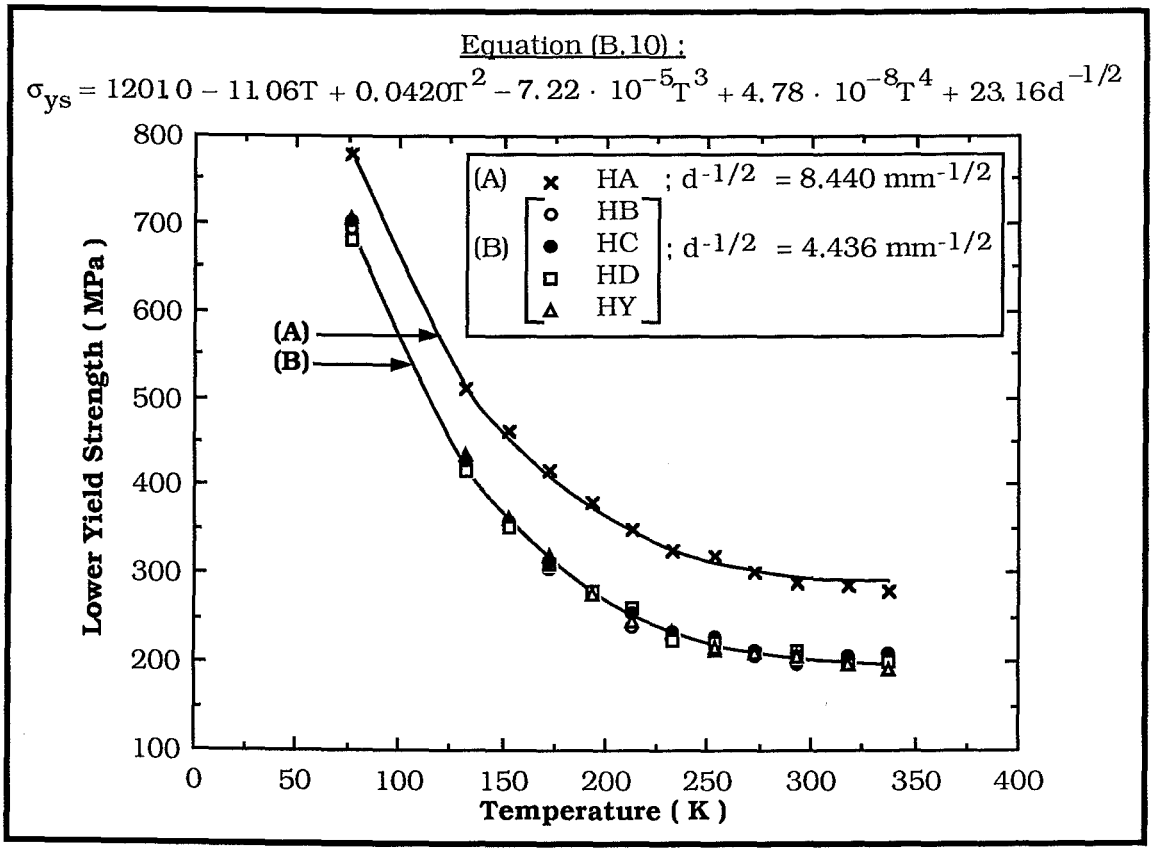

Figure B.10 : Lower yield strength (MPa) as a function of temperature (K) for Steel H; showing the predicted results for equation (B.10).

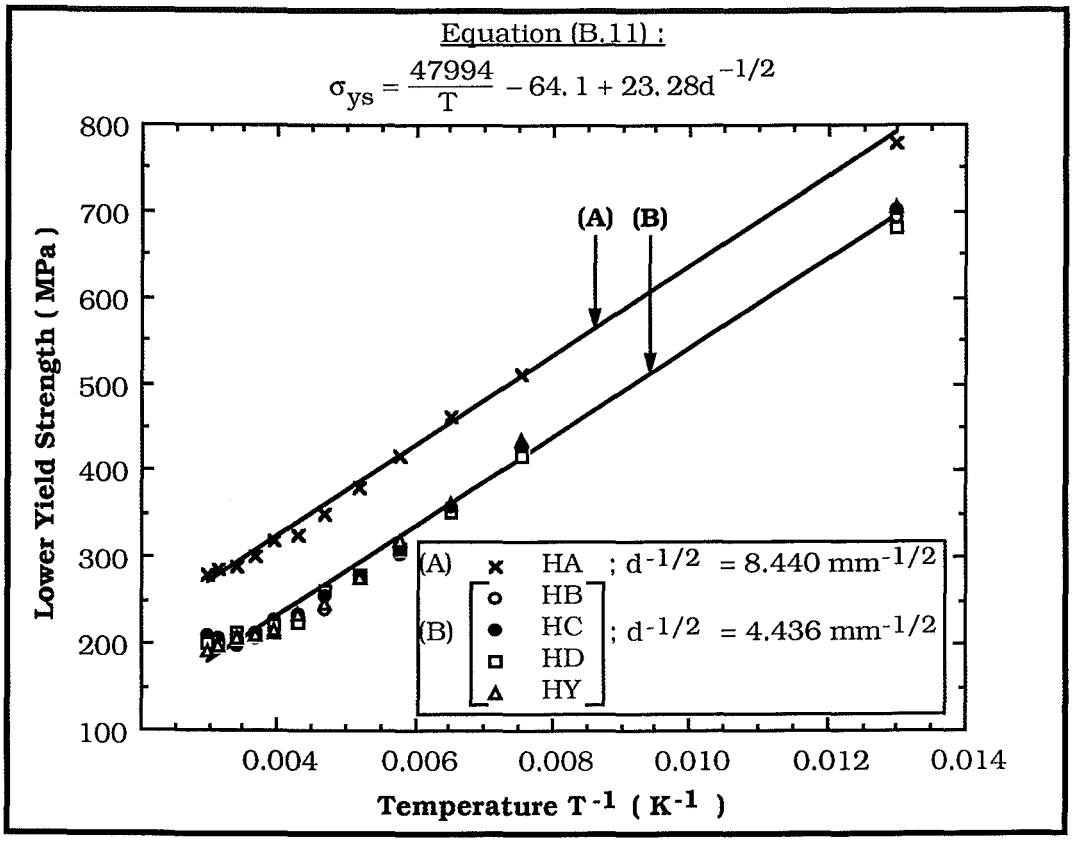

Figure B.11 : Lower yield strength (MPa) as a function of inverse temperature (K^{-1}) for Steel H; showing predicted results for equation (B.11).

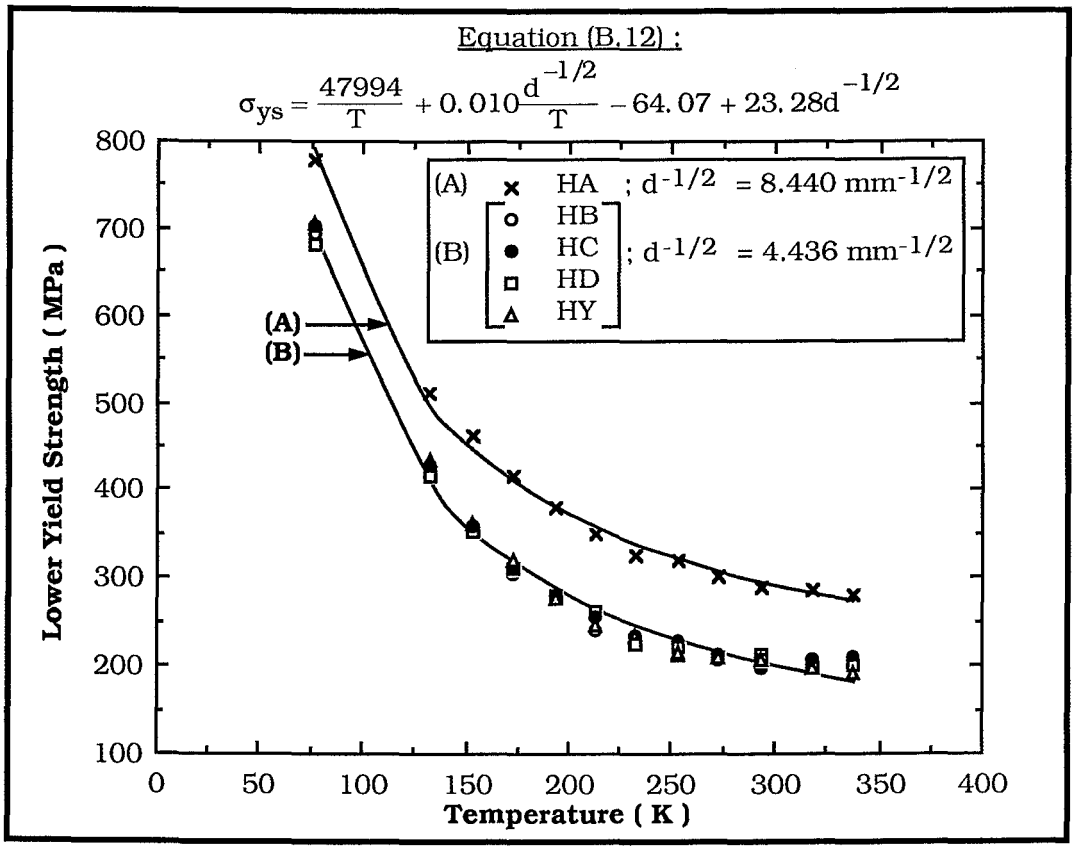

Figure B.12 : Lower yield strength (MPa) as a function of temperature (K) for Steel H; showing predicted results for equation (B.12).

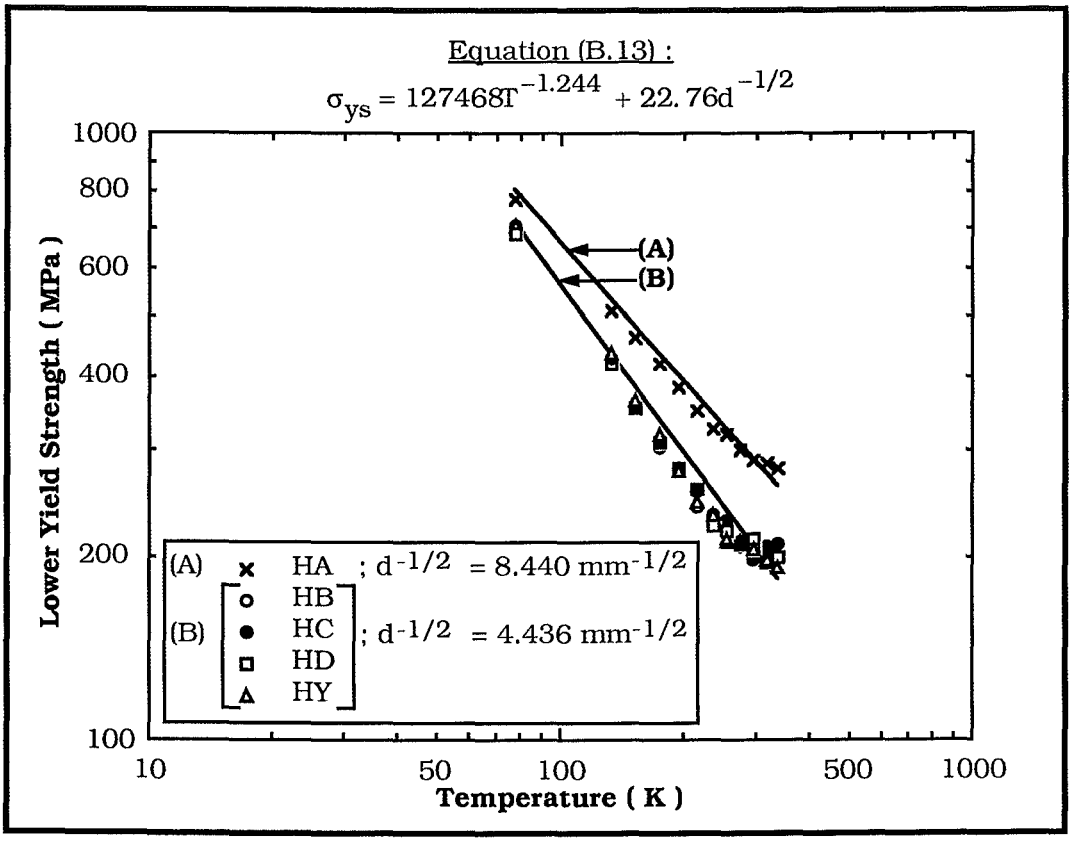

Figure B.13 : Lower yield strength (MPa) as a function of temperature (K) for Steel H on log-log axes; showing predicted results for equation (B.13).

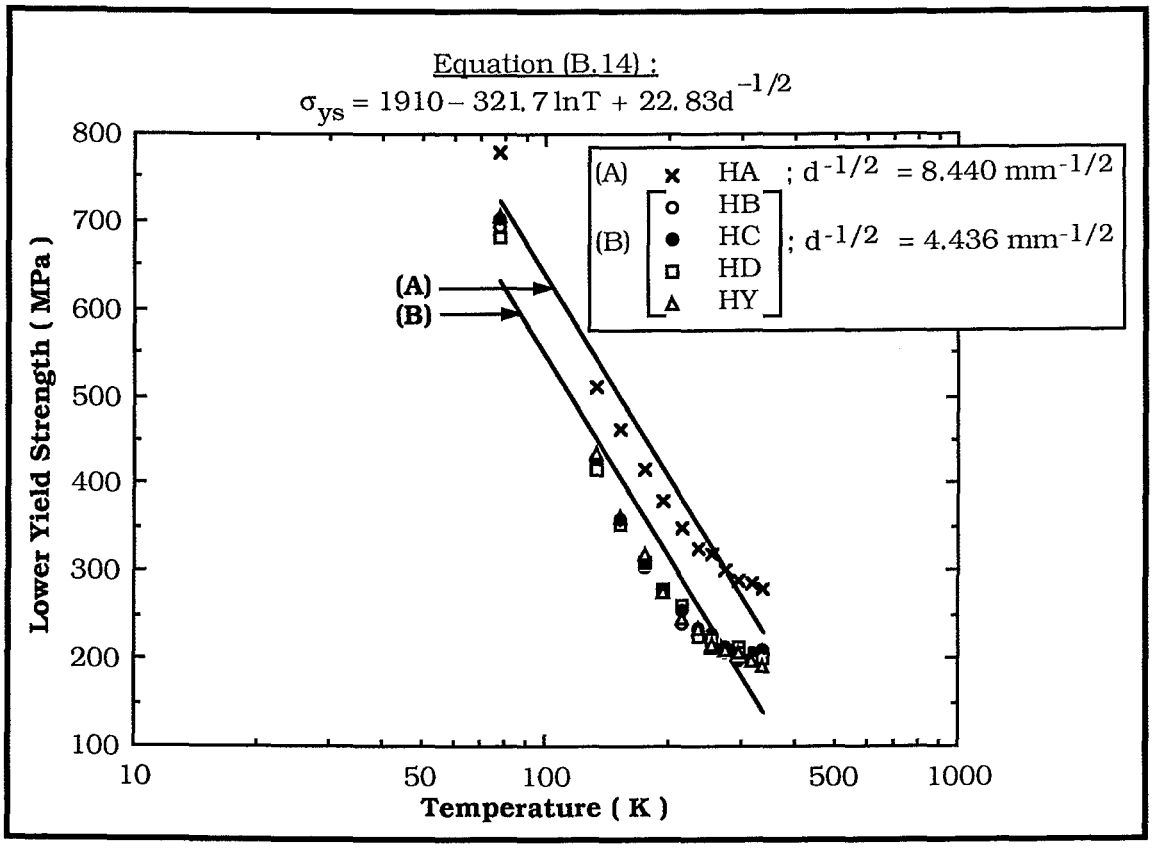

Figure B.14 : Lower yield strength (MPa) as a function of temperature (K) for Steel H on linear-log axes; showing predicted results for equation (B.14).

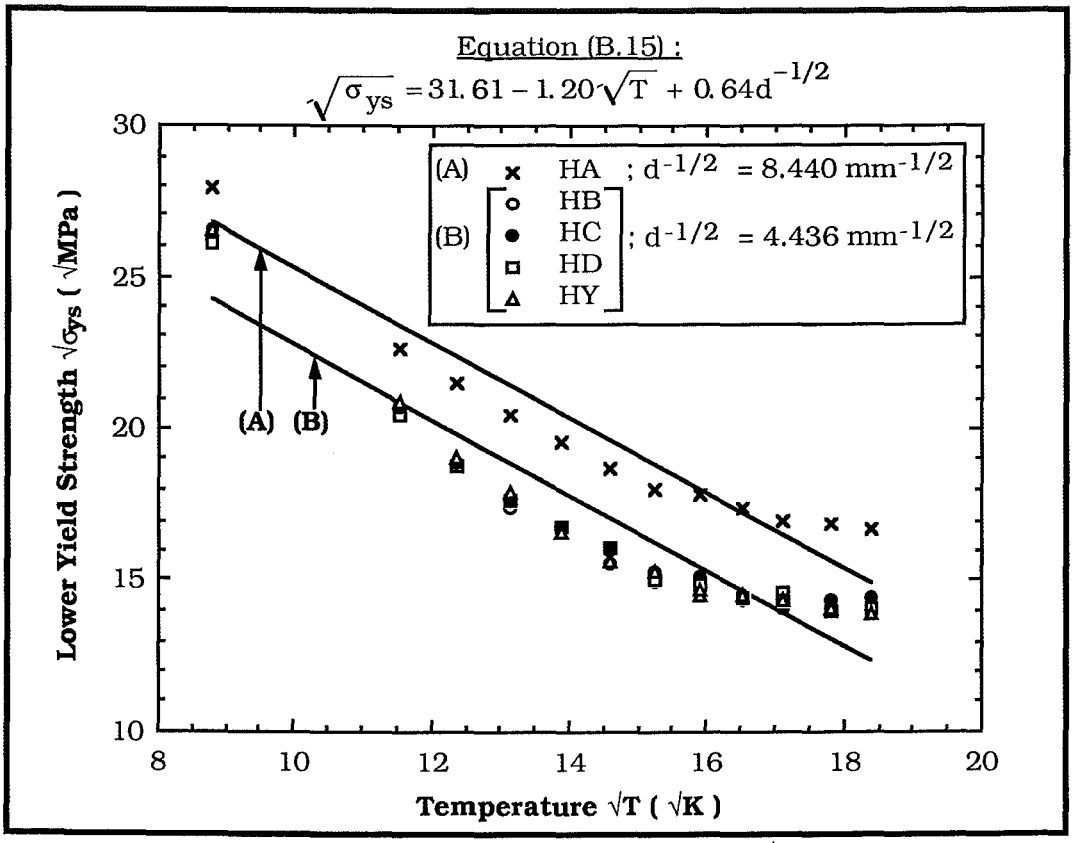

Figure B.15 : The square root of yield strength ($\sqrt{MPa}$) as a function of the square root of temperature ($\sqrt{K}$) for Steel H; showing predicted results for equation (B.15).

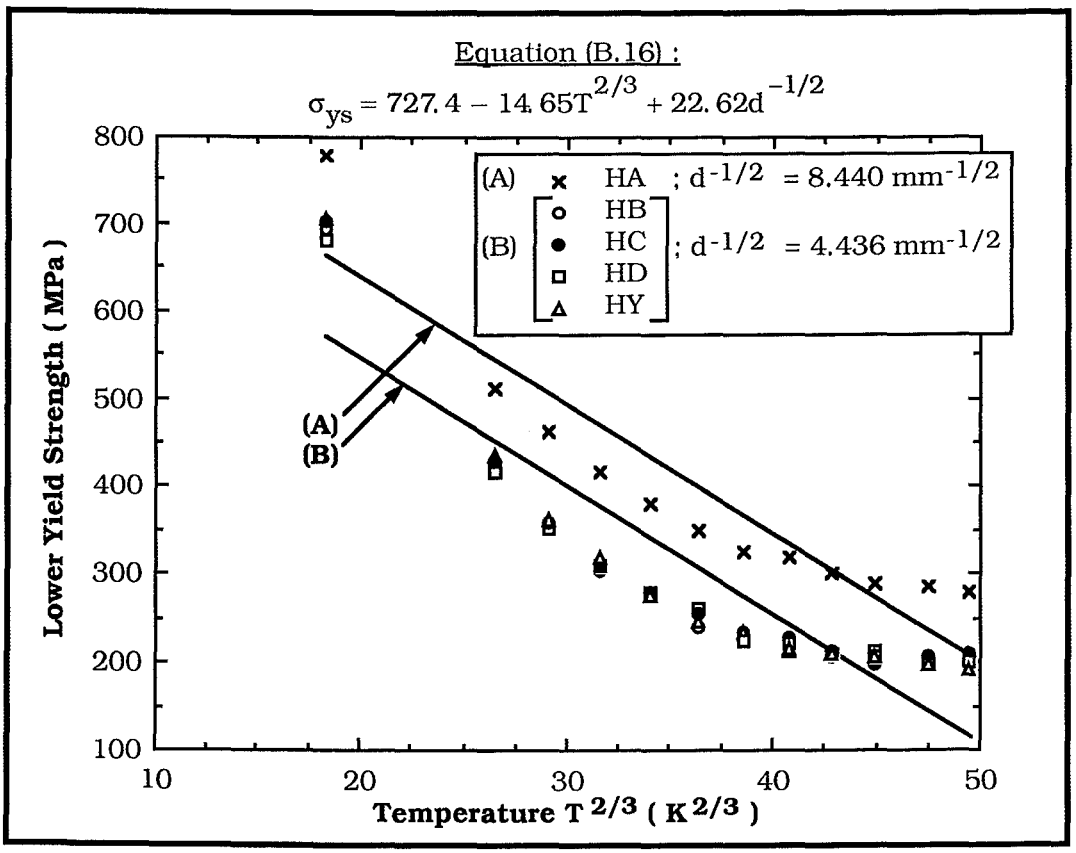

Figure B.16 : Lower yield strength (MPa) as a function of the 2/3 root of temperature ($K^{2/3}$) for Steel H; showing predicted results for equation (B.16).

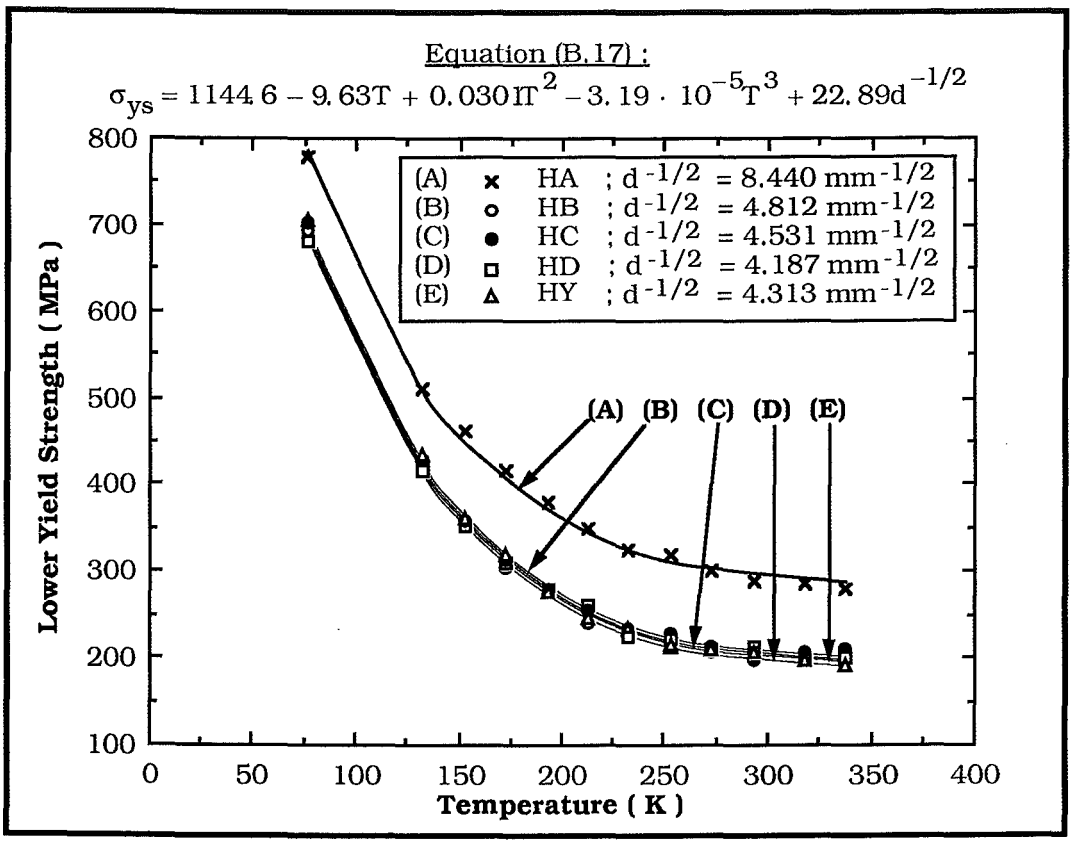

Figure B.17 : Lower yield strength (MPa) as a function of temperature (K) for Steel H; showing predicted results for equation (B.17).

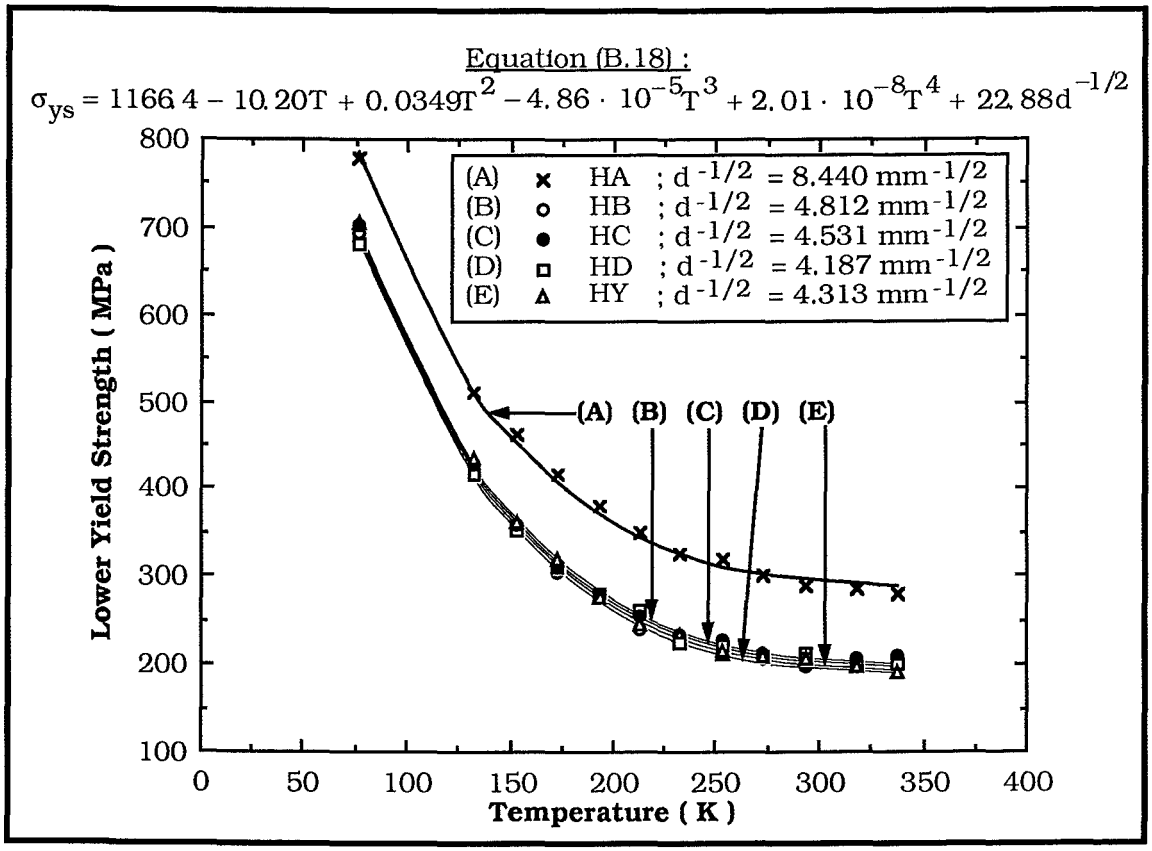

Figure B.18 : Lower yield strength (MPa) as a function of temperature (K) for Steel H; showing the predicted results for equation (B.18).

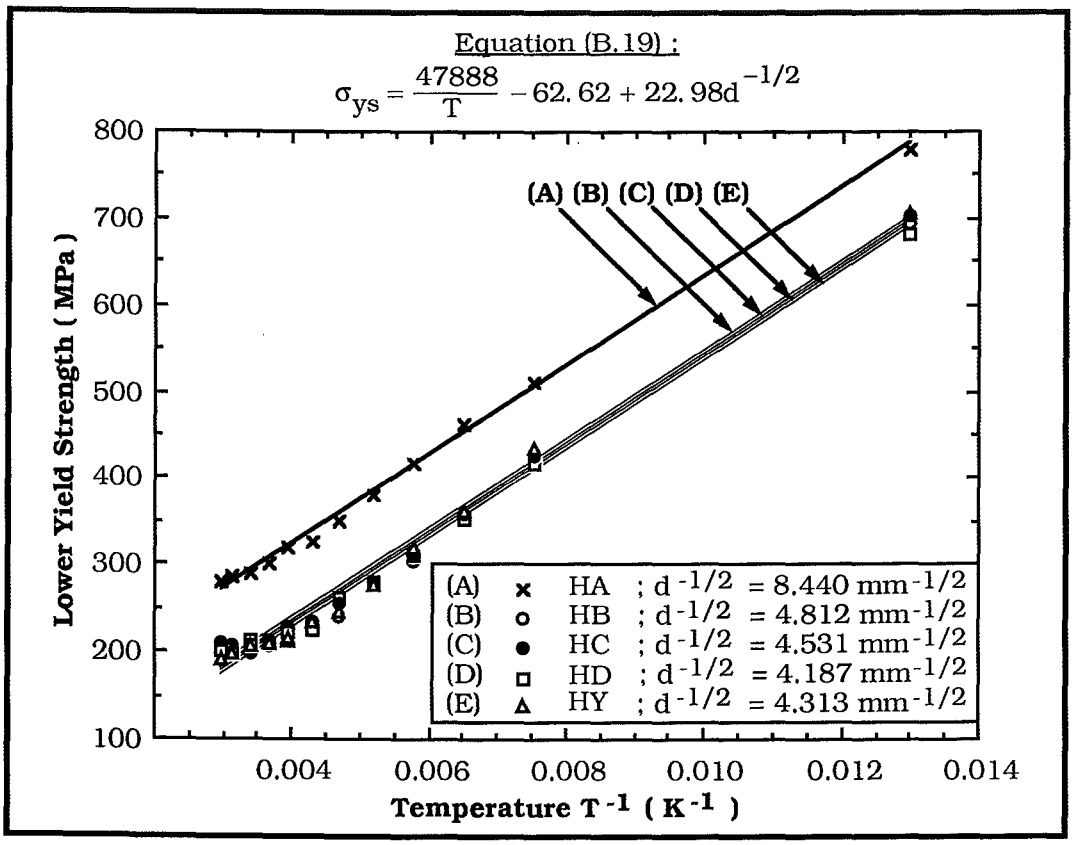

Figure B.19 : Lower yield strength (MPa) as a function of inverse temperature (K^{-1}) for Steel H; showing predicted results for equation (B.19).

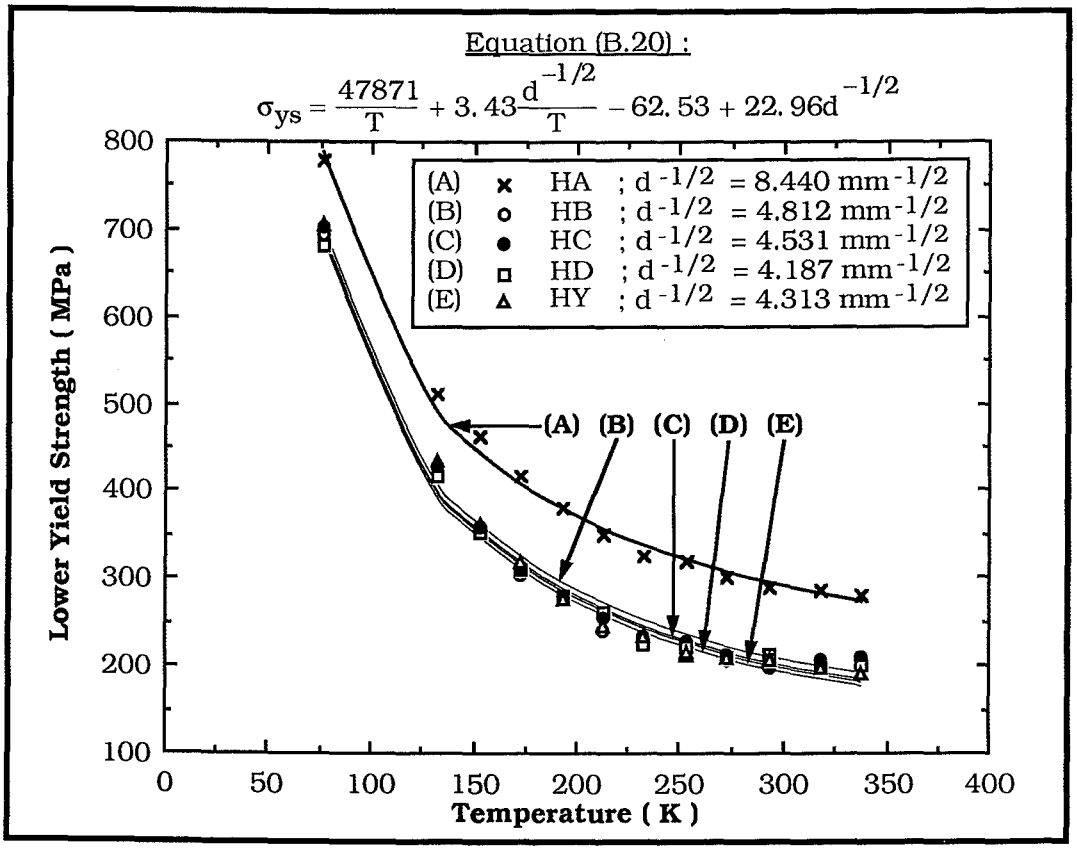

Figure B.20 : Lower yield strength (MPa) as a function of temperature (K) for Steel H; showing predicted results for equation (B.20).

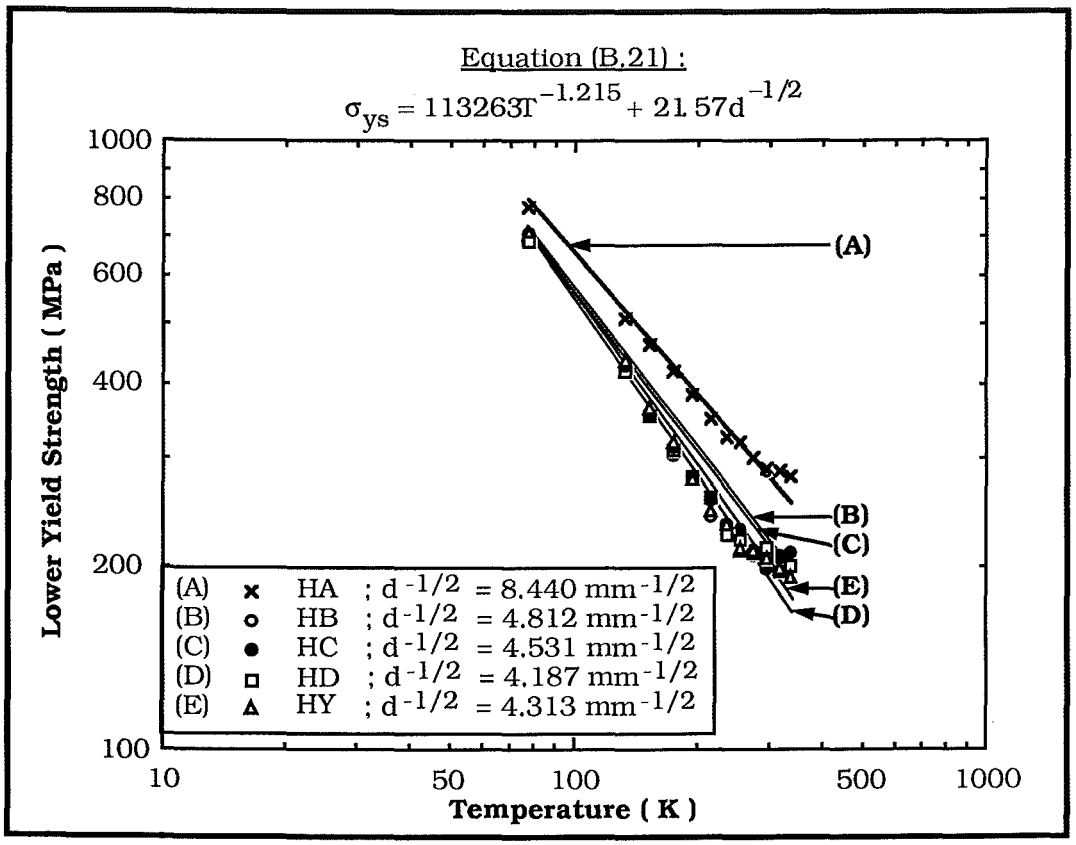

Figure B.21 : Lower yield strength (MPa) as a function of temperature (K) for Steel H on log-log axes; showing predicted results for equation (B.21).

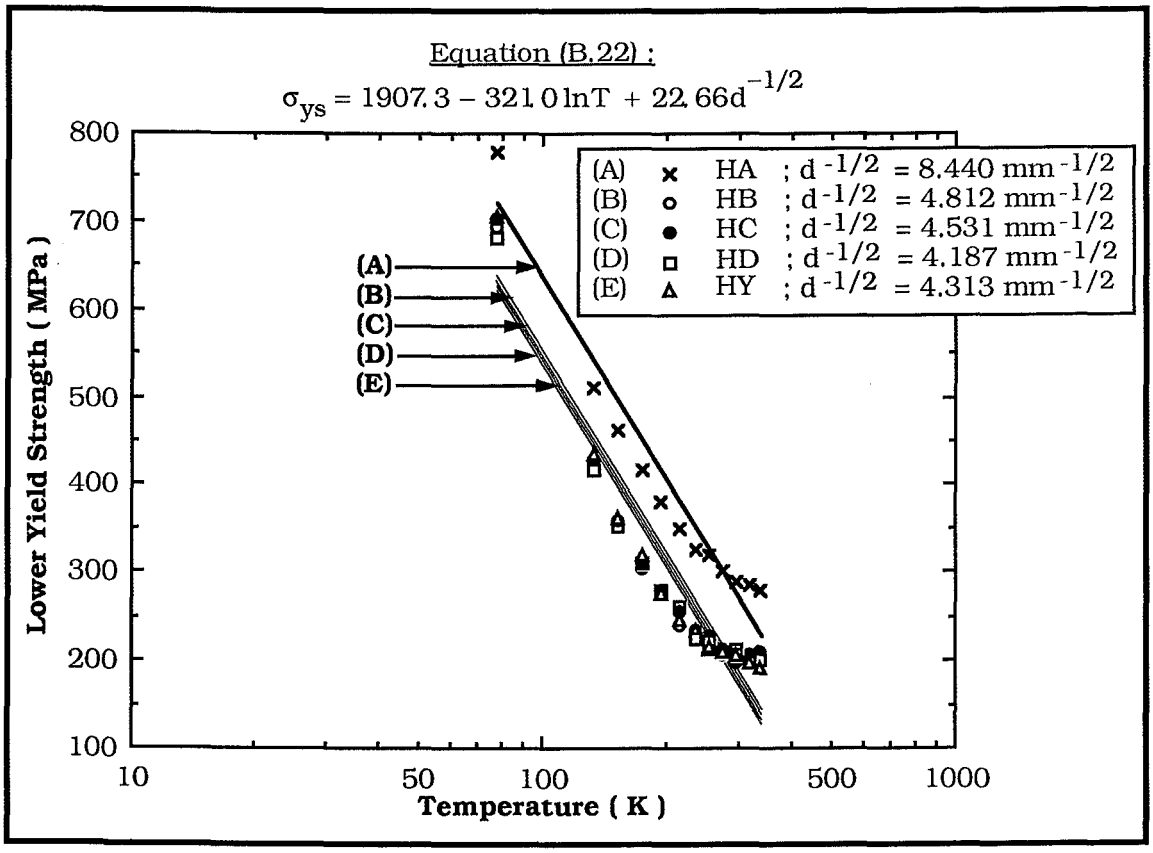

Figure B.22 : Lower yield strength (MPa) as a function of temperature (K) for Steel H on linear-log axes; showing predicted results for equation (B.22).

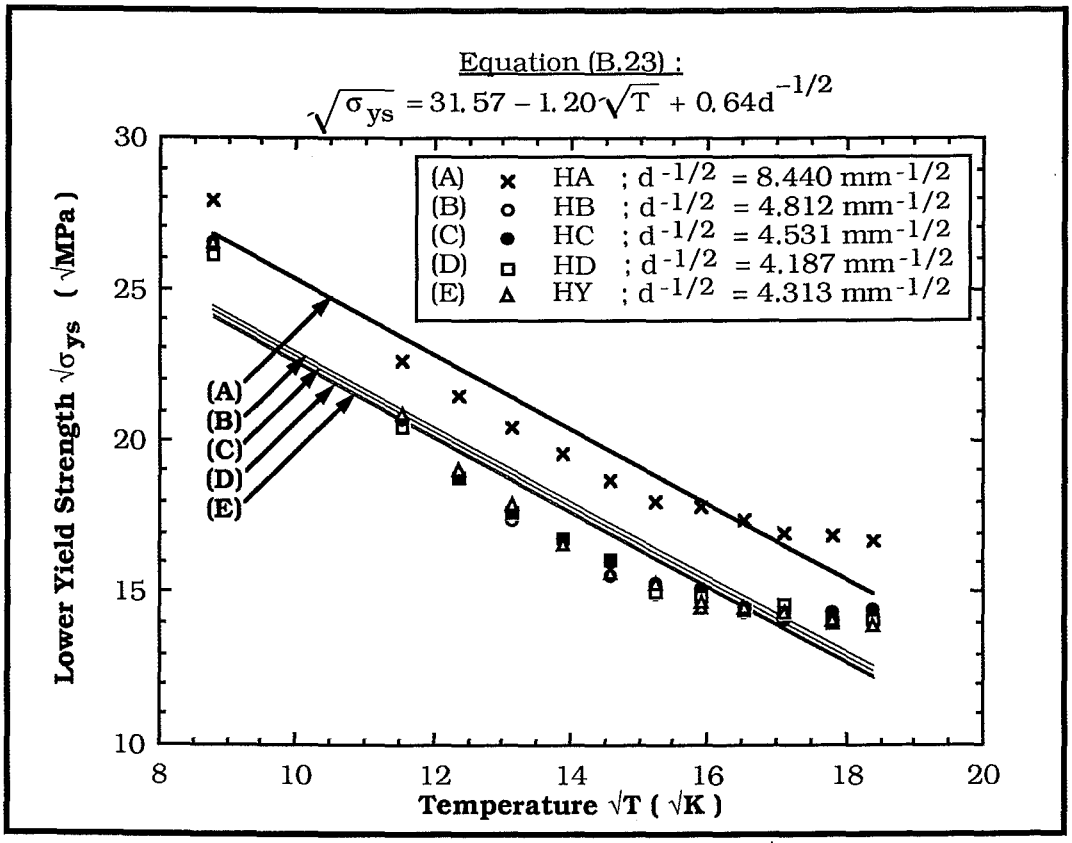

Figure B.23 : The square root of yield strength ($\sqrt{MPa}$) as a function of the square root of temperature ($\sqrt{K}$) for Steel H; showing predicted results for equation (B.23).

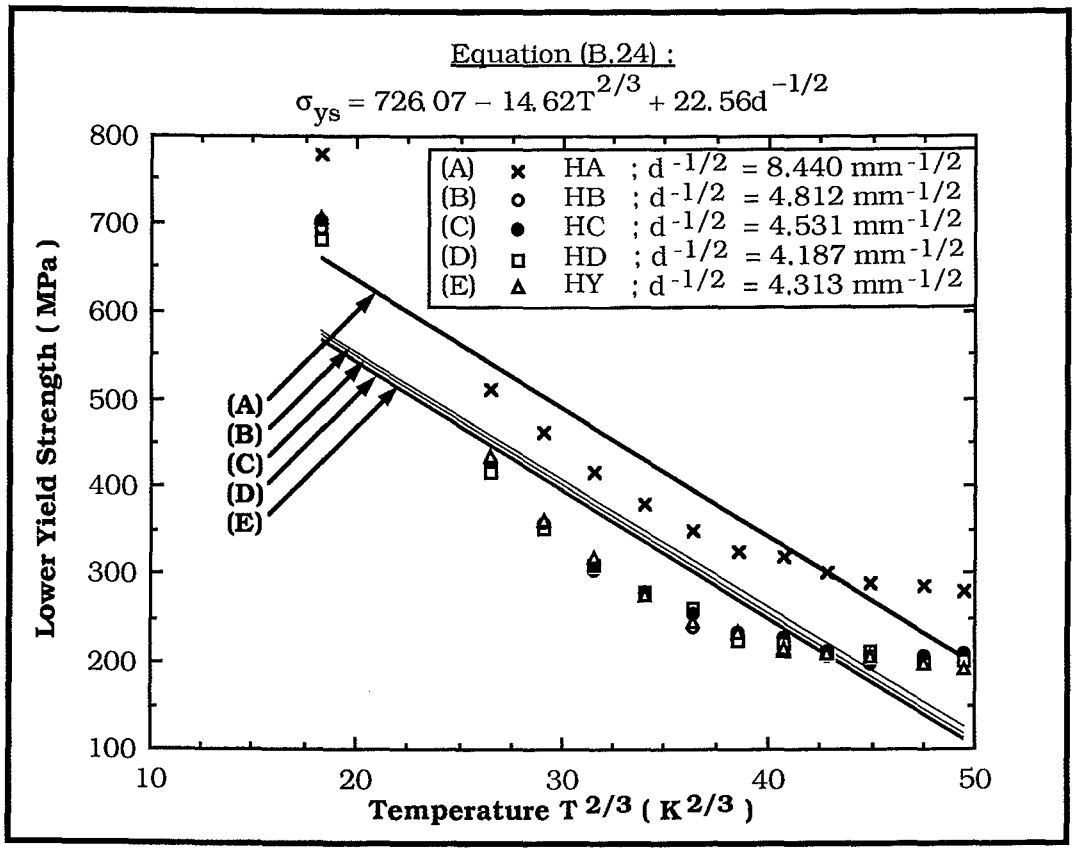

Figure B.24 : Lower yield strength (MPa) as a function of the 2/3 root of temperature ($K^{2/3}$) for Steel H; showing predicted results for equation (B.24).

APPENDIX C

Fatigue History of Fracture Toughness Specimens.

Table C.1
The Fatigue History of Fracture Toughness Specimens for Steel L.

Specimen I.D.	Maximum Load (kN)		$K_{f(max)}$	No. of Stress Cycles
	Initial	Final	MPa $m^{1/2}$	(x10^3)
LA1	3.0	2.0	8.82	633
LA2	4.3	3.2	14.29	308
LA3	4.3	3.1	13.20	327
LA4	4.3	3.1	13.01	325
LA5	4.3	3.2	14.07	220
LA6	4.3	3.1	13.45	418
LA7	4.1	3.1	13.51	336
LA8	4.4	3.1	13.24	230
LA9	4.2	3.1	12.97	328
LA10	4.3	3.1	12.85	258
LA11	4.1	3.1	12.88	325
LA12	4.4	3.1	13.83	234
LB1	4.3	3.1	13.67	393
LB2	4.2	3.1	13.45	241
LB3	4.2	3.6	15.25	315
LB4	4.2	3.1	13.18	502
LB5	4.2	3.2	13.61	361
LB6	3.9	3.1	12.80	280
LB7	4.0	3.1	13.24	427
LB8	4.4	3.1	13.33	335
LB9	4.4	3.1	13.04	282
LB10	4.3	3.1	13.18	287
LB11	4.2	2.5	11.03	503
LB12	4.4	3.1	13.50	320

Table C.1 continued.
The Fatigue History of Fracture Toughness Specimens for Steel L.

Specimen I.D.	Maximum Load (kN)		$K_{f(max)}$	No. of Stress Cycles
	Initial	Final	MPa $m^{1/2}$	($x10^3$)
LC1	4.4	3.1	13.37	454
LC2	4.1	3.1	13.16	378
LC3	4.3	3.1	13.28	365
LC4	3.1	3.1	14.20	450
LC5	4.4	3.1	13.79	352
LC6	4.4	3.1	13.81	332
LC7	4.4	3.1	13.70	266
LC8	4.4	3.1	13.55	355
LC9	4.4	3.1	13.69	372
LC10	4.5	3.1	14.07	320
LC11	4.5	3.1	13.15	298
LD1	4.5	3.1	13.54	317
LD2	4.5	3.1	13.73	321
LD3	4.5	3.1	14.22	383
LD4	4.5	3.1	13.95	337
LD5	4.5	3.1	13.33	391
LD6	4.3	3.1	13.59	297
LD7	4.4	3.1	13.92	425
LD8	4.4	3.1	13.11	391
LD9	4.4	3.1	13.49	391
LD10	4.4	3.1	13.49	361
LD11	4.4	3.1	13.10	358
LD12	4.4	3.1	13.51	285

Table C.2
The Fatigue History of Fracture Toughness Specimens for Steel H.

Specimen I.D.	Maximum Load (kN)		$K_{f(max)}$	No. of Stress Cycles
	Initial	Final	MPa $m^{1/2}$	($x10^3$)
HA1	4.4	3.1	13.03	248
HA2	4.4	3.1	13.34	243
HA3	4.4	3.1	14.16	202
HA4	3.7	2.7	11.43	487
HA5	3.9	2.7	11.56	430
HA7	3.9	2.7	11.75	441
HA8	3.9	2.7	11.70	412
HA9	3.9	2.7	11.50	474
HA10	3.9	2.7	11.55	390
HB1	3.9	2.7	11.28	343
HB2	3.9	3.3	15.92	342
HB3	3.9	2.7	11.21	331
HB4	3.9	2.7	11.52	381
HB5	3.9	2.7	11.59	321
HB7	3.9	2.7	11.52	281
HB8	3.9	2.7	11.48	335
HB9	3.9	2.7	11.89	328
HB10	3.9	2.7	11.79	316
HB11	3.9	2.7	11.67	393

Table C.2 continued.
The Fatigue History of Fracture Toughness Specimens for Steel H.

Specimen I.D.	Maximum Load (kN)		$K_{f(max)}$	No. of Stress Cycles
	Initial	Final	MPa $m^{1/2}$	($x10^3$)
HC1	3.9	2.7	11.28	489
HC2	3.9	2.7	11.59	330
HC3	3.8	2.7	11.68	440
HC4	3.9	2.7	11.64	363
HC5	3.9	2.7	11.53	431
HC6	3.9	2.7	11.47	306
HC7	3.9	2.7	11.71	402
HC8	3.9	2.7	11.89	450
HC9	3.9	2.7	11.70	434
HC10	3.9	2.7	12.12	406
HD1	3.9	2.7	11.54	405
HD2	3.9	2.7	11.31	412
HD3	3.9	2.7	11.46	379
HD4	2.7	2.7	11.55	378
HD5	2.7	2.7	11.70	383
HD6	3.9	2.7	11.55	374
HD7	3.9	2.7	11.31	395
HD8	3.9	2.7	11.70	376
HD9	3.9	2.7	11.50	389
HD10	3.8	2.9	11.77	405
HD11	3.9	2.7	11.23	371

Table C.3
The Fatigue History of Fracture Toughness Specimens for Steels LZ and HZ.

Specimen I.D.	Maximum Load (kN)		$K_{f(max)}$	No. of Stress Cycles
	Initial	Final	MPa $m^{1/2}$	($x10^3$)
LZ1	4.5	3.1	12.30	344
LZ2	4.9	3.4	12.77	1355
LZ3	4.9	3.8	14.59	1174
LZ4	5.3	3.7	15.18	669
LZ5	5.6	3.9	15.94	610
LZ6	5.6	3.9	15.89	722
LZ7	5.6	3.9	15.98	485
LZ8	5.6	3.9	15.58	465
LZ9	5.8	3.9	16.10	395
LZ10	5.8	3.9	16.38	395
LZ11	5.7	3.9	16.52	400
LZ12	5.8	3.9	15.52	385
HZ1	4.4	3.6	13.33	2163
HZ2	5.1	3.8	14.02	825
HZ3	5.8	3.9	15.53	280
HZ4	5.8	3.9	15.73	400
HZ5	5.5	3.8	14.85	455
HZ6	5.5	3.8	15.34	385
HZ7	5.5	3.8	15.68	485
HZ8	5.5	3.8	14.56	523
HZ9	5.5	3.8	15.76	430
HZ10	5.5	3.8	15.85	276
HZ11	5.5	3.8	15.43	430
HZ12	5.5	3.8	16.70	435

APPENDIX D

Results of Fracture Toughness Testing.

The tables presented in Appendix D contain the results of fracture toughness tests from -196°C to +65°C for Steels L, H, LZ and HZ. These include specimen identification, test temperature, yield strength, type of critical CTOD, critical CTOD load P_c, critical apparent fracture toughness load P_Q, critical CTOD found using equations (6.38) and (6.46), K_c found using equation (6.60) and K_Q found using equation (6.58) and whether or not this is a valid K_{IC} result. Instability (the critical CTOD) occurred at either spontaneous fracture (sf.) or at a maximum load (ml.).

Fracture appearance is given as either cleavage (cl.), microvoid coalescence (mc.) or for mixed mode of fractures as microvoid coalescence-cleavage (mc,cl) or as cleavage-shear lips (cl,sl.).

The apparent fracture toughness (K_c) at -196°C was calculated using the critical CTOD found using equation(6.46) and not equation (6.38).

Table D.1

Results of Fracture Toughness Tests for Steel L.

T °C	Spec. I.D.	σ_{ys} MPa	P_c kN	P_Q kN	δ_c (6.38) μm	δ_c (6.46) μm	K_c (6.60) MPa $m^{1/2}$	K_Q (6.58) MPa $m^{1/2}$	Valid K_{IC}	Inst. at	Fract App.
-196	LA9	765	6.27	6.27	11.9	2	18.7[1]	26.2	Yes	sf.	cl.
-140	LA2	531	6.72	6.72	11.5	3.6	37.3	29.7	Yes	sf.	cl.
-120	LA1	475	13.73	13.73	31	17	57.0	60.6	No	sf.	cl.
-100	LA6	432	16.47	15.90	56	26	74.2	69.0	No	sf.	cl.
-75	LA12	392	16.06	14.79	71.5	64	79.8	66.0	No	sf.	cl.
-67.5	LA7	383	16.10	15.35	71.5	53	78.9	66.9	No	sf.	cl.
-60	LA11	375	17.01	16.10	263	254	150	66.9	No	sf.	mc,cl
-50	LA3	365	17.10	15.25	358	358	172	64.9	No	sf.	mc,cl
-40	LA4	357	17.43	14.80	863	833	265	62.1	No	ml.	mc,cl
-20	LA5	345	16.60	13.25	936	784	271	58.3	No	ml.	mc.
0	LA8	337	16.85	14.30	843	755	254	61.1	No	ml.	mc.
+20	LA10	330	16.87	14.52	798	799	245	60.2	No	ml.	mc.
-196	LB8	731	5.69	5.69	12	2	18.2[1]	24.5	Yes	sf.	cl.
-140	LB1	475	6.14	6.14	11.5	3.3	35.2	27.1	Yes	sf.	cl.
-100	LB3	376	10.13	10.13	22	10.6	43.4	42.9	No	sf.	cl.
-67.5	LB4	327	13.98	13.26	64	33.5	69.0	56.4	No	sf.	cl.
-55	LB5	314	13.36	12.05	68	51	69.7	51.3	No	sf.	cl.
-47.5	LB2	307	13.65	12.55	80	63	74.7	54.5	No	ml.	cl,sl.
-40	LB12	302	12.86	12.00	129	127	94.1	52.3	No	sf.	cl.
-30	LB9	295	13.11	9.60	154	170	102	40.4	No	sf.	cl,sl.
-20	LB10	289	13.98	12.20	339	323	149	51.9	No	sf.	cl,sl.
-10	LB7	285	13.90	11.91	291	290	137	50.9	No	sf.	cl,sl.
0	LB6	281	16.35	12.20	1162	1085	273	50.4	No	ml.	mc,cl
+20	LB11	274	14.86	10.95	1219	1041	276	48.5	No	ml.	mc,cl

1. Value of K_c calculated using δ_c at -196°C for equation (6.46).

2. Instability either at spontaneous fracture (sf.) or maximum load (ml.)

3.Fracture Appearance either cleavage (cl.), microvoid coalescence (mc.) or shear lips (sl.), or a mixture of more than one type.

Table D.1 continued.
Results of Fracture Toughness Tests for Steel L.

T °C	Spec. I.D.	σ_{ys} MPa	P_c kN	P_Q kN	δ_c (6.38) μm	δ_c (6.46) μm	K_c (6.60) MPa $m^{1/2}$	K_Q (6.58) MPa $m^{1/2}$	Valid K_{IC}	Inst. at	Fract App.
-196	LC11	682	6.39	6.39	19	2.3	18.9[1]	27.1	Yes	sf.	cl.
-100	LC8	328	8.55	8.55	16.7	9.2	35.3	37.4	No	sf.	cl.
-67.5	LC9	279	11.74	11.12	64	41	63.7	49.1	No	sf.	cl.
-55	LC4	266	10.75	10.15	51	33	55.4	46.5	No	sf.	cl,sl.
-45	LC10	257	11.04	9.75	108	85	79.5	44.3	No	sf.	cl.
-30	LC3	247	10.83	10.45	65	50	60.4	44.8	No	sf.	cl,sl.
-25	LC1	244	13.40	9.85	250	254	118	42.5	No	sf.	cl,sl.
-10	LC2	237	13.53	10.10	336	330	135	42.9	No	sf.	cl,sl.
+10	LC5	229	12.78	9.05	354	338	136	40.3	No	sf.	cl,sl.
+25	LC7	224	13.61	9.62	521	480	163	42.5	No	ml.	mc,cl
+45	LC6	218	13.61	9.10	892	736	210	40.6	No	ml.	mc,cl
-196	LD9	667	5.81	5.81	13.1	2.1	17.8[1]	25.3	Yes	sf.	cl.
-120	LD8	356	7.30	7.30	7.7	5.8	25.0	30.9	No	sf.	cl.
-80	LD4	280	11.70	11.35	40	31.3	50.5	51.1	No	sf.	cl.
-60	LD2	255	11.12	9.92	78	62	67.3	43.9	No	sf.	cl.
-45	LD6	242	10.87	10.20	95	74	72.3	44.7	No	sf.	cl,sl.
-30	LD1	231	11.66	9.65	184	166	98.3	42.2	No	sf.	cl,sl.
-10	LD5	221	11.58	9.20	200	176	100	39.6	No	sf.	mc,cl
+10	LD11	214	13.36	8.70	402	374	140	36.8	No	sf.	cl,sl.
+25	LD12	209	13.94	9.42	1154	897	234	41.1	No	ml.	mc,cl
+45	LD10	203	12.61	8.95	476	428	148	38.9	No	ml.	mc,cl
+55	LD7	199	13.36	8.45	1338	956	246	37.9	No	ml.	mc,cl
+65	LD3	194	12.82	8.40	1063	798	217	38.5	No	ml.	mc,cl

1. Value of K_c calculated using δ_c at -196°C for equation (6.46).
2. Instability either at spontaneous fracture (sf.) or maximum load (ml.)
3.Fracture Appearance either cleavage (cl.), microvoid coalescence (mc.) or shear lips (sl.), or a mixture of more than one type.

Table D.2
Results of Fracture Toughness Tests for Steel H.

T °C	Spec. I.D.	σ_{ys} MPa	P_c kN	P_Q kN	δ_c (6.38) μm	δ_c (6.46) μm	K_c (6.60) MPa $m^{1/2}$	K_Q (6.58) MPa $m^{1/2}$	Valid K_{IC}	Inst. at	Fract App.
-196	HA3	783	5.56	5.56	17.2	2	18.9[1]	25.4	Yes	sf.	cl.
-120	HA1	455	7.80	7.80	17.9	5.2	43.0	32.8	Yes	sf.	cl.
-80	HA5	371	14.27	14.27	44	26	61.1	61.1	No	sf.	cl.
-55	HA 10	338	14.36	13.20	72	44.3	74.4	56.5	No	sf.	cl.
-40	HA2	325	13.61	12.59	68.8	46	71.3	54.2	No	ml.	cl.
-20	HA4	311	14.44	13.10	290	252	143	55.5	No	sf.	cl,sl.
0	HA9	303	10.50	9.40	201	195	118	40.0	No	ml.	cl,sl.
+5	HA8	302	16.18	12.85	1336	1080	303	55.7	No	ml.	mc,cl
+20	HA7	298	15.69	12.62	983	853	258	54.9	No	ml.	mc,cl
-196	HB10	727	5.64	5.64	18.4	2	18.2[1]	25.0	Yes	sf.	cl.
-80	HB11	315	8.17	8.17	15	9	32.8	35.3	No	sf.	cl.
-48	HB8	276	11.33	10.62	48	40.3	54.9	45.2	No	ml.	cl,sl.
-35	HB4	265	10.91	10.10	54	36.1	57.0	43.1	No	ml.	cl,sl.
-25	HB1	258	9.59	9.32	38.2	27.3	47.3	38.9	No	ml.	cl,sl.
-10	HB9	251	9.88	9.30	246	233	119	41.0	No	ml.	cl,sl.
+10	HB3	244	11.87	10.45	256	262	119	43.4	No	ml.	cl,sl.
+20	HB5	242	11.78	10.00	575	509	178	42.9	No	ml.	cl,sl.
+30	HB7	240	11.45	10.12	528	497	170	43.2	No	ml.	cl,sl.
+40	HB2	238	12.16	10.15	484	447	162	43.7	No	ml.	mc,cl

1. Value of K_c calculated using δ_c at -196°C for equation (6.46).
2. Instability either at spontaneous fracture (sf.) or maximum load (ml.)
3.Fracture Appearance either cleavage (cl.), microvoid coalescence (mc.) or shear lips (sl.), or a mixture of more than one type.

Table D.2 continued.
Results of Fracture Toughness Tests for Steel H.

T °C	Spec. I.D.	σ_{ys} MPa	P_c kN	P_Q kN	δ_c (6.38) μm	δ_c (6.46) μm	K_c (6.60) MPa $m^{1/2}$	K_Q (6.58) MPa $m^{1/2}$	Valid K_{IC}	Inst. at	Fract App.
-196	HC3	693	5.81	5.81	20.2	2	17.8[1]	25.1	Yes	sf.	cl.
-80	HC8	282	7.55	7.55	21	9	36.7	33.3	No	ml.	cl,sl.
-50	HC10	244	10.33	9.90	50	40	52.7	44.4	No	ml.	cl,sl.
-35	HC4	231	9.92	8.80	66	63.2	58.9	37.9	No	ml.	cl,sl.
-27.5	HC1	226	9.58	9.50	58	48	54.6	39.7	No	ml.	cl,sl.
-20	HC2	222	10.33	9.25	47	41	48.7	39.7	No	ml.	cl,sl.
-5	HC6	215	9.88	8.47	183	178	94.6	36.0	No	ml.	cl,sl.
+10	HC7	211	10.91	8.40	371	353	133	36.4	No	ml.	cl,sl.
+25	HC5	207	10.54	8.80	419	376	140	37.6	No	ml.	cl,sl.
+50	HC9	203	15.35	11.83	1497	1036	263	51.2	No	ml.	mc,cl
-196	HD5	686	5.64	5.64	13.4	2	17.7[1]	24.5	Yes	sf.	cl.
-80	HD7	274	9.46	9.46	28	13	41.8	39.6	No	sf.	cl.
-60	HD2	247	10.08	10.08	32.4	18.5	42.7	42.2	No	sf.	cl.
-40	HD1	227	10.21	10.00	46	38.3	48.7	42.7	No	ml.	cl.
-25	HD9	217	10.25	10.10	34	26	41.0	43.0	No	ml.	cl,sl.
-20	HD 11	214	10.29	9.30	47	43	38.7	47.8	No	ml.	cl,sl.
-10	HD 10	209	10.58	8.90	219	219	102	38.8	No	ml.	cl,sl.
+5	HD3	204	10.42	8.62	200	184	96.3	36.6	No	ml.	cl,sl.
+25	HD6	200	11.12	8.30	333	310	123	35.5	No	ml.	cl,sl.
+45	HD8	196	11.70	8.10	761	646	184	35.1	No	ml.	mc,cl
+65	HD4	192	12.03	8.30	806	697	188	35.5	No	ml.	mc,cl

1. Value of K_c calculated using δ_c at -196°C for equation (6.46).
2. Instability either at spontaneous fracture (sf.) or maximum load (ml.)
3. Fracture Appearance either cleavage (cl.), microvoid coalescence (mc.) or shear lips (sl.), or a mixture of more than one type.

Table D.3
Results of Fracture Toughness Tests for Steels LZ and HZ.

T °C	Spec. I.D.	σ_{ys} MPa	P_c kN	P_Q kN	δ_c (6.38) μm	δ_c (6.46) μm	K_c (6.60) MPa $m^{1/2}$	K_Q (6.58) MPa $m^{1/2}$	Valid K_{IC}	Inst. at	Fract App.
+20	LZ1	330	17.72	15.65	676	681	225	62.1	No	ml.	mc.
	LZ2		19.59	16.35	791	815	244	61.4	No	"	"
	LZ3		16.55	14.62	719	684	232	61.0	No	"	"
	LZ4		16.40	14.22	570	560	207	58.4	No	"	"
	LZ5		16.81	14.50	722	703	233	59.3	No	"	"
	LZ6		17.31	14.90	788	707	243	60.7	No	"	"
	LZ7		17.06	14.16	861	827	254	58.0	No	"	"
	LZ8		18.01	15.15	854	836	253	60.5	No	"	"
	LZ9		16.89	-	-	-	-	-	-	"	"
	LZ10		17.14	14.20	-	-	-	59.6	No	"	"
	LZ11		16.61	-	-	-	-	-	-	"	"
	LZ12		17.97	15.74	747	742	237	62.6	No	"	"
+20	HZ1	201	13.08	11.95	200	198	95.6	44.3	No	ml.	cl,sl.
	HZ2		12.67	11.51	253	243	108	42.5	No	"	"
	HZ3		11.35	10.20	280	251	113	40.6	No	"	"
	HZ4		11.68	9.60	408	368	137	38.7	No	"	"
	HZ5		12.34	11.01	-	-	-	43.0	No	"	"
	HZ6		12.01	-	-	-	-	-	-	"	"
	HZ7		11.26	10.0	345	313	126	41.3	No	"	"
	HZ8		12.51	10.59	244	239	106	40.6	No	"	"
	HZ9		11.55	10.32	389	356	133	42.8	No	"	"
	HZ10		11.59	10.20	319	293	121	42.5	No	"	"
	HZ11		11.88	10.60	304	293	118	43.1	No	"	"
	HZ12		10.73	9.35	346	297	126	41.1	No	"	"

1. Value of K_c calculated using δ_c at -196°C for equation (6.46).
2. Instability either at spontaneous fracture (sf.) or maximum load (ml.)
3. Fracture Appearance either cleavage (cl.), microvoid coalescence (mc.) or shear lips (sl.), or a mixture of more than one type.

APPENDIX E

Results of CTOD-Clip Gauge Displacement Correlation.

Table E.1
Results of Silicone-Rubber Replica Measurement of CTOD

CTOD (mm)	V_g (mm)	V_{CH} (mm)	Specimen I.D.
0.017	0.105	0.351	LZ9
0.022	0.250	0.571	LZ11
0.040	0.500	0.881	LZ10
0.065	0.750	1.073	LZ12
0.080	0.750	0.964	LD12
0.091	1.000	1.124	LC7
0.100	1.000	1.171	LZ3
0.160	1.250	1.310	LZ7
0.210	1.500	1.526	LZ1
0.213	1.500	1.512	LZ4
0.242	1.956	1.794	LB11
0.422	3.333	2.500	LZ5
0.737	5.088	3.500	LZ8
0.996	7.040	4.500	LZ6
0.021	0.250	0.548	HZ6
0.039	0.500	0.736	HD6
0.046	0.500	0.695	HZ5
0.091	0.750	0.857	HZ4
0.106	0.825	1.000	HZ7
0.128	1.000	1.000	HZ3
0.150	1.413	1.341	HC5
0.197	1.500	1.488	HB5(1)
0.200	1.500	1.325	HZ2
0.267	1.740	1.500	HZ11
0.399	2.717	2.000	HZ9
0.504	3.894	2.500	HZ12
0.750	4.706	3.000	HZ10
0.821	5.192	3.792	HA7
1.107	6.283	4.000	HZ8
1.283	7.799	5.050	HB5(2)

Table E.2
Comparison of Experimental, Predicted and ASTM CTOD from CTOD-V_g correlation.

V_g (mm)	V_p (mm)	ASTM δ_t Eqn. (6.46)	Exp'tal δ_t (mm)	Predicted δ_t (mm)	Grain size $d^{-1/2}$ ($mm^{-1/2}$)
0.105	0.0	0.003	0.017	0.013	9.939
0.250	0.0	0.015	0.022	0.030	9.939
0.500	0.075	0.034	0.040	0.061	9.939
0.750	0.250	0.063	0.065	0.093	9.939
0.750	0.500	0.088	0.080	0.095	4.218
1.000	0.475	0.092	0.100	0.125	9.939
1.000	0.700	0.117	0.091	0.128	4.941
1.250	0.760	0.134	0.160	0.157	9.939
1.500	1.000	0.175	0.210	0.189	9.939
1.500	1.025	0.171	0.213	0.189	9.939
1.956	1.655	0.250	0.242	0.255	7.262
3.333	2.825	0.441	0.422	0.442	9.939
5.088	4.500	0.695	0.737	0.705	9.939
7.040	6.475	0.970	0.996	1.023	9.939
0.250	0.0	0.015	0.021	0.031	4.187
0.500	0.238	0.051	0.039	0.063	4.187
0.500	0.050	0.028	0.046	0.063	4.187
0.750	0.360	0.072	0.091	0.095	4.187
0.825	0.450	0.085	0.106	0.105	4.187
1.000	0.550	0.100	0.128	0.129	4.187
1.413	1.100	0.173	0.150	0.186	4.531
1.500	1.425	0.242	0.200	0.200	4.187
1.500	1.175	0.179	0.197	0.195	5.995
1.740	1.410	0.227	0.267	0.230	4.187
2.717	2.350	0.357	0.399	0.389	4.187
3.894	3.505	0.494	0.504	0.596	4.187
4.706	4.395	0.638	0.750	0.751	4.187
5.192	4.810	0.665	0.821	0.738	8.440
6.283	6.010	0.912	1.107	1.084	4.187
7.799	7.495	1.029	1.283	1.292	5.995

Table E.3
Results of Stable Crack Extension for Steels L and H to ASTM Specification

CTOD (mm)	K_c (MPa $m^{1/2}$)	Δa_p (mm)	Specimen
0.065	69.8	0.121	LZ12
0.091	68.1	0.094	LC7[1]
0.100	86.6	0.189	LZ3
0.154	101.6	0.110	LB9
0.160	109.7	0.174	LZ7
0.210	125.5	0.307	LZ1
0.213	126.4	0.278	LZ4
0.242	122.8	0.191	LB11[2]
0.263	149.8	0.470	LA11
0.291	137.3	0.280	LB7[2]
0.358	172.4	0.520	LA3
0.422	178.0	0.847	LZ5
0.582	209.0	0.973	LA10
0.737	235.2	1.212	LZ8
0.996	273.4	1.842	LZ6[1]
0.091	64.5	0.204	HZ4[1]
0.106	69.6	0.275	HZ7[1]
0.128	76.5	0.238	HZ3[1]
0.150	84.0	0.281	HC5
0.197	104.1	0.141	HB5(1)[2]
0.200	95.6	0.636	HZ2
0.267	110.5	0.558	HZ11
0.290	143.2	0.310	HA4[2]
0.399	135.1	1.193	HZ9
0.504	151.8	1.850	HZ12[1]

1. These results included in analysis although outside exclusion lines.
2. These results excluded from CTOD-Δa_p analysis.